David Taylor Naval Ship
Research and Development Center
Bethesda, MD 20084-5000

DTIC FILE COPY

(1)

Proceedings of the Fourth International Cryocoolers Conference

Easton, MD
Sept. 25-26, 1986

AD-A211 760

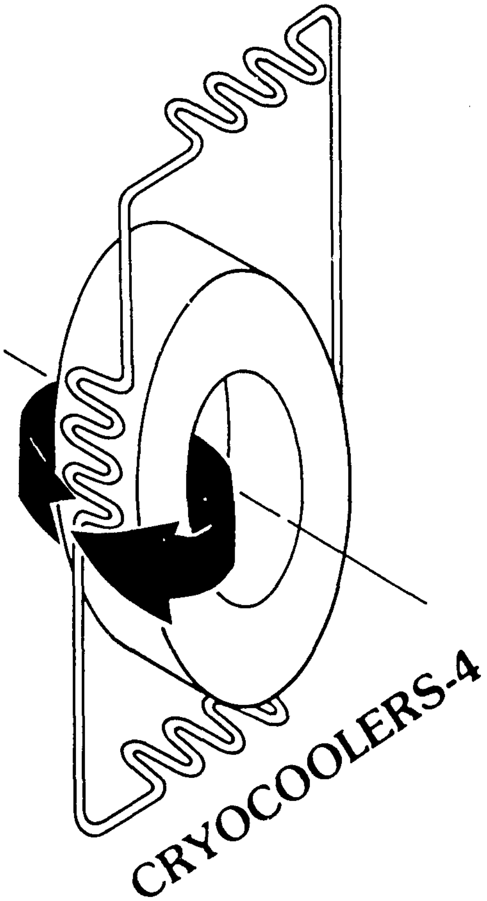

DTIC
ELECTE
AUG 17 1989
S B D

Edited by:
Geoffrey Green, George Patton, and Margaret Knox
David Taylor Naval Ship Research & Development Center
Annapolis, MD 21402-5067

Approved for public release; distribution is unlimited.

89 8 17 125

CONFERENCE ORGANIZING COMMITTEE

Chairman

Michael Superczynski
David Taylor Naval Ship R&D Center
Code 2712
Annapolis, MD 21402-5067
(301) 267-2149

Program Committee

Geoffrey Green, Co-Chairman
W. George Patton, Co-Chairman
David Taylor Naval Ship R&D Center
Code 2712
Annapolis, MD 21402-5067
(301) 267-3632

Peter Kerney
CTI Cryogenics

Ray Radebaugh
National Bureau of Standards

George Robinson
Massachusetts Institute of Technology

Advisory Board

John Barclay
LASL

Edgar Edelsack
Office of Naval Research

Yoshihiro Ishizaki
Consultant

Paul Lindquist
Wright-Patterson AFB

Ralph Longsworth
Air Products and Chemicals

Martin Nisenoff
Naval Research Laboratory

Samuel Russo
Hughes Aircraft Co.

Allan Sherman
NASA/Goddard

Joseph Smith
MIT

Walter Swift
Creare R&D, Inc.

Klaus Timmerhaus
University of Colorado

Graham Walker
General Pneumatics Corp.

Proceedings of the Fourth International Cryocooler Conference

Easton, MD
Sept. 25-26, 1986

Edited by
Geoffrey Green, George Patton, and Margaret Knox
David Taylor Naval Ship Research and Development Center
Annapolis, MD 21402-5067

Sponsored by
David Taylor Naval Ship Research and Development Center
Annapolis, MD 21402-5067

Approved for public release; distribution unlimited.

UNCLASSIFIED

SECURITY CLASSIFICATION OF THIS PAGE

REPORT DOCUMENTATION PAGE

1a. REPORT SECURITY CLASSIFICATION
UNCLASSIFIED

1b RESTRICTIVE MARKINGS

2a. SECURITY CLASSIFICATION AUTHORITY

2b. DECLASSIFICATION / DOWNGRADING SCHEDULE

3. DISTRIBUTION / AVAILABILITY OF REPORT
Approved for public release; distribution unlimited.

4. PERFORMING ORGANIZATION REPORT NUMBER(S)

5. MONITORING ORGANIZATION REPORT NUMBER(S)

6a. NAME OF PERFORMING ORGANIZATION
David Taylor Naval Ship Research & Development Center

6b. OFFICE SYMBOL (If applicable)
Code 2712

7a. NAME OF MONITORING ORGANIZATION

6c. ADDRESS (City, State, and ZIP Code)
Bethesda, MD 20084-5000

7b. ADDRESS (City, State, and ZIP Code)

8a. NAME OF FUNDING / SPONSORING ORGANIZATION

8b. OFFICE SYMBOL (If applicable)

9. PROCUREMENT INSTRUMENT IDENTIFICATION NUMBER

8c. ADDRESS (City, State, and ZIP Code)

10. SOURCE OF FUNDING NUMBERS

PROGRAM ELEMENT NO.	PROJECT NO.	TASK NO.	WORK UNIT ACCESSION NO.

11. TITLE (Include Security Classification)
PROCEEDINGS OF THE FOURTH INTERNATIONAL CRYOCOOLERS CONFERENCE

12. PERSONAL AUTHOR(S)
Green, Geoffrey; Patton, George; and Knox, Margaret, Editors

13a. TYPE OF REPORT
Proceedings

13b. TIME COVERED
FROM 860925 TO 860926

14. DATE OF REPORT (Year, Month, Day)
1987 October 30

15. PAGE COUNT
340

16. SUPPLEMENTARY NOTATION

17. COSATI CODES

FIELD	GROUP	SUB-GROUP

18. SUBJECT TERMS (Continue on reverse if necessary and identify by block number)
Crycoolers, Cryogenics, Cryopumps, Helium, Infrared Detectors, Refrigeration, Supercondctors, (AW)

19. ABSTRACT (Continue on reverse if necessary and identify by block number)

This document contains the proceedings of the Fourth Cryocooler Conference for electronic systems and sensors. Cryocoolers-4 was held September 25 and 26, 1986, in Easton, Maryland. About 170 people ~~attended, representing~~ 11 countries, 14 universities, 21 government laboratories, and 60 industrial companies. Thirty-one papers were presented, describing advancements and applications of cryocoolers in the temperature range below 80 K. Keywords: Compressors, Superconducting Coils, Reciprocating Magnetic Refrigerators, Magnetic Refrigerators, Helium Refrigerators, Liquid Helium Recondensing Refrigerators, Heat Exchangers, Stirling Cycle Refrigerators, Gas Compressors, Piston Compressors, Symposia

20. DISTRIBUTION / AVAILABILITY OF ABSTRACT
☑ UNCLASSIFIED/UNLIMITED ☑ SAME AS RPT. ☐ DTIC USERS

21. ABSTRACT SECURITY CLASSIFICATION
UNCLASSIFIED

22a. NAME OF RESPONSIBLE INDIVIDUAL
Michael J. Superczynski

22b. TELEPHONE (Include Area Code)
301-267-2149

22c. OFFICE SYMBOL
Code 2712

DD FORM 1473, 84 MAR

83 APR edition may be used until exhausted.
All other editions are obsolete

SECURITY CLASSIFICATION OF THIS PAGE

★U.S. Government Printing Office: 1985—639-012

0102-LF-014-6602

UNCLASSIFIED

CONTENTS

Page

ABSTRACT.. vii

INTRODUCTION AND SUMMARY.. vii

NOTE ON THE CRYCOOLER USER EXPERIENCE DATA COLLECTION CENTER...... ix

OPERATING CHARACTERISTICS OF A HYDROGEN SORPTION REFRIGERATOR PART 1: EXPERIMENT DESIGN AND RESULTS, by Kurt Karperos.......... 1

OPERATING CHARACTERISTICS OF A HYDROGEN SORPTION REFRIGERATOR PART II: A COMPARISON BETWEEN A SECOND ORDER ANALYSIS AND EMPIRICAL DATA, by Lawrence A. Wade.......... 17

HIGH RESPONSE HYDRIDE COMPRESSOR FOR REGENERATIVE CRYOCOOLER, by Y. Matsubara, M. Kaneko, J. Suzuki, and K. Hirosawa.......... 31

DEVELOPMENT OF AN 80-120 K CHARCOAL-NITROGEN ADSORPTION CRYOCOOLER, by S. Bard.......... 43

A SUPERCONDUCTING PULSE COIL WITH LOW AC LOSSES FOR USE IN MAGNETIC REFRIGERATORS, by P. Seyfert and G. Claudet.......... 57

RECIPROCATING MAGNETIC REFRIGERATOR, by G. Patton, G. Green, J. Stevens, and J. Humphrey.......... 65

MAGNETIC REFRIGERATION BASED ON MAGNETICALLY ACTIVE REGENERATION, by C.P. Taussig, G.R. Gallagher, J.L. Smith, Jr., and Y. Iwasa.......... 79

DESIGN LIMITATIONS ON MAGNETIC REFRIGERATORS IMPOSED BY MAGNETIC FORCES, by J.A. Barclay, M. Shnaider, C.R. Cross, F.C. Prenger, W.F. Stewart, and C.B. Zimm.......... 89

4.2 K REFRIGERATOR FOR SQUID MAGNETOMETER, by Takashi Ishige, Hidekazu Baba, Yasuo Kuraoka, Iwao Nakano, Gentaro Kai, and Shinichi Ishii.......... 99

AN EXPERIMENTAL STUDY ON A LOW-POWER PLASTIC CRYOCOOLER FOR HIGH-T_c SQUID, by Z.X. Huang, G.B. Chen, J.Y. Zhen, F.G. Zhang, S.M. Li, C.R. Jiang, and B.L. Wang.......... 107

REFRIGERATION EFFICIENCY OF PULSE-TUBE REFRIGERATORS, by Ray Radebaugh and Steffen Herrmann.......... 119

LONG-LIFETIME, CLOSED-CYCLE CRYOCOOLER FOR SPACE, by Javier A. Valenzuela, Herbert Sixsmith and Walter L. Swift.......... 135

REFRIGERATION AND HEAT PUMP SYSTEMS BASED ON He II VORTEX CONTROL, by T.H.K. Frederking, H.H.D. Tran, and R.M. Carandang.......... 147

DTIC COPY INSPECTED 5

Dist Special

A-1

Page

SMALL SIZE HELIUM REFRIGERATOR WITH MICRO TURBO-EXPANDERS, by S. Harada, T. Matsuda, S. Saito, and K. Ihara.............................. 159

LOW CAPACITY HELIUM LIQUEFIER: A ROSS-STIRLING ENGINE WITH ZIMMERMAN DISPLACER AND TWO STAGE COMPRESSOR WITH JOULE-THOMSON EXPANSION, by Graham Walker.. 169

PERFORMANCE OF VM COOLER COUPLED WITH TWO STAGE G-M COOLER, by M. Kaneko and Y. Matsubara.. 177

CLOSED-CYCLE LIQUID HELIUM DIP CRYOCOOLER, by Calvin Winter and Suso Gygax.. 189

RECONDENSING REFRIGERATOR FOR SUPERCONDUCTING NMR-CT, by T. Koizumi, K. Kuroki, Y. Tomita, Y. Kanazawa, and M. Suzuki.......................... 199

THE DESIGN, FABRICATION, AND TESTING OF A NOVEL TITANIUM-ALUMINUM HEAT EXCHANGER, by R.C. Sweet and R.L. Bronnes.................. 209

TEMPERATURE SENSITIVE VARIABLE AREA FLOW REGULATOR FOR JOULE-THOMSON NOZZLES, by K. Hedegard, G. Walker, and S. Zylstra................ 217

SYSTEM DESIGN REQUIREMENTS FOR INFRA-RED DETECTOR CRYOCOOLERS, by D. Marsden... 229

PARAMETRIC TESTING OF A LONG LIFE LINEARLY DRIVEN STIRLING CRYOGENIC REFRIGERATOR AFTER 20,000 HOURS OF OPERATION, by F.R. Stolfi.............. 241

DEVELOPMENTS OF A 4-5 K COOLING STIRLING CYCLE REFRIGERATOR, by H. Nakashima, K. Ishibashi, and Y. Ishizaki............................ 263

SPLIT-STIRLING CYCLE CRYOCOOLER OFF-DESIGN PERFORMANCE TESTS, by Forrest R. Cleveland.. 273

DEVELOPMENT OF THE STIRLING CYCLE COOLERS FOR THE IMPROVED STRATOSPHERIC AND MESOSPHERIC SOUNDER, by S.T. Werrett and G.D. Peskett.. 289

FIRST RESULTS ON A PROTOTYPE TWO STAGE MINIATURE STIRLING CYCLE COOLER FOR SPACEFLIGHT APPLICATIONS, by T.W. Bradshaw.................... 303

A DYNAMOMETER FOR TESTING LINEAR MOTORS FOR MINIATURE CRYCOOLERS, by Wilfred J. Gully and Robert L. Berry......................... 311

MINIATURE MULTISTAGE HIGH-PRESSURE GAS COMPRESSOR FOR LINDE-HAMPSON CRYOCOOLERS, by E. Atkins, G. Walker, and S. Zylstra............. 325

PROGRESS IN DEVELOPMENT OF OIL-FREE RESONANT-PISTON COMPRESSORS FOR CRYOGENIC APPLICATIONS, by Peter W. Curwen............................... 337

ABSTRACT

This document contains the proceedings of the Fourth Cryocooler Conference for electronic systems and sensors. Cryocoolers-4 was held September 25 and 26, 1986, in Easton, Maryland. About 170 people attended, representing 11 countries, 14 universities, 21 government laboratories, and 60 industrial companies. Thirty-one papers were presented, describing advancements and applications of cryocoolers in the temperature range below 80 K.

Key words: cryocoolers, cryogenics, cryopumps, helium, infrared detectors, refrigeration, superconductors

INTRODUCTION AND SUMMARY

This document contains the proceedings of the Fourth International Cryocooler Conference, which was hosted by the David Taylor Naval Ship Research and Development Center and held in Easton, Maryland, on September 25-26, 1986.

The first of the cryocooler conferences was held in 1980 at the National Bureau of Standards in Boulder, Colorado. Initially, this conference was designed to get the scientific and engineering community together to discuss the lastest development and advances in refrigeration for cryogenic sensors and electronic systems at temperatures below 20 K. The temperature range was increased to 80 K for the Second and Third Cryocooler Conferences, held at NASA Goddard Space Flight Center, Greenbelt, Maryland (1982) and National Bureau of Standards, Boulder, Colorado (1984).

The scope of the Fourth International Cryocooler Conference covered the scientific and technological development of small closed-cycle refrigerators and components applicable in the temperatures below 80 K. Some 170 participants from 11 countries, 14 universities, 21 foreign and domestic government laboratories, and 60 private industrial companies attended.

Thirty-one technical papers were presented, decribing advancements in many areas of cryocooler technology. These presentations of cryogenic systems included discussions of magnetic refrigerators, absorption coolers, space coolers, squid coolers, pulse tube refrigerators, and hybrid systems. Two special attractions on applications of these cryogenic systems were presented. The first was a videotaped performance of an infrared detection system installed on an A-6 fighter plane. This system had taken pictures of the Annapolis, Maryland area. The second was a film describing the development of the Japanese magnetically levitated high speed train.

The development and application of a small, compact, reliable and efficient cryocooler is essential if cryogenics is to become state-of-the-art technology. To this end, we feel that the papers presented at Cryocoolers-4 and included in this proceedings show significant progress in cryocooler technology.

The Editors

NOTE ON THE CRYOCOOLER USER EXPERIENCE DATA COLLECTION CENTER

UNIVERSITY OF CALGARY
ALBERTA, CANADA

A Center for compilation and collation of cryocooler user experience has been established in the Department of Mechanical Engineering, University of Calgary, Alberta, Canada by Professor Graham Walker.

Cryocooler users are invited to contribute their experience to the Center - both good news and bad news is welcome. To facilitate compilation it would be helpful if the contributions could be prepared in the following format:

Cryocooler Type: ______________________ Model No.: ______________

Manufacturer: Name and address/contact person or service representative.

Application: What is the cryocooler used for (no more than 1/2 page typed).

Experience:
Annual operating hours.
Duty cycle (period of continuous running).
Maintenance requirements: 1) scheduled
2) unscheduled
Failure modes - type and reasons for system being non-operational.
Operating Time/Elapsed Time between failure (defined as system not operational).
Any other relevant information.

Any contributions submitted will be strictly confidential and need not be identified when submitted. It would, however, be useful to have the contributor's name and telephone number for further information if required.

The data collected will be summarized and published annually in the technical press or by direct mail from the Center. Contributors will automatically be sent a copy of the annual report following their submission. Copies of the annual report will be available to anyone else for a small postage/handling fee.

Contributions should be submitted to:

Dr. Graham Walker
Dept. of Mechanical Engineering
The University of Calgary
Calgary, Alberta, Canada T2N 1N4
(403)-220-5772

OPERATING CHARACTERISTICS OF A HYDROGEN SORPTION REFRIGERATOR
PART 1: EXPERIMENT DESIGN AND RESULTS

Kurt Karperos

Aerojet ElectroSystems Co.
Azusa, CA 91702

A description of Joule-Thomson refrigerator operating characteristics with hydrogen $LaNi_5$ absorption compressors is presented. A continuous supply of high pressure gas is provided by the phased thermal cycling of four high heat transfer hydride compressors. Since the system operates with no moving parts, other than self actuating check valves, the system offers a potentially highly reliable alternative to mechanical refrigerators for long life space missions. The cooler does not require electrical power and can operate using a low grade energy source, e.g. waste heat. The data presented include pressure profiles for the compressors which indicate that sufficient heat transfer is achieved and that an excessive heat transfer rate leads to nonoptimum performance. Pressure and mass flow measurements show large fluctuations produced by changing sorbent sorbate equilibrium conditions and by large changes in compressor heat fluxes.

Key words: Absorption; adsorption; cryogenics; hydride; hydrogen; Joule-Thomson; refrigerator; sorption.

1. Introduction

Refrigeration through nonmechanical sorption compression of the refrigerant gasses has been demonstrated as a viable approach [1,2]* for providing reliable, long life, vibration free cryogenic cooling for advanced spaceborne surveillance systems. Mission refrigeration requirements will include temperatures from 6 to 125 Kelvin with cooling capacities of a few watts to tens of watts and 5 to 10 years of near 100% duty cycle, maintainence free service. Because sorption compressors have no moving parts they have the potential for highly reliable, long life operation. The refrigerators need no electrical power to operate except to drive very simple, low power control electronics. Compressors can be designed to run on direct solar energy or waste heat such as from a radioisotope power system.

---

*Numbers in brackets refer to literature references at the end of this paper.

As stated, the practical feasibility of sorption refrigerators has been proved. However to develop flight systems, cooler operating data beyond that which are provided by laboratory demonstration models are required. To fill this need, Aerojet undertook a program to develop and study the performance of a flight-like hydrogen $LaNi_5$ absorption refrigerator. This paper discusses the design philosophy and the operating characteristics of the refrigerator. Of particular interest are transient data that indicate dynamic features which must be considered in future analysis as well as compressor and system design.

2. Sorption Refrigerator Concept

The sorption process, in which gasses are physically adsorbed onto the sorbent surface or react with the sorbent and are absorbed into vacant interstitital sites, is an exothermic reaction. That is, heat is liberated when the gas is sorbed and taken up when the gas is desorbed. If the sorption reaction is reversible, as with charcoals, zeolites, and metallic hydrides, a refrigerant gas can be pumped by the cyclic heating and cooling of a suitable sorbent. Figure 1 shows a schematic of the Aerojet J-T refrigerator with hydrogen sorption compressors. In this system one of the compressors is heated to release high pressure gas. The gas flows through the precoolers and the recuperative heat exchangers to the J-T valve where it is expanded and cooled, and possibly partially liquefied. After absorbing the heat load the gas flows back via the heat exchangers to a second compressor which is cooled to sorb the low pressure gas. The direction of the gas flow from and to a compressor is controlled by self actuating check valves. The outlet valve opens and gas flows out of a compressor when the compressor is heated to the point where its pressure is slightly higher than the system high side pressure. Similarly, the inlet valve opens when the compressor is cooled so that its pressure drops below the system low side pressure. The only moving parts in the refrigerator are the long life check valves which operate at the warm end of the cooler. The compressors are merely pressure vessels equipped with a means to heat and cool them. As indicated in figure 2 a compression cycle is composed of four phases: heating, desorption, cooling, and absorption. A fully charged compressor is pressurized by heating it to the high equilibrium temperature at which point it desorbs into the high pressure side of the system. When depleted of hydrogen the compressor is cooled and it absorbs hydrogen from the low pressure side prior to repeating the cycle. To provide a continuous hydrogen flow the refrigerator includes four identical compressor units operated 90° out of phase.

As with other sorption refrigerator analyses [3,4], a simple second order model was used with heat exchanger ineffectiveness the only refrigeration loss. This assumption yields a simple relationship for the required refrigerant mass flow rate, m, for a given cooling load, $\dot{q}_L$

$$\dot{m} = q_L/\Delta h$$

where Δh is the enthalpy difference between the cool and warm streams at the warm end of the low temperature heat exchanger. The enthalpies were obtained, as a function of temperature and pressure, by assuming the compressors delivered a constant discharge and suction pressure, and the system pressure drop was zero so that the pressures at the heat exchanger were the sorption and desorption pressures. The warm stream inlet temperature was taken as the precooler temperature. The cold stream temperature was then calculated using the heat exchanger effectivity.

During the desorption phase, at pressure P_H and temperature T_H, the heat of reaction, required to liberate the hydrogen, is added to the compressor. The heat of desorption, $\dot{q}_d$, is given by

$$\dot{q}_d = \dot{m}H$$

where H is the heat of reaction per gram of hydrogen, 15480 J/g for $LaNi_5$ [5]. Prior to desorbing, the compressor is pressurized to the high pressure, P_H, by heating it from the low absorbing temperature, T_L, to the high equilibrium temperature, T_H. Writing the total thermal capacitance of the compressor housing and hydride bed as ΣMC, the sensible heat required is

$$\dot{q}_h = \Sigma MC(T_H - T_L)/\Delta t$$

where Δt is the phase time. The amount of energy required to liberate sufficient hydrogen to pressurize the compressor was assumed small compared to the sensible heat and was ignored.

With four identical compressor units operated 90° out of phase with equal span time, the approximate input power at any given time, $\dot{q}_i$, is then equal to the sum of the desorbing and heating powers

$$\dot{q}_i = \dot{q}_h + \dot{q}_d$$

The amount of hydride, M, required to supply the specified mass flow rate was obtained from the relation

$$M = \dot{m}\Delta t/\Delta C$$

where ΔC is the change in hydrogen mass concentration during desorption. The change in mass concentration is related to the change in atomic concentration, ΔX, by the ratio of the total number of hydrogen atoms which can be absorbed into the interstitial sites of the metal molecule, 6.12 for $LaNi_5$, to the atomic weight of the metal. A value of 0.7 was chosen for ΔX as it corresponds to the near full extent of the isotherm plateau.

The assumed idealized pressure curve for one compressor unit is shown in figure 3. The system design variables are given in table 1.

Table 1 Refrigerator Design Variables

Cooling load q_L = 2.5 watts

4 Compressors phased at 90 seconds (Δt = 90 sec)

Total cycle time: 360 sec (4 x 90)

Pressure ratio P_H/P_L: 4.05 mPa/.10 mPa

Operating temperatures: T_H = 130°C, T_L = 0°C

Hydrogen mass flow rate: $\dot{m}$ = 0.03 g/sec

Total heat of absorption: 41,000 Joules

Amount of hydride: 270 gm per compressor

Absorbing capacity: 3.86 gm H_2 (43.3 liters STP per compressor)

Amount of H_2 cycled: 2.65 gm (ΔX = 0.7)

3. Mechanical Design

Two compressor designs were developed to meet the system requirements. Schematics of the two designs are shown in figure 4. The hydride bed in the first concept is a narrow annular gap, 4.128 cm I.D. by 0.318 cm wide. The annular gap allows a large heat transfer area and avoids the singularity along the cylinder center line. Heating and cooling is provided by a surrounding fluid jacket with a passage on both the inside and outside diameters of the annulus. The thermal conductance of the hydride bed is enhanced by a 20% density copper foam matrix into which crushed hydride, 25 mesh, is sifted. The hydride, which upon exposure to hydrogen breaks down to a micron sized powder, is retained in the annulus by a 1 micron filter. The annulus depth is 25.40 cm. The second concept also uses a 0.318 cm wide copper foam filled annular sorbent bed; however, the inside diameter wall is a 1 micron cylindrical filter. This permits the hydrogen to pass only through the narrow width of the bed rather than its entire length as in the first concept, thereby reducing the flow resistance and resulting pressure drop across the sorbent bed. This configuration allows only a fluid passage along the outside diameter and as a consequence in order to achieve the same heat transfer area the compressor is twice as long as the first. The compressors are made from 316 stainless steel and are of all welded construction. The first and second concepts weigh approximately 2.8 and 4.1 kg respectively when filled with hydride.

Prototypes of the two compressor concepts were tested to determine their performance. No measurable difference in performance was found and the first, more compact, concept was selected for refrigerator testing. Figure 5 shows a photograph of a hydride compressor. The six mechanical fittings on the compressor flange are thermocouple feed throughs used only for test. The compressor was designed with a removable cover sealed with a metal O-ring and a metal backed teflon C-ring. After preliminary compressor performance tests it was determined that the seal leak rate was unacceptable and the compressor was welded shut for future tests.

The two recuperative heat exchangers are of a simple, tube-in-tube counter flow design. They are made from stainless steel tubing with a 0.475 cm O.D. by 0.041 cm wall inner tube slipped inside a 0.635 cm O.D. by 0.051 cm wall outer tube. The warm and cold heat exchangers are 12.2 m and 6.1 m long respectively.

A schematic of the J-T valve, based on a design by JPL, is shown in figure 6. The variable orifice size is controlled by the spring force on the ball. As the pressures up and down stream from the valve change the spring flexes to balance the forces on the ball. The resulting change in orifice size adjusts the mass flow rate through the valve. By reducing excursions in the pressure difference across the J-T valve, the valve provides less fluctuation in temperature at the cost of a changing refrigeration capacity. It was anticipated as has been reported [1], that the valve would be less susceptible to plugging by opening up to relieve pressure build up caused by the orifice fouling with frozen contaminant. However, this was not found to be the case. The clogging will be discussed in more detail below.

4. Test Setup

The compressor thermal control system was designed and assembled to model the behavior of a flight system, i.e. a closed loop system with a low grade heat source and radiator cooling, but with the components being commercially available hardware. A schematic of the system is shown in figure 7. It consists of high and low temperature fluid circuits which share a common path through the compressor. The compressors were thermally cycled using electrically operated ball valves to alternately circulate hot and cold fluid, Dowtherm J, through the compressor jackets (fig. 7). Fluid circulation was provided by two 3/4 hp centrifugal pumps. Liquid flow rates, approximately 30 liters/min, were monitored with rotameter type flowmeters and were regulated with gate valves. Expansion tanks were used to dampen hydraulic surges and to accommodate fluid expansion with temperature. A 6 kw process heater was used to simulate a flight heat source, e.g. a solar collector, radioactive isotope, or other heat source. A 12,000 Btu fluid chiller at -20°C simulated space radiator heat rejection.

The sorption refrigerator and test equipment were controlled by a computer driven data acquisition and control system. Interactive software provided operation in both manual and automatic modes. Hardware and software failsafes were incorporated to ensure graceful shutdown in the event of system failure.

The manual operation mode allowed complete system control by the test engineer except for data acquisition, which proceeded automatically after the data acquisition rate, typically every 15 seconds, and data storage medium were selected. The operation of the pumps, heater, chiller, and the valves, and thereby the temperature of the compressors, was controlled by keys at the computer terminal. The manual mode was used for compressor outgassing and activation, preliminary system checkout and diagnostics.

In the automatic mode the cyclic operation of the compressors was controlled by simple software interrupts from the computer's internal clock. The engineer selected the compressor cycle time and the computer generated the necessary commands to switch the valves and operate the heater, chiller, and circulation pumps. Data acquisition and storage proceeded as in the manual mode.

The pressure of each compressor and the high and low pressures of the refrigerator were measured. The hydrogen flow rate was measured with a mass flowmeter down stream from the compressor outlet check valves. Thermocouples were located in the gas streams at the inlets and outlets of each heat exchanger and precooler and on the liquid trap. Each of the hydrogen compressors was instrumented with thermocouples in the hydride bed. These were used during compressor performance tests, but were damaged when the compressor covers were welded and therefore not used during subsequent tests. Immersion thermocouples were located in the heat transfer liquid at the entrance and exit of the fluid heater and chiller and at each compressor fluid jacket.

5. Test Results

Operation of the refrigerator to 26.6 K and 0.21 watts (a discussion of refrigeration capacity and losses is found in Part 2, [6]) has demonstrated that system operation is very dynamic. Compressor suction and discharge pressures vary continuously during the cycle. The pressure profile for each compressor is extremely repeatable with small differences between compressors attributable to variations in check valve cracking and resealing pressures. The continuous variation in mass flow rate is also very repeatable. The changing pressure difference across the J-T valve and flow rate, and therefore refrigeration capacity working against a constant heat load, result in a fluctuating coldtip temperature.

The high and low side pressures at the J-T valve are formed by the upper and lower envelope of the four compressor pressures. Figure 8 shows the pressure envelope. The hydrogen mass flow rate associated with the pressures in figure 8 is shown in figure 9. As expected, changes in flow rate correspond to fluctuations in system pressure. Gross differences in the amplitude of flow rate peaks are attributable to the data sampling rate. Coldtip temperature stability is shown in figure 10. The temperature fluctuations are caused by changes in high and low side pressure and mass flow rate and are therefore in phase with the curves of figure 8 and 9. Because the frequency of fluctuations is very low it can be easily dampened and thermophonics would not be a problem.

Since the fundamental driver of sorption refrigerator operation is compressor pressure, the transient behavior of the system can be understood by examining the pressure profile for one compressor unit. Figure 11 shows the transient pressure for a compressor unit and also demonstrates the repeatability obtained.

At point A, the compressor is fully saturated with hydrogen and hot fluid is directed to it. Because of the initially large temperature difference between the fluid and the compressor, approximately 130°C, the heat fluxes are large and the compressor heats rapidly. Heating is nearly complete in 15 seconds. Because of the finite slope of the isotherm, and since the compressor has a full hydrogen charge, it is at a higher pressure than the other hot compressor, 90° ahead, which is partially desorbed. Therefore its outlet valve opens and it begins to deliver hydrogen, Point B. The sudden release of hydrogen causes hydride self cooling and the compressor pressure drops to Point C. With more heat input the compressor temperature recovers and its pressure rises to Point D. The fluid loop is, as it would be in a flight cooler utilizing low grade heat, a closed loop with a finite heating rate. The rapid initial heating of the compressor and release of hydrogen, caused by the initially large temperature difference between the heating fluid and the compressor, results in a drop in fluid temperature, the magnitude of which is a function of the fluid system heating rate and thermal capacity. This drop in fluid temperature results in a compressor pressure drop to Point E. From here the compressor continues to desorb to Point F where it is nearly depleted of hydrogen and its pressure drops quickly. The compressors cycle at Point G (the compressor shown remains hot, the compressors 90° ahead and behind change temperature). The compressor outlet check valve closes and with no hydrogen flow there is a slight decrease in the rate of pressure drop. However, as before at Point C, after fluid switching there is a decrease in fluid temperature producing the pressure drop to Point H. With the check valve closed recovery of the fluid temperature produces an increase in pressure.

At Point I cold fluid is directed to the compressor causing its pressure to drop to Point J. The effect of the finite slope of the isotherm plateau is repeated here. Although at the same temperature the compressor is at a lower pressure, being fully depleted, than the compressor 90° ahead. Therefore its inlet check valve opens and hydrogen is taken up. Because the absorption reaction kinetics are slower than the desorption kinetics, compressor heat transfer is great enough to overcome any self heating and there is no associated sharp jump in pressure. Similar to the heating loop there is a sharp change in fluid temperature when the fluid is switched. The resulting increase in pressure is not as dramatic since the compressor contains very little hydrogen. The increasing plateau pressure causes the pressure to rise to Point K where the fluid is again switched to the compressors 90° ahead and behind. The inlet check valve closes and the pressure momentarily drops, Point L, but rises again when the fluid warms, Point M. Gradual cooling of the fluid produces a drop in pressure until the compressor is again heated.

A major threat to sorption refrigerator reliability is clogging of the J-T valve by frozen contaminants. The operation of the self adjusting J-T valve was investigated to determine its ability to compensate for clogging. Figures 12 and 13 show the pressures up and down stream of the valve and mass flow rate through the valve while it was partially plugged. The valve was calibrated to provide a nominal flow rate of 0.015 g/s with a pressure drop across the valve of 3.95 MPa. In an attempt to clear the valve the temperature of the high pressure compressor and therefore its pressure was increased to provide a pressure drop of approximately 4.8 MPa. As can be seen in figure 13 there was no effect on the flow rate as it remained near 0.0025 g/s.

The valve performance is a direct result of sorption compressor behavior, in particular, its tendency to seek equilibrium. A hydride compressor heated to a given temperature will release hydrogen until the volume into which it is desorbing is at the equilibrium pressure or until the hydride is fully depleted. If contaminant freezes partially obstructing the orifice the upstream pressure will rise (down stream pressure will fall) but only to the equilibrium pressure defined by the compressor temperature. At that point the compressor will only desorb enough hydrogen to keep pressure constant. In the extreme case of complete valve plugging once the equilibrium pressure is reached no more hydrogen would be desorbed. The hydride compressors behave like pressure regulators. Any sorption compressor, be it absorption or adsorption, will have, by design, an upper pressure limit. When the J-T valve fouls the pressure can increase to that limit, but not above, at which point the self adjusting feature of the valve no longer works. The reliability of the design when coupled with a mechanical compressor has been demonstrated by its accumulated life on the JPL Deep Space Network Maser Receiver. It is the pressure regulating characteristic of sorption compressors which negates the valve self adjusting feature.

6. Conclusions

While a sorption refrigerator can be thought of as a thermal analog to mechanical refrigerators, the operation of sorption compressors is inherently different from mechanical compressor operation. As opposed to a constant volume mechanical compressor a sorption compressor is a constant pressure device. During both absorption and desorption the compressor seeks to regulate the gas pressure to its equilibrium pressure. Modeling and design of compressors and refrigerators must reflect this fundamental difference.

Past analysis of sorption refrigerators has assumed steady state operation. Detailed examination of refrigerator operation has demonstrated, as is expected in any real system, that operation is transient, with fluctuations in expansion pressures, mass flow rate, and coldtip temperature. Design improvements can be made to minimize fluctuations, including controlled heating and cooling of the compressors, surge tanks to accommodate mass flow transients, and high capacity heating and cooling systems; however, operation will remain dynamic. The fluctuations are very repeatable and are explained by known changes in compressor heat flux and sorbent sorbate equilibrium conditions. Such fluctuations are predicable, can be modeled, and accommodated by design.

7. References

[1] Jone, J.A., $LaNi_5$ Hydride Cryogenic Refrigerator Test Results, Second Biennial Conference on Refrigeration for Cryogenic Sensors and Electronic Systems, GSFC, Greenbelt, Md, Dec. 7-8, 1982.

[2] Bard, S., Development of an 80-120K Charcoal/Nitrogen Adsorption Cryocooler, Proceedings of the Fourth International Cryocooler Conference, Easton, Md, Sept. 25-26, 1986.

[3] Barhydt, K.H., General Computer Model for Predicting the Performance of Gas Sorption Refrigerators Vol. 1 and 2 NASA Jet Propulsion Laboratory, JPL D-2600, 29 Aug. 1985

[4] Jones, J.A. and Golben, P.M., Life Test Results of Hydride Compressors for Cryogenic Refrigerators, AIAA 22nd Aerospace Sciences Meeting, Reno, Nevada, Jan. 9-12, (1984).

[5] Huston, E.L. and Sanrock, G.D., Engineering Properties of Metal Hydrides, J of Less-Common Metals, 74 (1980) 435-443.

[6] Wade, L.A., Operating Characteristics of a Hydrogen Sorption Refrigerator Part II: A Comparison Between a Second-Order Analysis and Empirical Data, Proceedings of the Fourth International Cryocooler Conference, Easton, Md, Sept. 25-26, 1986.

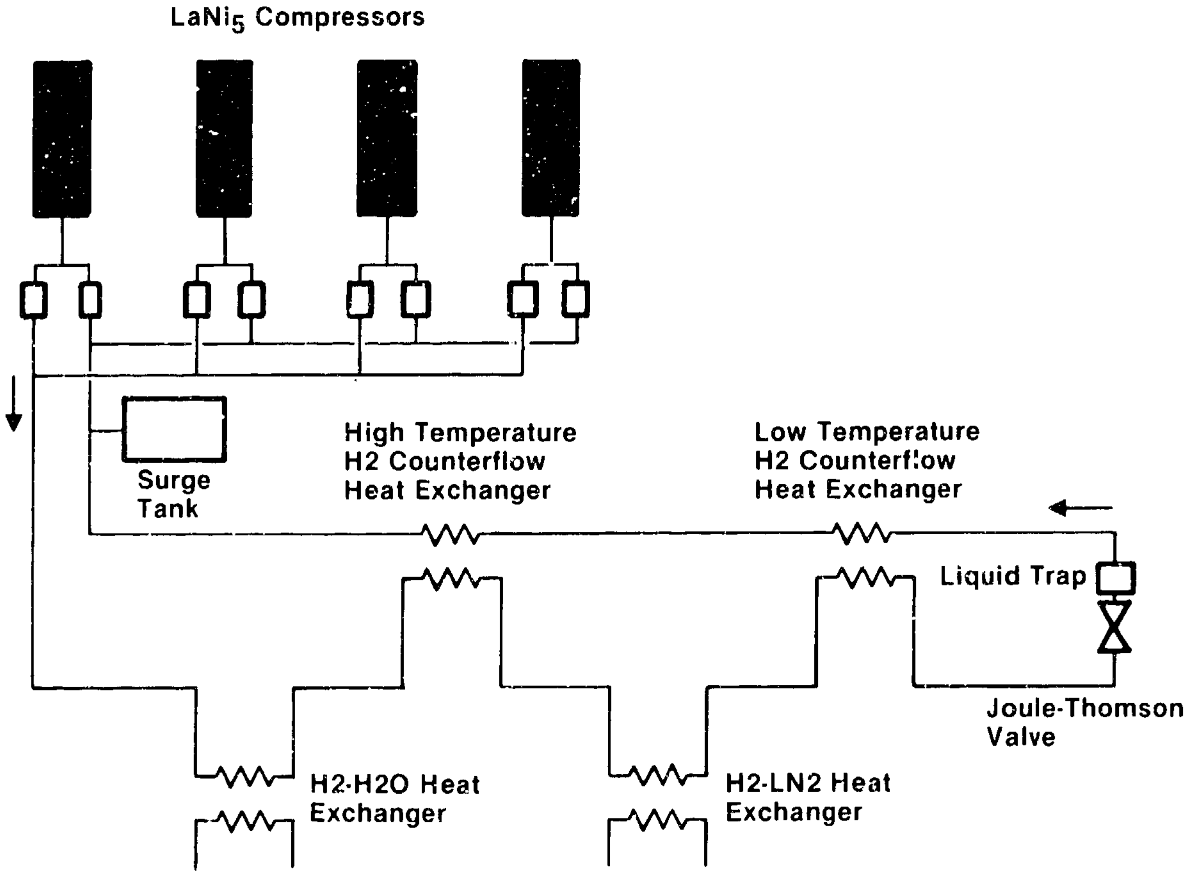
LaNi5 Compressors
Surge Tank
High Temperature H2 Counterflow Heat Exchanger
Low Temperature H2 Counterflow Heat Exchanger
Liquid Trap
Joule-Thomson Valve
H2-H2O Heat Exchanger
H2-LN2 Heat Exchanger

Figure 1 Hydrogen Sorption Refrigerator

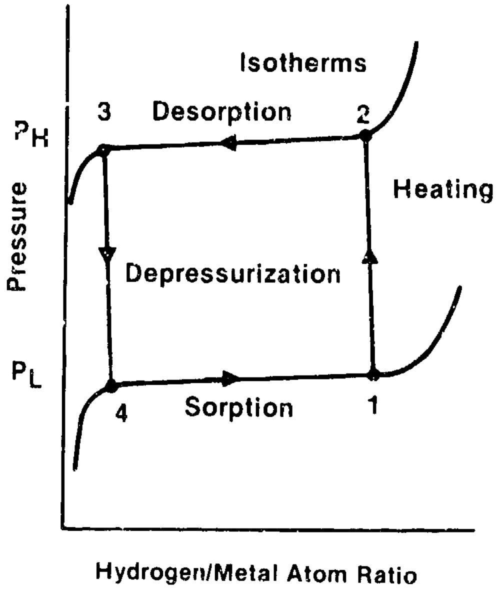
Isotherms
3
Desorption
2
P_H
Heating
Pressure
Depressurization
P_L
4
Sorption
1
Hydrogen/Metal Atom Ratio

Figure 2 Absorption Cycle

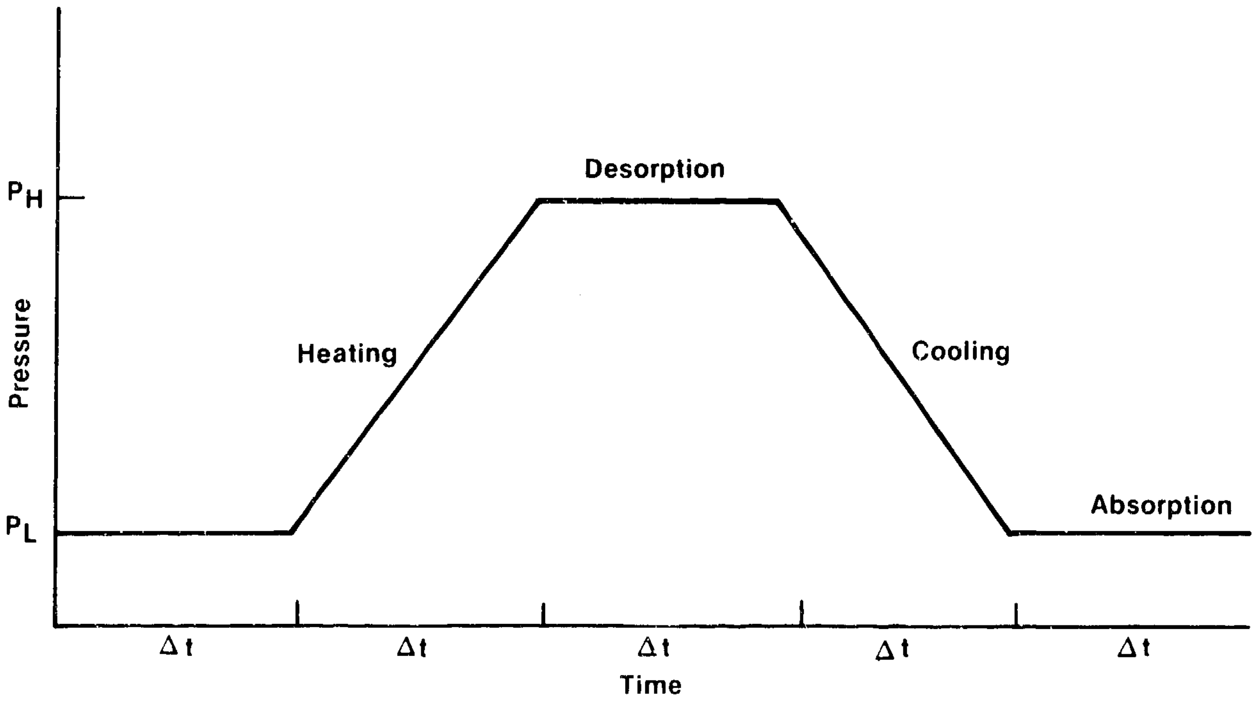
Desorption
P_H
Pressure
Heating
Cooling
Absorption
P_L
Δt
Δt
Δt
Δt
Δt
Time

Figure 3 Idealized Compression Pressure Profile

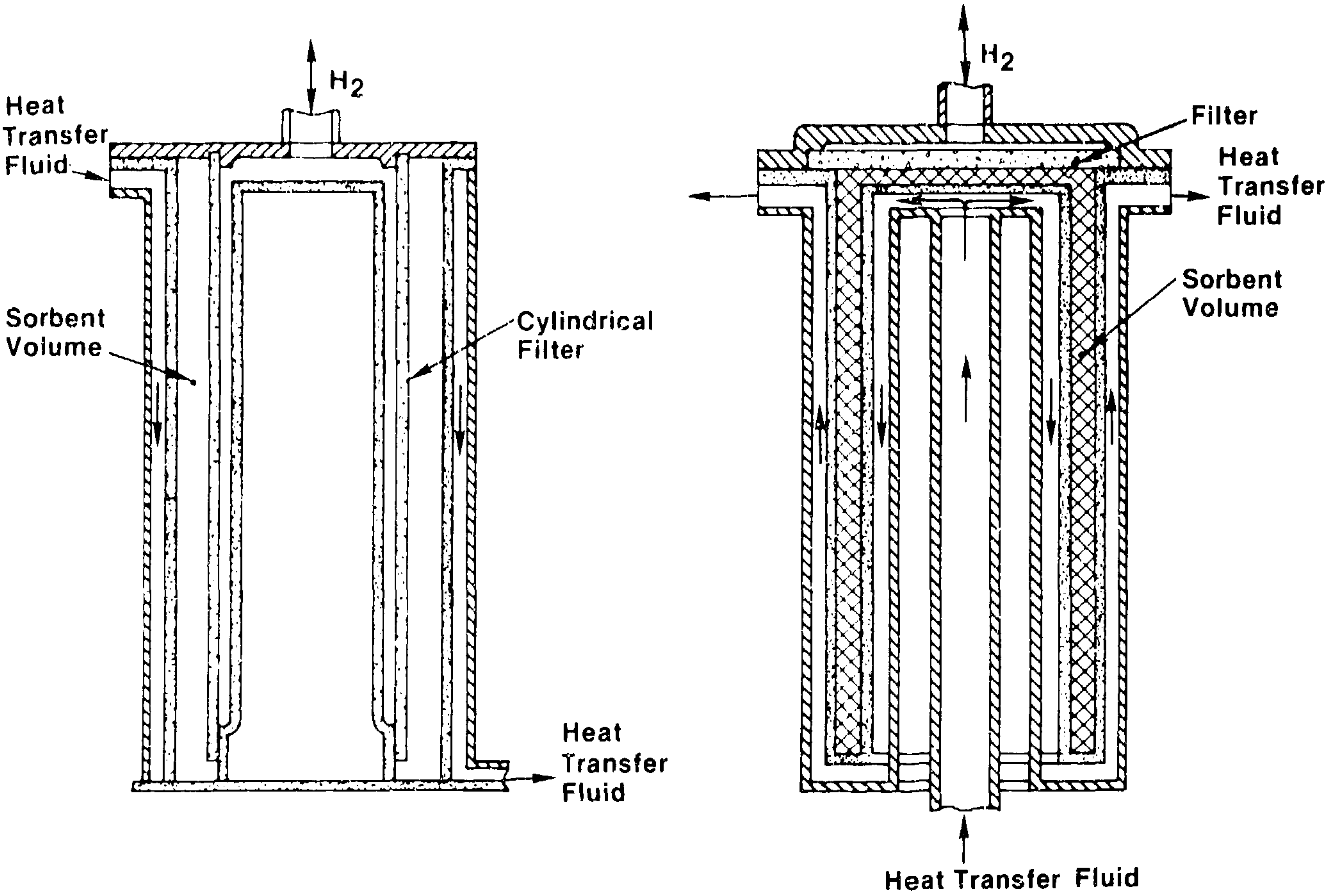
H2
Heat Transfer Fluid
Sorbent Volume
Cylindrical Filter
Heat Transfer Fluid
H2
Filter
Heat Transfer Fluid
Sorbent Volume
Heat Transfer Fluid

Figure 4 Compressor Concepts

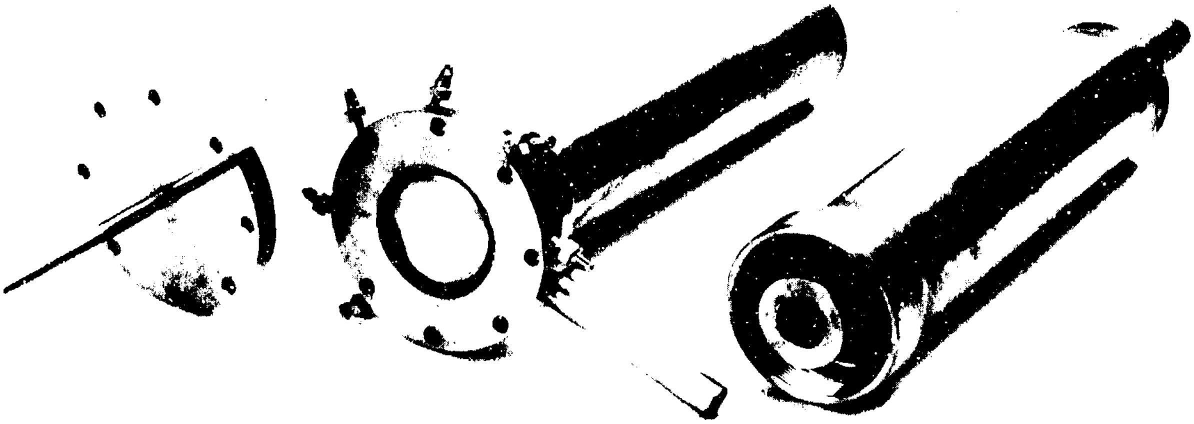

Figure 5 Hydrogen $LaNi_5$ Compressor

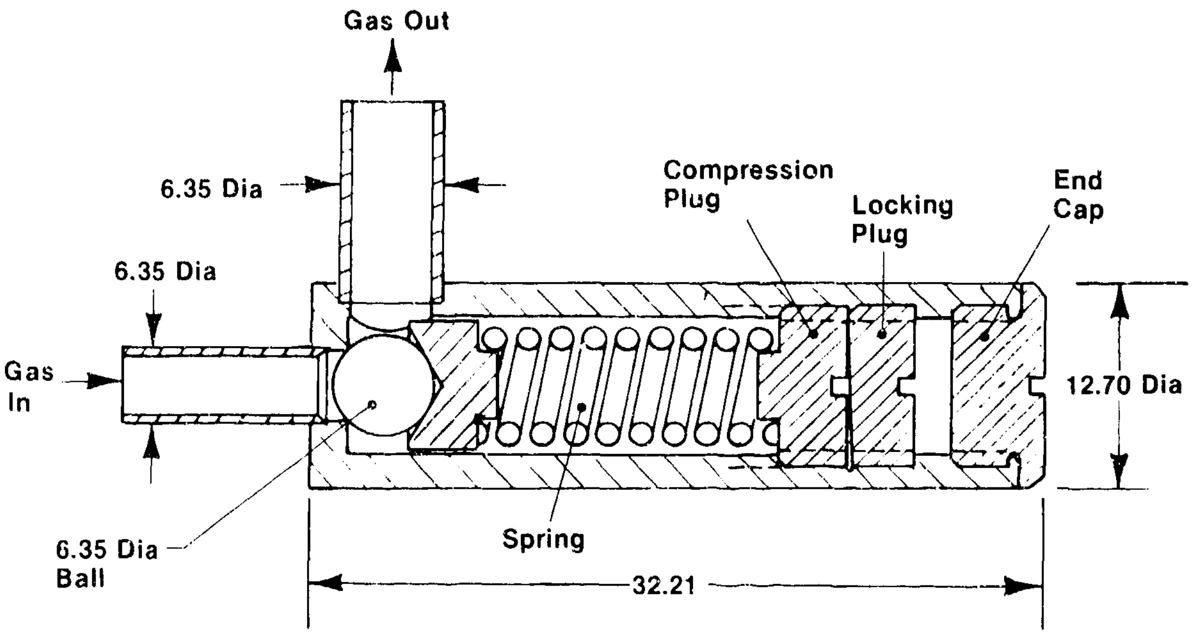
Gas Out
6.35 Dia
6.35 Dia
Gas In
Compression Plug
Locking Plug
End Cap
12.70 Dia
6.35 Dia Ball
Spring
32.21

Figure 6 Joule-Thomson Expander (Dim In MM)

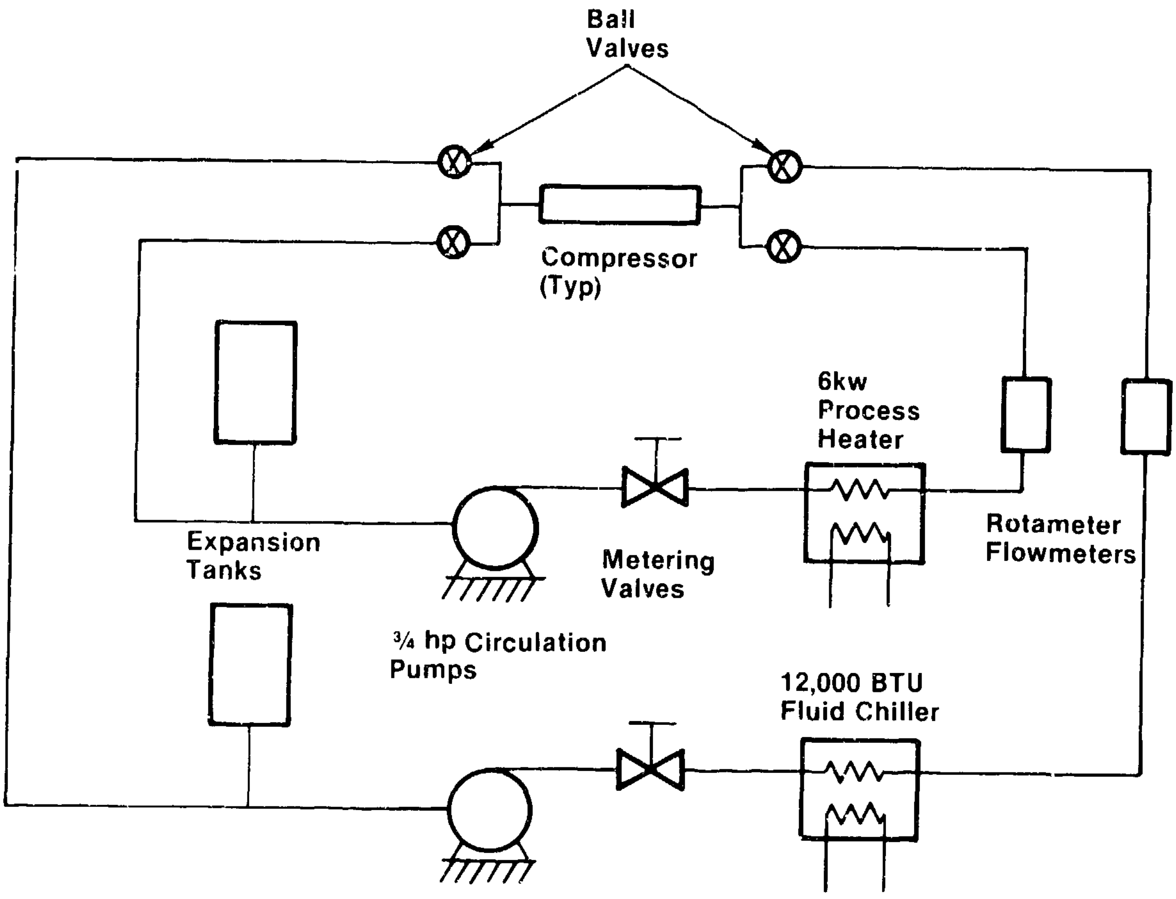
Ball Valves
Compressor (Typ)
6kw Process Heater
Expansion Tanks
Metering Valves
Rotameter Flowmeters
¾ hp Circulation Pumps
12,000 BTU Fluid Chiller

Figure 7 Fluid Loop Schematic

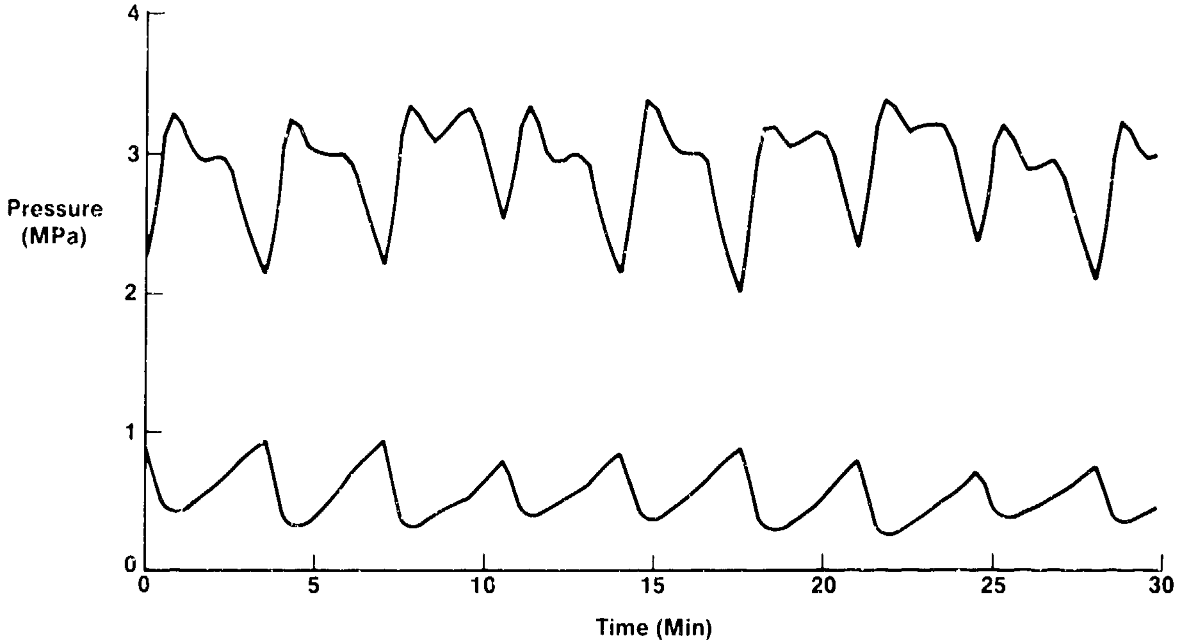

Figure 8 System Presure

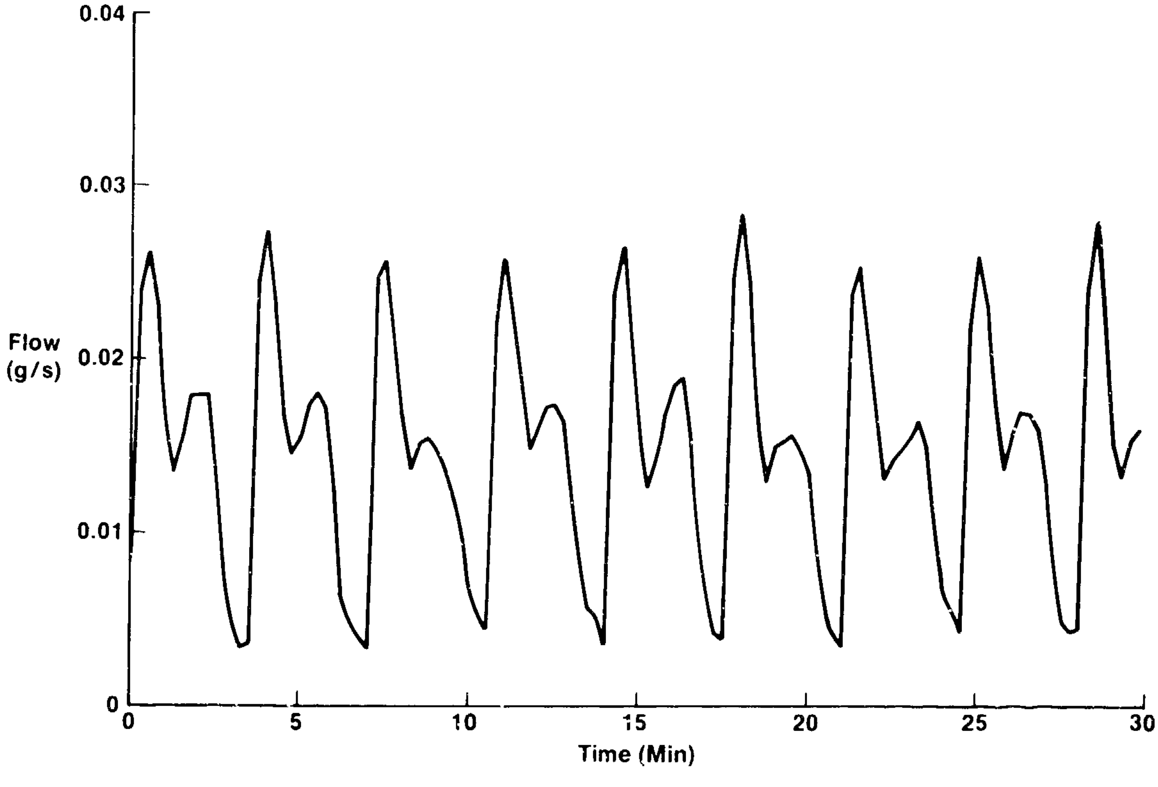

Figure 9 Hydrogen Mass Flow Rate

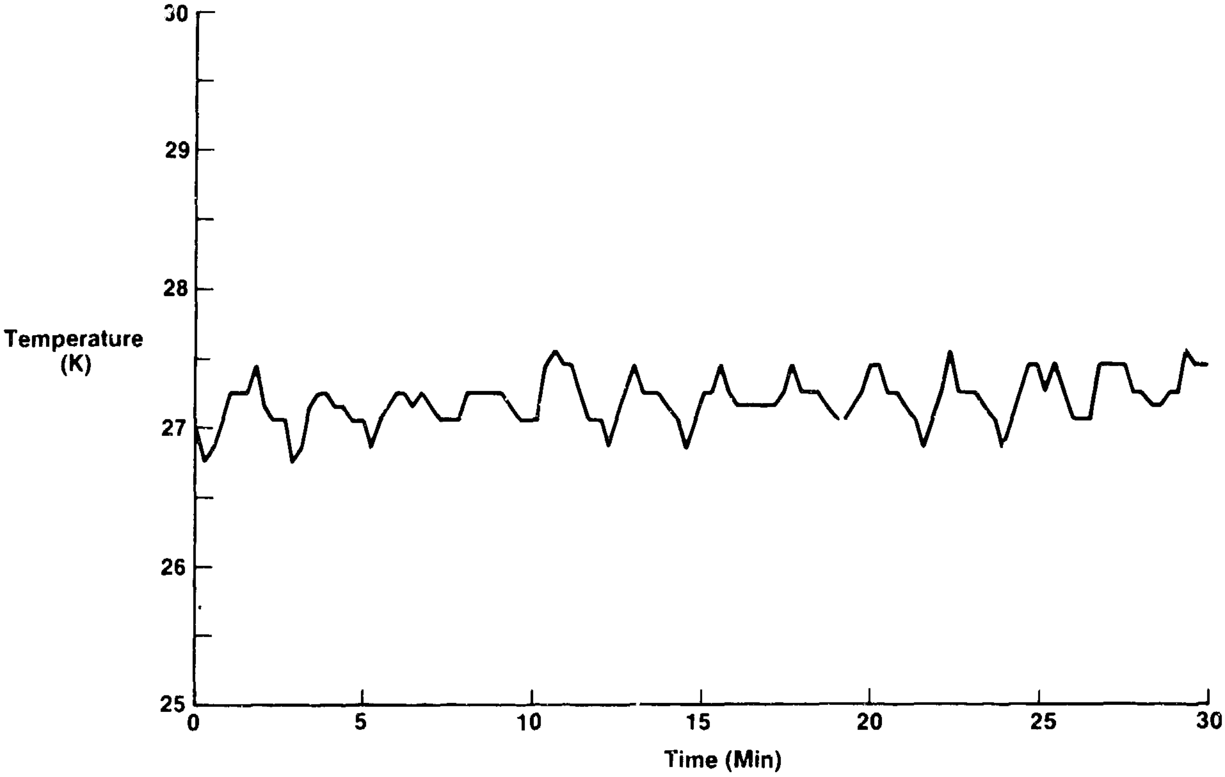

Figure 10 Cold Tip Temperature Fluctuations

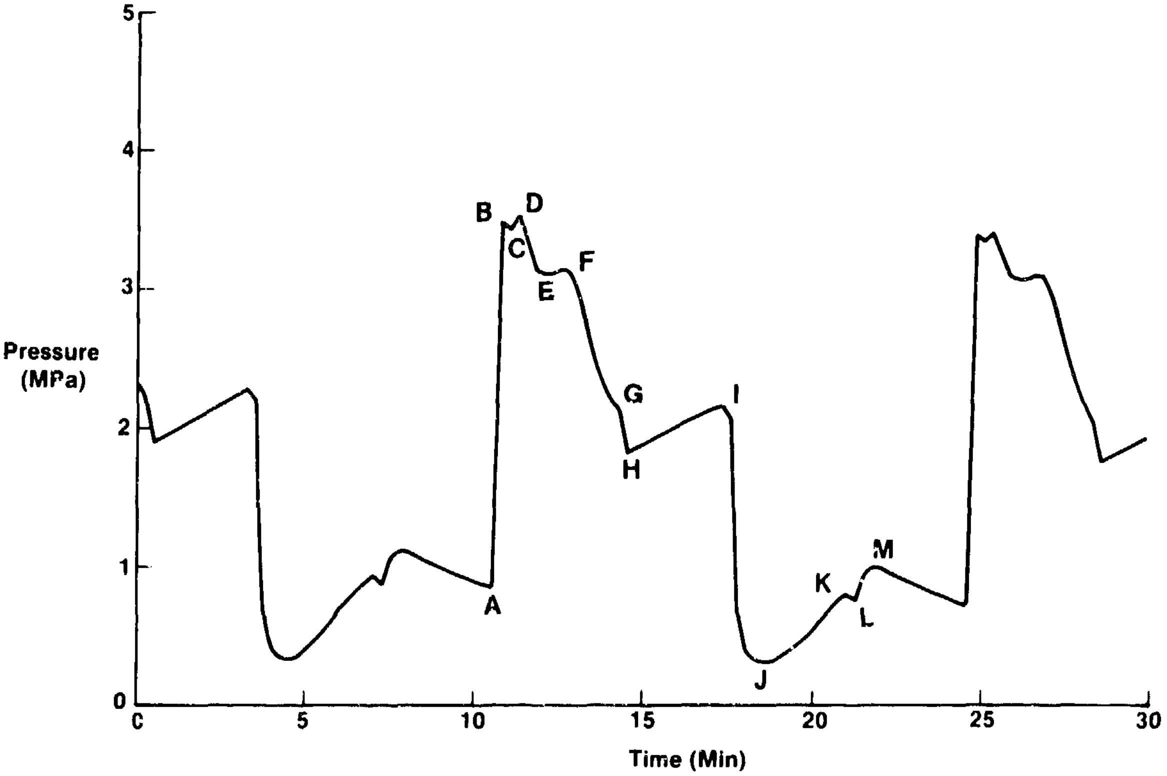

Figure 11 Compressor Pressure Profile

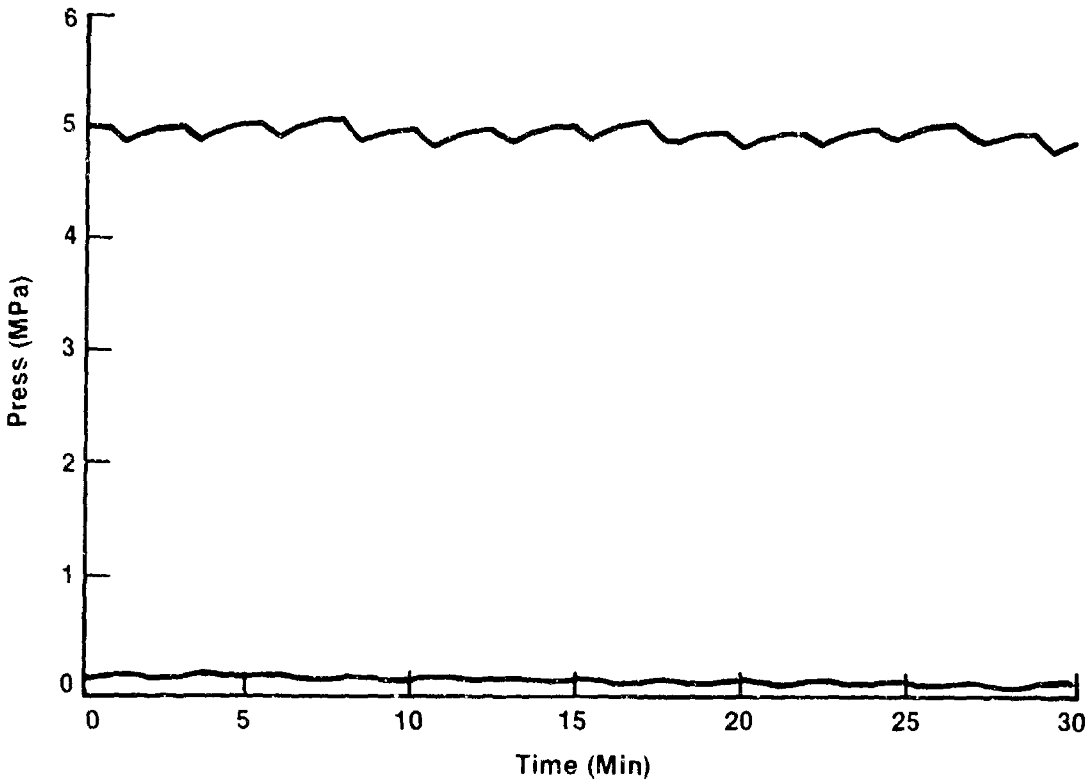

Figure 12 Clogged J-T Valve Pressure

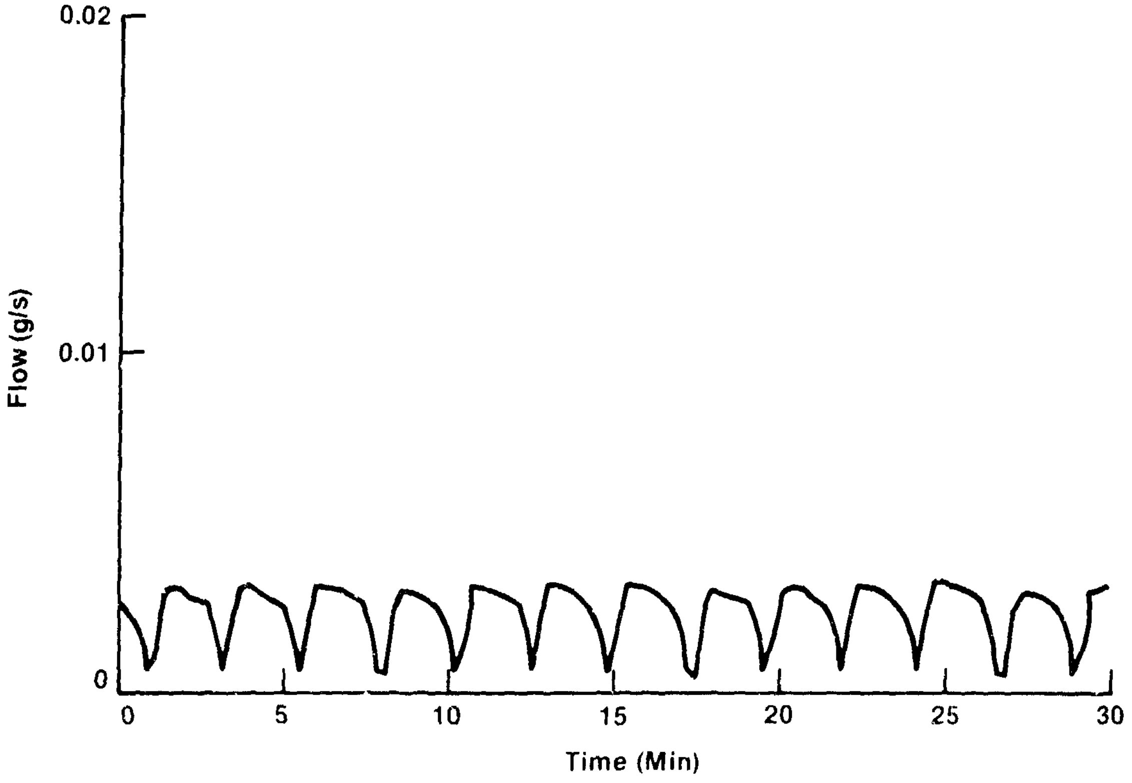

Figure 13 C'ogged J-T Valve Mass Flow

Preceding Page Blank

OPERATING CHARACTERISTICS OF A HYDROGEN SORPTION REFRIGERATOR
PART II: A COMPARISON BETWEEN A SECOND ORDER ANALYSIS AND EMPIRICAL DATA

Lawrence A. Wade

Aerojet ElectroSystems Co.
Azusa, CA 91702

Aerojet ElectroSystem has developed a hydrogen sorption refrigerator which has the potential to become a highly reliable alternative to mechanical refrigerators. The sorption refrigerator utilizes a Joule-Thomson (J-T) expander in combination with a $H_2/LaNi_5$ absorption compressor to minimize the number of wear susceptible mechanical parts. The performance of a flight qualifiable system is simulated by supplying heat to and removing heat from the compressor via fluid loops. The refrigerator was instrumented to allow its operating characteristics to be accurately determined. A general discussion of sorption refrigeration theory is presented and a second order refrigerator analysis model used to predict the refrigerator's performance is examined in detail. Empirical test data demonstrate that the analysis model accurately predicts the performance of a sorption refrigerator. It was determined that variations in the refrigerator mass flow rate and pressures have a strong impact on refrigerator performance.

Keywords: Absorption; adsorption; analysis; compressor; cryogenics; metal hydride; hydrogen; Joule-Thomson; mathematical model; refrigerator; sorption.

1. Introduction

Sorption refrigerators offer an inherently reliable solution for future satellite cooling requirements as they have no moving parts other than ambient temperature passive check valves. Earlier experiments demonstrated the feasibility of sorption refrigeration.[1][1] Aerojet ElectroSystems built and tested a sorption refrigerator to determine its operating characteristics. A $H_2/LaNi_5$

---

[1] Numbers in brackets indicate the literature references at the end of this paper. None of the equations in this paper are numbered.

refrigerator design was chosen for this experiment based on the results reported by previous investigators.[1,2] The design and performance details of this refrigerator are reported in an accompanying paper.[3]

Figure 1 shows a schematic of the hydride refrigerator design and a diagram of the corresponding temperature as a function of entropy. Tube-in-tube counterflow heat exchangers, with the high pressure gas flowing through the annulus and the low pressure gas flowing through the inner tube, are incorporated in the design. Liquid nitrogen is used to provide the 80 K precooling refrigeration. The refrigerant gas is expanded with a Joule-Thomson valve. The load to be refrigerated is applied to the liquid trap.

A rigorous second order analysis model was constructed to examine the performance of the sorption refrigerator. It can analyze cycles which incorporate either single or two phase refrigerant expansion. The program is modular in nature, so that changing the kind or order of the components can be done easily. The model is also useful for predicting the performance of proposed sorption refrigeration systems since it can analyze multistage refrigerators. A direct comparison of the analytical model to the refrigerator's measured performance and operating characteristics has yielded valuable insights into the complexities of how sorption refrigerators work.

2. Overview of sorption refrigeration theory

Sorption refrigerators are fundamentally different from most conventional ones in that the refrigerant is compressed thermally rather than mechanically. The sorption compressor absorbs gas at low pressure. The absorbed gas is then pressurized by heating the compressor. High pressure gas is desorbed and run through a counterflow heat exchanger to the expander. Cooling the depleted compressor returns it to the initial state. A design which uses four compressors, each of which is operated in a different part of the cycle, can continuously deliver high pressure refrigerant gas. As one compressor desorbs high pressure gas, a second will absorb the expanded low pressure gas. At the same time, a compressor which is full of absorbed gas is being pressurized by heating and another compressor which has been depleted of hydrogen is being cooled and thereby depressurized. When four compressors are used, they will work as two sets of opposing pairs. One absorbs while the other desorbs. One is pressurized while the other is depressurized. The minimum number of compressors needed to continuously supply high pressure refrigerant is three.

While some mechanical refrigerators (e.g. those which use the Vuilleumier cycle) also thermally compress the refrigerant, sorption refrigerators differ in that they make use of sorbent material for this purpose. This eliminates the need for moving mechanical parts. An additional advantage in pressurizing the refrigerant gas by heating a sorbent material, as opposed to directly heating the gas itself, is that a much greater pressure change is possible for a given temperature change. Heating $LaNi_5$ from 300 to 400 K will increase its equilibrium pressure by a factor of 40. If just the gas was heated, the ideal gas law shows that the pressure would increase by only one third. Using a material like $LaNi_5$ for the sorbent also has the advantage of resulting in a fairly small compressor design as the absorbed hydrogen has a greater density than does liquid hydrogen.[4] Input power is supplied to the sorption compressor in the form of heat.

Almost any expander can be used in combination with a sorption compressor to make a refrigerator. Due to their simplicity, Joule-Thomson valves have been selected for use on all reported sorption refrigerator designs. This is a naturally clean system, as no lubricants are required by the refrigerator. Some alternative designs shuttle the gas between two compressors which eliminates the check valves and thereby results in a refrigerator which has no moving parts. Turbo expanders appear to provide the most promising alternative to J T valves when high efficiency is required. However this does introduce a moving part into the cold end of the refrigerator.

While idealized theory indicates that perfectly continuous flows, temperatures, pressures and refrigeration are supplied by a sorption refrigerator, the experiments conducted at Aerojet indicate that refrigerator operating characteristics are actually very complex. The limited heat transfer and heat capacity available in real materials cause variations in the pressures, temperatures, and mass flow rate. Because the volume of the $LaNi_5$ increases by about 25% when fully hydrided, the void volume in the compressor increases by nearly 40% during desorption. This change in the compressor void volume, in combination with the gradual change in the $LaNi_5$ hydride equilibrium pressure when absorbing and desorbing refrigerant, also has a strong impact on refrigerator dynamics. Variations in the refrigerator pressures, temperatures and mass flow rate were found to be extremely regular. These variations occurred with the quarter cycle since four compressor units were used to make up the compressor bank. The fluctuations are slow in nature due to the refrigerator's nine minute cycle time. Figure 2 shows the mass flow rate, cold end temperature and pressure drop across the J-T valve as a function of time.

3. Detailed discussion of the second order analysis model

The model constructed to examine sorption refrigerator performance utilizes a second order analysis technique. A second order analysis is begun by calculating the ideal performance of a refrigerator. The heat flows and entropy productions which detract from the ideal cycle are then calculated. The difference between the ideal and the sum of the adjustments for the non-ideal behavior of the refrigerator gives the net refrigeration available. This program calculates the refrigerant mass flow rate, and input power required for a given geometry, operating pressure, net refrigeration and cold temperature. The program output includes the net refrigeration, the individual losses and the refrigerant enthalpy, temperature, and pressure at the entrance and exit of every component in the system.

This model includes a number of loss terms: environmental parasitic heat loads, heat exchanger inefficiency, pressure drop losses, heat exchanger longitudinal thermal conduction, and ortho to para conversion of the hydrogen gas. The heat exchanger inefficiency and the environmental parasitic heat loads are the dominant losses in the system. The pressure drop loss was very low in this system due to the low mass flow rate (normally between 0.01 and 0.02 g/sec.) However, in some of the proposed systems which have been examined, the pressure drop loss was also very important.

3.1 Code logic

A flow chart of the program code logic is shown in figure 3. The program is structured so that the heat balances in the cold heat exchanger, J-T valve and liquid trap are calculated. The mass flow rate is then increased until the required net refrigeration is delivered. After the correct mass flow rate has been determined, the required refrigeration which must be supplied by the precooler is calculated and the compressor input power is determined. When using experimental data to verify the program's accuracy, the net refrigeration requirement input to the program is varied by the programmer until convergence of the measured mass flow rate is achieved. The calculated temperatures and net refrigeration can then be compared to the measured valves.

The analyst inputs the precooler temperatures, the required net refrigeration, the heat exchanger geometries, the high and low pressures at the J-T valve and the estimated gas enthalpies at the inlets and outlets of each component. An initially low estimate of the mass flow rate required to deliver the specified net refrigeration is made by the program to ensure that the Newton-Raphson mass flow rate estimation routine achieves convergence. After estimating the required mass flow rate, the program calculates the gas stream flow areas and the gas properties at the estimated temperatures and pressures in the cold heat exchanger. The critical Reynolds number is calculated and the friction factors and heat exchange coefficients are determined. Using this information, the heat exchanger efficiency and the pressure drop are established. The gas enthalpies at the cold heat exchanger inlets are known as their temperatures and pressures are known. The gas enthalpy at the high pressure outlet is calculated by subtracting the difference between the low pressure inlet and outlet enthalpies from the high pressure inlet gas enthalpy since the enthalpy change in the high and low pressure streams along the heat exchanger are equal when the heat flow is balanced.

The pressure at the inlet of the high pressure side of the heat exchanger is calculated by adding the pressure drop through the heat exchanger annulus to the pressure at the J-T valve entrance. The pressure at the outlet of the low pressure side is the pressure at the liquid trap minus the pressure drop through the inner tube. The temperatures at the outlets of the heat exchanger are then calculated from the newly determined enthalpies. The new temperatures are used to determine the new average temperatures for the two streams and new gas properties are calculated. The program iterates until the heat exchanger effectivity, outlet temperatures, pressures, and gas properties have converged. The losses, the net refrigeration and the percent of the refrigerant which is liquefied are then calculated. If the calculated net refrigeration is less than that required, the estimated mass flow rate is increased and the program recalculates the heat exchanger performance and the refrigerator cold end heat balance. This continues until the desired net refrigeration is delivered.

Once the temperatures and pressures at the inlets of the warm heat exchanger have between determined, its performance can be calculated. The required precooler refrigeration and finally the input power to the compressor are calculated.

3.2 Equations

The symbols used are defined at the end of the text.

3.2.1 Compressor input power

The input power to the compressor is the sum of the power required to desorb the refrigerant, to heat the compressor when pressurizing the refrigerant, to desorb enough gas to pressurize the compressor void volume during pressurization and to make up the heat leaks from the compressor during desorption. These can be described by the following relations.

$$\dot{Q}_{in}=\dot{Q}_d+\dot{Q}_p+\dot{Q}_v+\dot{Q}_1$$

where

$$\dot{Q}_d=\Delta H*w$$

$$\dot{Q}_p=((M_h*c_{ph}+M_g*c_{pg}+M_{ss}*c_{pss})*(T_d-T_a))/t$$

$$\dot{Q}_v=(\Delta H*((P_h-P_1)-(n*R*(T_d-T_a))/V_v)*(V_v/(R*T_d)))/t$$

Hydrides expand when absorbing hydrogen and contract when desorbing hydrogen. The power required to desorb enough gas to pressurize the additional compressor void volume which develops as the hydride becomes depleted of hydrogen and shrinks was not included in this calculation.

3.2.2 Pressure drop and heat exchanger efficiency

The heat exchanger effectivity and pressure drop relations used in the model describe a curved tube-in-tube configuration. The relations have also been modified slightly to account for the effects of noncentricity on the tube-in-tube heat exchanger friction factors and heat exchange coefficients.[5]

The program assumes constant mass flow rates and pressures. Using the standard counterflow heat exchanger effectivity equation [6] resulted in effectivities better than 0.9998 being calculated. However, the variations in mass flow rate and pressures found in the sorption refrigerator cause increased heat exchange and pressure drop losses. To compensate for the over optimistic efficiencies calculated when the refrigerator flow variations were ignored, the effectivity of the counterflow heat exchanger was degraded by averaging the standard relation for $C_{min}/C_{max}=1$ and the relation which allows this value to vary. This resulted in a much more reasonable calculated effectivity of about 0.98.

The subscript 1 is used to indicate that the quantity being considered refers to the heat exchanger annulus. The subscript 2 is therefore used to refer to the inner tube of the heat exchanger. The equations for the pressure drop, heat exchanger effectivity and the associated friction factors and heat exchanger coeffecients follow.

$$\Delta P_1=2*f_1*L*w^2/(\rho_1*(D_3-d_2)*A_{c1}{}^2)$$

Ref
No.

$$\Delta P_2=2*f_2*L*w^2/(\rho_2*D_1*A_{c2}{}^2)$$

$$\varepsilon=((NTU/(1+NTU))+((1-e^{(-NTU*(1-C_r))})/(1-C_r*e^{(-NTU*(1-C_r))}))/2 \qquad [6]$$

$$Re_{crit}=20000.*(D_1/D_5)^{.32} \qquad [7]$$

For laminar flow:

$$f_1=0.985x10^{-4}+25.21*Re_1{}^{-1.011} \qquad [8]$$

$$(f_2=344*(D_1/D_5)^{.5})/(1.56+\log_{10}(Re_2*(D_1/D_5)^{.5}))^{5.73} \qquad [9]$$

$$h_1=(.9*k_1*Re_1{}^{.45}*Pr_1{}^{.5}*Gr_1{}^{.05}*(D_3/d_2)^{.8}*(\mu_{av}/\mu_w)^{.14})/((D_3-d_2)^{.6}*L^{.4} \qquad [10]$$

$$h_2=(1.84*k_2*Re_2{}^{5/6}*Pr_2{}^{1/3}*(D_1/D_5)^{.25}*(\mu_{av}/\mu_w)^{.14})/ \\ ((2+(10/(Pr_2{}^{2.}-1))^{.5})*D_1{}^{2/3}*L^{1/3}) \qquad [11]$$

For turbulent flow:

$$f_1=0.085*Re_1{}^{-0.25} \qquad [8]$$

$$f_2=0.00725*(D_1/D_5)^{.5}+0.0085*Re_2{}^{-0.25} \qquad [9]$$

$$h_1=0.020*k_1*Re_1{}^{.8}*Pr_1{}^{.4}*(D_3/d_2)^{.45}/(D_3-d_2) \qquad [12]$$

$$h_2=0.021*k_2*Re_2{}^{.85}*(D_1/D_5)^{.1}*Pr_2{}^{.4}/D_1 \qquad [13]$$

3.2.3 Gross refrigeration

When the refrigerant is expanded into a two phase flow, curve fit relations are used to describe its enthalpy and specific heat. The ideal gas law is used to describe the thermophysical properties when the refrigerant remains in a single phase after expansion. The effect of any inaccuracy in these relations on the predictive capability of this model is fairly strong. The primary effect occurs when the gross refrigeration is calculated. The gross refrigeration is a function of the difference between the enthalpy of the gas at low pressure and the cold precooler temperature, and the gas enthalpy at high pressure and the same temperature.

$$Q_{gross}=w*(H_6-H_2)$$

Because this difference can be very small relative to the enthalpies themselves, any error in the enthalpy values chosen will result in a large error in the calculated gross refrigeration.

3.2.4 Loss calculations

The dominant cold end losses for the Aerojet refrigerator are environmental heat leaks and the heat exchanger loss. For high capacity systems the pressure drop loss will also become extremely important. The losses included in this analysis are the environmental heat load, heat exchanger loss, pressure drop loss, ortho to para conversion of the hydrogen gas and longitudinal heat conduction along the heat exchanger.

The environmental heat load at the precooler and cold tip are calculated from the actual design. The primary source of heat leaks were thermal conduction paths down heater and thermocouple wires, and the pressure transducer capillary tubes. The heat leaks totalled 0.21 watts at the cold tip and 0.15 watts at the precooler.

The loss due to inefficiency in the precooler heat exchanger was not included in the model. Therefore, the gas exiting the precooler is assumed to be at exactly the same temperature as the precooler. The cold counterflow heat exchanger loss is one of the most significant. It is given by the following relation:

$$\dot{Q}_{hx}=(1-\varepsilon)*w*(h\ \text{[illegible]}\ h_5)$$

The pressure drop loss affects the refrigerator performance in two ways. It directly increases the gas temperature through frictional heating and it reduces the pressure range over which the refrigerant can be expanded. This directly reduces the available gross refrigeration. The loss of gross refrigeration was included in the model by using the pressures measured at the J-T valve when calculating the gas enthalpies. The frictional heating is described by:

$$\dot{Q}_{dp}=(\Delta P_1/\rho_1)+(\Delta P_2/\rho_2))*w$$

Hydrogen gas exists in two primary states ortho and para. The distinction between them is the relative nuclear spin of the two atoms that make up the hydrogen molecule. At room temperature, the two states of hydrogen reach an equilibrium condition which is referred to as normal hydrogen. Normal hydrogen consists of 75% ortho and 25% para hydrogen. The equilibrium balance swings to essentially 100% para hydrogen at the normal boiling point temperature. As the hydrogen converts from the ortho to the para state, 703.3 j/g are released. The rate at which this energy is released will be referred to as the ortho to para conversion loss. If left alone, the reaction rate for this conversion is very slow. However if a catalyst is present, the rate of reaction can be increased by several orders of magnitude. Metal oxides, copper, carbon and a number of other materials can act as a catalyst with varying degrees of efficiency. By avoiding materials which are known to be hydrogen catalysts, or which are susceptible to hydrogen embrittlement, the effects of this problem can be minimized. In the interests of being conservative, the reaction rate with an activated charcoal catalyst, 0.001 sec^{-1}, was assumed for this calculation. The ortho to para loss is given by:

$$\dot{Q}_{o-p}=0.001*w*703.3*(.75-Eq)*L_1/v$$

The thermal conduction along the heat exchanger is given by:

$$\dot{Q}_{cond}=k_w*(A_3+A_4)*\Delta T_1/L$$

The loss term $\dot{Q}_{de}$ is the difference between the enthalpy difference as a function of pressure at the 80 K precooler and the enthalpy difference as a function of pressure at the 297 K precooler. This term, the difference in the enthalpy differences, is the dominant loss when the required precooler refrigeration is calculated. It can be put in the form

$$\dot{Q}_{de}=w*((H_6-H_2)-(H_7-H_1))$$

3.2.5 Heat balances

The net refrigeration is calculated by the equation

$$\dot{Q}_{net}=\dot{Q}_{gross}-\dot{Q}_{hx}-\dot{Q}_{dp}-\dot{Q}_{env}-\dot{Q}_{o-p}-\dot{Q}_{cond}$$

The refrigeration which must be supplied by the 80 K precooler is given by the equation

$$\dot{Q}_{pc}=\dot{Q}_{whx}+\dot{Q}_{wdp}+\dot{Q}_{wo-p}+\dot{Q}_{wcond}+\dot{Q}_{de}-\dot{Q}_{hx}-\dot{Q}_{cond}$$

where the subscript w added to the front of the already defined subscripts indicated that these losses occurred in the warm heat exchanger. Note that the cold heat exchanger inefficiency loss and longitudinal conduction loss are treated as a refrigeration of the precooler. Table 1 shows the calculated losses and heat balance for a typical set of refrigerator operating parameters.

Table 1 Calculated Heat Balance of a Typical Refrigerator

	Cold Tip Net Refrigeration (watts)		Required Precooler Refrigeration (watts)
$\dot{Q}_{gross}$	+0.7827	$\dot{Q}_{de}$	+0.9390
$\dot{Q}_{env}$	-0.210	$\dot{Q}_{whx}$	+0.4224
$\dot{Q}_{hx}$	-0.1895	$\dot{Q}_{wenv}$	+0.150
$\dot{Q}_{o-p}$	-0.0071	$\dot{Q}_{wdp}$	+0.0094
$\dot{Q}_{cond}$	-0.0008	$\dot{Q}_{wcond}$	+0.0032
$\dot{Q}_{dp}$	-0.0004	$\dot{Q}_{o-p}$	+0.0025
		$\dot{Q}_{hx}$	-0.1895
		$\dot{Q}_{cond}$	-0.0008
$\dot{Q}_{net}$	+0.375	$\dot{Q}_{pc}$	+1.336

4. Comparison of the analysis to the measured refrigerator performance

The data was averaged over the thirty minutes or more to determine the values for the mass flow rate and pressures which were input to the analysis model. The refrigerator achieved an average cold tip temperature of 28.9 K and a gas temperature prior to expansion of 38.5K while delivering 0.25 watts of net refrigeration. The program predicted that the refrigerator should achieve a temperature of 28.9 K and a gas temperature prior to expansion of 38.5K with a net refrigeration of 0.28 watts. When the refrigerator was operated at a load of 0.60 watts, the gas temperature was 34.8 K after expansion and 45.6 K prior to expansion. The program predicted that the gas temperature would be 34.0 K after expansion and 45.9 K prior to expansion with a net refrigeration of 0.65 watts. The model therefore calculated the refrigerator cold end temperatures to within 2.4% and the net refrigeration to within 11%.

However, this close correspondence was achieved by degrading the predicted cold heat exchanger efficiency. The surges in mass flow rate which actually exist in the refrigerator result in higher pressure drops and heat exchanger inefficiencies than those calculated by using averaged pressures and mass flow rates. The difference between the degraded heat exchanger loss and the constant pressure and mass flow heat exchanger loss directly demonstrates the importance of the refrigerator dynamics to performance calculations. As the variations in pressures, temperatures and mass flow rates are extremely regular it should be possible to construct a model which duplicates the physical situation and is capable of determining the relative importance of each of these effects.

5. Conclusions

A detailed second order model has been constructed whose predictive capability has been verified against the measured performance of a flight like sorption refrigerator. The second order analysis model was found to be capable of predicting cold end temperatures to within 2.4% and the net refrigeration to within 11%. The program calculates the refrigerant pressures, temperatures, and enthalpies throughout the system. The heat flows and entropy productions in each of the refrigerator components are also calculated. While the model examines the refrigerator in a rigorous fashion, there are a number of assumptions made in its construction. The most important of these was the assumption that the refrigerant is supplied by the compressor at a constant pressure and mass flow rate. A model can be constructed which is capable of predicting the dynamic operating characteristics of a sorption refrigerator since the measured transients are extremely repeatable. This program would also prove valuable when designing the refrigerator to minimize the transients.

6. Symbols

A_3	inner tube crossectional area, cm^2
A_4	outer tube crossectional area, cm^2
A_c	crossectional travel free-flow area, cm^2
C_p	specific heat, J/mole-K
C_r	flow stream capacity rate ratio
D_1	inner diameter inner tube, cm
d_2	outer diameter inner tube, cm
D_3	inner diameter outer tube
D_5	coil diameter, cm
E_q	equilibrium mole fraction
f	fanning friction factor
G_r	Grashof number
H_i	gas enthalpy at state points in figure 1, J/g
k_i	gas thermal conductivity, mW/cm-K
k_w	tube material thermal conductivity, mW/cm-K
L	flow length, cm
M_h	hydride mass, g
M_g	hydrogen mass, g
M_{ss}	container mass, g
NTU	number of transfer units
n	moles of hydrogen at P_1
P_h	high pressure, Pa
P_l	low pressure, Pa
Pr	Prandtl number
R	gas constant, J/kg-K
Re	Reynolds number
T_a	absorption temperature, K
T_d	desorption temperature, K
t	cycle time, s
V_v	void volume cm^3
w	mass flow rate, g/s
ΔH	heat of desorption, J/g
ΔT_1	temperature difference along the heat exchanger, K
ε	heat exchanger effectivity
ρ_i	density at state points in figure 1, gm/cc
μ_{av}	average viscosity, g/cm-s
μ_w	viscosity of fluid next to the wall, g/cm-s

7. References

[1] Jones, J.A. and Golben P.M., Design, Life Testing, and Future Designs of Cryogenic Hydride Refrigeration Systems, Cryogenics 25, 212 (1985).

[2] Lehrfeld, D. and Boser O. in Absorption-Desorption Compressor for Spaceborne/Airborne Cryogenic Applications, Air Force Flight Dynamics Laboratory, Wright-Patterson Air Force Base, Ohio 45433, AFFDL-TR-74-21, March 1974.

[3] Karperos, K., Operating Characteristics of a Hydrogen Sorption Refrigerator, Part I: Experiment Design and Results, Proceedings of the 1986 Cryocooler Conference, Easton, Maryland, Sept. 25-26 1986.

[4] Reilly J.J. and Sandrock G.D., Hydrogen Storage in Hydrides, Scientific American, February 1980, pg. 118.

[5] Rohsenow, W.M. and Harnett, J.P. in Handbook of Heat Transfer, pages 7-107 to 7-110 (McGraw-Hill Book Co., Inc., New York, N.Y., 1973).

[6] Kays, W.M. and London, A.L. in Compact Heat Exchangers. pgs. xi to xiv (McGraw-Hill Book Co., Inc., New York, N.Y., 1984).

[7] Ito, H., Friction Factors for Turbulent Flow in Curves Pipes, J. Basic Engng, Trans. ASME D 81, 123 (1959).

[8] Rohsenow, W.M. and Hartnett, J.P., op. cit., pg 7-64.

[9] Rohsenow, W.M. and Hartnett, J.P., op. cit., pg 7-149.

[10] Chen, C.Y., Hawkins, G.A. and Solberg, H.L., Trans. ASME 68, 99 (1946).

[11] Rohsenow, W.M. and Hartnett, J.P., op. cit., pg 7-149 to 7-151 and Sieder, E.N. and Tate, G.E., Ind. Eng. Chem. 28, 1429 (1936).

[12] Wiegand, J.H., discussion of paper by McMillen and Larson, Trans. AIChE 41, 147 (1945).

[13] Rohsenow, W.M. and Hartnett J.P., op. cit., pgs 7-149 to 7-151.

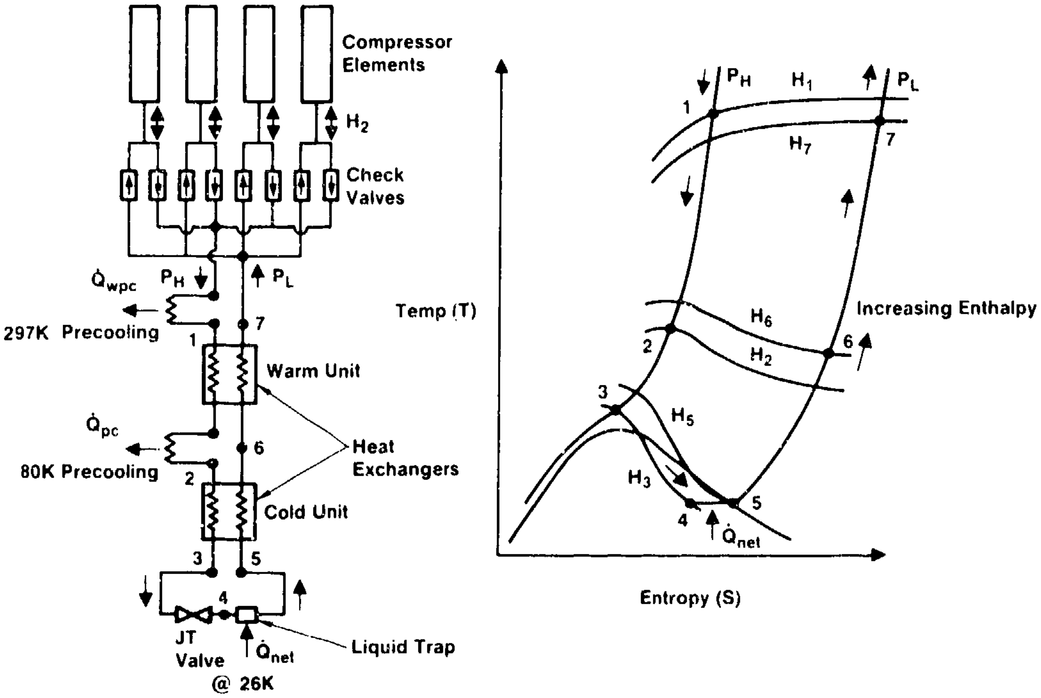
Compressor Elements
H_2
Check Valves
$\dot{Q}_{wpc}$
P_H
P_L
297K Precooling
1
7
Warm Unit
$\dot{Q}_{pc}$
6
Heat Exchangers
80K Precooling
2
Cold Unit
3
5
4
JT Valve
@ 26K
$\dot{Q}_{net}$
Liquid Trap
Temp (T)
Entropy (S)
P_H
H_1
P_L
H_7
H_6
H_2
H_5
H_3
Increasing Enthalpy
$\dot{Q}_{net}$

Figure 1 Schematic of Hydride Refrigerator with T-S Diagram

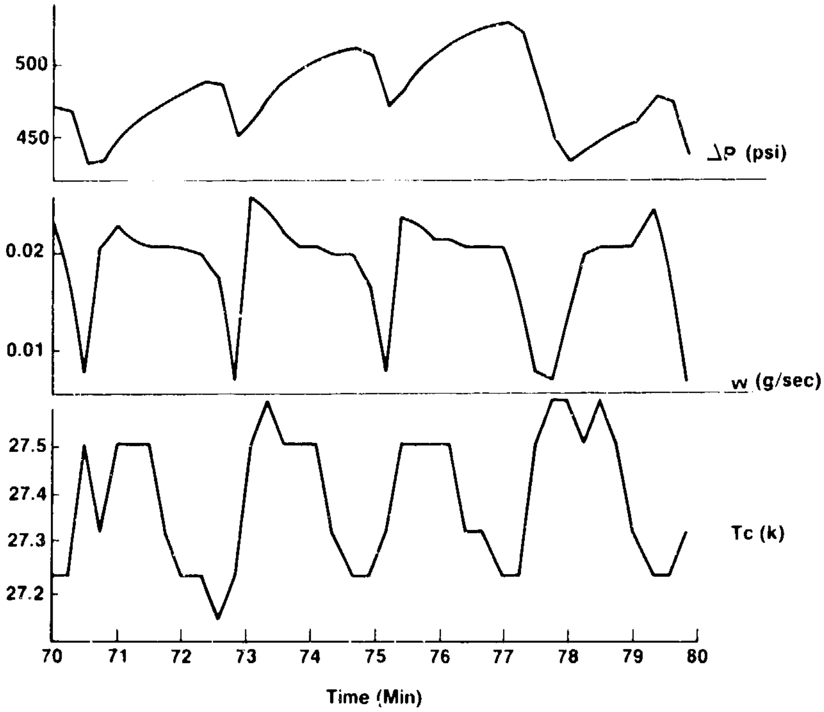

Figure 2 Mass Flow, Cold Temperature and Pressure Difference Across The J-T Valve as a Function of Time

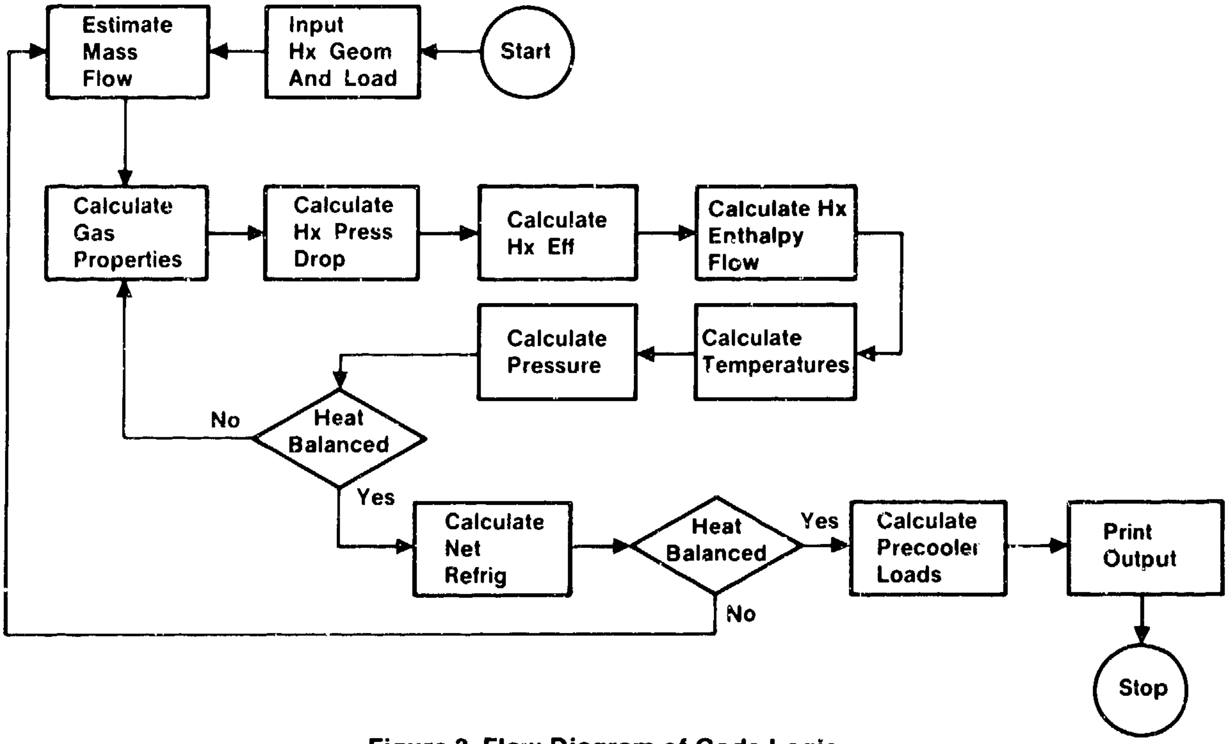
Estimate Mass Flow
Input Hx Geom And Load
Start
Calculate Gas Properties
Calculate Hx Press Drop
Calculate Hx Eff
Calculate Hx Enthalpy Flow
Calculate Pressure
Calculate Temperatures
No
Heat Balanced
Yes
Calculate Net Refrig
Heat Balanced
Yes
Calculate Precooler Loads
Print Output
No
Stop

Figure 3 Flow Diagram of Code Logic

Preceding Page Blank

HIGH RESPONSE HYDRIDE COMPRESSOR FOR REGENERATIVE CRYOCOOLER

Y. Matsubara

Atomic Energy Research Institute
Nihon University
Tokyo 101, Japan

M. Kaneko, J. Suzuki and K. Hirosawa

Suzuki Shokan Co., Ltd.
Tokyo 101, Japan

This paper describes the feasibility study of the high response hydride compressor for a regenerative cryocooler. The gas compression parts of the split Stirling or Vuilleumier cycle could be replaced with the gas absorption compressor, if the pressure response of the absorption compressor is high enough to drive the regenerative cryocooler directly. A metal hydride (LaNi5) has been used for the experiment of hydrogen absorption compressor which gives the equilibrium state of 12 atm at 80°C or 4 atm at 40°C. Our preliminary experiment indicates the pressure response of the order of seconds could be obtained. An application of the hydride compressor operating below 100°C to the gas compression parts of the regenerative cycle cryocooler has also been described.

Key words; absorption, desorption, hydride, thermal compressor, cryocooler, hydrogen, regenerative cycle, pulse tube, Vuilleumier cycle

1. Introduction

An increasing number of cryogenic applications require reliable and low cost cryocoolers. The gas sorption compressor could be substituted for the mechanical compressor of the cryocooler and enhance its reliability. The sorption compressor having intake and exhaust valves has been used in a high pressure Joule-Thomson cycle [1,2,3]; however, its application to the regenerative cycle is limited to Gifford-McMahon cycle [4] because of relatively slow operating speed of the sorption compressor.

However the gas compression part of the split Stirling on Vuilleumier cycle could be replaced with a sorption compressor, if the pressure response of the sorption compressor is high enough to drive the regenerative cryocooler directly. Its application to the pulse tube refrigerator is also interesting because there is a potential to realize a cryocooler having no moving parts. This paper describes the feasibility study of a high response hydride absorption compressor for regenerative cryocoolers.

2. Fundamental model of the pressure swing generator

To know the pressure response of the metal hydride, we considered the fundamental model as shown in Figure 1. It is constructed by the hydride receptacle having heat transfer wall and the hydrogen gas space with pressure gauge.

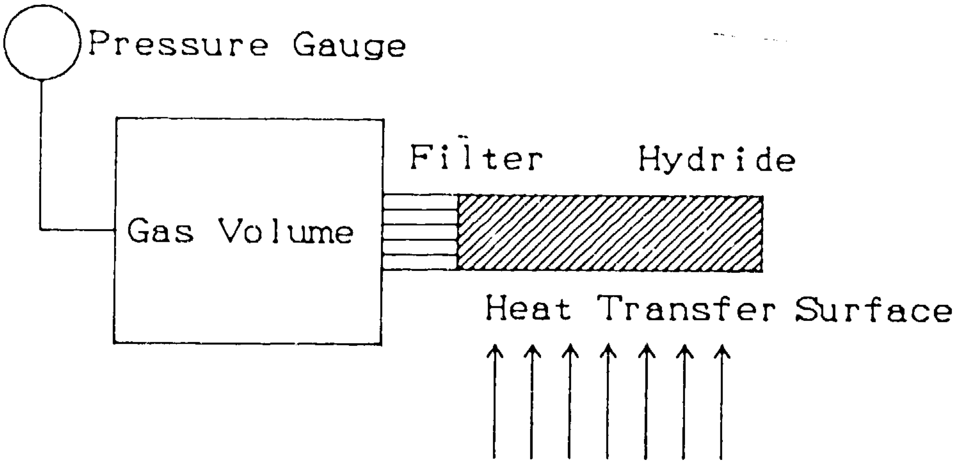

Figure 1. Fundamental model of the pressure swing generator.

The absorption and desorption process of this model is explained on the PCT (Pressure, Composition, Temperature) plane as shown in Figure 2(a). During the heating process of the heat transfer wall, hydrogen gas in the hydride is desorbed due to the increasing temperature of the hydride. As a result, the gas flows into the gas space and the pressure increase (A to B in Figure 2(a)). During the cooling process of the same wall, the pressure decreases due to the gas absorption effect (B to A in Figure 2(a)).

In general, the positive reaction heat is produced during the cooling process of the hydride and the negative reaction heat (cooling effect) is produced during the heating process. Therefore the fundamental equations of the process described above can be written as follows:

$$(Cs+Cw)\frac{dTs}{dt} = k*s(Tf-Ts)+QH \tag{1}$$

where the secondary fluid such as water for heating and cooling the heat transfer wall has been considered. In eq. (1), Ts is hydride temperature; Tf, secondary fluid temperature; Cs, heat capacity of the hydride; Cw, heat capacity of the wall material; k, thermal conductance; s, heat transfer area of the wall; and QH, reaction

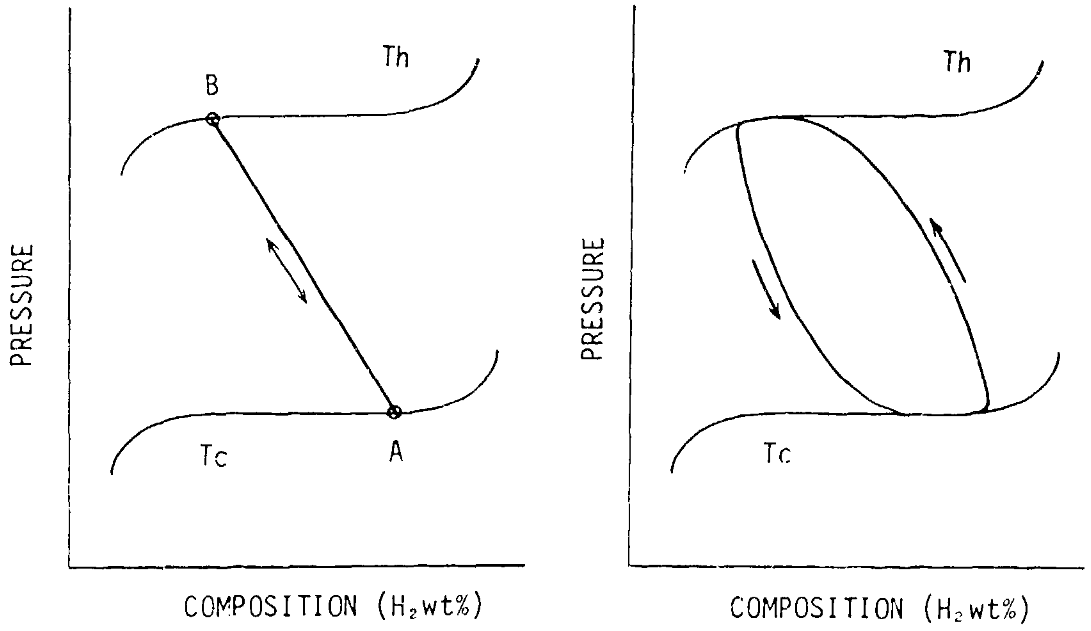

(a) Constant volume. (b) Variable volume.

Figure 2. PCT plane of metal hydride for pressure swing.

heat. The effects of the thermal conductivities of the hydride and the heat transfer wall are not considered in eq. (1) for simplicity. Therefore these effects should be included in the thermal conductance (k) with the heat transfer coefficient of the secondary fluid.

The pressure and the temperature relation within the plateau region on the PCT plane is defined as;

$$\ln(P) = \frac{\Delta H}{RTs} - \frac{\Delta S}{R} \tag{2}$$

where ΔH is the enthalpy change of the hydride due to the reaction heat; ΔS, entropy change of the hydride; and R, a gas constant (for hydrogen, R=4.12 J/g.K).

The reaction heat for unit mass (ms) within the hydride may be written as;

$$QH = \Delta H \frac{dms}{dt} \tag{3}$$

Considering the ideal gas, the state equation in the gas space is expressed as,

$$PV = 0.098(m - ms)\ RT \tag{4}$$

where P is pressure (kg/cm^2); V is volume of the gas space (cm^3); T is gas temperature in the gas space (K) which is assumed to be constant; and m is the total mass of the working gas (grams).

Summarizing these equations, we obtained the following differential equation for the hydrogen gas temperature within the hydride:

$$\frac{dTs}{dt} = \left\{ Cs+Cw+0.098\,\frac{V}{T}\left(\frac{\Delta H}{RTs}\right)^2 EXP\left(\frac{\Delta H}{RTs}-\frac{\Delta S}{R}\right)\right\}^{-1} k{*}s(Tf-Ts) \qquad (5)$$

The Runge-Kutta method was used to solve this equation. The pressure response followed by the step change of the secondary fluid temperature is obtained by eq. (2) and (5). One of the calculated results is shown in Figure 3. Fixed parameters are shown in Table 1. The values of ΔH and ΔS are those of LaNi5 obtained from our experimental data.

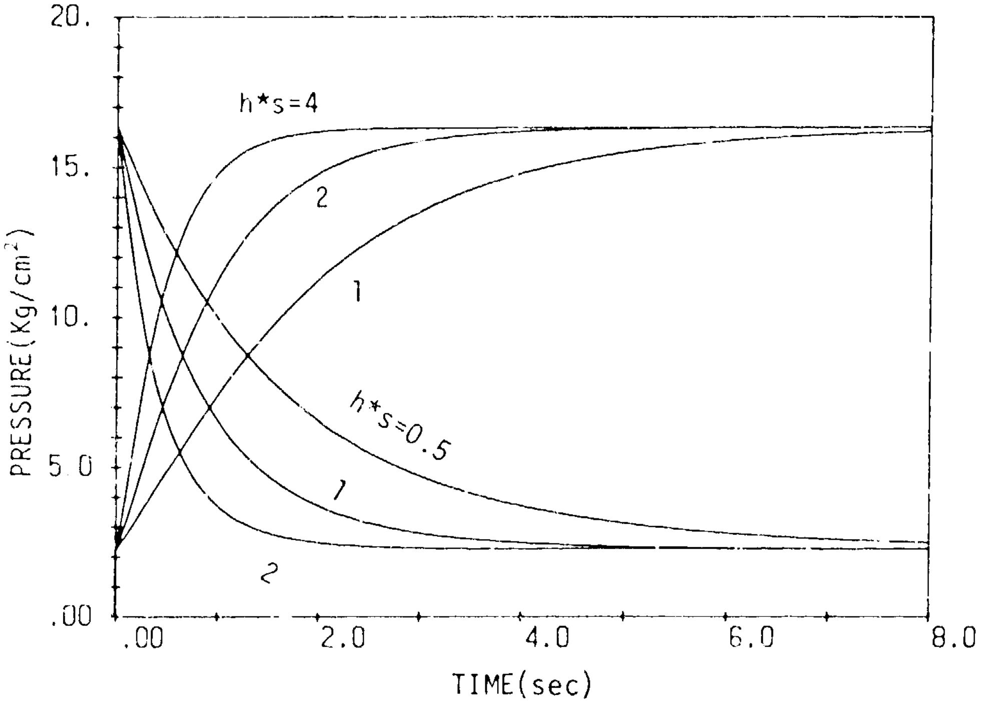

Figure 3. Pressure response following the step change of the second fluid temperature.

Table 1. Fixed parameters used in Figures 4 to 8.

Enthalpy change of LaNi5	ΔH	-1.56E4	(J/g)
Entropy change of LaNi5	ΔS	-55.6	(J/g.K)
Max. temperature of secondary fluid	Th	353	(K)
Min. temperature of secondary fluid	Tc	298	(K)
Sum of heat capacities	ΣCi	1.0	(J/K)
Heat transfer rate	k*S	10.0	(J/sec.K)
Max. gas volume	Vmax	6.0	(cm^3)
Min. gas volume	Vmin	1.0	(cm^3)
Phase angle of Tf and V	Ψ	40	(deg.)
Cycle frequency	f	30	(rpm)

3. Hydride compressor for regenerative cryocoolers

The regenerative cycle using a cold displacer instead of an expander operates with constant volume except the compression part of Stirling cycle, but the mass flow produced by the temperature difference at both ends of the displacer means the existence of an imaginary variable volume. Therefore it could be assumed that the cyclic change of the volume of the gas space in eq. (2) indicates the combination of a hydride compressor and the regenerative cryocooler using a cold displacer.

Figure 4 shows the cyclic response of the pressure (P) caused by the cyclic change of the gas volume (V) and the secondary fluid temperature (Tf) having the phase angle ( ) as indicated on the figure. The parameters listed on table 1 are also used in this calculation. In this case, the mass flow due to the absorption and desorption of the hydride is schematically shown in Figure 2 (b). The cooling effect at the cold end of the displacer may be obtained if the gas absorbed in the hydride moves counterclockwise on the PCT plane.

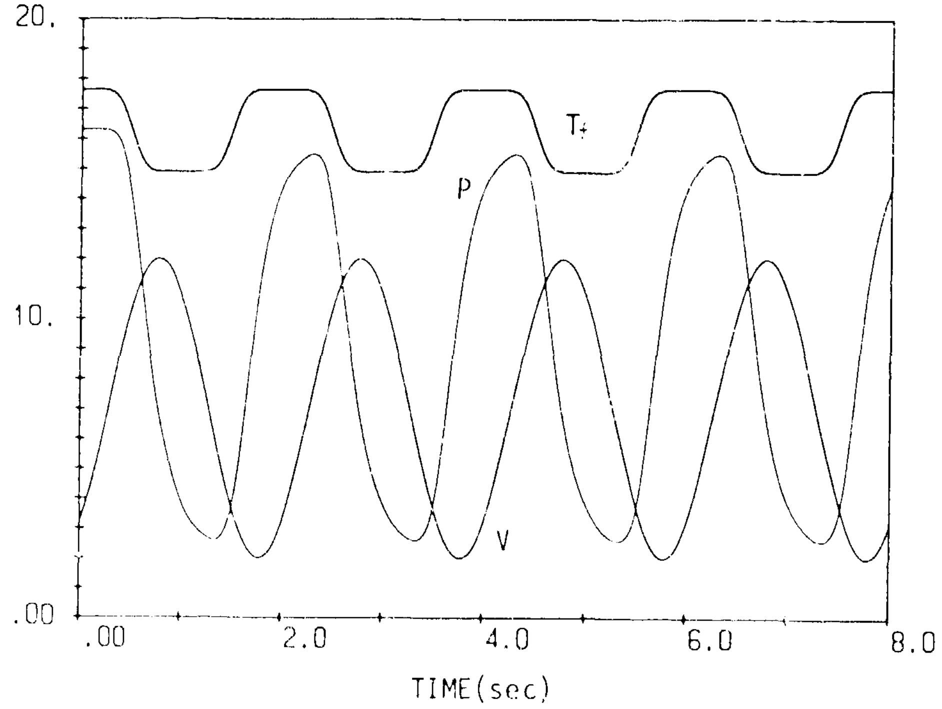

Figure 4. Cyclic response of the pressure (case (b) in Fig. 2).

Figure 5 shows the PV diagrams of different phase angles. In the case of $\Psi = 0$ degrees, the figure is similar to that of Stirling or VM cycle, but if the phase angle increases to 40 degrees, the figure is close to that of G-M cycle which gives maximum cooling power per unit expansion volume. The effects of the thermal conductance, heat capacity and the phase angle on the maximum pressure difference and the PV work (indicated as Q) are plotted on Figure 6 to 8 respectively. In these figures, fixed values of the parameters listed on table 1 are used except the parameter used on X axis. We found the effect of the heat transfer rate is most important

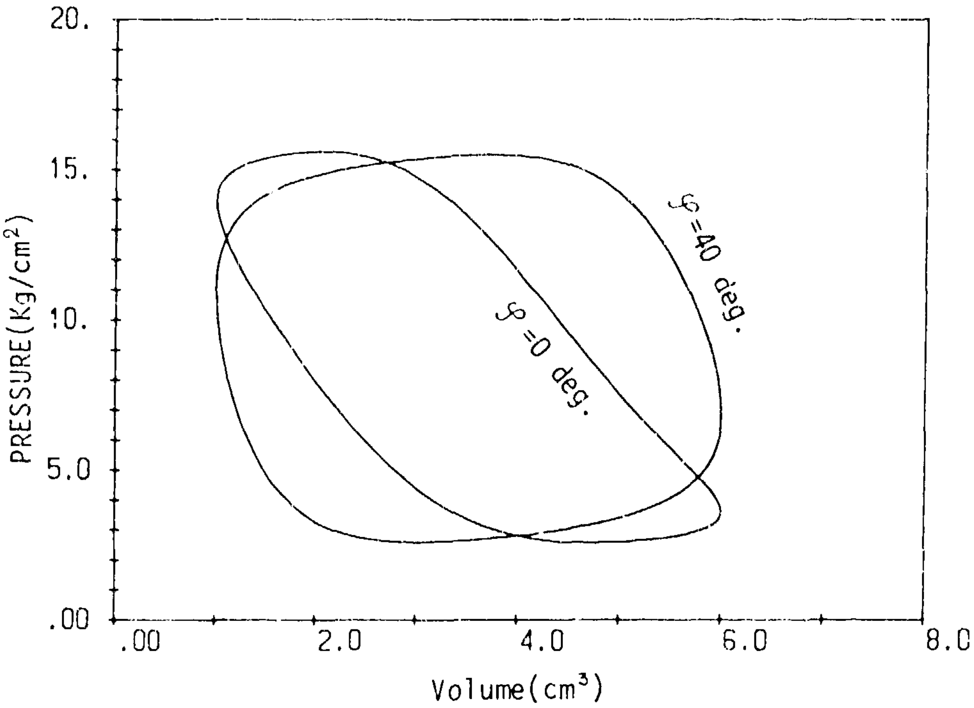

Figure 5. PV diagrams of the regenerative cycle.

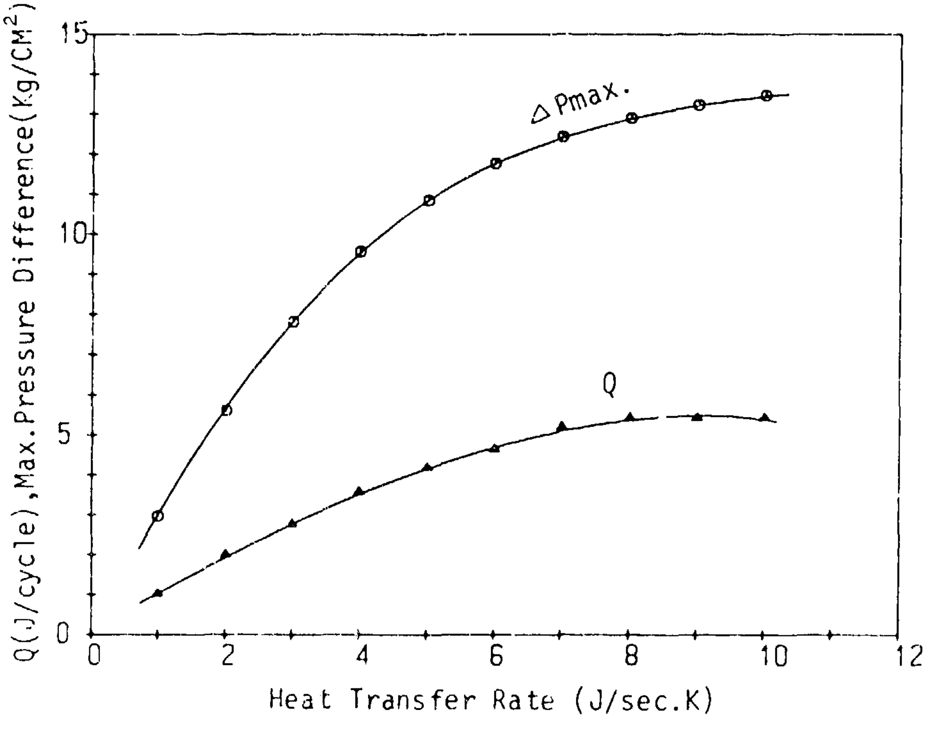

Figure 6. Effect of the heat transfer rate.

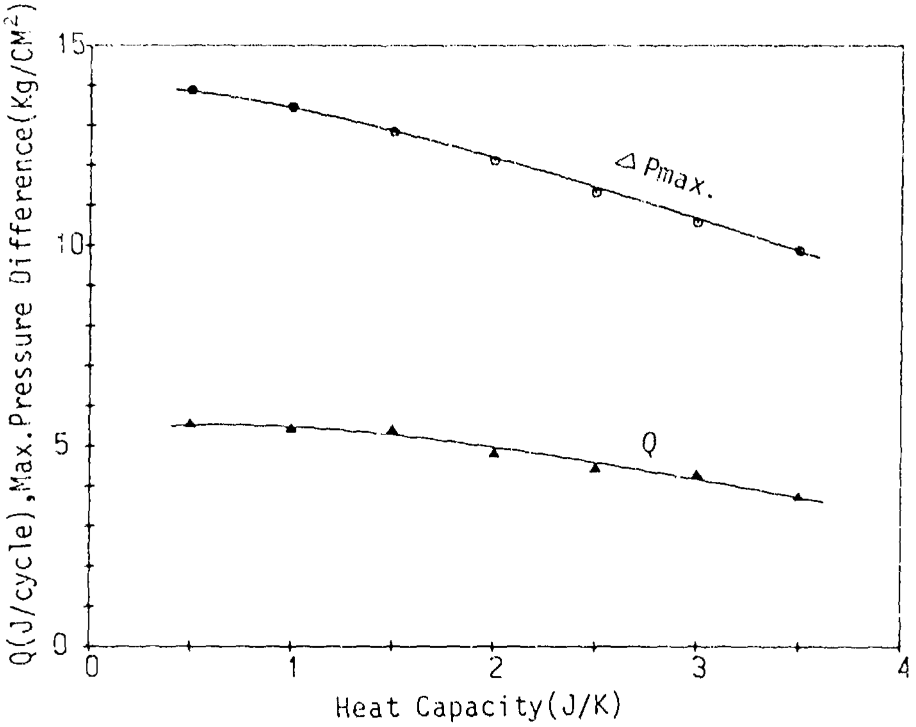

Figure 7. Effect of heat capacity.

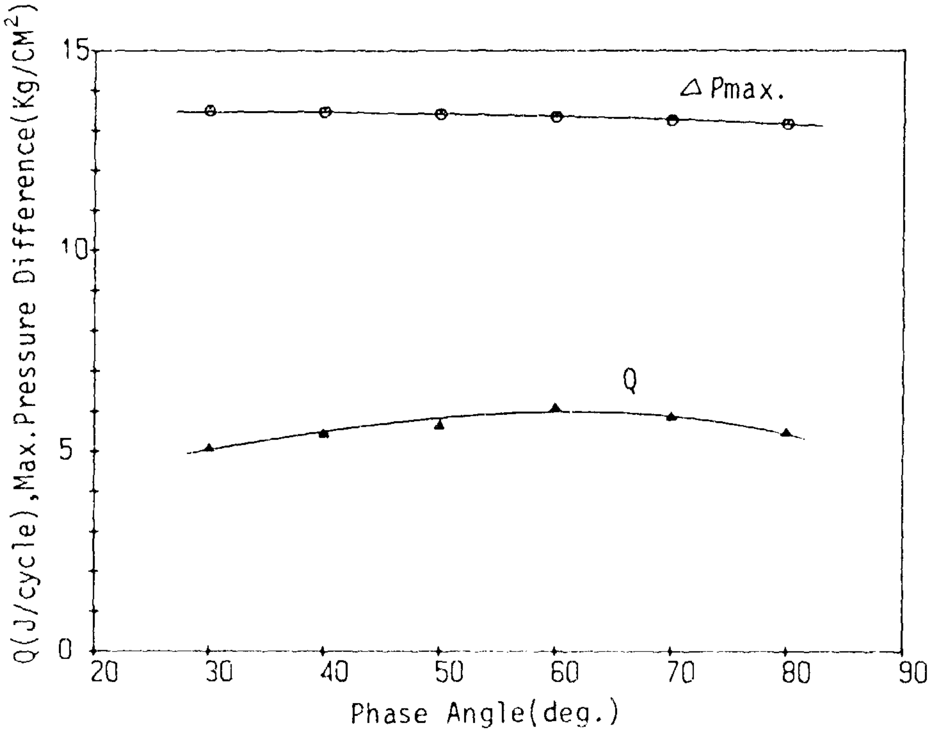

Figure 8. Effect of the phase angle.

to increase the maximum pressure difference; however, the increasing heat transfer area increases the heat capacity of the wall, which decreases the maximum pressure difference. Therefore we have to use the thin wall material having low specific heat.

Figure 8 indicates the effect of the phase angle is not significant; however, large phase angles may not be desirable for regenerator efficiency because the regenerator mass flow rate per unit expansion work may increase. This effect is well expressed by the shape of PV diagram.

4. Experimental Results

For the preliminary experiments, a number of stainless steel capillary tubes were used as the hydride receptacle for increasing the heat transfer area per unit mass of the hydride. The outer diameter of the tube is 1.6 mm, the thickness is 0.15 mm, and one end is closed and the other open to the gas space. The hydride we used here is LaNi5 powder of about 60 mesh. In the first experiment, we used seven capillary tubes, each having a length of 23 mm, as the hydride receptacle. The total mass of LaNi5 in the capillary tubes was 1.2 grams and the gas volume was about 1.1 cm^3. Hydrogen gas of 0.96 wt% has been absorbed at 293K. The secondary fluid is flowing water.

Figure 9 shows the desorption process when the water temperature increased from 298K (25°C) to 353K (80°C). Figure 10 shows the absorption process. To estimate the order of pressure response, we defined τm as the required time to reach the mean pressure following the step change of the secondary fluid temperature. The measured value of τm is about 0.9 seconds for desorption and is about 1.0 second for absorption. The pressure response has been significantly improved, but these values still do not satisfy the requirement of the regenerative cryocooler without valves.

In the second experiment, we used nine capillary tubes, each having a length of 29mm, as the hydride receptacle, as shown in Figure 11 (a). The cross section of the tube was flattened as shown in Figure 11 (b) for reducing the amount of LaNi5 per unit heat transfer area. The total mass of LaNi5 was 1.3 grams. The heat transfer area per unit LaNi5 was increased by about 50% in comparison to the first test device using seven circular tubes. One of the test results of cyclic pressure response is shown in Figure 12, where a constant volume gas space was 1.0 cm^3 and the cycle frequency was 30 rpm. The maximum pressure difference was 4.9 kg/cm^2 and a pressure ratio of 1.6 was observed under the temperature swing of the secondary fluid between 310 K (37°C) and 355 K (82°C).

Owing to the lack of an effective heating system for the secondary fluid, we could not obtain a higher temperature difference under the high flow rate of the secondary fluid. However if the secondary fluid heating system was improved, the hydride compressor described here could be applied to a regenerative cryocooler.

The most simple applications of this compressor unit will be a surface heat pumping cycle, which is known as a pulse tube refrigerator. The possible arrangement

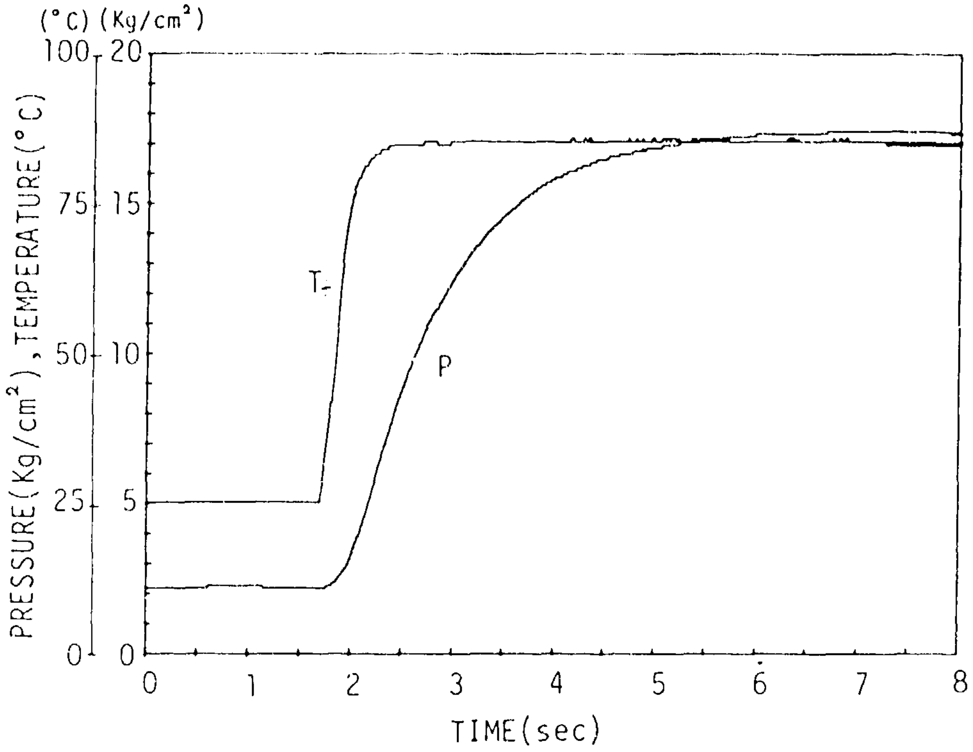

Figure 9. Experimental results of the pressure response (desorption).

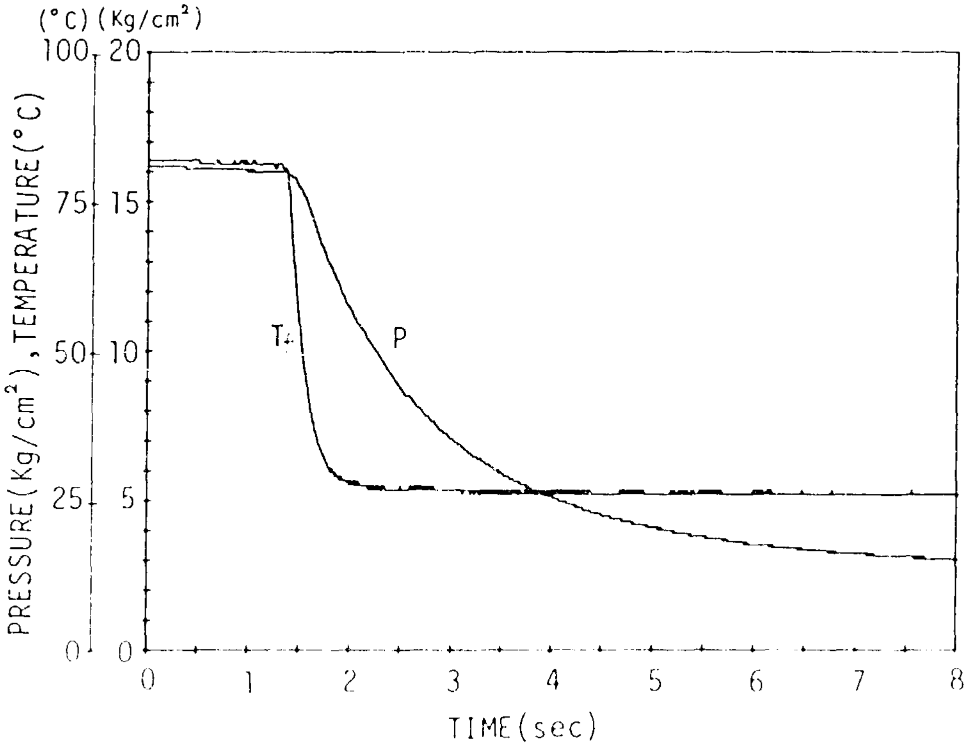

Figure 10. Experimental results of the pressure response (absorption).

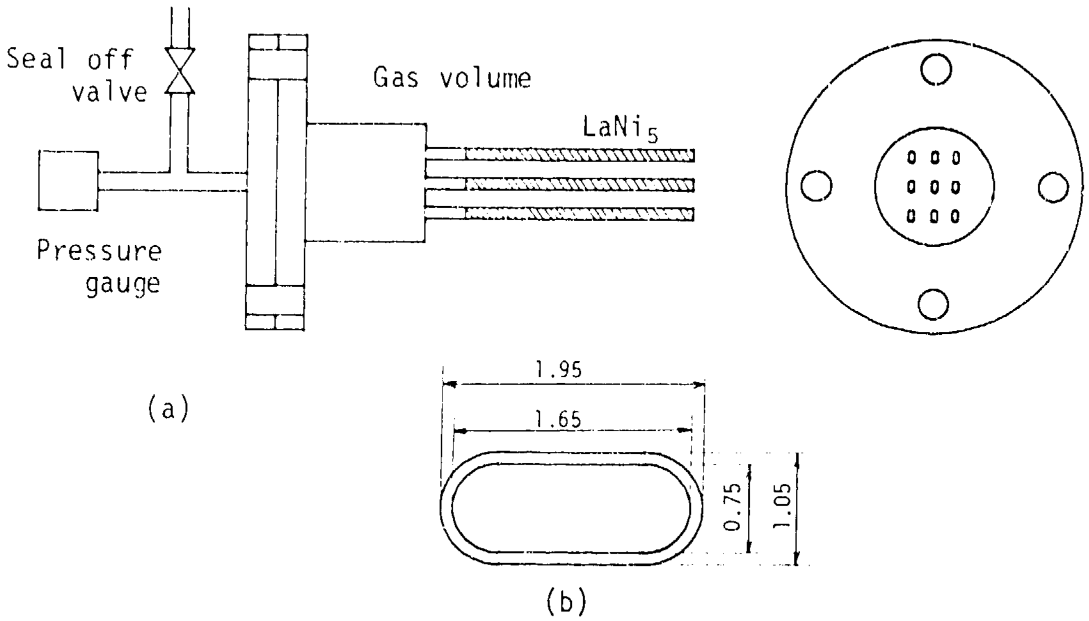
Seal off valve
Gas volume
$LaNi_5$
Pressure gauge
(a)
1.95
1.65
0.75
1.05
(b)

Figure 11. Schematic of the test device.

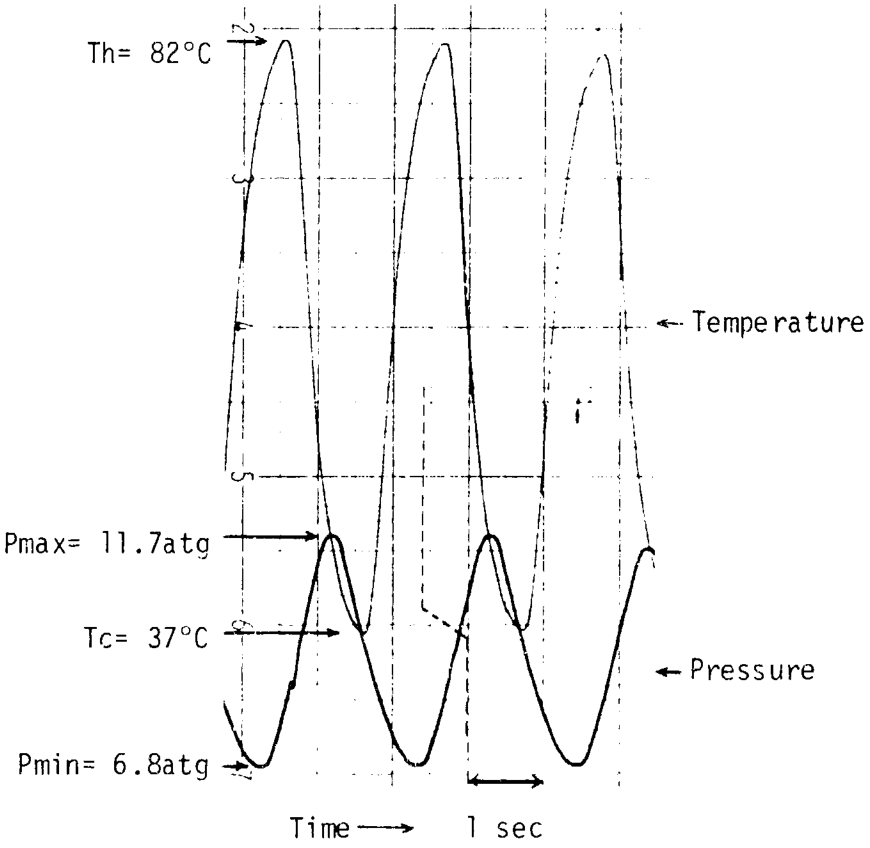

Figure 12. Experimental result of cyclic pressure response.

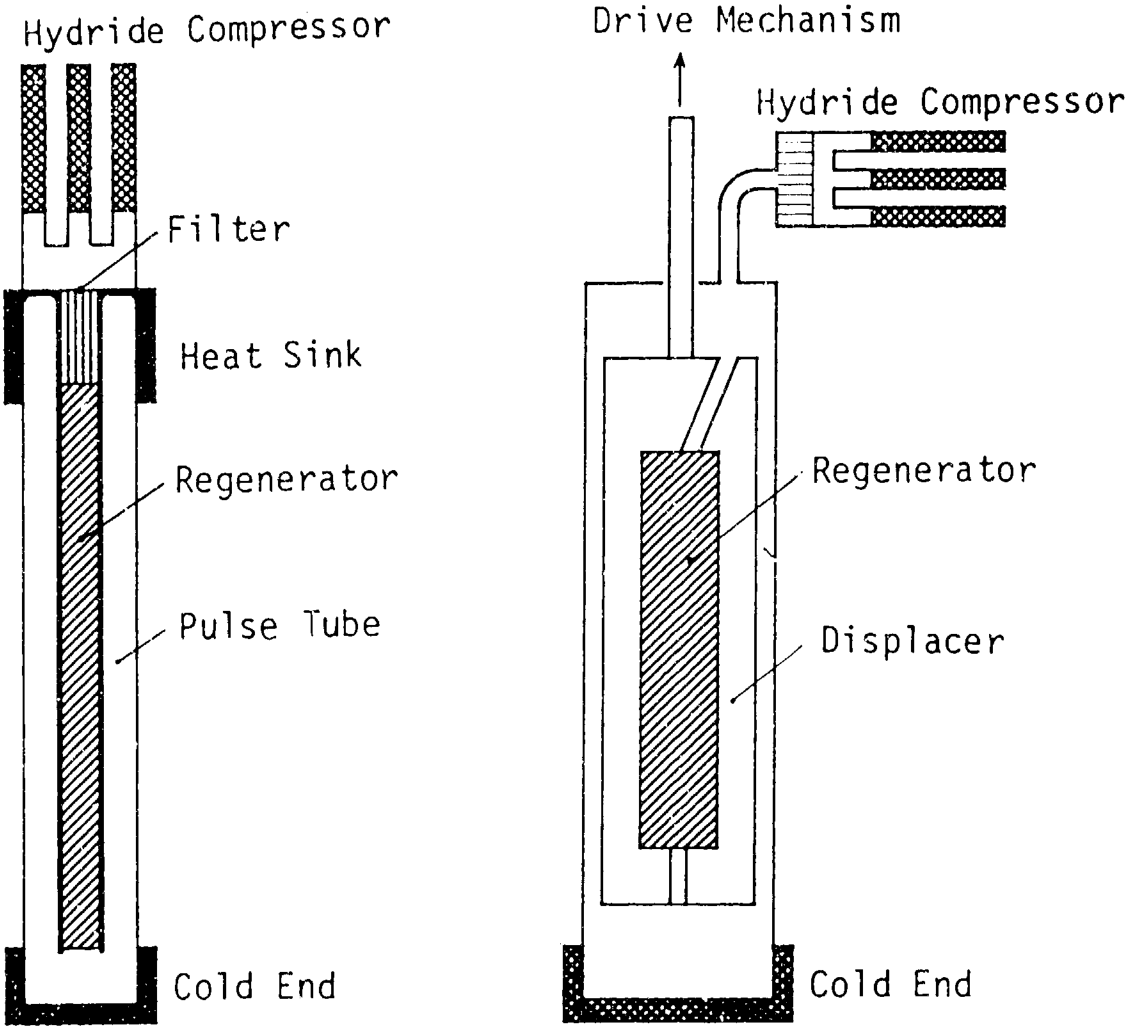
Hydride Compressor
Filter
Heat Sink
Regenerator
Pulse Tube
Cold End
Drive Mechanism
Hydride Compressor
Regenerator
Displacer
Cold End

(a) Pulse tube refrigerator (b) Regenerative cooler with displacer

Figure 13. Possible arrangement of crycoolers coupled with the hydride compressor.

of the pulse tube refrigerator coupled with this compressor unit is shown schematically in Figure 13(a). Figure 13(b) shows the application to a regenerative cryocooler having a displacer such as split Stirling or VM cycle.

5. Conclusion

A simplified scheme for realizing a high response hydride compressor was developed which can be used for the compression part of the regenerative cryocoolers directly without any valves. The parametric calculation and the preliminary experiments using LaNi5 as the hydride material give the following results:

(1) A high response hydride compressor, which could be applied to a pulse tube refrigerator or other regenerative cryocoolers having a cold displacer.
(2) To realize a high pressure response the amount of the hydride must be minimized. As a result, a low cost cryocooler could be realized.
(3) As a concrete design of the hydride receptacle, application of the thin walled and flattened capillary tubes was proposed.

However a number of problems which must be settled remain. These are:

(1) Prediction of the life time limits of the hydride due to degradation of performance.
(2) Low pressure drop filter design.
(3) System design of the secondary fluid for the specified application of the cryocooler.

We wish to acknowledge to M. Kawade (ETL) and Y. Baba (JECC), who gave us an opportunity to conduct this study.

6. References

[1] J.A. Jones, "LaNi5 Hydride Cryogenic Refrigerator Test Results", Refrigeration for Cryogenic Sensors, NASA Conference Publication 2287, p357-P373, (1983).

[2] C.K. Chan, "Optimal Design of Gas Adsorption Refrigerator for Cryogenic Cooling", Refrigeration for Cryogenic Sensors, NASA Conference Publication 2287, p323-p341, (1983).

[3] K.B. Sigurdson, "A General Computer Model for Predicting the Performance of Gas Sorption Refrigerators", NASA Conference Publication 2287, p343-p355, (1983).

[4] J.A. Jones, "Hydride Absorption Refrigerator System for Ten Kelvin and Below", Proceedings of the Third Cryocooler Conference, NBS Special Publication 698, p53-p64, (1985).

DEVELOPMENT OF AN 80-120 K
CHARCOAL-NITROGEN ADSORPTION CRYOCOOLER

S. BARD

Jet Propulsion Laboratory
California Institute of Technology
Pasadena, California 91109

The design, development, and testing of a charcoal-nitrogen adsorption cryocooler is described. The cryocooler was operated between 100 and 120 K and produced 0.5 W of cooling at 118 K. Designs and performance predictions of optimized 80 K and 118 K spaceborne systems are also presented. Because of their many attractive features, particularly the absence of wear-related moving parts and the ability to be combined in cascade refrigeration systems to provide cooling in the 4 to 150 K range, adsorption cryocoolers are an ideal choice for cryogenic cooling applications on many long duration space missions.

Key words: Adsorption; charcoal; cryocoolers; cryogenic; gas adsorption; Joule-Thomson; nitrogen; refrigeration; sorption.

1. Introduction

Development of reliable cryogenic systems for long duration spaceborne operation is becoming a high priority issue [1-5],[1] with typical applications including infrared sensors for detection, tracking and surveillance, gamma and X-ray astronomy, storage of cryogenic propellants and other fluids, and Josephson junction devices. Because they have no wear-related moving parts, non-mechanical adsorption cryocoolers have the potential for operating reliably for over 10 years, far longer than present mechanical systems. They also offer the potential of being relatively simple, require no maintenance, generate negligible vibration and electromagnetic interference, can recover from trace gas contamination effects, can be easily scaled to accommodate different heat loads, and can be powered by waste heat from a spacecraft nuclear or solar thermal energy source.

The ability to use chemical and physical adsorption processes to create a non-mechanical compressor for use in cryogenic refrigeration systems has been recognized for many years. A hydrogen refrigerator delivering 1 W at 25 K using a $LaNi_5$ hydride thermal chemisorption compressor has been demonstrated by Van Mal and Mijnheer [6], and again more recently by Jones [7]. The use of zeolite, silica gel and charcoal as adsorbents for various gases in cryogenic refrigerator systems has been described by Hartwig [8], Kidnay and Hiza [9], and Chan [10].

---

[1] Numbers in brackets refer to literature references listed at the end of this paper.

The first laboratory demonstration model of a charcoal/nitrogen adsorption cryocooler has been developed and successfully tested at JPL. Results of initial feasibility experiments are reported here along with optimal designs and predicted performance characteristics of 80 K and 117.5 K flight systems. The 80-120 K range is a typical requirement of many infrared detectors. The described flight systems can be used to cool detectors requiring these operating temperatures or as upper stages in a liquid helium (4-10 K), liquid hydrogen (14-30 K), or solid hydrogen (7-14 K) cascade system.

2. Principle of Operation

When a gas is brought into contact with a solid, intermolecular attractive forces cause some of the molecules to be retained at the solid surface. The number of molecules adsorbed at a given temperature and pressure is related to the surface area of solid adsorbent. Certain substances, notably charcoal, have a very porous structure. As a result, their effective surface areas are enormous, in some cases well over 1000 m^2/g [11,12], and they will adsorb large quantities of gas.

The amount of gas adsorbed increases as the adsorbent temperature is reduced. Gas is desorbed as the adsorbent temperature is raised, and in a closed container, moderately high pressures can be produced. By thermally cycling a number of canisters filled with charcoal, it is possible to provide an essentially continuous flow of high pressure gas, thus creating a non-mechanical compressor. Cooling can be achieved by expanding the compressed gas through a Joule-Thomson (J-T) valve. The only moving parts in the whole system are self-operating check valves. Since the check valves operate at room temperature and at very low frequency, about once every two minutes, they can be expected to last for many years.

2.1 Compressor Cycle

An idealized thermodynamic compressor cycle is shown as the dashed curve in figure 1, superimposed on charcoal/nitrogen adsorption isotherms. The compressor is cooled and depressurized between state points (d) and (a). Further cooling from (a) to (b) causes the inlet check valves to open, admitting gas into the compressor. Heating from (b) to (c) pressurizes the compressor. Additional heating from (c) to (d) causes the outlet check valves to open, allowing high pressure gas to flow out of the compressor.

The schematic in figure 2 shows four compressors integrated into a simple refrigeration system. A relatively constant gas flow rate can be produced by using four compressors, each operating in a different phase of the cycle at any time.

2.2 Refrigeration Cycle

The adsorption compressors can be integrated into a precooled Joule-Thomson (Linde-Hampson) refrigeration system [13], as shown in figure 2. The high pressure

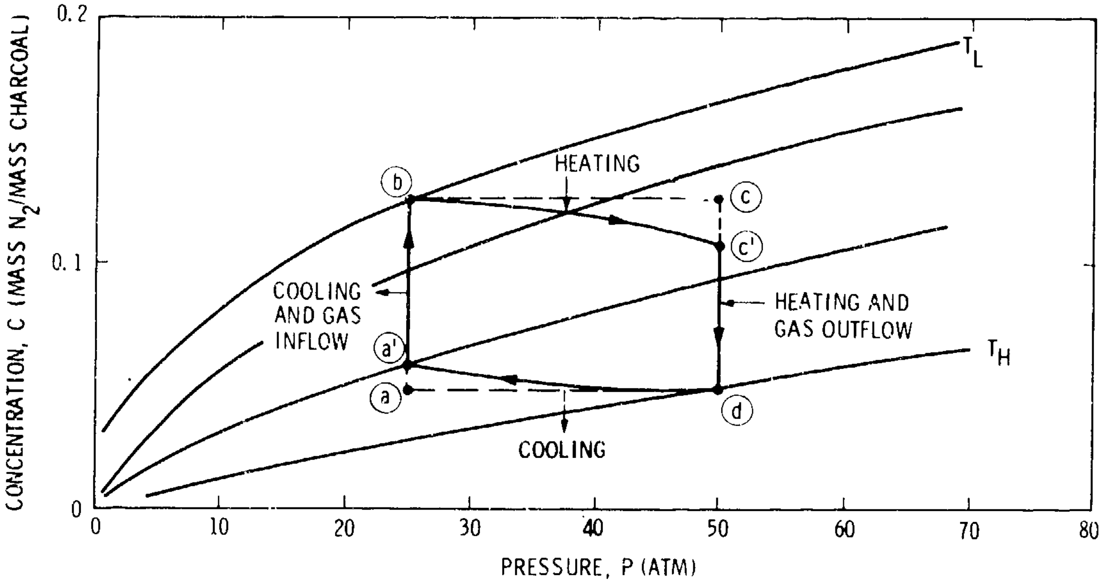

Figure 1 Charcoal/nitrogen adsorption compressor cycle.

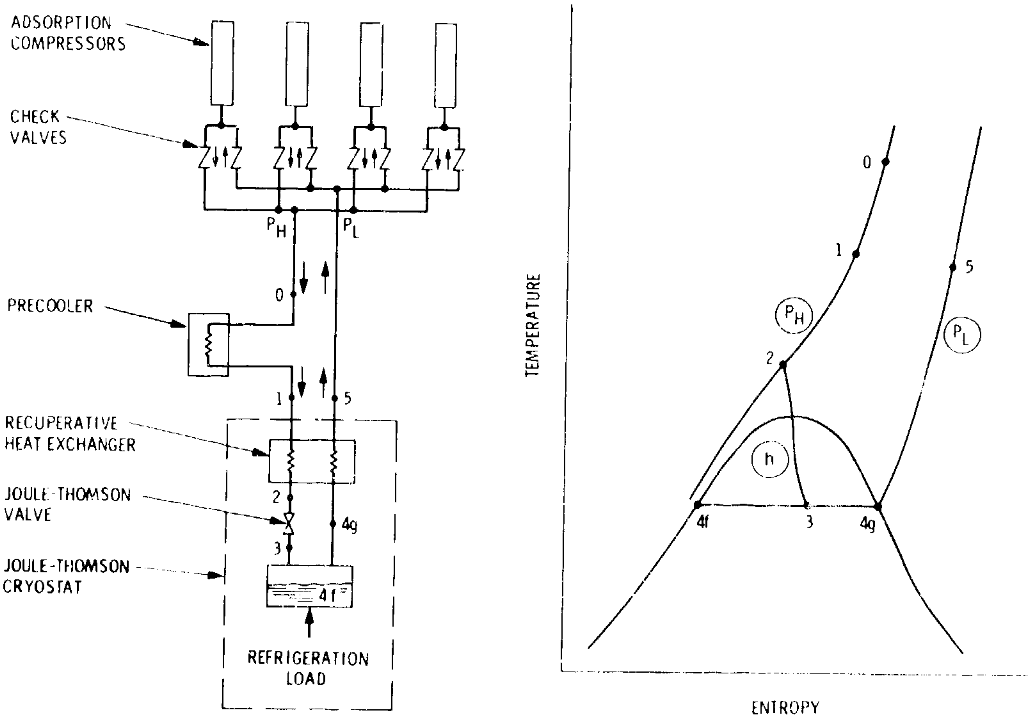
ADSORPTION COMPRESSORS
CHECK VALVES
P_H
P_L
PRECOOLER
0
1
5
RECUPERATIVE HEAT EXCHANGER
2
JOULE-THOMSON VALVE
3
4g
JOULE-THOMSON CRYOSTAT
4f
REFRIGERATION LOAD
TEMPERATURE
ENTROPY
0
1
5
P_H
P_L
2
h
4f
3
4g

Figure 2 Functional schematic and temperature-entropy diagram of an adsorption compressor precooled Joule-Thomson refrigeration cycle.

compressor outlet gas is first precooled (process 0-1) with passive radiators, a thermoelectric cooler, or a dry ice/alcohol bath (test configuration). The compressed gas is further cooled in a counterflow recuperative heat exchanger to condition (2) and then expanded isenthalpically through a Joule-Thomson (J-T) valve. If the gas at condition (2) is below its inversion temperature, it experiences a decrease in temperature. The temperature at (2) may be so low that expansion causes condition (3) to be located within the liquid-vapor envelope and the fluid will partially condense, as shown. At (3) it will exist partly as saturated liquid (4f) and partly as saturated vapor (4g). The refrigeration load vaporizes the liquid and the low pressure gas returns through the recuperative heat exchanger to the compressor (process 4g-5).

3. Analysis

The thermodynamic efficiency of a cryocooler is often expressed as the specific power requirement, SP, which is the input power required per watt of cooling. Expressions for SP, as well as the mass flow rate obtained from adsorption compressors, will now be derived.

The cooling capacity, $\dot{Q}_c$ is proportional to the gas mass flow rate, $\dot{m}$, and the difference in enthalpy between the heat exchanger outlet and inlet gas, i.e.

$$\dot{Q}_c = \dot{m}(h_5 - h_1) \tag{1}$$

The designer chooses the high and low operating pressures, P_H and P_L, and precooling temperature, T_1, which determines h_1, where the numerical subscripts refer to state points in figure 2. These parameters along with the heat exchanger effectiveness, give h_5. For an ideal compressor, the gas mass flow rate is given by

$$\dot{m}_{ideal} = m_s \Delta C/\Delta t \quad , \tag{2}$$

where m_s is the mass of solid adsorbent and C is the adsorbate concentration, given by the mass of gas adsorbed per unit mass of solid adsorbent. ΔC is the change in concentration in the compressor during the desorption phase of the compressor cycle, occurring during the time interval Δt. For the ideal compressor, $\Delta C = C_c - C_d = C_b - C_d$. The mass of gas liberated during compression is represented by $m_s \Delta C$.

As shown in [14], the void volume effect causes the flow rate produced by the compressors to be somewhat less than that given by eq. (2), as the real compressor cycle follows the solid curve in figure 1. The real flow rate, $\dot{m}$, is given by

$$\dot{m} = [m_s \Delta C + \Delta\rho(V_v + V_l)]/\Delta t \quad , \tag{3}$$

where V_l is the void volume in the plumbing line between the compressor and the check valves, which is a function of the system design and hardware. $\Delta\rho = \rho_b - \rho_d$ is the change in gas density from condition (b) to (d), which is always negative. The compressor void volume can be expressed [14] as

$$V_v = (m_s/\rho_s)[(1-f_o)/f_o - f_{micro}/f_s] \tag{4}$$

where ρ_s is the density of solid, non-porous, carbon (about 2.1-2.2 g/cm^3). The charcoal packing factor is given by $f_o=\rho_{eff}/\rho_s$, where the bulk charcoal density $\rho_{eff} = m_s/V_c$, and V_c is the total available volume in the compressor. f_{micro} and f_s are micropore and solid carbon particle volume fractions, and along with f_o are functions of the type and preparation of the charcoal. f_s and f_{micro} can be determined by mercury porosimetry and by examination of charcoal/nitrogen isotherms [11,12,14,15].

The differential heating required to liberate and compress the gas during any part of the compression and desorption phase of the compressor cycle (b-c-d) is given by

$$dQ_H = (m_s c_{ps} + m_c c_{pc})dT + m_g dh + m_s \Delta H dC \tag{5}$$

where $m_c c_{pc}$ represents the product of mass and specific heat of the compressor container and heat transfer enhancement matrix, c_{ps} is the solid adsorbent specific heat, and m_g is the gas mass. The differential change in temperature, gas enthalpy, and concentration are represented by dT, dh and dC, respectively. ΔH is the negative of the isosteric heat of adsorption given by the adsorption analogue of the Clausius-Clapeyron equation:

$$\Delta H = R[\partial(\ln P)/\partial(1/T)]_C \tag{6}$$

The specific power, SP, is defined as the reciprocal of the coefficient of performance, i.e.

$$SP = 1/COP = \dot{Q}_H/\dot{Q}_C \tag{7}$$

Given charcoal characteristics and adsorption isotherms, C(T,P), eqs. (1)-(7) can be solved, and eq. (5) can be integrated to determine the specific power requirement for any gas/sorbent combination under various operating conditions. A computer program which numerically solves these equations [16] was used to design the feasibility demonstration cooler and to obtain the optimum flight model designs described later.

4. Experiment

Figure 3 shows a functional schematic of the laboratory demonstration cooler. The precooler is a 194.7 K dry ice/ethyl alcohol bath. The four compressors are

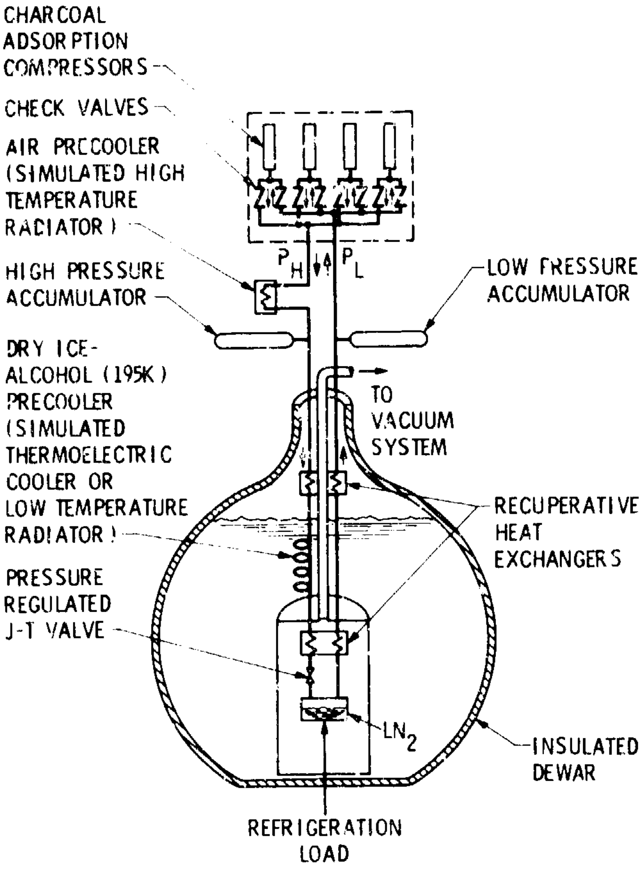
CHARCOAL ADSORPTION COMPRESSORS
CHECK VALVES
AIR PRECOOLER (SIMULATED HIGH TEMPERATURE RADIATOR)
HIGH PRESSURE ACCUMULATOR
DRY ICE-ALCOHOL (195K) PRECOOLER (SIMULATED THERMOELECTRIC COOLER OR LOW TEMPERATURE RADIATOR)
PRESSURE REGULATED J-T VALVE
P_H
P_L
LOW PRESSURE ACCUMULATOR
TO VACUUM SYSTEM
RECUPERATIVE HEAT EXCHANGERS
LN_2
INSULATED DEWAR
REFRIGERATION LOAD

Figure 3 Schematic diagram of the charcoal/nitrogen adsorption cryocooler laboratory demonstration system.

Figure 4 Charcoal/nitrogen adsorption cryocooler laboratory demonstration system.

each constructed of 1.59 cm (5/8 in) dia by 33 cm (13 in) long, 17-7 PH stainless steel tubes, heat treated to the TH1050 condition. This high strength steel enables the use of $3.56\text{x}10^{-2}$ cm (0.014 in) thin walls, which minimizes m_c in eq (5) and ultimately SP. A 6% density aluminum foam is linepress fit into the tubes in order to enhance the radial heat transfer through the charcoal. The tubes are filled with Barneby-Cheney type GI (BCGI) charcoal, which is first prepared by grinding it in a ball mill and filtering it through a 400 mesh (38 micron dia) sieve. A 0.5 micron sintered stainless steel filter is laser welded onto one end of the tube to prevent charcoal powder from contaminating the rest of the system. The nitrogen working fluid flows into and out of the same end of the tube, enabling the constant flow reversal to keep the filter unclogged.

Kapton film heaters are bonded to the outside of the compressor tube to heat the compressors to T_H~400 K. The average total input power at any time, Q_H, was

150 W throughout the test. The compressors are cooled to T_L=250 K by flowing a coolant in an insulated annular jacket surrounding each unit.

The high pressure gas produced by the compressors flows through the outlet check valves and is cooled convectively in air. The check valves open at a pressure differential of about 5 psi (0.34 atm, 0.034 MPa). The gas then flows through a recuperative heat exchanger, a coiled tube heat exchanger, and the J-T cryostat. The coiled tube heat exchanger precools the incoming gas to 194.7 K, and along with a vacuum chamber containing the recuperative heat exchanger and J-T valve, are all immersed in a dewar containing a dry ice/alcohol bath, as shown in figure 3. The large pressure, mass flow, and refrigeration load fluctuations predicted in [18] are avoided by the use of large 2.5 liter accumulator tanks located downstream of the compressor outlet and upstream of the inlet, and the pressure regulated J-T valve.

The J-T valve is a modified version of the pressure regulated adjustable check valve used by Jones [7], in which the desired pressure drop in the valve can be set by adjusting the check valve spring tension. Besides maintaining the desired pressure drop, the pressure regulated valve has the additional advantage of being less susceptible to contamination [7]. The effect of contaminants in the system are also reduced by the use of a molecular sieve and a sintered stainless steel filter directly upstream of the J-T cryostat.

Temperatures are measured with thermocouples mounted on each compressor and located at the cryostat inlet and outlet. A silicon diode temperature sensor is mounted on the J-T valve for accurate ($\pm$0.1 K) cold finger temperature measurements. Pressures are measured to $\pm$2 psia (0.14 atm, 0.014 Mpa) with pressure transducers mounted at each compressor and accumulator tank. Flow rates are measured by closing the J-T inlet valve for three to four minutes and monitoring the pressure increase in the calibrated accumulator volume as a function of time.

Figure 4 shows a picture of the adsorption cryocooler. Clearly visible near the top are the four ice covered faces of the compressor coolant jackets with their thermocouple, pressure transducer and heater feedthroughs. The flow control panel can be seen in the center of the picture and the inlet to the dry ice/alcohol precooler and J-T cryostat is at the lower right hand corner.

The system operation is controlled by a Hewlett Packard HP 9836CS minicomputer connected to an HP 3497 data acquisition/control system. Software was developed to continuously monitor temperature and pressure transducers, control system timing, open and close solenoid valves, and switch heater power supplies on and off.

5. Experimental Results

The system was operated for over 60 hours at various operating pressures and temperatures. Table 1 summarizes measurements of the high and low operating pressures and flow rates, and also shows comparisons to flow rates predicted by eq. (3). The experimental flow rates are all within 15% of predictions. The gross cooling loads and specific powers in the final columns of table 1 are calculated with eqs. (1) and (7) using the measured flow rates and pressures, assuming a heat exchanger effectiveness of 0.98.

A heater on the J-T valve was used to simulate useful cooling loads from a detector. Unfortunately, intermittent instability of the spring loaded J-T valve made it difficult to maintain a steady pressure drop over the time required to boil off any accumulated liquid N_2 and achieve steady state conditions. Therefore, accurate useful cooling load measurements could not be obtained. However, J-T parasitic heat loads, estimated from heat-up rates to be between 0.04 and 0.06 W, can be subtracted from the gross cooling loads in table 1 in order to estimate useful cooling loads. Note that the J-T instability problem was avoided in the system described by Jones [7] by using a metal-to-metal seat in the J-T valve.

Table 1. C/N_2 adsorption cryocooler test results (T_H=400 K, T_L=250 K, T_1=195 K).

P_L (atm)	P_H (atm)	T_C (K)	$\dot{m}_{predict}$ (g/sec)	$\dot{m}_{exper}$ (g/sec)	$\Delta\dot{m}\%$[a] (%)	Volumetric flow rate (sccs)	$\dot{Q}_C$ (W)	$SP=\dot{Q}_H/\dot{Q}_C$ (W/W)
9.3	29.0	102.8	0.019	0.017	-11	13.9	0.143[b]	629
10.8	27.2	105.1	0.026	0.022	-15	18.4	0.151[b]	596
13.2	37.9	108.4	0.021	0.024	14	19.9	0.272[b]	331
15.9	35.2	111.4	0.033	0.034	3	28.5	0.292[b]	308
18.8	57.1	114.7	0.017	0.018	6	14.8	0.336[b]	447
20.4	55.2	116.2	0.024	0.024	0	20.3	0.417	360
21.2	54.3	116.9	0.027	0.025	-7	20.8	0.405	371
22.2	53.3	117.9	0.030	0.030	0	25.0	0.453	331
22.3	53.2	117.9	0.030	0.032	7	26.9	0.484	310
23.4	51.7	118.8	0.034	0.032	-6	26.6	0.435	345
25.7	49.2	120.7	0.042	0.039	-7	32.2	0.426	352
26.4	48.0	121.2	0.045	0.042	-7	34.6	0.416	360
30.1	44.8	124.0	0.057	0.053	-7	44.5	0.335	447

[a] $\Delta\dot{m}\% = 100 \times (\dot{m}_{exper} - \dot{m}_{predict})/\dot{m}_{predict}$

[b] system operated with only 3 compressors for these cases

The system was originally designed to cool to below 120 K with a gross cooling capacity of 0.4 W. This goal was easily met with various operating conditions shown in table 1. For example, with P_L=22.3 atm (2.26 MPa) and P_H=53.2 atm (5.39 MPa), a cooling capacity of 0.48 W at 117.9 K was obtained with an SP value of 310 watts/watt.

An interesting phenomenon was observed due to the relatively low J-T parasitic heat loads. Operating temperatures below saturation were achieved because the heat load was low enough, and the flow rate high enough, that the J-T expansion occurred in the subcooled liquid region. For example, a cooling temperature of T_C=102 K was achieved for P_H=53.2 atm (0.39 MPa) and P_L=18.8 atm (1.9 MPa), although the saturation temperature corresponding to P_L=18.8 atm (1.9 MPa) is T=114.7 K. It may be possible to exploit this effect in a hydride chemisorption cryocooler by operating in the hydrogen subcooled liquid region, for cooling applications in the 10-15 K range [17].

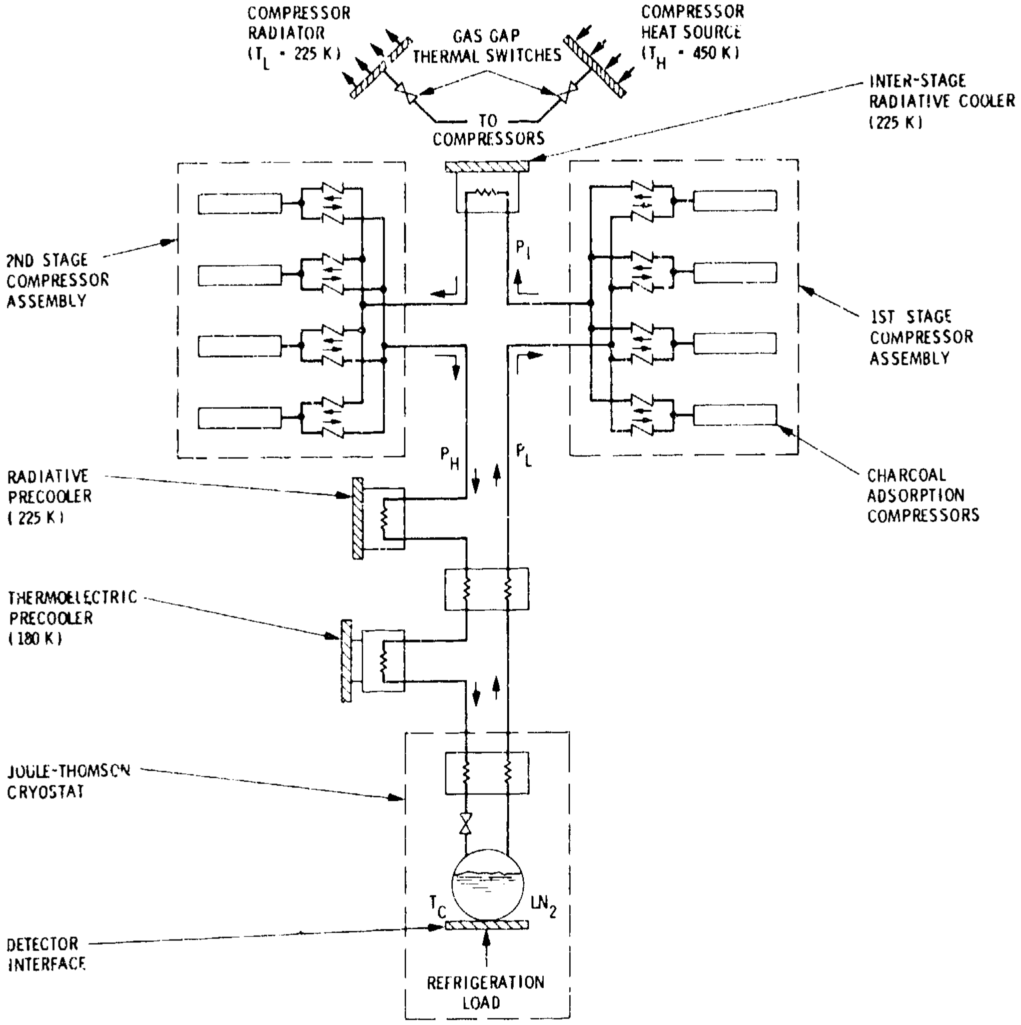
COMPRESSOR RADIATOR (T_L = 225 K)
GAS GAP THERMAL SWITCHES
COMPRESSOR HEAT SOURCE (T_H = 450 K)
TO COMPRESSORS
INTER-STAGE RADIATIVE COOLER (225 K)
2ND STAGE COMPRESSOR ASSEMBLY
P_I
1ST STAGE COMPRESSOR ASSEMBLY
P_H
P_L
CHARCOAL ADSORPTION COMPRESSORS
RADIATIVE PRECOOLER (225 K)
THERMOELECTRIC PRECOOLER (180 K)
JOULE-THOMSON CRYOSTAT
T_C
LN_2
DETECTOR INTERFACE
REFRIGERATION LOAD

Figure 5 Charcoal/nitrogen adsorption cryocooler flight system schematic.

6. Flight Model Design

The laboratory demonstration cooler was designed to demonstrate the feasibility of the charcoal/nitrogen adsorption refrigerator concept. The design was not optimized with regard to minimizing specific power requirements and system mass. Certain features of the design are peculiar to the laboratory, such as use of a compressor coolant fluid circuit and electrical film heaters to thermally drive the compressors.

An adsorption refrigerator used for an actual spacecraft application would require several design modifications. Compressor heating may be provided by a solar collector or a radioactive thermal energy source while cooling is provided by passive radiators. Thermal cycling can be achieved by using a simple gas-gap thermal switch [17]. The dry ice/alcohol precooler bath can be replaced with a thermoelectric cooler (TEC) operating at T_1=180 K. The TEC will require small amounts of electrical power (less than 15 W for $\dot{Q}_C=1$ W and $T_C=80\text{-}120$ K). Figure 5 shows a schematic of the flight system, including the TEC pre-cooler and two stages of compression. The advantage of multistage compression is discussed in a later section.

As indicated by eq. (3), the void volume in the compressor should be minimized in order to maximize the flow rate and minimize the specific power requirement. The packing factor, and micropore and solid particle volume fractions in the BCGI charcoal used in the feasibility demonstration cooler are estimated as $f_o=0.23$, $f_{micro}=0.396$ and $f_s=0.336$ [14,15]. Fifty percent of the available compressor volume is void space [14]. By using a high pressure pressing technique to reduce the interparticle void volume, Yang has achieved a packing factor of $f_o=0.326$ for BCGI [15], thus reducing the void volume to 29% of the total available compressor volume [14]. Further reductions to 23% void volume can be obtained by using Saran charcoal [12], prepared by the pyrolysis of Saran polymer (polyvinylidene chloride), which has an estimated $f_o=0.423$, $f_{micro}=0.379$ and $f_s=0.455$, and has the further advantage that it can be produced to specific geometric shapes. The flight predictions presented here all assume the use of Saran charcoal and a plumbing line void volume equal to that of the laboratory demonstration cooler, $V_1=7.4$ cm^2.

6.1 Optimum Operating Pressure

The low pressure operating condition, P_L, is determined by the desired cooling temperature, T_c, and is normally equal to the saturation pressure corresponding to T_c if condition (3) in figure 2 lies within the liquid-vapor envelope. There are two competing effects with regard to the choice of optimum high operating pressure, P_H. As P_H increases, the enthalpy difference, $h_5\text{-}h_1$, increases to some maximum value before decreasing again. If $\dot{m}$ remains constant, the increased enthalpy difference results in an increased Q_c. However, as P_H increases, ΔC decreases as indicated by figure 1, while $|\Delta\rho|$ increases. Equation (3) indicates that this causes a decrease in flow rate which in turn reduces Q_c.

Figure 6 shows the effect of varying P_H for $P_L=21.8$ atm (2.21 MPa), $T_c=117.5$ K, $T_1=180$ K, $T_L=225$ K, and $T_H=450$ K for the flight model design. The specific power is minimized at about $P_H=70$ atm (7.09 MPa) and has a value of SP=116 for the single-stage flight model design. The laboratory demonstration system curve, for $T_1=195$ K, $T_L=250$ K, and $T_H=400$ K is also shown in figure 6 along with the corresponding 117.9 K experimental data point. The experimental SP is within 10% of the predicted value. Note the 60% performance improvement for the flight system conditions relative to the laboratory demonstration system performance.

Further improvement in performance can be obtained by compressing the gas in two or more stages with intercooling between stages [14], with the configuration shown in figure 5. Multistage compression reduces the void volume effect by reducing $|\Delta\rho|$ while also increasing ΔC. The net effect tends to increase the flow rate and reduce SP. Figure 6 shows the effect of varying the high pressure, P_H, for a two-stage compressor system with an intermediate pressure, $P_I=70$ atm (7.09 MPa), under the identical conditions as for the single stage system. The minimum value of SP=95 is achieved at $P_H=130$ atm (13.2 MPa). An intermediate pressure of $P_I=70$ atm was demonstrated to be optimum in [14], although SP is affected by less than 5% if P_I is varied by ± 10 atm (± 1 MPa). The increased complexity of an extra series of compressors and check valves, intercooler heat exchanger, and electronic

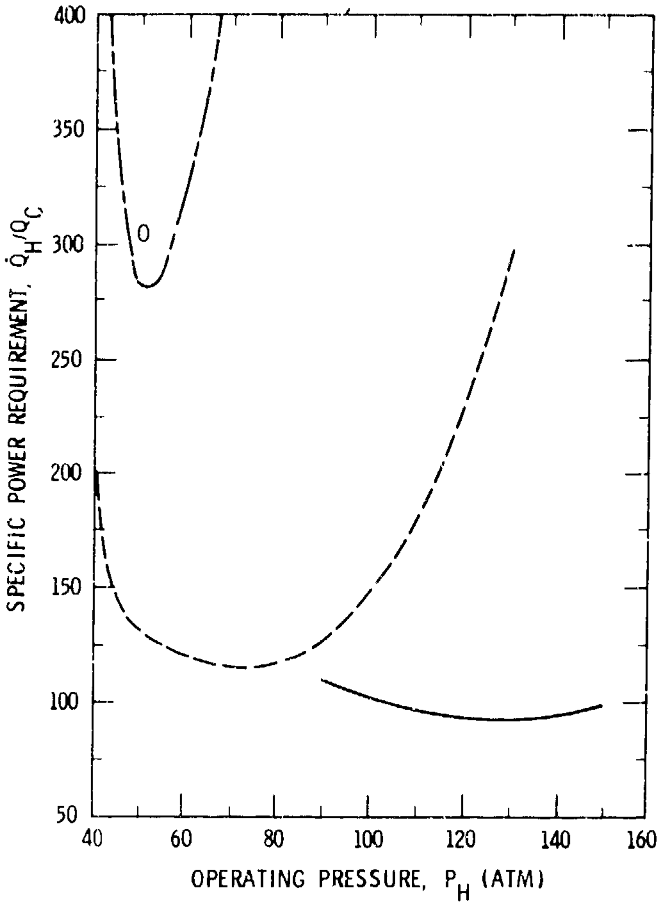

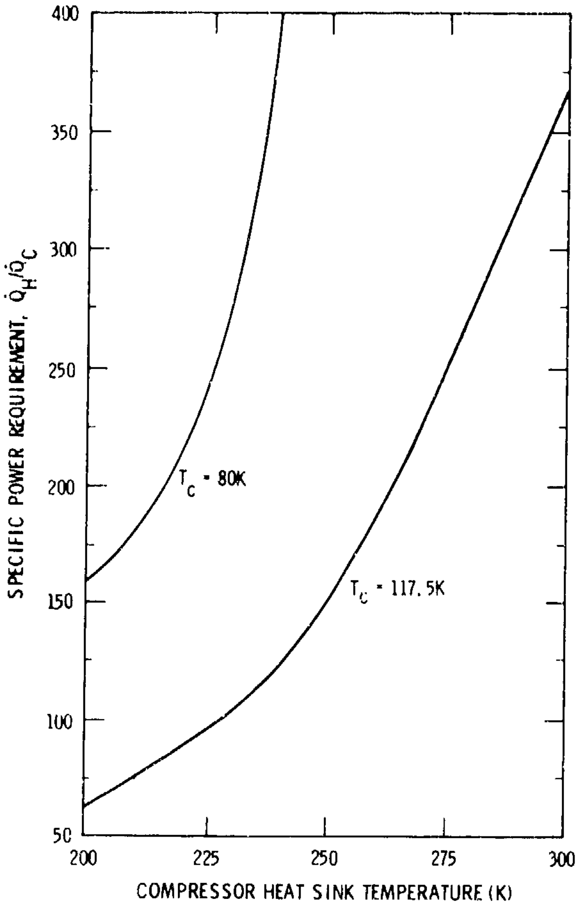

Figure 6 SP vs. P_H for a 117.5 K C/N_2 cryocooler, where:
------- single-stage flight system,
——— 2-stage flight system with P_I=70 atm (7.1 MPa),
— - — laboratory demonstration system (theoretical),
0 laboratory demonstration system (experimental).

Figure 7 SP vs. minimum compressor operating temperature for 80 K and 117.5 K flight systems (assumes optimized 2-stage compressor systems with T_H=450 K).

controls must be traded against the 18% improvement in performance over the optimum single stage compressor design.

The advantage of multistaging is more evident for a T_c=80 K adsorption cryocooler, with P_L=1.35 atm (0.14 MPa), T_1=180 K, and T_L=225 K. This low operating pressure results in a large $|\Delta\rho|$, which increases the void volume effect and also results in a lower available ΔC. The net effect is a reduced mass flow rate which makes a one stage compressor possible for only a small range of pressures (between 40 and 45 atm), resulting in an SP value of over 1000. Therefore, a single stage compressor system is unfeasible. With a first stage operating between P_L=1.35 atm (0.14 MPa) and P_I=20 atm (2.03 MPa), a second stage operating between P_I=20 atm and P_H=100 atm (10.1 MPa), a multistage compressor system can achieve SP=245. These are determined in [14] to be the optimum operating conditions for an 80 K C/N_2 adsorption cryocooler.

Table 2 summarizes optimized flight designs for the 80 K and 117.5 K systems. The mass estimates in the final column are for a complete flight cooler, including multistage compressors. Radiators contribute between 68% and 85% of the total system mass, depending on whether or not they can be shielded from planetary heat inputs. The SP values include the TEC electrical power. If the 180 K thermoelectric precooler was eliminated and replaced with a 225 K radiative precooler, then SP would increase to 151 and 381 for the 117.5 K and 80 K systems, respectively, although the need for any electrical input power would be completely eliminated.

Table 2. C/N_2 Adsorption Cryocooler Flight Design Summary

Refrig Temp T_C (K)	Low Pressure P_L (atm)	Intermed Pressure P_I (atm)	High Pressure P_H (K)	Heat Sink T_L (K)	Heat Source T_H (K)	TEC Power/ Cooling Power (W/W)	Specific Power SP (W/W)	System Mass* (kg)
80	1.35	20	100	225	450	14.3	245	16-36
117.5	21.8	70	130	225	450	14.7	95	7-14

*mass estimates assume low earth orbit; lower value is for radiators which are shielded from planetary heat inputs; higher value is for no shielding.

6.2 Compressor Low Temperature Limit

All of the flight designs discussed thus far and the comparisons shown in figure 6 have assumed a compressor low temperature limit of T_L=225 K. This is a temperature readily obtainable with reasonably sized passive radiators in many low Earth-orbiting applications [17]. The effect on SP of varying T_L is shown in figure 7 for the optimum conditions described in the previous section for the 117.5 K and 80 K coolers. Minimizing T_L is clearly advantageous, due to charcoal's increased nitrogen adsorption capacity below 250 K.

6.3 Alternate Sorption Systems

Preliminary calculations indicate that a 117.5 K charcoal/methane (C/CH_4) adsorption refrigerator may have a lower SP than the optimum charcoal/nitrogen system. The value of (h_1-h_5) will be greater for the C/CH_4 system, but it will be more difficult to obtain a high flow rate since P_L is very low, with a value of 1 atm (0.1 MPa). Just as for the 80 K C/N_2 system, the low P_L will result in a large $|\Delta\rho|$, and therefore a large void volume effect and also a low ΔC. More accurate performance predictions for the methane system and comparisons to the N_2 system are planned, once accurate charcoal/CH_4 adsorption isotherms are incorporated into the adsorption refrigerator computer program [16].

Preliminary calculations also indicate that various oxide chemisorption systems may have lower SP's than the C/N_2 or C/CH_4 systems. A cascaded 140 K charcoal/methane and 80 K oxide chemisorption system with an estimated overall specific power requirement of less than 160 W/W, with heat sink temperatures above 275 K, is currently being developed at JPL.

7. Conclusions

A charcoal/nitrogen adsorption cryocooler has been successfully tested, achieving its design temperature of 117.5 K with a cooling capacity of about 0.5 W. The high and low operating pressure was P_H=53.2 atm (5.39 MPa) and P_L=22.3 atm (2.26 MPa). The system required 150 W input power, resulting in a specific power requirement of SP=310 watts/watt.

An optimized flight design would require considerably lower input power than the laboratory demonstration cooler due to the use of a lower void volume charcoal, a lower precooling temperature achievable with a thermoelectric cooler, and use of multistage compression. Optimized 118 K and 80 K flight systems with multistage compression would have a specific power requirement of 95 and 245, respectively, as summarized in table 2. Lowering the compressor heat sink temperature from 225 K to 200 K reduces the specific power requirement to 62 and 159 for the 118 K and 80 K systems, respectively.

The successful laboratory testing of a charcoal/nitrogen adsorption cryocooler is an important first step in the development of a flight system. Because the adsorption cryocooler has no wear-related moving parts, generates negligible mechanical vibration and electromagnetic interference, and requires no electrical input power, it is an ideal choice for cooling science instrument sensors on many long duration space missions.

Acknowledgements

The support provided by Mark Herring and Alex Goetz, technical assistance provided by Jack Jones, Dennis O'Connor, and Walt Petrick, review of the manuscript by Jim Stultz and Donald Rapp, and the development of the adsorption refrigerator computer model by Katherine Barhydt is deeply appreciated. Special thanks are due to Ron Reynolds, whose technical skills have contributed greatly to this effort.

The research described in this paper was carried out at the Jet Propulsion Laboratory, California Institute of Technology under contract with the National Aeronautics and Space Administration.

8. References

[1] Johnson, A.L., "Spacecraft Borne Long Life Cryogenic Refrigeration Status and Trends," Cryogenics, 23, 339 (July 1983).

[2] Haskin, W. C., "Cryogenics in Space Systems," Meeting of the IRIS Specialty Group on Infrared Detectors, Boulder, CO, (August 2-4, 1983).

[3] Knox, L., Patt, P., and Maresca, R., "Design of a Flight Qualified Long-Life Cryocooler," Third Cryocooler Conference, Boulder, CO, (September 1984).

[4] Bradshaw, T.W., Delderfield, J., Werrett, S. T., and Davey, G., "Performance of the Oxford Miniature Stirling Cycle Cryocooler," CEC/ICMC Conference, Cambridge, MA, (August 12-16, 1985).

[5] Walker, G., "Cryocoolers," Vol. I, Plenum Press, New York, (1983).

[6] Van Mal, H. H. and Mijnheer, A., "Hydrogen Refrigerator For the 20 K Region With a $LaNi_5$ Hydride Thermal Absorption Compressor for Hydrogen," Proc. ICEC 4, IPC, Science and Technology Press Guilford, UK, (1972).

[7] Jones, J. A. and Golben, P. M., "Life Test Results of Hydride Compressors for Cryogenic Refrigerators," AIAA No. 84-0058, AIAA 22nd Aerospace Sciences Meeting, Reno, NV, (January 9-12, 1984).

[8] Hartwig, W. H., Steinfink, H., Masson, J. P. Woltman, A. W., Proc. 1976 Region V IEEE Conf, IEEE Cat. 76CH1068-6 Reg 5, (1976).

[9] Kidnay, A. J. and Hiza, M. J., Cryogenics, 10, 271 (1970).

[10] Chan, C. K., "Cryogenic Refrigeration Using a Low Temperature Heat Source," Cryogenics, 391 (July 1981).

[11] Flood, E. A., (ed), "The Solid-Gas Interface," Marcel Dekker, Inc., New York, (1967).

[12] Quinn, D. F., Barton, S. S., Dacey, J. R., Evans, M.J.B., and Holland, J. A., "Solid Adsorbents for Storage of CNG For Automotive Use-Saran Carbon," Alternate Energy Conference, Winsor, Ontario, (June 1985).

[13] Barron, R., "Cryogenic Systems, " McGraw-Hill, (1966).

[14] Bard, S. "Improving Adsorption Cryocoolers by Reducing Void Volume and Multistage Compression," Cryogenics, 26, 450 (August/September 1986).

[15] Yang, L. C., Vo, T. D., and Burris, H. H., "Nitrogen Adsorption Isotherms For Zeolite and Activated Carbon," Cryogenics, 22, 625 (December 1982).

[16] Sigurdson, K. B., "A General Computer Model For Predicting the Performance of Sorption Refrigerators," Second Cryocooler Conference, GSFC, Greenbelt, MD, (December 7-8, 1982).

[17] Jones, J. A., "Hydride Absorption Refrigerator System for Ten Kelvin and Below," Third Cryocooler Conference, Boulder, CO, (September 1984).

[18] Chan, C. K., "Dynamic Design of Gas Sorption J-T Refrigerator," Cryogenic Engineering Conference (CEC), Cambridge, MA, (August 14, 1985).

A SUPERCONDUCTING PULSE COIL WITH LOW AC LOSSES FOR USE IN MAGNETIC REFRIGERATORS

P. Seyfert, G. Claudet

Service des Basses Temperatures
Centre d'Etudes Nucléaires de Grenoble, 85 X
38041 Grenoble Cédex, France

A small superconducting magnet (useful bore 1.8 cm, 10 cm length) is used in pulsed operation to magnetize and demagnetize the working material in a magnetic refrigeration device. Design features are a winding made of special low loss multifilamentary NbTi conductor with very fine filaments, a coil former and casing made of non-metallic composite material. The results of loss measurements for field sweeps of up to 3 T with a repetition rate in the 1 Hz range are given and compared with calculations. The possibilities of utilizing such coils in magnetic refrigerators are briefly discussed.

Key-words : A.C. losses in superconductors; cryocoolers; cryogenics; low loss superconductors; magnetic refrigeration; superconducting pulse coils.

1. Introduction

An essential feature of magnetic refrigeration is the need of an appropriate method for obtaining periodically changing magnetic fields. Superconducting pulse coils surrounding the magnetic working material are one solution. They avoid relative motion of the magnetic components which is liable to cause cold seal leakage and frictional heating. They give rise, however, to specific heat losses which must be taken account of when assessing the loss inventory.

A few designs of magnetic refrigerators with ac superconducting magnets have been described and published [1,2,3,4][1]. It has become apparent from this work that special low loss superconducting wire must be used for the magnet to keep a.c.losses at tolerable level.

2. Experimental study and analysis

Recently new low loss NbTi material with particularly small filament diameter has been developped industrially [5,6]. We have taken this opportunity to make a pair of coils from that type of conductor and to study a.c. losses under practical conditions which simulate their use in magnetic refrigerators.

The two identical coils have a clear bore of 1.8 cm and a length of 10 cm. They were designed for the purpose of a magnetically active regenerator device under development at our laboratory [4]. Field profile in axial direction is not uniform but falls by 40 percent almost linearly over 7.5 cm from a peak field region near one end of the coil to a low field region near the other. The load characteristics of peak field on the axis is given by .062I T, where I is the transport current.

Both coils are wound from a NbTi wire specially developed to minimize ac losses [7]. It contains 13068 filaments of 1.8 µm diameter in a copper, cupro-nickel matrix. The bare wire has a diameter of .41 cm and is coated with electrical varnish for insulation.

The coil former made of epoxy fibreglass is provided with axial grooves which produce a number of cooling channels for the innermost layer of winding. Both coils were impregnated with vacuum-grease. For final use in the refrigerator device a vacuum-tight epoxy fibreglass casing will surround each coil to contain the helium coolant.

D C quench current was found to be very nearly 100 % of the short sample critical current, i.e. 69 A, in the most exposed turns of coil winding.

A.C. losses were measured using a calorimetric method [8]. The test coil was fed with transport current of triangular waveform. The investigation covered a range of frequency and amplitude that we anticipated for operation of our magnetic refrigerator device. Results are displayed in figures 1 and 2 and are shown in terms of energy release per current oscillation ("pulse").

Calculation of losses was started on the basis of analytical relations for the loss power per unit volume of superconductor. Preliminary analysis showed that losses in the present case would be due to hysteresis in the NbTi filaments and, to a much lesser degree, to so-called coupled eddy currents [9]. The following expression allows for both loss mechanisms.

---

[1] Numbers in brackets refer to the literature references listed at the end of this report.

$$P = \frac{\alpha \sqrt{\pi}\, D_f\, I_c}{8\, A} \left\{ 1 + \left(\frac{I}{I_c}\right)^2 \right\} \left| \frac{dB}{dt} \right| + \frac{\beta}{2\rho} \left(\frac{L_p}{2\pi}\right)^2 \left(\frac{dB}{dt}\right)^2 \qquad (1)$$

where P = loss power per unit volume of superconducting composite
D_f = diameter of superconducting filament
I_c = critical current of superconducting composite
A = cross-sectional area of superconducting composite
ρ = effective transverse resistivity of matrix
L_p = twist pitch of superconducting filaments
dB/dt = rate of transverse magnetic field change
I = transport current
α, β = dimensionless coefficients
and all values are to be entered in units of the SI system.

In a first approximation the dimensionless coefficients in eq.[1] may be set to $\alpha = 1$ and $\beta = 2$. That is how these formulae generally appear in literature. A more refined theory of loss calculation [10] shows non-negligible deviations from that assumption for the type of superconductor used in the present work. It was found [11] that this theory could be taken into account adequately by using eq.(1) with

$$\alpha = 1.28 \quad , \quad \beta = 63.0 \quad \text{and} \quad \rho = 2.3 \times 10^{-7} \text{ Ohm m} .$$

It should be noted that the above values depend on the structure of superconductor and therefore have no universal validity.

To obtain loss energy eq.(1) must first be integrated over the period of current oscillation. Since critical current and rate of field change depend on the local magnetic field which is not uniform at all within our test coil, eq.(1) has to be integrated also over the volume of the superconducting winding. Numerical solutions of this twofold integration are plotted as full curves in figures 1 and 2.

The experimental as well as calculated results shown in figure 1 appear to depend very weakly on pulse frequency. This clearly indicates that hysteresis is the predominant loss mechanism and that our model describes the relative magnitudes of hysteresis and coupling losses correctly.

Fig.1 and 2 both show that our calculations underestimate absolute values of total loss by 10 to 15 percent. That kind of agreement between theory and experiment seems to be usual for a.c. losses in superconductors [6,11].

As a first conclusion it may be said that we have found no particular problem in building small a.c. coils wound from special low loss superconducting wire and that it was possible to predict loss figures to a reasonable accuracy.

3. The use of superconducting pulse coils in magnetic refrigerators

In the light of the results presented above it seemed interesting to attempt an evaluation of the potential usefulness of superconducting pulse coils for magnetic refrigerators. We will discuss the question from the standpoint of thermodynamic efficiency and it should be understood that we only refer to the final design of magnetic refrigerators. In early stages of process development a.c. superconducting coils may be superior just because they allow flexibility in experimentation.

Evaluation of a.c. losses will be based on the results with the 1.8 μm filament dia. NbTi wire used for our coils. At present superconductors with still finer filaments are being developed industrially but it has turned out that hysteresis losses are no longer proportional to the filament diameter below ~ 1.4 μm [6]. It thus appears that reduction of losses by a factor of 2 to 3 over our results may be expected at best with such wires. That should be borne in mind for the following discussion.

For the boil-off due to current-leads we will assume that the heat leak per unit of optimized current and per lead has a value of 10^{-3} W/A and that the leads are designed for an optimum current equal to $I_m/\sqrt{3}$, where I_m is the peak value of the oscillating transport current.

At first we shall discuss the situation of magnetic refrigerators for the 4-20 K temperature range. That is the most unfavourable case since the magnet system has to be coupled to the cold reservoir and will thus draw directly on the available cooling capacity.

To illustrate the dramatic impact on refrigeration efficiency we consider the practical example of magnetically active regeneration. Projects of this type are under development at our laboratory [4] and at MIT [3]. We carried out numerical simulations of a cycle with cold source at 4.5 K and hot sink at 15 K. A GGG regenerator core fitting into the bore of the coils described in the preceding chapters was found to produce 0.05 J/cycle of refrigeration under a 2.9 T field swing. To achieve 2.9 T our coil needs 47 A and figure 2 shows that a.c losses will be about 0.18 J/cycle in that case. Heat leak from two current leads will add 0.11 J/cycle (at 0.5 Hz cycle frequency). Total heat load due to the magnet system thus amounts to 0.29 J/cycle which exceeds the available cooling capacity by almost a factor of 6 !

We don't claim that any magnetic refrigerator design for the 4-20 K range with a.c. superconducting magnet systems will give so disastrous results. We fear, however, that a satisfactory positive energy balance at the cold source may never be attained with this design option.

Next we consider the situation of magnetic refrigators for the 1.8 - 4.5 K temperature range. A superconducting pulse coil will be less detrimental to refrigeration efficiency in that case since the corresponding heat load can now be rejected to the hot sink.

We will again base our evaluation on practical examples. As yet two successful designs of 1.8 - 4.5 K magnetic refrigerators have been published. A very nice machine of an entirely static type using a superconducting pulse coil has been built and tested in Japan (2) and a reciprocating magnetic refrigerator was developed a few years ago at our laboratory (12).

The reciprocating refrigerator had a Carnot efficiency of 53 percent at 1.8 K with 1.35 W useful cooling power. As a result of loss analysis [4] it was found that 2.2 W instead of 1.35 W would have been available had it been possible to avoid leakage through the piston cold seal and frictional heating, both directly linked to the motion of the reciprocating piston.

We have calculated that an a.c. magnet system of sufficient size to achieve the same magnetic cycle as our reciprocating machine would have a loss of 0.27 W, including a.c. losses and leaks from current leads. Taking into account these numbers we have found that a static magnetic refrigerator could attain a Carnot efficiency of 74 percent at 1.8 K which would be a definite improvement over the results obtained until now.

It is true the actual efficiency of the static refrigerator reported in [2] was only 0.24. But according to the authors of that paper it should not be too difficult to modify the design so as to suppress a major source of losses in their first generation machine.

Our general conclusion to this chapter is therefore that a.c. magnets wound from low loss superconducting wires offer interesting prospects for magnetic refrigeration provided the magnet losses can be rejected to the refrigerator hot sink.

The authors are grateful to Alain Février and Julian R. Cave, both of CGE Marcoussis, for valuable discussions on a.c. losses in superconductors and for their help in working out the numerical values of α and β in eq.(1). Hoang Gia Ky of Alsthom Atlantique is ackowledged for providing extensive information on the NbTi wire delivered to us.

4. References

[1] Nakagome, H., Tanji, N., Horigami, O., Ogiwara, H., Numazawa, T., Watanabe, Y., Hashimoto, T., The helium magnetic refrigerator, Adv. Cryogenic Engineering, 29, 581-596 (1984).

[2] Hakaraku, Y. and Ogata, H., A static magnetic refrigerator for superfluid helium with new heat switches and a superconducting pulse coil, Japanese J. Applied Physics. 24, 1538-1547 (1985).

[3] Taussig, C.P., Gallagher, G.R., Smith, J.L. Jr, Iwasa, Y., Magnetically active regeneration, paper presented at the 1985 Cryogenic Engineering Conf. Boston, Massachusetts (USA), August 12-16, 1985, to be published in Adv. Cryogenic Engineering, 31.

[4] Claudet G.M., Magnetic refrigeration study at CEA Grenoble, paper presented at the 1985 Cryogenic Engineering Conf., Boston, Massachusetts (USA), August 12-16, 1985, to be published in Adv. Cryogenic Engineering, 31.

[5] Dubots, P., Février, A., Renard, J.C., Goyer, J.C., Hoang Gia Ky, Behaviour of multifilamentary NbTi conductors with very fine filaments under a.c. magnetic fields, Proc. 8th Int. Conf. Magnet Technology-MT8, Journal de Physique, 45 (colloque C1), 467-470 (1984).

[6] Dubots, P., Février, A., Renard, J.C., Tavergnier, J.P., Goyer, J.C., Hoang Gia Ky, NbTi wires with ultra-fine filaments for 50-60 Hz use : influence of the filament diameter upon losses, IEEE Trans-Magnetics, MAG-21, 177-180 (1985).

[7] Alsthom Atlantique, 9001 Belfort Cédex - France.

[8] Wilson, M.N., in Superconducting Magnets, p. 251 ff. Monographs on Cryogenics, Clarendon Press Oxford (1983).

[9] Ibid. p. 159 ff.

[10] Février, A., Losses in a twisted multifilamentary superconducting composite submitted to any space and time variations of the electromagnetic surrounding, Cryogenics, 23, 185-200 (1983).

[11] Février, A. and Case, J., Centre de Recherches de la CGE Laboratoires de Marcoussis, 91460 Marcoussis (France), Private communication.

[12] Lacaze, A.F., Béranger, R., Bon Mardion, G., Claudet, G. and Lacaze, A.A., Double acting reciprocating magnetic refrigerator: recent improvements, Adv. Cryogenic Engineering, 29, 573-579 (1984).

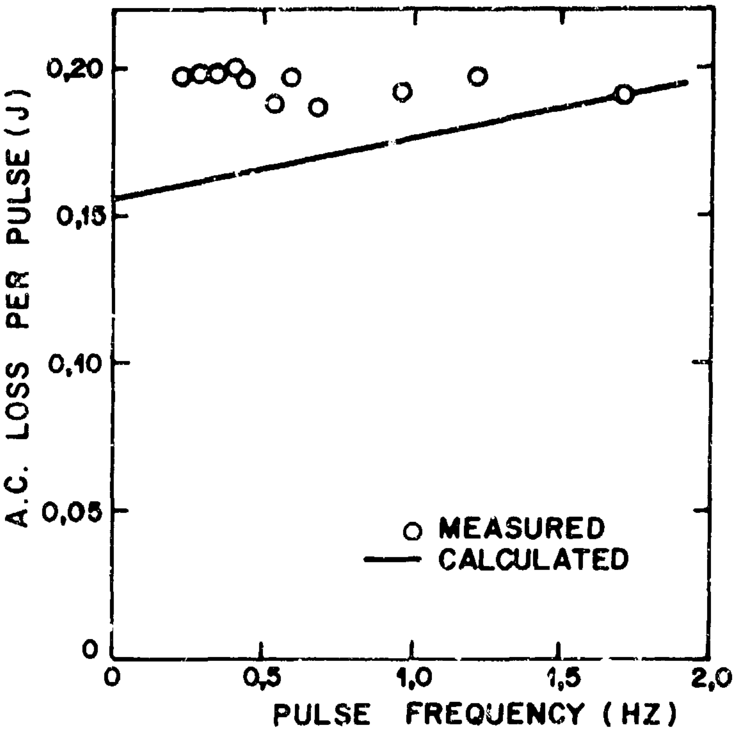

Fig. 1 AC loss vs. frequency in test coil subjected to triangular current pulses of amplitude I = 50 A

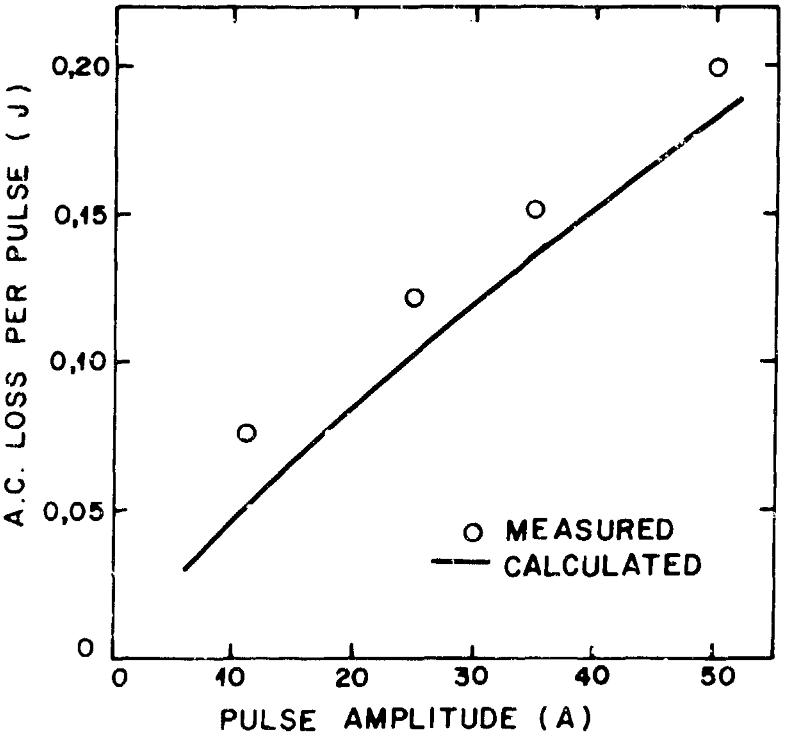

Fig. 2 AC loss vs. pulse amplitude in test coil subjected to nearly triangular pulses of frequency f = 0.5 Hz

RECIPROCATING MAGNETIC REFRIGERATOR

G. Patton, G. Green, J. Stevens, and J. Humphrey

David Taylor Naval Ship Research
and Development Center
Bethesda, Md. 20084-5000

An experimental apparatus was designed to investigate the magneto-caloric effect in a refrigerator near room temperature. This apparatus is representative of the first stage of a helium liquefier that would operate between 300 to 4.2 K. The active material used in these experiments was gadolinium with a Curie temperature of 293 K. This material was formed into a ribbon geometry, and configured into an active regenerator. The active regenerator is placed into a 7-tesla field which is periodically cycled in sequence with a periodically moving working fluid. A series of thermocouples located throughout the apparatus were used to measure the thermal characteristics of this apparatus and the results of these measurements are presented.

Key words: cryogenics; magnetic refrigeration; rare earth metals; regenerator, active.

1. Introduction

For a number of years the U.S. Navy has used gas-cycle liquefiers on board some of its ships to liquefy oxygen and nitrogen. The prospect of ships' using superconducting electric propulsion means that helium liquefaction also will be done afloat.

Having a shipboard liquefier that requires no compressors would be highly desirable. In the Navy compressors are considered to be "hull mounted" machinery and, as such, must be highly tolerant of shock and vibration while retaining the reliability and contamination-free performance necessary for long term liquefier operation.

Most of the magnetic refrigerators built to date are a hybrid of a gas cycle on the warm end coupled to a magnetic cycle on the cold. Because these devices still require a compressor, they are of little interest to the Navy at this time.

An all-magnetic cryogenic refrigerator interests the Navy because it could produce low temperatures without a compressor. In addition, a magnetic cycle is potentially more efficient than its gas cycle counterpart.

This paper discusses the construction and performance of a room temperature, reciprocating magnetic refrigerator which could represent the first stage of an all-magnetic cryogenic refrigerator.

2. The Magnetic Cycle

For these room temperature experiments we chose a reciprocating cycle that used gadolinium (Gd) as the active magnetic element. This experiment was based on the results of work done by Benford and Brown [1].[1] In our experiment, however, the magnet was pulsed to achieve a temperature change in the magnetic material rather than moving the magnetic material in and out of a constant field. Nitrogen gas at 4238 kPa pressure was chosen as a working fluid. Figure 1 shows a schematic of the refrigerator.

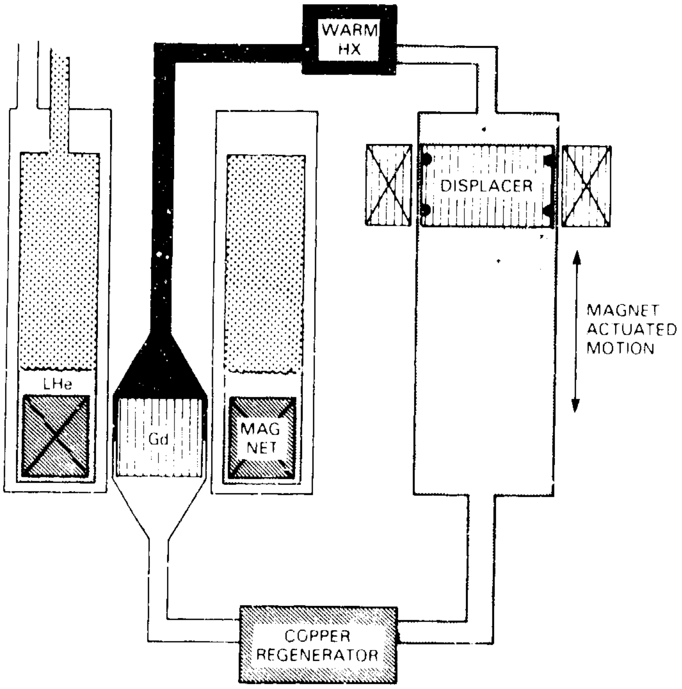

Fig. 1. Schematic of reciprocating magnetic refrigerator.

---

[1] Numbers in brackets refer to the literature references listed at the end of this paper.

The reciprocating magnetic cycle is divided into four phases. They are:

Phase 1. With the displacer held stationary, the magnet is ramped to full field. Internal entropy in the magnetic material (Gd) decreases, causing the material's temperature to increase by ΔT from T_0 to a temperature T_1.

Phase 2. While the magnet is held at full field, the displacer is moved down, forcing the working fluid (N_2 gas) through the copper regenerator, up through the magnetic material, and past the warm heat exchanger. During this movement, the working fluid absorbs heat from the magnetic material, which cools the material to a temperature near T_0. The heat is then rejected in warm heat exchanger. The displacer is stopped.

Phase 3. The magnet is ramped down to zero field. As the internal entropy in the magnetic material increases, the temperature falls below T_0 by some ΔT_1.

Phase 4. The displacer is moved up to its initial position. The working fluid moves through the magnetic material, where it is cooled, and then back through the regenerator, where it accepts heat.

The magnetic material is now cooler than its original temperature, T_0. The regenerator is cooler than its original temperature. Heat has been rejected at the warm heat exchanger, and the displacer and magnet are properly configured to initiate the next cycle.

3. The superconducting magnet

The superconducting magnet used in this device was fabricated at the David Taylor Naval Ship R&D Center (DTNSRDC). A photograph of the magnet is shown in Fig. 2.

The magnet contains 7,122 electrical turns of niobium titanium (NbTi) superconductor in 26 layers. It is 25.4 cm high and has a 8.3 cm bore diameter (I.D. of wire). At 225 amperes, the magnet produces a field of 7 tesla in the center of its axial length. Figure 3 shows the distribution of field strength along the axis of the magnet.

Superimposed on Figure 3 is a representation of the gadolinium magnetic material. This representation shows that the magnetic field has diminished to about 6.3 tesla at each end of the gadolinium.

4. Construction of the refrigerator

The regenerator and the active element both were constructed by winding narrow, embossed metal ribbon into discrete "pancakes" of material and stacking the pancakes. Figure 4 shows a segment of the copper regenerator unwound to reveal the "bumps" embossed on the copper ribbon. The magnetic material consisted of similar gadolinium ribbons. The ribbon shown is 1.77 mm (0.070 in.) wide and 0.2 mm (0.008 in.) thick with a bump embossed on it every 3.175 mm (0.125 in.). Figure 5 shows a regenerator segment wound and installed in a tube. The gas passages formed by the bumps on the ribbon can be seen easily in this photograph. This configuration provides about 40% void volume.

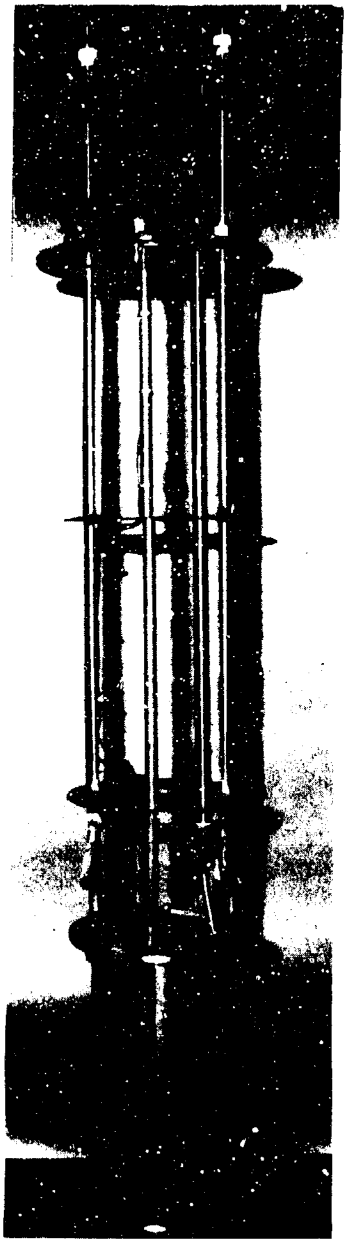

Fig. 2. Superconducting magnet used in the magnetic refrigerator.

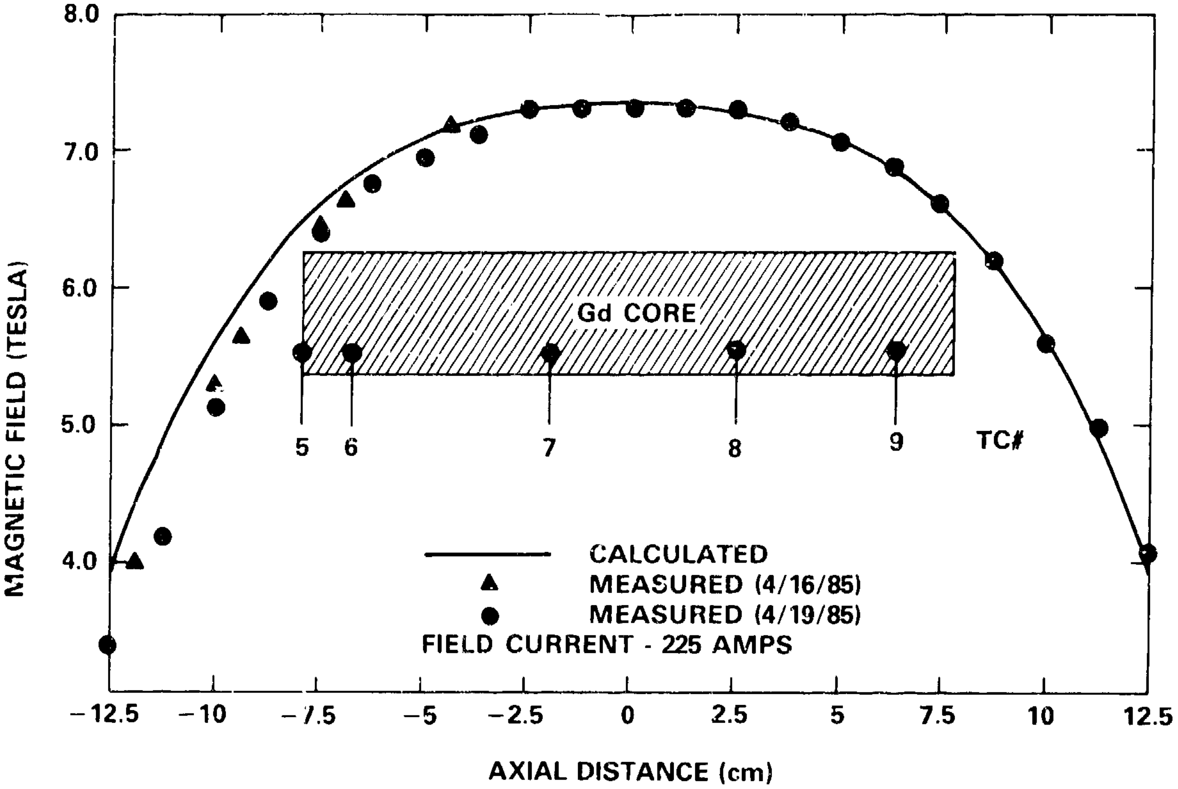

Fig. 3. Magnetic field vs. axial distance for the superconducting magnet.

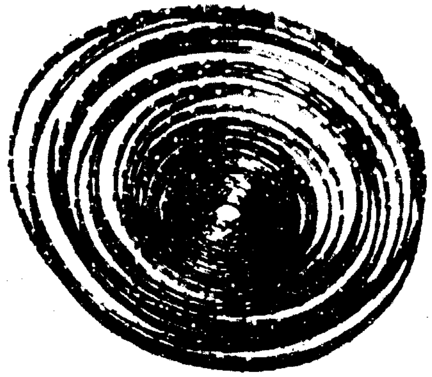

Fig. 4. Ribbon configuration used in the regenerator and active element.

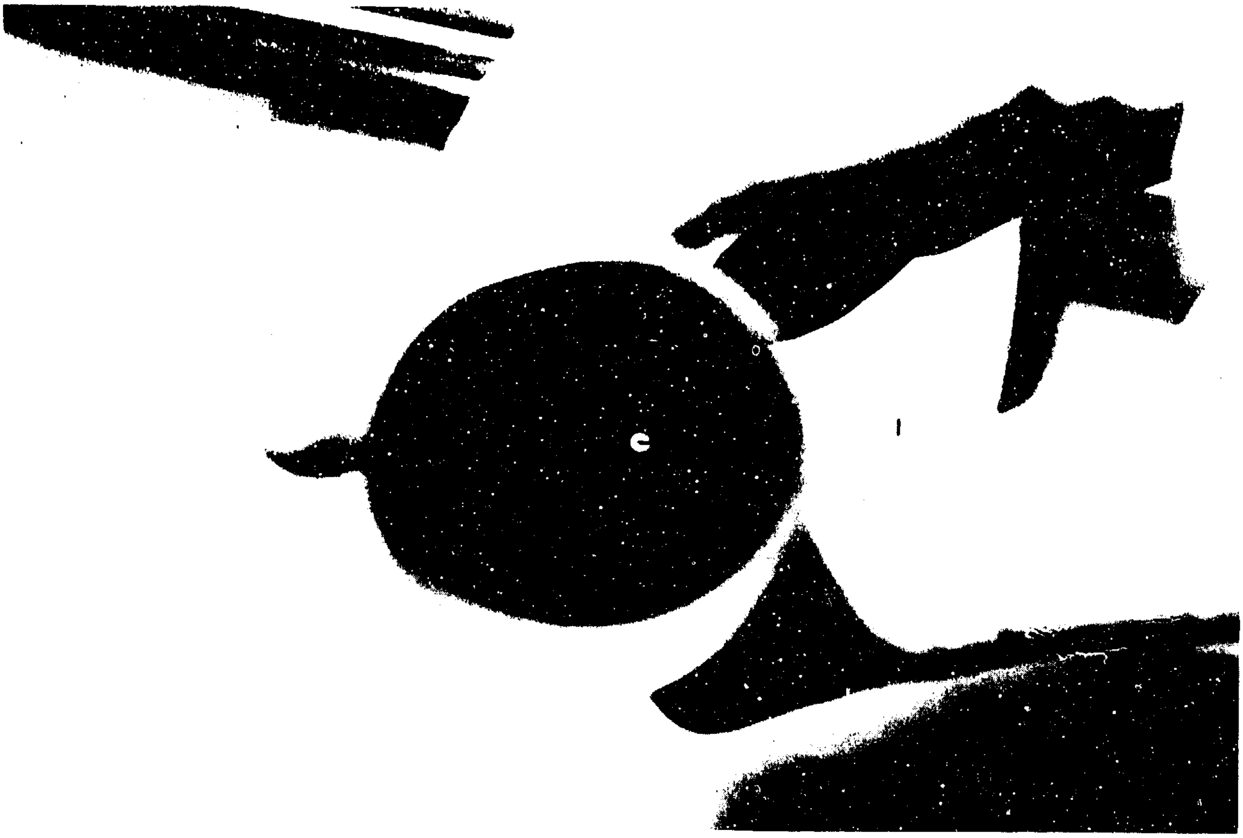

Fig. 5. Regenerator segment wound and installed in tube.

The spindle of the winding mechanism leaves a small hole and tab in the center of each wound segment. After stacking, the tab is broken off and a G-10 fiberglass or stainless steel rod is inserted through the center of all the segments to prevent gas flow through the hole left by the spindle.

The segments of the magnetic material and the copper regenerator were packed into a G-10 fiberglass tube. Figure 6 shows this tube with the components inside.

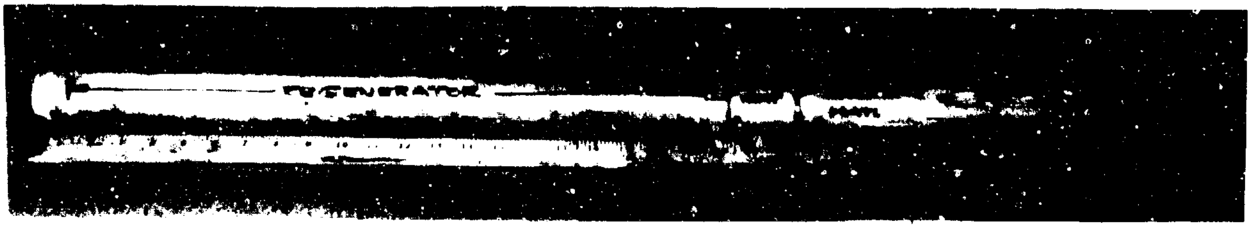

Fig. 6. G-10 fiberglass tube containing the regenerator and the magnetic material.

The copper regenerator is 3.18 cm in diameter and 61 cm long. The regenerator contains 2.47 kg copper. The magnetic material is 900 g of gadolinium sections 3.8 cm in diameter and packed 15.24 cm long.

Some preliminary experiments were conducted using the embossed gadolinium material to determine the adiabatic temperature change of the material as a function of temperature with a 7 tesla change in magnetic field. Figure 7 shows the results of these experiments and compares them to the data presented by Benford and Brown [1].

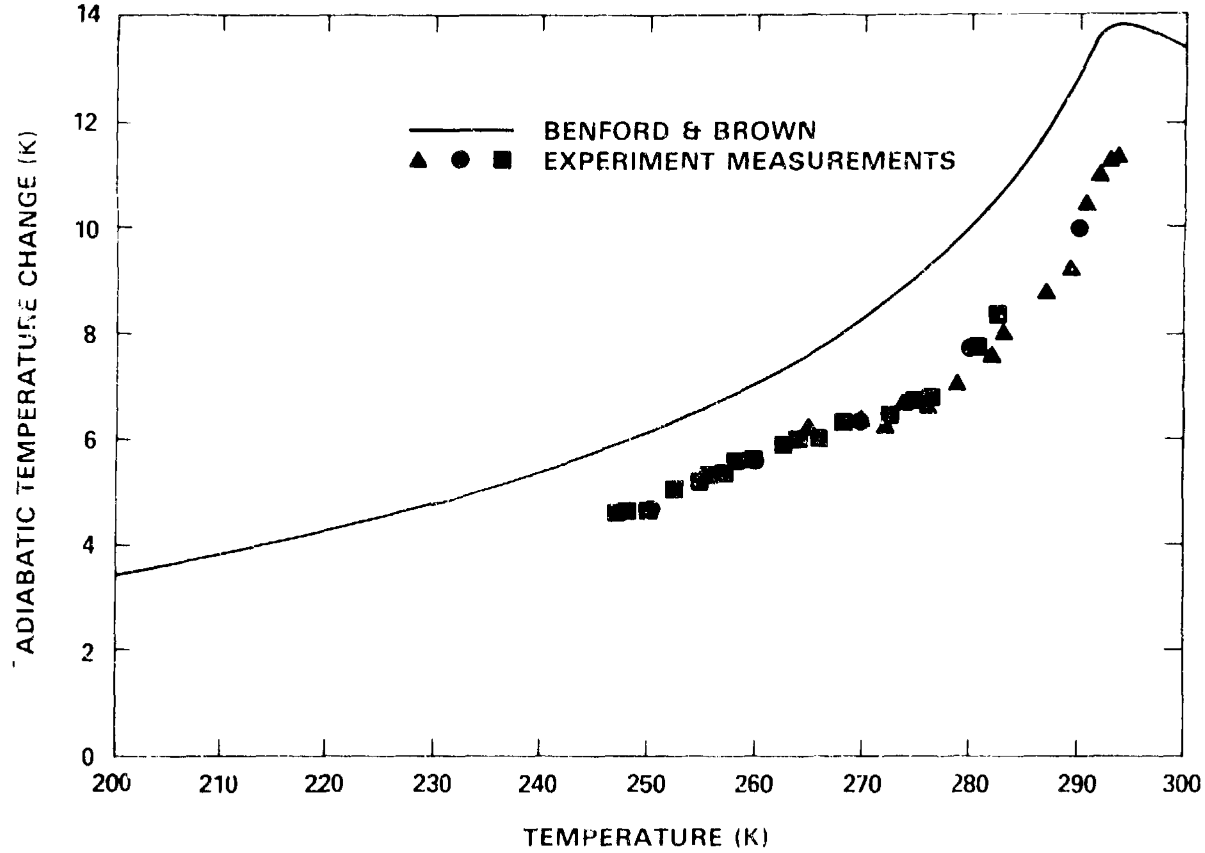

Fig. 7. Adiabatic temperature change in gadolinium subjected to a 7-tesla change in magnetic field at various temperatures.

The shortfall in adiabatic temperature change in this experiment as compared to Benford and Brown's results can be attributed to several factors:

1. About 15% of the difference in adiabatic temperature change can be attributed to the heat capacity of the nitrogen gas surrounding the gadolinium ribbon.

2. There is some heat transfer in the axial direction of the gadolinium material.

3. The G-10 fiberglass surrounding the gadolinium has some heat capacity which diminishes the adiabatic temperature rise.

4. The thermocouple preamplifiers used to interface into the computer data acquisition system has at least 1% error in their output.

These factors also act to reduce the reversibility of the adiabatic temperature change.

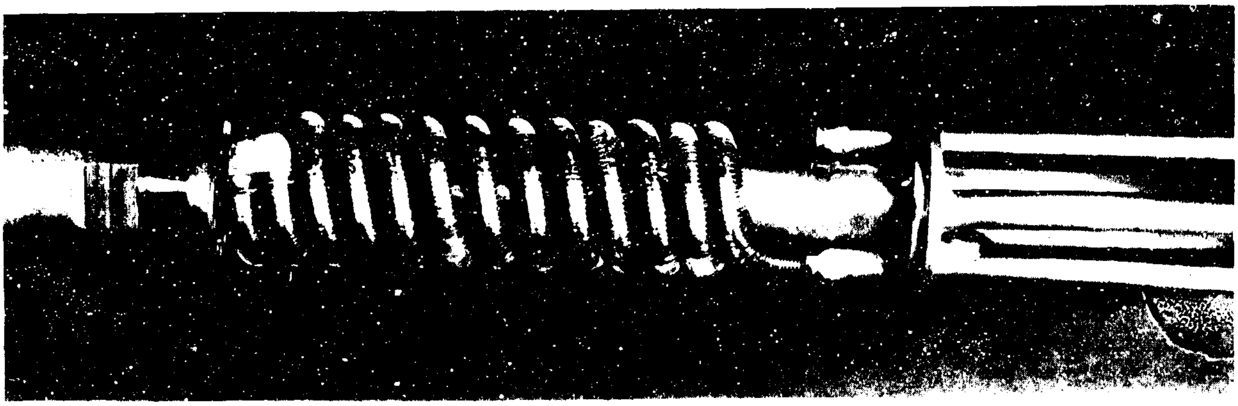

Fig. 8. Warm heat exchanger.

The warm heat exchanger is a finned-tube type and is shown in Fig. 8. Water is forced through the tubes in the heat exchanger to maintain the warm end at a constant room temperature.

The G-10 fiberglass tube and the warm heat exchanger were inserted into a 4.5-cm stainless steel tube with a vacuum jacket. Figure 9 shows the fiberglass tube, the warm heat exchanger, and the stainless case before assembly. The small stainless tube extending from the right end of the fiberglass carries the instrumentation and heater wires out through the center of the heat exchanger.

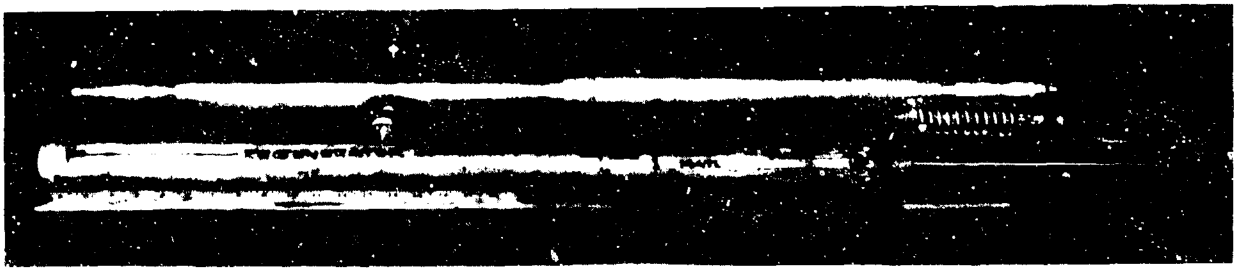

Fig. 9. Refrigerator components before assembly.

The components were assembled and the ends welded in the tube. The instrumentation wires were sealed with a hermetic feed-through and a swage-lock fitting on the center tube.

5. Instrumentation and control

Temperatures were measured in the refrigerator components with type T (copper constantin) thermocouples. These thermocouples were inserted through small holes drilled through the G-10 fiberglass tube and into the component material. Number 36 thermocouple wire was used to minimize heat conduction and response time. The thermocouple wire was placed in grooves machined in the outside of the fiberglass tube. Figure 10 shows some of the thermocouples in the magnetic material leading to the right end of the assembly, where they pass through the pressure-tight feed-through.

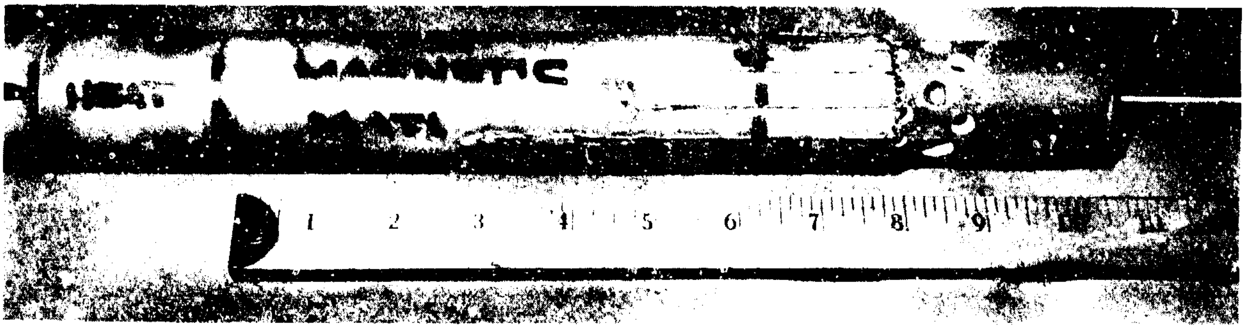

Fig. 10. Thermocouple installation in the G-10 fiberglass tube.

A total of 13 thermocouples are used as follows:

- 3 in the regenerator
- 1 on the heater
- 1 in the gas space between the regenerator and magnetic material
- 7 in the magnetic material
- 1 in the gas space between the magnetic material and the heat exchanger

The refrigerator was controlled and the data recorded using a small Digital Laboratory computer equipped with the necessary I/O modules.

The magnet current was controlled by the output of a computer digital-out line which operated the ramp-enable circuit in the magnet exciter. Current level for the magnet was fed back to an analog-in port of the computer using an analogous voltage from the ammeter on the exciter.

The displacer was controlled in a similar manner. The computer program operated through an analog-out line to an electronically controlled hydraulic valve to cause the displacer to go up, stop, or go down. Displacer position was sensed with a linear variable differential transformer (LVDT) attached to the displacer shaft and fed back to the computer through an analog-in port. Displacer speed was programmable also.

Temperatures, magnet current, displacer position, and cycle number were recorded on floppy disks and simultaneously displayed on the computer video terminal.

The control and data acquisition program was written in four segments which corresponded to the four phases of the magnetic cycle. Subroutines were invoked to display and store the data.

6. Refrigerator operation

The magnet required about 30 s to ramp between 0 and 225 A, either up or down, using a 10-V potential. The total time for one cycle was about 90 s.

The magnetic refrigerator was operated several times starting at room temperature (300 K). During each test, the refrigerator was allowed to operate until the cold end temperature stopped decreasing and remained steady. Between tests, the refrigerator was allowed to warm up throughout, and the displacer was cycled up and down with no magnetic field present to make sure that all parts of the regenerator and active material had reached thermal equilibrium.

The results of each test were compared to the results predicted by a mathematical model of the magnetic refrigeration cycle constructed at DTNSRDC, and operated through a NASTRAN Numerical Analysis Program.

The results of two test runs (run 1 and run 2) are discussed in this paper are the final two tests conducted to date. The refrigerator was warmed to room temperature between these runs as previously described.

The initial trials did not produce temperatures as low as predicted. Calculations showed that the mass flow of the nitrogen working fluid was too great as the cold end temperature fell, and that the displacer stroke (i.e. mass flow) is a function of temperature. Calculations were done for a number of cold end temperatures, and the results were used to construct the curve in Figure 11, which shows the displacer stroke as a function of the gadolinium cold end temperature when the working fluid pressure is held constant.

The control program was then modified to approximate the curve in Figure 11 with two straight line segments. The refrigerator was subsequently operated and produced the cooldown curves shown in Figure 12.

As expected, the refrigerator cooled most rapidly near the Curie point of the gadolinium (293 K) where the adiabatic temperature change is a maximum. During run 1, the temperature gradient, or temperature change per cycle at the cold end of the regenerator, had become very small by cycle 150. It was suspected that the mass flow of the nitrogen working fluid was still too great. The nitrogen pressure was reduced from 4238 kPa (600 psig) to 3204 kPa (450 psig). Figure 12 shows an increased cooling rate in run 1 between cycles 150 and 230.

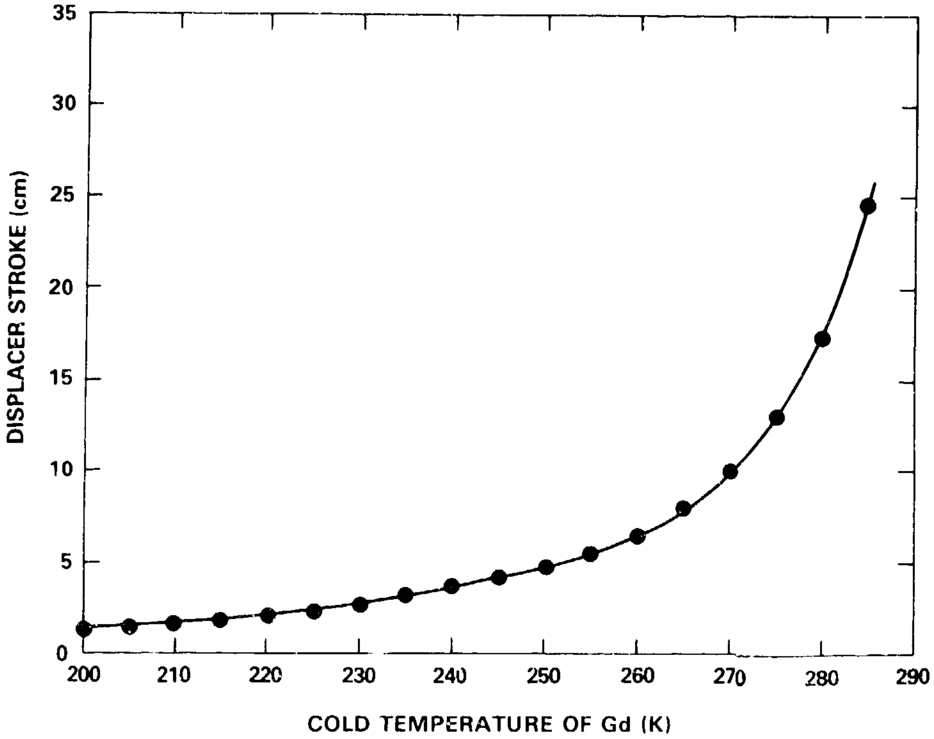

Fig. 11. Displacer stroke vs. cold end temperature of Gd.

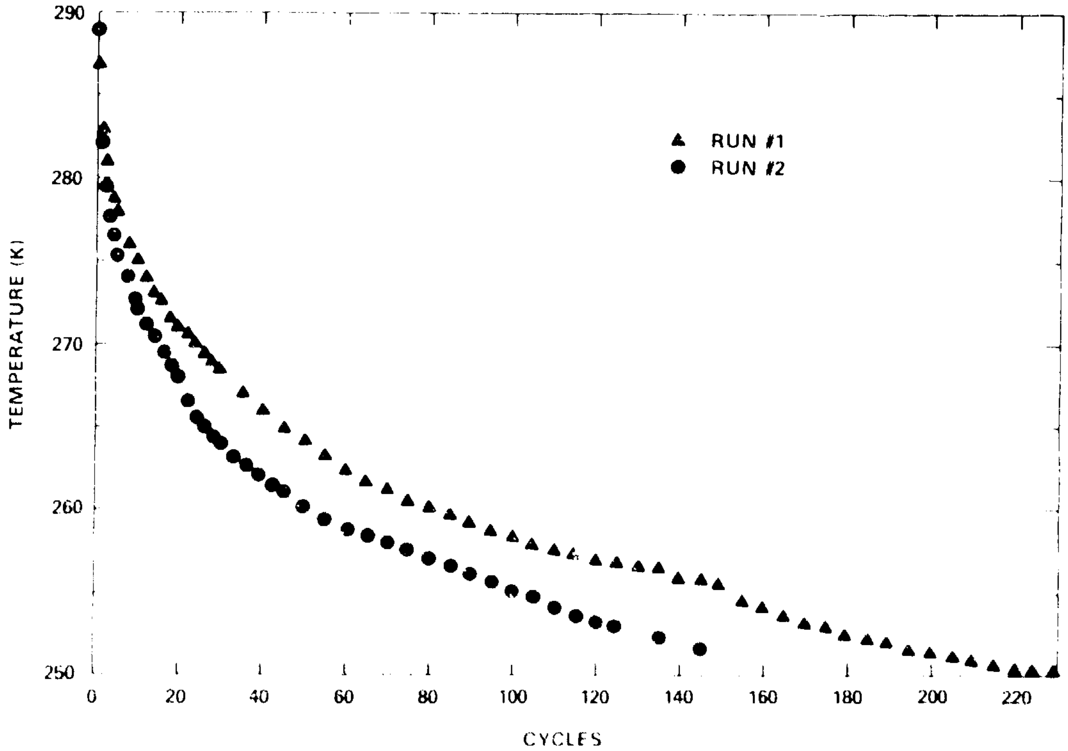

Fig. 12. Temperature in the cold end of the regenerator as a function of refrigerator cycles.

Run 2 was conducted with the nitrogen pressure reduced to 3204 kPa (450 psig). The cooling rate was greater throughout the run compared to run 1.

No tests were conducted to measure the refrigeration because a failure in the warm heat exchanger allowed water to leak into the gadolinium, producing oxidation in the gadolinium and greatly impeding the flow of nitrogen gas.

Results of the tests conducted, however, showed that a fairly large temperature span can be achieved with a single magnetic material. Dr. John Barclay [2] introduced the notion of an active magnetic regenerator using a number of magnetic materials having Curie points appropriately spaced to allow a much greater temperature span. Figure 13 shows three candidate materials for such a device.

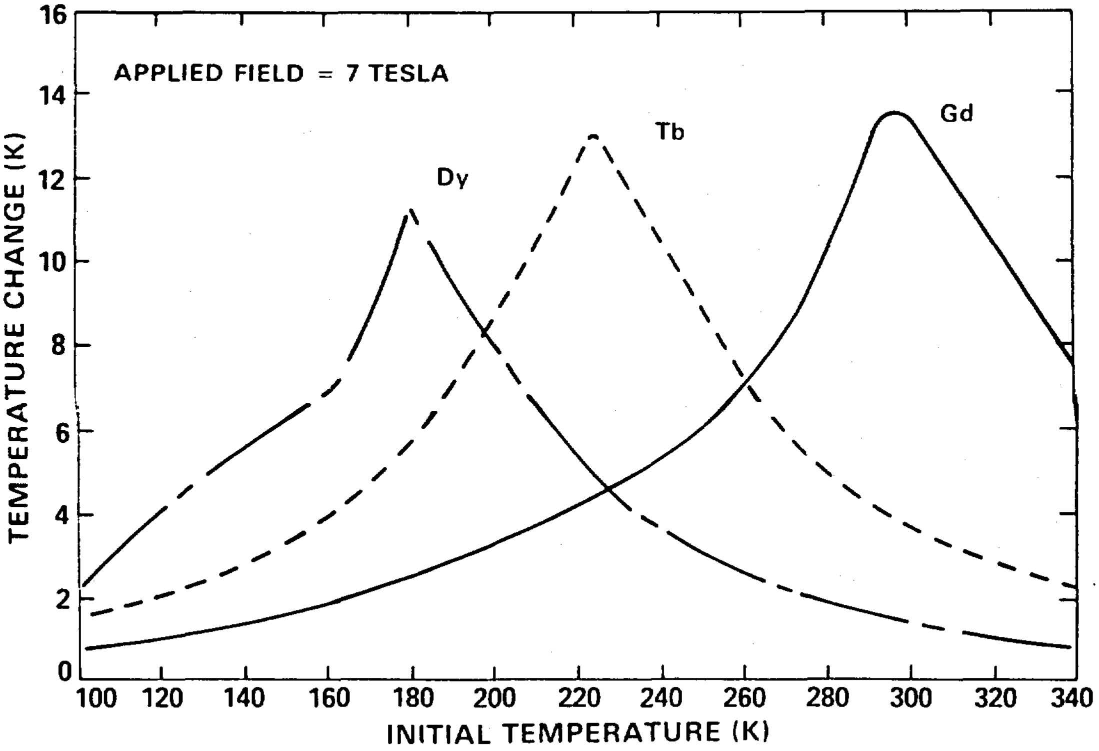

Fig. 13. Candidate materials for an active magnetic regenerator.

These three materials - gadolinium, terbium, and dysprosium, are all rare-earth elements whose magnetic characteristics overlap appropriately to produce active magnetic regeneration near room temperature with a cold end temperature possibly as low as 170 K.

Other characteristics, such as magnetic hardness and fabricability, affect the suitability of most materials for use in a device such as this. The main thrust of the future magnetic refrigeration program at the David Taylor Naval Ship R&D Center will be to identify those materials most suitable for incorporation into a refrigerator to achieve cryogenic temperatures.

6. References

[1] Benford, S.M., and G.V. Brown, "T-S diagram for gadolinium near the Curie temperature," J. Appl. Phys., Vol. 52, No. 3, pp. 2110-2112 (1981).

[2] Barclay, John, "An analysis of liquefaction of helium using magnetic refrigerators," Los Alamos National Laboratory Report LA 8991, Los Alamos, N. Mex. (Dec 1981).

Preceding Page Blank

MAGNETIC REFRIGERATION BASED ON MAGNETICALLY ACTIVE REGENERATION*

C.P. Taussig, G.R. Gallagher, J.L. Smith, Jr., and Y. Iwasa

Cryogenic Engineering Laboratory, Massachusetts Institute of Technology
Cambridge, MA 02139

A small experimental device to investigate magnetic refrigeration based on magnetically active regeneration is described. The device produced steady refrigeration power of 0.40 W at 3.79 K, rejecting heat at 5.51 K. An AC superconducting magnet excited a stationary GGG regenerator core with a stream of 3-atm helium transporting refrigeration from the cold reservoir to the hot reservoir.

Key words: magnetic refrigeration; gadolinium gallium garnet (GGG).

1. Introduction

The magnetic refrigeration project was initiated in 1983 at MIT. The fruit of our project to date is a small device that permits experimentation in magnetic refrigeration. The device is described in great detail in two theses completed recently, one by Taussig [1] and the other by Gallagher [2]. This paper is based on the two theses; however, because of the size limitation, most details are not included.

The concept of using magnetically active regeneration for the MIT device evolved after careful examination of the advantages and disadvantages associated with various concepts recently employed [3–7]. Almost all the magnetic refrigerators built operate on the magnetic analogy of one of three thermodynamic cycles: Carnot, Stirling, or Ericsson.

The Carnot cycle is simpler to implement than the cycles employing regeneration but has suffered from two basic difficulties. The magneto-thermodynamics of the magnetic refrigerant limit the temperature span, and low thermal conductance between the magnetic refrigerant and the reservoirs has limited performance. Regenerative machines constructed so far have had difficulties with mixing in the fluid regenerator. Both the Carnot and regenerative cycles have had losses associated with friction generated by relative motion of the magnetic components, and leakage and friction from the cold seals.

Stirling and Ericsson magnetic cycles offer enhanced performance for machines with larger temperature span. Their drawback is that they require heat transfer over their complete temperature span. Designers have typically employed regenerative heat exchange to implement these cycles. It is possible to use either a thermally stratified working fluid as the thermal storage element or to use the magnetic refrigerant itself as the regenerator as is the case with the MIT device.

---

* Work supported in part by the U.S. Airforce Flight Dynamics Laboratory and in part by Sumitomo Heavy Industries.

2. Design Concepts

A regenerative cycle was chosen for the MIT device because of its ability to span the 4K-10K temperature range of the machine with relatively low intensity magnetic fields. A second inherent advantage of regenerative cycles is forced-convection heat transfer. It was decided to use the magnetic refrigerant as the regenerator core to avoid the problems of mixing in fluid regenerators. To avoid the problem of cold seal leakage it was agreed that the regenerator core should be stationary. The helium working fluid would be circulated by warm sealed displacers. It was resolved that AC operation of a superconducting magnet would provide excitation for the magnetic refrigerant. This would eliminate friction caused by relative motion of the magnetic components. Recent advances in low-AC-loss superconductors makes this option realistic.

2.1 Simple Model of the Ideal Cycle

The MIT cycle can be idealized as a series of cascaded Carnot cycle refrigerators, as shown in Fig. 1. In one cycle, a mass of helium, m_s, flows from the cold reservoir at temperature T_{cold} and is heated as it flows across the tops of the heat pumps until it reaches the hot reservoir with a temperature greater than T_{hot}. An equal mass of helium flows from the hot reservoir and is cooled as it passes along the bottom of the heat pumps until it reaches the cold reservoir with a temperature less than T_{cold}, thus providing refrigeration to the cold bath. Figure 2 shows idealized temperature profiles for the cycle.

The temperature distribution is $T_h(x)$ in the stream being heated and the temperature profile is $T_c(x)$ in the stream being cooled. In this simple analysis, it is assumed that enough Carnot refrigerators are present so that each only heats or cools the working fluid by a differential increment in temperature. It is further assumed that the specific heat, c, of the working fluid is constant and that all interactions between the Carnot refrigerators and working fluid are lossless.

The energy balance for a complete cycle for one incremental refrigerator (Fig. 1) at x is:

$$W_{mag}(x) = Q_{rej}(x) - Q_{ref}(x) \tag{1}$$

$Q_{rej}(x)$ and $Q_{ref}(x)$ are each related to the energy balance of the respective helium flow:

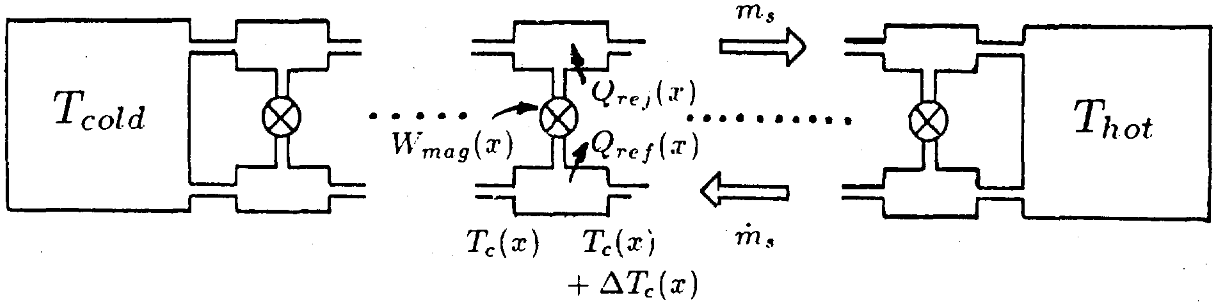

Fig. 1. Cascaded Carnot cycle refrigerators.

$$Q_{rej}(x) = m_s c dT_h(x) \tag{2}$$

$$Q_{ref}(x) = m_s c dT_c(x) \tag{3}$$

The entropy balance for the reversible cycle is given by:

$$\frac{Q_{rej}(x)}{T_h(x)} = \frac{Q_{ref}(x)}{T_c(x)} \tag{4}$$

By combining Eqs. 2 and 3 with Eq. 4 and integrating, we can show that the ratio $T_h(x)/T_c(x)$ is a positive constant greater than unity, independent of x.

$$\frac{T_h(x)}{T_c(x)} = \text{constant} = K \tag{5}$$

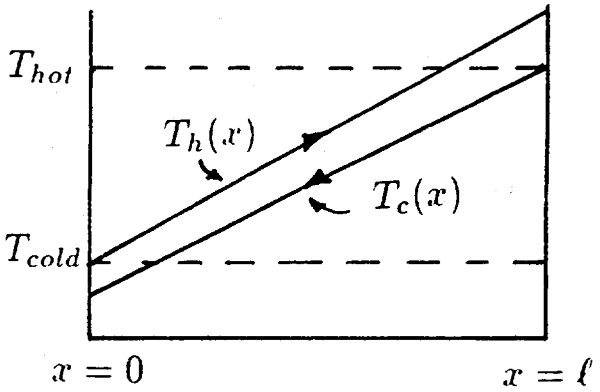

Fig. 2. $T_h(x)$ and $T_c(x)$ in the regenerator.

The functional dependence of the temperatures on position is not determined by Eq. 5. Consider the simple case of linear temperature profiles shown in Fig. 2.

$$T_h(x) = T_{cold} + ax \tag{6}$$

$$T_c(x) = \left(\frac{1}{K}\right) T_h(x) \tag{7}$$

Note that $T_h(0) = T_{cold}$ and $T_c(\ell) = (1/K)T_h(\ell) = T_{hot}$. The energy balance for the differential Carnot cycle at x shows the magnetic work input per unit length $W_{mag}(x)$ required as a function of position.

$$m_s c \left(\frac{dT_h}{dx} dx - \frac{dT_c}{dx} dx \right) - W_{mag}(x)dx = 0 \tag{8}$$

For the above linear temperature profiles, we can solve Eq. 8 for the magnetic work per unit length:

$$W_{mag}(x) = m_s c a \left(1 - \frac{1}{K} \right) \tag{9}$$

This result shows that for linear temperature profiles and constant-specific-heat working fluid, the magnetic work input per unit length is constant.

The refrigeration rate and efficiency of the ideal cycle depend on the temperature profile ratio, K. For a constant mass flow rate, $\dot{m}_s$, $\dot{Q}_{ref}$ is given by a power balance at the cold reservoir and $\dot{Q}_{rej}$ is calculated from a power balance at the hot reservoir:

$$\dot{Q}_{ref} = \dot{m}_s c(T_h(0) - T_c(0)) = \dot{m}_s c T_{cold} \left(1 - \frac{1}{K} \right) \tag{10}$$

$$\dot{Q}_{rej} = \dot{m}_s c(T_h(\ell) - T_c(\ell)) = \dot{m}_s c T_{hot}(K - 1) \tag{11}$$

The refrigerator's efficiency, η, can be defined as:

$$\eta \equiv \frac{\dot{Q}_{ref}/\dot{Q}_{rej}}{T_{cold}/T_{hot}} = \frac{1}{K} \tag{12}$$

The efficiency for the distributed Carnot cycle machines is $1/K$, which is less than 1. That is, Q_{ref} increases with K (Eq. 10), but η decreases (Eq. 12). The maximum efficiency for the cycle is less than the Carnot efficiency despite being completely reversible internally because the refrigeration and rejection are generated via thermal mixing in the reservoirs.

The distributed Carnot cycle is realized in four discrete processes. First the shuttle mass, initially in the hot reservoir, is driven through the core towards the cold reservoir. During this flow process (cold blow), the magnetic field is decreased in such a way that the temperature profile in the helium stream approximates that of $T_c(x)$ on Fig. 2. In the second step there is no flow. The core is adiabatically magnetized until the temperature profile becomes that of $T_h(x)$. During the third step (hot blow), the shuttle mass flows from the cold reservoir to the hot while the magnetization continues so as to maintain the temperature profile at $T_h(x)$. The fourth step completes the cycle by demagnetizing the core adiabatically while the shuttle mass resides in the hot reservoir returning the temperature profile to $T_c(x)$ in preparation for the next cycle to begin.

3. Experimental Apparatus

Figure 3 shows a schematic of the experimental apparatus. The apparatus consists of five major components: 1) gas handling system; 2) temperature control; 3) regenerator core; 4) magnet; and 5) cryostat. Some of these components are briefly described.

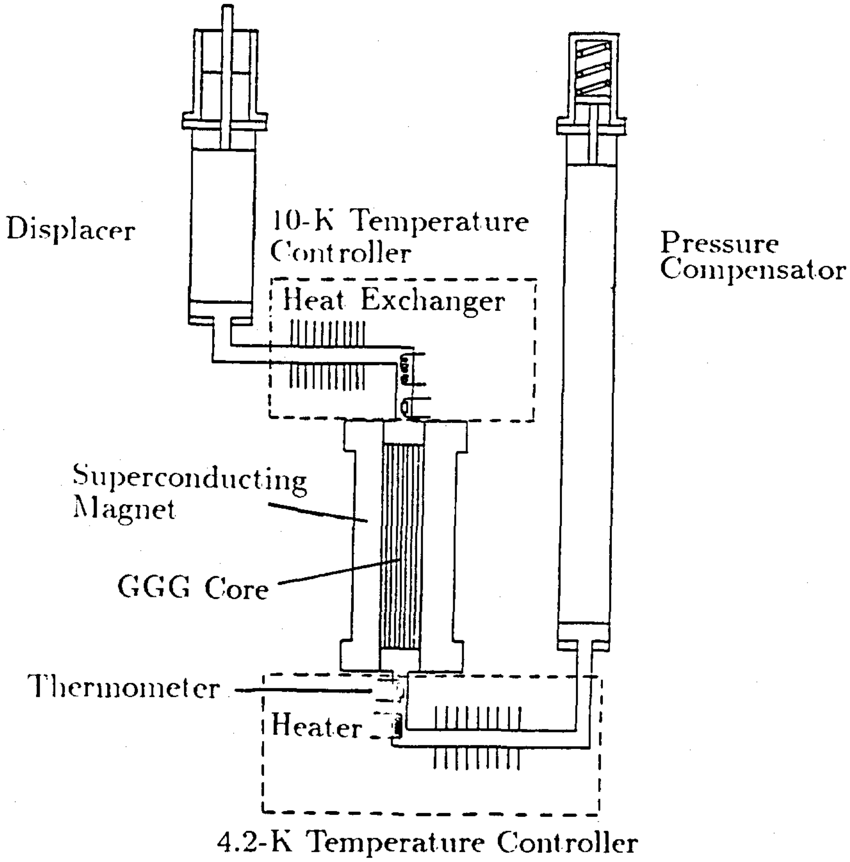

Fig. 3 Schematic of the MIT device.

3.1 Gas Handling System

The components of the gas handling system shuttle the 3-atm supercritical helium back and forth through the regenerator core. The two components of the gas handling system are the displacer and the compensator.

The displacer position is controlled by a stepper-motor-driven ball-screw. A computer sends position commands to a translator which converts the commands to current pulses in the switching sequence required to drive the windings of the stepper motor. Position commands can also be relayed manually to the stepper motor from the control panel.

The swept volume of the displacer is 620 cm^3 which is required to contain the shuttle mass (4.6 g) at 15 K and 3 atm. The displacer stroke of 76 mm was chosen to limit the shuttle losses which are proportional to the square of the stroke. The displacer cylinder length of 680 mm was selected as a compromise between providing a large liquid helium reservoir for the experiment and reducing axial-conduction heat leak. The large displacer bore of 102 mm (required to provide the swept volume) caused two difficulties. The large cross-sectional area of the displacer (81 cm^2) required to provide the swept volume led to a high actuation force and to large axial conduction through the displacer piston. To reduce the 2600-N force needed to move the displacer against the working gas both the rod and the piston were sealed and helium, regulated at slightly below the working pressure of the refrigerator, was introduced on top of the piston. The backing-gas reduces the actuation force sufficiently that a stepper motor with a small running torque can drive the displacer at acceptable rates. The backing gas has the additional advantage of minimizing the load on the seals at the top of the piston. The axial conduction through the displacer piston was reduced by constructing it as a hollow, evacuated, linen-phenolic unit with aluminized mylar radiation shields inside. The piston was glued together with a low-temperature epoxy. The external surface of the displacer piston was sealed with the same epoxy, then wet sanded to run smoothly in the 0.9-mm wall stainless steel cylinder.

The compensator is a passive element designed to maintain the refrigerator system pressure at 3 atm while the displacer moves the shuttle mass between the hot and cold ends of the refrigerator. The task of pressure regulation is simplified because the pressure drop through the core is small relative to the system pressure (4%). The compensator is a free-floating piston exposed to the working gas on one side and pressure regulated backing-gas on the warm side, an auxillary spring (not used in the preliminary experiments) is available as a mechanical aide. Friction is minimized by the use of a Bellofram rolling diaphragm for the main seal; the piston rod is sealed with a small diameter O-ring with minimal drag. The compensator piston is 38 mm in diameter and 1 m long. It is made from molded linen phenolic and like the displacer runs in a 0.9-mm wall thickness, type 304 stainless steel cylinder. The smaller bore of the compensator reflects the factor of 10 decrease in the volume required by the shuttle mass at the cold end of the regenerator. The compensator length was selected so that its working volume would always be immersed in 4.2-K liquid helium.

The working volume is charged through a separate valve and regulator. When running experiments the charging valve is closed and a fixed mass of helium is maintained in the working volume of the experiment. A mechanical bourdon-tube type pressure gauge connected to the warm end of the charging line monitors the working gas pressure at all times. A 4-atm pressure relief valve is connected to the charging line to prevent accidental over-pressurization of the system.

3.2. Regenerator

Gadolinium-gallium-garnet (GGG) was selected for the core material. A parallel plate configuration (Fig. 4) was chosen as the best geometry to provide the small dimension flow passages and low porosity mandated to minimize the loss mechanisms in an easy-to-fabricate package.

The complete internal geometry of the parallel plate regenerator core was specified by the four variables t, w, d, b, defined in Fig. 4. The variables were selected to minimize the applicable loss mechanisms subject to reasonable construction limitations. t and w determine the amount of axial conduction, the entrainment loss due to barrier material and, in part, the fluid-to-wall heat transfer loss. d and b control the fluid friction loss, the amount of helium entrainment, and share in the determination of the fluid-to-wall heat transfer irreversibility. The coupling between the two sets of variables is the fluid-to-wall heat transfer: d and b determine the magnitude of the heat transfer coefficient, but t and w determine how efficiently it is used. This independence of function allows the variables to be selected in two separate groups. The final dimensions chosen for the core are: wafer diameter=38 mm; total core length=270 mm; d =0.01 mm; b =0.25 mm; t =0.25 mm; and w =0.01 mm.

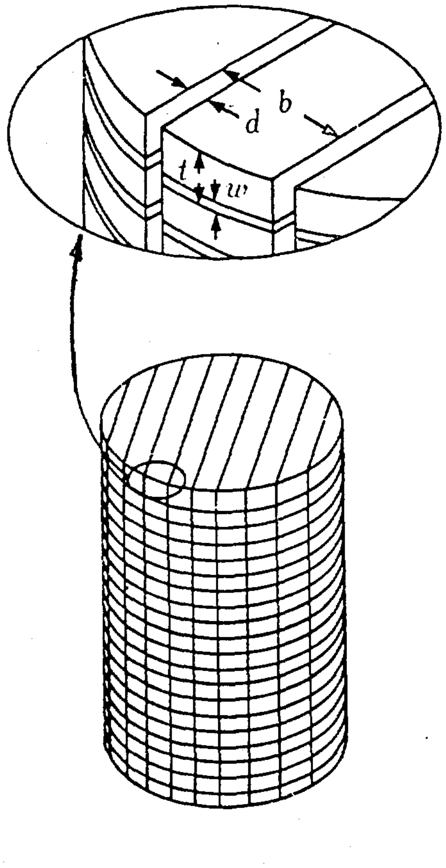

Fig. 4. Core geometry.

Construction of the parallel plate core starts with a series of GGG wafers which are bonded together with thin discs of thermal barrier material between them. The composite cylinder is then sawn lengthwise into parallel slabs which are then reassembled into a cylinder with thin spacers separating them on the edges to provide the parallel flow passages.

The container which houses the regenerator core is a vacuum jacket composed of two concentric stainless steel cylinders. It isolates thermally the regenerator core from the 4.2-K liquid helium environment and is magnetically transparent. Eddy-current heating in the walls of the container is negligible at the ~0.1-Hz operating frequency. The total radial thickness of the vacuum jacket is less than 1.5 mm. The vacuum space in the jacket is connected to a room temperature pressure-relieving pump-out valve. A fine strand of helically wound monofilament in the vacuum space prevents buckling.

3.3. Magnet System

The magnet system for the magnetic refrigerator consists of a superconducting solenoid, vapor-cooled current leads, a computer-controlled current supply, and a magnet protection system. Here only the superconducting magnet is briefly described.

The superconducting solenoid designed for this experiment has a bore of 44 mm and a total length of 345 mm. Within the 305-mm active length of the magnet the field is uniform within 6% from end to center. The magnet is designed to be operated in an AC mode and therefore is wound in an open fashion with spacers providing cooling between adjacent layers of wire. The measured AC losses produced in operating the magnet with a triangular current waveform between the amplitudes of 15 A and 105 A at ~0.1 Hz are ~1.5 W.

The losses are almost entirely due to hysteresis within the 9-μm diameter niobium-titanium superconducting filaments. The hysteresis loss is directly proportional to the filament diameter. Niobium-titanium superconductor with ~0.5-μm diameter filaments is commercially available. The use of 0.5-μm filament wires would reduce the hysteresis losses to less than 0.1 W.

3.4. Temperature Control

At either end of the regenerator core the supercritical helium entering the core is conditioned by temperature controllers. The purpose of the temperature controllers is to simulate constant temperature reservoirs of selected temperature.

4. Experimental Procedure

Once the dewar is filled with helium, the working volume is charged to 3 atm with the displacer at the bottom of its stroke. The charging valve is then closed. The backing-gas pressure is concurrently brought up to a pressure of 2 atm. The backing-gas is supplied by a standard gas bottle (120 atm charge) and will usually last for a day of experiments. The backing-gas cylinder can be replaced without contaminating the experiment if required.

The motion of the displacer and the magnet current are controlled by a computer. A program was written which allows keyboard input of the current and displacer waveforms. Before starting the cycle the computer initializes the magnet at the minimum field selected for the run and positions the displacer at the bottom of its stroke, thus placing the shuttle mass in the cold end of the refrigerator. The computer continues to operate the cycle under the selected conditions until it receives a keyboard interrupt which causes the computer to exit the cycle by returning the displacer to the bottom of its stroke and to ramp the magnet down to zero current.

The experimental data were collected with a data acquisition system. The system receives an instruction from the computer to begin data collection once an experimental run starts. The system internally stores the data until the run is over and then relays the data to the host computer. The measured quantities are: temperatures at the top end and the bottom end of the core, system pressure, compensator volume for m_s and $\dot{m}_s$, and magnet current for field.

5. Experimental Results and Discussion

Data were collected for three modes of operation: 1) helium circulation between the reservoirs without magnetic field change; 2) field changes without helium circulation—passive regenerator experiments; and 3) helium circulation between the reservoirs while the magnetic refrigerant was subjected to field changes—active regenerator experiments. For each run, the experiment was operated for approximately 30 cycles at a frequency of ~0.1 Hz. Cyclic steady state was achieved after 3 or 4 cycles for most operating conditions. In this paper, only results of the active regenerator experiments are presented.

5.1. Data Reduction For Mass Flow

For the preliminary experiments the only data reduction performed was that necessary to determine the refrigeration power to the cold reservoir and the heat rejection to the hot reservoir. To calculate these quantities the enthalpy fluxes to the reservoirs must be ascertained. The specific enthalpy at either end of the regenerator core was calculated based on the temperature measured by the local sensor and an assumed 3-atm pressure. The mass flux was calculated based on the change in compensator working volume. The state of the working fluid within the compensator was assumed to be 3 atm and 4.2 K. The temperature measured by the carbon resistor located at the exit of the compensator showed this temperature to be within 0.4 K of 4.2 K and, as will be shown, the mass flux is not very sensitive to uncertainty in this temperature. The pressure as indicated by the mechanical room temperature gauge was 3±0.2 atm. The rate of volume change was measured by the LVDT located on the room temperature compensator piston rod and its accuracy far exceeds the other experimental measurements. The uncertainty in the mass flow can be estimated assuming that all the uncertainty resides in the density. The uncertainty in density is $\sim$2% for the nominal value of 0.14 g cm^{-3}. Neglecting the uncertainty in the volume measurement the uncertainty in mass flux leaving the compensator is also $\sim$2%.

The accuracy in mass flow at points remote from the compensator depends on the rate of change in mass storage between the compensator and the point of interest. If the hot and cold blows were steady processes then the mass flow would be constant throughout the system. In the real unsteady case, the error in mass flow results from the volume of the plumbing between the point and the compensator and the change in density with time of the helium within. Consider the error in mass flow of helium entering the cold end of the regenerator core relative to the mass flow leaving the compensator. The volume of the plumbing between the compensator and the base of the core is approximately 27 cm^3. If this volume were to change temperature uniformly over 4.0K to 2.5K during a cold blow, a mass storage of 0.3 g would result. The resulting error in mass flow at the base of the core relative to the compensator mass flow would be 7%.

The error in mass flow at the hot end of the regenerator core is larger because of the additional mass contained in the core and because of the larger density variation with increasing temperature. Again, as a pessimistic estimate, if the density-averaged temperature of the entrained helium in the core dropped 1 K from an initial value of 6 K (a density swing of almost 3-fold) the total mass flow error including the error in the cold-end plumbing would be $\sim$30%.

5.2 Active Regenerator Experiments

The results from the preliminary experiments are very encouraging. The device generated steady refrigeration power of 0.40 W at 3.79 K, rejecting heat at 5.51 K. Cycling steady state was arrived at after only four or five cycles. The performance of the device was very sensitive to the timing of the magnetic field changes and much less sensitive to variations in the mass flow.

The same magnetic field waveform was used throughout the experiments: a constant slope form ramping from 1 T to 4 T in 5.25 s then back to 1 T in the next 5.25 s. This waveform was chosen because it was the fastest design sweep rate for the magnet.

Figure 5 shows a set of data for the 20th through 23rd cycles out of the 33-cycle run. The average mass flow rate was 2.0 g s^{-1}. The top traces are the cold-end temperature, T_{circ}(K), in solid line and hot-end temperature, T_ℓ(K), in dotted line; middle trace is the hot-end mass (in fractions, to a maximum value of 2.1 g), f_h; and bottom trace is magnet current, I(A).

The refrigeration provided to the cold reservoir and heat rejected to the hot reservoir were calculated (as described for the zero-field experiments) by converting the temperature data to enthalpy and numerically integrating the enthalpy fluxes for each cycle for each end of the core. The net refrigeration to the cold reservoir is calculated as the enthalpy exiting the cold reservoir on a hot blow less the enthalpy entering the cold reservoir during a cold blow. The net rejection is the enthalpy entering the hot reservoir on a hot blow less the enthalpy exiting the hot reservoir on a cold blow.

As can be seen from Fig. 5 the reservoir temperatures were not steady throughout the cycle. The cold-end reservoir temperature was estimated as the enthalpy-averaged temperature of the helium entering the bottom of the core during a hot blow (flow from cold reservoir to hot reservoir during magnetization). Similarly, the hot reservoir temperature is approximated by the cold blow stream temperature entering the top of the core.

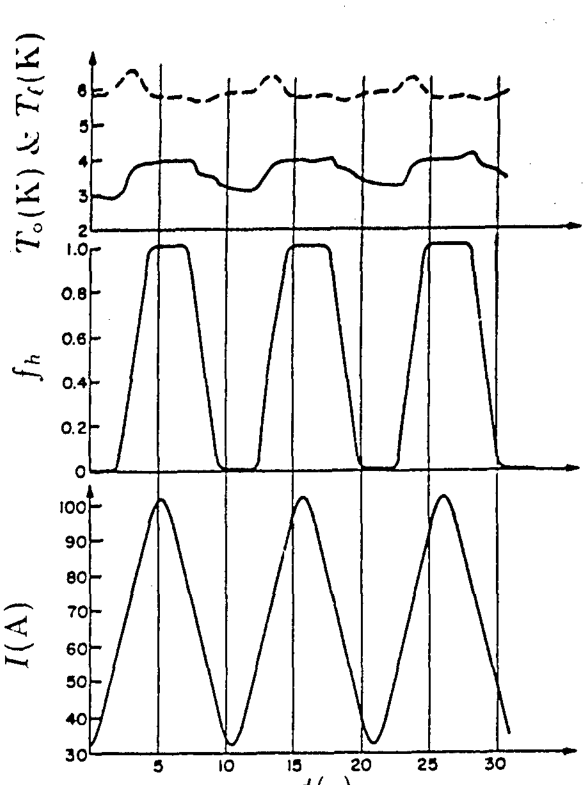

Fig. 5. Data from active regeneration experiments.

The calculations were performed on the last 29 cycles of the 33 cycle 2.0 g s^{-1} run. The first 4 cycles of the run had not established a cyclic steady state. The results of the analysis show an average of 0.40 W of refrigeration to the cold reservoir at 3.79 K. Average power of 3.0 W was rejected to the hot reservoir at 5.51 K.

The actual performance of the magnetically active regenerator differs from the results presented. The causes for the disparities can be grouped into two categories: one source is errors in measurement and calculation, the second is corruption of the experimental quantities by phenomena extrinsic to the experiment.

An example of the latter is the effect of pumping. The mechanical work input produced by the motion of the displacer and compensator is out of phase with the magnetic work input to the regenerator core. As a result, the pumping tends to heat the working fluid on a cold blow and cool it on a warm blow. Consequently, the pumping lowers the refrigeration produced by the magnetic effect. It is not possible to simply quantify the contribution of pumping on the measured results because of its complicated interaction with the magnetic work mode. The loss of refrigeration due to the pumping effect is probably small. The refrigeration loss measured in zero-field experiments with the same mass flow was 0.02 W. The greater temperature difference between the reservoirs in the active field experiments makes a larger density difference between the hot and cold reservoirs and therefore reduces the pumping work.

Sensor errors are examples of the former class of inaccuracies in interpreting the data. Two sources of temperature measurement errors are magnetoresistance of the carbon sensors and transient thermal sensor lag. As discussed above, the resistance of the carbon sensors increases with the applied field. Therefore the indicated temperature measured in the magnetic field will be lower than the actual temperature. The magnetic field error increases with field and decreases rapidly with increasing temperature, becoming insignificant at temperatures above 10 K.

Because the hot blow takes place at a higher average field than the cold blow, the indicated hot blow temperatures are underestimated more than the indicated cold blow temperatures. Helium's enthalpy increases monotonically with temperature. Therefore, the actual net rejection is larger than the indicated rejection and similarly the net actual refrigeration is larger than the indicated refrigeration.

Another source of error in the interpretation of time-dependent temperature data is sensor lag. Like the effect of magnetoresistance, the sensor lag causes both the calculated refrigeration and rejection to be smaller than the actual values.

The temperature errors produced either by magnetic field or by sensor lag are amplified in the calculation of the rejection and refrigeration by the multiplicative factor of the specific heat. The temperature error is particularly large in the calculation of the heat rejection, where hot-end temperatures are in the region of extremely high specific heat. The refrigeration calculation is less sensitive both because of the faster transient response of the transducer and because of the lower specific heat at the cold end.

6. Conclusions

The results demonstrate the successful implementation of magnetically active regeneration. The device generated steady refrigeration power of 0.40 W at 3.79 K, rejecting heat at 5.51 K. The experimental uncertainty could be greatly reduced by determining the temperature transducer lag via an *in-situ* measurement. The lag of the warm-end transducer, if found to be excessive, could be reduced easily by changing its mounting design. Further experiments must be carried out to establish the performance of the apparatus as a function of mass flow, relative timing of the processes, and temperature span of the cycle.

7. References

[1] C.P. Taussig, Magnetically active regeneration, (Ph.D. thesis, Department of Mechanical Engineering, MIT, Cambridge MA, October 1986).

[2] G.R. Gallagher, Analysis of a magnetically active regeneration, (M.S. thesis, Department of Mechanical Engineering, MIT, Cambridge, MA, September 1986).

[3] J.R. Van Geuns, A study of a new magnetic refrigerating cycle, Philips Research Report, Suppl. **6**, (1966).

[4] G.V. Brown, Magnetic heat pumping near room temperature, *J. Appl. Phys.* **47**, 3673 (1976).

[5] J.A. Barclay, O. Moze, and L. Paterson, A reciprocating magnetic refrigerator for 2–4 K operation: Initial results, *J. Appl. Phys.* **50**, 5870 (1979).

[6] C. Delpuech, R. Beranger, G. Bon Mardion, G. Claudet, and A.A. Lacaze, Double acting reciprocating magnetic refrigerator: first experiments, *Cryogenics* **21**, 579 (1981).

[7] H. Nakagome, N. Tanji, O. Horigami, T. Numazawa, Y. Watanabe, and T. Hashimoto, The helium magnetic refrigerator I—Development and experimental results, *Adv. Cryogenic Engr.* **29**, 581 (1984).

DESIGN LIMITATIONS ON MAGNETIC REFRIGERATORS IMPOSED BY MAGNETIC FORCES

J.A. Barclay, M. Shnaider, C.R. Cross, F.C. Prenger, W.F. Stewart, and C.B. Zimm

Astronautics Corporation of America
Astronautics Technology Center
Madison, WI 53716

One of the fundamental requirements in refrigeration is the addition of work during the execution of the thermodynamic cycle. In magnetic refrigerators that utilize the thermomagnetic properties of certain materials, the work is supplied in some cases by action against a magnetic force between the magnet and a moving magnetic material or in other cases by the magnet power supply where the material is stationary and the magnet is charged and discharged. In moving-material designs, the net force that must be supplied is a result of compensation of two rather large magnetic forces. During the motion of the magnetic material the force on the material changes direction and can cause large stresses on the magnetic material. It is important to understand the forces on the materials in any complete magnetic refrigerator design. We have carefully analyzed the magnetic forces for reciprocating-material and for rotating-material designs. The key result in the reciprocating design is that the magnetic forces on the magnetic material entering and leaving the magnet can not readily be totally compensated even when both material blocks are in a counterbalanced arrangement and are of the same temperature. This difficulty in compensation is a result of the difference in the gradients of the magnetic field in different regions of a solenoidal magnet. In rotating wheel designs, the forces are complicated because there is a resultant vertical force on magnetic material not located exactly at the midplane between the magnets

Key words: Design limits; magnetic forces; magnetic material; reciprocating; magnetic refrigerator; rotating.

1. Introduction

The operation of magnetic refrigerators is based on the magnetic field and temperature dependence of the entropy of certain magnetic materials. In order to make a useful refrigerator, the magnetic materials must be magnetized and demagnetized at appropriate times during a cycle. Among the several devices that have been developed [1-7][1], there are at least three major ways to achieve the cyclic magnetization and demagnetization.

The first way is to leave the material fixed in place and to charge and discharge the superconducting magnet (generally solenoidal), that produces the magnetic fields. Some of the advantages of this method are that the magnetic work required during the cycle is entered electrically and that the magnetic forces on the material are limited to compressive stresses if the magnetic material is centered in the magnetic field. The primary disadvantage of this approach is the relatively low efficiency caused by long cycle times and the large ratio of the work required to establish the field to the work required to execute the magnetic cycle.

The second way to cycle the magnetization of the material is to use a fixed solenoidal magnet and reciprocate the magnetic material in and out of the magnet. One advantage of this method is that the magnet can be charged, put in persistent mode, and then left undisturbed during the cycle with the work entered via a mechanical means attached to the magnetic material. One disadvantage of this method is that large periodic forces exist between the magnet and magnetic material as the material enters and leaves the magnet.

The third way to repeatedly magnetize and demagnetize the material is to rotate a continuous piece of material through a stationary magnetic field. One advantage of this method is that the attractive magnetic forces between the magnet and the working material entering and leaving the field are naturally compensated in the material except for those forces required by the cycle-work. One disadvantage of the rotating material method is the inefficiency of producing the magnetic field (generally in a gap between two coils).

This paper presents the results of an analysis of the magnetic forces for both the reciprocating and rotating magnetic material cases and identifies the design limits imposed by the stresses produced by large forces.

2. Theory of magnetic forces

In the development of a magnetic refrigerator there are two important forces that must be carefully considered during the design process. The first one is the Lorentz force produced by one current carrying element on another. This effect produces the forces between the magnets in the refrigerator (assuming a Helmholtz or other two magnet system) and the forces on the windings within the magnets. Such a force is calculated by the Biot-Savart and Lorentz-force laws combined as

---

[1] Numbers in brackets refer to the literature references listed at the end of this report.

$$d\mathbf{F} = \frac{\mu_0 \; i_1 \, d\mathbf{l}_1 \times (i_2 \, d\mathbf{l}_2 \times \mathbf{r})}{4\pi r^3} \tag{1}$$

where μ_0 is the permeability of free space, $\mathbf{r}$ is a vector from the first current element $i_1 d\mathbf{l}_1$ to the second current element $i_2 d\mathbf{l}_2$. While these forces are extremely important, they are not considered in this paper. Vectors are indicated by bold type.

The second force of concern in design calculations is the force between the magnetic material and the magnetic field described by

$$d\mathbf{F} = [(\mathbf{M} \cdot \nabla) \mathbf{B}_{app}] \, d\tau \tag{2}$$

or

$$\mathbf{F} = (\mathbf{m} \cdot \nabla) \mathbf{B}_{app} \tag{3}$$

where $\mathbf{M}$ is the magnetization, $\mathbf{B}_{app}$ is the applied magnetic induction, $d\tau$ is a volume element, and $\mathbf{m}$ is the magnetic moment. The moment $\mathbf{m}$ is assumed to be parallel to $\mathbf{B}_{app}$. In cartesian coordinates, eq. (3) expands to

$$\begin{aligned} \mathbf{F} = \; & \mathbf{i} \left(m_x \frac{\partial B_x}{\partial x} + m_y \frac{\partial B_x}{\partial y} + m_z \frac{\partial B_x}{\partial z} \right) \\ + \; & \mathbf{j} \left(m_x \frac{\partial B_y}{\partial x} + m_y \frac{\partial B_y}{\partial y} + m_z \frac{\partial B_y}{\partial z} \right) \\ + \; & \mathbf{k} \left(m_x \frac{\partial B_z}{\partial x} + m_y \frac{\partial B_z}{\partial y} + m_z \frac{\partial B_z}{\partial z} \right) \end{aligned} \tag{4}$$

where $\mathbf{i}$, $\mathbf{j}$, and $\mathbf{k}$ are unit vectors in the x,y, and z directions. The nine components of the force can lead to some subtle effects, especially because $\mathbf{m}$ is also a function of $\mathbf{B}_{app}$ and T. The treatment made here does not consider the effect of the shape or presence of the magnetic material on $\mathbf{B}_{app}$. Generally, the magnetic materials used in magnetic refrigerators are magnetically soft, not magnetically saturated, and shaped such that their effect on the field profile is estimated at not more than 10% of $\mathbf{B}_{app}$. The exact treatment would require the solution of the field equations in the presence of the magnetic material.

3. Results and discussion

The force calculations were perfomed using a computer code that solves eqs. (3) and (4) by calculating the magnetic field and the field gradients on a specified grid for a given coil geometry and current density. A table of magnetization of the material as a function of **B** and T as well as a temperature profile for the material during the cycle must be supplied for the computer code.

3.1 Reciprocating material

The geometry used in the reciprocating material case is shown in figure 1. A magnet which was approximately a right circular cylinder was used because it is close to the optimum shape for a solenoid [8]. The length of the cylinder of magnetic material was two thirds of the length of the magnet and the diameter two thirds of the bore of the magnet. For the purpose of calculation, the cylinder of magnetic material was axially sectioned into six segments. The force components were calculated on each segment as a function of position along the z axis as shown in figure 1. The cylindrical symmetry reduces the force components to F_Z and F_r as shown in the upper right corner of figure 1. The forces on the segment are primarily axial (along the z direction) but there is a radial component which changes direction as the material moves into the magnet. The magnitude of the axial force F_Z can be calculated for a specific material, temperature profile, and field strength. The results shown in figure 2 are for a maximum field of 6 T, gadolinium gallium garnet working material, and a temperature profile for a magnetic Carnot cycle with the cold end temperature at

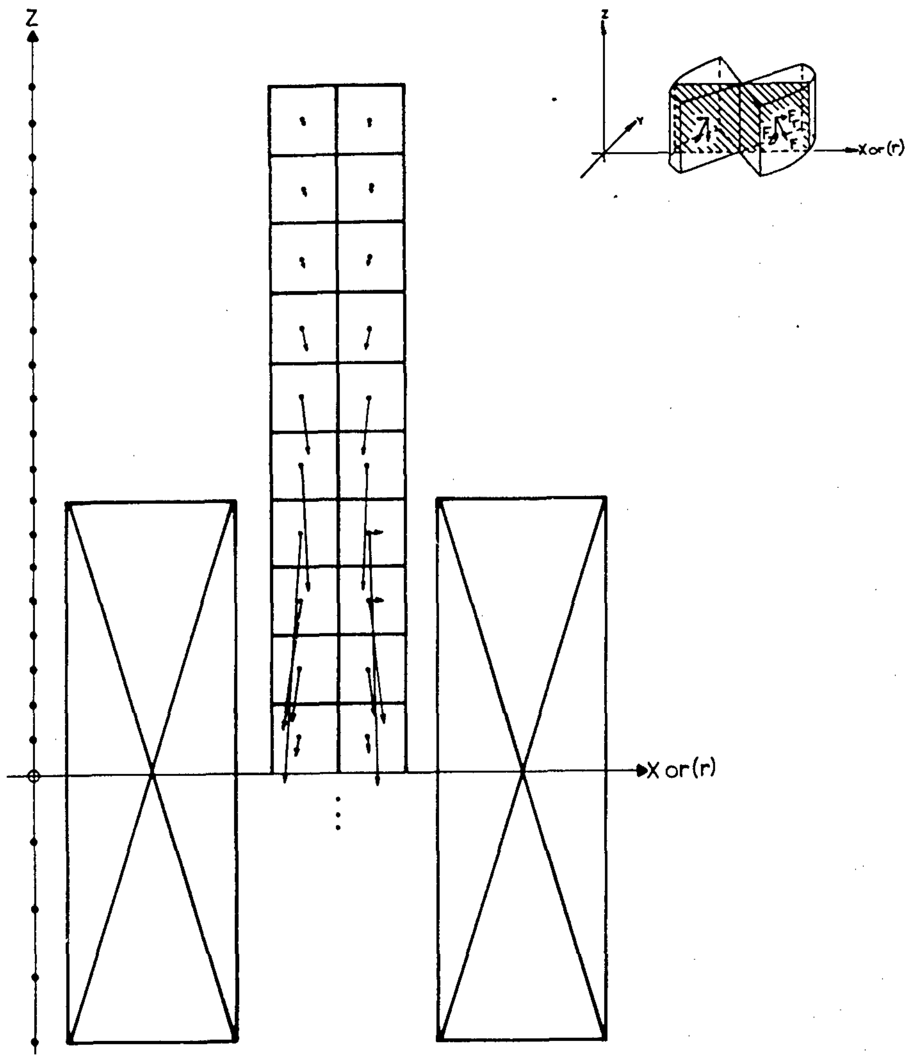

Figure 1. The magnetic forces on a segment of magnetic material as a function of position along the z axis of a solenoidal magnet.

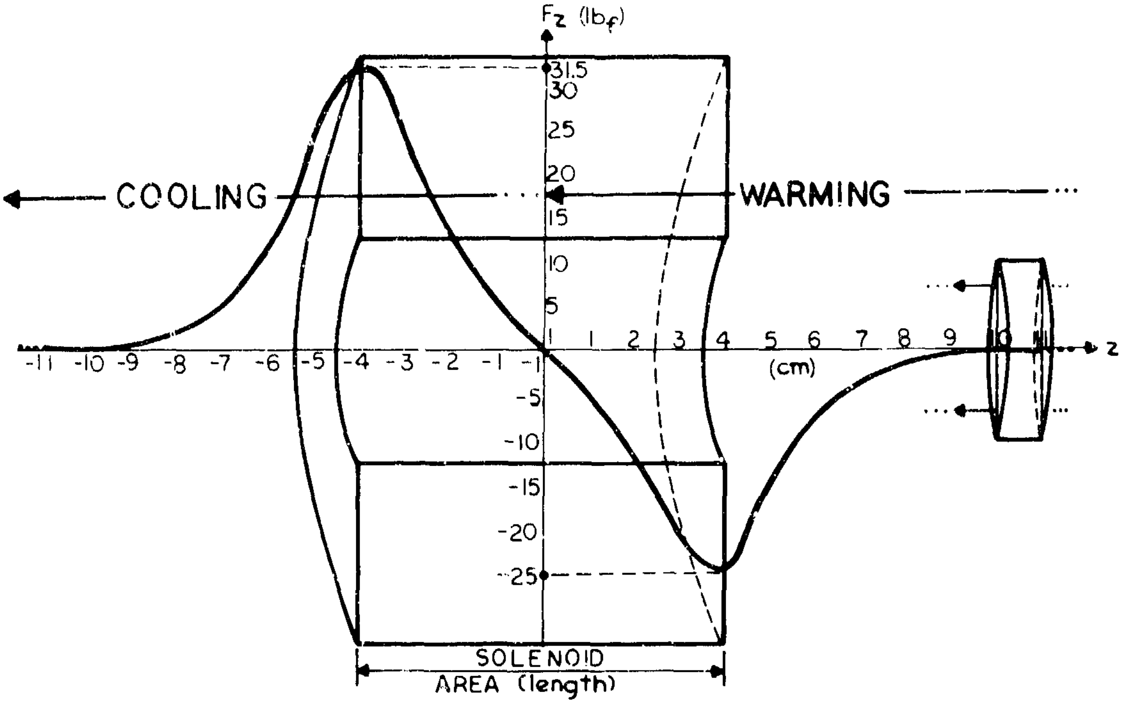

Figure 2. The axial force component on a magnetic material as a function of its distance from the center of a solenoidal magnet.

4 K. For the calculation of figure 2, the material is warmer when it enters the field than when it leaves the field. (This assumes heat transfer from the magnetic material when it is in the center of the magnet). The magnitude of the axial force is maximum near the ends of the solenoid where the field gradients are largest. Neither the shape nor the magnitude of the axial force is symmetric about the center of the solenoid because of the field and temperature dependence of the magnetization and because the magnetic field profile is not symmetric about the end of the solenoid. Therefore, it is unlikely that any compensation mechanism, such as using two matching cylinders of magnetic material at each end of the magnet, can completely cancel the magnetic force. The magnitude of the difference in force across the magnet is only 28.9 N (6.5 lb_f) in the example chosen but the total compressive load between the same two segments is 251.4 N (56.5 lb_f), or almost nine times larger because of the sign reversal of F_z.

3.2 Rotating material

The geometry used for the force calculations on a rotating material is shown in figure 3. The magnetic field is produced by two solenoids in a Helmholtz configuration with the magnetic material in the rim of a wheel rotating through the gap between the magnets. The magnetic material is sectioned into eight segments per quadrant as shown in figure 4. The direction of rotation and the position of the solenoids are also shown in figure 5. The magnetic forces are indicated as small vectors in the figure. Note that the resultant forces are toward the center of the magnet. In the case shown the center of the wheel rim was assumed to pass through the center of the solenoid. In

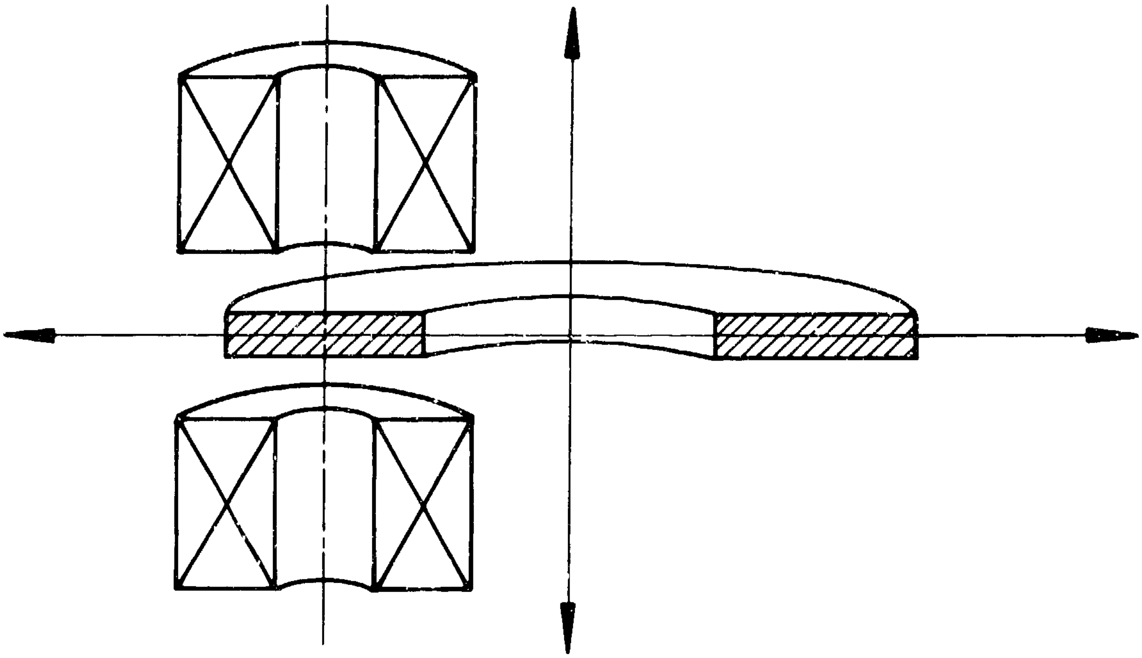

Figure 3. Geometry of a magnetic material in the rim of a wheel rotating between two superconducting solenoidal magnets.

figure 4, there are no z component forces because the segments are axially centered at the midplane between the two magnets. The x and y force components change direction as the segment moves and the resultant force reverses direction at $\Theta = 0^\circ$ (center of the magnet). Hence, the segments undergo a cyclic, compressive stress as they enter and leave the high field region. The magnetic material must be able to withstand this stress without fatigue or excessive deflection. The material must also be attached to the hub of the wheel securely to avoid undue motion.

The forces as a function of rotation angle on a single segment of the wheel are shown in figure 5. The magnetic material was gadolinium gallium garnet and the temperature profile was for a Carnot cycle with a 6 T maximum field. Heat transfer occurs in the high field region. The force components are shown as polar-coordinate components in figure 5. The force component, F_Θ, goes through a maximum as the magnetic material enters the field. The positions of the maximums relative to the magnet windings are shown in figure 5 also. The magnitude of the force in the cold part of the cycle is larger than that in the hot part This net force defines the torque required to turn the wheel as it refrigerates. Another interesting feature of the results in figure 5 is the radial force component. This force represents a net load on the wheel bearing. It is usually assumed that by careful positioning of the magnet center relative to the center of the wheel rim this force can be eliminated. However, the results shown in figure 5 indicate that this cannot be the case. The wheel bearing must withstand a non-uniform radial load.

If the wheel rim of magnetic material is not located in the magnet gap midplane, additional forces must be considered. If the same wheel as shown in figure 3 is moved upwards such that the lower edge of the material is located at the midplane, an unbalanced z component force occurs. The results for this case are shown in figure 6.

The z component is large enough to cause this or unsupported magnetic material segments to flex in the z direction as they transit the high field region. This force requires careful attention be paid to the method of attachment of the magnetic material to the wheel and that the material itself be able to withstand the load.

As shown in figure 5, a segment of magnetic material at the center of the magnetic field is subjected to a total compressive load of about 356 N (80 lb_f) for the specified field and temperature profiles, magnetic material, and geometry. However, the difference between the force on a magnetic material segment entering the magnet field and on one leaving the field is only 26.7 N (6 lb_f). The input power required to rotate the wheel is related to the force difference but the magnetic material is subjected to a much larger compressive load.

4.0 Closure

Forces generated in the working material of magnetic refrigerators as a result of interactions with the magnetic field have been analyzed for two common refrigerator configurations: a stationary magnetic field with either a rotating or reciprocating material motion. Contrary to what was expected apriori the results of the study revealed that nonzero, net forces on the magnetic material exist. These forces arise because of asymmetries in both the magnetic field profile and the temperature distribution within the magnetic material. Furthermore, these asymmetries are a necessary consequence of executing a true Carnot cycle, the method of refrigeration used in this study. These forces have

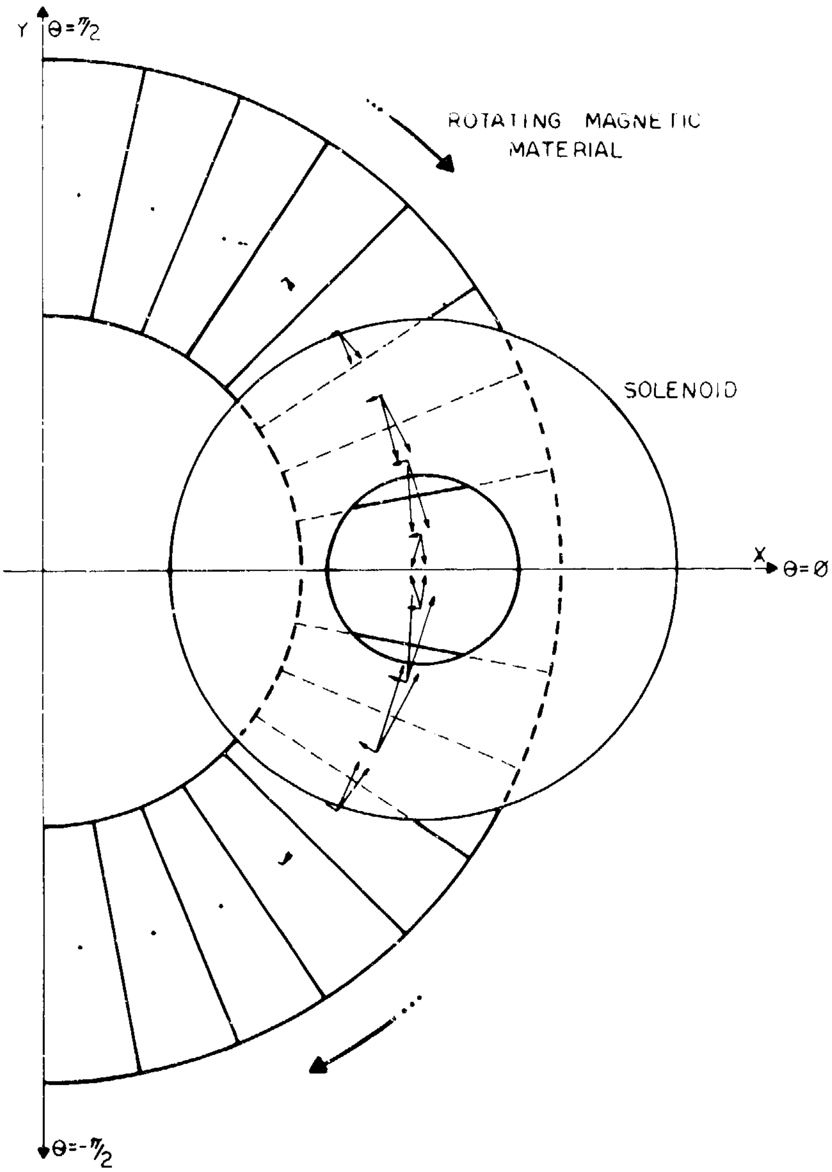

Figure 4. The magnetic forces on a segment of rotating magnetic material as a function of its path as it enters and leaves the magnetic field between two solenoids.

great significance in the design of magnetic refrigerators in such areas as materials selection, mechanical design, and structural support of the individual components. The results of this study demonstrate the need for careful modeling and analysis of candidate magnetic refrigerator designs.

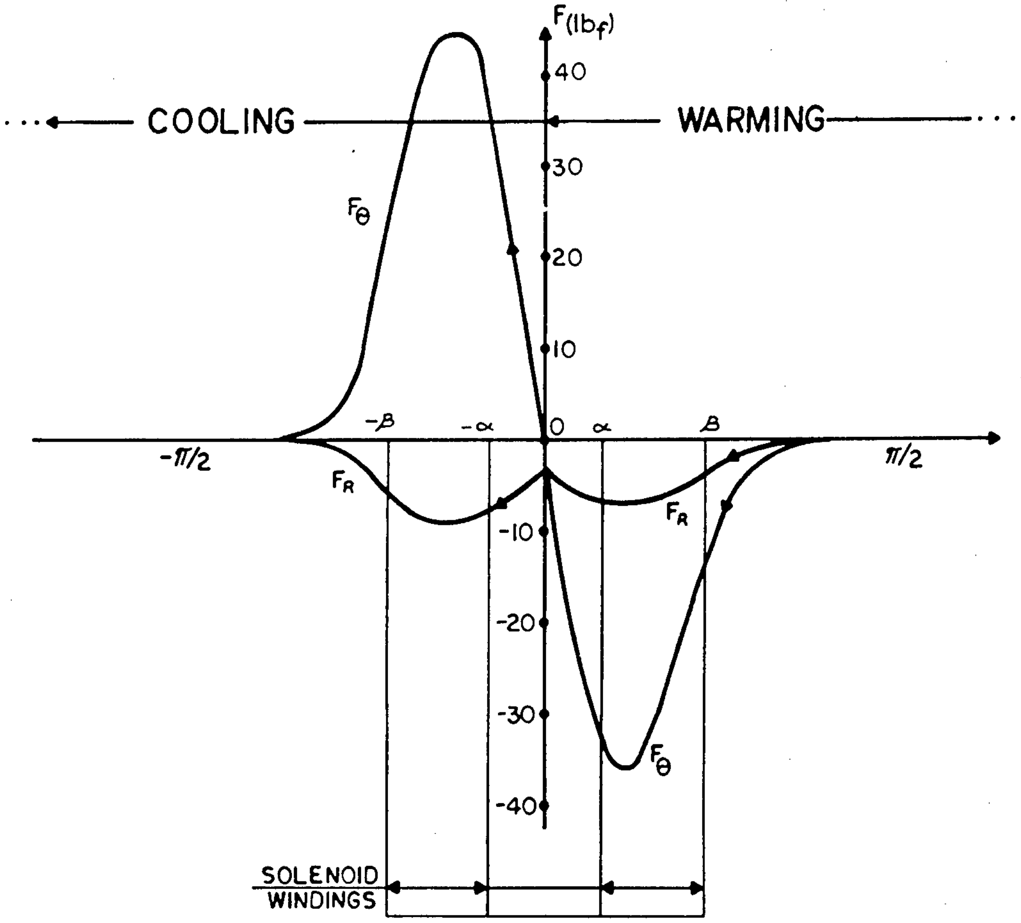

Figure 5. The radial and angular force components acting on a rotating magnetic material as a function of its angular position with respect to the location of the solenoidal magnets.

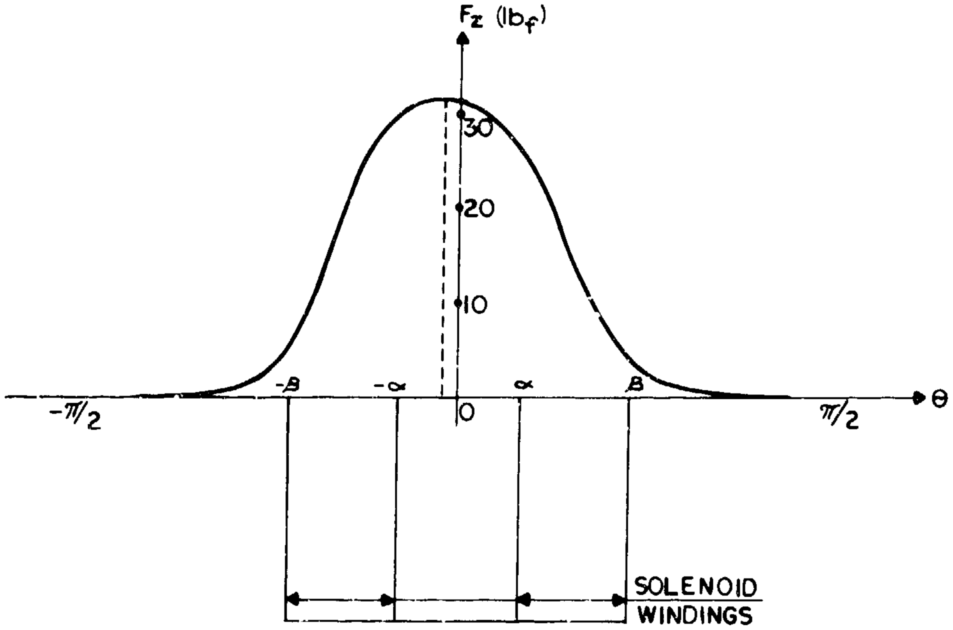

Figure 6. The unbalanced force component in the z-direction as a result of the magnetic material being offset from the midplane of the two solenoidal magnets.

5.0 References

[1] Barclay, J.A., Stewart, W.F., Overton, W.C., Candler, R.J., and Harkleroad, O.D., Experimental results on a low-temperature magnetic refrigerator, in Advances in Cryogenic Engineering [31], edited by R.W. Fast, 743-752 (Plenum Press, New York, N.Y., 1986).

[2] Claudet, G.M., Magnetic refrigeration study at CEA Grenoble, in Advances in Cryogenic Engineering [31], edited by R.W. Fast, 733-742 (Plenum Press, New York, N.Y., 1986).

[3] Deardorff, D.D., and Johnson, D.L., Magnetic refrigeration development, TDA Progress Report 42-78, 49-58, April-June 1984.

[4] Taussig, C., Gallagher, G., Smith, J.L., Kr., Iwasa, Y., Magnetically active regeneration, presented at Cryogenic Engineering Conference 85, Cambridge, Mass., August 12-16, 1985.

[5] Nakagome, H., Kuriyama, T., Ogiwara, H., Fujita, T., Yazawa, T., and Hashimoto, T., Reciprocting magnetic refrigerator for helium liquefaction, in Advances In Cryogenic Engineering, [31], edited by R.W. Fast, 763-769 (Plenum Press, New York, N.Y., 1986).

[6] Fujita, T., Yazawa, T., Hashimoto, T., Nakagome, H., and Kuriyama, T., An experimental study simulating the helium liquefaction process in a reciprocating magnetic refrigerator, in Advances In Cryogenic Engineering, [31], edited by R.W. Fast, 753-762) Plenum Press, New York, N.Y., 1986).

[7] Schroeder, E.A., Transient analysis of a magnetic refrigerator, David W. Taylor Naval Ship R & D Center report no. DTNSRDC-85/099, December, 1985.

[8] Thomas, E.J., and Bright, C.D., Optimizing the design of superconducting solenoids, Cryogenics 6, [2], 10-13 (Feb. 1966).

4.2 K REFRIGERATOR FOR SQUID MAGNETOMETER

Takashi Ishige, Hidekazu Baba, and Yasuo Kuraoka

Cryogenic Technology Development Center
HOXAN Corporation
16-2, Ninomiya 3-chome, Yatabe-machi
Tsukuba-gun, Ibaraki 305, Japan

Iwao Nakano, Gentaro Kai, and Shinichi Ishii

Japan Marine Science and Technology Center
2-15, Natsushima-cho, Yokosuka 237, Japan

A SQUID magnetometer has to be maintained at or close to liquid helium temperature for a long term. To realize this, a small closed-cycle refrigerator can be used for recondensation of liquid helium boil-off in a dewar. The design philosophy for such a refrigerator is as follows: The SQUID magnetometer generates little heating power at liquid helium temperature. If the size of the dewar is minimized on the most suitable condition, the heat loads to the dewar can be very small. Consequently a small recondensing power will be required. Thus the authors designed the dewar capacity to be about 500 cm^3 and the recondensing power to be 100 mW at 4.2 K.

Key words: SQUID; magnetometer; refrigerator; recondensation; liquid helium; dewar.

1. Introduction

Because of their high sensitivity, SQUID magnetometers are used for many applications, such as studies of magnetic properties in laboratories, biomagnetic measurements, geomagnetic measurements in the sea [1], etc. To achieve long-term operation with high reliability, some cooling systems are needed. Hence studies have been carried out on the cooling systems for SQUID magnetometers [2,3,4]. One way to realize long-term operation of SQUID magnetometers is to recondense liquid helium boil-off in a dewar combined with a small 4.2 K refrigerator. This paper describes the construction and some experimental results on a recondensing system for SQUID magnetometers.

As shown in Fig. 1, our recondensing system consists of three main components, a FRP (Fiber Reinforced Plastics) dewar, a G-M (Gifford-McMahon) cryocooler, and

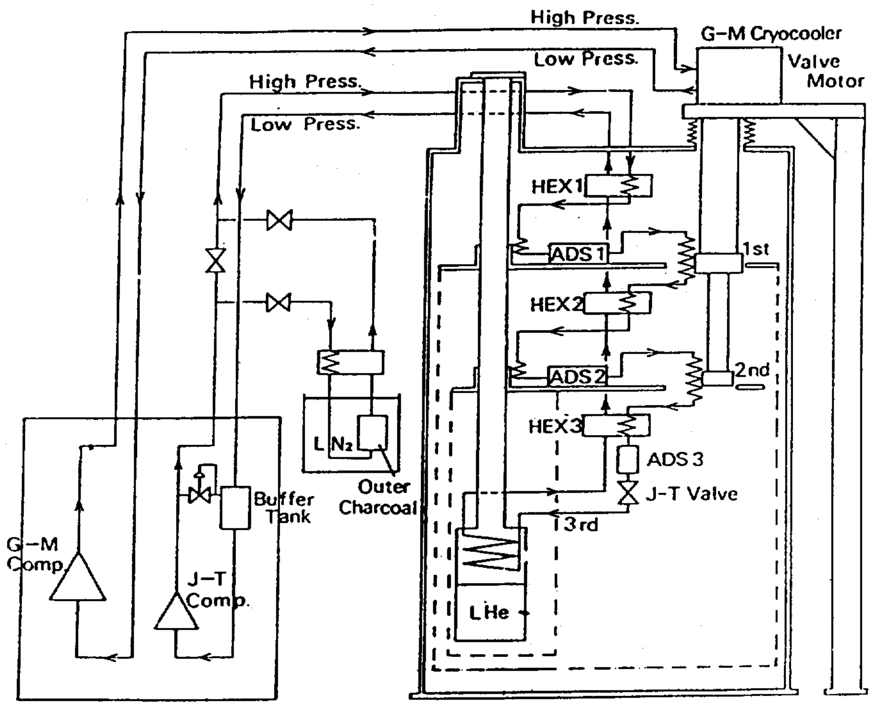
High Press.
G-M Cryocooler
Low Press.
Valve
Motor
High Press.
Low Press.
HEX1
ADS 1
1st
HEX2
ADS2
2nd
HEX3
ADS 3
J-T Valve
3rd
LN₂
Outer
Charcoal
Buffer
Tank
G-M
Comp
J-T
Comp.
LHe

Fig. 1. Flow diagram of recondensing system.

a J-T (Joule-Thomson) circuit with a recondensing heat exchanger. In particular, this system can be used for a commercial SQUID magnetometer, like a probe type.

Design requirements of the recondensing refrigerator are as follows:

(1) Maximum recondensing power of 100 mW at 4.2 K.
(2) Interference to the SQUID magnetometer from the refrigerator reduced to as little as 10 pT of the intrinsic noise level of the SQUID magnetometer.
(3) One year continuous operation of the recondensing state.

From these points, the refrigerator has been designed and constructed, and some performance data have been obtained. The thermal conditions and the mechanical vibration of the refrigerator are mainly discussed in this paper.

2. Design and construction

2.1. Heat loads

Figure 2 shows the refrigerator combined with the FRP dewar and a SQUID probe inside. It consists of a two-stage G-M cryocooler and a J-T circuit with a recondensing heat exchanger.

The high pressure gas in the J-T circuit is cooled by the first and the second counterflow heat exchangers and the first and the second heat stages of the G-M cryocooler. The cold high pressure gas is used for cooling the radiation shields and the neck tube of the dewar. The high pressure gas further cooled by the third heat exchanger is expanded at the J-T valve and generates refrigeration in the recon-

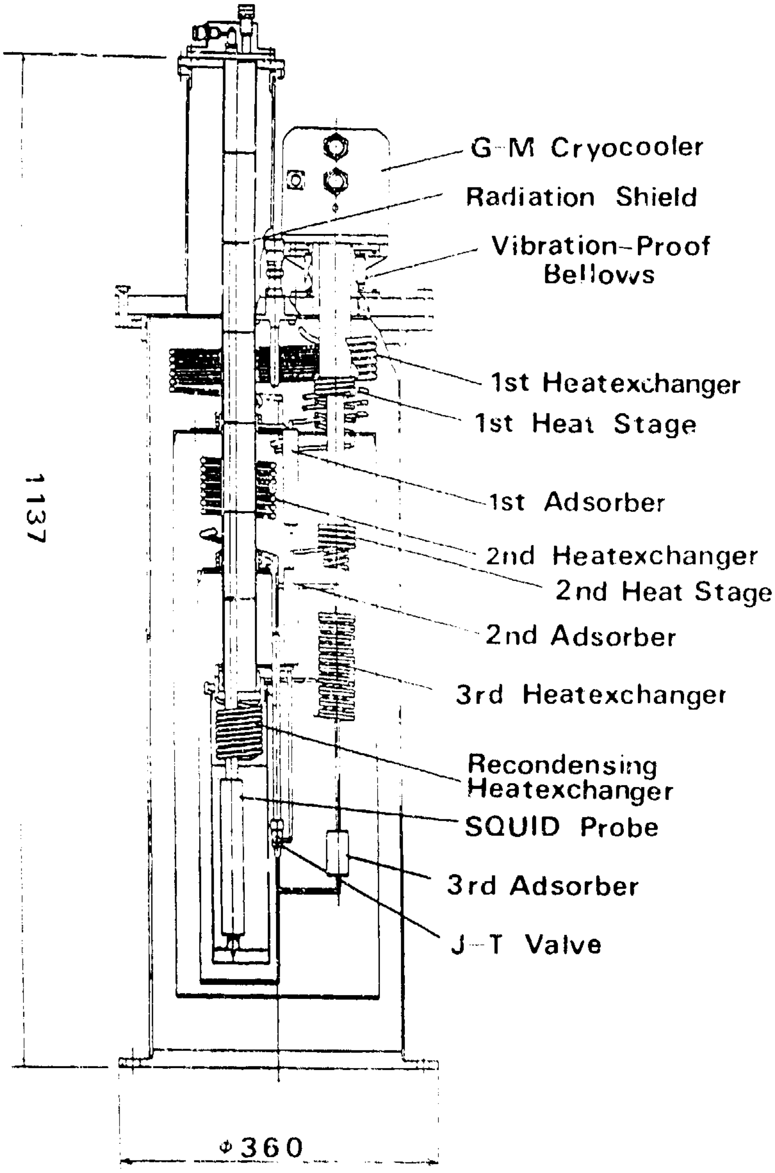
G-M Cryocooler
Radiation Shield
Vibration-Proof Bellows
1st Heatexchanger
1st Heat Stage
1st Adsorber
2nd Heatexchanger
2nd Heat Stage
2nd Adsorber
3rd Heatexchanger
Recondensing Heatexchanger
SQUID Probe
3rd Adsorber
J-T Valve
1137
Φ360

Fig. 2. Refrigerator and FRP dewar.

densing heat exchanger. The three heat exchangers are cooled by the return gas from the recondensing heat exchanger. The temperature distributions are given in this way. Therefore the mass flow rate of the J-T circuit is very important to estimate the heat loads to the recondensing cryostat. Then the mass flow rate is assumed to be 20 mg/s corresponding to the maximum recondensing power designed to be 100 mW.

Table 1 shows the estimated values of heat loads to the recondensing cryostat. It is found that the major part of heat loads to the J-T stage is thermal conduction. Four thermal paths were considered in estimating the thermal conduction, i.e., along the neck tube wall, through the helium gas in the neck tube, along the guide pipe of the J-T valve, and along the SQUID probe. The thermal path along the SQUID probe is dominant among them. It is about 24 mW from room temperature to 4.2 K, because the SQUID probe has no thermal anchor inside of the neck tube to be handled easily. However, the estimated total heat load of 41 mW to the J-T stage is low enough compared with the designed refrigeration power.

Table 1. Calculated heat loads to the recondensing cryostat.

Heat loads	Radiation	Conduction	J-T cooling	Total
1st stage (65 K)	1.2 W	0.44 W	1.4 W	3.0 W
2nd stage (18 K)	14mW	78mW	590mW	680mW
J-T stage (4.2K)	8mW	33mW	-----	41mW

2.2. FRP dewar

The FRP dewar is composed of completely non-magnetic materials such as GFRP (Glass Fiber Reinforced Plastics), aluminum alloy (A5052), stainless steel (SUS316L), and aluminized plastic film. The first and second thermal shields are constructed from several slip-formed aluminum-alloy-plates, which are electrically insulated from each other to prevent the attenuation of the magnetic signals from the environment. These shields are attached to the neck tube of the FRP dewar and cooled by the high pressure gas in the J-T circuit. The upper part of the neck, tube, whose temperature will be maintained over 80 K even when the dewar is in recondensing state, is copper- plated to prevent helium gas from permeating into the vacuum space of the dewar. Based on the size of the SQUID probe case, the volume of the liquid helium pot was defined as 500 cm^3. In typical operation, the liquid helium surface will be maintained at a level 2 cm below the recondensing heat exchanger.

2.3. G-M cryocooler

The G-M cryocooler is used for cooling the J-T gas at the first and second stages. Further, this cryocooler is designed to make use of a free displacer moved by differential fluidic forces with a gas brake mechanism for the purpose of diminishing mechanical vibration. This fluidic-driven displacer is composed of non-magnetic materials such as GFRP, teflon-based plastics, phosphor bronze, brass, lead, copper, and so forth, to reduce magnetic interference to the SQUID magnetometer. However, the cryocooler generates mechanical vibration caused by the pressure change in the cylinder and magnetic noise caused by the valve motor operation. Therefore, to minimize these effects to the SQUID magnetometer, the cryocooler is attached to the top flange of the FRP dewar through the vibration-proof bellows. Further, a vibration proof mechanism is used with the J-T circuit. Namely, the inlet and outlet tubes of the two heat stages, which are thermally connected to each stage of the G-M cryocooler, are made in coiled form so as not to transmit the vibration generated by the cryocooler to the SQUID probe. These vibration-proof mechanisms are expected to protect the SQUID probe from cryocooler vibration.

2.4. J-T circuit

The J-T circuit consists of three counterflow heat exchangers, two heat stages cooled by the G-M cryocooler, a recondensing heat-exchanger, and a J-T valve. The counterflow heat exchangers are made of solder-bonded copper tubes and are coiled in the vacuum space of the FRP dewar. In particular, indium solder has been used to fabricate the third heat exchanger instead of lead compound solder, whose transition temperature to superconducting state is higher than the temperature of the lower side of the third heat exchanger. The measured efficiencies of these heat exchangers are in good agreement with the calculated ones. The recondensing heat-exchanger, shown in Fig. 3, is made of a coiled copper tube of outside diameter 3 mm, and its surface area for recondensation is about 140 cm^2. This value is determined by heat transfer coefficients between recondensed liquid helium and the outer surface of copper tube, and between mist helium produced by J-T expansion and the inner surface of copper tube. The J-T valve consists of an orifice of diameter 1.4 mm and a tapered needle. The valve can be operated from a room temperature region through a thin wall tube made of cupronickel.

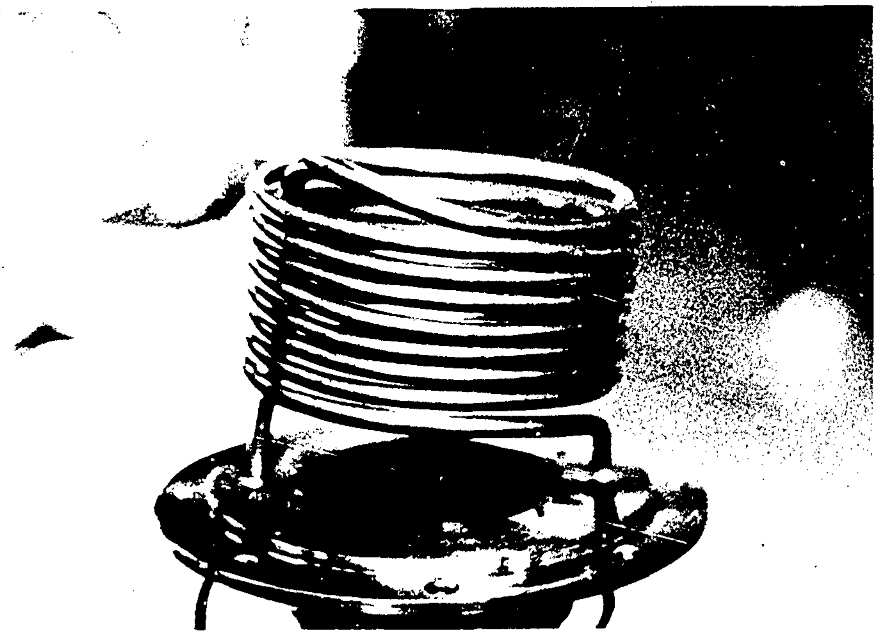

Fig. 3. Recondensing heat exchanger.

2.5. Compressors

Two compressors have been prepared to keep the purity of the J-T gas high. One is for the G-M cryocooler, the other is for the J-T circuit. The compressors diverted from Freon type have a rolling piston with oil lubrication. Hence, three stages of oil separators and a charcoal pot are installed to these units. In order to remove impurities, the J-T gas is cleaned up by an outer charcoal pot in liquid nitrogen before the G-M cryocooler is started.

2.6. SQUID probe

The SQUID probe guide is made of a FRP pipe with six radiation baffle plates outside, and three coaxial cables are inserted in it for tri-axial measurement of the geomagnetic field. The cables are made of cupronickel tubes and core cables, and plastic insulators. These materials are selected for low thermal conduction.

3. Experiments

The recondensing system combined with the SQUID magnetometer was operated in the following sequence:

- Purify the J-T gas by circulation through the outer charcoal pot in liquid nitrogen.
- Cooldown the recondensing cryostat by the G-M cryocooler.
- Transfer liquid helium from a vessel into the pot of the FRP dewar.
- Adjust the J-T valve and monitor the evaporation rate of liquid helium.
- When the evaporation rate goes down to zero, close the vent valve and monitor the vapor pressure of liquid helium in the pot.
- Adjust the pressure regulator at the suction line of the J-T compressor to keep the vapor pressure around 0.1 MPa (recondensing state at or close to 4.2 K).

The experimental data in the recondensing state is shown in Fig. 4. The vapor pressure in the helium pot was about 97 KPa, which corresponded to the liquid helium temperature of 4.17 K. Further, the maximum value of the pressure fluctuation was about 2 KPa, which corresponded to a temperature fluctuation of 20 mK. Consequently, the temperature in the recondensing state is stable enough to operate the SQUID magnetometer. In the recondensing state, the J-T compressor provided the mass flow rate of 20 mg/s at the discharge pressure of 1.5 MPa. From this chart a correlation can be found between the fluctuation of the pressure and that of the mass flow rate.

Figure 5 shows the temperature distribution in the recondensing refrigeration system. From these temperatures, the cooling power at the first and second stages is calculated; the first is about 5 W at 56 K, and the second is about 0.6 W at 18 K

The noise spectrum of the refrigerator was also measured. Noise peaks were observed at frequencies of 1, 2, 4, 6, 8, and 10 Hz. The noise peak of 1 Hz corresponds to the magnetic noise caused by the valve motor. However, the evaluation of such a magnetic noise is not discussed in this paper. The other noise peaks correspond to the mechanical vibration caused by the G-M cryocooler. These peaks were reduced below 67% by the vibration-proof mechanisms. However, the noise level is not low enough to realize the noise level required. Therefore a new vibration-proof mechanism with higher performance should be developed.

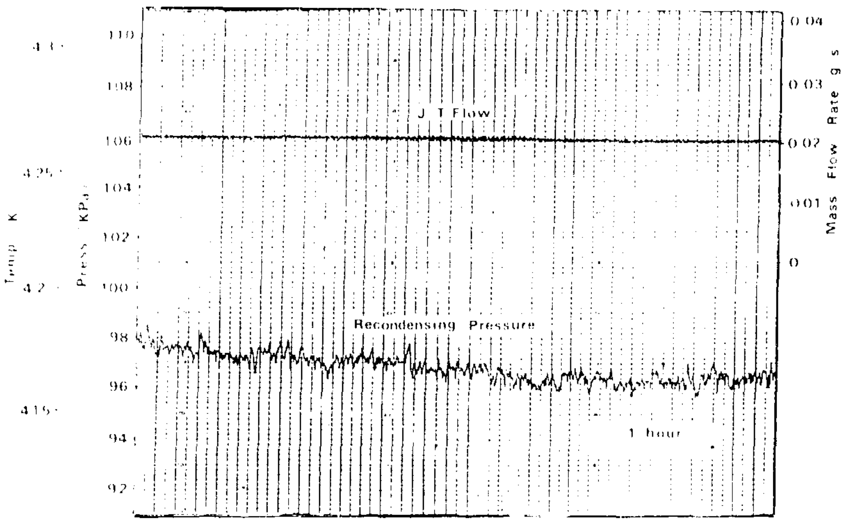

Fig. 4. Vapor pressure in the helium pot and J-T mass flow rate.

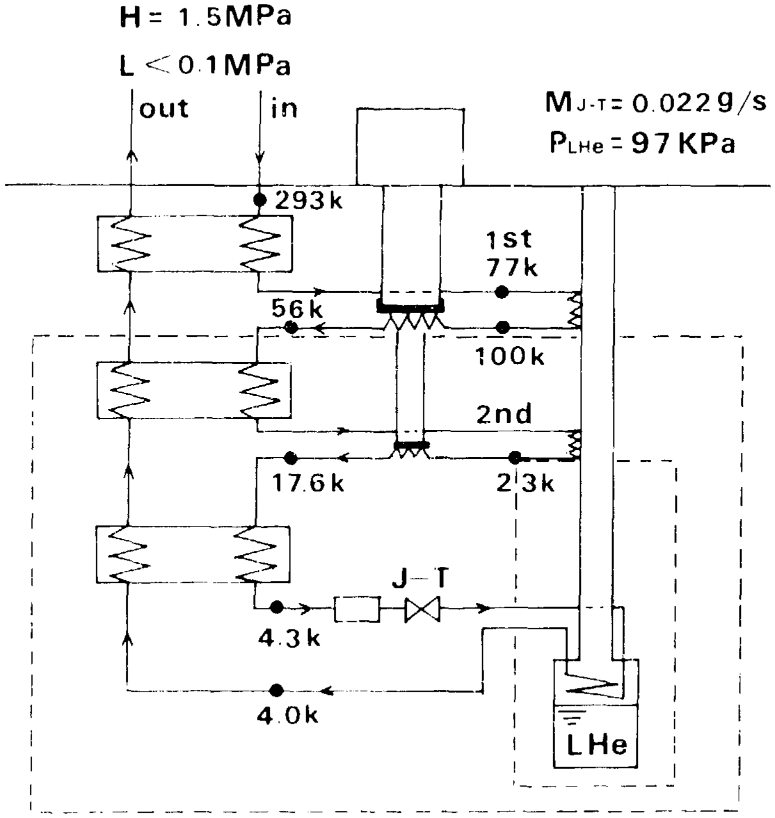
H = 1.5MPa
L < 0.1MPa
out
in
MJ-T = 0.022 g/s
PLHe = 97 KPa
293k
1st
77k
56k
100k
2nd
17.6k
23k
J-T
4.3k
4.0k
LHe

Fig. 5. Temperature distribution of the recondensing refrigeration system.

4. Conclusions

The recondensing state at 4.17 K was obtained using a small, closed recondensing refrigerator for cooling a SQUID probe. Further, the heat balance of the recondensing cryostat is in good agreement with the expected one.

The interference to the SQUID magnetometer is caused mainly by the magnetic noise from the valve motor and the mechanical vibration of the G-M cryocooler. The amplitude of vibration has been reduced by employing vibration-proof mechanisms, but the noise of the SQUID magnetometer was also reduced. Therefore a new vibration-proof mechanism with higher performance will be effective to minimize the interference to the SQUID magnetometer.

For long-term operation, two compressor units are prepared to keep the purity of the J-T gas high, one for the G-M cryocooler and the other for the J-T circuit. Further, the J-T gas is cleaned up by using an outer charcoal pot in liquid nitrogen before the G-M cryocooler is started.

The next steps of this study will be as follows:

- Further discussion about the influence of the magnetic noise caused by the valve motor or the compressors upon the SQUID measurement.
- Actual long-term operation of this system.

5. References

[1] I. Nakano, T. Emura, T. Hotta, Y. Tomoda, and H. Nagano, Ocean Bottom SQUID Magnetometer, Proc. ICEC-10, Helsinki, 31 July-3 August (1984) 830-833.

[2] D. B. Sullivan, J. E. Zimmerman, and J. T. Ives, Refrigeration for Cryogenic Sensors and electronic systems, NBS SP-607, Sup. of Doc., US Govt Print. Off., Washington, DC 20234, USA (1981) 186-194.

[3] N. Lambert, S. Barbanera, and J. E. Zimmerman, Versatile Experimental Low Power 4 K Cryocooler, Cryogenics, 26, [6], 341-345 (June 1986).

[4] G. Walker, Miniature Stirling Cryocoolers: Trends in Development, Cryogenics, 26, [7], 387-391 (July 1986).

AN EXPERIMENTAL STUDY ON A LOW-POWER PLASTIC CRYOCOOLER FOR HIGH-T_c SQUID

Z.X. Huang, G.B. Chen, J.Y. Zhen, F.G. Zhang,
S.M. Li, G.R. Jiang, B.L. Wang

Cryogenics Laboratory, Zhejiang University
Hangzhou, CHINA

This paper introduces a four-stage plastic cryocooler which is used for cooling a high-T_c SQUID and describes its performance, testing, and analysis. Refrigeration temperatures of each stage and the relationship between cooling capacity and filling pressure are measured. The influence of several thermodynamic parameters on machine performance is analyzed.

Key words: Cryocooler; cryogenics; low temperature; refrigerator; Stirling cycle; superconducting devices.

1. Introduction

At present, the interest in using a small closed cycle plastic cryocooler to cool a SQUID magnetometer instead of using a cryogenic non-magnetic liquid helium (LHe) Dewar flask is increasing(1). Experiments have shown that this kind of low-power Stirling cryocooler can match the requirements of a SQUID gradiometer (2).

In order to meet the demand of cooling a high-T_c SQUID, we built a plastic cryocooler as an experimental prototype in 1985. This is a split four-stage Stirling cryocooler. The lowest refrigeration temperature reached in a preliminary test was about 8K (3). Since then, we have run about 50 tests, and cumulative running time is more than 1600 hrs. In this paper, the cooldown process and refrigeration temperatures at each stage and cooling capacity at the 4th cold end under different refrigeration temperature of the cryocooler are reported. Based on the measurements, cooling losses at the 4th stage of the displacer are estimated and main factors that limit refrigeration temperature are analysed.

2. Test system and measurements

Figure 1 shows the experimental system of the cryocooler and its measurement system. Figure 1(a) is the test system. The displacer of the expander is made of nylon bar. It is operated inside a spun-glass epoxy cylinder. The regenerator consists of the radial clearance between the displacer and the cylinder. Through

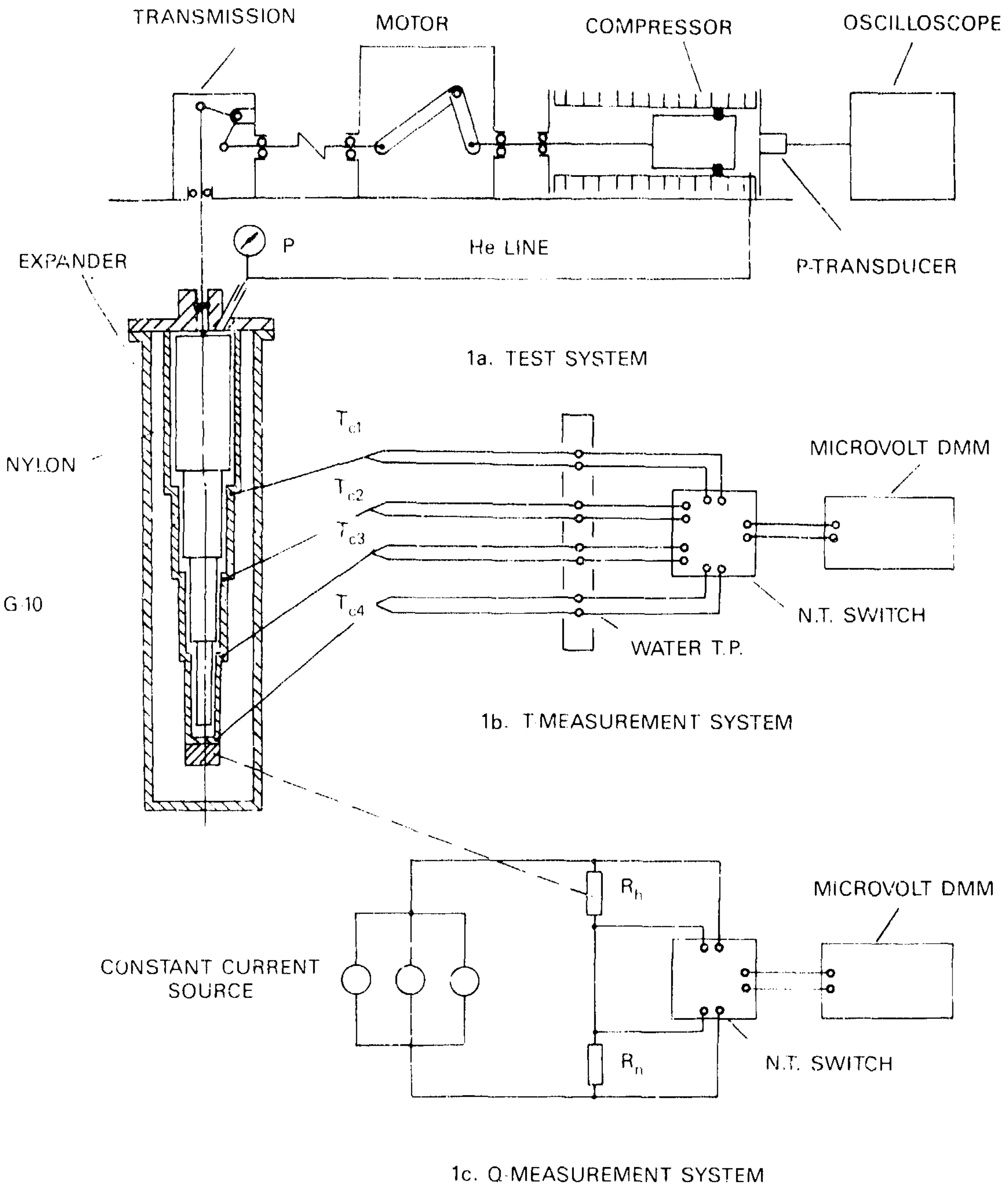
TRANSMISSION
MOTOR
COMPRESSOR
OSCILLOSCOPE
EXPANDER
P
He LINE
P-TRANSDUCER
1a. TEST SYSTEM
NYLON
G-10
T_{c1}
T_{c2}
T_{c3}
T_{c4}
MICROVOLT DMM
N.T. SWITCH
WATER T.P.
1b. T-MEASUREMENT SYSTEM
R_h
MICROVOLT DMM
CONSTANT CURRENT SOURCE
N.T. SWITCH
R_n
1c. Q-MEASUREMENT SYSTEM

Figure 1. 4-stage plastic cryocooler and its test system.

a phase matching mechanism, a phase angle of 90 degrees between the expander and the compressor chamber is maintained. Running frequency is 60 rpm. A pressure gauge ($0-10\times10^5$ Pa) indicating filling pressure, maximum running pressure and minimum running pressure of the system is installed in the He transfer line which connects the split compressor with the expander. There is a pressure transducer at the exit of the compressor. Helium pressure change in the compressor can be registered with a light oscilloscope.

Temperatures at each stage are measured by thermocouples set in corresponding cold head. Figure 1(b) shows the measurement system of refrigeration temperature. Thermocouples KP versus Au-0.03 at %Fe(¢0.2 mm) are used for measuring temperatures of 1st and 2nd stages, while thermocouples KP versus Au-0.07 at %Fe(¢0.1 mm) are used for 3rd and 4th stages. In order to obtain good thermal contact between thermocouple and measuring point, a small hole is drilled at each cold head (aluminum ring) where measuring connective point of the thermocouple is inserted, then some metal powder and vacuum grease are filled in. A total length of 2m of the thermocouple line is helically wound around the cylinder surface of the expander.

Thermocouples have been calibrated through the medium of LN_2, LH_2 and LHe normal boiling points to make relative calibration. Adopting standard table(4). to indicate temperatures, the maximum comprehensive error of the thermocouples is ± 0.5 K.

Cooling capacity is measured with compensation method of electricity-heat (see Fig. 1(c). Since refrigeration power of the cryocooler is very low (in the milliwatt range), heat loss due to the electrical leads must be minimized. Although the resistivity of a copper wire is very low at low temperature, copper is not a good candidate due to its high conductivity. Table 1 lists conductivities of pure copper, constantan and manganin at different temperatures. It is clear from Table 1 that the conductivity of constantan or manganin is only a few thousandths or less of that of pure copper. Heat loss will be greatly decreased when alloy materials are used as lead wire. In order to overcome the effect of Joule heating, a resistance value of heater must be increased to such an extent that the resistance of electrical leads is so much less than the total resistance that it can be neglected. For example, the heating resistance is 12KΩ, while the leads resistance of manganin is 250Ω , and so the error of calculation of cooling capacity due to electrical leads will be less than 2%. In the same time, the heat loss due to Joule heating can be decreased if small heating current is adopted under a certain heating load.

Table 1. The thermal conductivity of several materials at different temperatures (W/m•K)

Material	T, (K)				
	10	40	80	150	300
pure copper	1000	1000	400	400	400
constantan	3	14	18	20	23
manganin	2	7	13	16	22

3. Results and analysis

3.1. Cooldown process

Cooling curves of the cryocooler are shown in Figure 2. Helium pressure of 3.5×10^5 Pa is filled into the system. The cooling time is about 24 hours. It can be seen from Figure 2, that cooling rate of 4th stage is apparently getting large from a temperature of 80K and reaches a maximum value at 40-30K. It doesn't slow down until a temperature of 12K is reached.

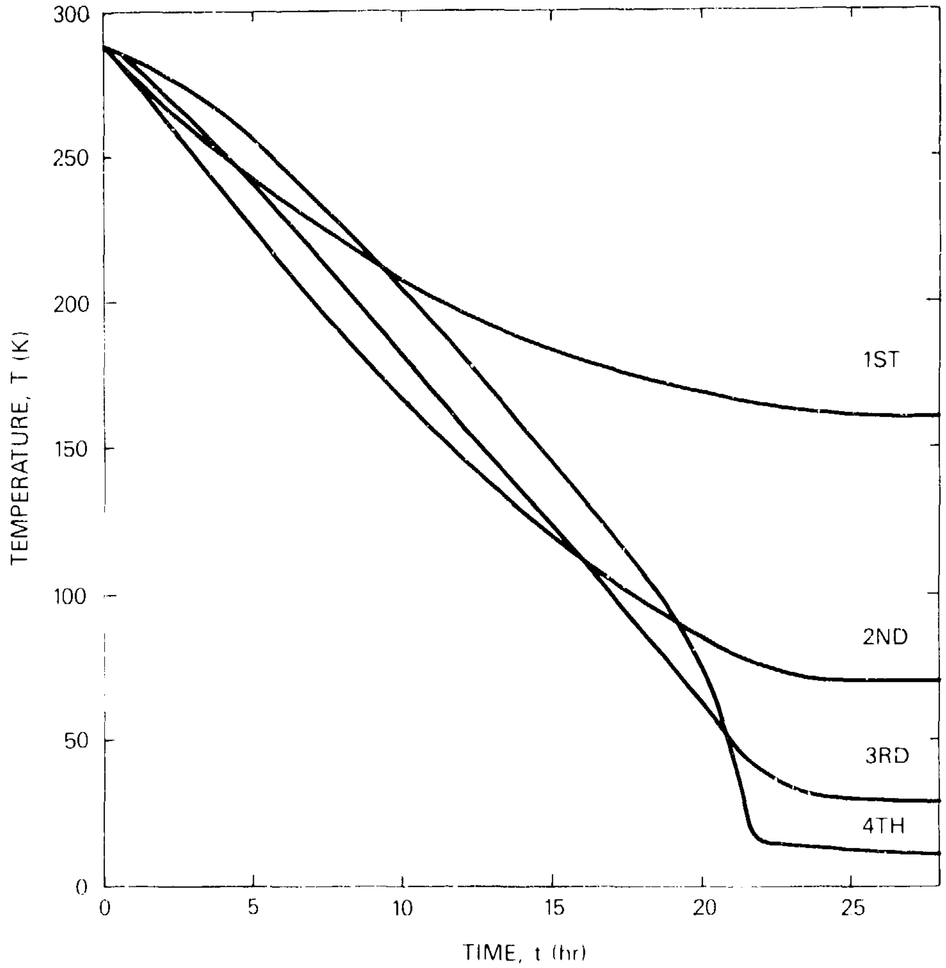

Figure 2. Temperature profile of the cryocooler during cooldown.

Main factors which influence refrigeration during cooldown to a stable state could be understood based on analyses of the refrigeration process. According to the 1st law of thermodynamics, the energy balance of working space is

$$dQ = dU + PdV - h_{in}dm_{in} + h_{out}dm_{out} \tag{1}$$

For an isothermal process, dU=0, the gross refrigeration capacity (8)

$$
\begin{aligned}
Q &= -\oint V dp = \oint p dV - \oint h_{in} dm_{in} + \oint h_{out} dm_{out} \\
&= Q_{ref} - Q_h
\end{aligned}
\tag{2}
$$

where $\alpha = T/V\ (\partial V/\partial T)_p$ - dimensionless bulk expansivity,

Q_{ref} - refrigeration capacity of an ideal gas;

Q_h - enthalpy deficit;

h,m - enthalpy and mass flux of the working medium, respectively. Thermodynamic calculation shows that the main cold losses of the displacer below a temperature of 80K are regenerative loss, axial conductive loss and shuttle transfer loss, while radiant heat flux through multilayer insulation and the heat conducted down electrical leads of alloy wire are fairly small.

For a given displacer, the shuttle heat transfer of a plastic displacer running at low speed can be shown (5) to be

$$Q_{shu} \approx C_{shu}\sqrt{K_n C_{vn}}\ (T_h - T_c) \tag{3}$$

where T_h and T_c are the temperatures of the hot end and the cold end of the stage, respectively;

K_n and C_{vn} are the conductivity and specific heat of the displacer. The variation of nylon's $\sqrt{K_n C_{vn}}$ with temperatures can be seen in Figure 3.

C_{shu} is a comprehensive constant.

Axial heat conducted down the nylon displacer and glass epoxy cylinder can be approximately given by

$$Q_{con} \approx C_{con}(K_n + K_e)\ (T_h - T_c) \tag{4}$$

where K_n, K_e are conductivity of nylon and glass epoxy respectively;

C_{con} is a comprehensive constant.

Regenerative loss of gas gap regenerator can be written as follows (6), When C_p is a constant (above 10K).

$$Q_{reg} \approx C_{reg}(MC_p)^2(KC_v)^{-\frac{1}{2}}(T_h - T_c) = C_{reg}(KC_v)^{-\frac{1}{2}}(T_h - T_c) \tag{5}$$

where K, C_v - conductivity and constant volume specific heat of regenerative material, respectively;

C_{reg} - a comprehensive constant.

The relationship of $(K_e C_{ve})^{-\frac{1}{2}}$ of glass epoxy material with temperature is shown in Figure 3. Nylon material has a similar form.

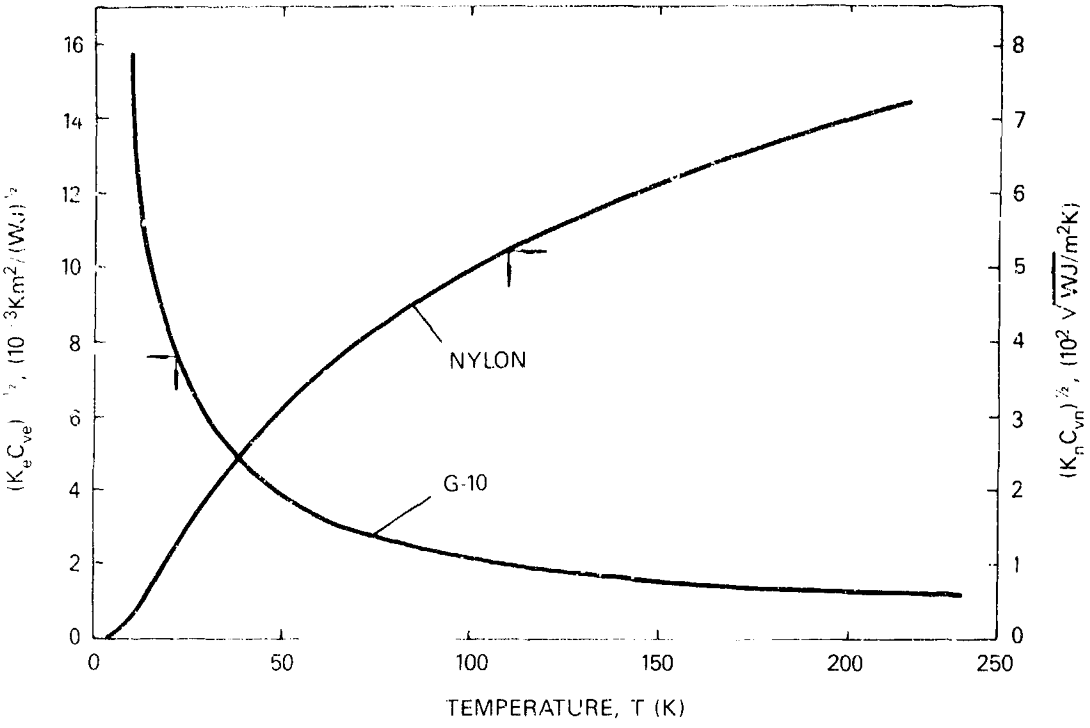

Figure 3. Thermophysical properties of glass reinforced epoxy and nylon versus temperatures.

In briefly, the total cold losses of the cryocooler, neglecting minor losses, at the ideal gas temperature range of 80-20K can be given approximately by

$$
\begin{aligned}
Q_{tot} &\approx Q_{shu} + Q_{con} + Q_{reg} \\
&\approx A[\sqrt{K_nC_{vn}} + (K_n+K_e) + (K_eC_{ve})^{-\frac{1}{2}}]\ (T_h-T_c)
\end{aligned}
\tag{6}
$$

It shows that total losses of the cryocooler in this temperature range are proportional to temperature difference (T_h-T_c) and are also functions of conductivity and specific heat of nylon and glass epoxy, which fall off with a decrease of temperature. The value of $(K_eC_{ve})^{-\frac{1}{2}}$ is getting large apparently in the range of 100-80K (Figure 3). That means regenerative loss of the cryocooler is increasing with a decrease of temperature. From Figure 2, we see when temperature is lower than about 80K, the temperature difference between 4th and 3rd stages becomes narrow. and 4th stage temperature catches up and equals to 3rd stage's at 40K, that is $\Delta T_{3-4}=T_3-T_4=0$. From equation (6) we can derive that a total of losses approximates zero at this point, so that cooling rate of 4th stage increases steeply.

As temperature further decreases, Q_{con} and Q_{shu} become smaller since specific heat and conductivity of nylon and glass epoxy are decreasing rapidly. They make a contribution to refrigeration and compensate the influence due to increasing Q_{reg}. Therefore, the cooling rate of 4th stage continues to increase and approaches a maximum value at or below 30K (see Figure 4). Then the increase of Q_{reg} offsets a

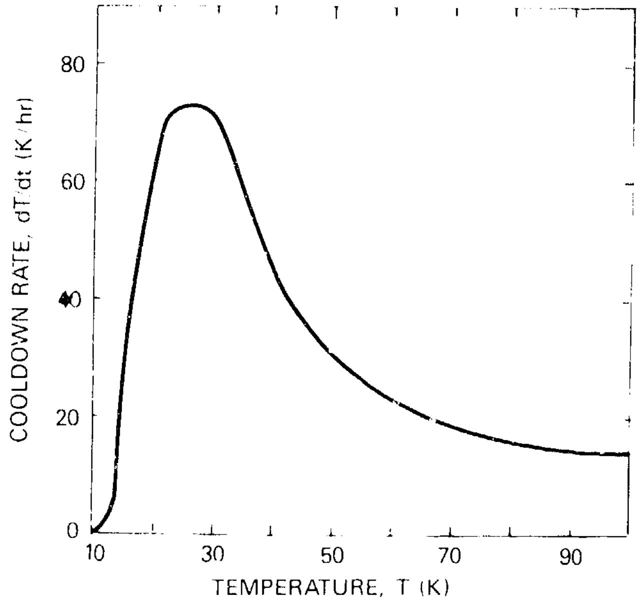

Figure 4. Cooling rate of 4th stage of the cryocooler.

drop of Q_{con} and Q_{shu}. It rises steeply, becomes the main loss, and limits the temperature of the 4th cold end.

3.2 4th stage cooling capacity of the cryocooler

Table 2 lists measured equilibrium temperatures in different stages of the machine after adding various electrical power to 4th cold end. These data are obtained with a filling pressure of 4.5×10^5 Pa. It can be seen from Table 2 that under certain conditions, the refrigeration temperatures of stages 1-3 can be maintained at constant values, while cooling capacity is exported, and the cryocooler is still operated normally.

Table 2. Heating power and corresponding equilibrium temperature of stages

Heating current (mA)	Voltage drop at heater (V)	Heating power (mW)	Each stage equilibrium T, (K)			
			T_{c1}	T_{c2}	T_{c3}	T_{c4}
0	0	0	171.7	80.4	32.2	11.2
0.2	2.32	0.46	171.7	80.4	32.2	11.2
0.5	5.81	2.90	171.7	80.4	32.4	12.2
0.7	8.14	5.70	171.7	80.4	32.6	13.0
0.8	9.31	7.45	171.8	80.4	32.9	13.5
1.0	11.66	11.66	171.8	80.4	33.0	15.2
1.1	12.80	14.08				16.6

According to the data of Table 2, the relationship of the 4th stage cooling capacity with temperatures is given in Figure 5. Measured output of cooling capacity of the machine is about 12 mW with a 4th stage refrigeration temperature of 15K.

3.3. The relationship of lowest refrigeration temperature with filling gas pressure - a valley pressure

Changing filling pressure, we measured refrigeration temperatures of each stage and the required time of equilibrium temperature of the 4th stage with no cooling capacity output. We can see from Table 3 that equilibrium time of the 4th stage decreases with a rise of pressure, while the refrigeration temperature does not simply fall with an increase of pressure. A curve (see Figure 6) is drawn according to 4th stage temperature and corresponding filling pressure listed in Table 3.

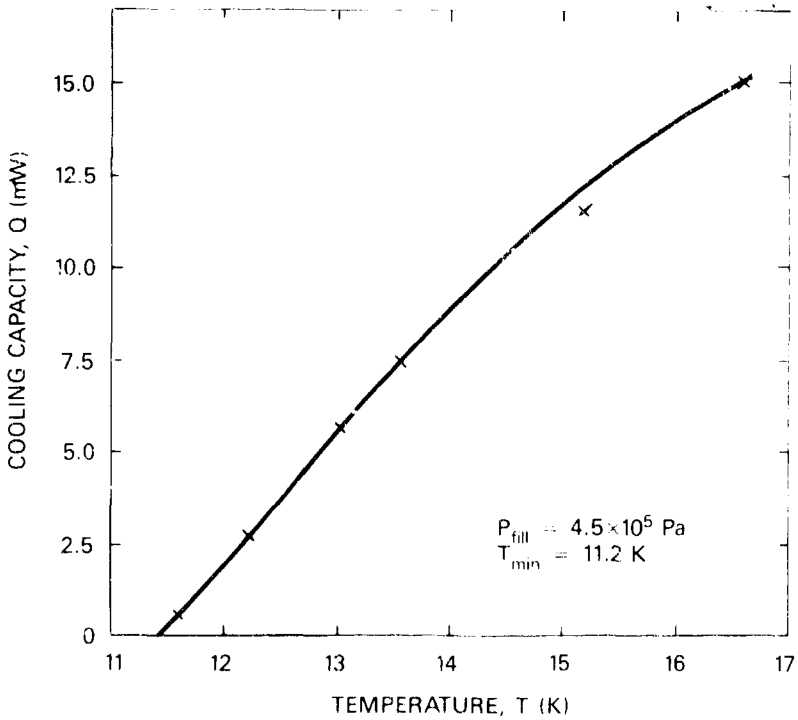

Figure 5. Relationship of cooling capacity with refrigeration temperature of the 4th stage.

Temperature decreases with a rise of filling pressure at the beginning and approaches a low point at a certain pressure; after that, refrigeration temperature increases with a rise of pressure, i.e., a valley pressure exists. It means that the lowest temperature may be obtained at the valley pressure. This temperature will tend to rise at either higher or lower pressure. The regular change couldn't be derived from theoretical equations since refrigeration temperature is a function of many thermodynamic parameters, such as specific heat of helium which is not only a function of pressure, but also is one of temperature. However, we can conclude qualitative relations from thermodynamics equilibrium of the cryocooler, and observe further influence of factors on the lowest temperature.

Table 3. Refrigeration temperature with filling pressure

Filling pressure (10^5 Pa)	Stage refrigeration temperature (K)				Equilibrium time of 4th stage (hr)
	1	2	3	4	
3.0	177	93	50	11.7	33
3.5	170	89	43	9.0	31
3.9	180	90	39	9.2	26
4.3	178	96	45	10.4	25
4.5	168	76	28	11.4	24

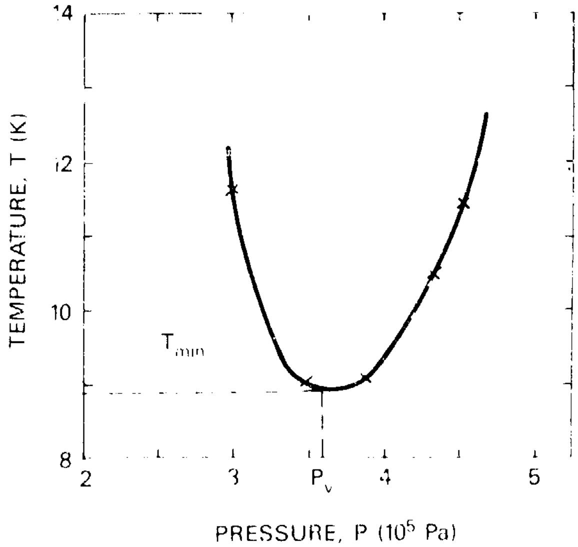

Figure 6. Filling pressure versus refrigeration temperature of 4th stage.

It was pointed out from previous calculation that when cooling temperature is below 15K, refrigeration power of the cryocooler is largely offset by regenerative loss. Refrigeration power of the cryocooler varies with average pressure, that is

$$Q_{ref} = n\pi P_{av} V_0 \frac{\delta \sin\theta}{1+\sqrt{1-\delta^2}} = C_{ref} P_{av} \frac{\delta}{1+\sqrt{1-\delta^2}} \tag{7}$$

where P_{av} = average working pressure of the machine, $P_{av} \approx P_{fill}$;
δ = $(P_{max}-P_{min})/(P_{max}+P_{min})$, dimensionless pressure parameter;
C_{ref} = a comprehensive coefficient.

Neglecting Q_{shu} and Q_{con} at close 10K, we have

$$Q = \bar{a}\, Q_{ref} \approx Q_{reg} \tag{8}$$

Using equation (5), (7) and (8), we obtain

$$T_c \approx T_h - B\left(\frac{\bar{a}}{C_p}\right)\left(\frac{P_{av}}{C_p}\right)\frac{\delta\sqrt{K_e C_{ve}}}{1+\sqrt{1-\delta^2}} \tag{9}$$

where T_h = hot end temperature of the stage;
B = a comprehensive coefficient.

The (a/C_p) term in equation (9) maintains an approximately constant value. When temperature is higher than 12K, C_p also maintains an approximately constant value. In this case, the influence of working pressure on refrigeration temperature of the machine is obvious. The temperature falls with a rise of pressure. When refrigeration temperature is lower than 12K, specific heat C_p of helium varies gradually with pressure (Figure 7), but the influence of pressure is still important. As a result, the refrigeration temperature falls off smoothly with an increase of pressure till a lowest temperature T_{min} is reached. The pressure corresponding to T_{min} is the valley pressure (Figure 7). Till then, the value of specific heat C_p becomes apparently larger, i.e., the term (P_{av}/C_p) becomes smaller if the pressure rises further. In that case, regenerative loss dominates all cold losses and refrigeration temperature must trend toward higher than T_{min}.

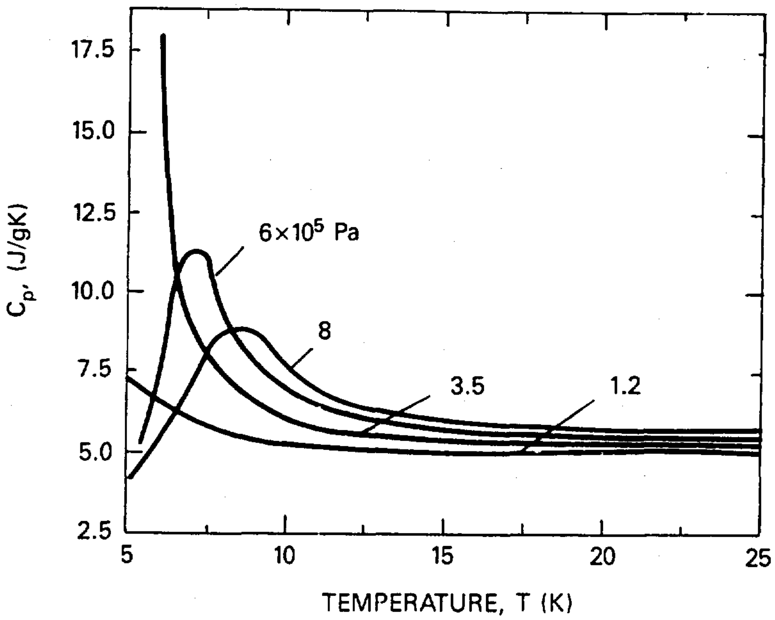

Figure 7. Variation of helium specific heat with temperature.

In short, net refrigeration power increases with a rise of pressure, if varying rate of the combined loss with pressure is less than that of theoretical cooling power with pressure, i.e., limiting refrigeration temperature will decrease with a rise of pressure. On the contrary, cooling power falls with an increase of pressure and limiting refrigeration temperature will rise. A valley pressure must exist. It may be suitable for a small cryocooler to operate in the vicinity of the valley pressure.

However, it seems difficult to choose an optimum pressure since there are a number of factors which influence refrigeration, in additional to difference of each test conditions such as extra friction, orientation effect of the displacer and inhomogeneous gas gap will seriously interfere with machine's normal operation.

4. Conclusions

4.1. In order to meet the demand for cooling a high-T_c SQUID, a split Stirling cycle plastic cryocooler has been built. The expandor of the machine is made of nylon rod and spun-glass epoxy, a gas gap is used as a regenerator. The lowest temperature of the 4th stage approaches about 9K. The 4th stage cooling power of 12mW is obtained at 15K with a filling pressure of 4.5×10^5 Pa. It could satisfy the requirement for cooling a Nb_3Sn SQUID.

4.2. Preliminary analysis on cooling process, refrigeration capacity, and filling pressure of the machine shows that the dominant factors which have a great influence upon machine's performance in the vicinity of 10K are the regenerative loss due to regenerator inefficiency and the enthalpy deficit due to helium non-ideal property. Therefore further improvement of the regenerator efficiency and optimum choice of the operating pressure may be the critical aspects for a cryocooler optimization.

4.3. The influence of helium non-ideality on Stirling cryocooler remains to be explored.

5. References

(1) Zimmerman, J.E. and Sullivan, D.B., A study of design principles for refrigerators for low-power cryoelectronic devices, NBS Technical Note, 1049, 1-19 (1982).

(2) Sullivan, D.B., Zimmerman, J.E. and Jues, J.T., ibid, 96-104.

(3) Chen, G.B. et al, Preliminary test report on a non-magnetic cryocooler, International Cryogenic Conference, Shanghai, China (1985).

(4) Sparks, L.L. and Powell, R.L., Low temperature thermocouples: KP normal silver and copper versus Au-0.02 at %Fe and Au-0.07 at %Fe, J. of Research of NBS - A. Physics and Chemistry, 76A, No. 3, 263-283 (1972).

(5) Radebaugh, R. and Zimmerman, J.E., Shuttle heat transfer in plastic displacer at low speeds, NBS SP-508, 67-74 (1978).

(6) Radebaugh, R., Analysis of regenerator inefficiency for Stirling cycle refrigerators with plastic displacer, NBS TN-1049, 52-57 (1982).

(7) McCarty, R.D., Thermophysical properties of helium-4 from 2 to 1500K with pressures to 1000 atmospheres, NBS SP-631 (1972).

(8) Daney, D.E., Cooling capacity of Stirling cryocoolers - the split cycle and nonideal gas effects, cryogenics, (Oct., 1982).

REFRIGERATION EFFICIENCY OF PULSE-TUBE REFRIGERATORS*

Ray Radebaugh and Steffen Herrmann

Chemical Engineering Science Division
National Bureau of Standards
Boulder, Colorado 80303

The pulse-tube refrigerator has the potential for high reliability because it has only one moving part and works well with pressure ratios of approximately 2. Recent work at NBS showed that an orifice type of pulse tube was capable of achieving 60 K in one stage.

This work describes measurements of the refrigeration capacity per unit mass flow as well as the thermodynamic efficiency of the cooling process which occurs within these pulse tubes. The effect of tube diameter, tube length, orifice setting and frequency were investigated. Efficiencies as high as 90% of Carnot efficiency were measured in some cases when compressor and regenerator losses were neglected. Gross refrigeration power at the optimum orifice setting was as high as 10 W at 80 K for a tube 12.7 mm O.D. by 240 mm long. It is shown that the performance of orifice pulse tubes is dependent on the tube volume and not on diameter and length, and heat transfer to the tube walls is detrimental to the performance. The regenerator losses can be relatively large since high mass-flow rates occur in these devices. With properly designed regenerators these refrigerators have great potential for the temperature range above about 15 K.

Key words: Cryocoolers; cryogenics; efficiency; pulse-tube refrigerator; refrigeration power; refrigerators; regenerators.

1. Introduction

The lack of reliability in small cryocoolers is a problem that has been studied for many years. One approach to increased reliability is the elimination

---

* Work funded by NASA-Ames Research Center.

of some of the moving parts in a mechanical refrigerator. Stirling refrigerators have only two moving parts--the compressor piston and the displacer. In 1963 Gifford and Longsworth [1] discovered a new refrigeration technique which eliminates the displacer from the Stirling refrigerator. They called it pulse-tube refrigeration, but we refer to it here as the "basic" pulse tube. Under Gifford's direction [2-5], basic pulse-tube refrigeration was advanced to the point where a temperature of 124 K was achieved with one stage, and of 79 K with two stages [4]. A single-stage unit with the warm end at 65 K achieved 30 K [4].

The principle of operation, as given by Gifford and coworkers [1-5] and by Lechner and Ackermann [6], is qualitatively simple. The basic pulse tube, shown in Figure 1, is closed at the top end, where a good heat-transfer surface must exist between the working gas (helium is best because of its high ratio of specific heats) and the surroundings, in order to dissipate heat. The open, bottom end also has a good heat-transfer surface to absorb heat from its surroundings. The open end is connected to a pressure-wave generator (in our case a compressor) via a regenerator. During the compression part of the cycle any element of gas in the pulse tube moves toward the closed end and at the same time experiences a temperature rise due to adiabatic compression. At that time the pressure is at its highest value. During the maximum in the pressure wave, the gas has sufficient time to be cooled somewhat by heat transfer to the tube walls. In the expansion part of the cycle the same element of gas moves toward the open end of the pulse tube and experiences cooling due to adiabatic expansion. During the relaxation period of minimum pressure, the gas is warmed by heat transfer from the tube walls. The net result of cycling the pressure in this manner is a "shuttle" heat-transfer process in which each element of gas transfers heat toward the closed end of the pulse tube. The heat pumping mechanism described here requires that the thermal contact between the gas and tube be imperfect, so that the compression and expansion processes are somewhere between isothermal and adiabatic. The best intermediate heat transfer generally occurs when the product of pulse frequency and thermal relaxation time between the gas and the tube walls is approximately unity.

In 1984 Mikulin, et al. [7] installed an orifice at the top of the pulse tube to allow some gas to pass into a large reservoir volume. This type of configuration is called the "orifice" pulse tube. Although the original work of Mikulin et al. [7] placed the orifice just below the isothermal section, our version of this modification placed the orifice above this section (Fig. 2). They applied the pressure wave by the use of valves and used air as the working gas even though the Joule-Thompson effect is not used as a cooling mechanism in the orifice. They were able to obtain a low temperature of 105 K using a pulse tube 10 mm in diameter by 450 mm long with maximum and minimum pressures of 0.4 MPa and 0.2 MPa at a frequency of 15 Hz. The net refrigeration capacity at approximately 120 K was 10 W. It is not clear from their report what fraction of gas passed through the orifice.

A low temperature of 60 K was achieved in our laboratory using helium gas with our version of the orifice pulse tube [8]. The tube was 12.7 mm in diameter by 237 mm long and operated at a frequency of 9 Hz with a valveless compressor.

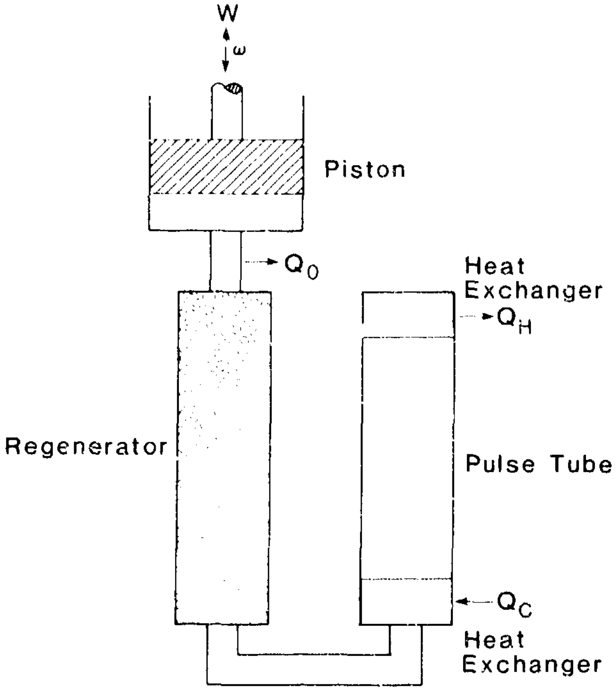
W
ω
Piston
Q0
Heat
Exchanger
QH
Regenerator
Pulse Tube
QC
Heat
Exchanger

Figure 1. Schematic of basic pulse-tube refrigerator.

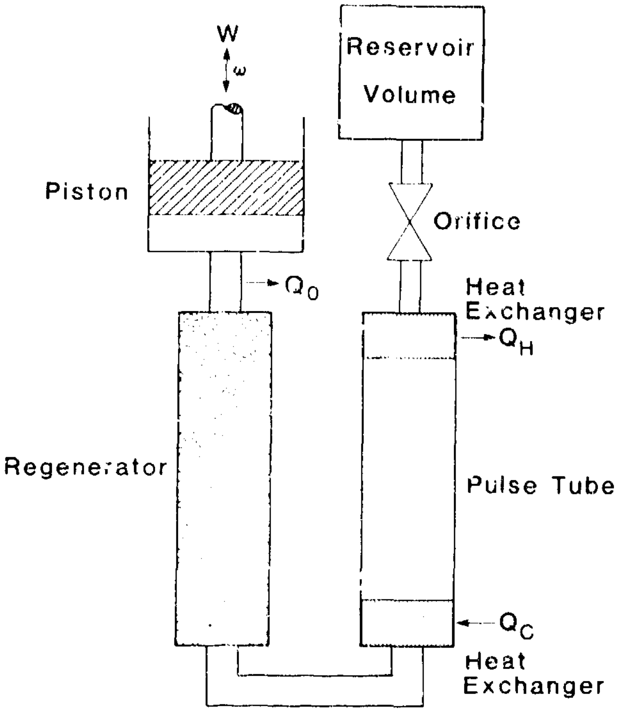
W
ω
Reservoir
Volume
Piston
Orifice
Q0
Heat
Exchanger
QH
Regenerator
Pulse Tube
QC
Heat
Exchanger

Figure 2. Schematic of orifice pulse-tube refrigerator.

Measurements of the efficiency of these pulse-tube refrigerators were never made. Also, no measurements exist of the refrigeration capacity per unit mass flow. Such a quantity is needed to design the compressor and regenerator for a particular pulse-tube refrigerator. The purpose of this work is to provide measured values of the efficiency and refrigeration per unit mass flow for both the basic and orifice pulse tubes. A much more comprehensive description of these measurements is given elsewhere [9]. The present work, however, does include results on one additional pulse tube, from which we are able to draw an important conclusion regarding tube size.

2. Theory

The refrigeration power of most refrigerators is usually expressed in terms of enthalpies of the inlet and outlet flow streams by using the first law of thermodynamics for continuous flow in an open system

$$\dot{Q} = \dot{W} + \dot{m}\,(h_e - h_i), \qquad (1)$$

where $\dot{Q}$ is the refrigeration power, $\dot{W}$ is the rate of work produced by the system,

$\dot{m}$ is the mass flow rate and h is the specific enthalpy at either the inlet or exit. However, all regenerative refrigerators, including the pulse-tube refrigerator, are not continuous-flow systems. In those cases we use time-averaged values to arrive at

$$\langle\dot{Q}\rangle = \langle\dot{W}\rangle + \Delta\langle\dot{H}\rangle, \tag{2}$$

where the time-averaged enthalpy flow for an ideal gas is

$$\langle\dot{H}\rangle = (C_p/\tau) \oint \dot{m}T dt. \tag{3}$$

In eq. (3) C_p is the specific heat at constant pressure, τ is the period of oscillation, T is temperature, and t is time. Consider the case where the system boundaries are drawn through the regenerator on the cold end and the heat exchanger on the hot end. There is no work term between these boundaries since there is no moving boundary. Therefore, eq. (2) shows that the refrigeration power is given by $\dot{Q} = \Delta\langle\dot{H}\rangle$, i.e., heat flow occurs at points where there is a discontinuity in the average enthalpy flow. To calculate enthalpy flow from eq. (3) we use the ideal gas law to relate temperature to pressure by

$$T = P/R\rho, \tag{4}$$

where R is the gas constant in mass units and ρ is the density. The enthalpy flow then becomes

$$\langle\dot{H}\rangle = (C_p A_g/R\tau) \oint uP dt, \tag{5}$$

where A_g is the gas cross-sectional area perpendicular to the flow direction and u is the flow velocity.

For sinusoidal velocity of amplitude u_1 and sinusoidal pressure variation of amplitude P_1, the enthalpy flow in eq. (5) is [8]

$$\langle\dot{H}\rangle = (C_p A_g/2R)\, u_1 P_1 \cos\theta, \tag{6}$$

where θ is the phase angle by which the dynamic pressure trails the flow velocity. Thus, $\langle\dot{H}\rangle$ is a maximum when u and P are in phase (θ=0) and is zero when $\theta=\pi/2$.

First we consider the basic pulse tube where phase shifts can occur only via heat transfer between the gas and tube walls. In that case three ranges of heat transfer may occur. Let τ_t be the thermal relaxation time between the gas and tube walls and ω is the angular frequency. For adiabatic conditions ($\omega\tau_t >> 1$) $\theta = \pi/2$, and from eq. (6) $\langle \dot{H} \rangle = 0$. For isothermal conditions ($\omega\tau_t << 1$) no temperature oscillation can occur and eq. (3) shows $\langle \dot{H} \rangle = 0$ when the amplitude of the temperature oscillation is zero. For intermediate conditions ($\omega\tau_t \approx 1$), θ is some value less than $\pi/2$ and by eq. (6) $\langle \dot{H} \rangle$ is nonzero.

For the case of the orifice pulse tube, the phase angle θ will be less than $\pi/2$ even with no heat transfer and according to eq. (6) the enthalpy flow is nonzero. In this type of pulse tube the enthalpy flow is zero only for isothermal conditions. In a Stirling refrigerator the phase shift of θ from $\pi/2$ is brought about by the use of a piston or displacer.

Because of isothermal conditions the enthalpy flow is always zero in the regenerator (perfect regenerator) and in the heat exchangers. Within the pulse tube itself the enthalpy flow is finite because of intermediate heat transfer ($\omega\tau_t \approx 1$) or because of the flow through the orifice.

At the boundary between the regenerator (or lower heat exchanger) and the pulse tube the enthalpy flow changes abruptly from zero to a finite value. According to eq. (2) there must be a heat flow into the system at that point. Between the cold and hot ends of the pulse tube no heat is exchanged with the surrounding. Thus, $\langle \dot{H} \rangle$ must remain constant within the entire pulse tube at equilibrium conditions. At the boundary with the hot heat exchanger the enthalpy flow suddenly drops to zero and heat flow out of the system must occur according to eq. (2). Because the magnitude of the change in enthalpy flow is the same at the two ends of the pulse tube, $\dot{Q}_C = \dot{Q}_H$ in figure 1 and 2. Thus, a measurement of $\dot{Q}_H$ gives the gross refrigeration power of the pulse tube. The required work input to drive the entire system occurs at the compressor, and an energy balance on the system requires a heat dissipation $\dot{Q}_O$ above the regenerator.

A question to be answered by this work was whether intermediate heat transfer within the pulse tube would improve the performance of the orifice pulse tube by bringing about an additional phase shift between u and P. As will be shown later it actually degrades the performance. Thus, orifice pulse tubes can work at much higher frequencies than the basic pulse tube for the same size of tube.

3. Experimental Techniques

3.1. Test Apparatus

The pulse-tube test apparatus provides a means for measuring the relevant parameters for determining the efficiency, refrigeration power, and mass flow. A schematic of the apparatus is shown in figure 3. The isothermalizers provide good heat transfer to the working gas by using two annular gaps 178 μm thick by 100 mm long. The gas volume in each isothermalizer is only $2.8\ \text{cm}^3$ and the number of heat transfer units is at least 4 for all studies discussed here. Laminar flow occurs in the isothermalizers for flow less than about 3.5 g/s. The largest average mass flow rates encountered here were about 2.9 g/s. A variable reluctance pressure transducer mounted on isothermalizer #2 measured the ΔP across the isothermalizer which gave the mass-flow rate after the flow coefficient was determined in a separate experiment. Accuracy of the mass-flow measurements are about ±15%, which made it difficult to determine the mass flow in the presence of large pressure oscillations. A commercial diode thermometer accurate to ±1 K and a resistance-wire heater were attached to isothermalizer #2 to measure the refrigeration power at various temperatures. The temperature at the bottom end of the pulse tube is the same as that of isothermalizer #2.

Isothermalizer #1 was added to allow boil-off gas from the liquid-N_2 container to absorb the regenerator loss so that the heat input to isothermalizer #2 would be the gross or intrinsic refrigeration power. However, for reasons we do not understand, the ΔT between the #1 and #2 isothermalizers could not be made zero even with the maximum LN_2 boil-off rate. With no cooling to isothermalizer #2 the ΔT for pulse-tube I at 6 Hz and 150 K was 7.6 K, and with the maximum

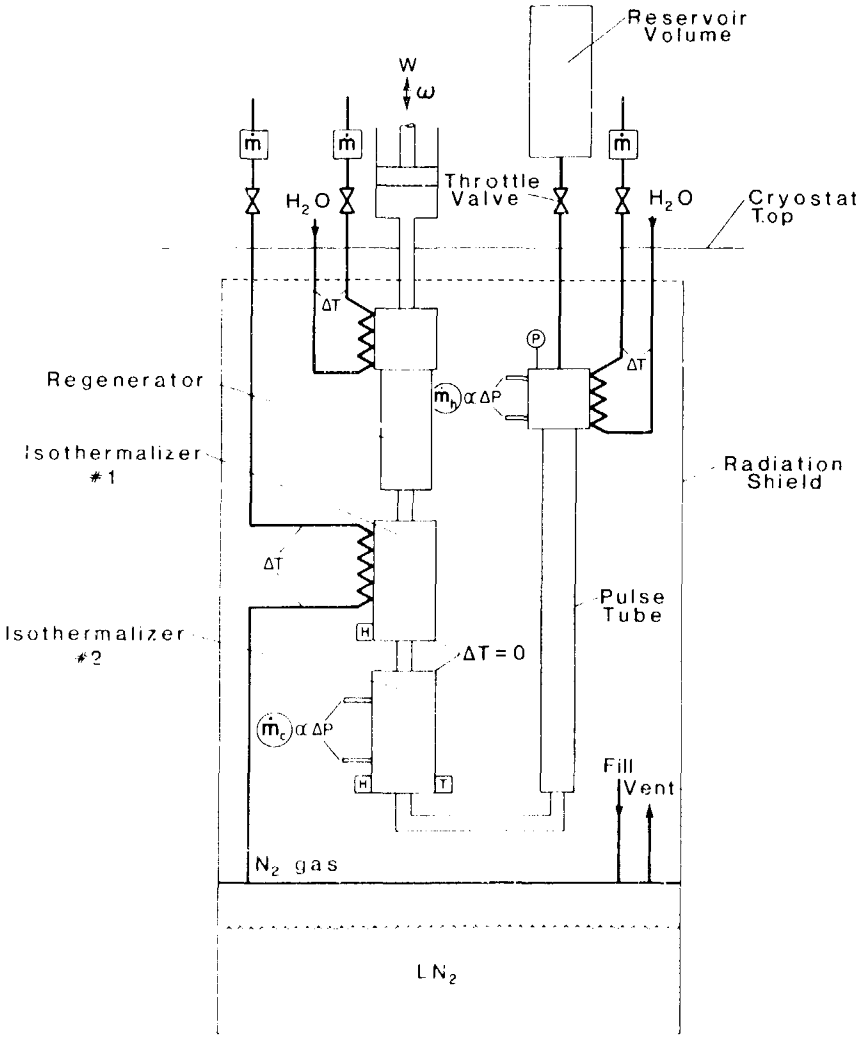
Reservoir Volume
W
ω
ṁ
ṁ
ṁ
H₂O
Throttle Valve
H₂O
Cryostat Top
ΔT
P
ΔT
Regenerator
ṁh α ΔP
Isothermalizer #1
Radiation Shield
ΔT
Pulse Tube
Isothermalizer #2
H
ΔT = 0
ṁc α ΔP
H
T
Fill
Vent
N₂ gas
LN₂

Figure 3. Schematic of test apparatus to measure intrinsic behavior of various pulse-tube refrigerators.

cooling of 12 W the ΔT was reduced to 6.9 K. At that condition the heat input to isothermalizer #2 was much greater than the heat output at the hot end of the pulse tube. Thus, all measurements reported here did not use the N_2 boil-off gas for cooling and the gross or intrinsic refrigeration power was determined from the heat rejected at the hot end since those two heat flows must be equal according to the first law of thermodynamics. The heat rejected is determined within ±5% by measuring the flow rate of water passing through the heat exchanger at the top end of the pulse tube and measuring the temperature rise of the water with a thermocouple attached to the inlet and outlet water streams as indicated in figure 3. The absolute pressure in the pulse tube is measured within ±10 kPa accuracy with a transducer mounted on the hot end.

The orifice consists of a 15-turn needle valve outside the cryostat, and the reservoir volume is 1.0 L. Mass flow in and out of the reservoir volume was determined from measurements of the pressure oscillation within the reservoir volume, which was of the order of 1% of the absolute pressure. The regenerator was a stainless steel tube 19 mm diameter by 127 mm long filled with 1050 discs of 150 mesh phosphor-bronze screen. The gas volume is about 16.2 cm^3. Conduction loss along the regenerator was measured in a separate experiment and found to be represented to within ±20% by

$$\dot{Q}\ (\text{conduction}) = 2.5\ (\text{W}) - 0.0086(\text{W/K})T \qquad (7)$$

At 100 K the conduction is then 1.6 W. Theoretical calculations based on curves of effectiveness vs. heat transfer units in Kays and London [10] give a regenerator loss (at 6 Hz and a mass flow rate of 2 g/s) which can be represented by

$$\dot{Q}_{reg} = 15(\text{W}) - 0.05(\text{W/K})T. \qquad (8)$$

At 100 K the regenerator loss is then 10.4 W and is the dominant loss.

The pressure oscillation was generated by a commercial compressor which has glass-filled Teflon piston rings in order to operate with no oil lubrication in the cylinder. The top head of the compressor, which contained the inlet and outlet reed valves was removed and replaced with a simple steel plate with a single tube attached. This commercial compressor has a volume displacement of about 300 cm^3 in each of two cylinders, although only one cylinder was used in these experiments. A considerable amount of void space exists between the compressor and the pulse tube, otherwise a smaller compressor could be used. The compressor is driven with a three phase motor whose speed is controlled by a variable frequency drive. Compressor speeds from 1 Hz to 12 Hz are obtainable with this system. All the measurements reported here were done with an absolute pressure of 1.0 MPa (10 atm) and a pressure ratio of about 2.6.

3.2. Measurement Methods

Because the compressor in our system was not sized optimally for our test apparatus and because its efficiency is not particularly high, it is of little value to give overall system efficiencies for the pulse tubes measured here. A more accurate comparison between efficiencies of the pulse-tube refrigerator and other refrigerators is best done by using the intrinsic efficiency of just the cooling process and neglecting the compressor and heat exchanger losses. This intrinsic or thermodynamic efficiency is determined by using the measured mass flow rate and pressure to calculate the volume variation of an ideal isothermal compressor with no dead volume between it and isothermalizer #2. Using the ideal gas equation of state gives the compressor-volume variation as

$$V_o(t) = m_o(t)\ RT_o/P(t), \qquad (9)$$

where the compressor temperature, T_o, is 300 K, $P(t)$ is the instantaneous pressure within the system, and $m_o(t)$ is the instantaneous mass of helium gas within the ideal compressor given by

$$m_o(t) = \int_o^t \dot{m}_o(t')dt'. \qquad (10)$$

In eq. (10) $\dot{m}_o(0)$ is assumed to be zero and for small time t' it is assumed to be positive (toward compressor). The thermodynamic work input for the closed cycle is then

$$W = \oint P dV_o. \qquad (11)$$

For a frequency f the average work rate is

$$\langle\dot{W}\rangle = Wf, \qquad (12)$$

and the average mass flow rate at the bottom of the pulse tube is

$$\langle\dot{m}_{pt}\rangle = \langle\dot{m}_c\rangle = 2f\Delta m_c, \qquad (13)$$

where Δm_c is the maximum change in mass over one half-cycle measured at isothermalizer #2. The thermodynamic efficiency relative to the Carnot efficiency is

$$\eta = \dot{Q}(T_o - T_c)/\dot{W}T_c, \tag{14}$$

where $\dot{Q}$ is the gross refrigeration power and T_c is the temperature of the cold end of the pulse tube. The reported efficiency values have an inaccuracy of about ±15%, which is dominated by the inaccuracy of the mass flow rate measurement.

3.3. Pulse Tubes

Experiments were conducted on the pulse tubes listed in table 1. All tubes were made of type-304 stainless steel. The top end is soldered into a copper end piece which contains several discs of 80-mesh copper screen to enhance the heat transfer from the gas to the copper walls. The diameter of these screens is slightly larger than the pulse tube's inside diameter. Enough screens are added (about 50% packing fraction) to give a gas volume in this isothermal section of 10% of the pulse tube volume. The copper end piece is slid into a hole of another copper piece which has the copper coils for the cooling water. Vacuum grease is used to make thermal contact between the two copper pieces. A stainless steel tube of 2 mm i.d. leading to the needle valve at the top of the cryostat is soldered to a short tube projecting from the copper piece on the end of the pulse tube.

Table 1. Dimensions of pulse tubes

Pulse tube #	Length (mm)	outside dia. (mm)	wall thickness (mm)	gas volume (cm^3)
I	240	12.7	0.51	25.7
II	240	6.4	0.30	6.3
III	120	12.7	0.51	12.9
IV	120	19.1	0.71	29.5

The bottom end of the pulse tube is soldered to another copper fitting which allows the tube to be connected to the 6.4 mm o.d. copper tube leading to isothermalizer #2. The copper fitting also has about ten copper screen discs inside to act as flow straighteners and prevent turbulent flow in the pulse tube.

4. Results

Measurements were made at frequencies of 3 Hz, 6 Hz, 9.5 Hz, and 11.5 Hz for pulse tubes I and II; 6 Hz and 9.5 Hz for pulse tube III; and 6 Hz for pulse tube IV. Measurements of refrigeration power, efficiency, refrigeration per unit mass flow, and percent of mass flow through the orifice were made on all tubes for several orifice settings (including zero) at temperatures from about 270 K down to the minimum. Results of all these measurements on the first three pulse tubes are given in detail in Reference 9. The most significant and representative results are discussed here.

The refrigeration power, the refrigeration per unit mass flow, the efficiency, and the fraction of gas passing through the orifice for pulse tube I at 6 Hz are shown in figures 4, 5, 6, and 7, respectively. In figure 6,

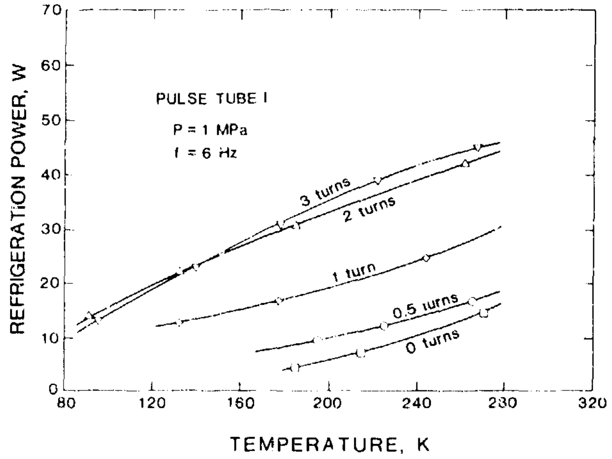

Figure 4. Gross refrigeration power vs. temperature for pulse tube I at 6Hz for various orifice settings.

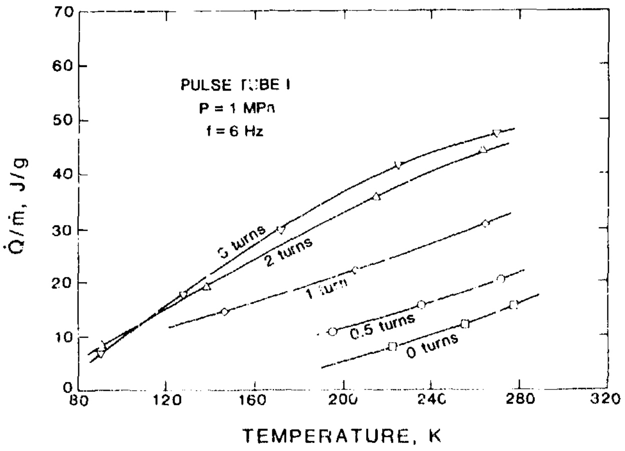

Figure 5. Gross refrigeration per unit mass flow at cold end of pulse tube I at 6 Hz.

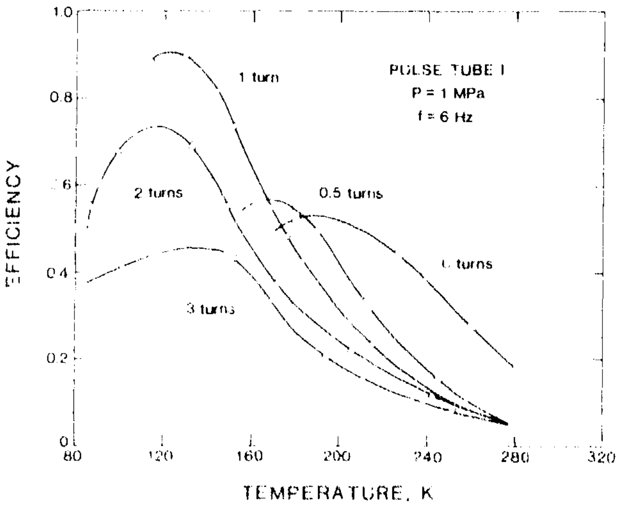

Figure 6. Intrinsic cooling efficiency relative to Carnot at 6 Hz for pulse tube I for various orifice settings.

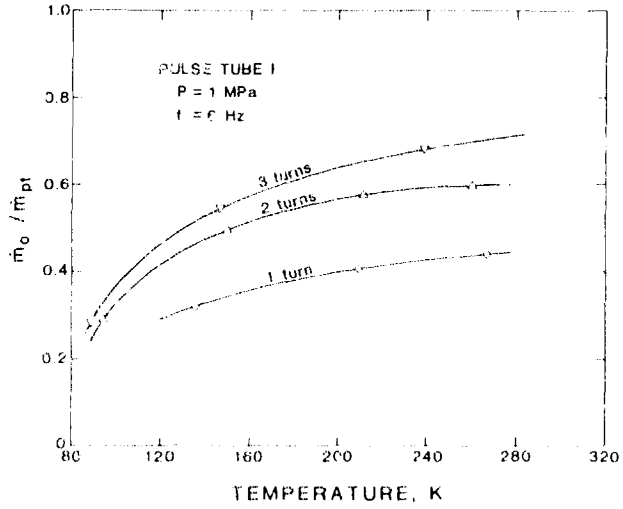

Figure 7. Ratio of mass flow through orifice to mass flow at the cold end of pulse tube I at 6 Hz.

$\dot{m}$ is defined by eq. (13). Note that two or three turns of the orifice needle valve gives the maximum refrigeration power which is about five times that with the orifice closed. The gross refrigeration-power of 10 W at 80 K is quite impressive as are the efficiencies of about 40% to 80% at 100 K. The higher efficiencies occur at lower orifice settings where the refrigeration powers are not as great. Thus, a compromise is necessary in the operation of a practical refrigerator. As the orifice is opened, the mass flow rate increases slightly but the refrigeration per unit mass flow increases nearly the same as the refrigeration power. The amount of gas which passes through the orifice for the maximum refrigeration power is about half the flow rate at the cold end of the pulse tube. Because the flow through the orifice is shifted in phase by nearly $\pi/2$ from the flow at the cold end of the pulse tube, it does not change the magnitude of the total flow significantly.

Figures 8 and 9 show how the efficiency varies with frequency for pulse-tube I with 0 and 3 orifice turns. With 0 turns the pulse-tube refrigeration requires intermediate heat transfer to the walls, which is why the efficiency is highest at the lower frequencies. The very low efficiency at 9.5 Hz is not understood. With the orifice at 3 turns, heat transfer is not required; hence the efficiency is better at higher frequencies. In fact, the low efficiency at the lower frequencies may suggest that heat transfer is not desirable for the orifice pulse tube.

Figure 10 shows the refrigeration power of pulse tube I and II as a function of frequency. At low frequencies the refrigeration power of pulse tube II is less than ¼ that of pulse tube I even though the cross-sectional area and volume are ¼ that of pulse-tube I. The factor of 4 reduction does occur at higher frequencies, however. These results also suggest heat transfer degrades the performance since heat transfer occurs more readily in the smaller diameter pulse tube II at the lower frequencies.

Results from measurements on pulse tube III, which has one-half the length of pulse-tube I, showed similar efficiency values but the refrigeration power was about one-half that of pulse tube I. The optimum orifice setting was at a slightly lower value of 2 turns instead of 2-3 for pulse tube I.

One may question whether the one-half refrigeration power of pulse tube III is due to its shorter length or due to its smaller volume. Pulse tube IV (nearly same volume as tube I but shorter length and larger diameter) was then tested and found to have essentially the same refrigeration power as pulse tube I for the orifice at 3 turns.

5. Discussion

The best results were obtained with pulse tube I and IV, so most of the discussion pertains to those. The measurements of the pulse-tube refrigerator show it to have rather high intrinsic cooling efficiencies. Figure 11 shows the range of useful efficiencies as a function of temperature compared with those from other refrigeration systems. Because the Stirling refrigerator must have shuttle and friction heat loses associated with the displacer motion, the cooling

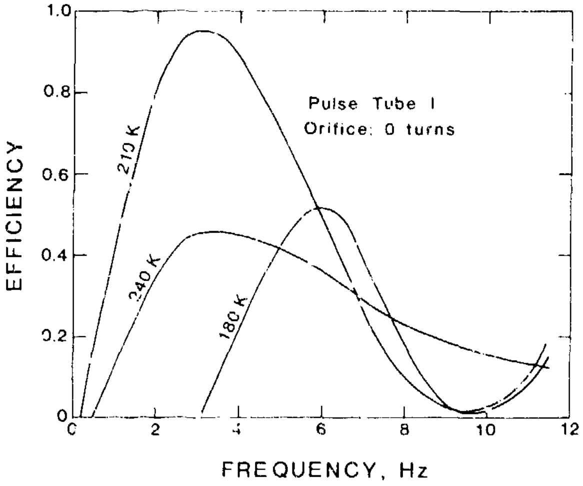

Figure 8. Intrinsic efficiency as a function of frequency for pulse tube I with a 0-turn orifice setting.

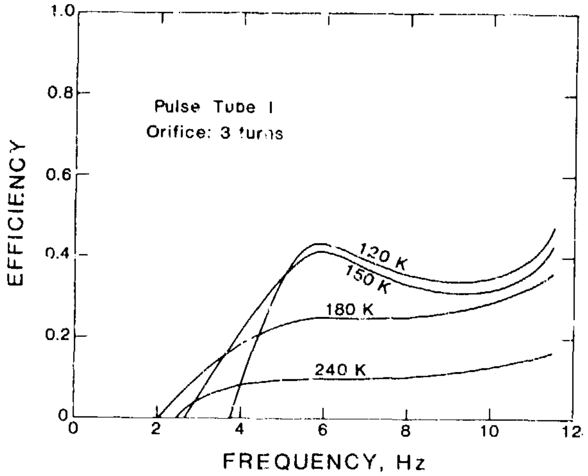

Figure 9. Intrinsic efficient as a function of frequency for pulse tube I with a 3-turn orifice setting.

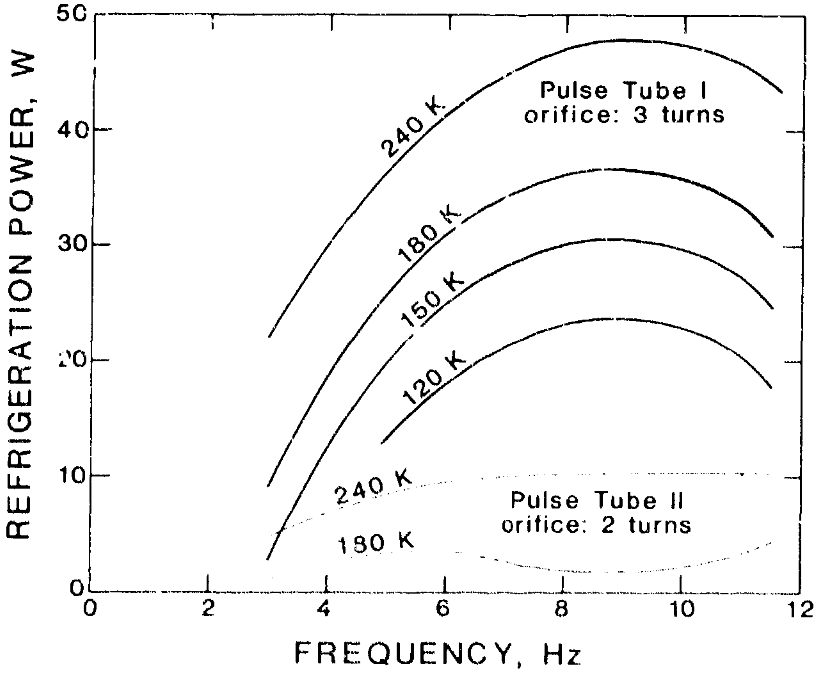

Figure 10. Gross refrigeration power as a function of frequency for pulse tubes I and II.

efficiency of an actual Stirling refrigerator will be somewhat less than indicated in figure 11, which makes it comparable to the pulse-tube refrigerator.

The refrigeration absorbed per unit mass of helium gas is given by

$$q_r = 2\,\dot{Q}/\langle \dot{m}_{pt} \rangle \tag{15}$$

because of the definition of $\langle \dot{m}_{pt} \rangle$ from eq. (13). Figure 12 shows how the reduced refrigeration power per unit mass, q_r/RT, varies with temperature for pulse tube I, where the pressure ratio was 2.6. Shown for comparison is the value for an ideal Stirling refrigerator operating with sinusoidal volume variations at $P_{max}/P_{min}=2.6$ calculated from the Schmidt analysis [11]. Also shown are values for continuous isothermal expansion with the same pressure ratio, and values for the Joule-Thomson refrigerator at the same pressure ratio and at the higher pressure ratios normally used. For a real Stirling refrigerator q_r will be smaller because of adiabatic expansion effects as well as shuttle and friction loss terms not present in the pulse tube refrigerator. The results in figure 12 show that a disadvantage of the orifice pulse-tube refrigerator compared with a Stirling refrigerator is the greater mass flow required to achieve the same amount of refrigeration, which means a larger or better regenerator is required.

An attempt is made here to answer the question of why heat transfer within the pulse tube degrades the performance when the orifice is open. Figure 13 shows the temperature as a function of position along the pulse tube. For the basic pulse tube an element of gas can only relax back to the tube wall temperature through heat transfer as shown by the path followed by an element of gas. For the orifice pulse tube an element can be cooled below the wall temperature as shown by path 2-3 during expansion of the gas by flow through the orifice. Likewise, during path 4-1 the element is heated above the wall temperature by compression of the gas within the pulse tube due to flow back through the orifice. If heat transfer were to occur, the gas element could not be cooled or heated beyond the wall temperature. The greater area enclosed by the element on the left in figure 13 shows qualitatively why the orifice pulse-tube has greater refrigeration power than the basic pulse tube.

6. Conclusions

The orifice pulse tube is capable of reaching 60 K in one stage. The intrinsic efficiency of this device has been shown to be nearly comparable to that of a Stirling refrigerator and greater than that of the Joule-Thomson refrigerator. The refrigeration per unit mass flow is about four times less than that for a Stirling refrigerator operating with the same pressure ratio. Because the pulse-tube refrigerator has only one moving part, and that is at room temperature, it has the potential for high reliability and could replace Stirling, Gifford-McMahon, and Joule-Thomson refrigerators in some cases for temperatures down to about 15 K by using multiple stages. The low temperature limit will be determined primarily by the regenerator loss.

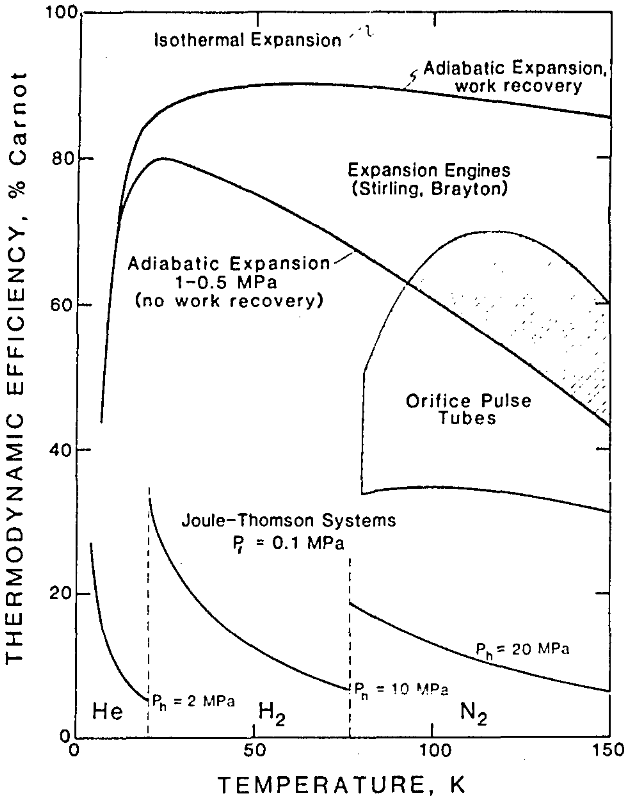

Figure 11. Comparison of the intrinsic cooling efficiency for pulse-tube refrigerators with that of other refrigerators.

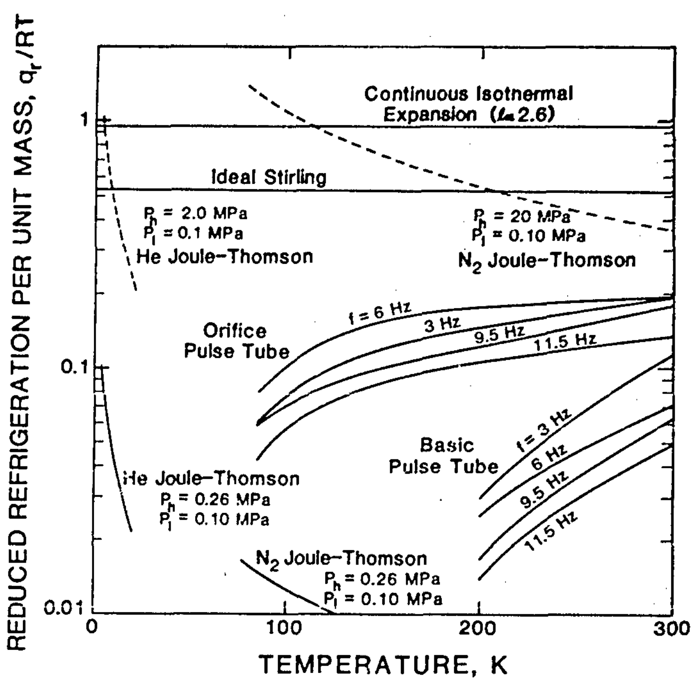

Figure 12. Comparison of the gross refrigeration power per unit mass flow for various refrigerators. All curves except the two dashed lines are for P_h/P_l = 2.6.

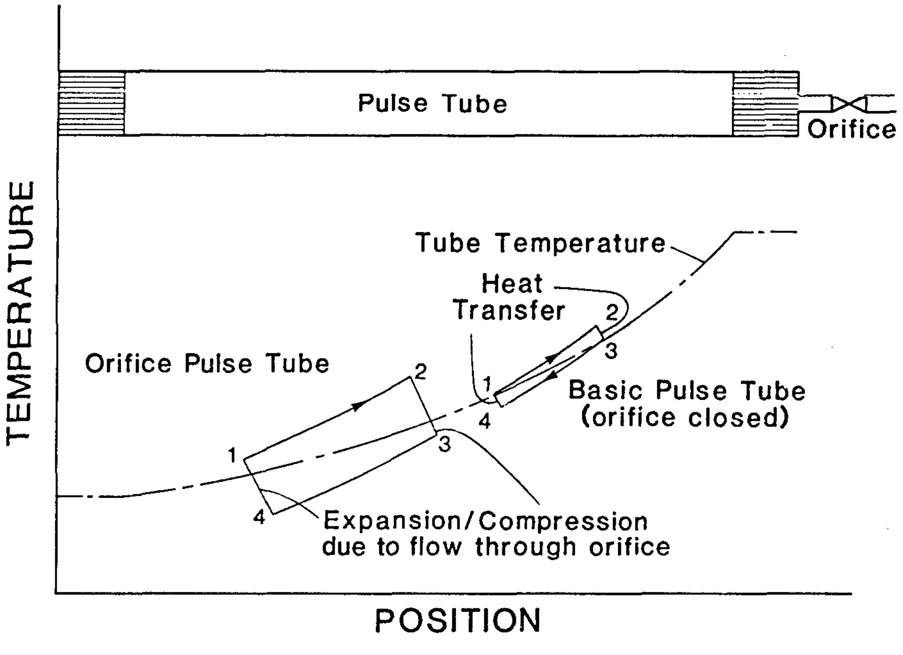
Pulse Tube
Orifice
TEMPERATURE
Tube Temperature
Heat Transfer
Orifice Pulse Tube
Basic Pulse Tube (orifice closed)
1
2
3
4
1
2
3
4
Expansion/Compression due to flow through orifice
POSITION

Figure 13. Temperature as a function of position for an element of gas in a pulse tube for the orifice open and for the orifice closed.

Construction of much of the apparatus was done by David R. Smith and is greatly appreciated. We acknowledge the assistance of C. King of Alabama Cryogenic Engineering and P. Storch during measurements of pulse-tube IV. Discussions with J. Zimmerman, C. King, and B. Louie were most helpful.

7. References

[1] Gifford, W.E. and Longsworth, R.C., Pulse-tube refrigeration ASME paper No. 63-WA-290 presented at Winter Annual Meeting of the American Society of Mechanical Engineers, Philadelphia, Pennsylvania (Nov. 17-22, 1963.)

[2] Gifford, W.E. and Longsworth, R.C., Pulse tube refrigeration progress, "Advances in Cryogenic Engineering", Vol. 10B, Plenum Press, New York (1965), p. 69.

[3] Gifford, W.E. and Longsworth, R.C., Surface heat pumping, "Advances in Cryogenic Engineering", Vol. 11, Plenum Press, New York (1966), p. 171.

[4] Longsworth, R.C., An Experimental Investigation of pulse tube refrigeration heat pumping rates, "Advances in Cryogenic Engineering", Vol. 12, Plenum Press, New York (1967), p. 608.

[5] Gifford, W.E. and Kyanka, G.H., Reversible pulse tube refrigeration, "Advances in Cryogenic Engineering", Vol. 12, Plenum Press, New York (1967), p. 619.

[6] Lechner, R.A. and Ackermann, R.A , Concentric pulse tube analysis and design, "Advances in Cryogenic Engineering", Vol. 18, Plenum Press, New York (1973), p. 467.

[7] Mikulin, E.I., Tarasov, A.A. and Shkrebyonock, M.P., Low temperature expansion pulse tubes, "Advances in Cryogenic Engineering", Vol. 29, Plenum Press, New York, (1984), p. 629.

[8] Radebaugh, R., Zimermann, J., Smith, D.R., and Louie, B., "A Comparison of Three Types of Pulse Tube Refrigerators: New Methods for Reaching 60 K", Advances in Cryogenic Engineering, Vol. 31, Plenum Press, New York, (1986), p. 779.

[9] Herrmann, S. and Radebaugh, R., Measurements of the Efficiency and Refrigeration Power of Pulse-Tube Refrigerators, NBS Technical Note 1301 (1986).

[10] Kays, W.M., and London, A.L., *Compact Heat Exchangers*, 3rd ed., McGraw-Hill Book Co., New York, (1984).

[11] Walker, G., *Cryocoolers*, Plenum Press, New York, (1983).

Preceding Page Blank

LONG-LIFETIME, CLOSED-CYCLE CRYOCOOLER FOR SPACE

Javier A. Valenzuela
Herbert Sixsmith
Walter L. Swift

Creare Inc.
Hanover, NH 03755

A simple, reliable, long-lifetime cryocooler for space applications is being developed. The cryocooler is designed to provide 5 watts of refrigeration at 70 K with a target power-to-load ratio of 30 watts per watt. The reverse-Brayton cycle will employ turbomachines operating in gas bearings to achieve long life. This paper presents the results of the cycle analysis and optimization and describes the design and expected performance of the three key components: turbocompressor, turboexpander, and high effectiveness heat exchanger.

KEY WORDS: Cryocooler, Refrigeration, Turbomachines

NOMENCLATURE

c_p	specific heat
COP	coefficient of performance
k	specific heat ratio
p	pressure
P	power
PR	Pressure Ratio
Q	heat flow
T	temperature
α	See Eq. 13
β	See Eq. 14
ε	heat exchanger effectiveness
η	efficiency

SUBSCRIPTS

A	aerodynamic
C	compressor
E	expander
H	high pressure stream
HX	heat exchanger
I	inverter, inlet
L	load, low pressure stream
M	motor
p	pressure
S	sink

1. Introduction

Several alternative approaches to long-lifetime cryocooling are currently under development through funding by various U.S. Government agencies [1]. Among these approaches, the Turbo-Brayton concept has been identified as having high potential reliability but it is expected to be used only in the higher temperature and high heat load applications. However, recent developments at Creare have succeeded in extending the range of possible turbine sizes lower than ever before. This has been accomplished concurrently with the development of small, robust gas journal bearings and a robust thrust bearing [2,3]. We have succeeded in producing turbine rotors 0.125" diameter which have operated successfully to speeds of 750,000 rpm. It is believed that a turboexpander of approximately this size, operating near 500,000 rpm is a key element in a reverse-Brayton cycle using neon to supply 5 W of cooling at 70 K. Furthermore, it is believed that the availability of this class of turbomachinery will extend the application of the Turbo-Brayton concept to temperatures near 10 K with heat loads of about 1 W.

This paper presents the status of an R&D program aimed at the development of a single-stage, reverse-Brayton (SSRB) cryocooler to provide refrigeration of 5 W at 70 K. A schematic of the cycle is shown in figure 1. This cycle has potentially several advantages over other cycles currently under development. The main advantages are:

- Reduced Electronics. The turboexpander includes a "room" temperature brake wheel to load the turbine instead of a high speed alternator operating at cryogenic temperatures. The brake is a simple closed loop which rejects heat to the main cycle thermal bus. Speed control is unnecessary which eliminates control electronics. The expander is capable of operation at 150% of design speed during cooldown. Design speed is fixed by a preset orifice to throttle flow in the brake circuit. The only electronics required is the fixed frequency compressor power supply.

- High Cycle Efficiency. The turbine is a high specific speed (three dimensional blade) design. It has inherently high efficiency. A similar prototype 0.3125" diameter machine developed at NBS, Boulder had a measured peak efficiency of 0.798 including all heat leaks.

- Reliable Long-Life Bearings. The proposed expander design uses tilting-pad self acting journals and a robust pressurized thrust bearing. Tests at Creare have shown that there is no noticeable deterioration in the journal bearings after two and a half years of continuous operation including more than 650 scheduled stop/starts.

- No Vibration. Both the compressor and the expander operate on gas bearings at rotational speeds of the order of ten kilohertz. The mass of the shafts is only a few grams and any shaft vibration resulting from residual shaft unbalance is effectively damped by the gas bearings.

The key components in the cryocooler are the turbocompressor, the turboexpander, and the main heat exchanger. At present we have completed the analysis and optimization of the cycle and have developed preliminary layouts for these three components. The specifications of the turboexpander are similar to those of other expanders we have built in the past few years and those designs will be adapted for this applications. We are currently building the high speed turbocompressor and expect to start development of the high-effectiveness heat exchanger in early 1987. We anticipate that an engineering model of the cryocooler will be tested in early 1988.

2. Cycle performance

Cycle analyses and optimization were performed in order to select the best suited cryogen for the cycle and to determine the operating conditions of the key components. While the analysis was performed numerically using detailed thermodynamic models of the compressor, aftercooler, heat exchanger, and expander, a simplified, closed-form calculation procedure is presented here to better illustrate the performance trades between the various components. The results of this simplified analysis are within 10 % of those obtained by the detailed calculations and provide a good basis for estimating the range of performance of a turbomachinery-based, single-stage, reverse-Brayton cryocooler.

The cryocooler coefficient of performance (COP) is defined as the ratio of the cooling load to the electrical power input to the compressor motor controller:

$$\mathrm{COP} = \frac{Q_L}{P_{C,E}} \qquad (1)$$

In addition to the cycle load, Q_L, there is a heat leak , Q_E, to the cold end by conduction along the turboexpander shaft and support tubes. The effect of this heat leak on the cycle performance can be conservatively estimated by assuming that the heat is added to the gas stream after the expansion process. That is, the expander heat leak effectively increases the load by Q_E. The COP can then be expressed as:

$$\mathrm{COP} = \left[\frac{Q_L}{Q_L + Q_E}\right] \left[\frac{Q_L + Q_E}{P_{C,E}}\right] \qquad (2)$$

The COP can also be expressed in terms of the temperature rise in the load and in the compressor as:

$$\mathrm{COP} = \eta_I \, \eta_M \left[\frac{Q_L}{Q_L + Q_E}\right] \left[\frac{c_{P,L} \, \Delta T^{*}_{L}}{c_{P,S} \, \Delta T_C}\right] \qquad (3)$$

The asterisk on the load temperature indicates that the expander heat leak has been added to the load.

The preferred cryogens for refrigeration at around 70 K are neon or helium and both behave as perfect gases at this temperature. The specific heats in eq. (2) are therefore the same and cancel out. Moreover, as can be seen in figure 1, the temperature drop available for the load is the difference between the temperature drop in the expander and the temperature difference in the heat exchanger. Hence eq. (3) can be expressed as:

$$\mathrm{COP} = \eta_I \, \eta_M \left[\frac{Q_L}{Q_L + Q_E}\right] \left[\frac{\Delta T_{E,A} - \Delta T_{HX}}{\Delta T_C}\right] \qquad (4)$$

As indicated in eq. (4), one effect of the heat exchanger losses is to reduce the temperature drop available for the load. As the load temperature is decreased for a fixed heat exchanger effectiveness, the heat exchanger temperature difference increases and the COP decreases correspondingly (for constant pressure ratio). Eventually, the temperature difference across the heat exchanger becomes equal to the expander temperature drop and the COP becomes zero. Therefore, the lowest temperature that can be achieved in the SSRB cycle is limited by the heat exchanger effectiveness.

A second effect of the heat exchanger losses is related to the heat exchanger pressure drops. Because of the heat exchanger pressure drops, the pressure ratio in the expander is less than that of the compressor, as illustrated in figure 2. The losses associated with the heat exchanger pressure drops can be expressed as the difference between the temperature drop the expander would have if the heat exchanger pressure drops were zero and the actual expander temperature drop:

$$\Delta T_{E,p} = \Delta T^{*}_{E,A} - \Delta T_{E,A} = \eta_{E,A} \, T_{E,I} \left[\left(\frac{p_L + \Delta p_L}{p_H - \Delta p_H}\right)^{\frac{k-1}{k}} - \left(\frac{p_L}{p_H}\right)^{\frac{k-1}{k}} \right] \qquad (5)$$

Since the heat exchanger pressure drops are normally much smaller than the pressures p_L and p_H, eq. (5) can be approximated as:

$$\Delta T_{E,p} = \frac{\eta_{E,A}(T_L+\Delta T_{HX})(k-1)}{k} \left[\frac{p_L}{p_H}\right]^{\frac{k-1}{k}} \left\{ \left[\frac{\Delta p_L}{p_L}\right] + \left[\frac{\Delta p_L}{p_H}\right] \right\} \qquad (6)$$

The effect of the heat exchanger pressure drops on the cycle performance can be accounted for by adding this temperature drop to the actual temperature difference across the heat exchanger.

An overall heat exchanger effectiveness can be defined as:

$$\epsilon^*_{HX} = 1 - \frac{\Delta T_{E,p} + \Delta T_{HX}}{T_S - T_L} \qquad (7)$$

This is the effectiveness which should be used when comparing the performance of two heat exchangers of different design.

Substituting $\Delta T_{E,A}$ from eq. (5) into eq. (4) and expressing the expander and compressor temperature drops in terms of the compressor pressure ratio and the respective aerodynamic efficiencies results in an expression for the COP which explicitly separates the compressor, expander, and heat exchanger losses:

$$COP = COP_{CARNOT} \cdot \eta_C \cdot \eta_E \cdot \eta_{HX} \qquad (8)$$

where the Carnot coefficient of performance is defined as:

$$COP_{CARNOT} = \frac{T_L}{T_S - T_L} \qquad (9)$$

the compressor efficiency is given by the product of the inverter, motor, and aerodynamic efficiencies:

$$\eta_C = \eta_I \cdot \eta_M \cdot \eta_{C,A} \qquad (10)$$

the expander efficiency is the product of the aerodynamic efficiency, the heat leak loss, and a loss term related to the mechanical power lost in the expander brake:

$$\eta_E = \eta_{E,A} \cdot \left[\frac{Q_L}{Q_L + Q_E}\right] \cdot \left[\frac{T_S - T_L}{T_S}\right] \tag{11}$$

and the heat exchanger overall efficiency is given by:

$$\eta_{HX} = \left[\frac{1 + \Delta T_{HX}/T_L}{1 - \Delta T_{HX}/T_S}\right] \left[\frac{1 - \frac{1}{\alpha} - \beta}{\alpha - 1}\right] \tag{12}$$

where

$$\alpha = (PR_C)^{\frac{k-1}{k}} \tag{13}$$

$$\beta = \frac{\Delta T_{HX} + \Delta T_{E,P}}{\eta_{E,A} (T_L + \Delta T_{HX})} \tag{14}$$

$$\Delta T_{HX} = (1 - \varepsilon_{HX}) (T_S - T_L) \tag{15}$$

From the form of eq. (12) it is apparent that there is value of the pressure ratio which maximizes the overall heat exchanger efficiency. As α approaches one, the efficiency becomes negative and as α becomes very large the efficiency approaches zero. Therefore, for some intermediate α the efficiency has a maximum. That is indeed the case, as illustrated in figure 3. The overall heat exchanger efficiencies shown in figure 3 were calculated for a specific heat ratio of 1.65. This value is close to that of either helium or neon.

Figure 3 brings forth two important features of the SSRB cycle:

1. There is a minimum pressure ratio required to even reach the desired load temperature. This minimum pressure ratio increases rapidly as the heat exchanger effectiveness is decreased.

2. There is an optimum pressure ratio which is a function of the heat exchanger thermal and pressure losses. The higher the performance of the heat exchanger, the lower the pressure ratio required to achieve maximum cycle performance. The optimum pressure ratio is given by:

$$PR_{C,OPT} = \left[\frac{1 + \sqrt{\beta}}{1 - \beta}\right]^{\frac{k}{k-1}} \qquad (16)$$

This last point is particularly important for a turbomachinery driven cycle because the pressure ratio which can be achieved in a single stage centrifugal compressor is limited by the rotor tip velocity. To avoid exceeding the yield strength of the material, the impeller tip velocity must be kept below about 500 m/s. The maximum pressure ratios which can be achieved are therefore about 2.4 for neon and 1.2 for helium. The pressure ratio is much lower for helium because it has a density five times lower than that of neon.

It is clear from the results shown in figure 3 that neon is a better choice of cryogen for this application. In order to use helium effectively at a pressure ratio of 1.2, a heat exchanger with an effectiveness of 0.995 or higher would be required.

Equations (8) through (16) were used to calculate the performance of the SSRB cycle for loads in the range from 1 to 10 W and load temperatures in the range from 30 to 250 K. The results are shown in figure 4 as a percentage of the Carnot efficiency. The calculations were made for a cycle with a sink temperature of 260 K, an overall compressor efficiency of 0.5, an expander aerodynamic efficiency of 0.8, a heat exchanger overall effectiveness of 0.985, and an expander heat leak given by

$$Q_E = 0.015\ (T_S - T_L) \qquad (17)$$

where Q_E is in watts and T_S and T_L in degrees Kelvin. This value of the heat leak corresponds to that calculated for 3.2 mm diameter turbines presently under development.

As shown in figure 4, the cycle efficiency is a strong function of both the load and the load temperature. For a 5 W load at 70 K the overall cycle efficiency is about 10 % of Carnot. If the load is reduced to 1 W the efficiency drops to about 5 % of Carnot and if the load is raised to 10 W the efficiency increases to about 14 % of Carnot. As shown in figure 5 taken from [4], the performance of the SSRB at 70 K compares favorably with that of other cycles.

The SSRB cycle efficiency, when expressed as a fraction of the Carnot efficiency, decreases at higher load temperatures because, as the load temperature increases, the mechanical power output of the expander also increases rapidly. In the present system the expander power is not recovered and hence it constitutes a loss to the system. One could use a turboalternator to recover this power. However, most applications of interest are at temperatures of 100 K or lower and the work which could be recovered is only a small fraction of the compressor input power.

Based on these analyses, the SSRB cycle specifications for providing 5 W of cooling at 70 K rejecting heat to a 260 K thermal bus were developed. The resulting operating conditions and power flows are shown in figure 1. In these calculations we conservatively assumed an overall compressor efficiency of 0.33 yielding a COP of 8.3% of Carnot.

2. Component design

The three key components in the SSRB cycle are the turbocompressor, the turboexpander, and the heat exchanger. Preliminary layouts for these three components are shown in figures 6-8.

The compressor consists of a solid rotor induction motor running on self-acting, tilting-pad gas bearings. A double sided impeller is used to balance axial loads. Axial location of the shaft is accomplished by a magnetic thrust bearing located at the end of the shaft opposite the impeller. A water jacket surrounding the motor stator provides cooling. All the materials in the compressor are metallic, with the exception of the teflon insulation in the stator wires. Gas stream contamination is therefore expected to be negligible.

The turboexpander preliminary layout is shown in figure 7. It consists of a solid shaft mounted on self-acting, tilting-pad gas bearings and having a 3.2 mm turbine impeller machined at one end and a 6.4 mm brake impeller at the other. The gas bearings and the brake impeller operate warm, at the 260 K sink temperature. The turbine end of the shaft is cold, a few degrees below the 70 K load temperature. The warm and cold ends of the expanders are connected by thin-walled titanium tubes to minimize heat leak to the cold end. The rotational speed of the expander is 570,000 rpm.

The heat exchanger preliminary layout is shown in figure 8. It consists of a stack of 200 perforated copper plates supported by thin-walled stainless steel tubes. The plates have concentric rings of 0.2 mm wide slots through which the gas flows in counter direction. The loss mechanisms included in the calculation of the heat exchanger performance are:

- gas film resistance,
- cross-stream metal conduction resistance,
- metal and gas axial conduction,
- flow maldistribution losses,
- pressure drop losses, and
- losses due to using a finite number of plates.

The geometry of the heat exchanger was optimized to obtain a minimum weight design.

3. Conclusions

It can be concluded that a single-stage, reverse-Brayton cryogenic system employing a single-stage centrifugal compressor and a radial inflow turbine can be used effectively to cool loads greater than 1 W in the temperature range from 30 to 150 K. Because the turbomachines run in gas bearings this cryocooler has the potential for long-life and should provide virtually vibrationless operation. Work is presently progressing on the development of the three key hardware components: the miniature, high-speed turbocompressor, the miniature turboexpander, and the high-effectiveness heat exchanger.

The work reported in this paper is being performed under the sponsorship of the NASA Goddard Space Flight Center through their SBIR program. The NASA technical monitor is Dr. Max Gasser.

5. References

[1] Johnson, A.L., Spacecraft-borne long life cryogenic refrigeration - status and trends, in Refrigeration for Cryogenic Sensors, edited by M. Gasser, 47-80, (NASA CP-2287, 1983).

[2] Sixsmith, H. and Swift, W.L., A miniature tilting pad gas lubricated bearing, in Refrigeration for Cryogenic Sensors, edited by M. Gasser, 189-196, (NASA CP-2287, 1983).

[3] Sixsmith, H. and Swift, W.L., A robust thrust bearing for cryogenic turbines, (Cryogenic Engrg. Conf., Colorado Springs, CO, Aug. 1983), in Advances in Cryogenic Engineering, edited by R.W. Fast, 525-532, (Plenum Publ. Corp., New York, NY, 1984).

[4] Strobridge, T.R., Cryogenic refrigerators - an updated survey. National Bureau of Standards Tech. Note 655 (Supt. Documents, U.S. Govt. Printing Off.) (12 pp.) (1974).

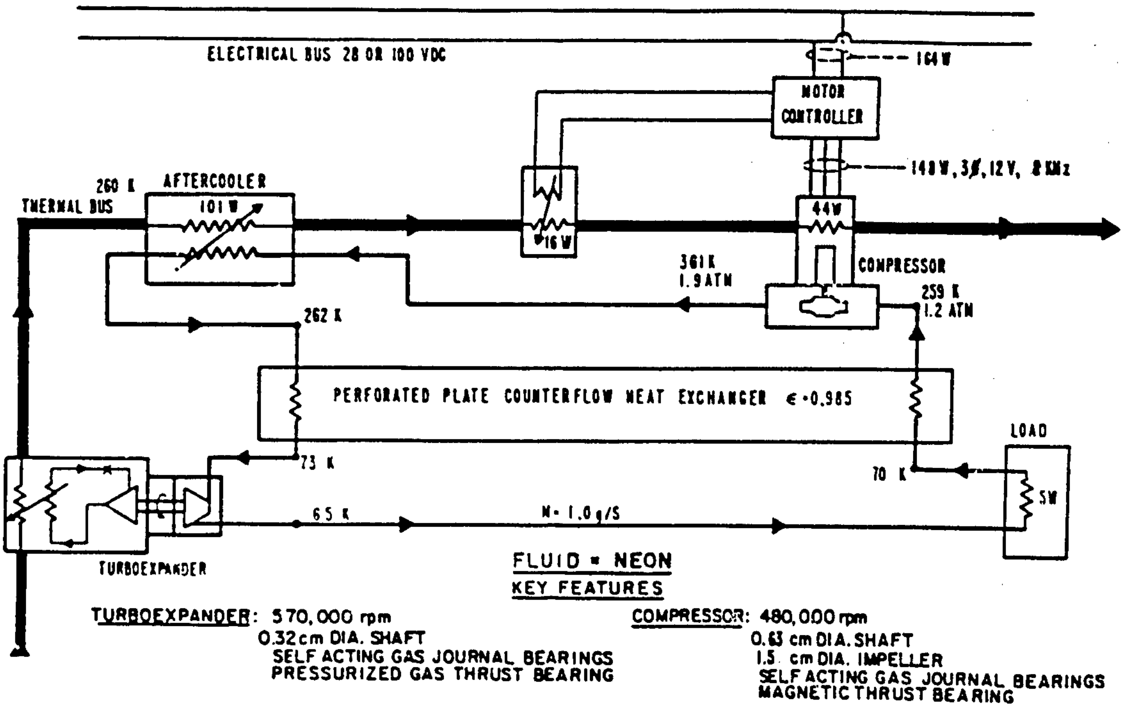
ELECTRICAL BUS 28 OR 100 VDC
164 W
MOTOR CONTROLLER
148 W, 3∅, 12 V, 8 kHz
260 K
AFTERCOOLER
THERMAL BUS
101 W
16 W
44 W
361 K
1.9 ATM
COMPRESSOR
259 K
1.2 ATM
262 K
PERFORATED PLATE COUNTERFLOW HEAT EXCHANGER ε = 0.985
LOAD
73 K
70 K
5 W
8 W
65 K
ṁ = 1.0 g/S
TURBOEXPANDER
FLUID = NEON
KEY FEATURES
TURBOEXPANDER: 570,000 rpm
0.32 cm DIA. SHAFT
SELF ACTING GAS JOURNAL BEARINGS
PRESSURIZED GAS THRUST BEARING
COMPRESSOR: 480,000 rpm
0.63 cm DIA. SHAFT
1.5 cm DIA. IMPELLER
SELF ACTING GAS JOURNAL BEARINGS
MAGNETIC THRUST BEARING

Figure 1. *SINGLE-STAGE, REVERSE-BRAYTON CRYOCOOLER*

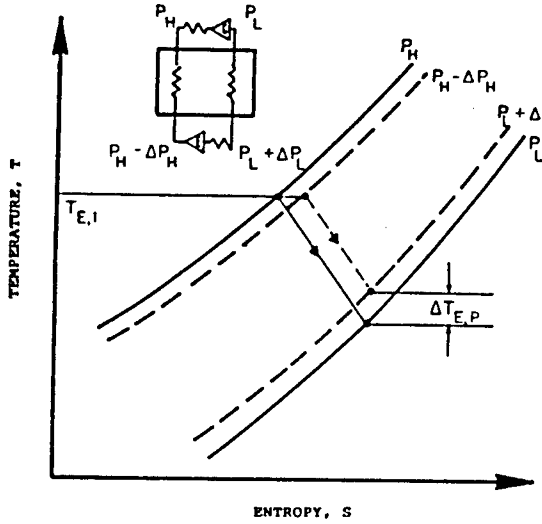
TEMPERATURE, T
ENTROPY, S
P_H
P_L
P_H - ΔP_H
P_L + ΔP_L
P_H - ΔP_H
P_L + ΔP_L
T_E,I
ΔT_E,P

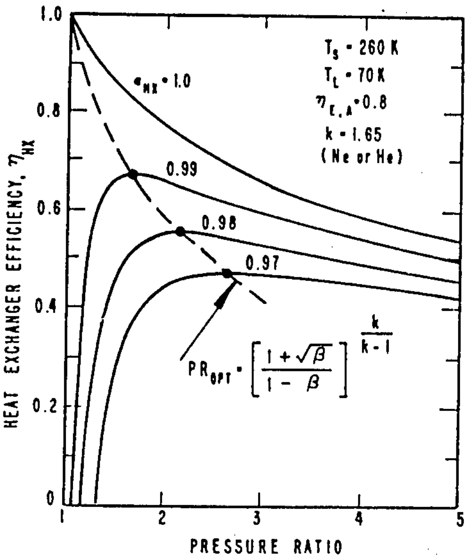

Figure 2. *EFFECT OF HEAT EXCHANGER PRESSURE DROP OF EXPANDER PERFORMANCE*

Figure 3. *HEAT EXCHANGER EFFICIENCY AS A FUNCTION OF PRESSURE RATIO*

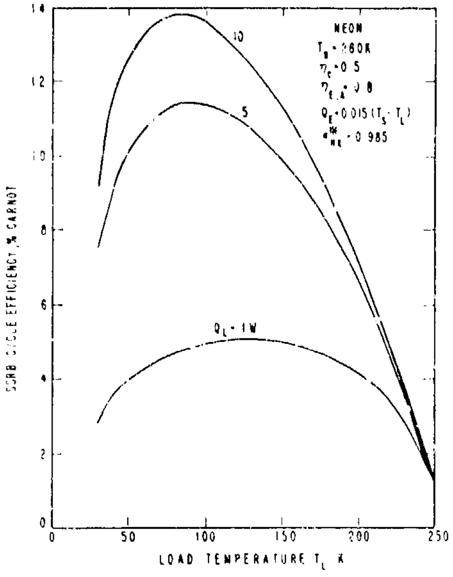

Figure 4. ***OVERALL SSRB CYCLE EFFICIENCY***

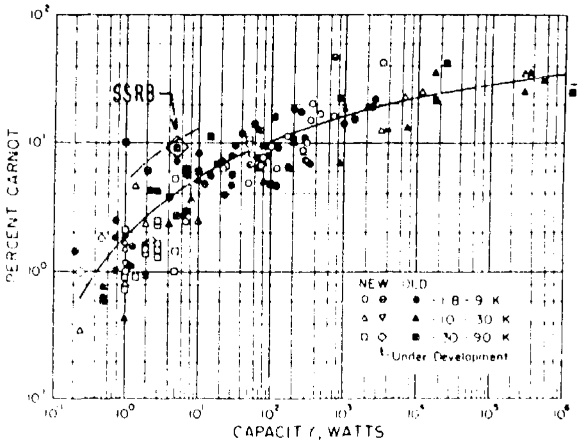

Figure 5. ***COMPARISON WITH OTHER CRYOGENIC COOLING SYSTEMS [4]***

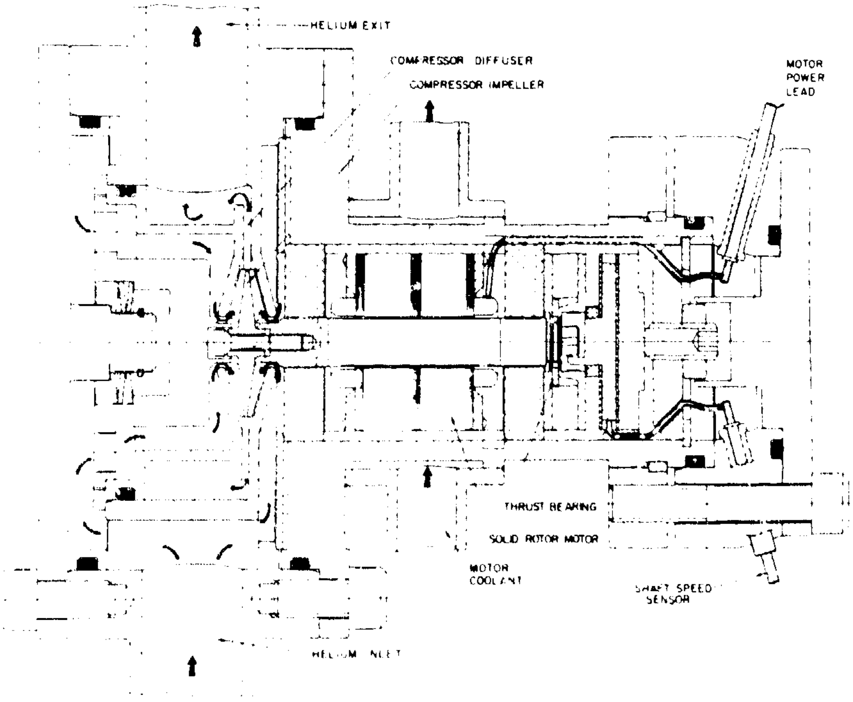
HELIUM EXIT
COMPRESSOR DIFFUSER
COMPRESSOR IMPELLER
MOTOR
POWER
LEAD
THRUST BEARING
SOLID ROTOR MOTOR
MOTOR
COOLANT
SHAFT SPEED
SENSOR
HELIUM INLET

Figure 6. ***TURBOCOMPRESSOR LAYOUT***

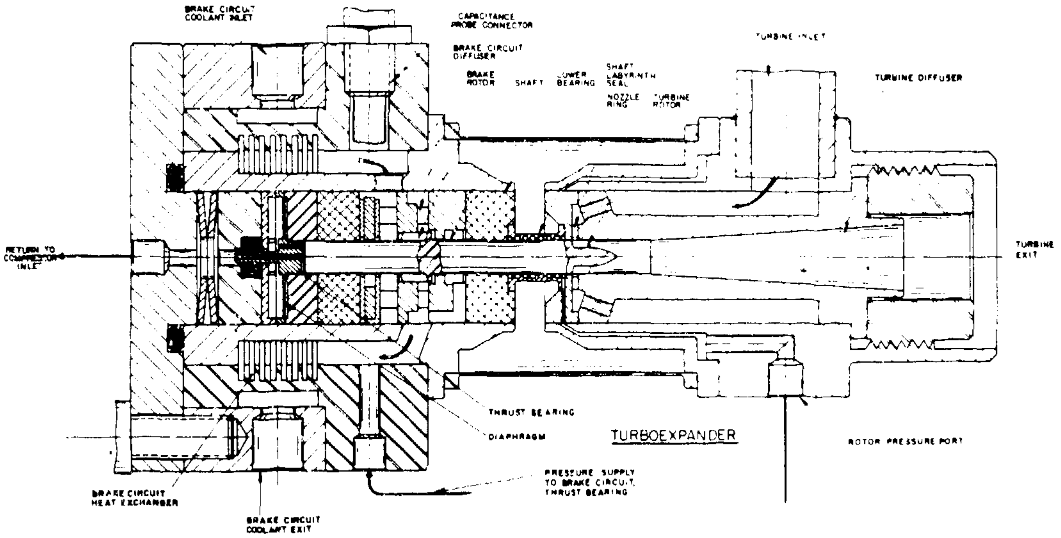
BRAKE CIRCUIT COOLANT INLET
CAPACITANCE PROBE CONNECTOR
BRAKE CIRCUIT DIFFUSER
BRAKE ROTOR
SHAFT
LOWER BEARING
SHAFT LABYRINTH SEAL
NOZZLE RING
TURBINE ROTOR
TURBINE INLET
TURBINE DIFFUSER
RETURN TO COMPRESSOR INLET
TURBINE EXIT
THRUST BEARING
DIAPHRAGM
TURBOEXPANDER
ROTOR PRESSURE PORT
PRESSURE SUPPLY TO BRAKE CIRCUIT, THRUST BEARING
BRAKE CIRCUIT HEAT EXCHANGER
BRAKE CIRCUIT COOLANT EXIT

Figure 7. ***TURBOEXPANDER LAYOUT***

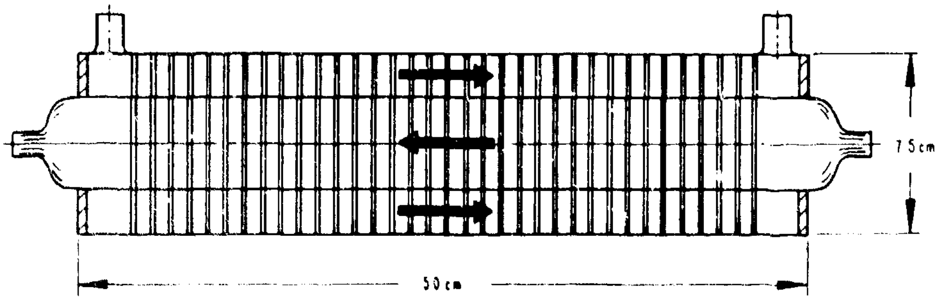

Figure 8. ***HEAT EXCHANGER LAYOUT***

REFRIGERATION AND HEAT PUMP SYSTEMS BASED ON He II VORTEX CONTROL

T.H.K. Frederking, H.H.D. Tran and R.M.Carandang

University of California, Los Angeles 90024 CA

The utilization of thermomechanical forces permits pressure increases in pumps without moving parts. This topic has become an interesting option for liquid transfer at microgravity. In addition, the thermomechanical pump (fountain effect pump) may be used to energize refrigerators, substituting for the usual mechanical pump. In the present thermodynamic studies, cyclic variations of the fluid equilibrium state are investigated including performance parameters. In contrast to attainment of low temperatures, the emphasis is on heat pumping tasks at temperatures between 1.5 K and the lambda temperature.

Key words: He II; thermodynamic cycles ; fountain effect; refrigerator/heat pump systems.

I. Introduction

Increased use of liquid He II as a coolant near 1.8 K has included application of the fountain effect (thermomechanical effect). Examples are vapor-liquid phase separators and fountain effect pumps (FEP). Another type of application addressed in the present studies is the use of FEP - induced pressurization for refrigeration purposes and heat pumping. An original version of such a system, based on the control of the dynamics of quantized vortices, has been proposed and tested by Staas and Severijns [1] [1]. This Staas-Severijns cooler has aimed at the attainment of low temperatures down to 0.7 K . In contrast, the present work emphasizes heat pumping in the range of the temperature (T) encountered in space cryogenics and in superconducting magnets for high magnetic fields based on NbTi/Cu. The system applicability appears to be not restricted to these examples and general features are presented: First, the vortex dynamics is discussed. Subsequently, simplified refrigerator operation is considered. The next subject is the FEP pressurization device. Heat pumping performance is considered for one of the simplest cycle-options, and an outlook is given.

---

[1] Numbers in brackets refer to the literature references listed at the end of this paper.

2. Vortex Dynamics and Two - Fluid Aspects

The quantum liquid He II has a high heat transport rate in conventional refrigerator ducts, unless the flow cross section is severely restricted. Therefore T - gradients are small in usual flow passages. In order to generate sizable temperature differences, needed for the application of thermomechanical forces, fine porous media, called superleaks or superfilters, are used. The limiting case is the "ideal superleak" with "zero" heat flow. The porous medium permits resistanceless flow (="superflow") up to its critical velocity (v_{sc}). As the pore size is reduced, at a specified temperature, the v_{sc} - value attainable is increased. At v_{sc}, liquid circulation and flow resistance is initiated. Because of quantization of the liquid circulation, a finite energy is needed for vortex motion onset with velocity com - ponents perpendicular to the main flow direction, i. e. vortex shedding . The energy needed is large for very fine pores. For FEP purposes, critical velocities of the order of 10 cm/s have been considered convenient in laboratory work. Because of the energetic restrictions, the fine plugs may be regarded as "vortex pinning devices" below v_{sc} . In the ideal thermodynamic treatment of changes of state, the ideal superleak constitutes a perfect vortex pinning component.

Once a vortex is activated above v_{sc} , a Magnus force provides vortex shedding e.g. from walls toward the fluid interior. This phenomenon leads to a finite difference in chemical potential (μ)[*]. In the ideal superleak $d\mu = 0$ is observed up to the critical velocity. Small vortex shedding rates of real plugs are expected to cause only small departures from the ideal thermodynamic change of state. Therefore, ideal processes involving changes of state at constant chemical potential are useful for performance assessment. It appears that minor vortex shedding rates cause only small departures from the ideal performance values of FEP units.

We have a flow system described in usual hydrodynamic terms supplemented by the superflow thermodynamics. The two - fluid model is useful . The existence of two interpenetrating fluid media is postulated: There exists a viscous normal fluid component and an inviscid superfluid component (at"concentrations " (ρ_n/ρ) and (ρ_s/ρ) adding up to unity). The flow field is subdivided accordingly: There is a normal fluid flow pattern and a superfluid flow field. Because of the fine pores, the normal fluid motion is considered negligible, in particular in the limit of perfect immobilization of superleaks. Thus, in the present context , attention is on the superfluid described by

$$D\vec{v}_s/Dt = -\nabla\mu = \nabla P/\rho - S\nabla T - (1/2)(\rho_n/\rho)|\vec{w}|^2 \qquad (1)$$

with $\vec{w} = \vec{v}_n - \vec{v}_s$ = relative velocity ; S entropy per unit mass; ρ liquid density). For steady, one-dimensional flow with negligible $|\vec{w}|^2$ term, we have a simple truncated form of the preceding equation

---

[*] In part of the low temperature literature, the Gibbs free energy is customarily denoted as μ . In the present discussion , this notation is adopted with μ =chemical potential per unit mass.

$$\mathrm{grad}\ (\ \mu + v_s^2/2) = 0 \qquad (2)$$

where the kinetic term is small outside the narrow passages formed by the porous medium. The momentum equation of the model , $\vec{j} = \rho\ \vec{v} = \rho_s\ \vec{v}_s + \rho_n\ \vec{v}_n$, for normal fluid locked in the plug, reduces to the simple condition

$$\rho\ \vec{v} = \rho_s\ \vec{v}_s \qquad (3)$$

Thus, the superfluid critical speed v_{sc} is related to the critical velocity of the observed mass flow by $v_c = v_{sc}\,\rho_s/\rho$.

In the terrestrial gravity field, the fountain effect is quantified readily by inclusion of the gravitational contribution to the generalized chemical potential function ($\mu + g\Delta z + v_s^2/2$) ; (z vertical position coordinate). In a thermostatic device, Equations (1) and (2) have in common the limit of the thermomechanical gradient, at zero flow, of

$$\mathrm{grad}\ P = \mathrm{grad}\ P_T = \rho\ S\ \mathrm{grad}\ T \qquad (4)$$

(London pressure gradient). When a jet geometry allows a speed v , downstream of the superleak, the limit of ideal flow without losses leads to a fountain height of $\Delta z = v^2/(2\ g)$.

There are two types of fluid processing components in general: First, the porous plugs needed for the thermomechanics and second, ducts and conventional devices, such as heat exchangers. In the latter category, significant vortex shedding may take place causing dissipation of flow power. At sufficiently high flow rates, both fluids may move with nearly the same speed. In this case, interaction of the normal fluid with the vortices causes "near - classical " flow. For instance, in a duct with a diameter beyond the order of 10^{-2} cm. roughness - dependent friction may be observed readily, as in Newtonian turbulent fluid flow . Therefore, classical equations have been used in the analysis of this aspect of the Staas-Severijns refrigerator [1] . Alternate use of vortex pinning components and of vortex shedding components implies controlled processing of vortex systems giving rise to the designation of "He II vortex refrigerator" , (or of " superfluid vortex fridge"). The various dissipation aspects in wide and narrow passages have been reviewed by Hammel [2] giving details of basic thermophysics of the He II modes of motion.

3. Simplified Vortex Refrigerator Operation: Concepts

In the discussion of this section, simplified refrigeration concepts are invoked. Up to this time, little has become known about performance figures. In line with applied thermodynamics conventions, the coefficient of performance is defined as the ratio of the refrigeration load to the net work. The thermal efficiency of thermal to mechanical energy conversion is defined as the ratio of the net work to the heat input. Macro-thermodynamics is used. For instance, at a superficial glance one may refer to the FEP device as "compressor". The reverse case of mechano-caloric cooling in a plug may be referred to as "expansion device", (or "ideal superleak expander"). Caution is needed though to avoid a literal interpretation in terms of classical ideas which may lead to non-physical consequences .

A schematic diagram of the original system of the Staas-Severijns vortex refrigerator is shown in Figure 1. There are "compressor" and "expander " peculiarities elucidated by the two-fluid model for $d\mu = 0$. "Compression" is actuated by the heater (H) which supplies thermal energy. As superfluid passes through the device at $d\mu = 0$, normal fluid left behind tends to accumulate entropy upstream.

Therefore, heat is to be removed in order to keep temperatures, at a specified location, time - independent. In the aftercooler (AC), the temperature is brought back to the bath temperature. In the "expander", application of the pressure difference generated in the FEP, forces superfluid through the plug. This results in cooling by the mechano-caloric effect. The refrigeration load (Q_R) is supplied in the cold box (CB). Finally, the capillary (CAP) connects the cold box to the bath.

Figure 2 indicates a scheme with a valve (V) replacing the capillary system. In principle, other means are available, e.g. a valve at the inlet. This option is not favored for a saturated liquid bath, as it may lead to pressure reduction and cavitation. This danger is avoided with pressurized liquid He II. It is noted that in Reference [1] a set of capillaries has been employed in order to test the flow conditions in the entropy carrying tubes downstream of the cold box.

4. Fountain Effect Pump Performance

The fountain effect unit is the driver for the vortex refrigerator. Therefore, its performance exerts an important influence on the coefficient of performance (COP) of the refrigeration process. Recent work on FEP use for liquid transfer in space [3] has prompted a critical inspection of various performance measures. Two types of effectiveness or efficiency figures have become known. One relates to the liquid yield, ultimately available at the receiver, during transfer from one vessel to another one. The other measure is the energetic effectiveness ε_e. Because of generally small values obtained for ε_e, there has been a sufficient incentive to improve the energetics of the FEP, e.g. by heat pump - assisted FEP units [4]. Ideal changes of state at $d\mu=0$ are referred to in the subsequent discussion of the FEP.

The energetic effectiveness is defined as the ratio of the flow power at the pump outlet, $\dot{W}_F$, to the heat input rate, $\dot{Q}$, energizing the pump. Neglecting the

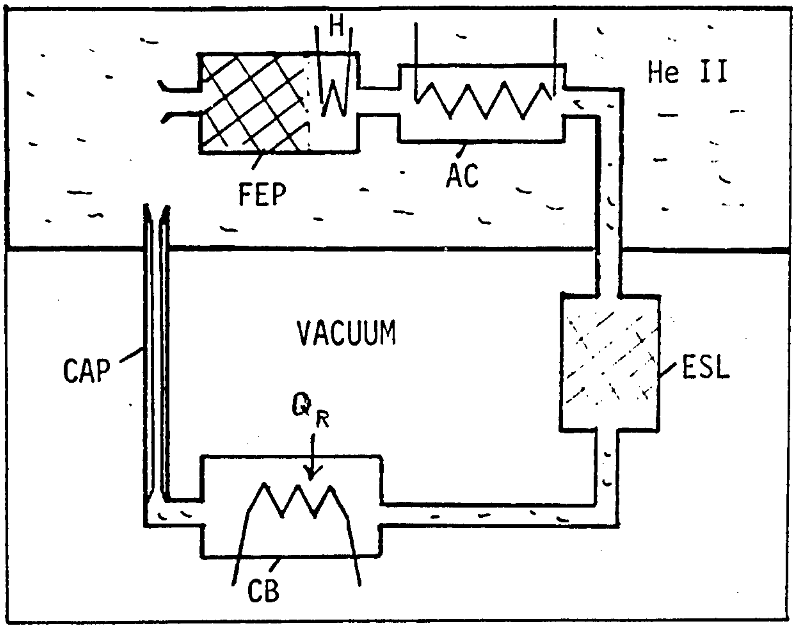

Figure 1. Vortex refrigerator, schematically; AC aftercooler, CAP capillary, CB cold box, ESL "expansion superleak", FEP fountain effect pump, H heater; Refrigeration load Q_R is absorbed in the cold box.

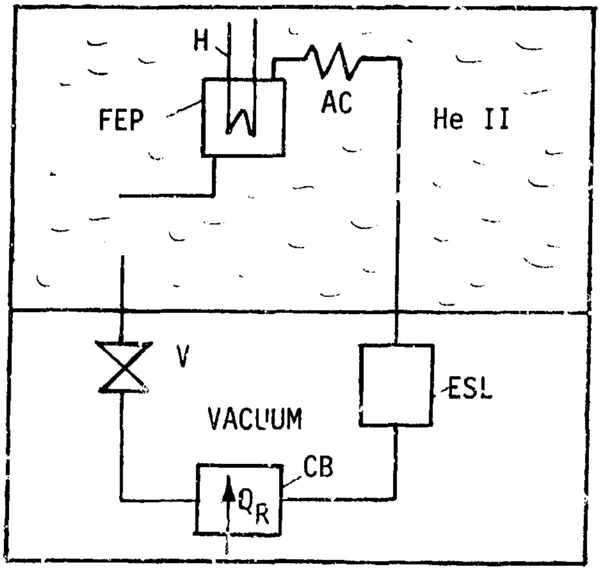

Figure 2. Vortex refrigerator, schematically; V valve, (other components as in Figure 1).

mass loss and using Equation (4), one obtains

$$\varepsilon_e = \dot{W}_F / \dot{Q} = \bar{S}\Delta T / S T \qquad (5)$$

$\bar{S}$ is the mean entropy for the range from the bath temperature T to the temperature (T + ΔT) at the pump exit. For very small temperature differences, $\bar{S}$ becomes equal to the bath value S(T), and the effectiveness simplifies to

$$\varepsilon_e = \Delta T/T \quad ; \quad \Delta T \ll T \qquad (6)$$

A comparison with the thermal efficiency of a Carnot cycle shows that the FEP effectiveness, in this limit, is equal to that efficiency for a low temperature environment. More specifically, the comparison Carnot power cycle receives heat at the temperature (T + ΔT) and rejects heat at T.

Figure 3 presents a comparison of the FEP effectiveness with the thermal efficiency (η_T) of the related Carnot power cycle. According to Carnot's theorem, the η_T - values constitute the best performance results available ideally. It is seen that ε_e is always below η_T . The effectiveness is about 50 % lower than the Carnot limit. There is a common asymptote at low ΔT. The parameter adopted in Figure 3 is the bath temperature upstream of the FEP unit. At sufficiently high ΔT, the FEP performance tends toward an asymptote, near 15 % of the ideal heat pump-assisted FEP unit [4] .

Figure 4 shows the heater power requirements. Figure 4a is a plot of the heat input rate per mass flow rate ($\dot{Q}/\dot{m}$), starting at a temperature of 1.6 K versus the temperature difference across the ideal pump. The upper curve is the ideal requirement of the simple FEP . The real pump will need a somewhat larger power because of departures from the ideal change of state characterized by $d\mu = 0$. The lower curve depicts the power requirements, $\dot{W}/\dot{m}$, per unit mass, of the heat pump-assisted

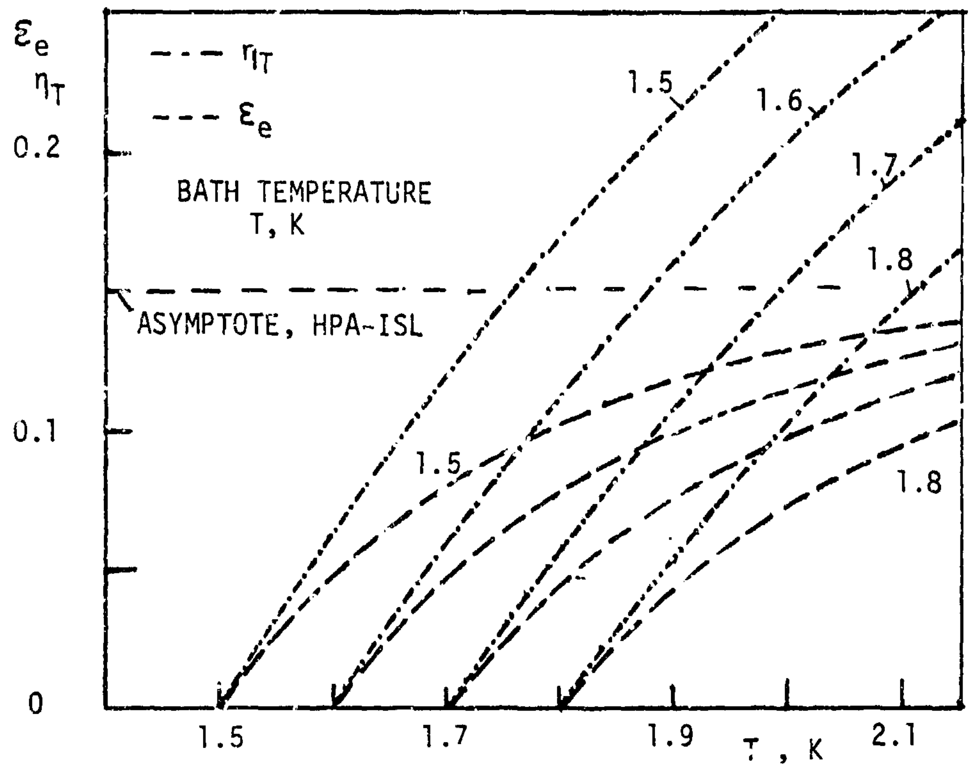

Fig.3. Energetic effectiveness ε_e and thermal efficiency η_T of ideal systems for various bath temperatures;(HPA-ISL heat pump-assisted ideal superleak).

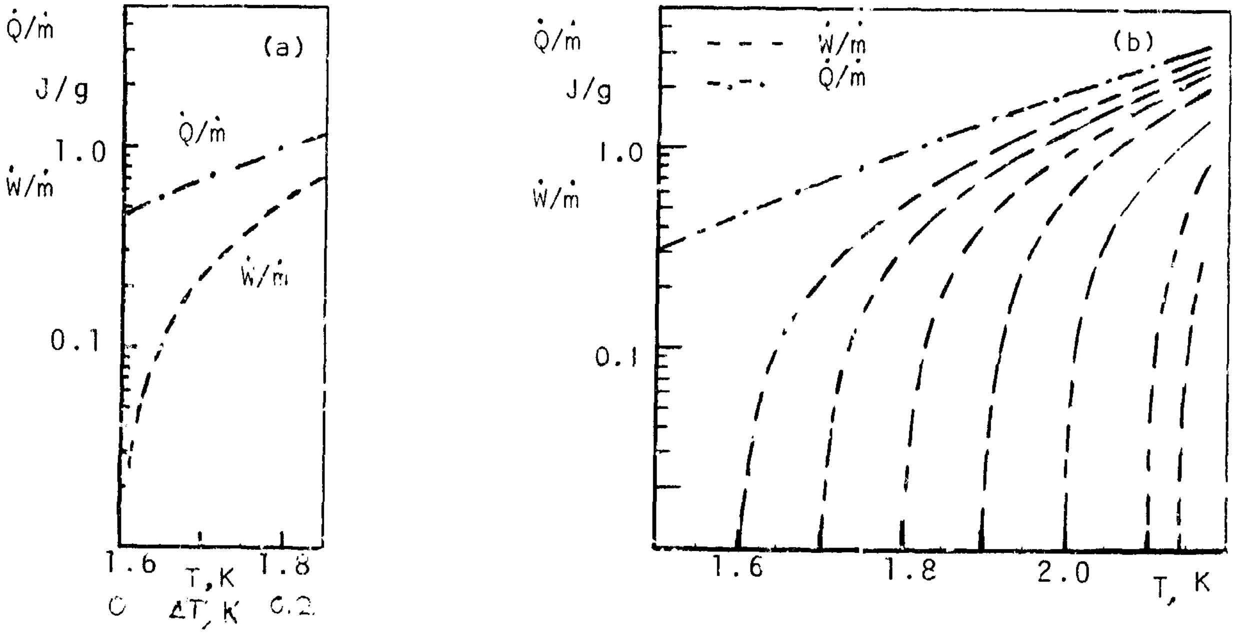

Fig.4. Heater input ($\dot{Q}/\dot{m}$) and power input ($\dot{W}/\dot{m}$) functions for ideal FEP systems; a. power required versus ΔT , bath temperature 1.6 K; b. parametric plot of the power required vs. T for various bath temperatures.

FEP unit. This power is low at low ΔT and rises monotonically with an increase in the temperature difference.

Figure 4b summarizes the power input requirements in one graph making use of a parametric representation with the bath temperature (upstream temperature) as parameter. It is seen that there is a unique ideal heater power function ($\dot{Q}/\dot{m}$) given by the ideal superleak constraint : ($\dot{Q}/\dot{m}$) is the value of $S\,T$ at the pump exit. For instance, for a mass flow rate of $\dot{m} = 40$ g/s , or a volumetric flow rate of about 1000 liters/hour, a heater power of the order of 40 Watts is required near 1.8 K. At large temperature differences, the heat pump assistance is no longer attractive as the power requirement approaches that of the simple FEP unit.

5. Refrigeration - Heat Pump Cycle Example

One important assumption in the preceding and in the present treatment is attainment of local thermodynamic equilibrium . Other system conditions of the present section are as follows: steady operation, steady flow of liquid and of the two fluids, simplified changes of state using ideal conditions, such as isobaric changes in heat exchangers, and ideal superleak processes at constant chemical potential. A simplifying tool is the introduction of the ideal heat pump-assisted FEP ($d\mu = 0$) and a related state change in the "expander " subsystem. Furthermore, for quick estimates the contribution from the integral $\int S\,dT$ may be neglected in the T-range near 1.8 K, as discussed elsewhere [4] . The changes of state are listed in Table 1.

TABLE 1 . STATE CHANGES OF THE SIMPLE CYCLE μ-P-μ-P

Sequence i - j	Constraint	Subsystem/Component
1 - 2	$d\mu = 0$	Ideal FEP,heat pump-assisted
2 - 3	$dP = 0$	Isobaric aftercooler ($T_3 = T_1$)
3 - 4	$d\mu = 0$	Ideal superleak"expander"
4 - 1	$dP = 0$	Absorption of the refrigeration load Q_R

The cycle is sketched in the T-S plane and in the P-T plane in the insets of Figure 5. After processing of fluid in the FEP, the aftercooler brings the temperature back to the bath temperature T_1. Subsequent "expansion" brings about a low temperature, and finally the change of state from T_4 to T_1 is assumed to be available for the absorption of the refrigeration load.

The temperature T_4 has been plotted for various pressure increases in Figure 5. For instance, the pressure rise in the FEP unit, starting from 1.8 K, produces a T_4 -value near 1.63 K; (pressure difference achieved across the FEP of about 100 milli-bar). Figure 5 includes the equivalent Carnot cycle temperature, for an "environment" of 1.8 K, which has the same refrigeration load as the μ-P-μ-P cycle under consideration. Both temperatures are displayed versus Q_R .

Coefficients of performance of the Carnot cycle $(COP)_{CARNOT}$ are shown in Fig.6 versus T . As the initial "environmental temperature" , e.g. 1.8 K , is lowered by a small reduction $\Delta T \ll T$, the COP is the reciprocal η_T - value of the power process.

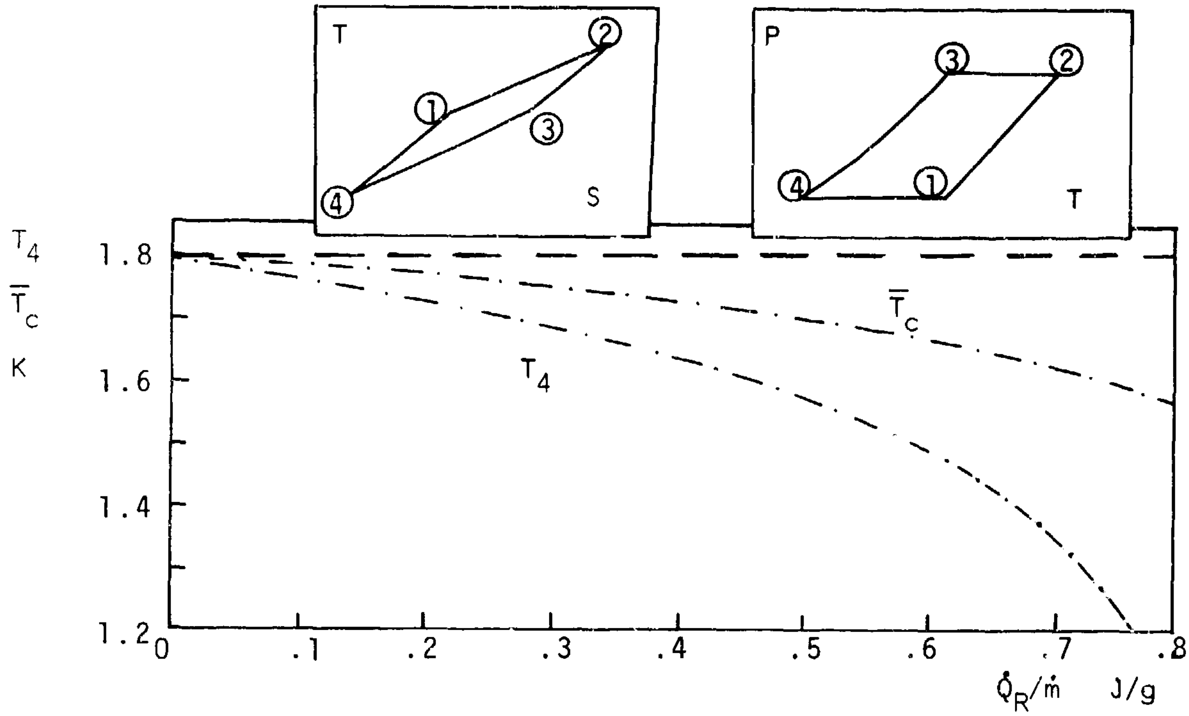

Fig.5. Lowest temperature T_4 of the ideal μ-P-μ-P cycle and equivalent Carnot cycle temperature $\overline{T}_c$ vs. refrigeration load $\dot{Q}_R/\dot{m}$; "environmental" T = 1.8 K = initial bath temperature T_I; Inset : Cycle in the T-S diagram, schematically and cycle in the P-T diagram , schematically.

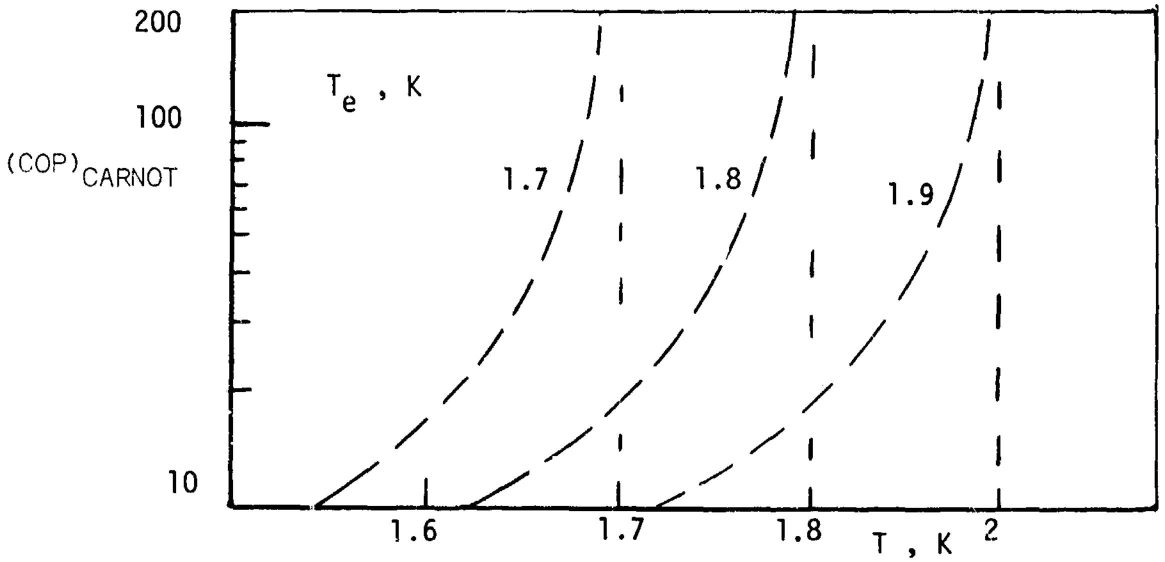

Fig. 6. Coefficients of performance of the Carnot cycle, $(COP)_{CARNOT}$ versus T for different "environmental temperatures" Te .

6. Perspectives

Simplified changes of state, with heat pump assistance of the FEP process, and a similar "expander assisted" pressure reduction, have been considered. The implementation of near - ideal conditions by external means may require considerable component developments. Therefore other approaches toward improvement of the very simple cycle ought to be considered. One possibility is a counterflow heat exchanger. Another one is via"Carnotization" by means of multi-stage operation.

Figure 7 depicts a schematic diagram of a vortex refrigerator with a counterflow heat exchanger increasing the T - range covered by the heat pump process. The counterflow avoids excessive entropy production brought about otherwise by a large temperature difference between the "high pressure" stream and the"low pressure" stream.

The other option of Carnotization is brought about by multi-stage "compression" and multi-stage"expansion" . Figure 8 presents an example of a three-stage FEP - system with aftercoolers (AC). The inset of this figure is a sketch of the multistage cycle . As the number of stages is increased, the Carnot case is approached more and more. While the low density change makes classical expansion less attractive, the possibility of multi-stage "compression" has received attention, e.g. Ref.[5] for the special case of He^3 - He^4 dilution refrigeration, and Reference [6] for the T-range near 1.8 K in the space cryogenics work of recent years.

In the final assessment, a major point is the FEP performance. The ideal energetic effectiveness figures of at most 15 % are not very attractive. A major advantage of the FEP - supported system is the generally high reliability due to the absence of moving components (aside from valve positioning). The most attractive issue appears to be the possibility of"waste heat"utilization (e.g. vessel heat leaks, instrument dissipation rates). For high field magnets, an example of liquid circulation has been presented in Ref.[7].For space cryogenics systems, the use of a cooler-activated FEP unit is a viable option. Also heat might be"piped" from solar energy concentrators to the FEP without the use of photo-voltaics. Further recent results are in Ref. [8] .

In summary, attractive features of the He II thermomechanics are available for specific refrigeration and heat pumping tasks.

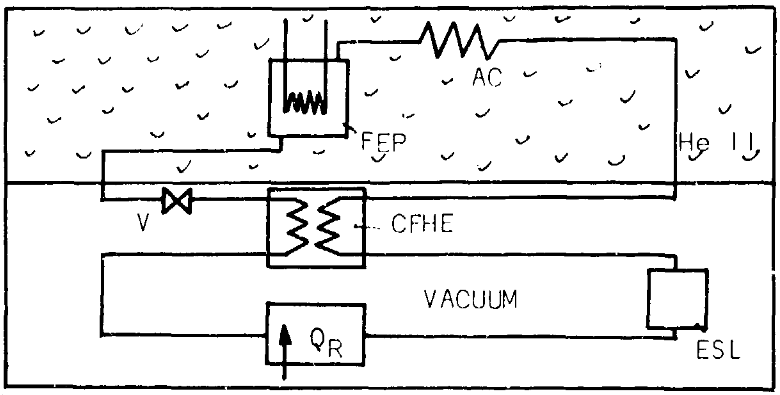

Figure 7 . Vortex refrigerator with a counterflow heat exchanger (CFHE), schematically; AC aftercooler , CB cold box ; ESL "expansion superleak" , FEP fountain effect pump with heater; V valve .

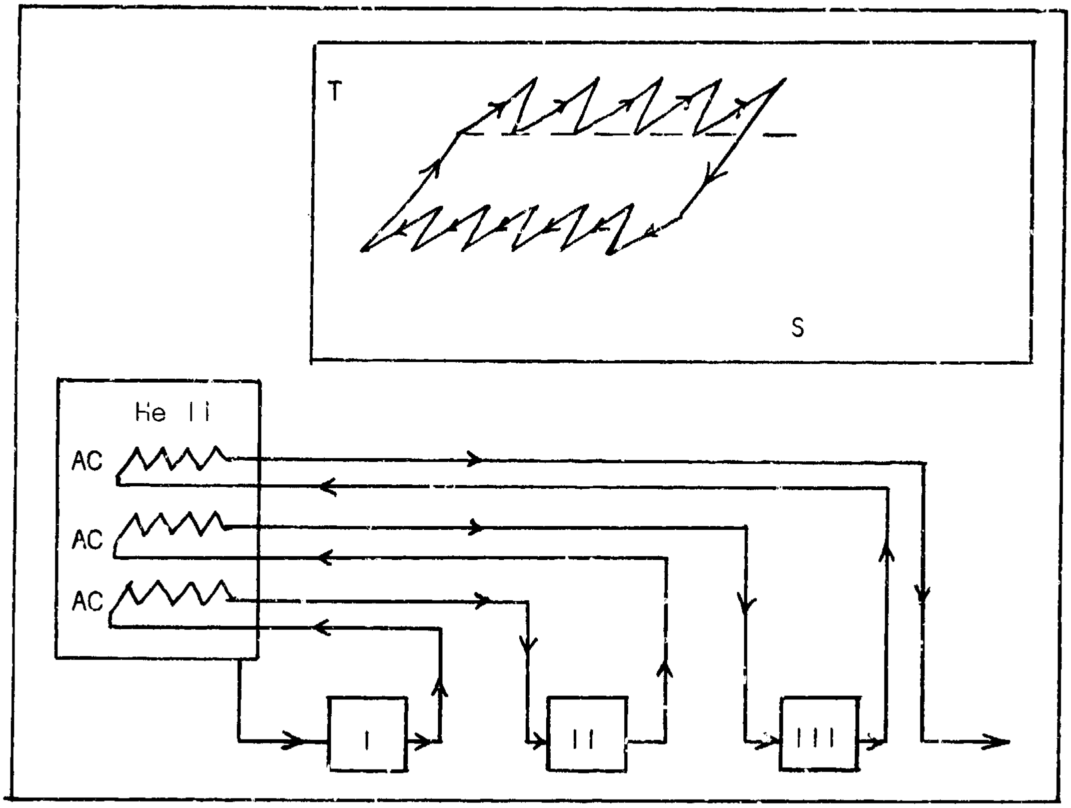

Figure 8. Example of multi-stage "compression" with three stages of FEP units designated as I, II, III ; AC after coolers in He II supply tank (schematically ; inset : Temperature - Entropy diagram for multi-stage "compression and "expansion" , schematically.

Acknowledgments. This work has received initial "seed" support from the Academic Senate Grant # 3526 , UCLA. Also NASA Summer 1986 support in the area of thermal components is acknowledged in this context (# NAG 2 - 412). The following students participated in the efforts : Kenny Hom, Alana Lee and David Ono. Their input is recognized with thanks. Further the help of Y.S. Yi is gratefully acknowledged.

7. References

[1] Staas F.A. and Severijns, A.P., Vorticity in He II and its Application in a Cooling Device, Cryogenics 9, 422 - 426 (1969).

[2] Hammel, E.F., Dissipation and Critical Velocities in Liquid Helium, LT-10, 10th Int. Conf. Low Temp. Phys. 1966, plenary paper.

[3] Kittel, P. , Helium Transfer in Space Workshop, Cryogenics 26, 59-60 (1986).

[4] Frederking, T.H.K. et al., Fountain Effect-Based Cycles and Related Changes of State, paper 07-4, ICEC-11, 11th Int. Cryog. Eng. Conf. Berlin 1986.

[5] Severijns, A.P., A Novel He^3-He^4 Dilution Refrigerator with Superfluid He^4 Circulation, Cryogenics 20, 115 - 121 (1980).

[6] Kittel, P. Liquid Helium Pumps for In Orbit Transfer, Space Cryog. Workshop,

Noordwijk, Holland, April 1986.

[7] Hofmann, A., Thermomechanically Driven He II Flow, An Option for Fusion Magnets with Internally Cooled Conductors, ICEC-11, 11th Int. Cryog. Eng. Conf. Berlin 1936.

[8] Hofmann, A. Khalil A., Kraemer, H.P. , Weisend, J.G., Srinivasan, R. and Vogeley, B., Investigations of Fountain Effect Pumps for Circulating Pressurized Helium II, ICEC-11, 11th Int. Cryog. Eng. Conf. Berlin 1986.

SMALL SIZE HELIUM REFRIGERATOR WITH MICRO TURBO-EXPANDERS

S. Harada, T. Matsuda

Mechanical Engineering Research Laboratory
Hitachi, Ltd., Tsuchiura, Japan

S. Saito, K. Ihara
Kasado Works, Hitachi, Ltd., Kudamatsu, Japan

A Claude cycle helium refrigerator with two-stage expansion micro-turbines has been developed. The refrigeration capacity of this refrigerator is proved to be 70 W at 77 K and 5 W at 4.5 K. The refrigerator design and test results are described in this paper. This refrigerator can meet the rapidly increasing demands for maintenance and vibration free systems which are applicable to cryoelectronic devices such as the NMR-CT and Josephson computers.

Key words: Expansion micro-turbines; helium refrigerator; NMR-CT; Josephson computers

1. Introduction

In the field of small helium refrigerators, a Gifford-MacMahon or Solvay cycle helium refrigerator with regenerative reciprocating expander are commonly used. But, for the application to cryoelectronic devices such as NMR-CT and Josephson computers which require a maintenance and vibration free refrigerator especially, the Claude cycle refrigerator with turbo-expander is possibly more suitable. Several attempts [1] had been made, in the past, to develop a micro turbo-expander, which is a key component for developing vibration free Claude cycle machines, but no successful application has been reported yet. This paper describes the design [2] and test results of a turbo-expanded Claude cycle helium refrigerator.

2. Specification and construction of a small size helium refrigerator

2.1 Specification of a small size helium refrigerator

Typical specifications of a small size helium refrigerator with micro turbo-expanders which has been recently developed are listed in Table 1. The liquefying method is a conventional Claude cycle with a refrigeration capacity of 70 W at 77 K.

Table 1. Design specifications of the refrigerator

Item	Unit	Specification
Refrigeration cycle	---	Claude cycle
Refrigeration capacity	W	5 at 4.5 K 70 at 77 K
Inlet pressure	MPa	1.62
Outlet pressure	MPa	0.12
Turbine efficiency	%	50
Compressor	--	Single-stage screw

2.2 Construction of a small size helium refrigerator

A small size helium refrigerator is shown in Figure 1. It consists of a compressor unit for compressing helium gas, a cold box which houses two micro turbo-expanders, five heat exchangers and a Joule-Thompson valve (J-T valve). The first stage heat exchanger is a cylindrical fin-tube and shell type. And the second to the fifth stages are perforated plate type heat exchangers. An external view of the cold box (ϕ400 mm in OD and 600 mm in height) containing these major components is shown in Figure 2.

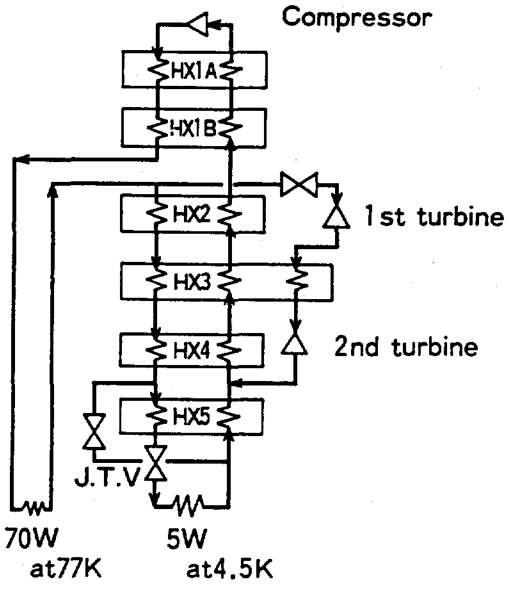

Figure 1. Flow diagram

Figure 2. Cold box (OD 400 x 600 H)

2.2.1 Micro turbo-expander

The micro turbo-expander is a vital component for small size helium refrigerator development. The performance of a refrigerator depends upon the efficiency of the two turbines. Design specifications of these micro turbo-expanders are listed in Table 2. The rotational speed of the first stage and the second stage turbo-expanders are 816,000 rpm and 519,000 rpm respectively.

Table 2. Design specifications of micro turbo-expanders

Specification	Unit	1st stage	2nd stage
Rotation speed	rpm	816,000	519,000
Inlet pressure, P_1	MPa	1.62	0.61
Inlet temperature	K	77	19
Outlet pressure, P_2	MPa	0.61	0.12
Out temperature	K	65	14
Mass flow rate	g/s	2.8	2.8

The turbo-expander consists of a radial inward flow reaction turbine and a centrifugal brake fan mounted on the upper and lower ends of a 4 mm diameter shaft, supported by self-acting gas bearings as shown in Figure 3. The turbine wheel with an attached shroud has a diameter of 6 mm and is stablized using Rayleigh step type thrust bearings as shown in Figure 4.

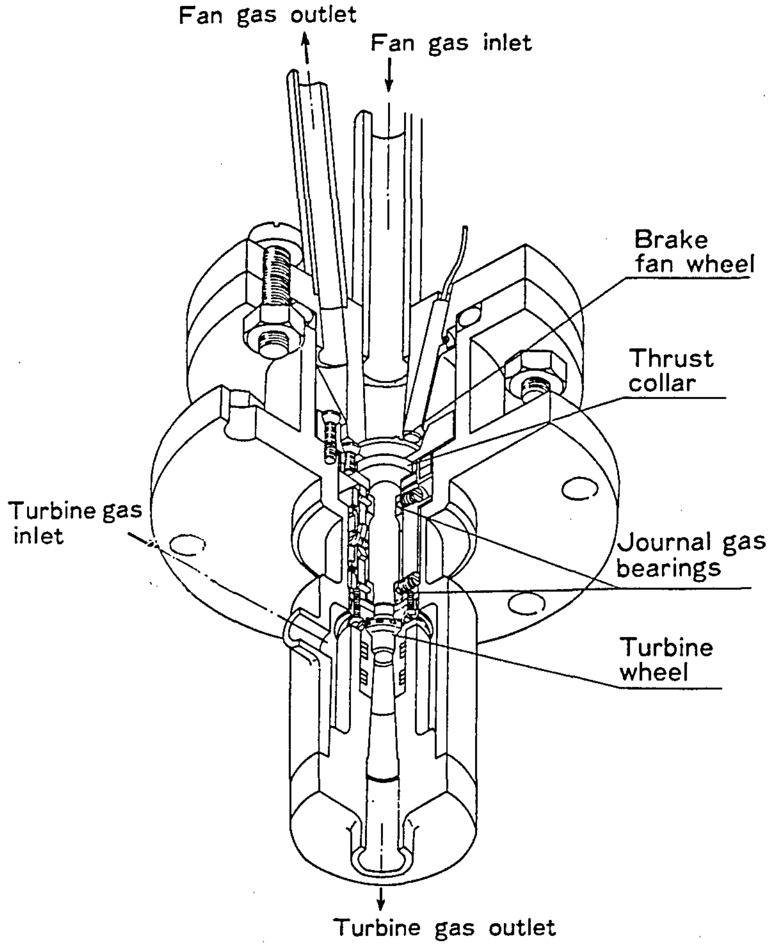

Figure 3. Cut away view of micro turbo-expander.

For journal bearings, which are vital components for attaining stable high speed operations, we have developed a tilting pad type bearing. A test shaft of 4 mm diameter and 24.5 mm length has been successfully driven up to 850,000 rpm using helium gas at room temperature conditions.

The turbine inlet temperature was verified as acceptable for rotations at LN_2 (77 K) temperature level. The measured vibration of the shaft for the first stage turbine is plotted against shaft speeds in Figure 5. During these tests there was no sign of shaft whirl.

The temperature of the turbine wheels remains very low (20 K to 77 K), while the brake fan room has a temperature of 330 K. This temperature difference is significant in that it tends to lower the adiabatic efficiency of the turbine due to heat leakage. To prevent such heat leakage, the turbine casing was thinned and thermal insulation was provided between the turbine wheels and the bearing room. Full consideration was given during seal construction to the prevention of high pressure and low temperature gas leakage at the turbine inlet into the bearing room and turbine outlet.

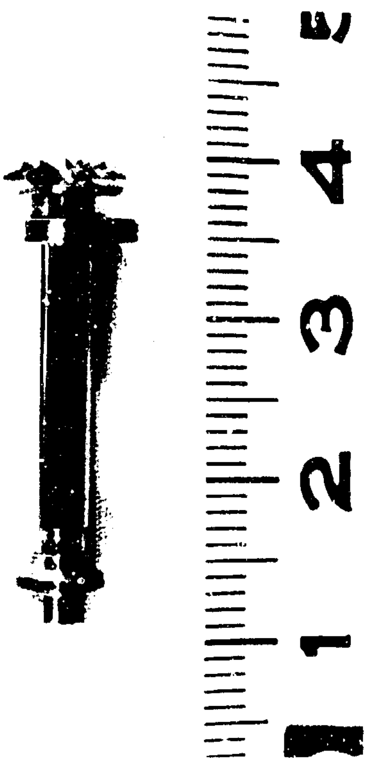

Figure 4. Shaft assembly.

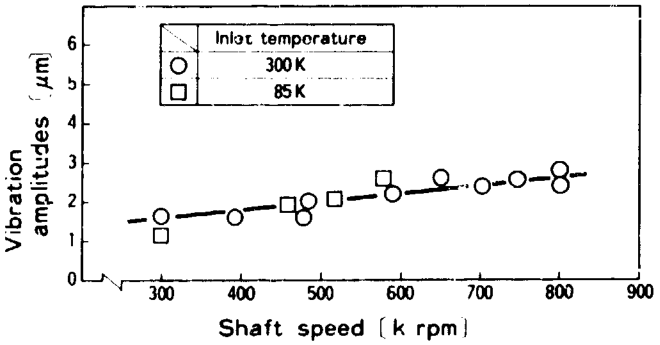

Figure 5. Vibration amplitudes of 1st stage turbo-expander shaft.

2.2.2 Heat exchanger

For large size helium refrigerators, aluminum plate fin type heat exchangers are commonly used. However, this type of heat exchanger is not adaptable for a small size refrigerator unit because of excessive size. To resolve this problem, a compact perforated-plate heat exchanger [3] was developed. The heat exchanger employed for the first stage is a conventional cylindrical fin tube and shell type, but the second to fifth stages which are arranged inside the cylindrical body consist of perforated-plate type heat exchangers. The cold box in which major components are compactly arranged is shown in Figure 6.

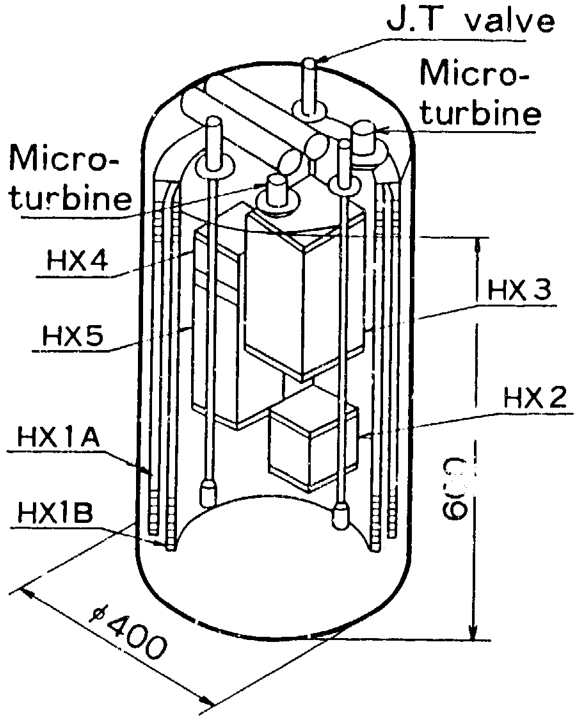

Figure 6. Cold box major component layout.

A schematic diagram of the perforated-plate heat exchanger is shown in Figure 7. A perforated heat transfer sheet of copper and an insulating sheet of stainless steel with a number of fluid channels are stacked and bonded together using a diffusion bonding method. This heat exchanger can provide a larger transfer area per unit volume (1,500 m^2/m^3 or larger), which has made it possible to reduce the size of heat exchanger. The fifth stage heat exchanger of the above refrigerator is only one-fourth of the size of a conventional aluminum plate fin heat exchanger.

2.2.3 Compressor

A single-stage screw compressor [4] was developed for use in this refrigerator system. Specifications for this compressor are listed in Table 3, and a photograph of the compressor unit is shown in Figure 8. This unit is composed of a single stage hermetic screw compressor, three stage oil separators, a heat exchanger and a control valve. The level of impurity of helium gas leaving the unit is less than 0.002 ppm, and an adiabatic efficiency as high as 76 to 78% has been achieved.

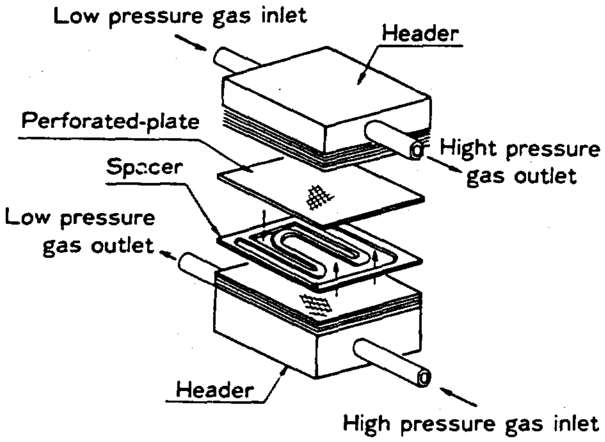

Figure 7. Compact perforated-plate heat exchanger layout.

Table 3. Design specifications of the compressor

Variables	Unit	Design Value
Gas Suction Pressure	MPa	0.11
Gas Delivery Pressure	MPa	1.87
Gas Delivery Temperature	C	35
Gas Delivery Flow Rate	g/s	3.5
Oil Content of Delivery Gas	Vol. ppm	0.1

3. Test results and discussion

The adiabatic efficiency of the turbo-expanders is plotted against the velocity ratio, U/Co, in Figure 9. The first turbo-expander indicates an efficiency of 34 to 44 % for turbine inlet temperatures ranging from 55 K to room temperature. These efficiencies were measured as a function of the velocity ratio, which varied between 0.28 and 0.5. The design value of U/Co was 0.5 with an efficiency (η) of 50 %. Since the rotational speed of the first stage turbo-expander was limited to 740,000 rpm, which was lower than the design speed (816,000 rpm), an increase in the turbine efficiency may be anticipated. The second turbo-expander indicated an efficiency between 30 and 70 % for a turbine inlet temperature variation between 19 and 100 K. This temperature variation corresponded to a velocity ratio, U/Co, of 0.26 to 0.52, as indicated in Figure 9. Performance of the second stage turbo-expander satisfied the design target of $\eta = 50$ %.

For example, the test results of the refrigerator are listed in Table 4. Both micro turbo-expanders were successfully and stably operated at near design values

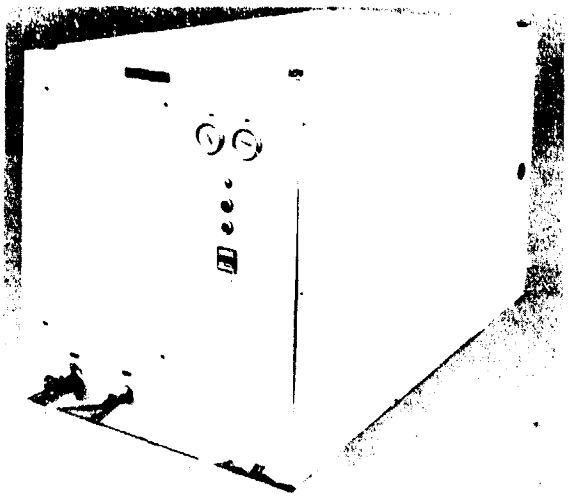

Figure 8. Compressor unit.
(800 W x 1520 L x 950 H)

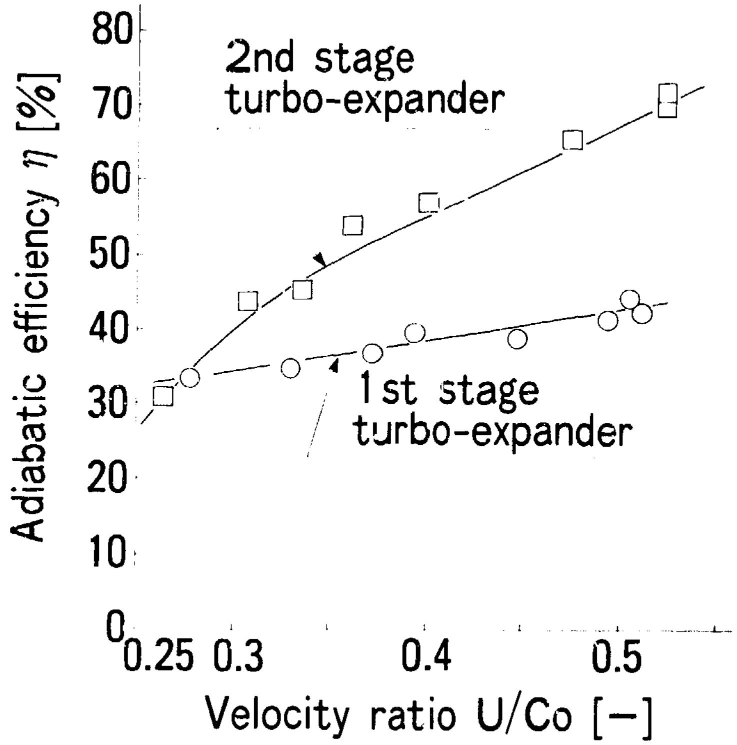

Figure 9. Micro turbo-expanders efficiency.

Table 4. Test results of the refrigerator

Item		Test Result
Refrigeration Capacity		5W at 4.5K 70W at 77K
1 st Exp. Turbine	Speed	740,000 rpm
	Efficiency	44 %
2 nd Exp. Turbine	Speed	470,000 rpm
	Efficiency	70 %

and their efficiency during liquefying of helium was 44 % and 70 % respectively. Refrigeration capacity of this refrigerator was proved to be 70 W at 77 K and 5 W at 4.5 K, and these results satisfy the design levels. This refrigerator accomplished a stable refrigeration capacity when operated for an extended time of more than 500 hours.

4. Conclusions

A low vibration and maintenance free small size helium refrigerator with micro turbo-expanders, which is applicable for refrigeration in superconducting NMR-CT or Josephson computers, has been developed. This refrigerator has a refrigeration capacity of 70 W (at 77 K) and 5 W (at 4.5 K). In the future, it is intended, through continuous operations over longer periods of time, to provide established reliability and improve efficiency of the turbine.

5. References

[1] D. B. Colyer., "Miniature Cryogenic Refrigerator Turbo-alternators," Advances in Cryogenic Engineering, vol. 14, Plenum Press, New York, P405 (1969).

[2] H. Izumi et al., "Development of Small Size Claude Cycle Helium Refrigerator with Micro Turbo-expander," CEC 85, DC-9.

[3] S. Harada et al., Proceeding of 31st Meeting of the Cryogenic Association of Japan, Tokyo, P.46 (1984).

[4] N. Arai et al., "Scroll and Screw Compressors: The Latest Compressor Technology for Air Conditioning and Refrigeration," Hitachi Review, vol. 34, No. 3, P.141 (1985).

LOW CAPACITY HELIUM LIQUEFIER: A ROSS-STIRLING ENGINE WITH ZIMMERMAN DISPLACER AND TWO STAGE COMPRESSOR WITH JOULE-THOMSON EXPANSION

Graham Walker

Professor of Mechanical Engineering
University of Calgary
Alberta, Canada, T2N 1N4
Consultant, General Pneumatics Corp.
Scottsdale, Arizona 85260

Abstract

Superconducting systems with liquid helium bath cooling require a low capacity, maintenance free helium liquefier to recondense the helium vapor 'boil-off'.

A novel concept to fill this need is presently under development at the University of Calgary. It consists of a Stirling refrigerator incorporating four stages of expansion with a displacer similar to that devised by J. Zimmerman.

The Stirling engine incorporates the piston drive linkage devised by A. Ross which virtually eliminates piston side thrust and the evils thereof. The Ross linkage is coupled also to a two stage helium compressor supplied with low pressure helium vapor and compressing it to 20 atm. with intercooling and aftercooling to ambient temperature.

The compressed gas is cooled to progressively lower temperatures by the four expansion stages of the Stirling cryocooler. It is passed at very low temperatures (i.e. 10 K approx.) to a final stage recuperative Giaque-Hampson type heat exchanger and the Joule-Thomson expansion nozzle. Some fraction of the helium liquefies on expansion, the remainder returns (with new vapor boil-off) to the low pressure compressor suction inlet.

This integral machine is driven electrically and has the potential to operate automatically and unattended for very long periods of time. It is anticipated the unit will work at variable conditions according to the demand in terms of the volume or mass rate of flow of the helium boil-off vapor.

Key words: Helium liquefier, Stirling cryocooler, Zimmerman displacer, J-T expansion.

1. Introduction

Superconducting systems are customarily cooled by liquid helium bath. Meticulous effort is made to thermally isolate and insulate the bath and contents from the environment. Nevertheless, some small 'heat leak' is intrinsic to all systems and, in addition, there may be some internal thermal generation in the cooled system. This heating will progressively vaporise some of the liquid helium so that replenishment is necessary from time to time.

Paper presented at 4th International Cryocooler Conference, September 25-26, 1986, Easton, Maryland, U.S.A. (D.T. Naval Ship R and D Center, Annapolis, Maryland, U.S.A.)

This 'topping-up' process is relatively expensive and, moreover, to be done efficiently and effectively, needs people with high levels of skill and expertise. The lack of liquid helium supplies and the personnel to manage it can prove catastrophic to the continued operation of the superconducting apparatus. While tolerable for laboratory operations this situation would not be conducive to the widespread use of superconducting apparatus, for example, nuclear magnetic resonance (NMR) apparatus in hospitals and health clinics.

There is, therefore, a need for a cryocooler capable of reliquefying the helium boil-off from storage dewars or otherwise providing cryogenic refrigeration to virtually eliminate the need for periodic resupply of the liquid helium. The cryocooler should be operable by anyone with no special skills or knowledge beyond operating a switch, and be reliable in operation for extended periods without maintenance. Routine replacement of the cryocooler at six or twelve month intervals may be acceptable but extension of this period to two or even five years is preferred. The cost of the cryocooler, both capital and operating, should be such that the 'payback period', the time when savings on liquid helium equal the cost of the cryocooler, should be less than two years, and, preferably, about one year.

Discussions with potential users of the cryocooler lead to the conclusion that a reliable unit capable of reliquefying 8 to 10 liters of liquid helium per day would readily find commercial acceptance. Some potential users with the need for higher capacity seem willing to incorporate the use of multiple low capacity cryocoolers to meet their needs.

The cost limit for such a cryocooler is difficult to establish for much depends on the cost and availability of liquid helium and skilled staff. In general terms, an annual cost of $20,000 is frequently quoted for helium replenishment and this may constitute a broad target figure for the annual cost limit for the helium liquefier. This would include the annual depreciation of the capital and installation cost, the annual operating cost for electric power, water for cooling and other services, the maintenance cost for replacing the cryocooler at annual or semi-annual intervals and the cost for refurbishment of the used machine.

2. A Low Capacity Helium Liquefier

A novel form of helium liquefier intended to fulfill the above requirement is at the earliest stage of development at the University of Calgary. The proposed liquefier is shown in Figure 1. It involves no new scientific principles but simply combines several disparate elements of existing technology in an arrangement thought to be novel.

It can be described in elementary terms as a mechanical refrigerator used to precool compressed helium prior to isenthalpic expansion (J-T expansion) with consequent liquefaction of some of the compressed helium.

The mechanical refrigerator is a Stirling cryocooler. This operates on a closed regenerative thermodynamic cycle with compression and expansion of the working fluid at different temperature levels. The basic technology of Stirling refrigerators has been summarised by Walker [1].

The form of Stirling cryocooler used for the machine shown in Figure 1 is of the two-piston variety rather than the piston-displacer machines often used.

One piston reciprocates in a cylinder called the compression space at temperatures near ambient. The other piston reciprocates in a cylinder called the expansion space. During normal operation the working fluid is compressed and expanded over a pressure ratio (p_{max}/p_{min}) in the range 1.6:1 to 2:1. Heat is abstracted from the surrounds of the expansion cylinder to the working fluid. That heat, plus the heat equivalent of the work input to drive the refrigerator is rejected from the working fluid to the ambient temperature water coolant in a heat exchanger called the cooler located adjacent to the compression space.

In the proposed Stirling cryocooler the expansion piston is a long thin element of solid nylon stepped along its length so there are four different diameters. Its design follows the principles developed and so lucidly enunciated by J. Zimmerman [2], including the use of articulated lower stages to minimise the precision of concentricity required of the piston and cylinder.

The stepped piston reciprocates with a short stroke in a long thin cylinder of epoxy-fiberglass tubing with diameters only slightly in excess of the expansion piston. As the piston moves in the cylinder the annulli formed between steps in the piston and cylinder diameter change in volume so there are in essence four separate expansion spaces. The four expansion spaces are thermally isolated from each other, relatively speaking, and in normal operation achieve progressively lower refrigeration temperatures, say 80 K for the upper space, 10 K for the lowest space and intermediate temperatures of say 40 and 20 K. Zimmerman employed aluminum foil tubes of high thermal conductivity to effectively use the refrigeration produced at the higher temperatures to 'shield' the environs of the lower temperature spaces. Of course the expansion cylinder is contained in a thermally insulated shell (vacuum or methane foam) to eliminate radiation and convected heat transfer.

A regenerative heat exchanger is a vital element of a Stirling cryocooler. This can be of the dense mesh wire screen or packed bed type shown in Figure 1 in the conduit coupling the compression and upper stage expansion spaces. It can also be of the regenerative annulus type shown in Figure 1 in the low clearance annular space connecting the various expansion spaces along the expansion piston. This follows the practice of Zimmerman [2] and utilizes the contribution of Radebaugh et al [3] to the design of regenerative annular heat exchangers.

The compression and expansion pistons are driven by a novel mechanical linkage devised by A. Ross [4] particularly for Stirling power generators. Figure 2 is a line diagram of the Ross linkage showing the loci of the extremities of the yoke coupled to the reciprocating pistons. It can be seen the loci are narrow 'figures of eight', almost a straight line so the piston side forces customarily arising from a crank/connecting rod linkage are virtually eliminated. This is

---

*Numbers in brackets refer to the literature references listed at the end of report.

particularly significant for Stirling machines intended for long periods without maintenance for it minimises the side loads supported by the unlubricated seals and guide rings on the piston. The linkage causes the pistons to move with near-sinusoidal motion and with a phase difference close to the 90° for optimum operation (see Walker [5]).

The same linkage can be used to drive the pistons of the two stage helium compressor shown in Figure 1 with water-cooled intercooling between stages and aftercooling of the compressed gas. Twenty atmospheres is, approximately, the optimum initial pressure for helium in a Joule Thomson expansion for it is close to the apex of the isoenthalpes at low temperature (10 to 15 K). With helium vapor available at atmospheric pressure, a pressure ratio (p_{max}/p_{min}) of 10 to 1 can be readily achieved with a two stage helium compressor using conventional automatic ball-check or reed valves.

The compressed gas leaving the compressor and aftercooler enters the inner tube of a long insulated double pipe heat exchanger connecting the compressor with the J-T valve located below the bottom (fourth expansion stage of the Stirling expansion cylinder). In transit from the compressor/aftercooler outlet to the J-T expansion valve the high pressure helium conduit is routed so as to be progressively cooled by the four levels of refrigeration generated by the Stirling cryocooler. This is supplementary to the cooling achieved by heat exchange with the low pressure return helium vapor flowing in the outer annulus of the double pipe heat exchanger *en route* to compressor inlet.

Following final precooling of the compressed helium to 10 to 15 K at the fourth expansion stage of the Stirling cryocooler the compressed helium passes to a conventional final stage Giaque-Hampson coiled tube heat exchanger with the actual J-T expansion nozzle at the lower end.

Isenthalpic expansion of the precooled compressed helium in J-T nozzles will result in conversion of a fraction of the helium to the liquid state for delivery by gravity feed or otherwise to the helium pool in the storage dewar (it is anticipated that where possible the J-T expansion will occur in or very close to the storage dewar).

The fraction of expanded gas, very cold but not liquefied, will return via the outer sheath of the Giaque-Hampson heat exchanger and the outer annulus of the double pipe heat exchanger to the compressor inlet. It will be supplemented by fresh vapor generated within the storage dewar. In transit to the compressor inlet the low pressure vapor will be warmed to near ambient temperature by heat transfer with the high pressure helium en route to the expansion nozzle.

The system requires a single electric drive motor, probably a conventional 125 V or 220 V A.C. motor with thyristor speed control to effect simple regulation. The refrigeration output of the Stirling cryocooler is, to a first approximation, a linear function of both the machine speed and mean pressure level of the working fluid. The speed of the drive motor and the pressure level of the helium working fluid (bled from the high pressure delivery of the high pressure compressor) can, in principle, be regulated readily by interactive feedback control using the criterion of helium vapor pressure in the storage dewar.

Any commercial J-T expansion nozzle may be incorporated with the system provided the flow characteristics are compatible. The preferred nozzle is the new temperature sensitive, annular expansion unit described by Hedegard et al [6]. This is preferred because of its demonstrated tolerance to relatively contaminated gases. This is valuable for extended operation for it minimises or even eliminates the need for effective filtration of the compressed gas. Another advantage of the Hedegard J-T nozzle is the facility with which adjustment of the fluid flow rate can be readily accomplished even in the course of operation.

3. Conclusion

The unit described above is at the earliest stage of development but no extension of the technological boundaries are anticipated and relatively straightforward engineering development is involved.

4. Acknowledgement

Research and development on Stirling cryocoolers at the University of Calgary is supported by the Canadian National Science and Engineering Research Council.

5. References

[1] Walker, G., Cryocoolers, Vol. 1 and 2, Plenum Publishing Corp., New York (1983).

[2] Zimmerman, J. and Sullivan, D.B., A study of design principles of refrigerators for low power cryoelectric devices, NBS Tech. Note 1049 (1982).

[3] Radebaugh, R. and Louie, B., A simple first step to the optimisation of regenerator geometry, Paper 19, pp. 177-198, Proc. Third Cryocooler Conf., NBS Spec. Pub. 698 (1985).

[4] Ross, A., The inverted yoke drive Stirling engine, Paper No. 859074, Proc. 20th Intersoc. En. Conv. Eng. Conf. (IECEC), Miami, Fla., Aug. 1985, Publ. Soc. Auto Eng., Warrendale, Pa.

[5] Walker, G. and Fauvel, R., Ross-stirling engines: variations on a theme, Paper no. 869132, pp. 610-616, Proc. 21 Intersoc. En. Conv. Eng. Conf. (IECEC), San Diego, Aug. 1986, Publ. Am. Chem. Soc., Wash., D.C.

[6] Hedegard, K., Walker, G. and Zylstra, S., Temperature sensitive, variable area flow regulator for Joule-Thomson nozzles, Proc. 4th Int. Cryocooler Conf., Easton, Md., Sept. 1986, (D.T. Naval Ship R&D Center, Annapolis, MD).

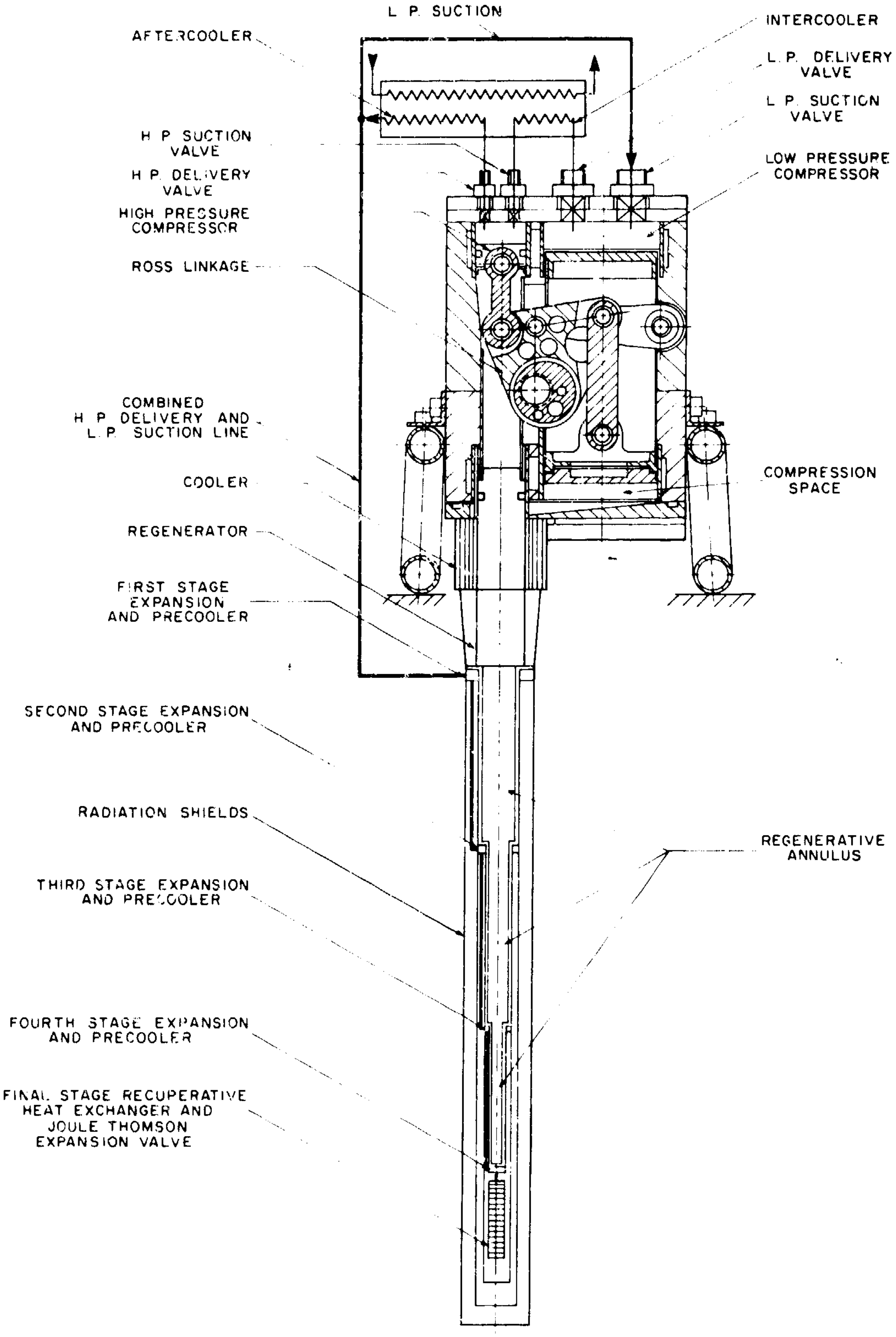
L. P. SUCTION
AFTERCOOLER
INTERCOOLER
L. P. DELIVERY VALVE
L. P. SUCTION VALVE
H. P. SUCTION VALVE
H. P. DELIVERY VALVE
HIGH PRESSURE COMPRESSOR
LOW PRESSURE COMPRESSOR
ROSS LINKAGE
COMBINED H. P. DELIVERY AND L. P. SUCTION LINE
COOLER
COMPRESSION SPACE
REGENERATOR
FIRST STAGE EXPANSION AND PRECOOLER
SECOND STAGE EXPANSION AND PRECOOLER
RADIATION SHIELDS
REGENERATIVE ANNULUS
THIRD STAGE EXPANSION AND PRECOOLER
FOURTH STAGE EXPANSION AND PRECOOLER
FINAL STAGE RECUPERATIVE HEAT EXCHANGER AND JOULE THOMSON EXPANSION VALVE

Figure 1

LOW CAPACITY HELIUM LIQUIFIER : A ROSS-STIRLING CRYOCOOLER WITH FOUR STAGE ZIMMERMAN DISPLACER, TWO HELIUM COMPRESSION STAGES AND JOULE THOMSON EXPANSION

UNIVERSITY OF CALGARY APRIL 1986

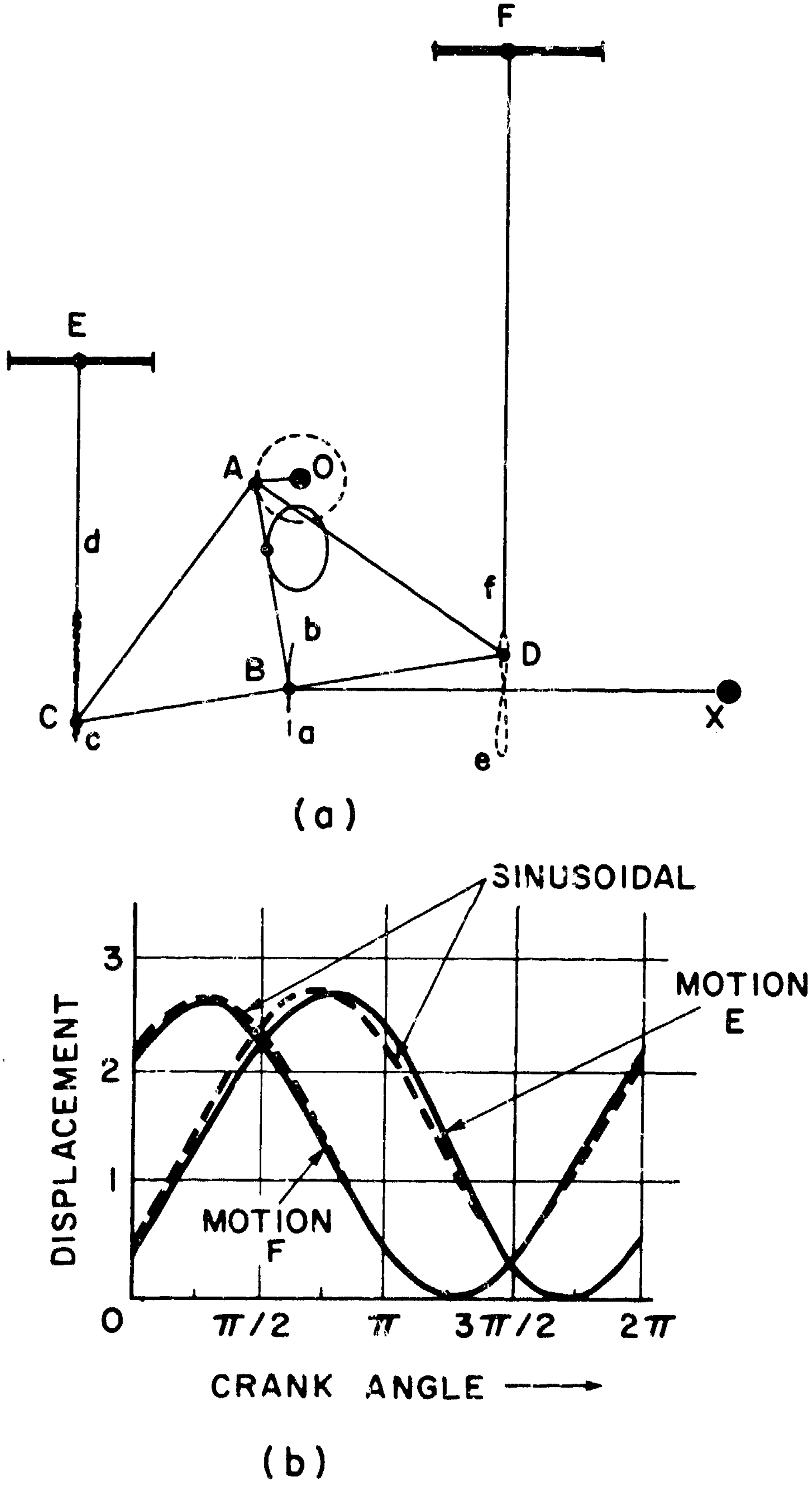
F
E
A
O
d
f
b
B
D
C
c
a
X
e
(a)
SINUSOIDAL
3
MOTION
E
2
DISPLACEMENT
1
MOTION
F
O
π/2
π
3π/2
2π
CRANK ANGLE ⟶
(b)

Figure 2 The Ross Linkage

Preceding Page Blank

PERFORMANCE OF VM COOLER COUPLED WITH TWO STAGE G-M COOLER

M. Kaneko and Y. Matsubara

Atomic Energy Research Institute
Nihon University
Tokyo 101, Japan

This paper describes the performance of the 4.5K Vuilleumier (VM) cycle cryocooler coupled to a commercial two stage Gifford-McMahon (G-M) cycle cryocooler. The compression part of Vuilleumier cryocooler works between room temperature and the first stage temperature (~80K) of a G-M cryocooler, so that the trouble caused by high temperature (>300°C) operation could be avoided. Another advantage of operating below room temperature is that a high pressure ratio can be obtained easily. Before it flows into the expansion space, the working gas of the Vuilleumier cryocooler is precooled using the G-M cooler's second stage cold end (at ~15K). In the low temperature region, especially below 10K, the temperature swing caused by the gas expansion becomes noticeable because of the low specific heat of the cold end material. In this paper, the effect of a helium gas damper on the temperature stability is also discussed.

Key words: Vuilleumier cycle, Gifford-McMahon cycle, cryocooler, gap regenerator, thermal damper, helium

1. Introduction

The development of reliable, low cost, easily operated cryocoolers has been required for superconducting and other cryogenic devices. In our previous work, we demonstrated a Gifford-McMahon (G-M) cycle cryocooler operating below 5K. This cooler was precooled to a temperature of about 10K using another commercially available Gifford-McMahon cryocooler[1]. The reliability of long term operation would be improved by use of a Vuilleumier (VM) cycle cooler operated below room temperature or by use of an annular gap regenerator. Operating the Vuilleumier cooler below room temperature would free it from the gas impurity problem caused by high temperature operation and the consequent degradation of performance caused by gas leakage through wearing piston seals.

*Research associate from Suzuki Shokan Co., Ltd.

In the previous cryocooler conference we described a Vuilleumier cryocooler in which the compression part was operated between room temperature and liquid nitrogen temperature. That system consists of two Vuilleumier cryocoolers, one precooled to about 16K by the second. The ultimate temperature was 5.4K, and acceptable heat load was about 10mW at 7K[2].

To establish an acceptable apparatus for the long-life operation, the system of a two-staged Vuilleumier cryocooler precooled by a commercially available two-staged Gifford-McMahon cryocooler was selected. The design and experimental results are described in this paper.

2. Design

Figure 1 shows the profile of the Vuilleumier (VM) cryocooler coupled with a two-stage Gifford-McMahon cryocooler which is commercially available for such uses as cryopumps. All of the cylinders are made of 304 stainless steel and other metals to prevent leakage of helium gas into the vacuum vessel. The components have been carefully joined with Ag containing solder. The compression part of the Vuilleumier cryocooler is operated between room temperature and a cold source temperature (approximately 80K) provided by the first stage of the Gifford-McMahon cryocooler. Therefore the compression ratio of working helium gas depends on the cooling temperature of the first stage of Gifford-McMahon cryocooler. This allows us to find the best pressure ratio for the Vuilleumier cryocooler. The physical dimensions are shown in table 1. In the compression part, a gap regenerator is used and the displacer is made of the cured phenolic resin reinforced by cotton cloth. It is 47mm in diameter and about 190mm in length. The radial clearance of the displacer section is about 0.1 to 0.2mm. The heat injection part, which is 35mm long at room temperature, is made of brass. It is heated only by heat from the drive motor. The heat rejection part is covered by a 30mm wide copper band, which is thermally balanced with a copper bridge. The stroke of the compression part is 15mm.

Table 1. Physical dimensions of Vuilleumier cryocooler.
(All values in millimeters.)

	Compression Part	1st Stage Expansion Part	2nd Stage Expansion Part
Cylinder O.D.	ϕ48	ϕ15	ϕ12
Cylinder thickness	0.5	0.5	0.5
Displacer O.D.	ϕ47	ϕ13.9	ϕ10.9
Displacer length	190	360	300

The expansion parts consist of two stages. The expansion intake stroke is 5mm. The structure and the displacer material are the same as those used in the compression part. The first and second cylinders are made of 304 stainless steel and have an outer diameter of 15mm and 12mm respectively. Both cylinders have a 0.5mm thickness. The first stage displacer, which is about 13.9mm in diameter and

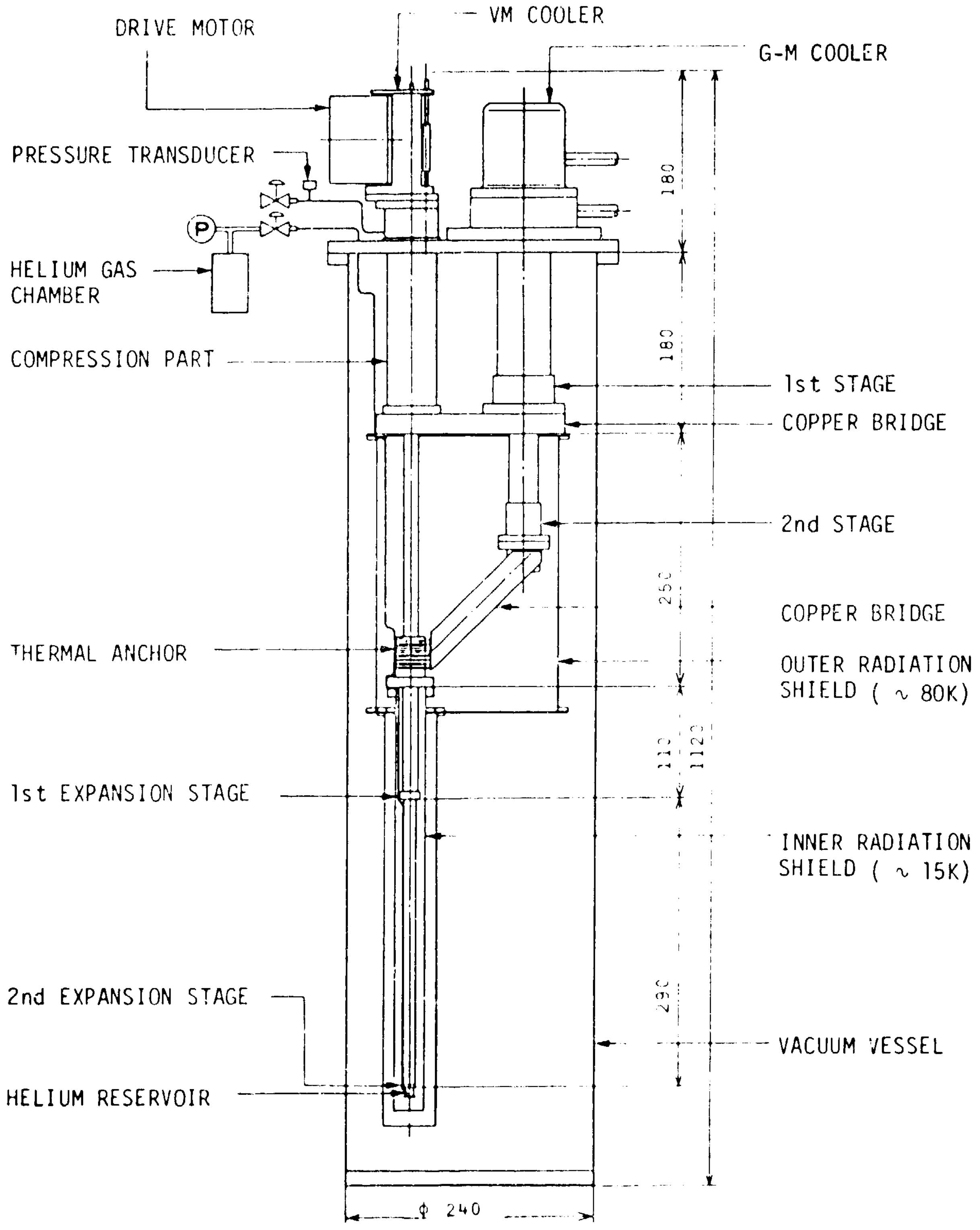
DRIVE MOTOR
VM COOLER
G-M COOLER
PRESSURE TRANSDUCER
P
HELIUM GAS CHAMBER
COMPRESSION PART
1st STAGE
COPPER BRIDGE
2nd STAGE
COPPER BRIDGE
THERMAL ANCHOR
OUTER RADIATION SHIELD (∿ 80K)
1st EXPANSION STAGE
INNER RADIATION SHIELD (∿ 15K)
2nd EXPANSION STAGE
VACUUM VESSEL
HELIUM RESERVOIR
180
180
250
110
1120
290
ϕ 240

Figure 1. VM cryocooler coupled with two stage G-M cryocooler.

360mm in length, consists of two parts that are carefully connected with pins to reduce physical stress. The displacer can be moved freely and it has 50 to 70μm in radial clearance. The second stage displacer is approximately 10.9mm in diameter and 300mm in length. The structure is the same as the first stage; clearance is about 20 to 45μm.

The working gas coming from the compression part of the VM cooler is precooled below 15K by the thermal anchor of the second stage Gifford-McMahon cryocooler and flows into the first expansion volume. Using a stepping motor to drive a double scotch yoke mechanism, any operation cycle speed is available, and the displacer moves in sinusoidal wave motion. Various angles between the expansion and compression displacers can be selected. This machine needs perfect stem seals for the displacer drive rods (ϕ4mm), but it must be possible to remove the stem seals by covering the drive mechanism portion with metal caps. The strain gauge type pressure transducer which is connected to the heat injection volume by capillary tube is used to minimize the dead volume.

A schematic diagram of the Vuilleumier cryocooler cold end is shown in Figure 2. Carbon glass resistance and germanium resistance temperature sensors are used at the cold end and the sample holder, respectively. A gauge-type electric heater is attached to the sample holder to simulate heat load. Copper or brass components are joined with pure indium, which has high thermal conductivity in the liquid helium temperature range. Helium flows into the brass reservoir through a 304 stainless steel capillary during the gas condensing process. To reduce the conduction heat through lead wires of cold sensors, phospher bronze instead of pure copper wires are used. It is necessary to reduce the temperatuere oscillation which is induced by the displacer motion. Zimmerman and Sullivan[3] have succeeded in reducing the temperature oscillation at 8.5K using a brass thermal damper containing helium. The reduction ratio (β) of a temperature oscillation having a sinusoidal wave can be expressed as follows,

$$\beta = \frac{\Delta Ts}{\Delta Tc} = \exp\left(-L\Big/\sqrt{\frac{\pi}{a \cdot \tau_0}}\right)$$

where ΔTc and ΔTs are the temperature oscillation at the cold end and the sample holder respectively, L is the length of the thermal damper (helium reservoir containing helium gas), τ_0 is the period of oscillation, and a is the thermal diffusivity of the damper. This thermal diffusivity is defined as

$$a\ [\mathrm{cm}^2/\mathrm{sec}] \equiv \frac{\lambda}{\rho \cdot c}$$

where λ(W/cm-K) is thermal conductivity, c (J/g-K) is specific heat and ρ(g/cm^2) is density. Choosing a small a value improves the thermal damping effect. Although the temperature of the sample holder is increased by heating, a good damping effect on the temperature oscillation can be obtained when low thermal conductivity materials are used. For these reasons, brass is preferable as the damper material rather than pure copper. Especially if the helium in the reservoir is liquified in operation below 5K, the use of brass might increase this damping effect significantly.

The refrigeration capacity of the particular Gifford-McMahon cryocooler used is 10W at 80K and 1W at 15K. This G-M cryocooler has sufficient cooling capacity that it can provide acceptable performance when it is used in combination with the VM cooler. According to Vuilleumier cycle analysis using the isothermal model,

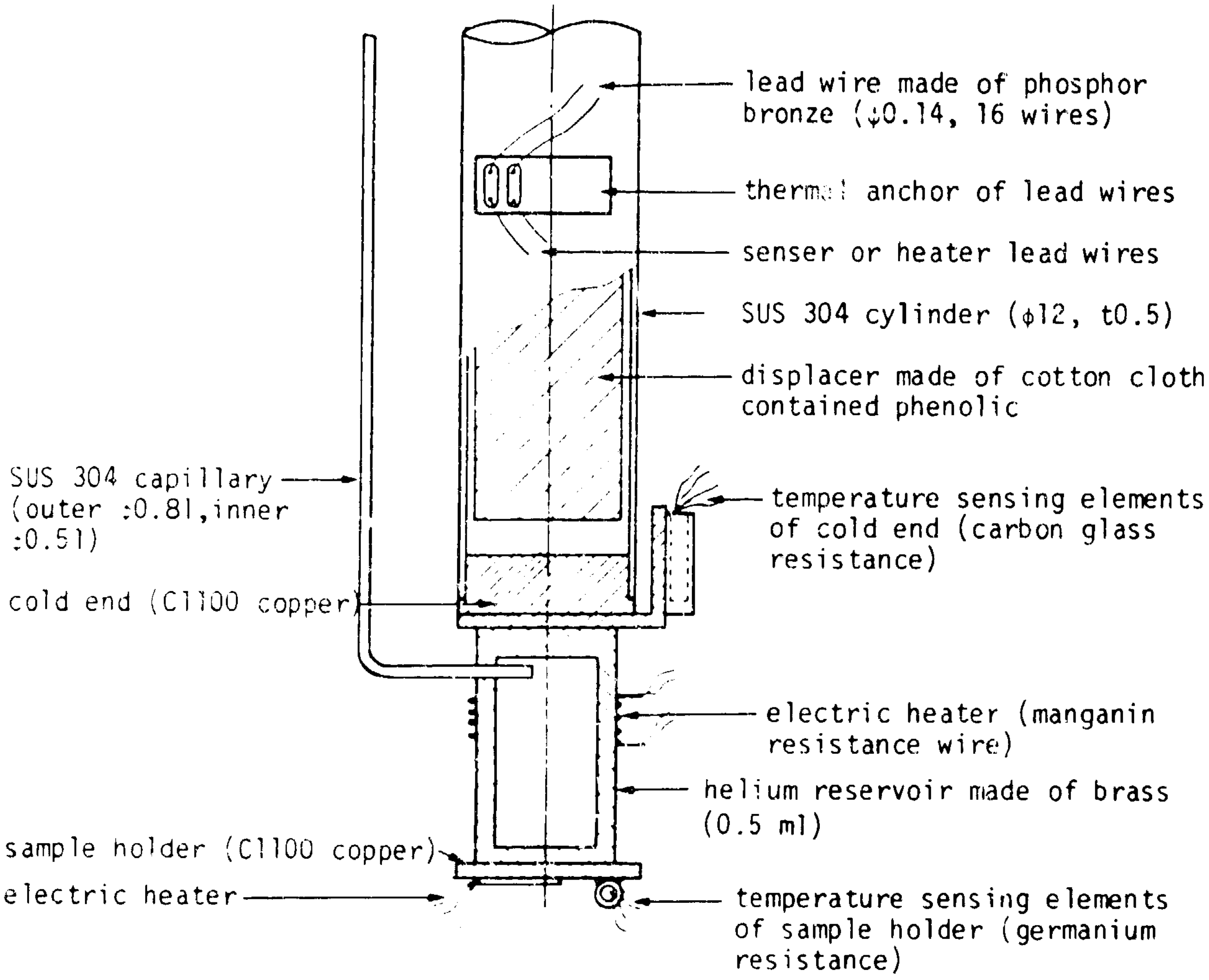
lead wire made of phosphor bronze (φ0.14, 16 wires)
thermal anchor of lead wires
senser or heater lead wires
SUS 304 cylinder (φ12, t0.5)
displacer made of cotton cloth contained phenolic
SUS 304 capillary (outer :0.81, inner :0.51)
temperature sensing elements of cold end (carbon glass resistance)
cold end (C1100 copper)
electric heater (manganin resistance wire)
helium reservoir made of brass (0.5 ml)
sample holder (C1100 copper)
electric heater
temperature sensing elements of sample holder (germanium resistance)

Figure 2. Schematic diagram of cold end portion of VM cryocooler. Parts are joined using pure indium.

the compression cycle work which the first stage of the G-M cryocooler must accept is less than 1W at 80K. Analysis conditions are: cycle speed, 60 rpm; base pressure, 0.1MPa; and pressure ratio, 2.3. In addition, there are several thermal losses such as regeneration loss, conduction loss, radiation loss, shuttle loss, etc. The radiation loss is especially noticeable. This system has radiation shields made of electro tough pitch copper (C1100) that are 1mm thick at the 80K level and 0.5mm thick at the 15K level. Superinsulation technique is also used.

3. Experiment

The experiment was carried out under proper thermal isolation. A mechanical rotary pump was used for initial evacuation. The cryopump effect was used after the seal-off valve was closed. The residual helium pressure was kept below 10^{-4}Pa (10^{-6} Torr). Thermal radiation that heated up the outer and inner shields was at acceptable levels. For the outer radiation shield, bottom side temperature was 87K and cooling side temperature was 81K. For the inner radiation shield, these temperatures were 14K and 13K. In this system, the ultimate temperatures of the first and the second stage of Gifford-McMahon cryocooler were 72K and 12.5K, respectively, when the Vuilleumier cryocooler was not operating. Therefore the heat loads on the first and the second stages were estimated at 7W and almost 0W, respectively, by using the cooling capacity data which was taken without any cooling objects. In the same way, when the Vuilleumier cryocooler was operated under the conditions of about 30rpm and mean working pressure of about 0.3MPa (3atm), the heat load on each cooling station was estimated at 10.7W at 81K and less than 0.1W at 13.2K. The system can be operated at any value of expansion compression phase angle; however, the results of the isothermal model calculation[4] indicated 80° as the optimum value, and was the value used in this paper.

It took approximately 8 hours for this particular Gifford-McMahon cryocooler to reach its working temperature level because it had to cool the masses of the copper radiation shield and copper thermal bridges. Both the cooldown time and ultimate temperature of this particular Vuilleumier cryocooler depend upon the mean working pressure or the cycle speed. Results and conditions of the Vuilleumier cryocooler operation in the cooldown period are given in table 2, and the temperature profile is described in Figure 3. The duration the cooldown time can be reduced by increasing the working pressure or cycle speed. In the case of the ideal gas, the cycle work is proportional to the mean pressure and cycle speed. If the cooldown time is inversely proportional to the cycle work of the expansion space, cooldown time for case 1 will become 12 hours. In this calculation cooldown time of the Gifford-McMahon cooler's first stage (8 hours) is not affected by the Vuilluemier cooler's mean working pressure or cycle speed. Considering the heat load of the helium reservoir, cooldown time of 15 hours is acceptable. In case 1, the ultimate temperature was 5.3K, which was higher than the critical temperature (5.201K). In case 2, the temperature reached was below the critical point.

Figure 4 shows the measured value of cold end temperature, pressure and displacement value of Vuilleumier cryocooler. The working pressure, which changed in a sinusoidal fashion, was mesured by using a pressure transducer at room temperature. The displacement volume, which also changed sinusoidaly, was measured by using a linear displacement convertor. In both cases [A] and [B] of Figure 4 the

Table 2. Cooldown time and conditions of operation.

	Conditions			Cooldown			
	Mean Pressure	Cycle Speed	He Reservoir*	Working State of G-M Cooler		VM Cooler	
	Pm (MPa)	(rpm)	(MPa)	1st (80K)	2nd (13K)	Cooldown Time	Ultimate Temp.**
Case 1	0.49	37	0.5	8 hours	2.5 hours	15 hours	5.3-5.5K
Case 2	0.28	19	-----	8 hours	2.5 hours	22 hours	5.2-5.5K

* Initial charged pressure at room temperature.
** With variation as shown in Figure 3.

helium reservoir (Figure 2) was not attached to the cold end. We can find the interesting point in the temperature wave in [B] and [C]. However the stroke in which that small perturbation, or "crick" occurred was different. In case [B], a constant temperature region appears during the gas expansion stroke. When the data were taken, mean temperature was slowly increasing by heating of 2.4mW. The last state was the same as [A]. In case [C], the helium reservoir was loaded, the crick appears during the gas compression stroke, and seems especially to occur when the pressure goes over the critical pressure (2.245 atm). This pressure-temperature relation is described on the T-S diagram shown in Figure 5. This T-S diagram was drawn using a computer program of McCarty's helium properties[5]. The symbols of [A], [B], and [C] are the same as those in Figure 4. In the case of [C] it is supposed that the particular crick is caused by the entrance to the supercritical region. In the case of [B] it is supposed that particular crick is caused by the latent heat of phase transition. The initial and the final part of crick region is shown in Figure 5 by the symbol of (●). Comparing [A] and [G] shows that increasing cycle speed increases refrigeration. The same discussion could be carried out from the comparison of [E] and [F]. The ultimate temperature of 4.3K was obtained in case [E].

Figure 6 shows the cooling capacity of this Vuilleumier cryocooler with helium reservoir. The data from [C] and [D] in Figure 5 are included in Figure 6. When the mean working pressure was about 2atm, the transition occurred between the cooling capacity of 4mW and 5mW. In this region the amplitude of the temperature change was unstable. In the region of over 5mW, there is no liquid in the expansion space, and therefore the temperature changes sinusoidally. A cooling capacity of about 3mW with a temperature swing of 4.7 to 4.9K was obtained. In the operation of over critical pressure, the temperature obtained was not below the critical point. In this particular Vuilleumier cryocooler, low pressure operation gives more cooling capacity than high pressure operation. The reason is that the performance of the regenerator is limited by heat capacity. In such a low temperature region the regenerator is short of heat capacity, and this regenerator loss should be larger than the P-V work of the gas.

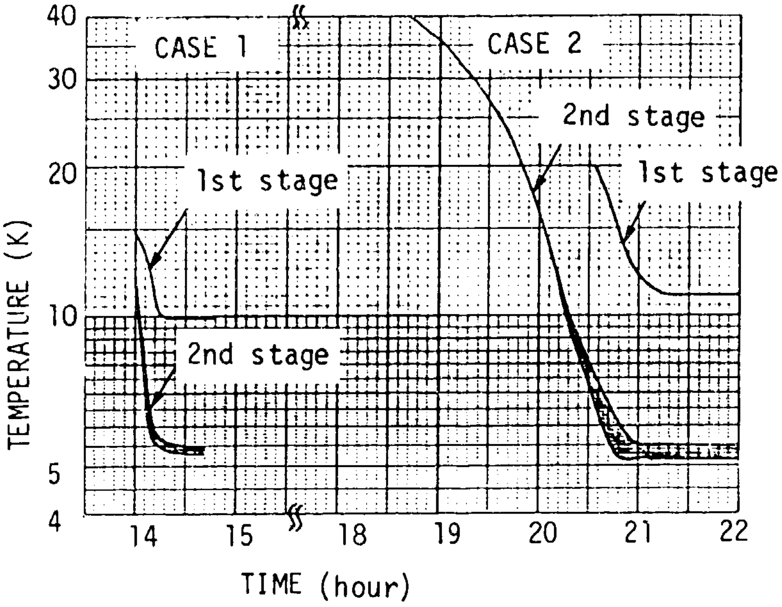

Figure 3. Cooldown of VM cryocooler.
CASE 1; mean pressure of 4.8 atm, 37 rpm, helium reservoir of 4.9 atm
CASE 2; mean pressure of 2.8 atm, 19 rpm, without helium reservoir

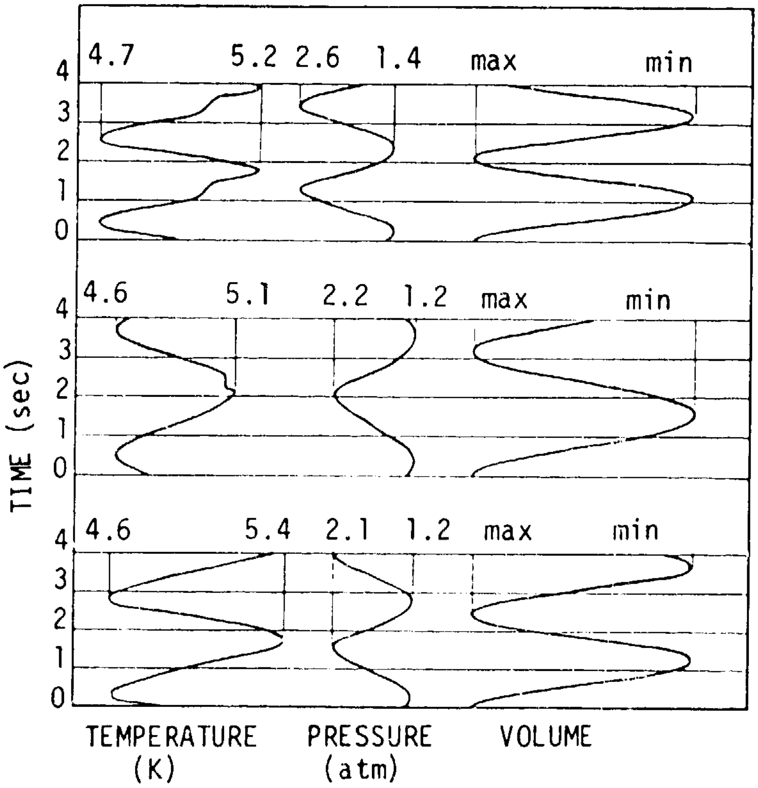

[C] with helium reservoir
cycle speed of 28 rpm
electric heat load of 4.5 mW

[B] without helium reservoir
cycle speed of 19 rpm
electric heat load of 2.4 mW
(during transition period)

[A] without helium reservoir
cycle speed of 24 rpm
electric heat load of 3.7 mW

Figure 4. Experimental results.

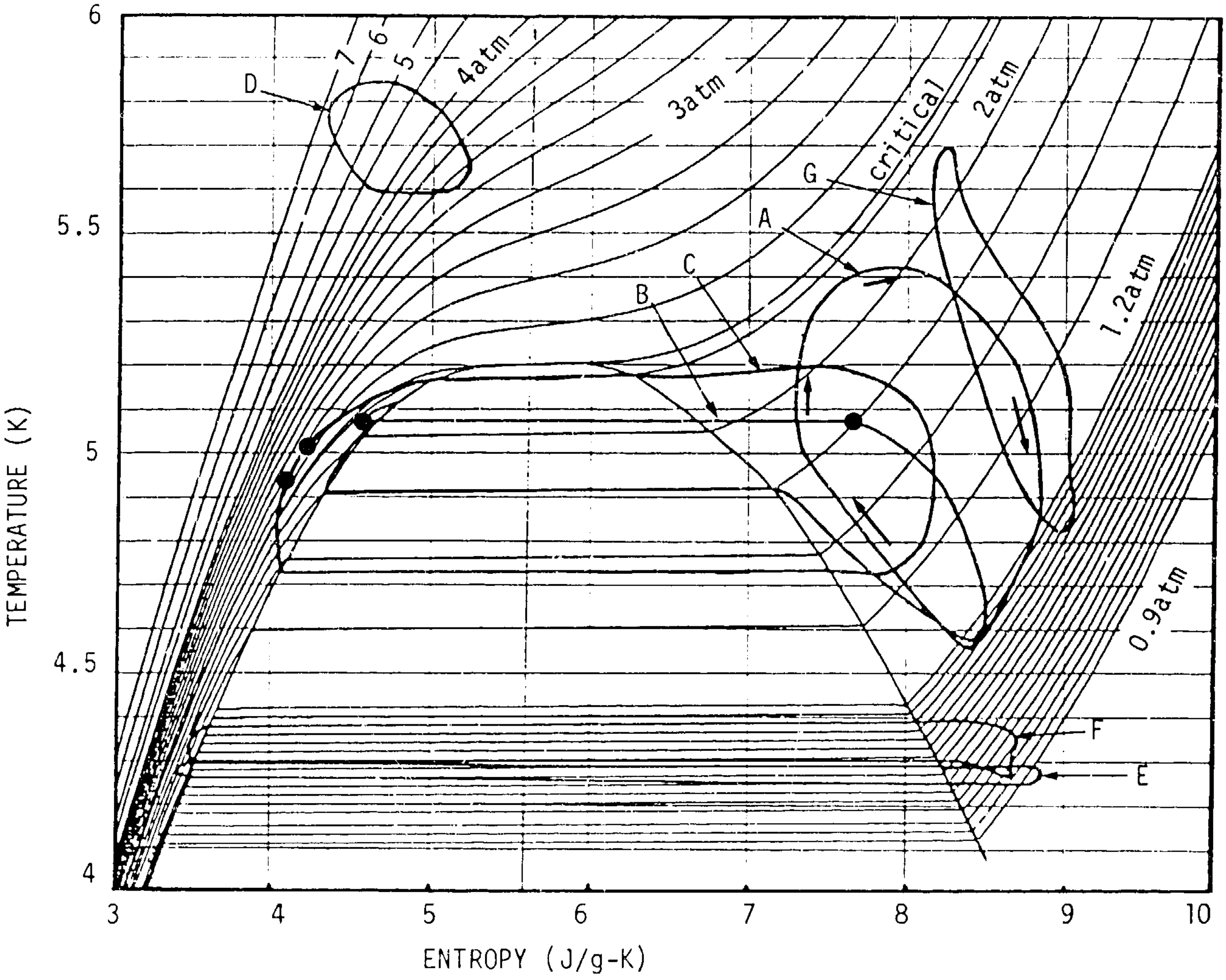

Figure 5. Cooling cycle of the second expansion volume of the VM cryocooler on the T-S diagram of helium.

[A]. without helium reservoir, 24rpm, 3.7mW.
[B]. without helium reservoir, 19rpm, 2.4mW.
[C]. with helium reservoir, 28rpm, 4.5mW.
[D]. with helium reservoir of 2.6atm, 28rpm, 3.7mW.
[E]. with helium reservoir of 1.2atm, 28rpm, no heat load.
[F]. with helium reservoir, 4.7rpm, no heat load.
[G]. without helium reservoir, 19rpm, 3.3mW.

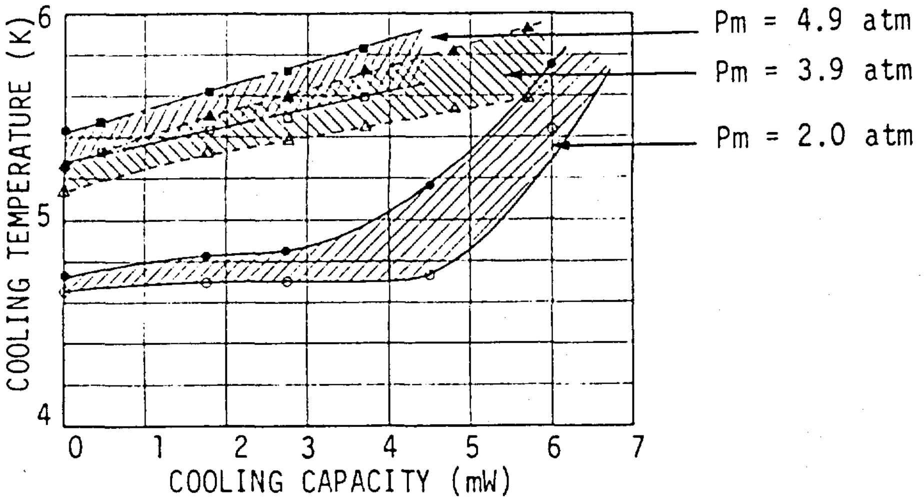

Figure 6. Cooling capacity of the VM cryocooler.
Pm is mean pressure and operating cycle speed is 28 rpm.
The hatching area shows the temperature variation.

This experiment did not involve research into the thermal damping effects of the helium reservoir shown in Figure 2. Therefore the temperature of the sample holder was not measured at all, even if the helium was conducted to the reservoir. Figure 7 shows the damping effect of helium reservoir using a different set of Vuilleumier cryocooler and damper. The temperature of both the cold end and the sample holder was about 6.1K. Amplitude of the temperature oscillation at the cold end was about 400mK and is shown on Figure 7 by the closed circles. The amplitude of the temperature oscillation at the sample holder is shown in two lines, one having the same frequency as the cryocooler and the other showing the maximum swing caused by the unstable motion of this cooler. Using high pressure helium gas, a good damping effect was obtained. When the pressure of the helium reservoir was 7atm, the temperature oscillated at 2Hz with an amplitude of 1.5mK and the maximum amplitude change was 5mK. Therefore the reduction ratio is equal to 0.013 and the thermal conductivity of the damper is estimated at about 0.036 (W/cm-K) at 8K.

4. Conclusion

We have succeeded in operating a two-staged Vuilleumier cryocooler below 4.5K. The cryocooler was coupled with a commercially available two-staged Gifford-McMahon cryocooler. A cooling capacity of 4mW was obtained at a temperature below 5K. In spite of the condition that only a phenolic regenerative displacer was used in this experiment, this cryocooler reached liquid helium temperature with a fractional cooling capacity. Sufficient heat transfer was realized in the annular gap regenerator by using a long displacer (shown in table 1) and low cycle speed. In this study, we found the phenolic displacer can be used as a regenerator, although it is necessary to improve the regenerative heat capacity to obtain large cooling capacity.

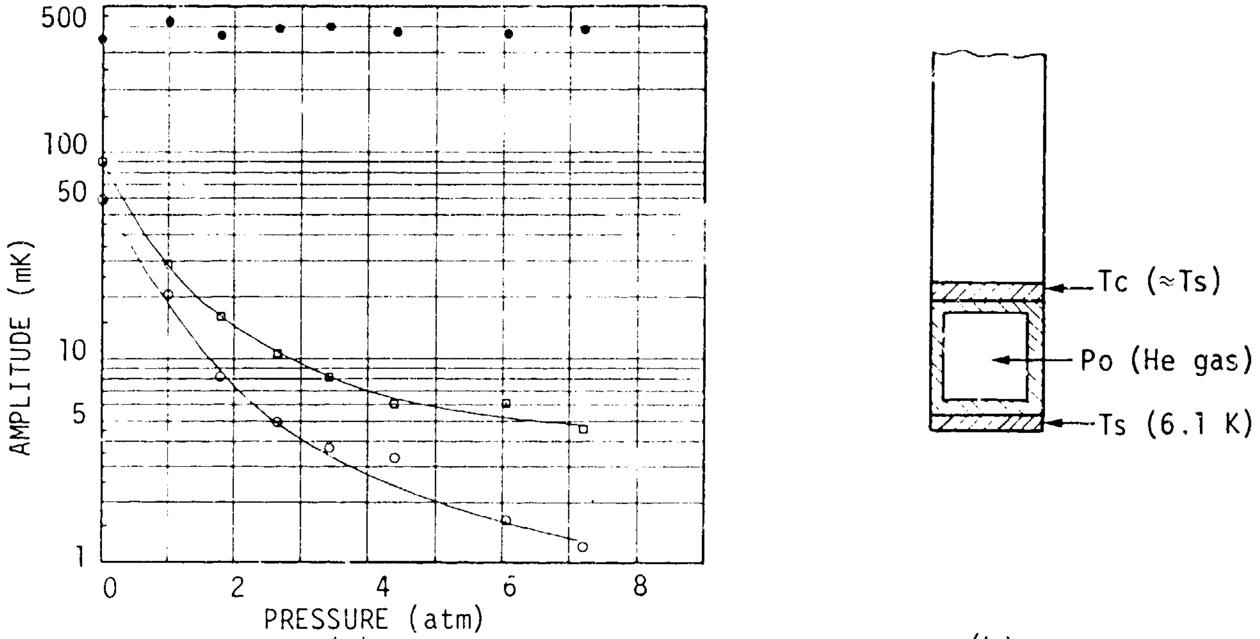

(a)

(b)

Figure 7. Damping effect of helium reservoir.
(a); Amplitude of temperature oscillation of each stage.
○ shows the amplitude of oscillation of Ts at 2 Hz which is equal to the cycle speed of the cooler operation.
☐ shows slow changes in temperature because of unstable motion of the cooler. This amplitude is the maximum change.
● shows the amplitude of oscillation of Tc. The maximum and the minimum pressure is 2.1 atm and 1.5 atm in a cycle respectively.

5. References

[1] Y. Matsubara and K. Yasukochi, "An Application of Gap Regenerator/Expander Precooled by Two Stage G-M Refrigerator", Refrigeration for Cryogenic Sensors, NASA Conference Publication 2287, p157 p168, (1983).

[2] Y. Matsubara and M. Kaneko, "Vuilleumier Cycle Cryocooler Operating Below 8K", Proceedings of the Third Cryocooler Conference, NBS Special Publication 698, p234 p239, (1985).

[3] J.E. Zimmerman and D.B. Sullivan, A Study of Design Principles for Refrigerations for Low Power Cryogenic Devices, NBS Technical Note 1049, (1982).

[4] Y. Matsubara and M. Kaneko, "Simple Analysis of Multistage Vuilleumier Cycle Cryocooler", Proceedings of SCEC 85, A 31, (1985).

[5] R.D. McCarty, Thermophysical Properties of Helium -4 from 2 to 1500K with Pressures to 1000 Atmospheres, NBS Technical Note 631, (1972).

CLOSED-CYCLE LIQUID HELIUM DIP CRYOCOOLER

Calvin Winter
Quantum Technology Corp.
6237-148 Street, Surrey, B.C., Canada V3S 3C3

Suso Gygax
Simon Fraser University
Department of Physics, Burnaby, B.C., Canada V5A 1S6

Performance results of the QUANTUMCOOLER closed-cycle liquid helium dip cryocooler demonstrate 1/4 watt of cooling power at liquid helium temperature. The dip dewar access port allows easy introduction of devices into the liquid helium bath without breaking any vacuum seals. In this manner devices to be cooled can be changed in a few minutes. It is ideally suited for cooling superconducting devices, samples, infra-red detectors and microwave amplifiers. Reliability and cooling power data from 5000 hours of operation is presented. No deterioration of the flow rate in the Joule-Thomson circuit has been detected during the more than 3000 hours of continuous operation at liquid helium temperatures.

Key words: cryocooler; helium dewar; Joule-Thomson valve; liquid helium.

1. Introduction

We are describing here in some detail a complete liquid helium dewar system containing its own closed cycle liquifier. It was developed to fulfill a number of specific design criteria. It is felt that with careful design a cooling power of 1/4 W at 4.2 K is sufficient for a large class of applications. A two-stage Gifford-McMahon (G-M) refrigerator followed by a Joule-Thomson (J-T) expander was chosen to provide helium liquifaction. A bath of liquid helium is essential for excellent temperature stability. It also provides greatly increased effective cooling power for intermittent heat loads such as sample cooling. However, the liquid helium space should be easily accessible to allow for quick immersion and removal of equipment. The liquifier proper should be a self contained unit to be used in a number of different dewar configurations. Some possible applications are: cooling of infrared and microwave detectors; cooling of superconducting magnets of modest size; cooling of superconducting electronics; experimental measuring dewar for resistivity, T_c, tunnelling and similar measurements; helium transfer system to replenish large capacity but low heat load dewars. In all these situations closed systems are desirable, making helium recovery mandatory.

A dip dewar version, QUANTUMCOOLER 4.2 (TM), was designed and built by Quantum Technology. After 2000 hours of test runs at liquid helium temperatures it was delivered to SFU's Low Temperature Lab and started on 16 May 1986. The liquifier has been running continuously ever since and has now logged over 3000 additional hours of continuous operation at liquid helium temperature without any sign of flow rate deterioration in the J-T loop. The dip dewar is used for resistivity and tunnelling measurements on thin film structures.

2. Principle of construction

One of the main features is the complete separation between the liquifier system and the accessible liquid helium space. The closed loop liquifier produces its own small quantity of liquid in a heat exchanger after the J-T expander. This liquid is not accessible, it is part of the closed loop. Instead of being surrounded by a vacuum, the liquifier sits in a specially designed well of a dewar which contains the actual accessible liquid helium bath. This liquid is obtained through condensation of helium gas in thermal contact with the closed loop liquifier. In this way, two important advantages are achieved. Small leaks in the liquifier are of no great concern, since it is surrounded by another helium space not a vacuum. This principle was already used to great advantage in the Collins liquifier. The accessible helium, being separate from the J-T loop, does not have to be particularly pure. Contaminations will freeze out in the dewar space and can simply be removed by turning the liquifier off, letting them evaporate.

The addition of a J-T loop to a G-M cryocooler to achieve operation at liquid helium temperature is not new. A large number of papers have been written on such systems [1][1]. The dewar construction is shown in figure 1. A prototype was already discussed in an earlier paper [2]. A similar dewar was independently proposed by Longsworth as a solution to the interfacing problem between refrigerators and cryostats [3].

The QUANTUMCOOLER (TM) design is compatible with almost any two-stage Gifford-McMahon refrigerator. A water cooled Air Products DISPLEX (TM) 202 was used in this model. The G-M refrigerator operates with an inlet pressure of 0.65 MPa (95 psia) and an outlet pressure of 2.2 MPa (320 psia). Gas returning from the J-T loop at a pressure between 0.005 and 0.2 MPa (0.7 and 30 psia) is compressed by a J-T compressor up to the inlet pressure of the G-M compressor. Thus the J-T and G-M compressors are in effect working in series to provide an overall compression ratio adjustable between 11 and 440. The schematic is shown in figure 2. The J-T loop, 'clog-proof' J-T expander, J-T compressor, helium purifiers and helium recovery compressor are Quantum Technology Corp. products.

3. Dewar

The dewar space consists of two interconnected spaces: the liquifier well and

---

[1] Numbers in brackets refer to the literature references listed at the end of this report.

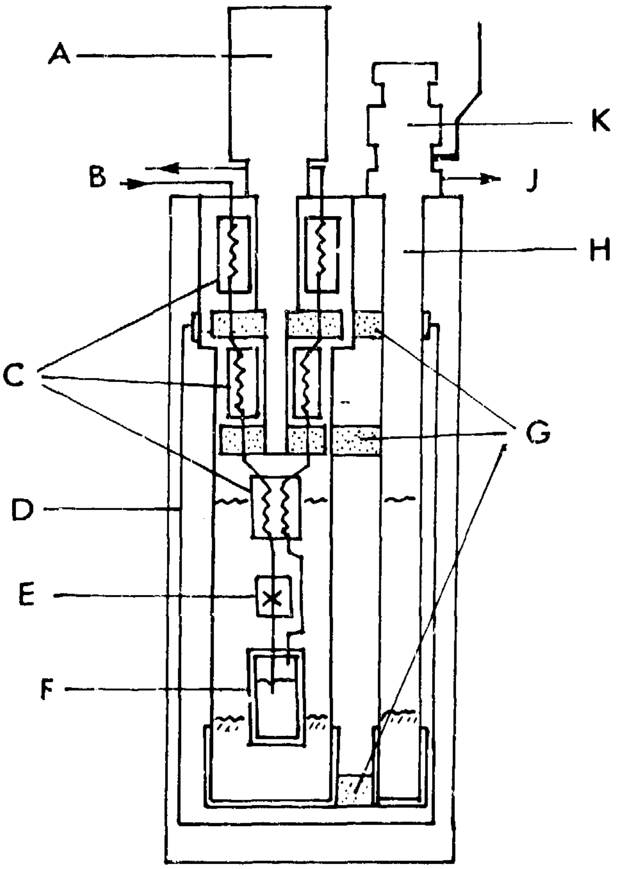

Figure 1 Schematic of dewar (not to scale)
A: G-M cryocooler. B: J-T loop. C: heat exchangers. D: heat shield. E: J-T valve.
F: condenser. G: thermal links. H: dip tube. J: recovery. K: ball valve.

the dip access tube. A special construction allows for efficient heat transfer between the 80 K and 15 K cold stages of the refrigerator and the dewar wall. The bottom of the dewar space is made entirely of copper. A heat shield anchored at 80 K and sheets of superinsulation are placed in the permanentely sealed vacuum space. Temperature monitors are attached to the various isothermal blocks. The dip tube with 7/8 inch clearance (22.2 mm) is closed at the top with a ball valve with a sliding O-ring seal above it. This gives easy access for the equipment being lowered into the helium bath.

The helium in the dewar space is part of a separate closed system. The pressure is usually maintained above atmospheric pressure to prevent accidental air contamination. The overpressure also assists in the condensation of the helium gas. A small helium recovery compressor stores the unused helium gas in a 115 liter tank rated at 1.2 MPa (175 psia). In this way 1/2 liter of liquid helium can be stored as gas and reused conveniently.

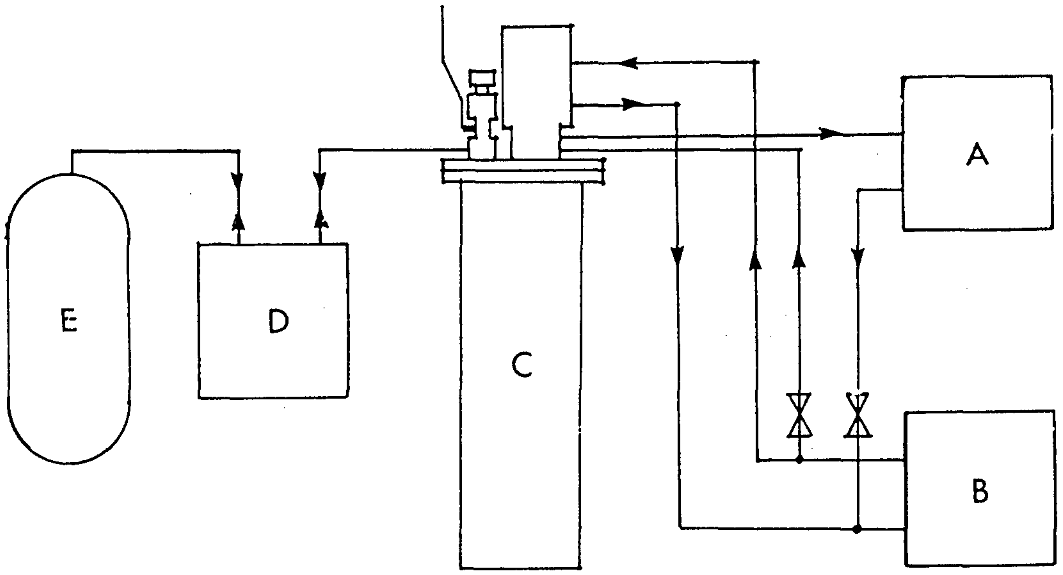

Figure 2 Schematic of gas flow
A: J-T compressor. B: G-M compressor. C: dewar. D: recovery compressor. E: storage.

4. Compressors

The G-M compressor from Air Products was not modified. The Quantum Technology J-T and the recovery compressors are based on hermetically sealed oil lubricated units chosen for their reliability and proven performance. Helium places heavy demands on any compressor due to the large temperature rise during compression. Effective cooling is important for compressor reliability as well as for preventing cracking of the lubricant and contamination of the helium gas. Special cooling and filtration was used in our units. The compressors are protected against lubrication failure, cooling failure or electrical overload by automatic power cutout devices. The total power consumption of the compressors is 2 kW. The J-T compressor is equipped with digital readouts to monitor the J-T loop flow and the return gas pressure.

5. Helium purity

The dip tube space is tolerant of relatively impure helium. Over one liter of air as impurity is required before mechanical blockage can occur. Thus the helium in this space must be maintained at 99.9% pure or better. The published helium purity requirements for the G-M cryocooler is only 99.995%. This is because G-M cryocoolers are relatively insensitive to impurities until a sufficient accumulation of solid contamination causes an increase in the friction of the sliding displacer.

J-T coolers are much more demanding. The vapor pressure of solid air at 4 K is well below 10^{-11} Pa (10^{-16} atm). This means that any contaminants in the system will eventually accumulate at the low temperature end. Furthermore, the conventional J-T valve has such a tiny orifice that it is easily plugged. In a recent paper, Lester and Benedict [4] estimate that the volume of solid required to plug a conventional J-T valve is about 10^{-6} cm^3. If the impurity is a frozen gas this corresponds to about 10^{-3} standard cm^3 of gas. Assuming a gas charge of 10^5 standard cm^3, the system must initially be charged with helium of a purity of 99.999 999% (8 nines). The impurities are then soon trapped at the cold end. However, if the cryocooler is to operate, as ours has, for 5000 hours with a flow rate of 100 standard cm^3/sec a total of 10^9 standard cm^3 of gas has gone through the J-T loop. This would require that, in operation, the gas entering the J-T loop would have to be better than 99.999 999 999 9% (12 nines) pure. As Lester and Benedict point out this is impractical because outgassing from surfaces alone produces more impurities. In practice, a J-T cooler of that type will only operate for a few minutes before plugging, not for 5000 hours.

We have devoted several years of research to this problem. Our solution is a combination of careful purification of the helium when charging the system, the use of room temperature and cold filters to remove impurities in the gas as well as a proprietary 'clog-proof' Joule-Thomson valve.

One major problem encountered during the research was the lack of instrumentation which could measure suitably small impurity levels in helium. This meant that every time we wanted to test the helium purity the cryocooler had to be operated for days or weeks, while carefully monitoring the flow to see if it dropped. To overcome this problem, Quantum Technology developed an instrument, the QUANTUMDETECT (TM), to quickly detect and measure the amount of impurity in a helium gas flow. It operates by freezing out impurities at a low temperature. The sensor is mounted on a dip tube suitable for use in the QUANTUMCOOLER or in a dewar of liquid helium. The full scale reading is 30 milligrams of impurity and the sensitivity is 3 milligrams. This instrument enabled us to measure and identify (by their sublimation temperatures) impurities in our system. This was an important aid in the development of the purification system and in reliability testing of the cryocooler.

A specially designed liquid nitrogen cooled helium purifier, the QUANTUMPURE (TM), is used when charging the cryocooler with readily available 99.999% ultra high purity helium. This is the only time when liquid nitrogen is required.

Tests of the 'clog-proof' J-T valve under simulated conditions clearly demonstrate that it will not clog. Naturally, once sufficient impurities freeze in the J-T loop the loop will become plugged. However, the plug does not occur in the J-T valve and its formation requires many orders of magnitude more contaminants than for a conventional J-T valve. Hence the name 'clog-proof' valve.

Carefully designed cold filters and heat exchangers trap impurities which enter the J-T loop in operation. During reliability testing, we deliberately introduced measured volumes of air into the J-T loop. We found that 100 standard cm^3 caused a noticable decrease in the flow through the J-T loop, but did not plug it. This is 100,000 times more impurities than the estimate by Lester and Benedict for a conventional J-T valve (without filtration). We can estimate the purity of the gas entering our J-T loop in operation as follows. Since no decrease in flow occurred during 3000 hours of operation, which forced 10^9 standard cm^3 of helium through the J-T loop, less than 100 cm^3 of impurities could have accumulated. Thus the purity of helium at the room temperature entrance to the J-T loop must exceed 99.999 99% (7 nines) when the system is in operation.

6. Operation

6.1 Start-up

The Quantumcooler 4.2 is very easy to operate. Cooldown is achieved by turning on the power switches on the G-M, J-T and recovery control units. No attention is required during cooldown, in operation or during warmup. Power failures can do no harm. The cooldown times are as follows: 17 hours from room temperature to 15 K and 2 hours from 15 K (G-M compressor running) to 4.3 K. The relatively long initial cooldown is due to the somewhat poor thermal contact between heat shield and 80 K stage and could easily be improved.

6.2 Temperature control and stability

The equilibrium temperature of the dip dewar is determined by the pressure at the outlet of the J-T expander. Since both liquid and gaseous helium are present, the temperature is determined by the vapor pressure of helium. The pressure at the room temperature end of the J-T gas return line is adjustable by means of a regulator on the J-T compressor. This allows the operator to vary the equilibrium temperature between the critical point of helium (5.2 K) and the lowest temperature for continuous operation (2.7 K). The lower temperature limit is determined by limitations of the J-T compressor. There is a small pressure difference between the J-T expander and the J-T compressor, due to the pressure drop in the heat exchangers. This has only a small effect (a few tenths of a degree) on the equilibrium temperature.

The pressure in the dip dewar space is independently controllable by the operator. Normally it is set to a pressure above the J-T return pressure to allow a pool of helium to be liquified. During the liquifaction process the temperature of the liquid is determined by the pressure of the gas in the dip tube space. However, once the equilibrium liquid level is reached, only a thin layer of liquid at the top is at that temperature. The remainder is cooled to a colder temperature determined by the J-T return pressure. This stratification of the liquid helium is stable due to the low thermal conductivity and rapid variation of the density of the liquid with temperature. We do, in fact, routinely maintain a bath temperature of 2.7 K at a pressure of 0.13 MPa (19 psia). Only a thin layer at the top of the bath is at 4.5 K which is the boiling point at that pressure.

The temperature stability in the liquid bath is excellent. The thermal time constant is several hours due to the high specific heat of liquid helium. This completely damps out any possible short term temperature fluctuations. Long term temperature fluctuations are only about 0.03 K in 1000 hours without any electronic regulation.

The 1/2 liter pool of liquid helium may be intentionally boiled for two purposes. In one case the G-M and J-T systems are switched off and helium is allowed to boil off and is returned (via the helium recovery compressor) to the recovery tank. This allows over four hours of operation at liquid helium temperature without any mechanical noise or vibration. In the second case, a reduced pressure is applied to the dip tube space to achieve lower temperatures. Using the QUANTUMCOOLER (TM) recovery compressor a temperature as low as 2.2 K can be reached. The limit is given by the fixed compression ratio of the recovery compressor. Using an external vacuum pump temperatures far below 2 K can be maintained for three hours before all the helium is boiled off. The temperature distribution is now very homogeneous. The only disadvantage is the loss of protection against accidental air intake into the dip dewar space inherent in all pumped liquid helium reservoirs.

6.3 Cooling power

The cooling power of the QUANTUMCOOLER (TM) is nominally 1/4 watt at liquid helium temperature. Naturally, the exact cooling power depends on the flow through the J-T circuit and the temperature of operation. As can be seen from figure 3 the temperature of operation remains relatively constant independent of the heat applied until a limit is reached. This is when the applied heat exceeds the cooling power and the J-T loop starts to warm up. The warming in the J-T loop causes a decrease in gas density which causes a decrease in flow rate which causes a decrease in cooling power. This positive feedback results in a sharp rise in temperature and hysteresis in the temperature-heat curves. When operation at the lowest possible temperature is desired the flow through the J-T loop (and hence the cooling power) is deliberately decreased because of the limited capacity of the J-T compressor.

The bath of liquid helium makes these temperature-heat curves difficult to measure because the bath can support large heat loads for hours simply by boiling off some helium. The rate of boiling is determined by the difference between the applied heat and the cooling power. As a result it takes hours or days to reach equilibrium when the applied heat is close to the cooling power.

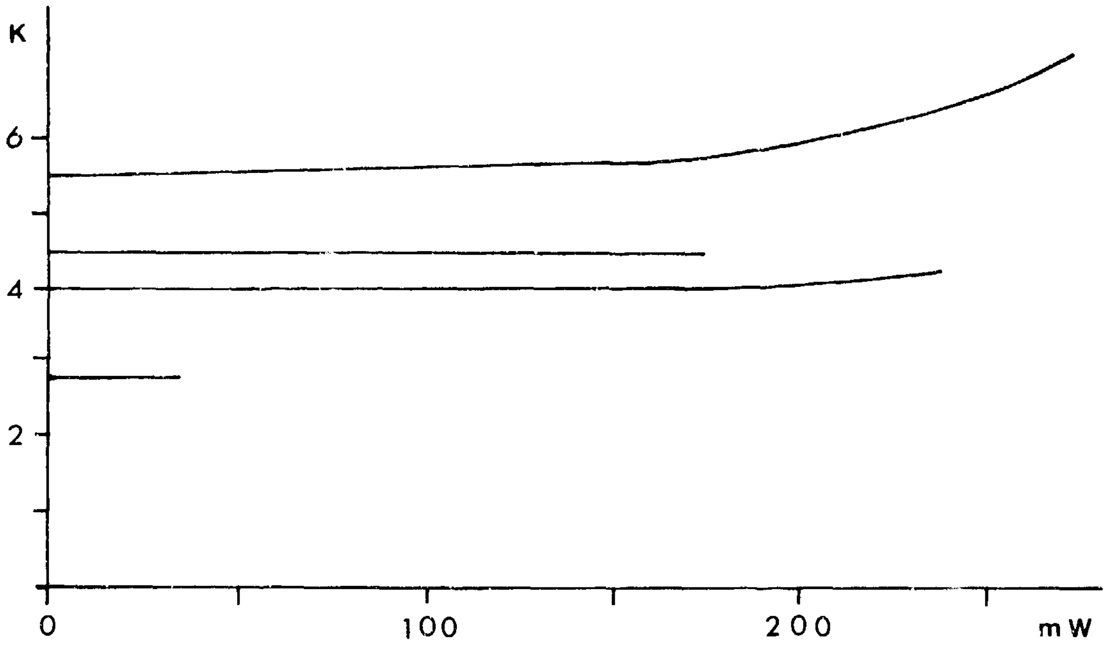

Figure 3 Cooling power for different settings of flow rate and back pressure

6.4 Dip tube access

Gaining access to the liquid helium bath is straightforward. The only precaution one has to take is to make sure that no large quantities of air are introduced into the dip dewar. Maintaining positive pressure in the dewar space, at least while the access valve is open, is essential. As a safety feature, a combination of timer and pressure sensor will turn off the G-M and J-T compressors if the valve has been left open to the atmosphere too long.

The equipment to be introduced into the helium bath must not evaporate all the helium. Very light objects can be inserted and dipped into the liquid helium bath immediately, cooling from room temperature to 4.2 K in a few seconds. With heavy objects, it is prudent to hold them at the 70 K stage for precooling because the 5 W cooling power available there can remove most of the heat content without needlessly boiling off any liquid helium.

7. Conclusions

The closed-cycle liquid helium dip cryocooler presented here has been in operation for over 5000 hours and is still running. In normal operation only two controls are used. One determines the return pressure in the J-T loop and hence the temperature. The other controls the flow rate in the J-T loop and hence the cooling power. No adjustments are required during cooldown or warmup. Careful attention to the design and fabrication have resulted in a reliable trouble-free cryocooler system. The long running time is attributed to the special purification and filtration of the helium as well as to the novel 'clog-proof' J-T valve.

We are grateful for the valuable advice from Ken Myrtle and the technical help and ingenuity of Russel Barton. Financial support by the Science Council of British Columbia as well as NSERC is gratefully acknowledged. DISPLEX is a trademark of Air Products and Chemicals Inc. QUANTUMCOOLER, QUANTUMPURE and QUANTUMDETECT are trademarks of Quantum Technology Corp.

8. References

[1] see: Cryocooler Conferences, U.S. Dept. of Commerce, NBS Special Publications #508 (1978), #607 (1981) and #698 (1984). A good source is also the series: Advances in Cryogenic Engineering (Plenum Press).

[2] Gygax, S., Cheap helium liquifiers, Physica 126B, 134-137 (1984)

[3] Longsworth, R. C., Interfacing small closed-cycle refrigerators to liquid helium cryostats, Cryogenics 24, 175-178 (1984).

[4] Lester, J. M., and Benedict, B., Joule-Thomson valves for long term service in space cryocoolers, Proc. Third Cryocooler Conf., NBS Special Publication #698, 257-266 (1984).

Preceding Page Blank

RECONDENSING REFRIGERATOR FOR SUPERCONDUCTING NMR-CT

T. Koizumi, K. Kuroki, Y. Tomita,
Y. Kanazawa, and M. Suzuki

Cryogenic Design Section
Precision Products Group
Sumitomo Heavy Industries, Ltd.
Tanashi-City, Tokyo 188, Japan

This paper mainly describes a compact closed-cycle helium refrigerator (3.5W at 4.3K) and a recondensing system using the refrigerator of the evaporated helium gas of superconducting NMR-CT at Medical Center of Chiba University in Japan. The cycle of this refrigerator consists of a two-stage Sumitomo's modified Gifford-McMahon cycle refrigerator and a Joule-Thomson loop. For the recondensing system, direct-mounted-type refrigerator unit has been selected. After removal of magnet current lead from S.C.M. cryostat of the NMR-CT, the recondenser connected to the end of transfer tube of the refrigerator unit is inserted through the magnet current lead entry. The refrigerator provides its helium mist coolant to the recondenser located in the gas phase of the liquid helium vessel of the S.C.M. cryostat and refrigerator's helium mist coolant in the recondenser suppreses gas phase pressure inside the liquid helium vessel. It indicates recondensation of evaporated helium gas inside the liquid helium vessel.

Now we have been successfully accumulating running data of this recondensing system and no electromagnetic brake against the refrigerator operation from the S.C.M. cryostat has been observed and also no NMR image distortion has been caused by the refrigerator operating near the S.C.M. cryostat.

Key words: Compact heat exchanger; cryogenic refrigerator; helium recondenser; NMR-CT; superconducting magnet

1. Introduction

Nuclear magnetic resonance (NMR) has now become an exceptionally powerful investigative technique in the life science and the material science. In the field of medicine, NMR-CT is used especially for imaging of humans to examine medical diagnosis.

All NMR use magnets, while a few instruments use permanent magnets and electromagnets, most instruments use superconducting magnets because the large bore high field, high homogeneity, and high stability are required to the magnets. It promises to provide the first large scale commercial market for cryogenic component because as the key component of S.C.M. NMR-CT, the superconducting magnet is essentially needed. To maintain the superconducting magnet in NMR-CT at liquid helium temperature, liquid helium of 0.4 l/h and liquid nitrogen of 1.0 l/h are usually consumed (1)[1], so such cryogen transfer is needed at regular intervals.

We have developed a recondensing refrigerator system of the evaporated helium gas of the S.C.M. NMR-CT. Without liquid helium refill, the system has made it possible to operate S.C.M. NMR-CT continuously. This paper mainly describes the results of the performance of the recondensing refrigerator system.

2. Recondensing system

There are some practical cryogenic refrigeration system for S.C.M. NMR-CT. The S.C.M. cryostat in which the radiation shields are cooled by axillary refrigertors such as two stage G-M refrigerator, can do away with the need for liquid nitrogen and can reduce liquid helium consumption to less than half but not to zero.

Our purpose is to provide a refrigeration system to need not refill liquid helium by recondensing the evaporating helium gas within the cryostat.

3. Layout of system design

Layout of the refrigeration system for the S.C.M. NMR-CT is shown in fig. 1. The refrigeration system consists of refrigerator unit, compressor unit and gas helium line.

The refrigerator unit has the transfer tube and the recondenser is connected to the end of transfer tube. Also, this refrigerator unit is suspended from the ceiling with the lift and can be moved up and down using the lift.

The compressor unit is installed in adjacent room and combined to the refrigerator unit with the interconnecting gas helium line. The refrigerator unit on the lift is moved to just above the S.C.M. cryostat. And after removal of magnet current lead, this refrigerator unit is precisely moved down with the lift. The recondenser is inserted through the magnet current lead entry and located in the gas phase of the liquid helium vessel of the S.C.M. cryostat.

[1] Numbers in brackets refer to the literature references listed at the end of this report.

4. Compact helium refrigerator

Flow diagram of compact helium refrigerator for the S.C.M. NMR-CT is shown in fig. 2. The refrigerator unit is the combination of a two stage Sumitomo's Gifford-McMahon cycle refrigerator and a Joule-Thomson loop. This Sumitomo's Gifford-McMahon refrigerator is the modification of so called Gifford-McMahon refrigerator. Sumitomo's Gifford-McMahon refrigerator (SRD-208) have been widely used as a cryopump refrigerator.

The Sumitomo's SRD-208 has a hybrid mechanism of displacer by simultaneous use of drive motor and highpressure helium gas, and meets such a requirement of a small, compact, noiseless and reliable refrigerator.

The Joule-Thomson loop itself consists of three heat exchangers and Joule-Thomson valve. The heat exchangers are laminated metal-plastics heat exchangers (2) of light weight and high efficiency, developed for the on-board refrigerators in Japanese National Railways Superconducting Magnetic Levitated Train Project.

The recondenser is a vertical condenser type where condensation takes place on the outer surface. To enhance condensation heat transfer surface, a vertical shallow-fluted tube is used.

The compressor unit is constructed with two hermetic type compressors, oil separator, adsorber, storage tank, and control safety devices.

Capacity of the refrigerator is 3.5W at 4.3K and electrical power is about 7.5KW. Noise level of refrigerator unit and compressor unit are about 51(dB) and 54(dB), respectively. A photograph of the refrigerator is shown in fig. 3.

5. Preliminary test

Preliminary tests conducted are as follows;

(a) Refrigerator reliability test
(b) Recondensing test
(c) Refrigerator operation test under magnetic field
(d) Influence of refrigerator to S.C.M. NMR-CT image

Test results are mentioned briefly.

(a) Refrigerator reliability test

We have already developed several prototype refrigerators of 3.5W at 4.3K refrigeration capacity and we have been running these refrigerators more than 15000 hours successfully ever since.

(b) Recondensing test

Fig. 4 shows the recondensing test apparatus. In this test, heat load is given by electric heater immersed into the liquid helium. Test results are shown in fig. 5 and fig. 6. Fig. 5 shows the relation between equilibrium pressure versus heater input. In this test, the distance between recondenser and liquid helium level is kept constant, 100mm, and only J-T flow is changed as a parameter.

Fig. 6 shows test results at constant J-T flow rate. Parameter is only distance of recondenser and liquid helium level. The higher the distance is, the higher equilibrium pressure of the vessel is observed. This means slight liquid helium temperature rise in this vessel.

(c) Refrigerator operation test under magnetic field

By assuming that only motor of the refrigerator will be affected by magnetic field, we have tested magnetic effect to the refrigerator, and it is confirmed it can be operated until 1000 gauss.

(d) Influence of refrigerator to NMR-CT image

We have measured phantom image distortion according to the change of location of the refrigerator. The results are as follows;

When this refrigerator is located at 30 gauss line, no image distortion is observed. But at 100 gauss line, a slight distortion is observed, so at 100 gauss line location, shimming procedure of S.C.M. cryostat is to be needed.

6. Installation and performance

We installed the compact helium refrigerator to the S.C.M. NMR-CT at Medical Center of Chiba University in March, 1986. Fig. 7 is a photograph of the recondensing system of the S.C.M. NMR-CT at Chiba University. The relation of the liquid helium level and the pressure of liquid helium vessel and the running time is shown in fig. 8. After this initial running, the gas helium vent line of the S.C.M. cryostat was closed. the pressure of the vessel began to rise. After a few days, we have controlled the J-T valve in order to adjust operation condition. Finally we have established stable operating condition. However long large slow variation of equilibrium pressure (0.110-0.114MPa) will be observed. We think this variation will be caused by several conditions, such as environmental and other unknown conditions. Also fig. 8 shows that the liquid helium level was almost kept constant, that means helium loss became zero.

7. Conclusions

The recondensing system of evaporated helium gas has made it possible to operate the S.C.M. NMR-CT without the liquid helium refill. The electromagnetic effect of the magnetic fields of S.C.M. cryostat to the refrigerator operation has not been observed and also NMR-image distortion to be induced by refrigerator operation has not been observed owing to shimming procedure. During operation, there were no indications of contaminant freeze out in this refrigerator system. This successful operation data and performance of the recondensing refrigerator has been confirmed its versatile adaptability to S.C.M. NMR-CT system.

The authors are greatly indebted to Professors N. Arimizu and S. Uematsu for giving us a chance of this experiment and variable instruction. Also the authors wish to express their thanks to Picker International, T.F.P. (Toray-Fuji-Picker International Inc.) for their cooperation and Oxford Magnetic Instrument, F.O.T. (Furukawa Oxford Technology Ltd.) for their kind advice and technical assistance.

8. References

(1) Larbalestier, D., Fisk, G., Montgomery, B., and Hawksworth, D., High-field superconductivity, Physics Today, March, 24-33 (1986).

(2) Koizumi, T., et al., A small and light weight heat exchanger for on-board helium refrigerator, NASA Conference Publication 2287, 179-188 (1983).

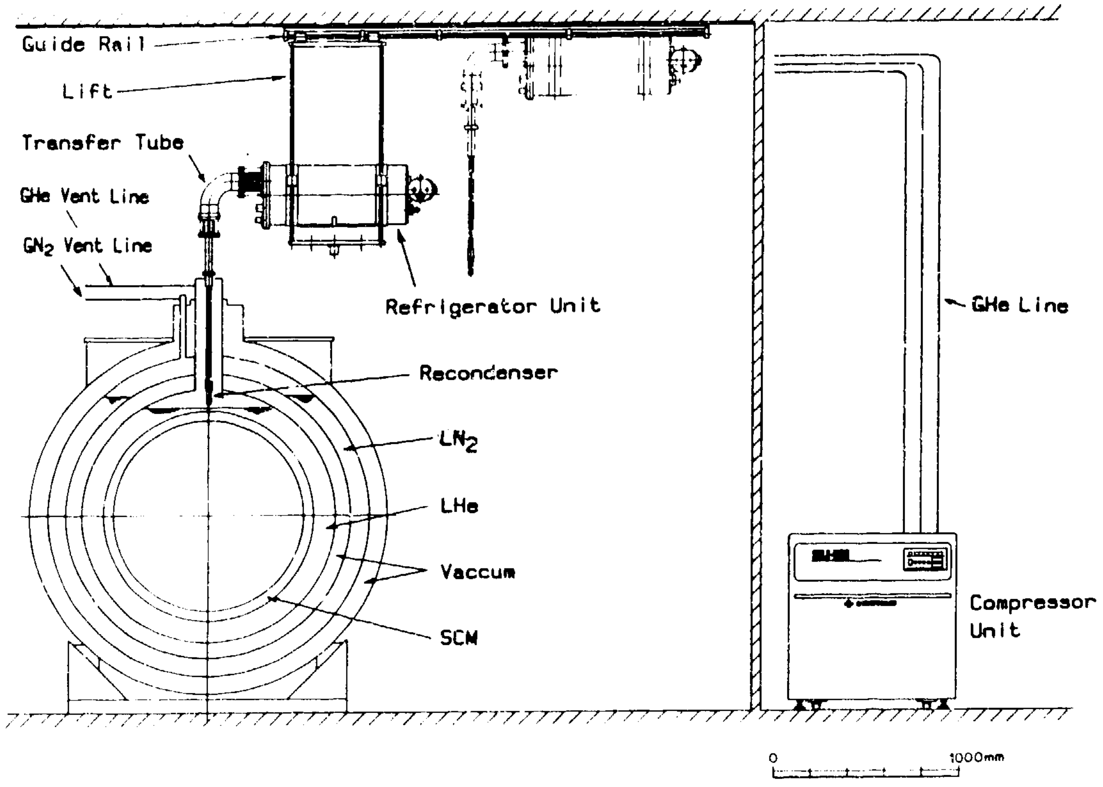
Guide Rail
Lift
Transfer Tube
GHe Vent Line
GN$_2$ Vent Line
Refrigerator Unit
GHe Line
Recondenser
LN$_2$
LHe
Vaccum
SCM
Compressor Unit
0
1000mm

Fig. 1 Layout of compact helium refrigerator for superconducting NMR-CT

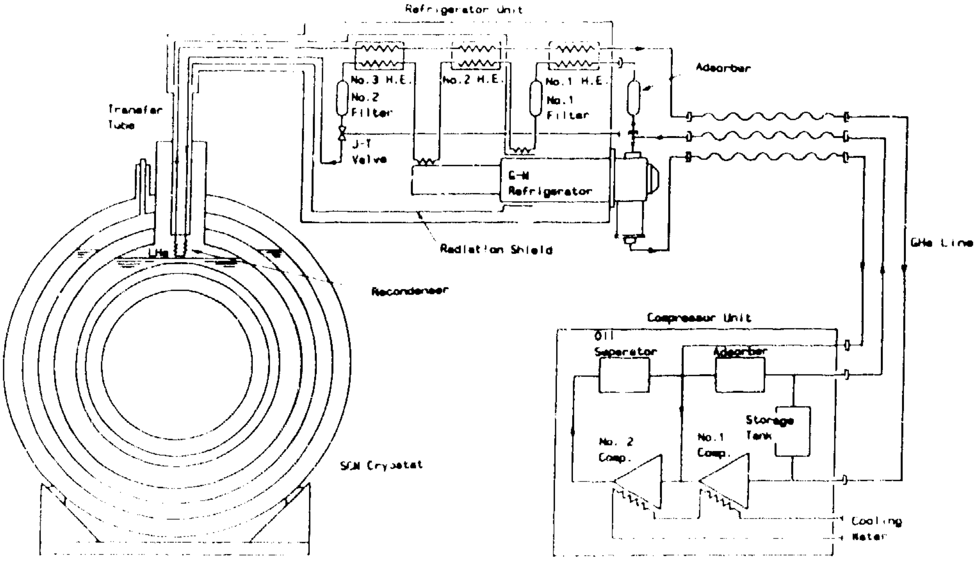
Refrigerator Unit
Transfer Tube
No.3 H.E.
No.2 Filter
J-T Valve
No.2 H.E.
No.1 H.E.
No.1 Filter
Adsorber
G-M Refrigerator
Radiation Shield
LHe
Recondenser
GHe Line
Compressor Unit
Oil Separator
Adsorber
Storage Tank
No. 2 Comp.
No. 1 Comp.
SCM Cryostat
Cooling Water

Fig. 2 Flow diagram of compact helium refrigerator for superconducting NMR-CT

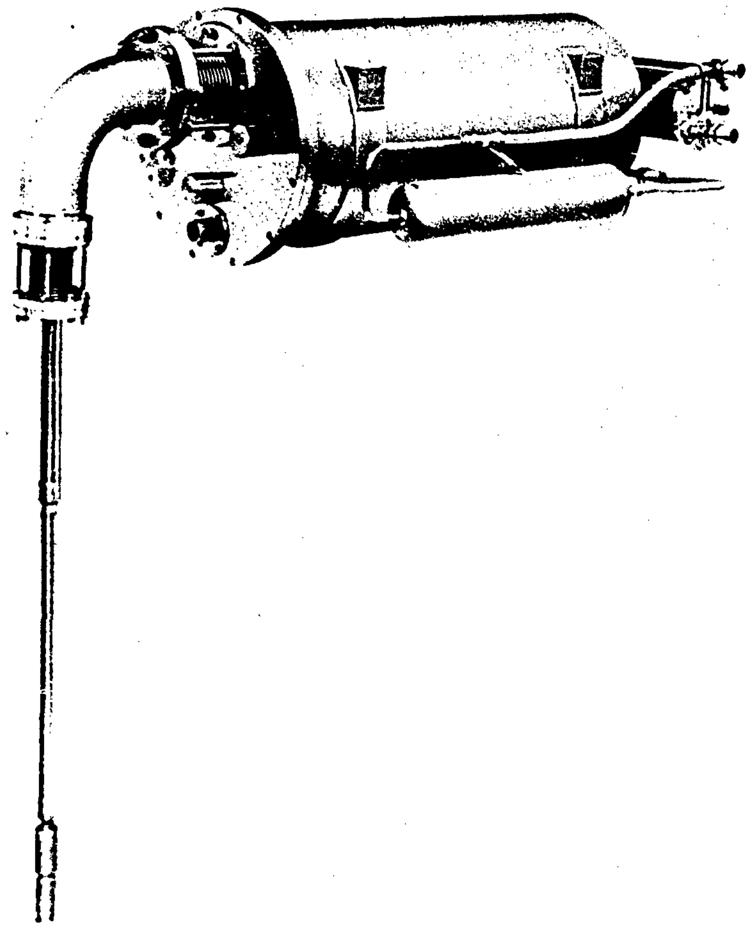

Fig. 3 The recondensing refrigerator

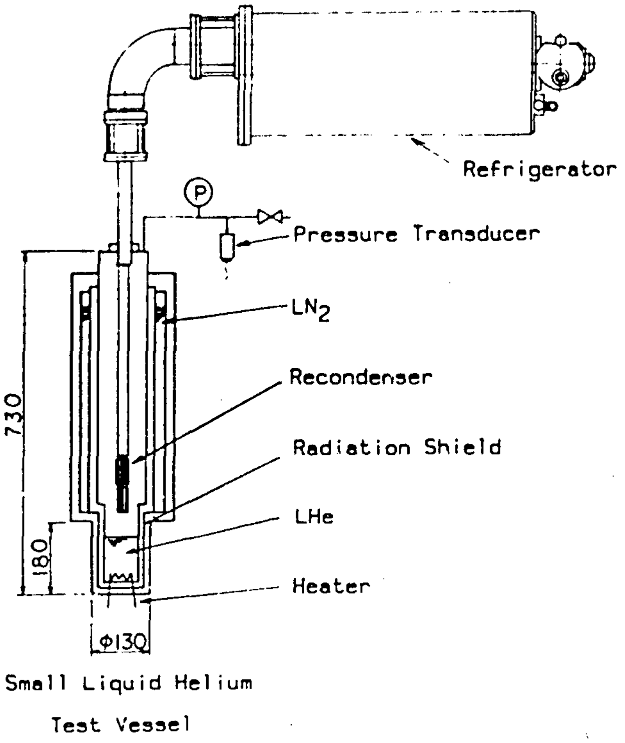
Refrigerator
P
Pressure Transducer
LN$_2$
Recondenser
Radiation Shield
LHe
Heater
730
180
Φ130
Small Liquid Helium
Test Vessel

Fig. 4 Apparatus of recondensig test

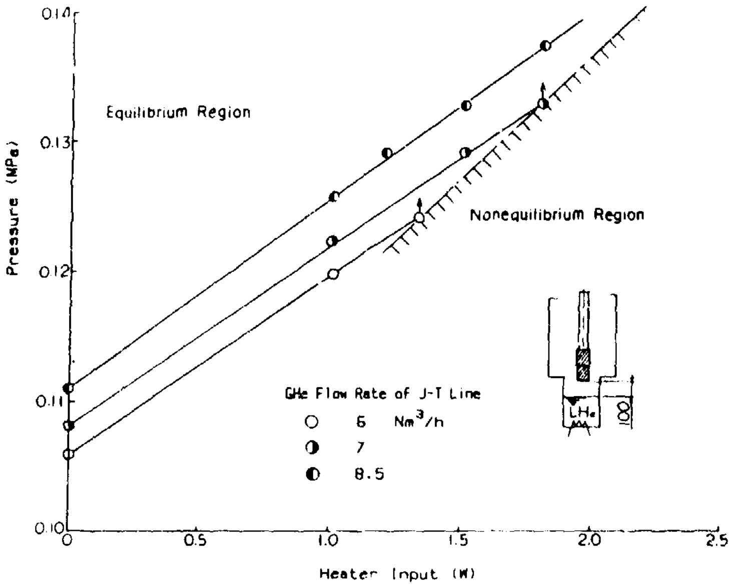

Fig. 5 Pressure versus heater input (1)

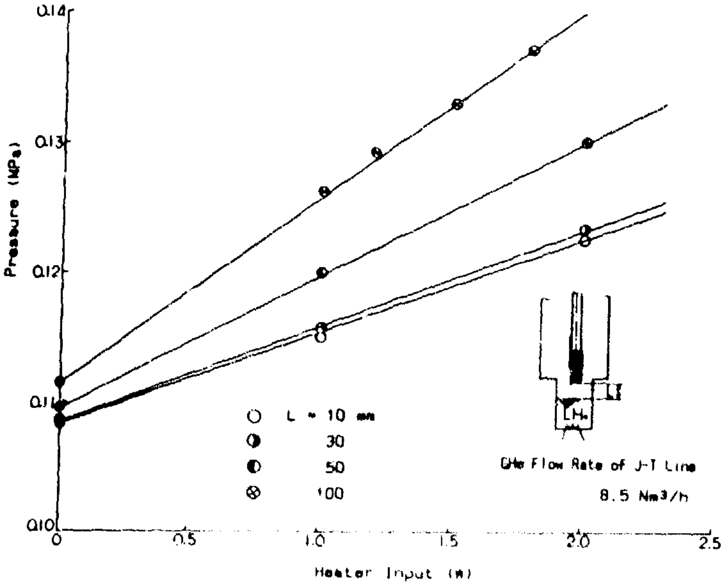

Fig. 6 Pressure versus heater input (2)

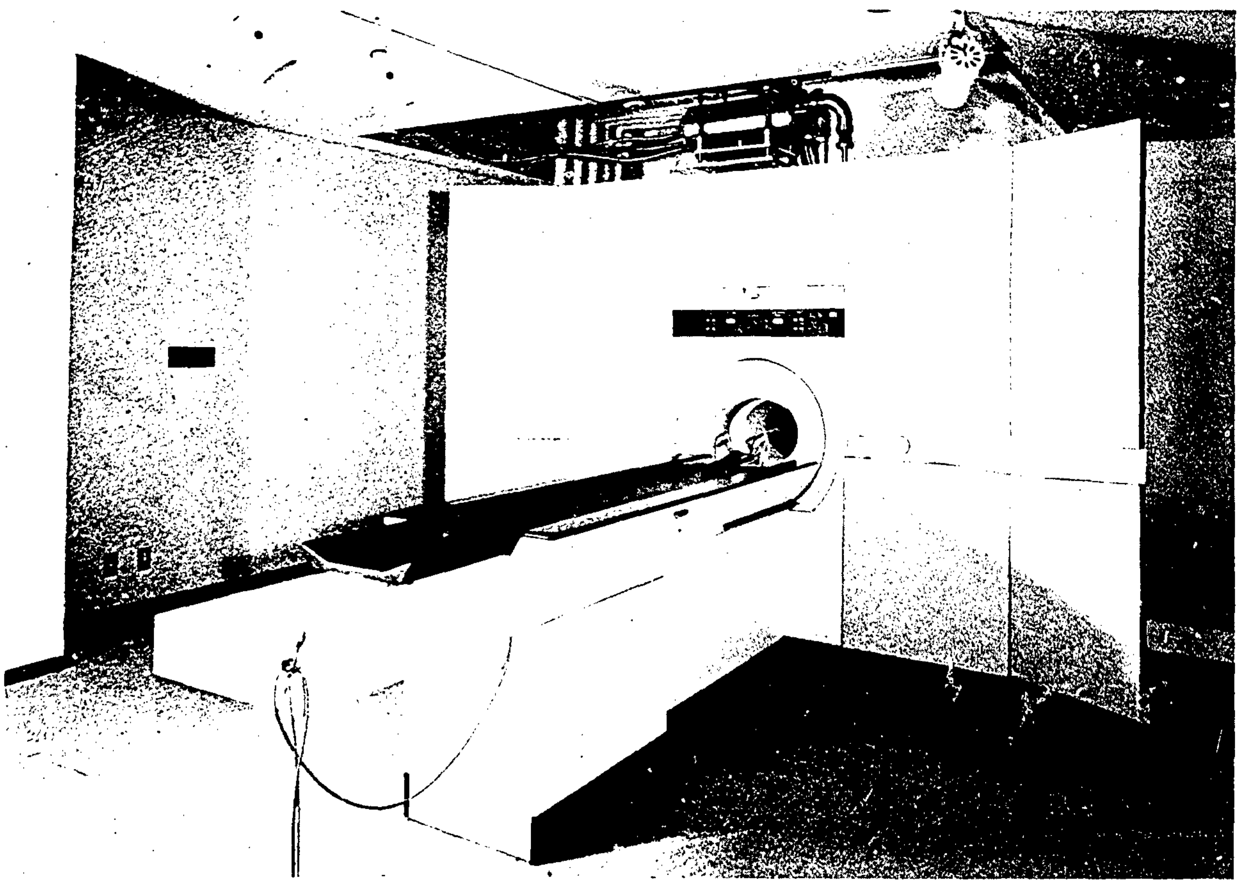

Fig. 7 The recondensing refrigerator system of the S.C.M. NMR-CT

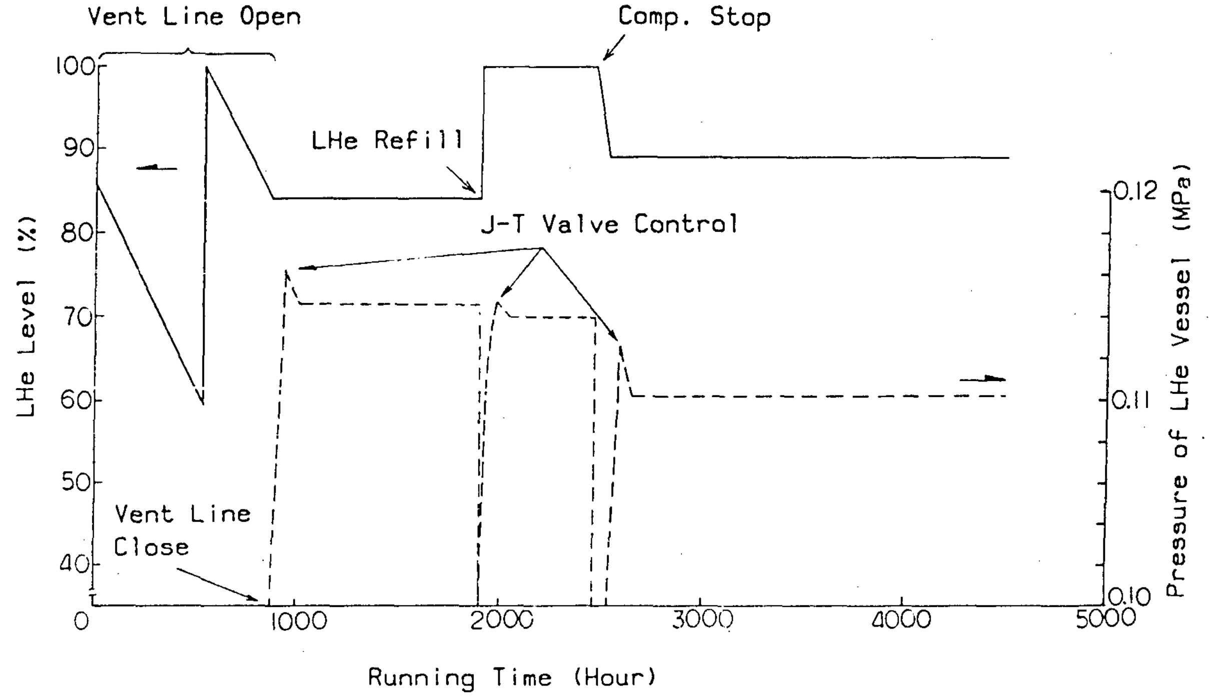

Fig. 8 Performances of compact helium refrigerator installed superconducting NMR-CT

Preceding Page Blank

THE DESIGN, FABRICATION, AND TESTING OF A NOVEL TITANIUM-ALUMINUM HEAT EXCHANGER

R.C. Sweet and R.L. Bronnes

PHILIPS LABORATORIES
North American Philips Corporation
Briarcliff Manor, New York 10510

Special techniques for constructing a novel titanium-aluminum heat exchanger for use as the expansion chamber in a Stirling cycle cryogenic refrigerator are described. The relatively high thermal conductivity of aluminum, the poor conductivity and high strength of titanium, and the light weight features of both materials are used to advantage in a unique heat exchanger configuration. To retain the helium working gas, the titanium-aluminum surfaces have to be hermetically sealed, and the structure has to withstand a large number of temperature cycles. Since both metals are highly reactive, conventional sealing techniques (brazing) tend to load the joint interface with undesirable constituents. To attain the required hermeticity, a novel assembly technique was therefore developed, whereby the aluminum component is vacuum melted within a titanium receptacle. The fabrication of a particular heat exchanger configuration, as well as test results on the structure and on the aluminum-titanium interface are presented.

Key words: Aluminum-Titanium joining, Cryogenic heat exchangers, Stirling-cycle refrigerator exchanger components. Testing aluminum-Titanium joints.

1. *Introduction*

In order to reduce the weight of a Stirling cycle cryogenic refrigerator and to improve the vibration characteristics of its cold end (or expansion chamber), a novel cold-side heat exchanger was developed. The new design utilizes the high thermal conductivity of aluminum, and the comparatively low thermal conductivity and high mechanical strength of titanium. To meet design and performance specifications, especially the need to retain the helium working gas, the aluminum had to be hermetically bonded to the titanium [1][1]. Following its fabrication, the heat exchanger is tungsten inert gas (TIG) welded to the mating portion of the refrigerator, which contains helium at a pressure as high as 1000 psi. The heat exchanger, a prototype of which is shown in Fig. 1, must survive temperature cycling between 292°K and 77°K without failure.

It would not be possible to construct a hermetic and structurally sound heat exchanger if aluminum had to be joined to titanium by any of the conventional joining methods. A major difficulty in selecting any such method is that the coefficient of thermal expansion (or contraction) of aluminum is approximately twice that of titanium. Welding aluminum to titanium is not feasible, and the use of mechanical fasteners is technologically unacceptable.

We solved the problem of joining these highly reactive metals by vacuum melting aluminum in titanium cups to form composite structures. These structures were then sectioned and machined into heat exchangers. Since the pressure vessel of the refrigerator, i.e. the part mating with the heat exchanger, was made of the Ti-5Al-2.5Sn alloy, the cups were made of the same alloy to simplify the TIG welding during final assembly. For the aluminum part of the exchanger we selected 1100 alloy, because it is a good heat conductor is low in contaminants and it is readily available. The melting was done in a vacuum environment in order to minimize oxidation of these highly reactive metals. The cups were 6.4 cm high, 4.06 cm in diameter with a 3.2 mm thick wall section, and weighed approximately 105 grams. The bottoms of the cups were made from 0.81 mm thick sheet which were TIG welded to the wall section. The closely fitting aluminum inserts measured 5.4 cm high and 3.42 cm in diameter, and weighted approximately 134 grams.

The cups and inserts were chemically cleaned to remove surface contaminants which could prevent the aluminum from wetting and bonding to the titanium. The parts were assembled and heated in a vacuum furnace (10^{-6} Torr indicated pressure) for 12 minutes at 958°K to melt the aluminum. Directional solidification from the bottom, upward, was used to confine final shrinkage cavities to the top portion of the aluminum. A cup, an insert, and a composite structure are shown in Fig. 2. The work-up of the final structure provided that the porous tops of the composite structures were discarded, and the dense lower portions were machined into heat exchangers.

A final step in the developmental program was to automatically cycle the heat exchangers between 292°K and 77°K while maintaining 6.9 MPa of helium to test the bond strength of the titanium-aluminum interface as well as the reliability of the titanium-to-titanium TIG weld. Each cycle required 26 minutes, during which time temperatures and pressures were continuously monitored and recorded. Heat exchangers tested in this manner for as many as 5000 cycles did not fail.

---

[1] Numbers in brackets refer to the literature references listed at the end of this report.

Optical metallography was selected as the principal method of examining the critical aluminum-titanium interface for voids which would impede the required heat transfer, and for excessive amounts of the brittle titanium-aluminum intermetallic compounds which would weaken the bond.

2. *Sample Preparation*

Two longitudinal cuts, 90 degrees apart, were made on each of the composite structures by means of a water-cooled cut-off wheel to provide the maximum length of the titanium-aluminum interface for examination, Fig. 3. Each quarter section was then cut into three metallographic samples by means of a Buehler ISOMET diamond saw. The metallographic samples were mounted in plastic to facilitate handling during surface preparation.

Although the conventional etching reagents worked well on the polished aluminum and titanium surfaces, the interfaces were difficult to etch. However, we did obtain good results when the polished surfaces were swab-etched with 0.25 volume percent aqueous hydrofluoric acid for several seconds.

3. *Results and Discussion*

The first part of the metallographic examination was to determine whether the aluminum wet and bonded to the titanium over the entire contact surface to achieve the required hermeticity. Since we did not find any voids in the aluminum-titanium interface, it was evident that the chemical etching step removed surface contaminants, the vacuum environment in the furnace prevented oxidation during the heating cycle, and that the aluminum wet and bonded to the titanium.

The second part of the examination was to determine the quality of the bond between the two metals. Molten aluminum will alloy with the surface of the titanium, forming a layer of hard, brittle, intermetallic compounds [2]. Since the thermal expansion/contraction coefficient of aluminum is about twice that of titanium, the interface would be highly stressed as the assembly cools and the aluminum contracts. The titanium-aluminum interface is representatively shown in Fig. 4 and 5. There is no evidence of separation, nor is there an excessive amount of intermetallic compound. The most striking illustration of the strength of the bond between the two metals is shown in Fig. 6. The two arrows indicate cracks which developed in the 0.032 inch thick base as the aluminum contracted during cooling. There was no evidence that the aluminum separated form the titanium even though the deflection measured 1.5 mm. The dark line between the aluminum and titanium is an artifact caused by the different polishing rates of the two metals. The aluminum-iron-silicon impurities are visible in the aluminum matrix.

The third part of the metallographic study was to examine the microstructure of the aluminum-titanium interface for incipient damage after 5000 cycles between 292°K and 77°K. We could not find any damage in the interface, nor could we find any difference from the microstructure shown in Fig. 4 and 5.

4. *Summary*

We have described a novel method for vacuum melting aluminum in titanium cups to form composite structures which have a minimal thickness of the brittle intermetallic compounds in the interface. We have shown that these structures can be machined into heat exchangers which when pressurized with 6.9 MPa or more of helium, will withstand better than 5000 cycles between 292°K and 77°K with no evidence of failure. The technique is being used to prepare heat exchangers for use in a new design of Stirling refrigerator.

5. *Acknowledgement*

The authors acknowledge the technical contributions of M. Cobb, R. Eggleston, J. McKinlay.

6. *References*

[1] Meehan, H., Sweet, R., Novel Titanium-Aluminum Joints for Cryogenic Cold Finger Structures. Cryogenic Engineering Conference, Aug. 1981, San Diego, CA.

[2] Hansen, M., Constitution of Binary Alloys, 139 (McGraw-Hill Books Co., Inc., New York, N.Y., 1958).

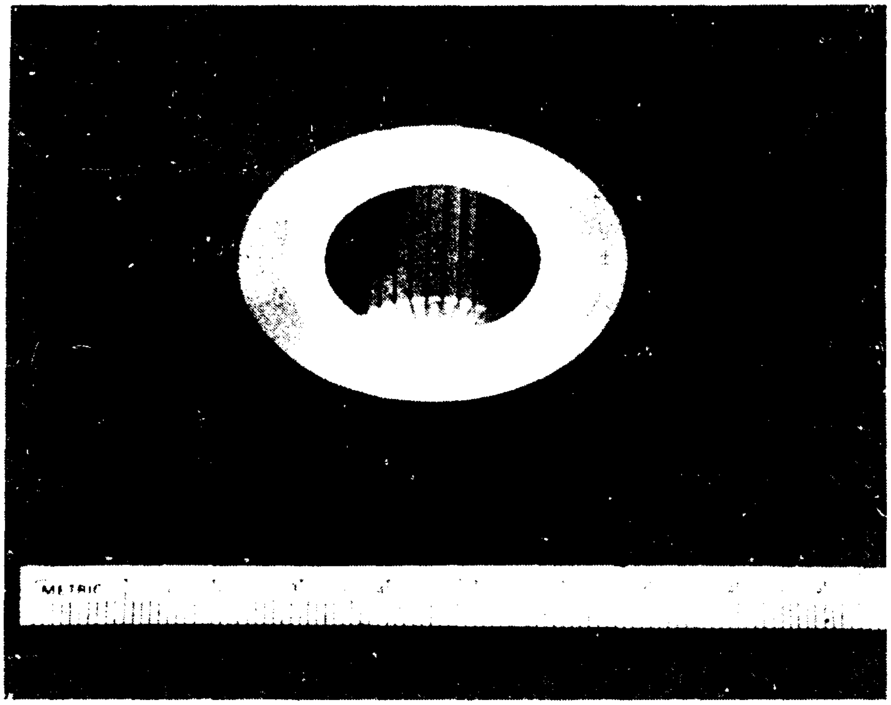

FIGURE 1 MACHINED Al/Ti COMPOSITE STRUCTURE

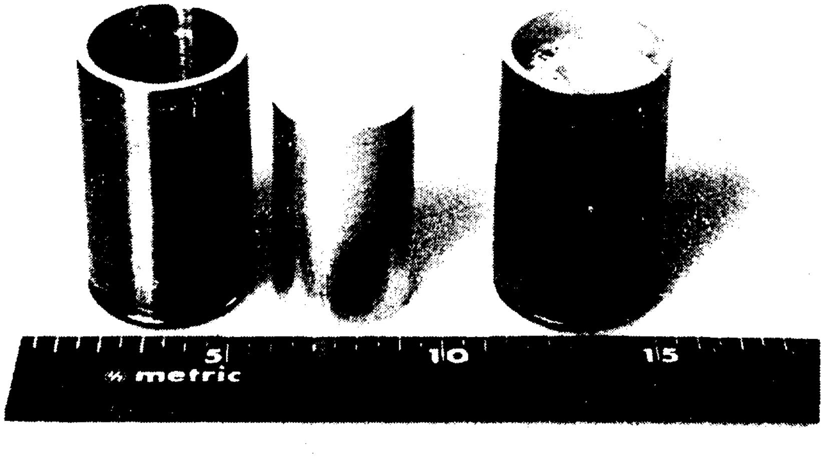
5
10
15
metric

FIGURE 2 COMPONENTS AND CAST STRUCTURE

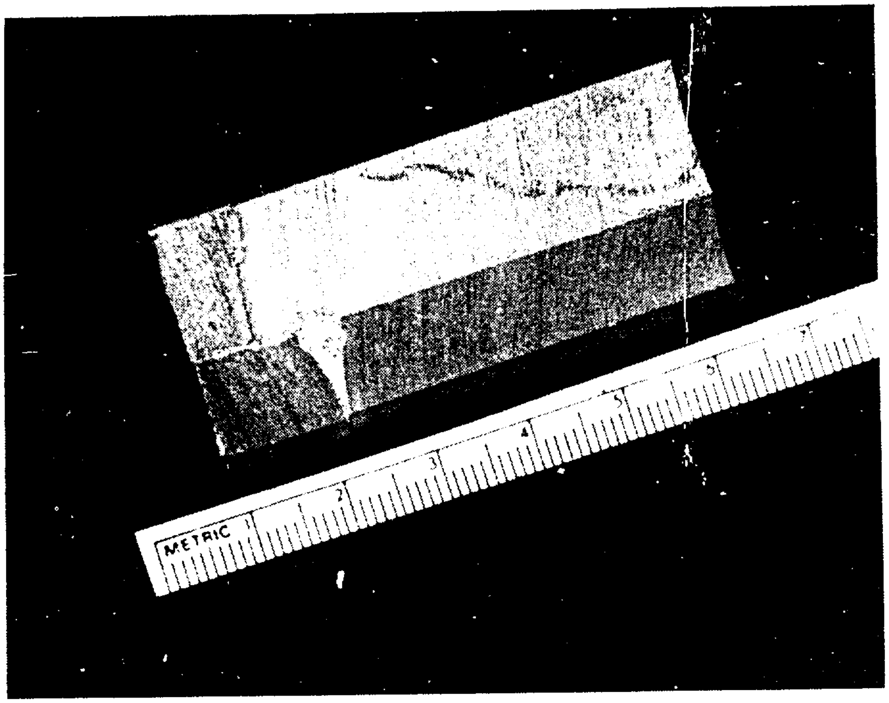
METRIC
1
2
3
4
5
6
7

FIGURE 3 QUARTERED SECTION OF COMPOSITE

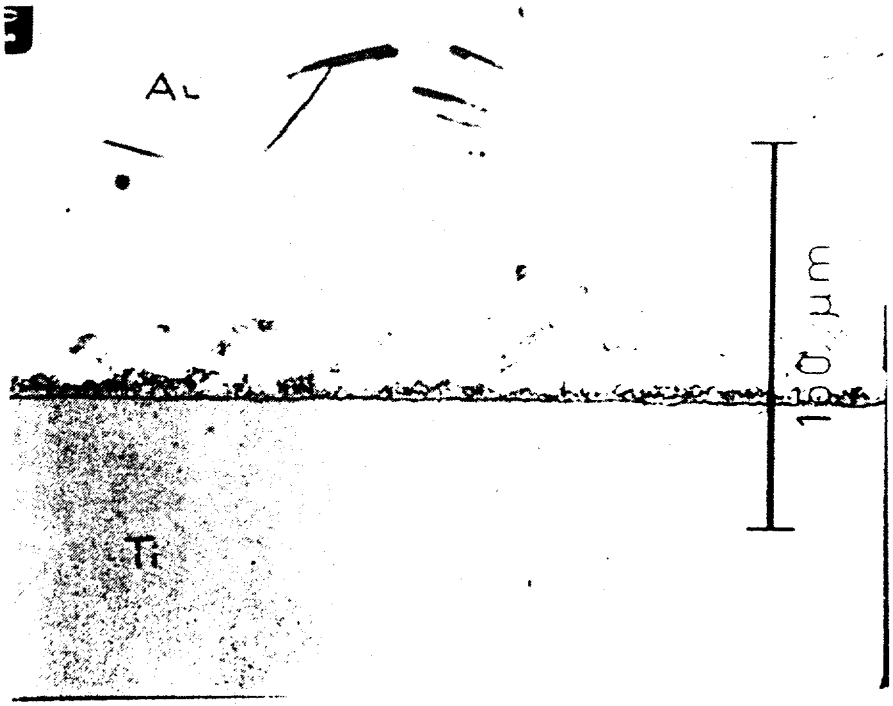

FIGURE 4 INTERFACE OF Al/Ti JOINT

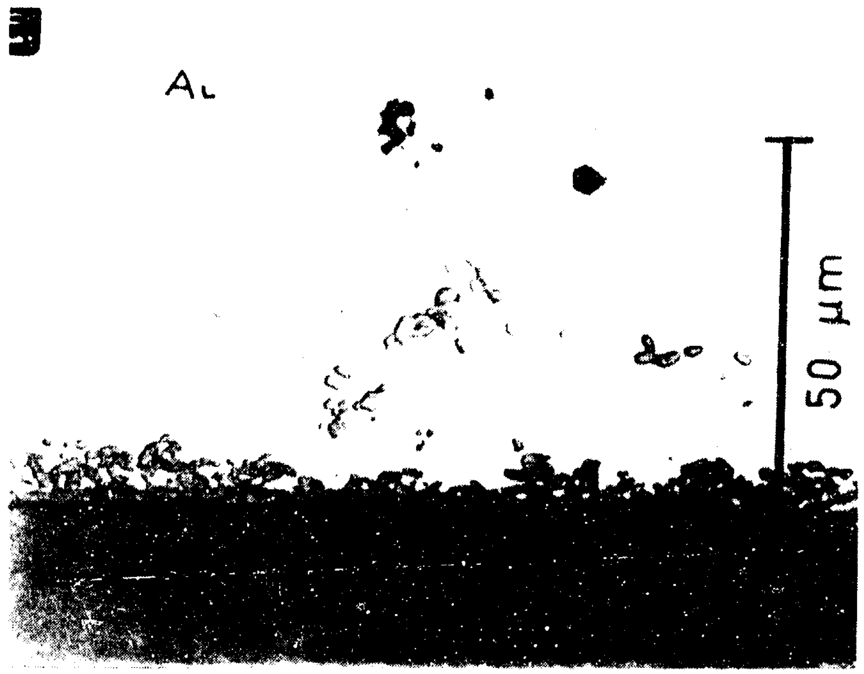

FIGURE 5 INTERFACE JOINT

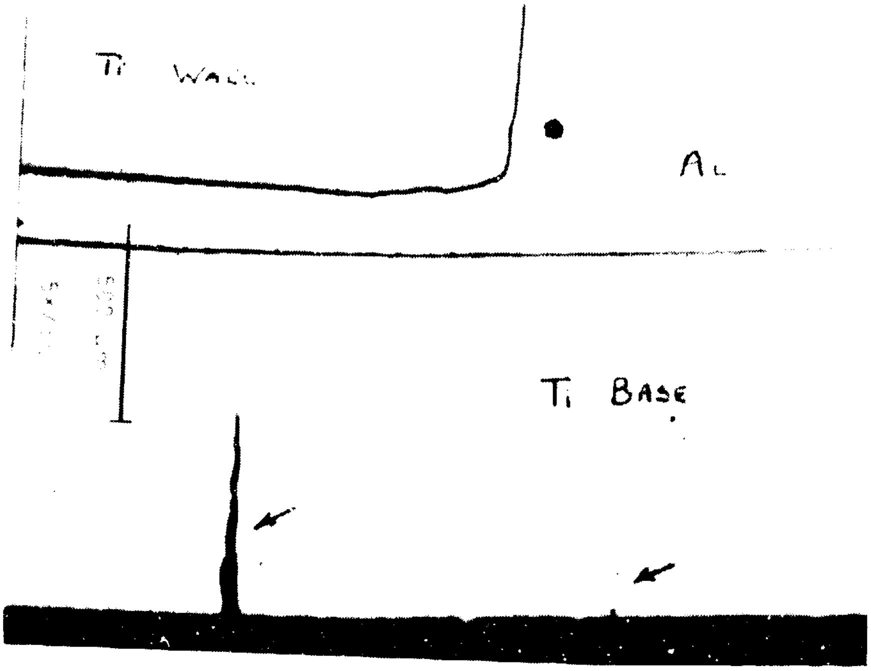
Ti Wall
Al
Ti Base

FIGURE 6 CORNER SECTION CAST STRUCTURE (THE BASE PORTION IS DISCARDED IN FABRICATION)

Preceding Page Blank

TEMPERATURE SENSITIVE VARIABLE AREA FLOW REGULATOR FOR JOULE-THOMSON NOZZLES*

K. Hedegard, G. Walker, S. Zylstra
General Pneumatics Corporation
Western Research Center
Scottsdale, AZ 85260
(602) 998-1856

Gas liquefiers utilize isenthalpic (Joule-Thomson) expansion of cooled, compressed gas to generate refrigeration. Effective usage of the compressed gas requires a variable mass flow rate; high initial flow with progressive reduction to the operating condition, and intermittent flow according to load demand thereafter. A common problem with J-T nozzles is blockage of the flow orifice by condensed contaminants in the expanding fluid.

A novel concept for a Joule-Thomson nozzle tolerant of higher levels of fluid contamination with the desired variable mass flow rate was investigated. Prototype miniature cryostats were designed, fabricated and tested to verify the concept.

Cryostat structural elements composed of materials having different coefficients of thermal expansion were combined to achieve a variable flow rate according to load demand. The problem of orifice blockage by condensed contaminants was resolved by design for expansion of the compressed gas in a tapered annulus with annular labyrinth flow spoilers acting as catchment reservoirs. The experimental prototype cryostats were equipped with a micrometer flow adjustment capable of precise flow control over a wide range, permitting the same cryostat to be used in a variety of applications or in the same application for a wide variety of flow regimes.

Key Words: Joule-Thomson expansion, differential thermal expansion, tapered annulus, labyrinth spoilers

---

*Supported in part by the National Aeronautics and Space Administration Contract No. NAS10-11144

1. Introduction

Miniature Joule-Thomson (J-T) Cryostats are widely used today in a variety of military and civil gas liquefaction applications. Refrigeration is produced through the constant enthalpy expansion of a compressed gas through a Joule-Thomson nozzle. Optimum usage of the compressed gas requires a variable mass flow rate; high initial flow with progressive reduction as the operating temperature is achieved, and intermittent flow according to load demand from that point on. Currently available cryostats provide the desired variable mass flow rate with very accurate control, although for reliable operation require the use of high purity gas to prevent the build up of condensed contaminants which block the flow orifice.

A novel concept for a J-T cryostat featuring temperature sensitive flow regulation, and a flow orifice tolerant of higher gas contaminant levels, is presently under development at General Pneumatics Corporation's Western Research Center. The progression of this development effort is the subject of this paper.

2. Joule-Thomson Expansion

Joule-Thomson, or isenthalpic, expansion is an irreversible thermodynamic process resulting in a change in gas temperature due to a change in gas pressure at constant enthalpy. The flow of high pressure gas is restricted by the small diameter orifice of the J-T nozzle. Flow pressure is degraded through substantial fluid friction within the narrow confines of the flow orifice, so the down stream pressure is low. No work has been done, and no heat has been transferred, so the enthalphy is the same after expansion as it was before. If the gas before expansion is below the inversion temperature, a decrease in temperature will be experienced during expansion. Furthermore, if the initial fluid temperature is sufficiently low, the gas will undergo a phase change during expansion with the resulting flow comprised of two distinct fluids, saturated liquid and saturated vapor.

3. Background

The evolution of miniature J-T liquefiers began with the development of the fixed orifice cryostat in the late 1950's [1-4]. This type of cryostat operates satisfactorily, although uses an excessive amount of compressed gas due to the non-regulated flow. Operational reliability is very dependent on gas purity since contaminants such as solid particulates, water vapor, carbon dioxide, etc. will condense out during expansion and accumulate within the J-T orifice, eventually causing complete blockage.

Significant improvements in flow rate control were achieved in the 1960's with the advent of the demand flow (J-T) cryostat [5-7]. Control of the flow rate is accomplished through restriction of the orifice flow area by the insertion of a needle activated by a vapor pressure thermometer and/or gas filled metal bellows arrangement.

This system provides the desired variable mass flow rate necessary for optimum usage of the compressed gas, in addition to improved temperature stability (thermophonic variation), and reduced gas flow noise (microphonics). The needle valve/flow orifice arrangement is much less susceptible to complete blockage than the fixed orifice nozzle, although still requires high purity gas for reliable operation.

4. Temperature Sensitive Variable Area Flow Regulator for Joule-Thomson Nozzles

A novel concept for a J-T nozzle with the desired variable mass flow rate, and a high tolerance to fluid contamination, was conceived by Dr. Graham Walker [8]. This novel concept features temperature sensitive flow regulation through the interaction of structural components having substantially different coefficients of thermal expansion. Tolerance to higher levels of fluid contamination is achieved through expansion of the fluid within a converging annular flow orifice. This orifice is equipped with labyrinth flow spoilers to aid the frictional degradation of the fluid flow and to act as catchment reservoirs for the condensed contaminants. A locking micrometer adjustment is provided to allow presetting of the initial flow over a wide range, or extremely accurate adjustment of the steady state flow while in operation.

5. Cryostat Configuration and Design Considerations

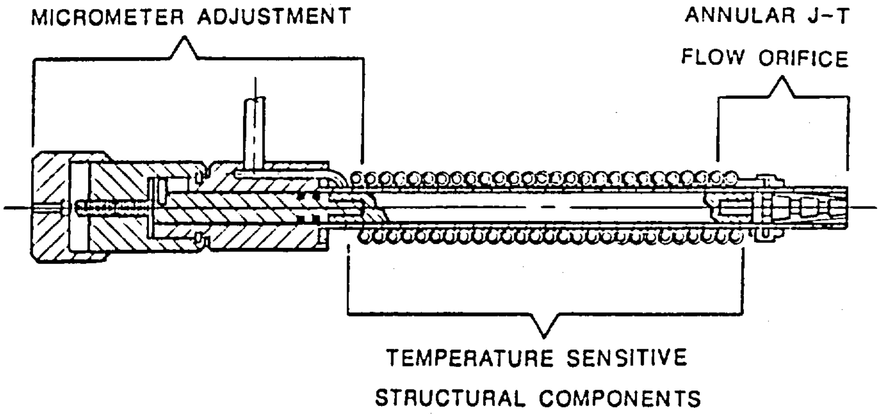

Figure 1: Areas of Development Concentration

The prototype cryostat developed for concept verification is composed of three main sections shown in figure 1: the temperature sensitive structural components, the annular J-T flow orifice, and the micrometer flow adjustment.

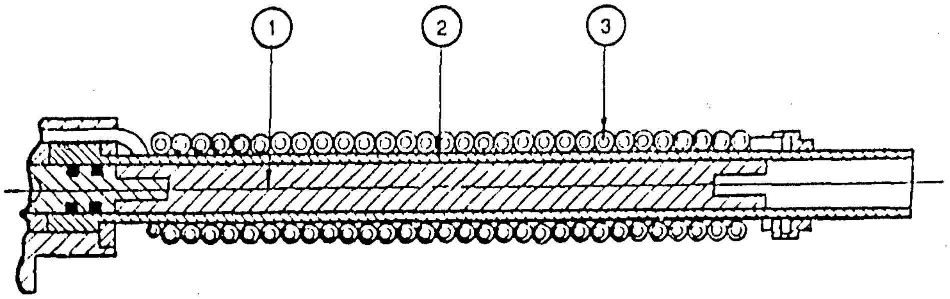

Figure 2: Temperature Sensitive Structural Components

Figure 2 is a partial section view of the cryostat showing the temperature sensitive structural components and the Giaque-Hampson finned tube contra-flow heat exchanger. The structural components consist of materials having substantially different coefficients of thermal expansion. The core (1) is made of a carbon fiber epoxy composite which exhibits a very low coefficient of thermal expansion. The core is enclosed by a sheath (2) made of aluminum, which has a very high coefficient of thermal expansion combined with a high thermal conductivity. Figure 3 below shows the coefficients of thermal expansion for these materials. The Giaque-Hampson heat exchanger (3), used to precool the incoming compressed gas, is helically wound around the sheath with close adjacent contact maintained between individual coils and the outside diameter of the sheath. The relative position of the core and sheath are fixed on the micrometer adjustment end so that the temperature induced contractive movement between the components takes place at the flow orifice end.

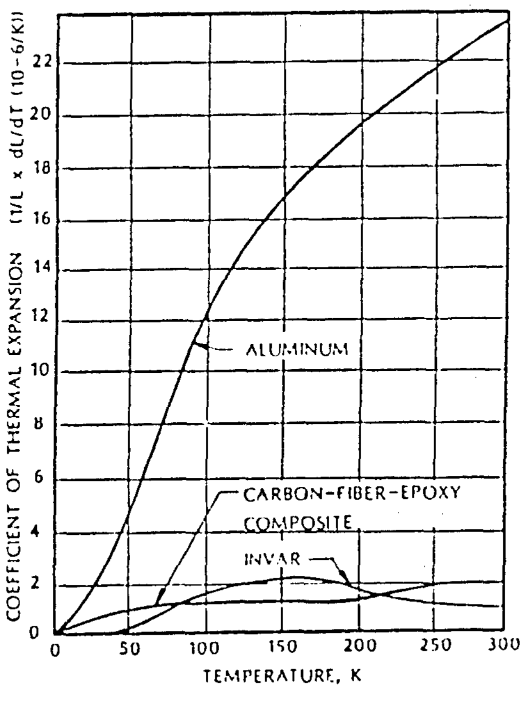

Figure 3: Coefficients of Thermal Expansion of Invar, Aluminum, and Carbon Fiber Epoxy Composite Material

The differential contractive movement between the component materials is termed the flow variability range. The resulting flow variability range is dependent upon the length of the core and sheath and the total temperature change they undergo from ambient temperature to the gas liquefaction temperature.

Diametral contractive movement of the sheath and core also occurs, although is of concern only in the area of the sheath containing the annular J-T flow orifice.

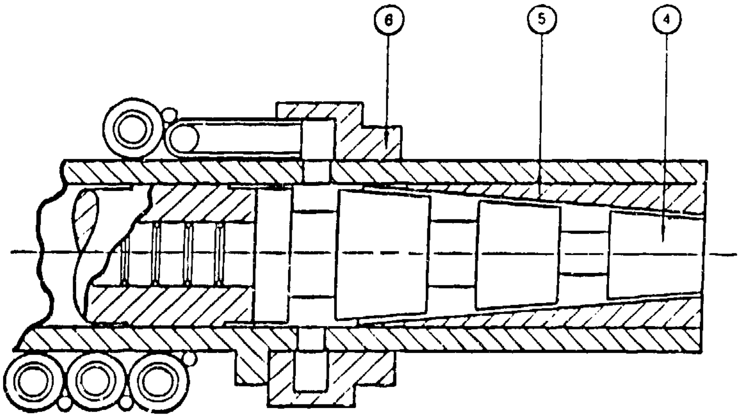

Figure 4: Converging Annular J-T Flow Orifice

Figure 4 is a partial section view of the cryostat showing the converging annular J-T flow orifice. The annular flow passageway is formed by axially locating the tapered tip (4) within the tapered seat (5). Labyrinth flow spoilers are machined in the tapered tip to aid flow degradation and to act as catchment reservoirs for condensed contaminants. A high pressure tube adaptor (6) is provided to direct the gas flow from the heat exchanger tube to the annular flow orifice. This adaptor also serves the function of dampening the pulsating pressure wave associated with use of a high pressure miniature compressor. The tip is made of invar 36, a material with a very low coefficient of thermal expansion (see Figure 3), and high durability to withstand the erosional effects of the high velocity compressed gas. The seat and tube adaptor are made of aluminum to facilitate joining with the sheath.

In a conventional J-T nozzle, flow pressure is degraded through fluid friction within the small diameter flow orifice. The small surface area of the orifice periphery is subject to the build-up of gas contaminants which freeze and condense when the gas expands. Expansion of the gas through a comparatively large diameter annular passageway substantially increases this peripheral surface area while maintaining approximately the same flow area. This increased peripheral surface area is the primary reason this J-T nozzle is less susceptible to blockage due to the build up of condensed contaminants. In addition, the labyrinth flow spoilers act as catchment reservoirs for the condensed contaminants, thus increasing reliability. They also serve the secondary function of promoting flow degradation through the generation of turbulence walls. It is anticipated that with further development these turbulence walls could conceivably permit even greater reliability by allowing an increase in the diametral separation of the tip and seat with no change in the mass flow rate, although at this stage of development this phenomena has not been well studied.

The included angle of the taper is dependant upon the flow variability range and the desired quantity of flow. For a given variability range, an increase in the included angle will cause a large flow rate change per axial movement, while a decrease in the included angle will cause a smaller flow rate change per axial movement. Therefore, it is necessary to match the nozzle included angle to the cryostat flow variability range to achieve a specific cooldown and/or steady state flow rate.

Integration of the two sections that have been discussed thus far will produce a unit capable of temperature sensitive flow regulation with expansion through an annular J-T nozzle. This non-adjustable configuration is well suited for applications where a specific cooling capacity is required, and variation of cooling capacity is unnecessary.

The addition of a micrometer flow adjustment greatly increases the versatility of the cryostat by allowing variation of the flow over a wide range. The adjustment mechanism permits the same cryostat to be used in a variety of applications, or in the same application over a wide variety of flow regimes.

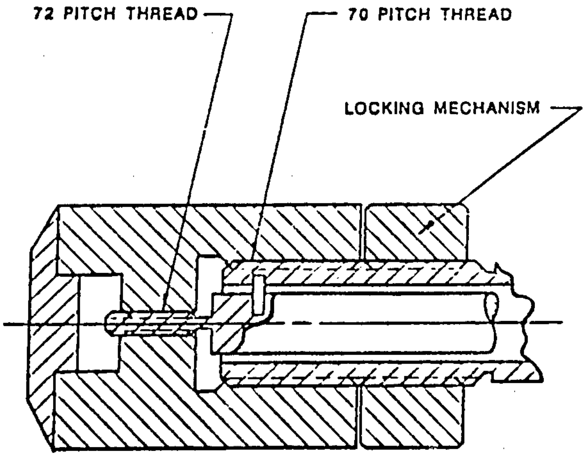

Figure 5: Differential Thread Micrometer Adjustment

The micrometer flow adjustment has undergone several generations of design in an effort to develop a single adjustment mechanism suitable for use in all anticipated miniature J-T cryostat applications.

Figure 5 is a cross section view of the first locking micrometer flow adjustment that was designed, fabricated, and tested. Adjustment is achieved through differential thread movement, where the linear advancement is the difference in the lead between two threads of close pitch. This mechanism provided extremely accurate flow adjustment, although was limited in range due to the limited length of thread engagement possible within the restricted size parameters suitable for use with a miniature J-T cryostat.

Extremely accurate adjustment is required to form the narrow annular expansion passageway between the tapered tip and tapered seat, and the highest degree of positional accuracy is required when a large included angle is used in the annular expansion orifice. As a result, an adjustment mechanism suitable for use with all orifice configurations must be capable of meeting the stringent positional requirements of the largest anticipated included angle configuration. On the other hand, the range of adjustment required depends upon the length of the temperature sensitive structural components and the resulting flow variability range. So the single adjustment mechanism must also be capable of traversing the extended adjustment range associated with a cryostat of maximum anticipated length.

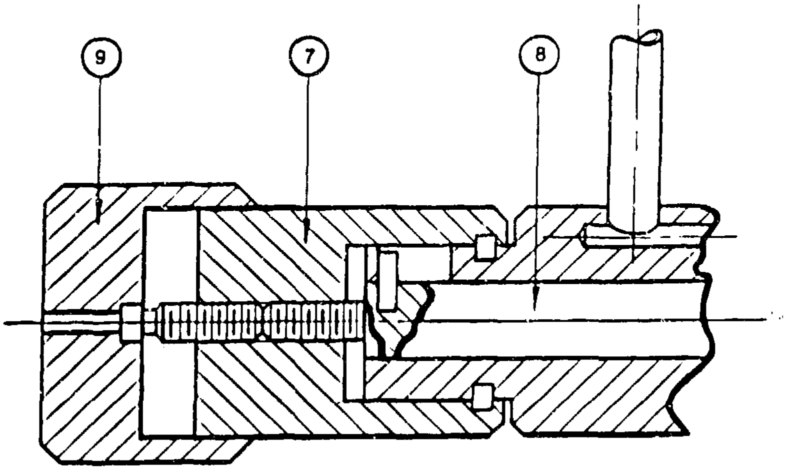

Figure 6: Single Thread Micrometer Adjustment

Figure 6 is a cross section view of the second generation adjustment design which was used successfully on the concept verification prototype. This adjustment mechanism translates rotary motion into linear motion through an adjustor (7) that is held in a fixed axial position, though is allowed to rotate in either direction, and is coupled to the core sleeve (8) by way of a fine pitch threaded section. A locking cap (9), operating as a jam nut, retains the core sleeve position once the flow adjustment is made. Integration of the micrometer flow adjustment with the cold end of the cryostat is achieved through attachment of the core to the core sleeve and the sheath to the micrometer body. This single thread locking micrometer adjustment provided adequate positional accuracy and retention over an adjustment range suitable for use with the prototype cryostat. Succeeding generations of design have resulted in a single adjustment mechanism currently under development that allows increased positioning accuracy and retention, with an extended range of flow adjustment, suitable for use with any flow regime and resulting variability range anticipated in a miniature J-T cryostat.

6. Cryostat Operation

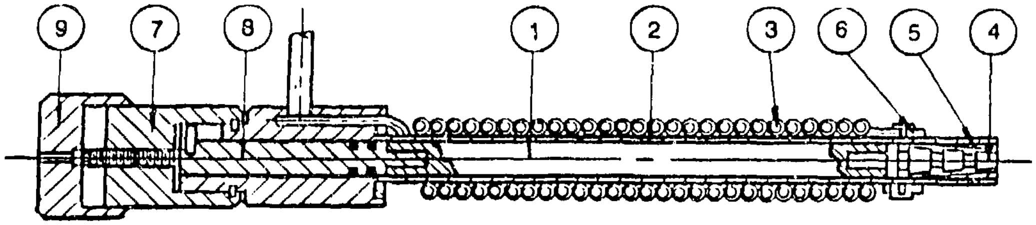

Figure 7: Temperature Sensitive Variable Area Flow Regulated Cryostat with Annular J-T Expansion Nozzle

Figure 7 is a fully integrated cross section view of the prototype cryostat used for concept verification. A total of three prototype cryostats were fabricated and tested, the only difference being in the number of labyrinth spoilers used on the tapered tip. Throughout the extensive testing series no significant difference in performance was noted as the result of the number of flow spoilers along the tapered tip, except at very low flow rates with the tapered tip separated from the tapered seat by a small axial distance. This was one of the most surprising and unexpected aspects of the study. The provision of flow spoilers utilizes the same design principles of labyrinth seals used extensively in turbomachinery to contain high pressure fluid by means of high energy flow dissipation. Appreciable difference in flow characteristics were anticipated with different numbers of flow spoilers.

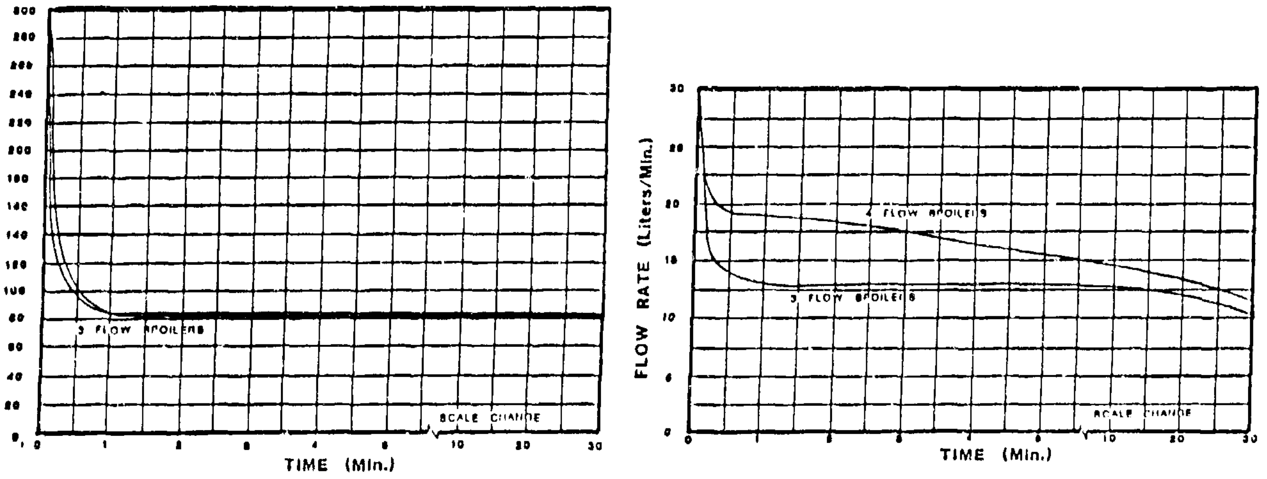

Figure 8: Typical Test Results of Temperature Sensitive Variable Area J-T Expansion Nozzles

Figure 8 shows typical results of the test program in respect to temperature/time correlations and volume flow rate/time history correlations of the prototype cryostats having three and four flow spoilers in the expansion annulus. There is no significance in the different volume flow rates of the two levels shown on the volume flow rate/time history graph. The difference arises from the fact that the startup flow rates were different in the two cases. These different startup flow rates were selected from a large number of measurements, and were chosen simply to separate the curves for clarity.

The minimum temperature achieved on the temperature/time graph is above the nitrogen boiling point; this variation may be attributed to inherent heat leaks associated with the dewar fabricated in-house for the testing series. As noted, the cryostats achieved cooldown within one minute of startup, with the desired progressive reduction in flow as the operating temperature was reached.

The resultant flow variability range and annular orifice geometry resulted in approximately fifteen litres/minute flow reduction regardless of the startup flow rate. Varying the position of the tapered tip within the tapered seat with the micrometer flow adjustment allowed wide variation of the startup and steady state flow rates.

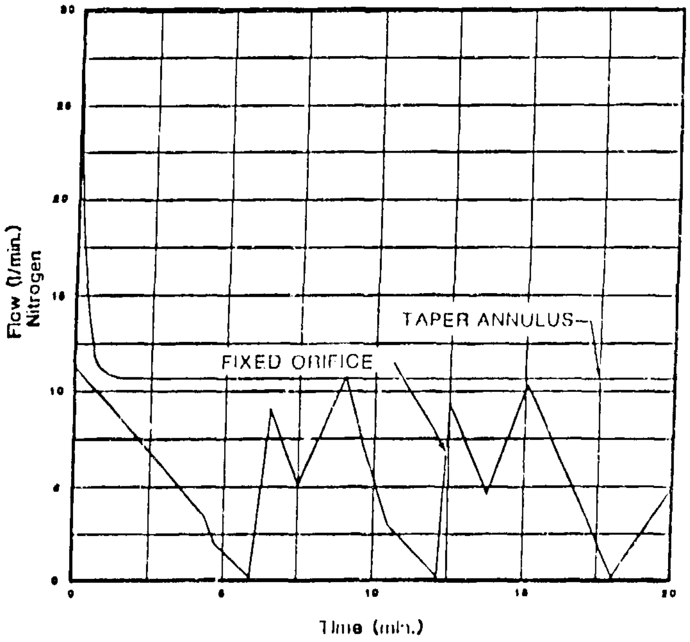

Figure 9: Volume Flow Rate as a Function of Time (Showing Fixed Orifice Blockage Due to Contamination Build Up)

Verification of the annular J-T nozzles tolerance to increased levels of fluid contamination was achieved through comparative testing against a commercially available fixed orifice J-T cryostat. Figure 9 is a graph showing the comparison of volume flow rates as a function of time during a comparative testing sequence.

No provision was made for filtration of the high pressure gas in the prototype cryostats, and relatively low purity nitrogen was used as the working fluid, so test results reflect a worst case condition. The micrometer flow adjustment was used to match the prototype cryostat steady state flow rate to that of the fixed orifice cryostat at equal gas pressure levels.

The test sequence graphically shown took place approximately ninety minutes after initiation of the test series, and the six minute time span represents the least amount of time the fixed orifice cryostat operated until complete blockage occurred. At the beginning of the test sequence the fixed orifice cryostat operated approximately sixty minutes before suffering complete blockage. After blockage would occur, the cryostat was allowed to warm up to ambient temperature before a new test sequence would begin.

At no time during the many hours of testing did the prototype annular cryostat suffer complete blockage; in some instances a reduction in flow would occur, but as soon as the temperature would begin to rise the flow would increase to a point above the steady state rate, then return to its previous level.

7. Conclusion

The novel concept for a temperature sensitive variable area flow regulator for Joule-Thomson nozzles was verified through the design and testing of three prototype cryostats. The study showed the excellent flow regulation characteristics as a result of the temperature sensitive structural components. The possibility for easy adjustment and wide variation in initial or final fluid flows in the expansion nozzle using the micrometer flow adjustment was verified also. And most importantly, the ability of the expansion unit to operate for many hours with no flow interruption by contaminant blockage when using the same contaminated nitrogen gas that would result in blockage of a fixed orifice J-T expansion unit within six to sixty minutes of operation.

8. References

[1] Parkinson, D.H. (1959). "Some Problems in the Design of Helium Liquefier Based on the Joule Thomson Effect." Proc. X Int. Cong. of Ref. Prog. in Ref. Sci. Technol. 1, 53-57, (Publ. Pergamon Press, Oxford).

[2] Parkinson, D.H. (1967). "Miniature Refrigeration Systems - A Review." Proc. XII Int. Cong. of Ref./Prog. in Ref. Sci. and Tech., Vol. 1, 69-77, Madrid (IIR, Paris).

[3] McInroy, J. (1967). Miniature Joule-Thomson Coolers." Proc. XII Int. Cong. of Ref./Prog. in Ref. Sci. Technol. 1, 59-68, Madrid (IIR, Paris).

[4] Nicholds, K.E. (1968). "Low Temperature Devices for Laboratory Operation." Proc. 2nd Int. Cryo. Eng. Conf., pp. 65-66, Brighton Iliffe, Sci. and Tech. Publ. Guildford, U.K.

[5] Nicholds, K.E. (1970). (a) "Performance of Self-Regulating Joule-Thomson Minicoolers." pp. 277-282. (b) "Miniature Cryogenic Cooling Systems for and Upper Atmosphere Infrared Research Programme," pp. 283-286, Proc. 3rd Int. Cryog. Eng. Conf., Berlin, Iliffe Sci. and Tech. Publ. Guildford, U.K.

[6] Stephens, S. (1970). "A Self-Regulating Miniature Joule-Thomson Refrigerator." Appl. Cryogen. Technol. 3.

[7] Buler, J.S. (1971). "A Self-Regulating Rapid-Cooling Joule-Thompson Cryostat." Adv. Cryog. Eng. 16, 205-213.

[8] U.S. Patent Application No. 793,268, "Joule-Thomson Apparatus With Temperature Sensitive Annular Expansion Passageway". Graham Walker, (1985) Assignor to General Pneumatics Corporation.

SYSTEM DESIGN REQUIREMENTS FOR INFRA-RED DETECTOR CRYOCOOLERS

D. Marsden

British Aerospace
Air Weapons Division
Hatfield
Hertfordshire
England

Infra-red sensor systems incorporating cryocoolers are required to be qualified to the appropriate environmental specification. Evaluation of system component performance and the effect of relevant interfaces will allow overall system performance to be predicted and some optimisation to be made.

The Stirling Cycle cryocooler developed by British Aerospace Air Weapons Division, and its interactions with Infra-red reconnaissance system sensors are described. Results from thermal mapping, vibration and detector sensitivity tests are included. The electronic control and Built-In test equipment (BITE) are described and the possible implications of maintainability requiremetns discussed.

Key words: Cryocooler; detector cooling; Infra-red systems.

1. Introduction

The use of cryocoolers in military systems requires a demonstration of adequate performance when subjected to anticipated levels of vibration and acceleration and over the required ambient temperature range. The cryocooler/sensor interfaces can significantly affect operating conditions and cooler performance and therefore estimates of the various interactions are required before overall performance levels can be predicted.

British Aerospace has developed a cryocooler for use in military infra-red systems, based on earlier work done at Oxford University. It is currently used in the British Aerospace range of Linescan infra-red reconnaissance equipment. The Linescan qualification programme has shown the significant effects interface characteristics can have on cooler performance, particularly in terms of external vibration and performance variation with ambient temperature. The effect of cooler performance variations on overall sensor performance has also been assessed. The results illustrate the value of some system modelling at an early design stage to allow both performance sensitivity and optimisation studies to be carried out.

2. Specification

2.1. Performance

The cryocooler is required to cool the sensitive material of a Mullard R185 Infra Red detector to operating temperatures, throughout the full environmental envelope of the overall system. Cool down time will not exceed 10 minutes. The external diameter of the cold finger inside the detector bore is limited by the detector type to 6.7 mm maximum. The thermal interface between the cold finger and the detector substrate is constrained within this diameter and is required to accomodate the differential thermal contraction between the encapsulation and stainless steel cold finger.

2.2. Life

Operating life is required to be in excess of 4,000 hours and the total life shall be not less than 10 years. An overall leak rate of better than 5×10^{-7} torr litres/sec is required.

2.3. Power Consumption

The power required by the cryocooler system is to be less than 80VA from a 200V, 400Hz 3 phase supply. Power to the cryocooler itself is typically 40VA.

2.4. Maintenance Philosophy

The cryocooler system forms groups of modules within Line Replaceable Units (L.R.U.'s). Line Replaceable Units are replaceable at first line, modules at second line. L.R.U.'s are required to be fully interchangable, without adjustment and the associated Built-In Test Equipment (BITE) is required to locate faults to the relevant L.R.U. at first line.

These requirements can have significant effects on system installation, packaging, or design.

3. Hardware

3.1. Cryocooler

The B.Ae. Cryocooler produced to satisfy the above specification is shown in figure 1.

It is a Split Stirling Cycle design with a compressor, or pressure modulator and a displacer joined by a transfer pipe. Both major assemblies have linear drive motors with fixed permanent magnets and spiral spring suspension to ensure accurate drive rod alignment. A design of such relative complexity was chosen because of its ability to withstand severe environmental conditions and in particular, high vibration levels.

Non contact clearance seals are used on both the compressor piston and the displacer drive rod, to ensure a long operational life. The clearances are maintained, by the spring suspension systems. Linear variable displacement transformers (L.V.D.T.'s) are fitted to both major assemblies to provide position feedback information to the control system.

Nominal stroke lengths are 8.0mm for the compressor piston and 4.0mm for the displacer regenerator contained within the cold finger of the displacer assembly. Drive frequency is 52 Hz.

A particular installation of the cryocooler can position the compressor and displacer independantly in any axis, with a transfer pipe length of up to 500 mm.

3.2. Control System

The electronic control system is required to drive the motor coils of the two major assemblies at the chosen drive frequency, with their displacements separated by the optimum phase angle. Servo position control loops around the two motors, using position information from the L.V.D.T. outputs ensure that the required motion is generated to an accuracy of better than 0.1 mm, even under extreme conditions of external vibration and acceleration. The schematic circuit design is shown in figure 2.

The reference waveforms for both drive motors are synthesised, with the appropriate phasing, from the two PROM's and D to A convertors shown in the reference generator section. Phasing is determined by the individual PROM content

The two servo position loops consist of main drive amplifiers, the relevant motor drive coil and an L.V.D.T. The 9.6 KHz L.V.D.T. input signals are also synthesised using the PROM and D to A convertor shown. Power to the control system is derived from a 400 Hz, 200V, 3 phase supply.

Built in test equipment (BITE) is included in the control system, but is not shown in figure 2, to provide cryocooler and detector status information to aircraft systems. Three BITE output signals are provided;

a) Power supply phase dropout

b) Electronics fault indication

c) Cryocooler fault indication

The system installation or maintenance philosophy can require a system fault to be located to the cryocooler or control system level. It is therefore necessary for the BITE system to also monitor several extra parameters, including regulated power supply outputs, detector temperature sensor signals, L.V.D.T. signals and drive coil voltages and currents. The associated hardware can form an appreciable part of the total control system.

A feedback signal of detector substrate temperature is used, by the control system, to vary compressor stroke length and thereby heat lift. It is provided to reduce the variation of substrate temperature with ambient conditions and to prevent overcooling i.e. a substrate temperature of below 75 K.

4. Integration

4.1. General

Although cryocooler performance can be specified in isolation, the various system interactions of a cooler and detector in a sensor assembly can result in significant performance variation. It is necessary to quantify the various influences on cooler performance, in terms of heat lift and to then establish the effect of this variation on overall sensor performance. A typical installation system flow diagram is shown in figure 3.

4.2. Detector Heat Load

The variation of detector heat load with both substrate and ambient temperatures must be known or modelled before comparison with engine performance data can indicate the operational substrate temperature range.

A typical linearised heat load model (for the Mullard R185 detector) is;

$$HL = (T_A - T_S)\tau + W\,(T_A^4 - T_S^4) + X\,(T_S - 80) + \varrho \qquad (1)$$

Where:

HL = heat load (mW)

T_A = ambient temperature (abs)

T_S = substrate temperature (abs)

τ = constant

W = constant

X = constant

ϱ = detector bias current heat load at 80K.

The expression represents the sum of conductive, radiative and electrical heat loads. The resulting head load values are shown in figure 4.

The increase in heat load with substrate temperature is caused by detector element resistivity changes. It has been assumed that the detector bias field is generated by a constant current supply. The bias field voltage will therefore vary with element resistance i.e. substrate temperature. The effect of this variation on detector performance should be assessed before acceptable substrate temperature ranges are specified. Relative performance variations for particular substrates are shown in figure 6.

4.3. Cryocooler Performance

Cooler performance in terms of nett heat lift, is usually quantified by a series of thermal mapping tests, due to the difficulty of accurately modelling the high parasitic losses such as shuttle heat transfer and cold finger heat leakage. The results can be expressed in the following form, for a given charge pressure;

$$H = \left[\alpha + ((T_S - 80)B) + ((293 - T_{CH})\lambda)\right]\theta^X \qquad (2)$$

Where:

H = nett heat lift from T_S to T_{CH} (mW)

α = nett heat lift from 80K to 293K (mW)

T_S = substrate temperature (K)

T_{CH} = compressor temperature (K)

B = constant. (Performance sensitivity to substrate temp.)

λ = constant. (Performance sensitivity to cylinder head temp.)

θ = function of compressor pressure ratio

X = constant.

Typical values for the British Aerospace 6.7mm cooler are:

B = 20 mW/K

λ = 2.8 mW/K

X = 2.3

Typical performance values are shown in figure 4.

Equations (1) and (2) can be used to predict the operational substrate temperature range, and the effect of changes to other system parameters discussed below.

System maintainability requirements usually result in the cold finger/ detector clearance volume not being evacuated and therefore convection losses can reduce performance levels in a detector to below those predicted from tests done with vacuum insullation. It is therefore desirable to validate at least some points of the mapping exercise with a cooler/detector combination.

4.4. Cooler Installation

Cooler performance, as described by equation (2), varies with compressor temperature by, typically, 2.8mW/K. The relationship between cylinder head temperature and ambient conditions will be determined by both the design of the installation, and the power dissipated by the compressor. The British Aerospace 6.7mm cooler dissipates approximately 35 watts in the compressor and up to 3 watts in the displacer.

Figure 4 allows the effects of variations in thermal performance of the mounting interface of substrate temperature to be assessed. A 10 K reduction in cylinder head temperature will result in a fall in substrate temperature of approximately 1.5 K. It is therefore possible to assess the benefits of alternative mounting arrangements or the extra complexity of forced air cooling in terms of system performance.

Typical installations without forced air cooling will have a temperature difference of about 20 - 30 K between the mounting structure and the compressor cylinder head. This assumes that there are no significant heat sources located close to the compressor or its heat sink zone.

4.5. Vibration

Military vibration specification levels are usually applied to the entire Line Replacable Unit (L.R.U.) and therefore levels experienced by the individual modules within the assembly will depend on the gains of the mounting structure. Several installations with gains significantly above 1 have been tested and therefore the cooler is required to withstand higher levels of vibration than originally specified.

The British Aerospace cooler has been tested to MIL STD 810B Method 514 (Curve J) in all three axes. Full performance was maintained, throughout. The relevant vibration levels are shown in figure 5.

In addition, at set frequencies, threshold levels of vibration for satisfactory operation were established, above which the BITE of the control system detected overstroking and shut down. These levels are also shown in figure 5 and are between 10 - 20g. The cooler has also been vibrated; and survived, levels in excess of 70g.

If structural gains are found to be unacceptably high the use of anti-vibration mounts will result in a thermal barrier being introduced into the system. Thermal modelling must then be carried out to assess the likely effect on substrate temperature range, using equations (1) and (2).

4.6. Control System Performance

The control system performance, in terms of tolerance to changes in compressor or displacer transfer functions, will influence both overall performance sensitivity to ambient temperature and the interchangability of the cooler and control system.

4.6.1. Ambient Temperature Variation

The cooler performance variation with compressor temperature shown in figure 4 is, in part cuased by reductions in stroke length with increasing temperature and charge pressure. A typical compressor stroke length sensitivity of 0.075% per °C gives a 7.5% variation over an environmental temperature range of 100°C. This is estimated to account for up to 50% of the 2.8mW/°C variability shown in figure 4.

4.6.2. Interchangability

The maintenance philosophy of a particular installation may require full interchangability between coolers and control systems, if they are defined as separate modules. It is then necessary to quantify the full tolerance bands of LVDT sensitivity, mechanical assembly, control system reference waveform settings and BITE overstroke detection levels. The resulting tolerance tiering will reduce an individual cooler's stroke lengths. The performance levels shown in figure 4 are obtained from coolers set up to meet full interchangability requirements.

4.7. Substrate Temperature Variations

The variation of substrate temperature with ambient and compressor temperatures is described above. The effect of this variation on detector performance will influence the overall effectiveness of the sensor. The performance of certain detector materials in the 8 - 13 μ band is believed to vary with both substrate temperature and cut-off wavelength (λ_c); as shown in figure 6. Curves A and B indicate acceptable substrate temperature operating ranges of 75-100K and 75-85K respectively. For a given encapsulation, the latter requires a significantly higher level of cooler performance.

5. Summary

The use of cryocoolers in military sensor systems requires the various system interactions to be understood and quantified. The British Aerospace cooler has now successfully completed two sets of flight trials in high performance military aircraft as part of Linescan systems and information gained during the respective qualification programmes has allowed the various system requirements to be assessed.

An example of Linescan flight trial imagery, using a cryocooler cooled detector is shown in figure 7.

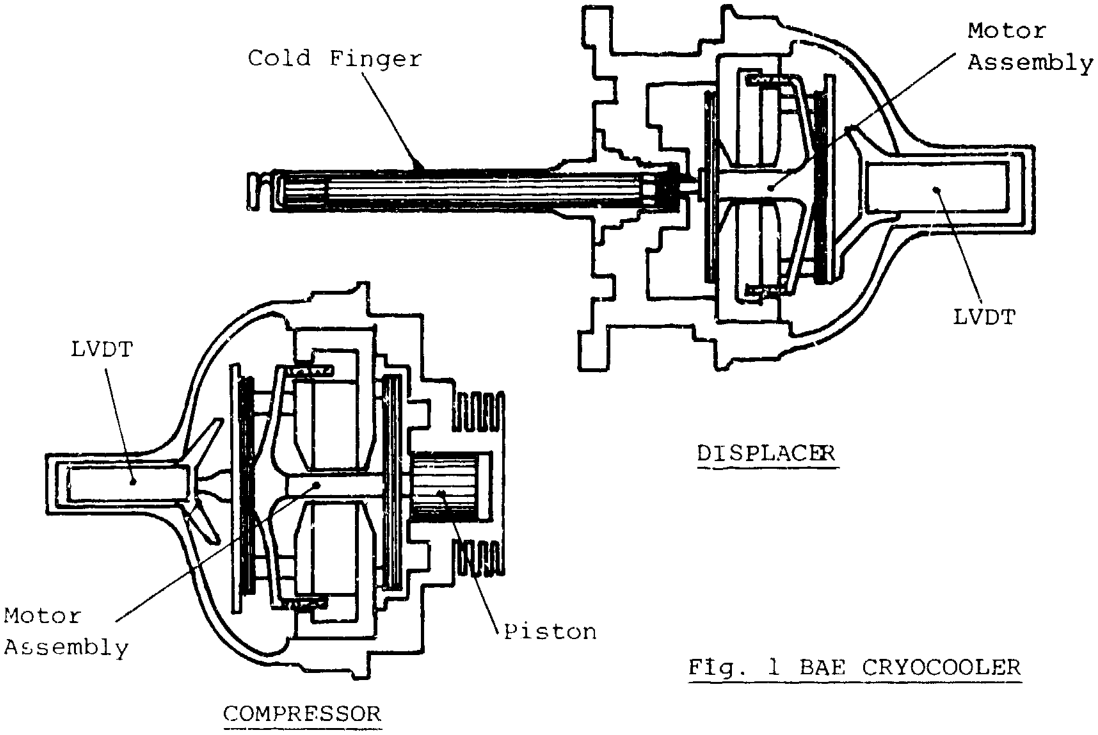
Cold Finger
Motor Assembly
LVDT
DISPLACER
LVDT
Motor Assembly
Piston
COMPRESSOR

Fig. 1 BAE CRYOCOOLER

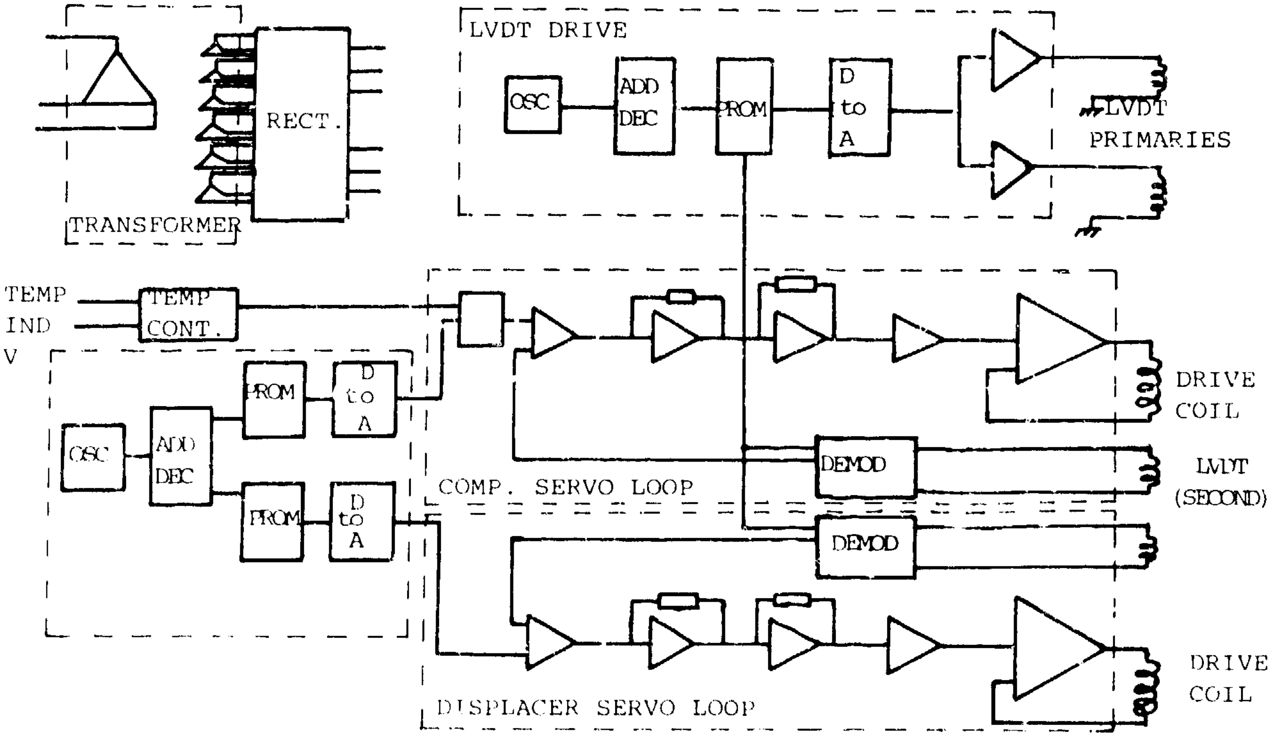
TRANSFORMER
RECT.
LVDT DRIVE
OSC
ADD DEC
PROM
D to A
LVDT PRIMARIES
TEMP IND V
TEMP CONT.
OSC
ADD DEC
PROM
D to A
PROM
D to A
DRIVE COIL
DEMOD
LVDT (SECOND)
COMP. SERVO LOOP
DEMOD
DRIVE COIL
DISPLACER SERVO LOOP

FIG. 2 - CONTROL SYSTEM

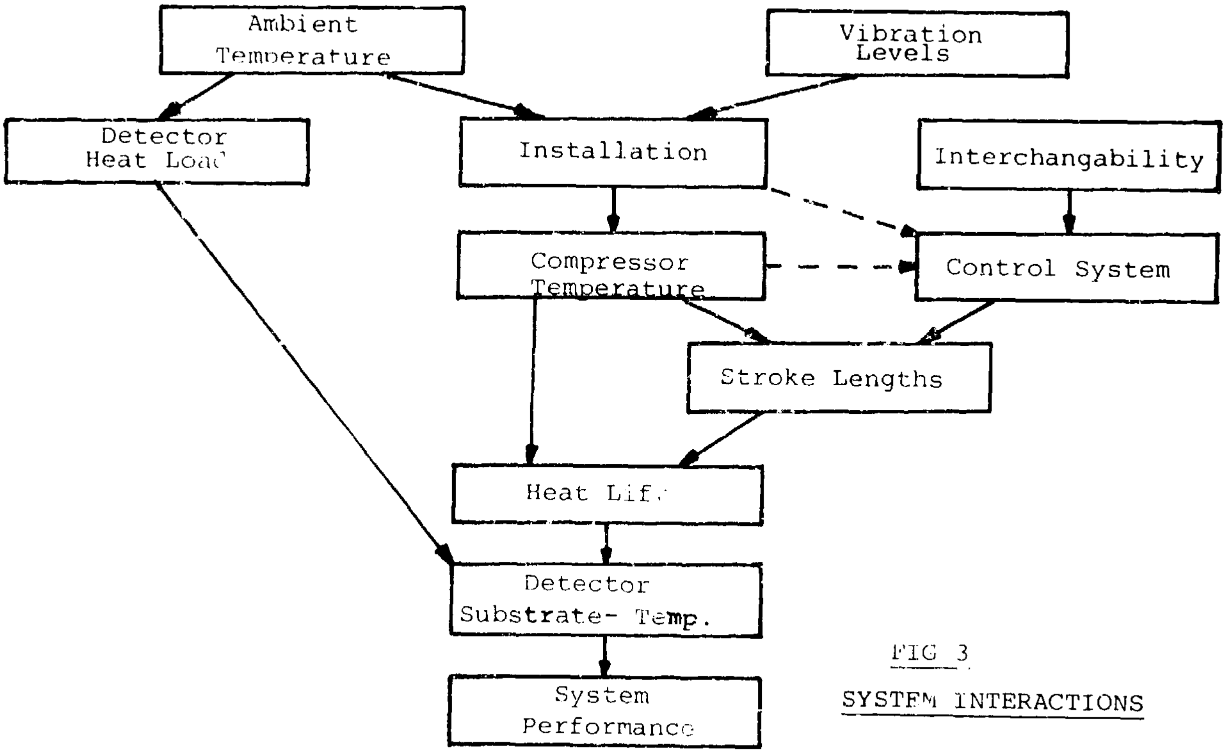
Ambient Temperature
Vibration Levels
Detector Heat Load
Installation
Interchangability
Compressor Temperature
Control System
Stroke Lengths
Heat Lift
Detector Substrate- Temp.
System Performance

FIG 3

SYSTEM INTERACTIONS

FIGURE 4 - CRYOCOOLER PERFORMANCE

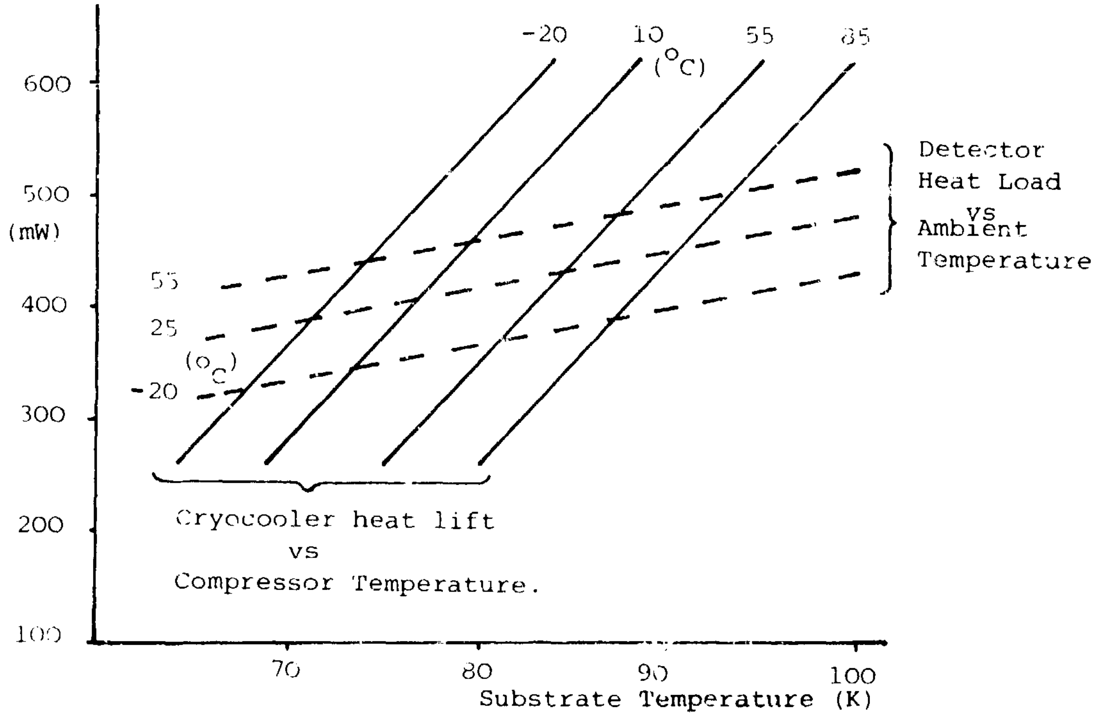

FIGURE 5 - VIBRATION TEST LEVELS

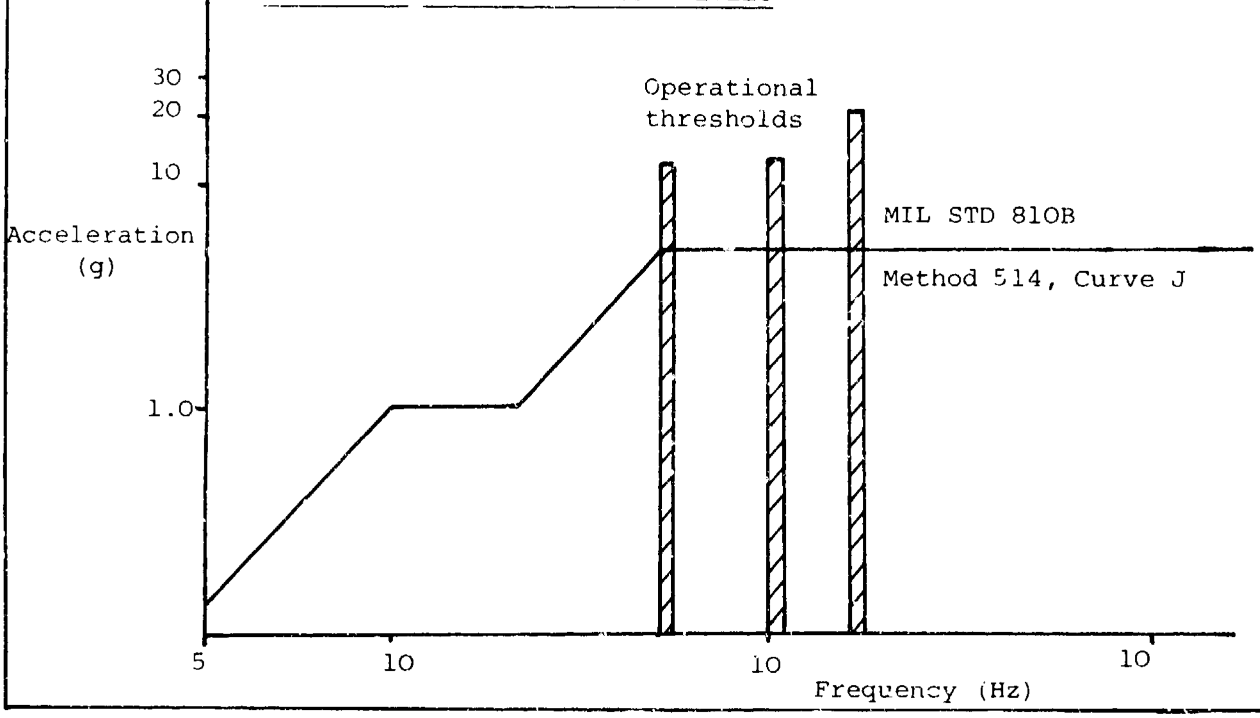

FIGURE 6 - DETECTOR PERFORMANCE

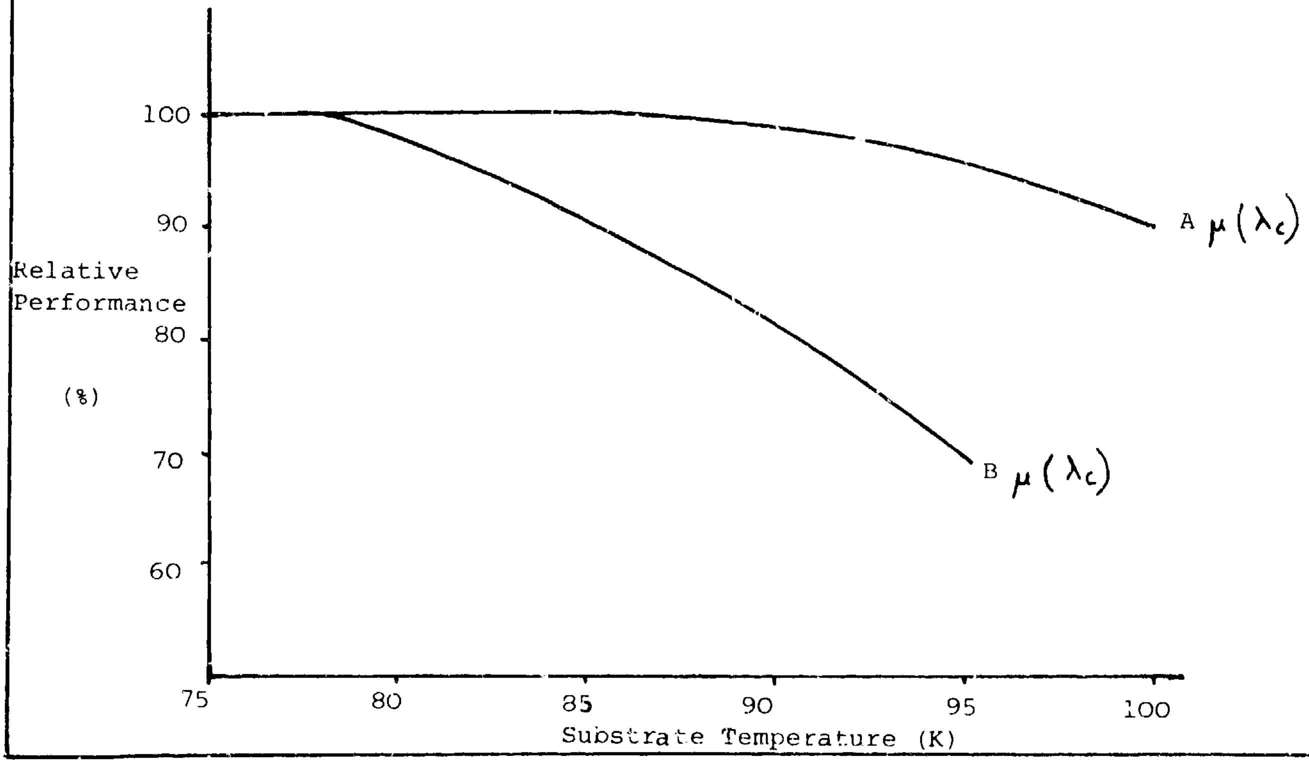

Horizon

Full field
of
View

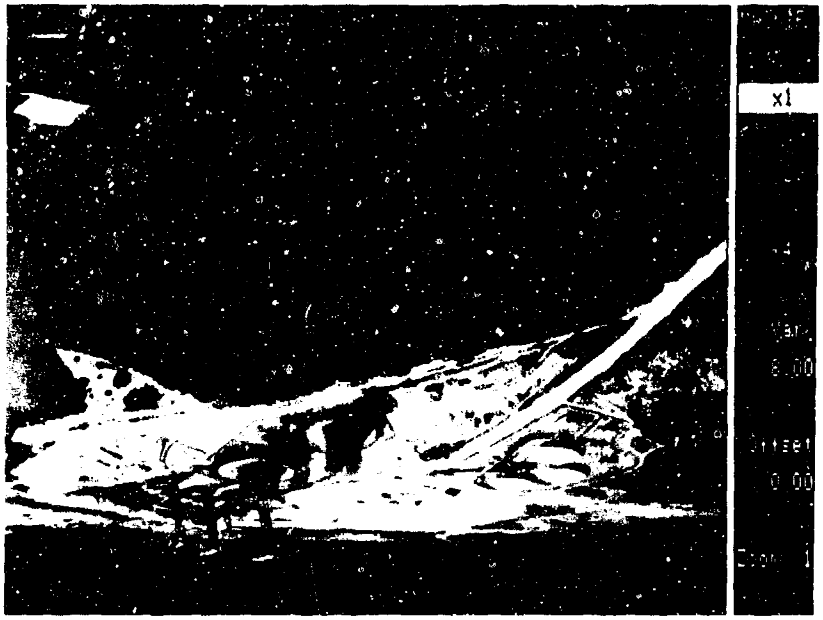
x1
Var
6.00
Offset
0.00
Zoom 1

Horizon

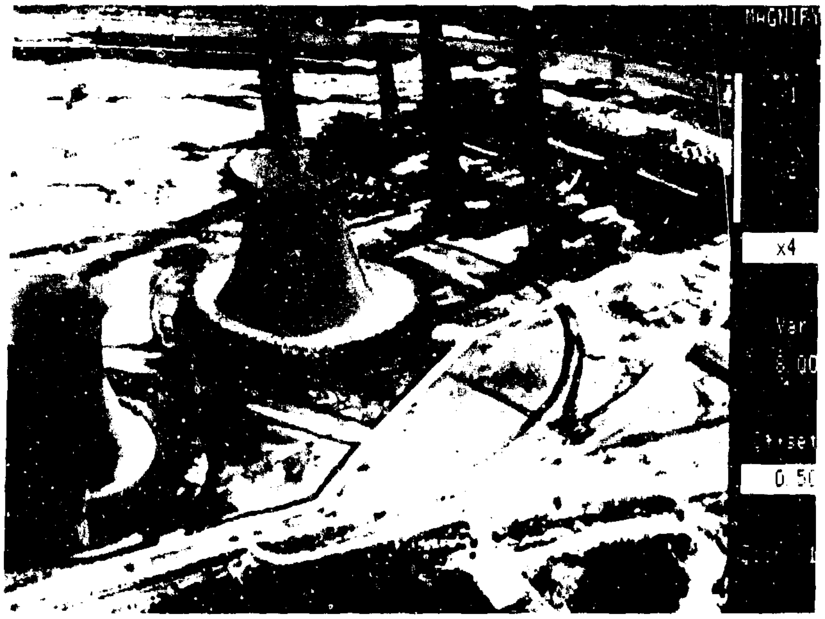
MAGNIFY
x4
Var
6.00
Offset
0.50

Selective Enlargement

(x4)

Fig. 7 - LINESCAN 4000 IMAGERY (CHESAPEAKE BAY AREA, MAY 1986)

PARAMETRIC TESTING OF A LONG LIFE LINEARLY DRIVEN STIRLING CRYOGENIC REFRIGERATOR AFTER 20,000 HOURS OF OPERATION

F.R. Stolfi

PHILIPS LABORATORIES
North American Philips Corporation
Briarcliff Manor, New York 10510

A novel Stirling cycle cryogenic refrigerator, built for long-life spaceborne missions, has surpassed 20,000 hours of operation. The refrigerator incorporates electro-magnetic bearings, clearance (i.e. non-contacting) seals and electronically controlled linear motions. This last feature, which is accomplished with the aid of two linear motors, position transducers and a highly accurate electronic feedback system, permits parametric evaluation of the Stirling cycle during operation. Such dynamic evaluation was not possible with previous systems. This paper discusses the results of parametric tests performed after the system was operated successfully for over 20,000 hours, never having to be disassembled for maintenance or inspection. The results are compared with those obtained from earlier tests reported previously.

Key words: Spaceborne cryogenic refrigerator; Stirling cycle; parametric testing; life testing; electronic feedback control; magnetic bearings.

1. Introduction

Philips Laboratories designed, fabricated, and tested a unique Stirling refrigerator prototype which can operate for many years without the need for periodic maintenance and without performance degradation, and has proven the design with more than 20,000 hours of operation. The refrigerator overcomes one of the principal limitations to the widespread application of cryogenic refrigeration systems, namely their relatively short maintenance-free life. Philips Laboratories has thus produced a system which is compatible with spaceborne applications. This was accomplished by suspending the moving parts of the refrigerator electro-magnetically, which eliminated contact and the associated wear and which permitted the use of clearance (rather than contact) seals. The electro-magnetic suspension was further enhanced by an electronically controlled direct (linear) drive. This last feature, which involves the use of two linear motors, position transducers and a highly accurate electronic feedback control system, produces the system capability which forms the basis for the tests described here. These tests are essentially a repeat of tests that were performed on the refrigerator after it had operated for 1,000 hours and have been previously reported [1]. The test results are meant to provide designers with an understanding of the basic operation of the Stirling cycle and give potential users some indication of the capabilities of this refrigerator under off design conditions. These repeated tests, after an additional 20,000 hours of operation (21,000 hours total) and more than 3 years of elapsed time give an indication of how little the refrigerator has aged in terms of performance even under off-design conditions.

Since the purpose of a cryogenic refrigerator is to produce cold at very low temperatures with high efficiency, its performance criteria are readily defined. Input power, cold production (output power) and operating temperature are very important characteristics. And, the magnitude of these characteristics (e.g. the input power required to produce a certain amount of cold) depends on the refrigerator geometry (e.g. the size of the components) and on its operating parameters. Thus, a measure of any existing cryogenic refrigerator's capabilities is the way in which these criteria - input power, cold production and temperature - vary with given operational parameters.

2. *The Cycle*

In this design, the reciprocation of the piston and displacer is sinusoidal, with the displacer motion leading that of the piston by about 70°. The p-v (pressure vs. volume) diagram for an ideal (isothermal) cycle is shown in figure 1b, the approximate position of the piston and displacer at the transitions being noted in figure 1a. The variations in the volume of the expansion space and the volume of the compression space due to the motions are shown in figure 1c.

For the ideal cycle, the cold production Q (in Watts) is proportional to the operating frequency (in radians/second), the amplitude of the displacer (in meters), the amplitude of the piston (in meters), the mean pressure (in Newtons/square meter), the surface area of the displacer (in square meters) and the sine of phase angle between piston and displacer motions. Similarly, the mechanical power P which must be provided to the cycle (in Watts) is proportional to the operating frequency (in radians/second), the amplitude of the displacer (in meters), the amplitude of the piston (in meters), the mean pressure (in Newtons/square meter), the surface area of the piston (in square meters), and the sine of phase angle between piston and displacer motions [1].

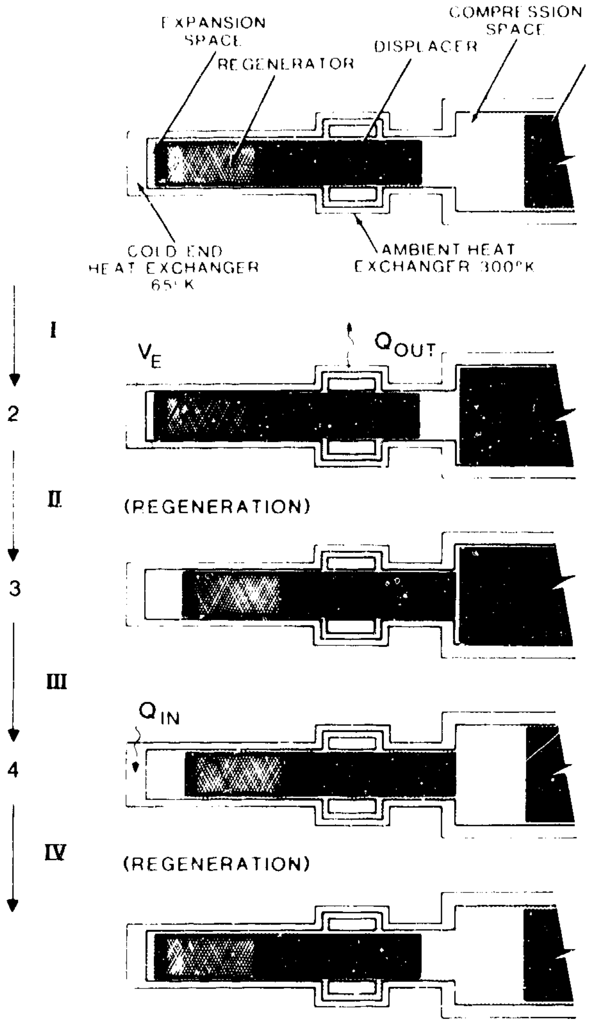
EXPANSION SPACE
REGENERATOR
DISPLACER
COMPRESSION SPACE
PISTON
COLD END HEAT EXCHANGER 65°K
AMBIENT HEAT EXCHANGER 300°K
I
2
II
3
III
4
IV
V_E
Q_{OUT}
(REGENERATION)
Q_{IN}
(REGENERATION)

(a) Phases.

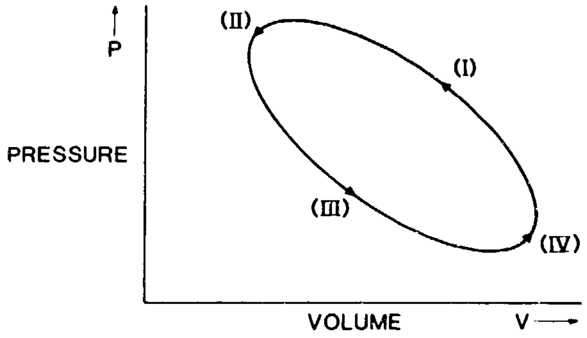

(b) p-v Diagram.

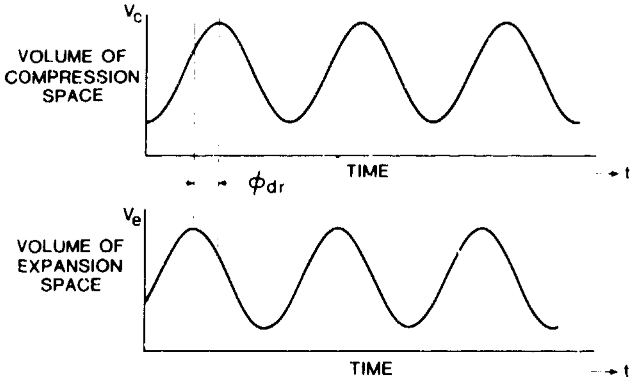

(c) Volume Variations.

Figure 1. Phases, p-v diagram and volume variations for ideal Stirling cycle.

For the ideal Stirling cycle, the thermodynamic efficiency is,

$$\eta = \frac{Q}{P} = \frac{Te}{Tc - Te} \tag{1}$$

where, Te = temp. of expansion space (cold finger) (°K)
Tc = temp. compression space (ambient heat exchanger) (°K)

and equals that of the Carnot cycle.

The actual efficiency of a refrigerator is less than Carnot because losses in the cycle cause the input power to increase or the cold production to decrease. Factors which directly effect the input power include mechanical loss (friction) in the drive, flow losses, and adiabatic losses (i.e. where the refrigeration process differs from the isothermal ideal). Factors which reduce the cold production include flow, insulation and conduction losses, as well as losses due to the non-ideal nature of the regenerator and heat exchangers.

The regenerator, often called the heart of a Stirling refrigerator, stores thermal energy during one half cycle to release it during the other half and thereby increase efficiercy. A temperature gradient is established along the regenerator in the direction of flow, which allows the gas to be cyclically cooled down and heated. In an ideal regenerator (perfect heat transfer), the process is perfectly reversible. Also the pressure drop across an ideal regenerator is zero. In an ideal heat exchanger, the temperature of the gas is constant, exactly equal to the temperature of the heat exchanger walls, regardless of the amount of heat being transferred. All real regenerators and heat exchangers differ from the ideal to some extent.

3. *Description of the refrigerator*

The design philosophy for this refrigerator was impelled by the importance of extending maintenance-free lifetime. The design was motivated by the common failure modes of existing refrigerators. In general, the useful life of a conventional Stirling refrigerator is limited by two major factors: wear and outgassing. Wear is present in most mechanical devices which have moving parts. Bearings and pressure seals wear out; mechanical rubbing and the associated friction generate potentially harmful particles. The other problem is the outgassing products (impurities) of organic materials such as lubricants and seals in the refrigerator working spaces. These impurities are "gettered" (attracted) by the low temperature regions in the machine and eventually clog critical passages. Since both surface wear and the presence of impurities result in thermal degradation, the simplest and perhaps the only realistic approach to longevity is to eliminate both.

The Philips refrigerator is designed to produce 5 Watts of refrigeration at 65°K for 5 years or longer. Four major features of the unit led to the long life achieved: a purely linear drive with linear motors and an electronic control system, electro-magnetic bearings, clearance seals, and an all metal-ceramic working-gas envelope. The synergistic combination of these four features has eliminated wear and impurities. The details of the refrigerator design are described in reference [2].

A cross sectional view of the linear drive and the linear motors is shown in figure 2. The drive produces the required linear piston and displacer motions directly, i.e. without the use of a crankshaft or linkages. The motors are of the moving-magnet type, which have the advantage that no flexing power leads are required. The directly coupled drive eliminates the mechanical drive losses associated with conventional refrigeration devices. Direct coupling requires an axial control system to maintain the proper piston and displacer amplitudes and the phase relationship dictated by the Stirling cycle. The capabilities and versatility of this control are important aspects of this novel refrigerator design and form the system basis which makes this type of testing possible. This feature is discussed in more detail in paragraph 5.0.

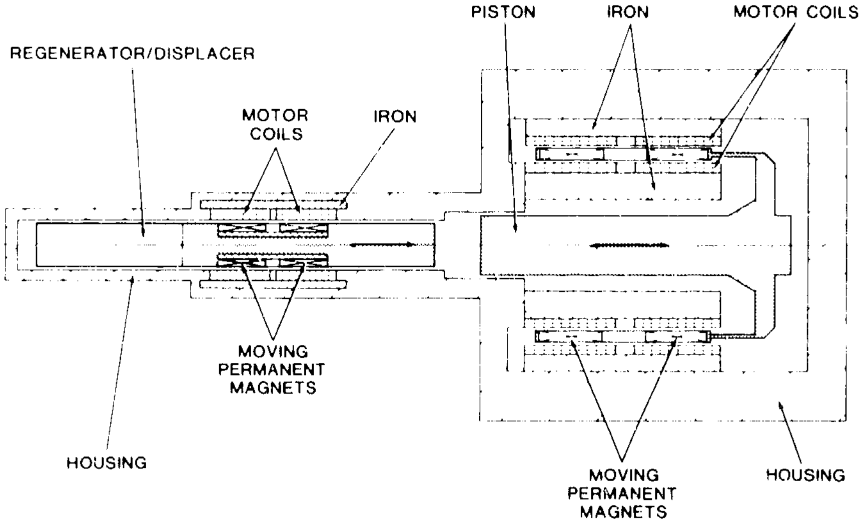

Figure 2. Cross-sectional view of linear drive showing displacer and piston motors.

A photograph of the refrigerator is shown in figure 3. The displacer section is at the left; cold is produced at the far left tip (cold ginger). The refrigerator is a single-stage expansion Stirling design (i.e., only one cryogenic temperature, 65°K, is produced) and has a constant diameter for the displacer bore. The piston subassembly together with a passive (spring/msss) countermass is on the right.

The moving displacer contains the regenerator, a moving-magnet linear motor, and a non-contacting element for the axial position transducer. The regenerator is fabricated from layers of a phosphor bronze wire mesh which has a high thermal capacity and remains porous to the reciprocating flow of the helium gas working fluid. The electro-magnetic bearings which support the displacer also form the clearance seals, forcing the gas through the regenerator and through the ambient heat exchanger. The heat exchanger is maintained at ambient temperature by a water jacket; its surface also permits the attachment of a heat pipe instead of the jacket. A vacuum Dewar (now shown) lined with super insulation (multi-layers of foil and mesh) thermally insulates the cold finger.

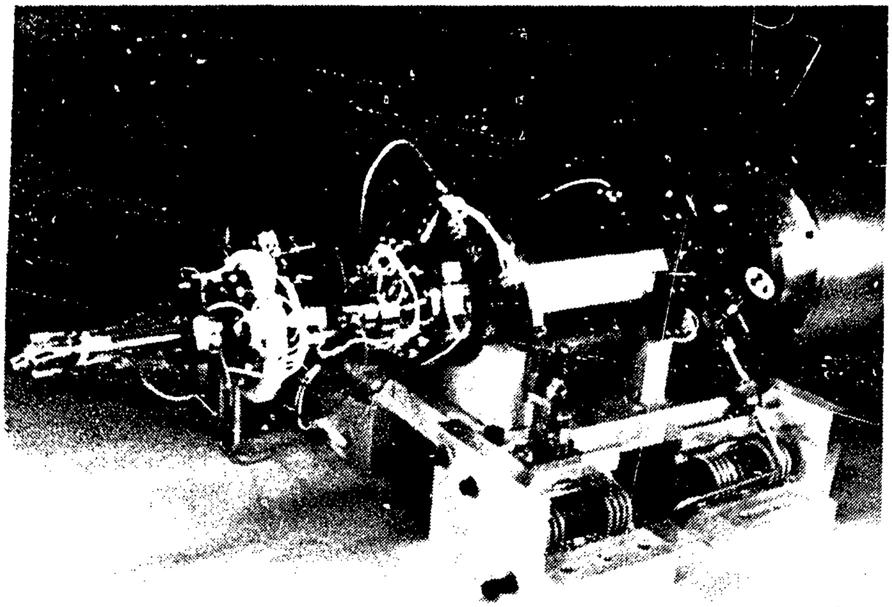

Figure 3. Photograph of refrigerator.

The piston is directly coupled to its moving-magnet linear motor and to a non-contacting element for its axial position transducer. The electro-magnetic bearing near the compression space forms a clearance seal to the compression pressure; the bearing at the rear of the piston is used for support but forms no seal.

4. *Overview of the Testing*

The parameters of interest are characteristic variables of the Stirling cycle. For simplicity, in each test one parameter was varied while the others were held constant at the nominal values shown in the following table.

By varying only one parameter at a time, the effect of the one parameter on the output variables can be easily observed. This test differed slightly with the one performed at 1000 hours, in which the nominal values of the parameters differed between tests and were chosen so that the parameter which was varied could have a wide excursion. It is felt that the present test procedure is more reasonable from a user standpoint. The difference in the tests produced small differences in the measured output but did not change the trends in the data.

Table 1. Nominal operating parameters

Piston Amplitude = 7.0 mm.
Displacer Amplitude = 3.0 mm.
Piston/Displacer Phase = 67 deg.
Mean Pressure = 240 psi.
Water Inlet Temperatures
  Ambient Heat Exchanger = 11°C
  Piston Case = 16°C

Given the limited scope of the testing, some care must be exercised in the interpretation of results. "Optimal" performance with only one variable changing does not mean that a better operating condition does not exist. The operating parameters are not independent in general. This fact also means that if two parameters are varied, the net result on performance may not the sum of the results of varying each one independently.

A schematic representation of the refrigerator test setup is shown in figure 4. Three pieces of laboratory equipment are required for normal operation: two water coolers and a vacuum station. The water cooler for the ambient heat exchanger removes the heat of compression and the ohmic loss of the displacer motor. The water cooler for the piston housing removes only the ohmic loss from the piston motor. The vacuum station produces the thermally insulating vacuum in

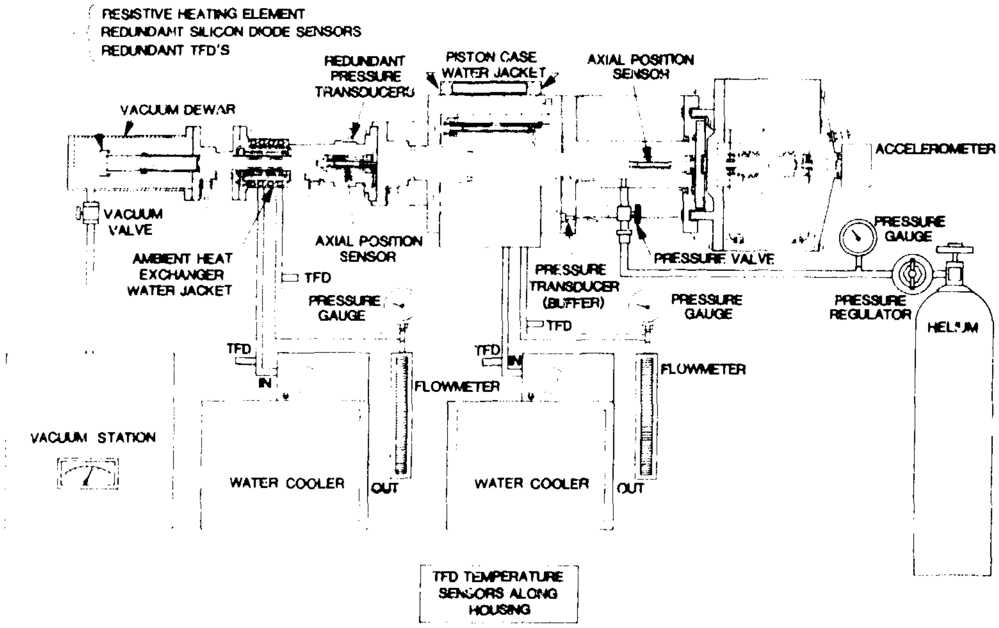
RESISTIVE HEATING ELEMENT
REDUNDANT SILICON DIODE SENSORS
REDUNDANT TFD'S
REDUNDANT PRESSURE TRANSDUCERS
PISTON CASE WATER JACKET
AXIAL POSITION SENSOR
VACUUM DEWAR
ACCELEROMETER
VACUUM VALVE
AXIAL POSITION SENSOR
PRESSURE GAUGE
AMBIENT HEAT EXCHANGER WATER JACKET
TFD
PRESSURE VALVE
PRESSURE TRANSDUCER (BUFFER)
PRESSURE GAUGE
PRESSURE GAUGE
PRESSURE REGULATOR
TFD
HELIUM
TFD
TFD
IN
IN
FLOWMETER
FLOWMETER
VACUUM STATION
WATER COOLER
OUT
WATER COOLER
OUT
TFD TEMPERATURE SENSORS ALONG HOUSING

Figure 4. Schematic representation of refrigerator under test.

the Dewar. The refrigerator was instrumented with transducers to measure temperature, pressure, radial and axial position, coolant flow, and case acceleration [3].

The approach for each test followed a similar procedure. The temperature of the cold tip was first reduced to the nominal 65°K with no heat load applied. This required supporting the piston and displacer with their electro-magnetic bearings, engaging the safety interlock system, and reciprocating the piston and the displacer.

Once the desired cold temperature (65°K) was reached, a resistive heater (load) on the cold tip was turned on, a given parameter was varied and its effect on the other system parameters was measured. The resistive heater was adjusted to maintain the cold temperature at 65°K. The signals measured were either slow-varying dc (e.g., cold temperature) or primarily single-frequency ac (at the operating frequency) with a large amount of noise and higher harmonics (e.g., piston motor current). To measure the former, a dc voltmeter was employed, and the measured quantity was considered stable when no notable change was observed for about 5 min. The latter was measured with an instrument employing a standard signal processing technique, namely, heterodyning with the input reference oscillator used for locking. The refrigerator typically required one hour to settle between data points. In this paper, db is defined as 20 log (quantity). Measured data points are noted; data for the original test (after 1000 hours) is noted by open squares and, data for the present test (after an additional 20,000 hours) is noted by solid circles. The curves in the figures are computer-generated using either a linear or polynomial least-squares routine. Curves for the original data are solid lines; curves for the new data are dashed.

Several second order effects could have caused the refrigerator to degrade over life. First, permanent magnets, of which the motors are constructed, degrade over time. For this application. Samarium-Cobalt ($SmCo_5$) magnets were chosen because they tend to degrade very little. During fabrication, the magnets were "stabilized" with a reverse magnetic field and elevated temperature. Thus, magnet degradation was expected to be small. Also, since the piston and displacer motions are exactly controlled by a control system with a large loop gain (see section 5 below), small changes in the motors are not expected to greatly change the cold production or the cold temperature. (Changes such as magnet strength, which effect motor efficiency, however, may raise the input power required to produce a given amount of cold.) Second, some settling may have occurred in the mesh that forms the regenerator. Such settling may increase conduction losses and flow losses. Settling may also reduce flow losses. Thus, the effect of settling on performance is not clear. Finally, much of the equipment peripheral to the refrigerator has changed over the last three years. The seals, instrumentation and mechanical pump in the vacuum station had to be replaced, leading to higher vacuum in the Dewar and thus lower insulation loss. The water cooler for the ambient heat exchanger had to be replaced and water has to be periodically added to the cooler to make up for evaporation. Thus, both the flow and heat conductivity of the water may have changed from the initial test. The temperature of the water at the inlet of the heat exchanger is the same, however, since this is set by a control on the cooler.

5. Axial control system

As an aid to understanding how parameters can be varied during refrigerator use, the operation and accuracy of the axial control system will be discussed next. A block diagram of the control system is shown in figure 5a. The piston amplitude, displacer amplitude, frequency, and piston/displacer phase angle are set with dc voltages which are adjusted at the control panel. The frequency and phase control electronics employ local feedback loops to maintain the accuracy of the reference signals for the displacer and piston closed loop position servomechanisms in spite of component drifts. The reference signal to the piston lags the signal to the displacer, producing the desired piston/displacer phase angle. The two closed loop position servomechanisms then control the motions of the piston and displacer with a high degree of accuracy and low harmonic content.

Although the closed-loop position servomechanisms for the piston and displacer look similar in Figure 5a, they vary considerably in frequency response because of the extreme differences in the frequency response of their motor and system dynamics. The displacer, as the measured dynamics of figure 5b indicates, is nearly a pure inertial load. (The additional rolloff which begins at 400 Hz is from filtering in the axial position sensor). Principally, the force produced by the motor serves only to accelerate and decelerate the mass. Since the motion is sinusoidal, with the displacer returning to its axial center position after each half cycle, there is no net displacement and no work is done. The mechanical output power is reactive (power factor of 0), and therefore, the electrical input power to the motor is only the ohmic loss dissipated in having to produce the required force. Ignoring the inductive reactance, therefore,

$$Pd = Id^2 \ Rd = \omega^4 \ x^2 \ Rd / Kd^2 \qquad (2)$$

where Pd = average electrical input power to displacer motor (W)
Id = current in displacer motor (A)
Rd = motor armature resistance (Ω)
ω = operating frequency (rad/sec)
x = peak displacement amplitude (m)
Kd = motor force constant (N/A) (i.e. Force = $Kd\ Id$)

The piston, on the other hand, is designed to resonate on the gas spring of compression (the effective "spring" of gas being compressed in a closed cylinder) which leads to highly efficient electromechanical operation. Its motor and system dynamics, as shown in the measured dynamics in figure 5b, has a spring-mass resonance characteristic (along with the position sensor filtering). The reactive inertial force is balanced by the reactive gas spring force, and the motor only produces a real (as opposed to reactive) force term which supplies the required mechanical input power to the thermodynamics (power factor of 1). The electrical input power to this motor can thus be separated into two terms: one resulting from supplying the real mechanical input power to the thermodynamics and one relating to the balanced reactive inertial power and gas spring power. For normal operation, the piston is in resonance and the net reactive power is zero; however, for the

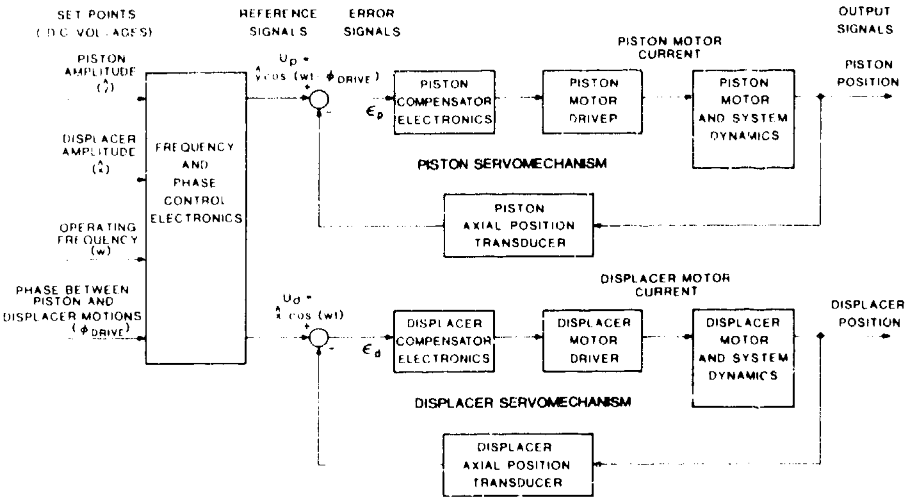
SET POINTS
(D.C. VOLTAGES)
PISTON AMPLITUDE ($\hat{y}$)
DISPLACER AMPLITUDE ($\hat{x}$)
OPERATING FREQUENCY (w)
PHASE BETWEEN PISTON AND DISPLACER MOTIONS (ϕ_{DRIVE})
FREQUENCY AND PHASE CONTROL ELECTRONICS
REFERENCE SIGNALS
ERROR SIGNALS
$U_p = \hat{y} \cos (wt - \phi_{DRIVE})$
$U_d = \hat{x} \cos (wt)$
+
-
ϵ_p
ϵ_d
PISTON COMPENSATOR ELECTRONICS
PISTON MOTOR DRIVER
PISTON MOTOR CURRENT
PISTON MOTOR AND SYSTEM DYNAMICS
PISTON SERVOMECHANISM
PISTON AXIAL POSITION TRANSDUCER
OUTPUT SIGNALS
PISTON POSITION
DISPLACER COMPENSATOR ELECTRONICS
DISPLACER MOTOR DRIVER
DISPLACER MOTOR CURRENT
DISPLACER MOTOR AND SYSTEM DYNAMICS
DISPLACER SERVOMECHANISM
DISPLACER AXIAL POSITION TRANSDUCER
DISPLACER POSITION

a. Block diagram.

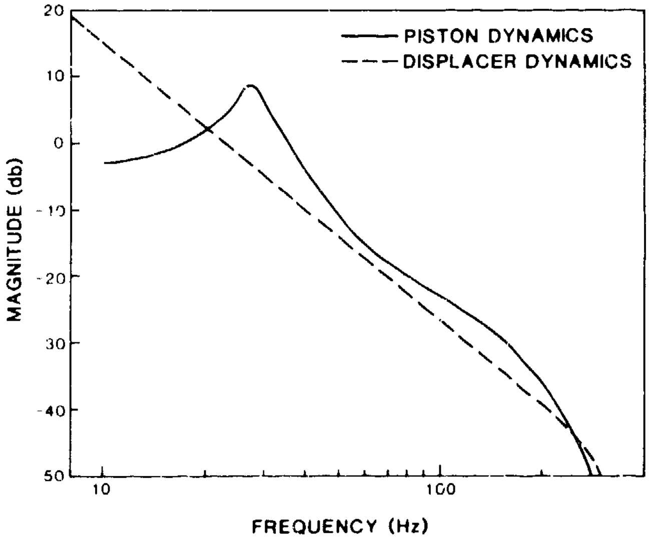

b. Frequency responses - displacer and piston motor and system dynamics.

Figure 5. Axial control system.

parametric tests discussed here, the piston does come out of resonance slightly. It should be noted that the piston operates at its resonant point with high accuracy (small error in the control loop) because of the high open-loop gain at that frequency (see Ref. [4]).

The dynamics of a gas spring are different from those of a mechanical spring in two important respects. First, the damping in a gas spring is generally higher than in a mechanical spring. Thus, power is dissipated at resonance which must be supplied by the linear motor, and the quality factor (the spring q) of the system is low. Second, because of gas properties, flow losses and leakage past the compression seal, the stiffness of the gas spring is a function of frequency and is slightly nonlinear (i.e. it has some higher harmonic components). These disadvantages of the gas spring are outweighed by the advantage of having a spring for resonance with no mechanical contact, no danger of fatigue failure and no possibility of fracture.

6. *Test results*

6.1 *Operating frequency*

Figure 6 shows the variation of applied load power (cold production) and figure 7, the variation of electrical input power to the motors, with changes in the operating frequency. Several effects contribute to the shape of these curves. First, it should be realized that both the ideal cold production and the ideal mechanical input power to the Stirling cycle vary linearly with operating frequency (since both are proportional to the number of times that the p-v curve is traversed per unit time). Secondly, many losses such as those due to flow and imperfect regeneration are functions of gas velocity and therefore of operating frequency. Some losses, such as that caused by the fluid friction of the flowing gas or that resulting from the temperature oscillation of local sections of the regenerator package over a cycle (since the transfer rate between the gas and the regenerator is finite), increase with increasing frequency. Others, such as the clearance seal leakage decrease with increasing frequency. Finally, as discussed, the nature of the displacer and piston motor and system dynamics means that the magnitude and phase of the input power for each are functions of the operating frequency.

For the small range of frequencies considered, the motor and system dynamics produce by far the most significant effect. The displacer power increases as the fourth power of the operating frequency, as noted in Equation 2 and the piston power has a resonant mass-spring characteristic (with some nonlinear effects produced by the gas spring).

The variation of piston and displacer motor force with operating frequency are shown in figure 8 and 9, respectively. The displacer motor force varies approximately as the square of the operating frequency as would be true of the purely inertial system, and the piston motor force exhibits the spring-mass characteristic (minimum force at resonance with a slight nonlinearity). From this, it is apparent that the system dynamics dominate the response and any change in the losses with frequency is not as significant. There was little change between the data taken after 1000 hours and that taken after the additional 20,000 hours. The strong dominance of the piston system dynamics on this test and the fact that the

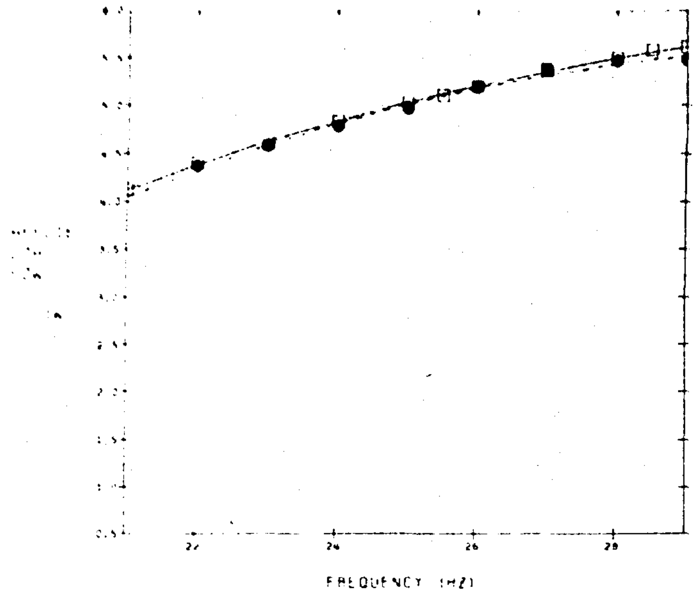

Figure 6. Applied load power vs. operating frequency.

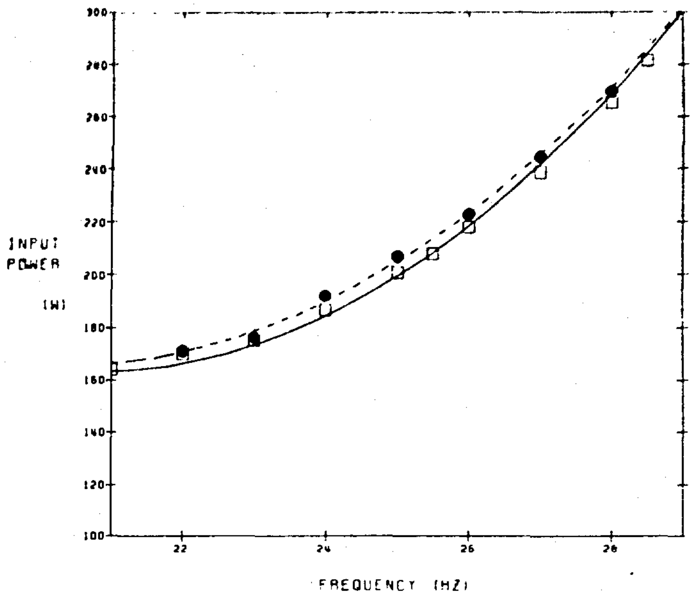

Figure 7. Electrical input power to motors vs. operating frequency.

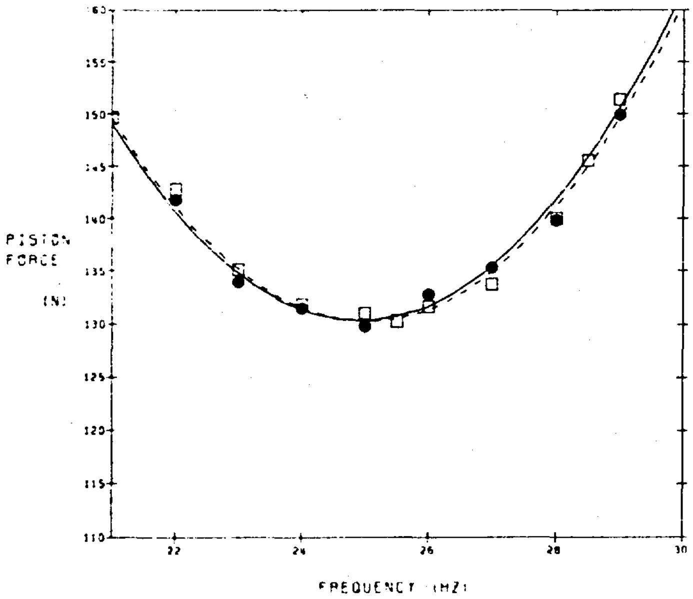

Figure 8. Piston motor force vs. operating frequency.

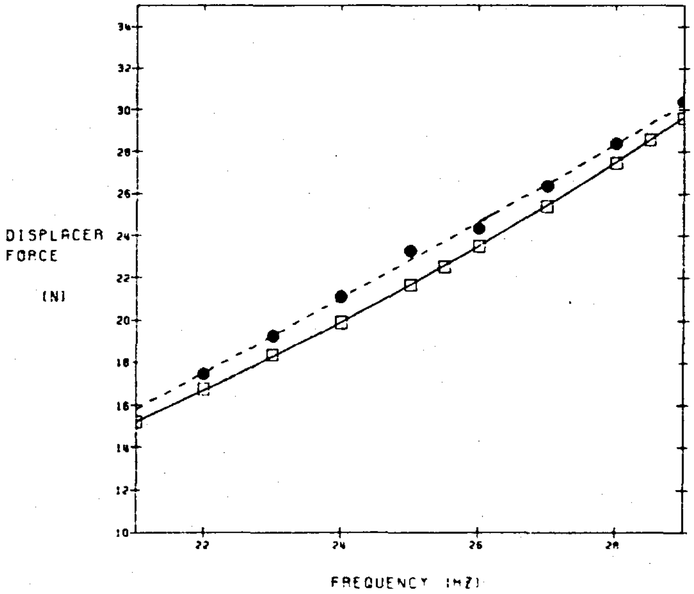

Figure 9. Displacer motor force vs. operating frequency.

piston dynamics has changed little over life, is responsible for this. Also, a comparison between table 1 and Appendix A of [1] shows that the nominal operating parameters for the two tests were nearly identical.

The displacer motor force, in figure 9, is measured by measuring the displacer motor current and using the measured force constant (Kd in Newtons / Amp) from tests of the displacer motor before the refrigerator was first assembled [4]. There are several reasons why the displacer motor force in the test after 20,000 hours may be greater than in the test after 1000 hours. The force constant may be reduced (meaning that more current is required to produce the same force). This can occur through aging of the permanent magnets or because the magnet strength has been reduced by the saturating magnetic fields generated by the coil in this motor [3]. The displacer motor section of this refrigerator, under the ambient heat exchanger, also experiences the highest temperatures.) Also, settling of the regenerator mesh resulting in higher flow losses would increase the motor force. Since the refrigerator has never been disassembled, the exact reason for the higher force is not known. It should be noted that because of the action of the control system, the effect of changes in the displacer motor are small in terms of cold production.

Some caution should be exercised in interpreting this data. Since this is a test in which only one parameter is varied, conclusions can not be drawn about what is the best frequency at which to operate the refrigerator. Both the mean charge pressure and the piston/displacer phase affect the resonant frequency of the gas spring to some extent. The "optimum" operating frequency must take all such effects into account. Such multi-parameter tests are beyond the scope of this paper.

6.2 Displacer amplitude

The variations of applied load power (cold production) and electrical input power to the piston and displacer motors with displacer amplitude are shown in figures 10 and 11, respectively. For the ideal cycle, the applied load power is proportional to displacer amplitude (discussion in section 5). Several losses, however, are functions of displacer amplitude; the most notable of these associated with the regenerator, referred to as shuttle loss. As the displacer moves, the regenerator passes over different portions of the housing. As a result, there is a mismatch between the temperature gradient along the housing wall and the temperature gradient along the regenerator, and the mismatch increases for increasing amplitudes of oscillation. This mismatch results in heat transfer between the displacer and the housing walls and thus a loss.

Another important effect in this test and in the one which follows relates to the changes in the refrigerator dead volume. Dead volume is the designation given to those regions in the working space of the refrigerator which do not change in volume as the displacer and piston move (i.e., do not participate in the thermodynamic cycle (fig. 12)). Dead volume includes the heat exchanger space, connecting passages, and the unfilled space in the regenerator. Relevant to this test, dead volume also includes those regions in the expansion and compression space which are not swept by the peak amplitude of the displacer motion.

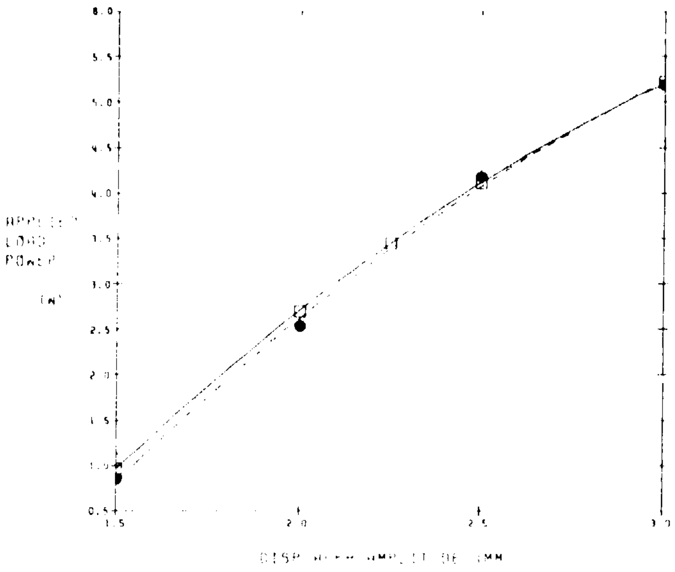

Figure 10. Applied load power vs. displacer amplitude.

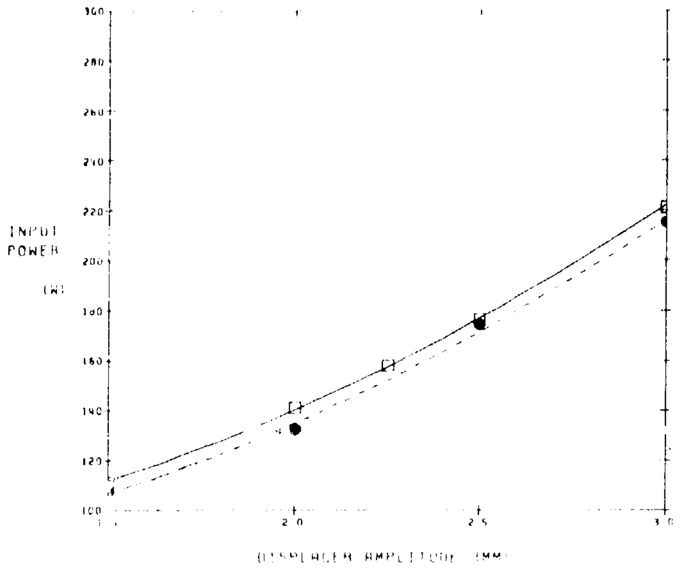

Figure 11. Electrical input power to motors vs. displacer amplitude.

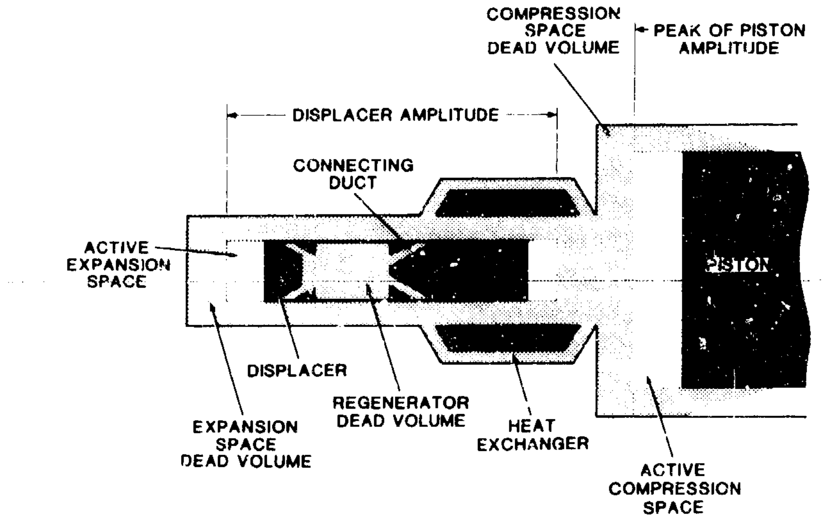
COMPRESSION SPACE DEAD VOLUME
PEAK OF PISTON AMPLITUDE
DISPLACER AMPLITUDE
CONNECTING DUCT
ACTIVE EXPANSION SPACE
PISTON
DISPLACER
REGENERATOR DEAD VOLUME
HEAT EXCHANGER
EXPANSION SPACE DEAD VOLUME
ACTIVE COMPRESSION SPACE

Figure 12. Schematic of dead volume (shaded). (Clearances are out of proportion for clarity.)

A discussion of dead volume is given in Appendix B of Reference [3]. For this paper, several comments will suffice. In general, dead volume reduces the cold production of a refrigerator. Often, the dead volume also reduces the required mechanical input power so that the refrigerator efficiency remains roughly constant. The magnitude of the effect of a given region of dead volume on the cold production or mechanical input power depends on the absolute temperature of that region. The colder the region, the greater the effect.

The electrical input power to the piston motor versus displacer amplitude is shown in figure 13. As discussed above, the input power to the piston motor has two terms: one related to gas spring resonance and one related to producing the thermodynamic work. Since the displacer amplitude has little effect upon the gas spring resonance, the electrical input power to the piston motor is only that which is required to do the thermodynamic work. For the ideal cycle, the mechanical input power required by the thermodynamics is proportional to displacer amplitude. The piston must also supply the work required to overcome the shuttle loss. Further, from the above discussions about dead volume, the mechanical input power should also be inversely proportional to the displacer amplitude (i.e. the mechanical input powerpower required from the piston should decrease as the displacer amplitude increases because the dead volume decreases and this effect is independent of the mechanical input power required to produce cold). Thus, variations in the displacer amplitude produce opposing effects. In figure 13, the electrical input power to the piston motor varies approximately as the square of displacer amplitude. The test data after 20,000 hours shows slightly more efficient piston operation than that after 1000 hours. Since the nominal operating parameters between the two tests are similar, it is believed that the improved efficiency comes from the changes in the external equipment - the improved vacuum station and water cooler.

Consider now the electrical input power to the displacer motor versus displacer motor versus displacer amplitude in figure 14. Since the displacer is an

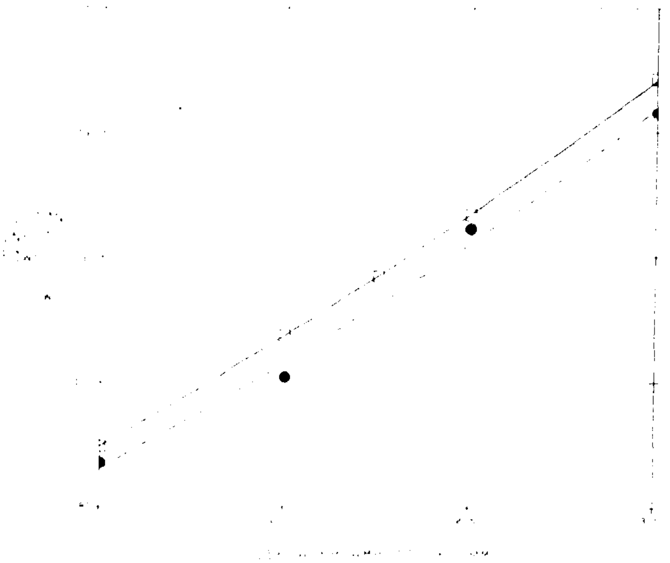

Figure 13. Electrical input power to piston motor vs. displacer amplitude.

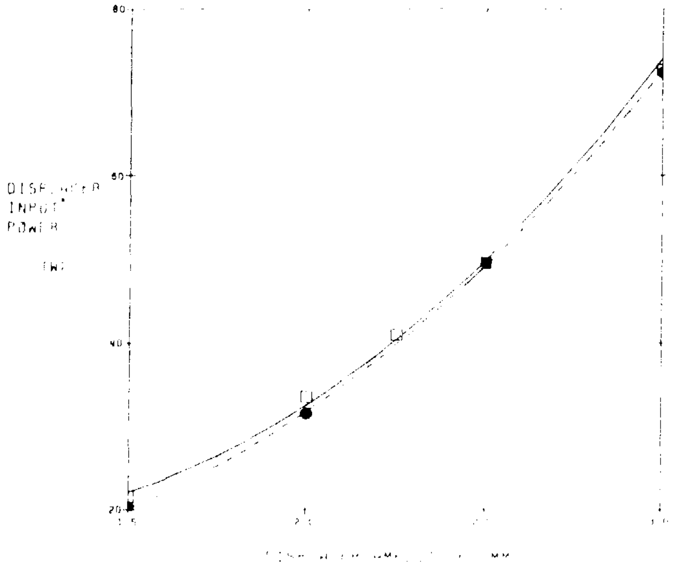

Figure 14. Electrical input power to displacer motor vs. displacer amplitude.

inertial load, the electrical input power is expected to vary as the square of the displacer amplitude (Equation 2), as observed.

6.3 Piston Amplitude

The change in applied load power and in electrical input power to the piston and displacer motors with piston amplitude is shown in Figures 15 and 16, respectively. For the ideal cycle, the applied load power and electrical input power are proportional to piston amplitude. This characteristic was indeed observed. Flow losses and the effects of dead volume both change with piston amplitude tending to cancel. The flow losses increase with increasing amplitude because the peak oscillating pressure and volumetric flow rate increase as more volume is displaced by the piston. The dead volume decreases by the amount above the piston in the compression space as the piston amplitude increases (fig. 12 above). As discussed, this dead volume effect is negligible because the volume is at the temperature of the ambient heat exchanger (warm).

Again, comparing the data taken after 1000 and 20,000 hours, it should be noted that the variation in load power with piston amplitude changed slightly, and that the input power required to produce this load was reduced to a greater extent. There were minor differences in the nominal operating points between the two tests, but the increased efficiency occurred, presumably, because of improvements in the external equipment.

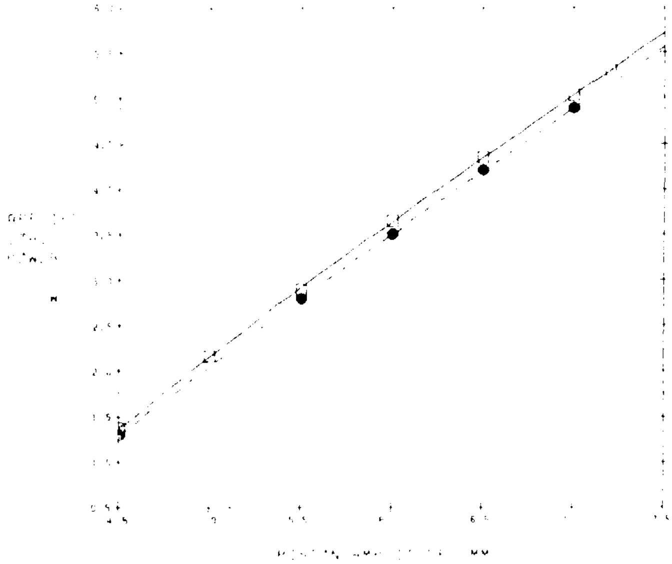

Figure 15. Applied load power vs. piston amplitude.

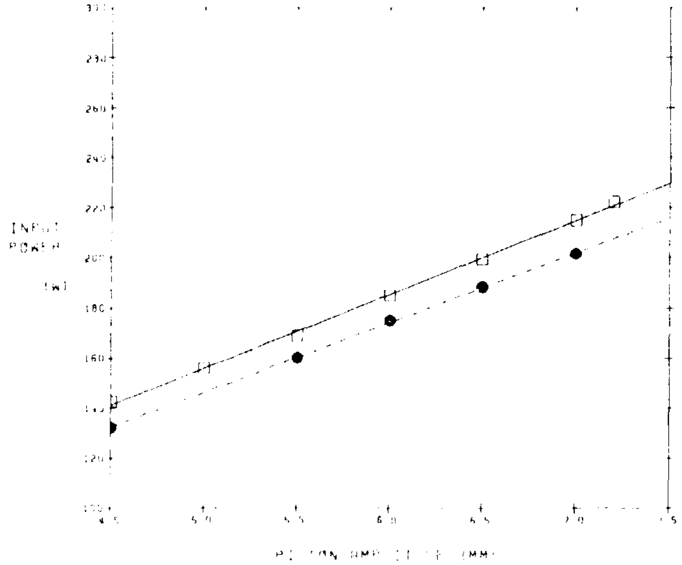

Figure 16. Electrical input power to motors vs. piston amplitude.

6.4 Piston/Displacer Phase

Figure 17 shows the variation in applied load power and figure 18, the variation of electrical input power to the piston and displacer motors as a function of piston/displacer phase. For the ideal cycle, the load power and electrical input power should vary as the sine of the phase. This is the approximate shape of the curves in the figures. The piston/displacer phase also influences flow losses and piston gas spring resonance to a lesser degree. These effects are more easily observed in the variations in the piston and displacer motor force shown in figures 19 and 20, respectively. From the figures, it should be noted that the variations in force are less than ± 10%.

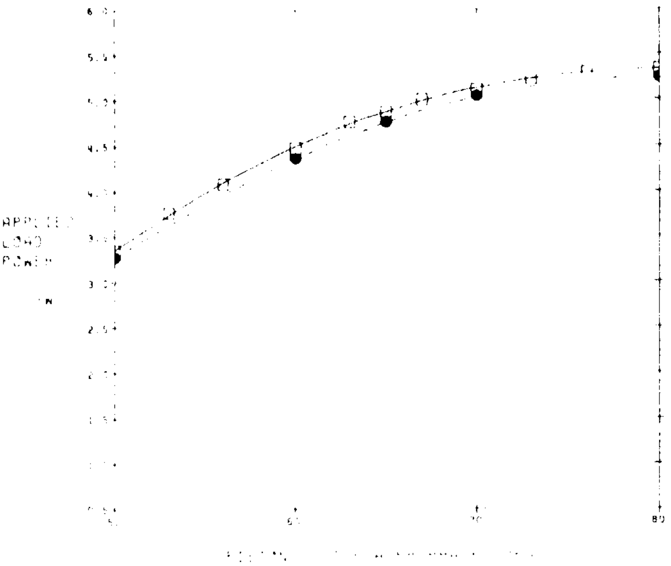

Figure 17. Applied load power vs. piston/displacer phase

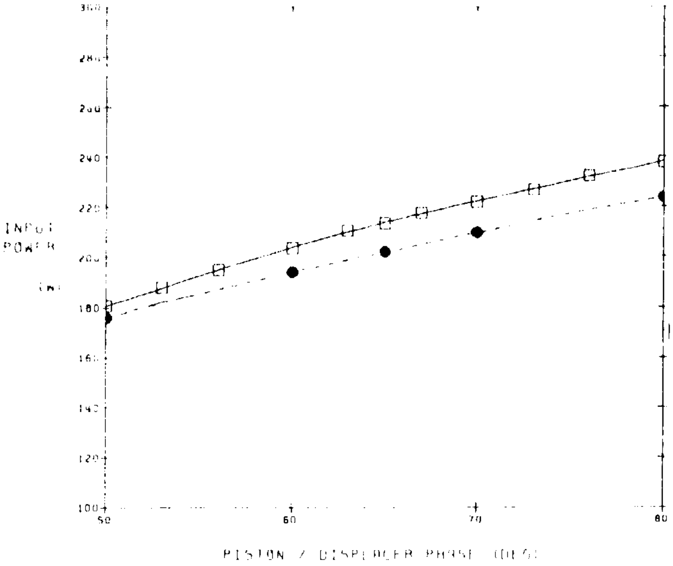

Figure 18. Electrical input power to motors vs. piston/displacer phase.

Some care must be taken in comparing the data taken after 1000 and 20,000 hours of operation. The variation of load power and input power with piston/displacer phase are somewhat reduced. However, in comparing the nominal values in table 1 above and Appendix A of [1], it is noticed that the piston stroke in the 20,000 hour data is much less than that in the 1000 hour data. This presumably caused the reduction. In general, however, the efficiency of the refrigerator increased, which can be observed in the graph of total efficiency (cold production/input power) versus phase shown in figure 21. The peak in efficiency before the 90° piston/displacer phase predicted by the ideal theory occurs because of the effect of phase on flow losses and on the resonance of the piston gas spring. The increase in displacer motor force shown in figure 20 is presumably due to the effects noted in the frequency parametric test.

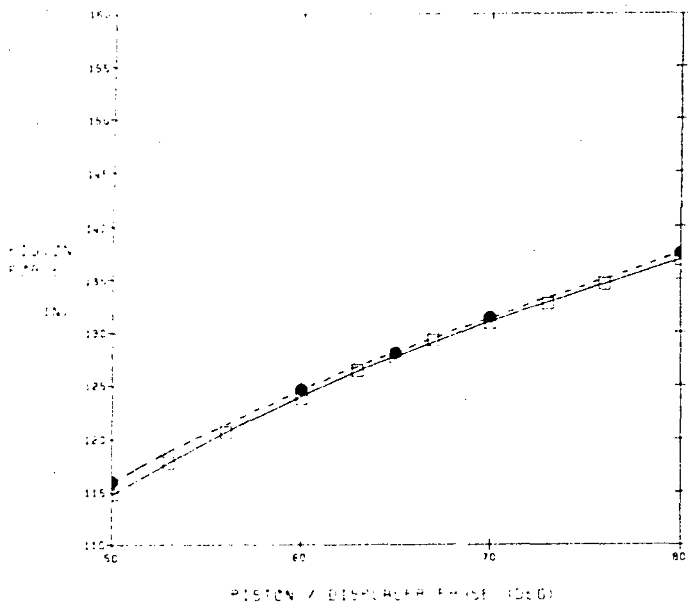

Figure 19. Piston motor force vs. piston/displacer phase

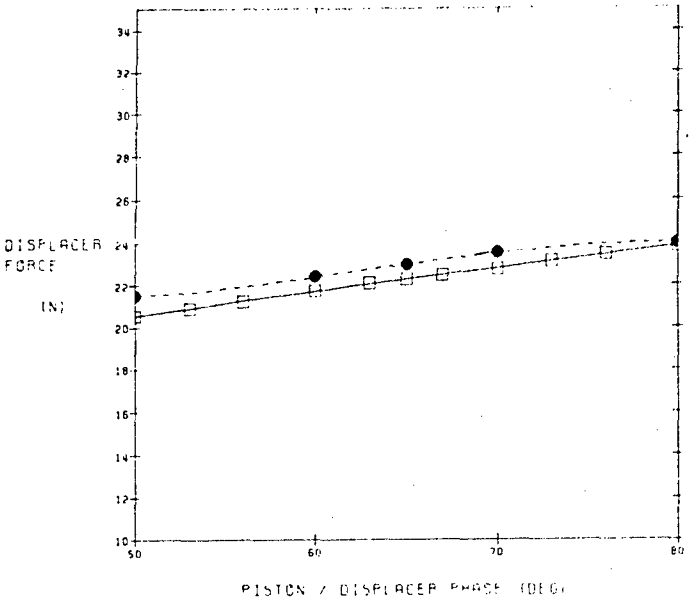

Figure 20. Displacer motor force vs. piston/displacer phase.

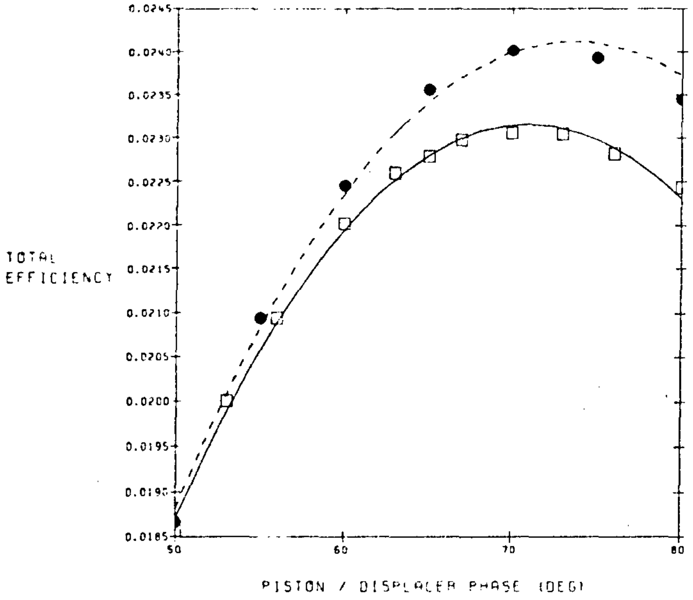

Figure 21. Overall efficiency vs. piston/displacer phase.

7. *Performance versus time*

The refrigerator continued to operate after this parametric data was taken. On September 22, 1986, the refrigerator exceeded 23,000 hours of operation at the nominal operating point of 65°K with a cold production of 5 Watts and continues to operate without problems. During this time, the refrigerator was stopped and restarted over 400 times. The cold temperature (along with several other operational parameters) is being measured with a digital data acquisition system. Measurements are taken every 15 minutes using a sampling frequency of 1 kHz. The samples are averaged over 2 seconds to reduce noise. As of this date, no temperature degradation other than two instances noted below, has been observed to the accuracy of the silicon diode sensors (0.1°K). With the constant cold production, the cold temperature is also measured to be stable within ± 0.2 K (i.e., temperature fluctuations including noise induced by the silicon diode thermometer are also about 0.1°K). During this period, the refrigerator has never had to be disassembled for maintenance or inspection.

The electro-magnetic bearings along with their radial position sensors are left on continually even if the refrigerator is not operating or is undergoing tests. As of September 22, 1986, the bearings have logged over 33,000 hours of operation.

On two distinct occasions, the refrigerator operated for a continuous run of over 1000 hours (approximately 1 1/2 months). In each case, after 1100 hours, the cold temperature slowly rose 1 degree (to 66°K) and leveled off. It is believed that this effect is due to whatever small impurities may be contained in the refrigerator eventually becoming attracted to the regenerator. In each case, after the refrigerator was allowed to warm up, operation returned to normal.

A small helium leak (approximately 1 psi per day) has developed in one of the housing flanges. A technique to weld the flanges shut, which is proposed for the final version of the refrigerator and which was demonstrated in a test fixture, was not used in this refrigerator. The helium loss is presently being made up with a helium bottle.

The electronics which control and drive the refrigerator use only commercial parts (instead of space qualified parts) and no redundancy was attempted. Several times during the life test, a commercial electronic part failed. In all cases, the safety interlock system responded correctly and safely shut down the machine. The failed part was replaced and the life test continued. The final version of this refrigerator for actual spaceborne employment will use space qualified, redundant electronics.

8. Conclusions

A novel feature of this refrigerator, namely, full electronic control of the motion of its moving parts, was utilized to characterize the capabilities of the refrigerator under parametric changes. The characterization is useful both for designers of the next generation of the refrigerator and for potential users. Designers have both an indication of the accuracy of their "optimal" design point and a determination of the tolerance of the design point to changes in operational parameters. Potential users have an indication of the operation of the refrigerator under off-design conditions which will broaden the range of potential applications.

In comparing the data for tests run after 1000 hours of operation and after 20,000 hours of operation, it is noted that the variation of output (applied load power) has changed only slightly. This is a result of the accuracy of the control system which maintains operating parameter levels in spite of minor changes in the internal dynamics. Over life, however, the refrigerator displacer motor appears to have changed slightly, becoming slightly less efficient. This is observed in the slight differences in the variations in displacer motor force. In general, however, the refrigerator appears to be slightly more efficient, as noted in the variation of input power with various parameters (except frequency where the effect is presumably masked by the more dominating effect of system dynamics). It is believed that this is most probably due to changes in the equipment external to the refrigerator (the improved vacuum station and water cooler).

Some care must be taken in the interpretation of results. In each test only one parameter was varied and its effect was measured. The data shows the quantitative influence of the parameter on the operation of the refrigerator. In general, however, the effect of each parameter is not independent, and thus the combination of two test results will not show the combined effect of varying the two parameters. This also means that more "optimal" off-design operating points than those shown in this paper generally exist. These off-design points are achieved by varying more than one parameter, depending on the operating point desired. Also, it should be recalled in comparing the two sets of data, that the nominal operating point between the two tests differed slightly.

In spite of the limited scope of this work, the versatility of this refrigerator must be appreciated both as a tool for understanding the Stirling cycle and as a general instrument for a wide variety of cryogenic applications. The capability of having parameters electronically controlled and able to be changed in operation, which made this study possible, sets this design apart from refrigerators built in the past. The small amount that performance degraded after an additional 20,000 hours of operation, even to off design conditions, demonstrates this refrigerator to be a reliable long life machine.

This work was supported by the NASA Goddard Space Flight Center (contract no. NAS5-25172).

9. References

[1] Parametric Testing of a Linearly Driven Stirling Cryogenic Refrigerator. by F. R. Stolfi and A. Daniels, Proceedings of the Third Biennial Conference on Refrigeration for Cryogenic Sensors and Electronic Systems, Boulder, Co., September 1984.

[2] A Magnetically Suspended Linearly Driven Cryogenic Refrigerator. by F. Stolfi, M. Goldowsky, J. Ricciardelli and P. Shapiro, Proceedings of the Second Biennial Conference on Refrigeration for Cryogenic Sensors and Electronic Systems, Greenbelt, Md, December 1982.

[3] Philips Laboratories, Division of North American Philips Corp., Design and Fabrication of a Long-Life Stirling Cycle Cooler for Space Applications, Phase I and II - Engineering Model, Final Report: Sept. 1978 - Dec. 1982, by F. Stolfi, M. Goldowsky, C. Keung, L. Knox, E. Lindale, R. Maresca, J. Ricciardelli, P. Shapiro, NASA contract NAS5-25172, Briarcliff Manor, N.Y., March 1983.

[4] Philips Laboratories, Division of North American Philips Corp., Final Report for Parametric Testing of Engineering Model Refrigerator, by F. Stolfi, NASA contract NAS5-26688, Briarcliff Manor, N.Y., February, 1984.

Preceding Page Blank

DEVELOPMENTS OF A 4-5 K COOLING STIRLING CYCLE REFRIGERATOR

H.NAKASHIMA

Machinery Systems Laboratory
Railway Technical Research Institute J.N.R.

K.ISHIBASHI

2nd R & D Center, Aisin Seiki Co.,Ltd

Y.ISHIZAKI

Energy Conversion Technology Inc.

The object of this development is a Stirling cycle refrigerator achieving temperatures in the 4-5K region without the use of Joule-Thomson loop. Rare earth metal compounds were used for the regenerator matrix and metal bellows were used for the compressor and the displacer for the purpose of improving the cryogenic performance.

The refrigeration capacity of 0.55 watts below 5 K was confirmed in the first step tests of cooling from about 15 K. The results were reported at ICEC 10(1984). In the next step, a new test apparatus which can test the performance of cooling down from about 80 K was constructed. Measurements of the dynamic change of temperature and pressure were carried out with the phase angle and the displacement of the bellows as parameters. According to the test results obtained up to now, the refrigeration capacity is more than 2 watts below 5 K.

Key words: Liquid helium ; metal bellows; rare earth metal; refrigerator; regenerator; Stirling cycle;

1. Introduction

This paper describes the development of a 4-5 K cooling Stirling cycle refrigerator without the use of Joule-Thomson loop.

The special merit of the Stirling cycle refrigerator is that the mechanical structure is simple and high efficiency can be expected. At present, however, Stirling cycle refrigerator requires a Joule-Thomson loop to be added to the regenerative cycle to obtain sufficient refrigeration power at liquid helium temperatures.

The aim of this research is to prove the possibility of a 4-5 K directly cooling Stirling cycle refrigerator. The research can be divided into the next four steps.

Step 1 : Cooling down from about 15 K to 4-5 K. The purpose is to investigate refrigeration performance at cryogenic region. In this step the basic characteristics of special regenerators were investigated.

Step 2 : Cooling down from 30 K to 4-5 K. This step was very important, because the Stirling cycle refrigerator technique at temperatures higher than 30 K is already generalized. Two stages of displacers were introduced to achieve this goal. After this step, the remaining problem was how to connect a newly developed refeigerator to already developed Stirling cycle refrigerators.

Step 3 : Cooling down from about 80 K to 4-5 K.

Step 4 : Cooling down from room temperature to 4-5 K.

Comparison between the new regenerator using rare earth metal compounds and the ordinary regenerator using small lead balls was made. As a result of this test, superiority of the former was confirmed. Furthermore attainment of temperatures as low as 3.74 K and a refrigeration capacity of 0.55 W at the 4 K level has been confirmed. [4]

This report describes the test results obtained in step 3, that is, the test cooling down from about 80 K to 4-5 K.

2. Test apparatus

Fig.1 shows the appearance of the test apparatus for the 4-5 K cooling Stirling cycle refrigerator. Fig.2 shows the schematics of the apparatus. The main features of this test apparatus are as follows.

(a) This test apparatus is composed of two separate Stirling cycle refrigerators, i.e. a main refrigerator cooling down from 30 K to 4-5 K and a sub-refrigerator cooling down from 80 K to about 30 K.

The reason for this division into two temperature ranges is that it has become clear that the working pressure is a very important parameter to achieve 4-5 K cooling and it should be in the range of 1.0 ~2.0atm. If the entire refrigerator is designed at such a low pressure level, the volume of the refrigerator will become fairly large and the efficiency may be decreased. Both the main and sub-refrigerators are connected by a heat exchanger to each other, i.e. the after-cooler of the main refrigerator is cooled by the cold gas helium supplied from the sub-refrigerator.

Another feature of this apparatus is that metal bellows are used instead of pistons and cylinders for one compressor and two displacers. The merit of using metal bellows is that the heat leakage due to the shuttle motion

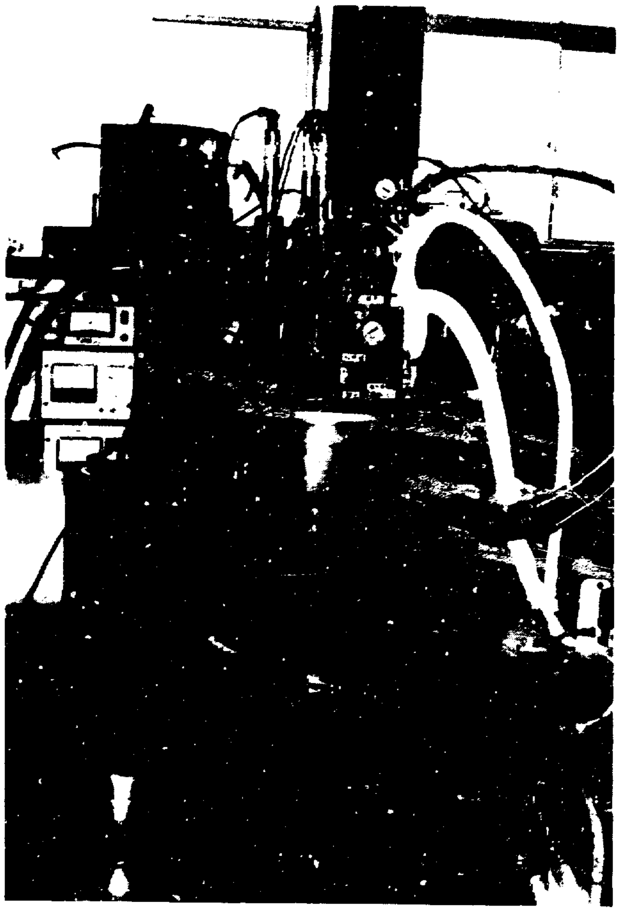

Fig.1 Appearance of the test apparatus

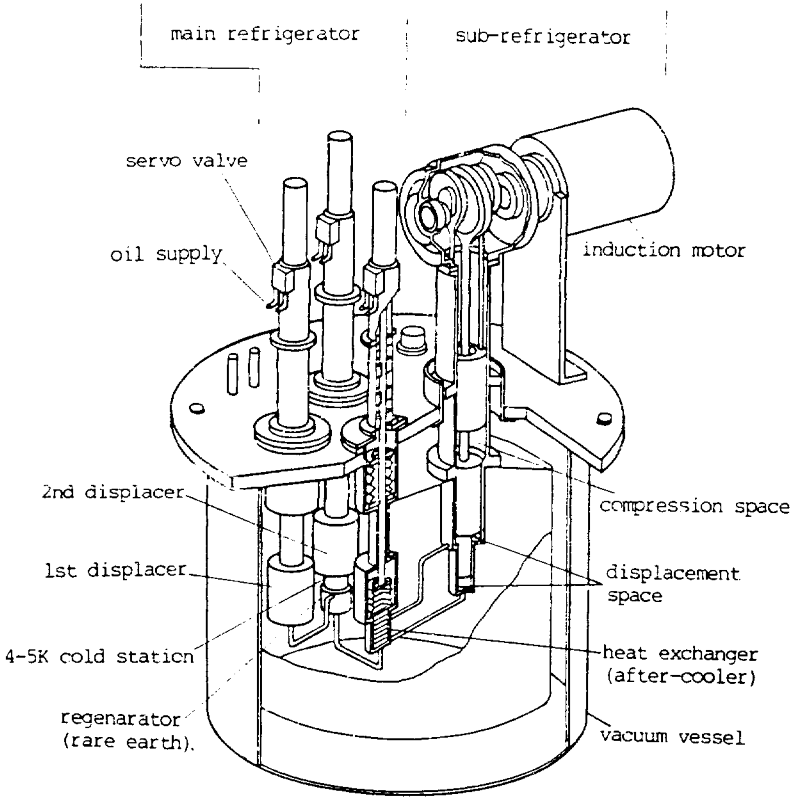
main refrigerator
sub-refrigerator
servo valve
oil supply
induction motor
2nd displacer
1st displacer
4-5K cold station
regenarator
(rare earth).
compression space
displacement
space
heat exchanger
(after-cooler)
vacuum vessel

Fig.2 Schematics of the test apparatus

of the piston does not occur. On the other hand, there is a demerit in that the dead space of the cold region increases and the reliability might be decreased. Nevertheless, bellows were selected for the purpose of realizing approximate ideal conditions.

(b) Regenerator

The regenerator used for the sub-refrigerator is composed of metal meshes and small lead balls, which are not different from those used in ordinary regenerators. The main refrigerator regenerators are composed of two blocks matching the temperature regions. For the higher temperature region (30-10 K) small lead balls are used (1st regenerator), and for the lower temperature region (15-4 K) rare earth metal compounds are used (2nd regenerator).

In the 2nd regenerator, rare earth metal compounds GdRh and GdErRh are used. These materials were selected because of their low temperature specific performance. Considering the properties of each material, GdErRh was used for the lowest temperature region (less than 10 K).

The regenerators are removable, so that different types of regenerators at the same condition may be compared.

(c) Compressor and displacers

As already mentioned the compression and the displacers of the main refrigerator are composed of metal bellows. Each space inside the bellows is filled up with blocks in order to minimize the dead space.

(d) Heat rejection

The heat rejection from the compression area of the sub-refrigerator is made by means of liquid nitrogen which is supplied from an outside source. The heat rejection from the main refrigerator is made by means of the sub-refrigerator.

(e) Heat load

The heat load on the main refrigerator at the cold end was applied by an electrical resistance heater attached midway between the second displacer and the second regenerator.

(f) Variable parameters

The test apparatus is designed so that a variety of parameters may be varied. For instance, the cyclic speed, the stroke and the phase angle between compression and displacer motions are variable on the main refrigerator.

The variations was accomplished by using a oil pressure servo actuator mechanisms for the displacement control of the bellows. Each condition can be readily set by adjusting the electrical signal.

The sub-refrigerator can be controlled simply by regulating the frequency of power suply.

(g) Measurements

Many kinds of sensors were set around the main refrigerator so that precise data can be obtained. For instance, the transducers for temperature and pressure were installed at the entrance to each bellows. These transducers can measure not only the statical change but also the dynamical change in one cycle of motion.

3. Testing method

The measurement of the refrigerator performance was executed by controlling the electric current of the heater at each setting of the parameter such as the pressure, the cycle and stroke of the bellows and the phase angle between the compression and the displacer motion. At each condition, the temperatures and the pressures were recorded by data processing computers.

4. Test results

Fig.3 shows the typical test results on the relation between refrigeration performance and the temperature at the cold end. The maximum refrigeration capacity of 2.3 W was confirmed when the cold end mean temperature was maintained at less than 5 K. As shown in fig.3, the refrigeration performance depends on the working pressure, i.e. when the working pressure is low, the attainable temperature may be low, but the temperature increases rapidly in proportion to the heat load. On the other hand when the pressure is high, the attainable temperature is high and the refrigeration capacity is large.

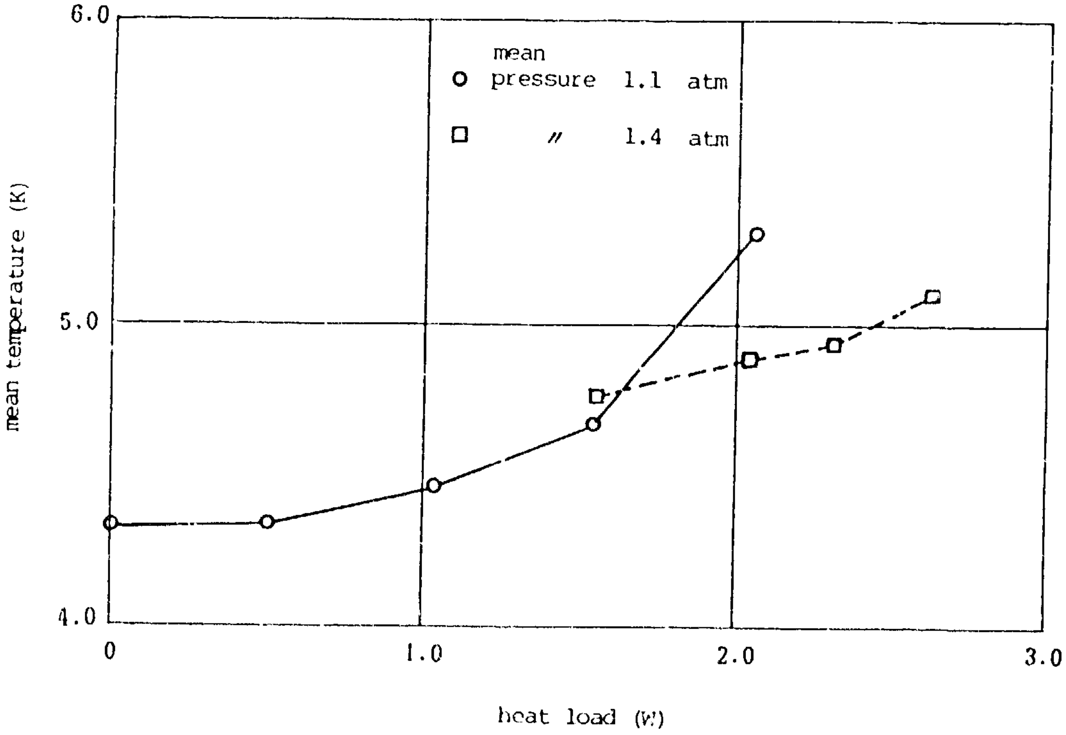

Fig. 3 Test result of refrigeration load and mean temperature at cold end (cooling down about 80 K)

Fig 4a,4b and 4c show the cyclic changes of the cold end temperature and the pressure. This temperature is measured by a Ge sensor inserted into the gas flow just outside of the bellows. The pressure is also measured at almost the same place. The outputs from these sensors pass through signal conditionors amplifier and then to a micro computerbased data logging system.

Fig.4a shows the data at zero heat load, and fig.4b and 4c show the data at an increased heat load. As shown in fig.4a, the cold end temperature decreases as the expansion begins, and it increases as the compression begins. It is notable that these values change very closely following the saturated curves of helium.

When the heat load increases, these values gradually deviate from the saturated curves, as shown in fig.4b and 4c. The data suggest that part of the gas helium is liquefied in a mist like state. This phenominon is especially prominent in the 0 W data (fig 4a). With increased heat load the quality of the mist is most likely deteriorated as can be seen from fig.4b.

At the condition of fig.4c, helium does not seems to be liquefied at any moment.

Comparing these data, it is notable that the minimum temperature in each cycle is not so different from each other (especially between fig.4b and 4c). Instead, the maximum temperature rises as the heat load increases.

Fig.5 shows a P-V diagram of the same data as shown in fig.4c. The work done to the compressor as calculated from this P-V diagram was approximately 43.9 W, and the works done by the displacers were 2.1 W (1st displacer) and 2.7 W (2nd displacer), respectively. The Carnot efficiency estimated experimentally was about 25% for the main refrigerator.

Fig.6 shows the measured temperature distribution on the flow diagram of this test apparatus which also is the same data shown in fig.4c and fig.5. As shown in this figure, 4-5 K cooling is achieved by cooling down from about 87 K.

5. Discussion

The possibility of 4-5 K cooling Stirling cycle refrigerator has been proved using a test apparatus for cooling down from about 80 K.

One of the features of cryogen obtained by this refrigerator is that the amplitude of the temperature fluctuation is rather large. The main use of these refrigerators is to recondense the helium gas. It is therefore necessary to confirm if such temperature fluctuation would pose a serious problem or not.

To investigate this problem, we installed a small LHe tank in which a heat exchanger for recondensing helium gas was housed between the 2nd displacer and the 2nd regenerator.

As the result of this test, the condensation of helium gas using this type of refrigerator was confirmed without difficulty.

This study has been performed using special coordination funds of the Science and Technology Agency of the Japanese Government. The authors would like to gratefully acknowledge the important support given by Mr. Yoshihiro Kyotani of the Japanese National Railways and Mr. Tatsuo Tani of Aisin Seiki Co., Ltd.

Fig.4a P-T diagram

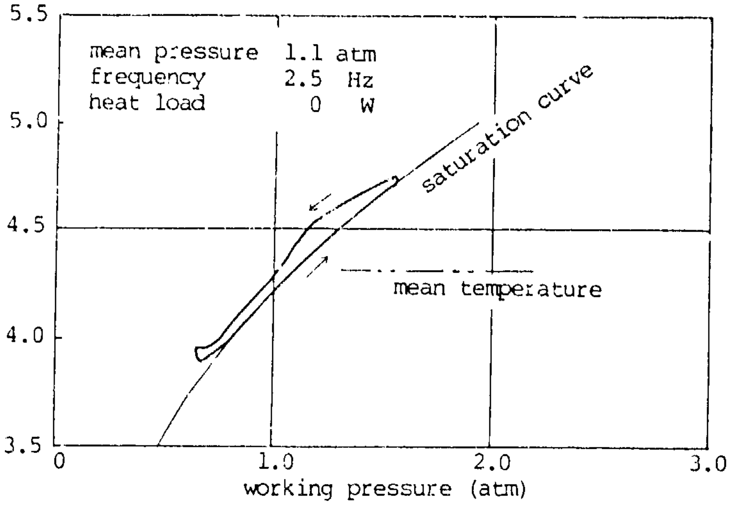

Fig.4b P-T diagram

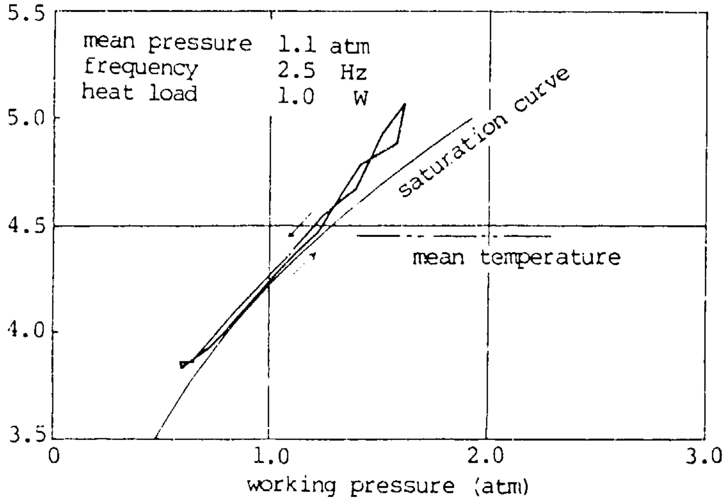

Fig.4c P-T diagram

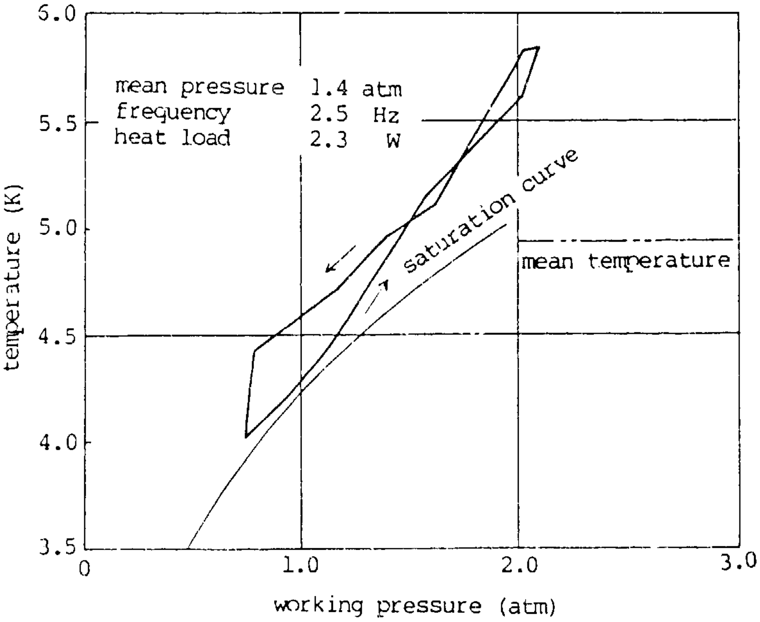

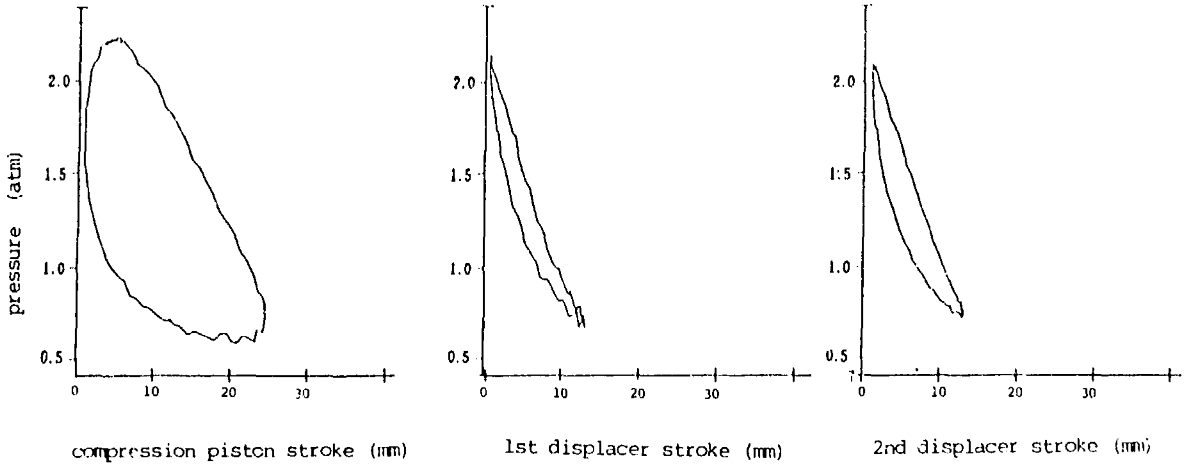

Fig.5 P-V diagram (1.4 atm , 2.5 Hz , 2.3 W)

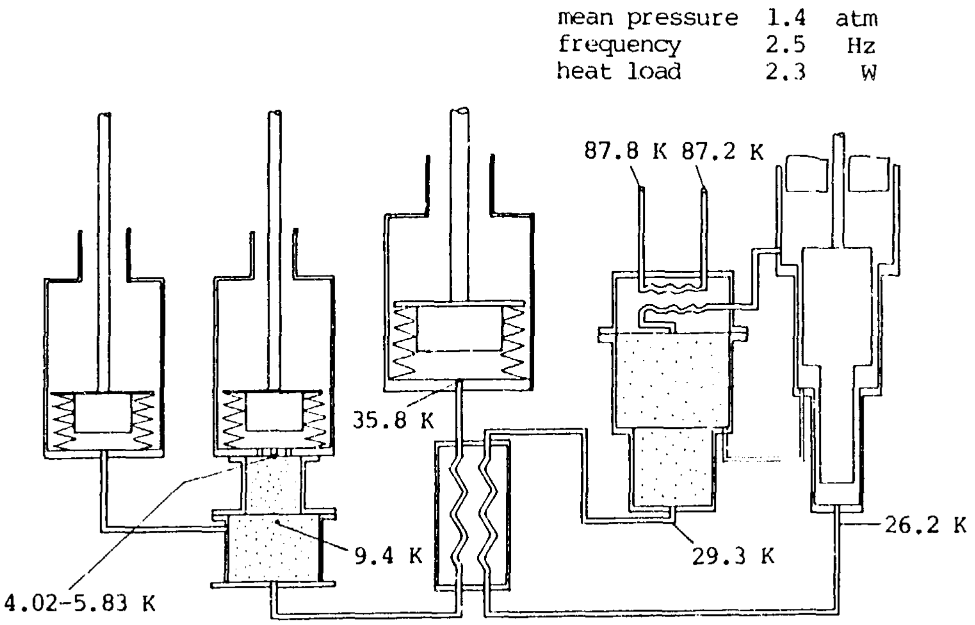
mean pressure 1.4 atm
frequency 2.5 Hz
heat load 2.3 W
87.8 K
87.2 K
35.8 K
9.4 K
29.3 K
26.2 K
4.02-5.83 K

Fig.6 Temperature distribution

6. Reference

〔1〕 Zimmerman, J.E. and Sullivan, D.B. 'A milliwatt stirling cryocooler for temperatures bellow 4 K'. Cryogenics, March (1979), pp.170-171.

〔2〕 Buschow, H.J., Olijhoek, J.F. and Miedema, A.R. 'Extremely large heat capacities between 4 and 10 K'. Cryogenics, May (1975), pp.261-264.

〔3〕 Daniels,A. and du Pre, F.K.'Triple expansion Stirling cycle refrigerator'. Proc. of CEC,E-5,Boulder (1970)

〔4〕 H.Nakashima, K.Ishibashi, and Y.Ishizaki, 'Stirling cycle refrigerator test result below 5 K'. ICEC 10, July (1984)

SPLIT-STIRLING CYCLE CRYOCOOLER OFF-DESIGN PERFORMANCE TESTS

Forrest R. Cleveland

Aerojet ElectroSystems Co.
Azusa, CA 91702

This paper presents the results of a series of performance tests conducted on a commercially available cyrocooler. The specific unit tested was a Magnavox MX7043 one-watt, split-Stirling cycle, linear-resonant cryocooler. The purpose of the tests was to determine cooler performance over a wide range of test conditions for which the cooler was not specifically designed.

The cooler is made for ground operation (1 atm) over a limited range of environmental temperatures (-40 C to +55 C) with both cooler components at nearly the same temperature. These tests were performed in a vacuum at temperatures as low as -100 C, with the cooler components at widely different temperatures.

Net refrigeration was determined as a function of cooler component temperatures (compressor, coldhead, and coldtip) and applied voltage. An algorithm was developed to describe this relationship over the ranges of the test variables.

Also determined was the input power split between the compressor and coldhead. The input power appears as waste heat at both components, and must be removed to hold component temperatures constant. The fraction of input power appearing at the coldhead was found to be a linear function of the temperature difference between the compressor and coldhead.

Key words: Cryocooler; cryogenics; performance; refrigerator; Stirling cycle; testing.

1. Introduction

A Magnavox MX7043 cryocooler is to be used by Aerojet Electro-Systems (AESC) on a space experiment. In order to accurately predict the behavior of the experiment with a thermal math model, a computer algorithm describing cooler performance is required. This paper presents that algorithm, together with supporting algorithms for cooler impedance, the power split between components, and long-term degradation.

The cooler is made for ground operation (1 atm) over a limited range of environmental temperatures (-40 C to +55 C) with the cooler components at nearly the same temperature. The AESC experiment will be conducted in space over a much broader range of environmental temperatures with the cooler components generally at widely separated temperatures. The tests reported herein are the first performance tests conducted on this cooler under conditions not originally intended by the designers (vacuum and temperatures lower than -40 C).

The cooler consists of two components joined by a transfer tube: The compressor and the coldfinger subassembly. This is shown in figure 1. In the following discussion, "coldtip" refers to the point at which refrigeration is produced: the copper tip of the coldfinger. "Coldhead" refers to the warm end of the coldfinger subassembly.

2. Test setup and procedure

All test variables were recorded at steady-state conditions. The on-orbit operation of the cooler, however, will be under transient conditions responsive to changes in the experiment environment. It is assumed that the steady-state performance of the cooler, with specific values of the test variables, is identical to its performance under transient conditions with the same instantaneous values of the variables.

All testing was performed in a laboratory bell jar, and a vacuum of at least 3e-6 torr was maintained throughout all tests. Two separate coldplates were serviced by liquid nitrogen (LN_2) and warm air for temperature control. One coldplate was dedicated to the compressor, the other to the coldhead. Both cooler components were separated from their coldplates by aluminum collars. The purpose of these collars was to act as heat flow meters to determine the input power split between cooler components. The collars were calibrated by means of heaters. The test setup is shown in figure 2.

There are five variables of interest in these tests. Four are independently set. The fifth is then measured as a function of the other four. The five variables are: compressor temperature, applied voltage, coldhead temperature, coldtip temperature, and net refrigeration. Tests were conducted with compressor temperatures of 313 K (+40 C), 253 K (-20 C), and 193 K (-80 C); with applied voltages of 24 v, 22 v, 20 v, and 16 v rms; with various coldhead temperatures ranging from 323 K (+50 C) to 173 K (-100 C); and with coldtip temperatures of 110 K, 100 K, and 90 K.

With so many variables to be examined, the following approach was adopted. First, a specific compressor temperature was selected at which to gather several data points. This was maintained by the coldplate servicing the compressor, driven by a computer-sensed temperature feedback circuit. The compressor is the largest thermal mass component, and consequently the component which takes longest to reach steady state. Second, a specific voltage was applied to the cooler. The test setup did not permit controlling this variable automatically. This, together with the cooler component temperatures, determines the power generation in each cooler component. Third, a specific coldhead temperature was selected. This was maintained by the coldplate servicing the coldhead and driven by an independent computer-sensed temperature feedback circuit. Finally, the net refrigeration was measured at the coldtip temperatures cited above. This was accomplished with a third computer-sensed temperature feedback circuit to vary the power generation at the coldtip in order to maintain the desired coldtip temperature.

All temperatures were measured with 36-gage copper-constantan (type T) thermocouples (TCs). A calibration was performed on all TCs prior to testing. This calibration consisted of dipping the TC beads into an LN_2 bath. Readings ranged from 79.13 K to 79.66 K. This is 1.77 K to 2.30 K high at LN_2 temperatures. No corrections were made to coldtip temperatures in fitting the data. The algorithm, then, underestimates net refrigeration.

3. Results

A total of 352 measurements were made representing 164 distinct test points. As a general rule, data were recorded twice for each test point to verify stability. The lowest coldtip temperatures achievable were also recorded, though these test points were not included in formulating the algorithm. Only a subset of the 164 test points was selected for the algorithm. This consisted of 125 test points which excluded all zero net refrigeration points occurring below a 90 K coldtip temperature. This made the algorithm a mathematically simpler surface.

3.1 Performance algorithm

The following algorithm fits the subset of 125 test points within reasonable accuracy. This is a working algorithm to describe cooler performance over the ranges of the test variables. There may exist others which are better in terms of closeness of fit, but there are none which are simpler mathematically and give as close a fit.

The data for which this algorithm was developed are shown in figures 3 through 11. Each figure is for a specific compressor temperature and applied voltage. The figure itself is a three-dimensional plot of net refrigeration (vertical axis) versus coldtip and coldhead temperatures (horizontal axes). What each figure depicts is a performance surface.

Geometrically, the algorithm for early-life (non-degraded) performance is a surface which is best described by the term "parabolic cylinder". It is that surface generated by moving a line parallel to itself along a parabola as a base. It opens downward in the direction of negative net refrigeration, and slopes downward in the direction of low coldtip temperatures. It has no rotation about the net refrigeration axis.

$$Qn = A * (Tct - Tmin) - B * (Tch - Topt)^2$$

where Qn = net refrigeration, w
A & B = proportionality "constants"
= functions of V & Tcmp (see below)
V = applied voltage, v rms $(12 < V < 30)$
Tcmp = compressor temperature, K $(193 < Tcmp < 313)$
Tct = coldtip temperature, K $(80 < Tct < 120)$
Tmin = temperature of zero refrigeration, K
= function of V & Tcmp (see below)
Tch = coldhead temperature, K $(173 < Tch < 323)$
Topt = temperature of maximum refrigeration, K
= 200 K (peak of parabolic surface)

$$Tmin = a0 * (V - V0)^2 + a1 * (Tcmp - T0)$$

where: V0 = 24 v rms a0 = .37
T0 = 73 K a1 = .16

$$A = b0 * (V - V1)^2 - b1 * (Tcmp - T1)$$

where V1 = 7 v rms b0 = 5.9 e-5
T1 = 1033 K b1 = 1.3 e-5

$$B = c0 - c1 * (V - V2)^2$$

where: $c0 = d0 + d1 * (Tcmp - T2)^2$

$V2 = 20$ v rms $\quad d0 = 3.4$ e-5
$T2 = 304$ K $\quad d1 = 3.3$ e-9

$c1 = d2 + d3 * (Tcmp - T2)^2$

$d2 = 1.7$ e-7
$d3 = 7.6$ e-11

This algorithm is not intended to accurately represent performance very far outside the range of the test variables. For example, it gives a reduction in net refrigeration with increased applied voltage for voltages above about 30 v rms. This is probably incorrect. The algorithm is not good at voltages above about 30 v rms. As a second example, the algorithm does not give zero net refrigeration for zero applied voltage. This is clearly incorrect. The algorithm is not good at voltages below about 12 v rms.

3.2 Supporting algorithms

Three supporting algorithms are required for a complete description of cooler operation. The first concerns cooler impedance, which relates applied voltage to input power. The performance algorithm above involves applied voltage as one of the variables. It is the power associated with this voltage, however, which determines the cooler temperature. The impedance algorithm allows input power to be calculated from applied voltage and cooler component temperatures.

The second supporting algorithm concerns the power split between compressor and coldhead. How the input power is split between these two components must be known in order to calculate temperatures for them. The power split algorithm gives the fraction of input power appearing at the coldhead.

The third supporting algorithm concerns expected performance degradation with operating time. This is important for calculations well into the life of the experiment. Cooler performance must be derated with operating time. The degradation algorithm gives the derating factor.

3.3 Impedance algorithm

Cooler impedance is a linear function of coldtip temperature in the range 90 to 110 K. The intercept is a function of coldhead and compressor temperatures, but is independent of applied voltage. The slope is a function of compressor temperature and applied voltage, but is independent of coldhead temperature. This is expressed as follows:

$$R = V^2/P = e0 + e1 * Tct$$

where R = impedance, ohms
P = input power, watts
$e0$ = $f1(Tch, Tcmp)$
$e1$ = $f2(Tcmp, V)$

The intercept, e0, is linear with coldhead temperature. It can be calculated from the following expression:

$$e0 = g0 + g1 * Tch$$

where $g0 = 4.348 + .01822 * Tcmp$

$g1 = 6.060\ e\text{-}3 + 4.498\ e\text{-}5 * Tcmp$

The slope, e1, is linear with applied voltage. It can be calculated from the following expression:

$$e1 = h0 + h1 * V$$

where $h0 = .1069 - 8.008\ e\text{-}6 * (Tcmp - 283)^2$

$h1 = -\ 3.095\ e\text{-}3 + 3.010\ e\text{-}7 * (Tcmp - 275)^2$

The maximum percentage error for this algorithm is 8.0%; the average percentage error is 2.3%. The maximum absolute error is 1.26Ω; the average absolute error is 0.39Ω.

3.4 Power split algorithm

The fraction of input power appearing at the coldhead is a linear function of the temperature difference between compressor and coldhead. Both intercept and slope are functions of compressor temperature and applied voltage.

$$fch = j0 + j1 * (Tcmp - Tch)$$

where fch = fraction of input power appearing at coldhead

$j0 = -.586 + 9.53e{-3} * Tcmp - 1.39e{-5} * Tcmp^2 - .0172 * V$

$j1 = (Tcmp - 128)^{.33} / (1345 - 113.2 * V + 4.274 * V^2)$

This algorithm fits most of the data quite well, as shown in figures 12a through c. It misses rather badly in three instances. It predicts high for 24 v rms applied voltage, 313 K compressor temperature, and 80 K temperature difference. It also predicts high for 20 v rms applied voltage, 253 K compressor temperature, and 70 K temperature difference. It predicts low for 20 v rms applied voltage, 193 K compressor temperature, and 20 K temperature difference.

3.5 Degradation algorithm

Cooler performance is expected to decline with increased operating time. This is shown in figure 13. Data were taken on five UA7035 Philips cryocoolers. These are 1/4-watt split-Stirling cycle units, similar to the 1-watt MX7043. (Philips manufactures the MX7043; Magnavox markets it in the U.S.) These data give the following:

$$q/q0 = k0 + k1 * t + k2 * t^2 + k3 * t^3 + k4 * t^4$$

where $q/q0$ = actual-to-initial refrigeration ratio
t = time of operation, hrs
$k0 = 1.0$
$k1 = - 7.7189\ e{-6}$
$k2 = - 1.3921\ e{-9}$
$k3 = + 2.7729\ e{-13}$
$k4 = - 6.3517\ e{-17}$

This is accurate to within 0.6% of the average of the five coolers, and implies zero net refrigeration at 11,618 hours, or one and a third years.

4. Conclusion

A performance algorithm for an MX7043 Cryocooler has been presented, together with supporting algorithms for cooler impedance, power split between components, and long term degradation.

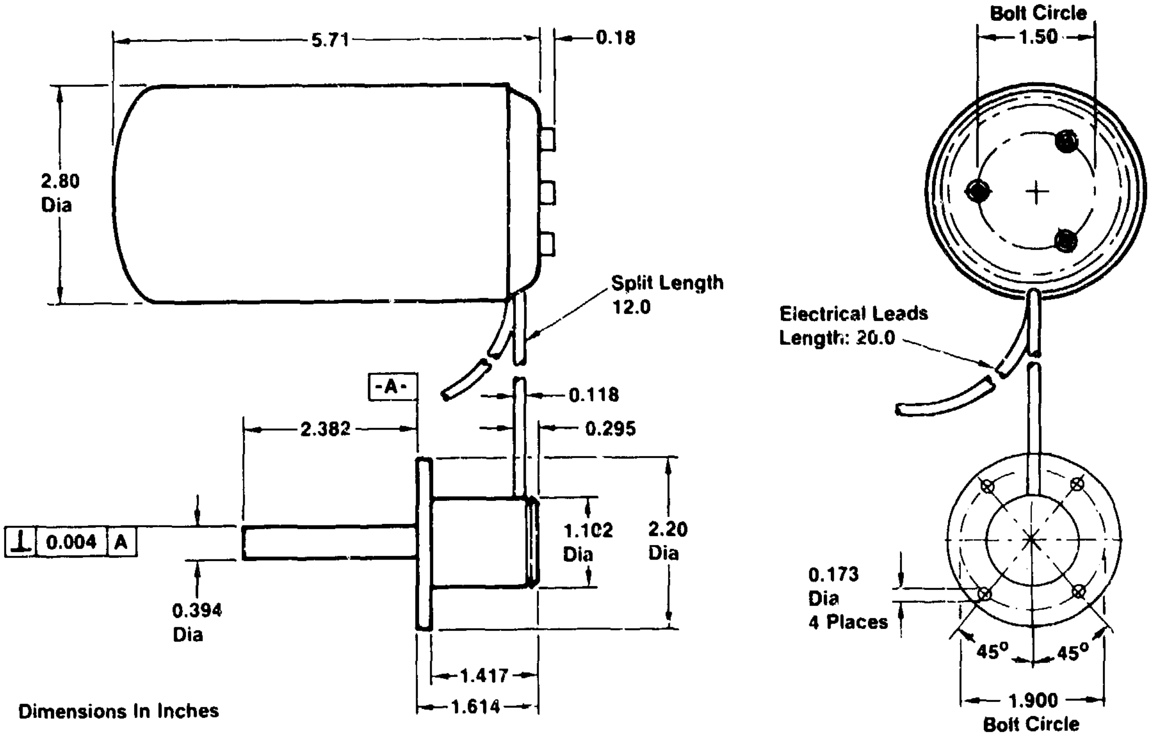
5.71
0.18
Bolt Circle
1.50
2.80
Dia
Split Length
12.0
Electrical Leads
Length: 20.0
-A-
0.118
2.382
0.295
0.004 A
1.102
Dia
2.20
Dia
0.394
Dia
0.173
Dia
4 Places
45°
45°
1.417
1.614
1.900
Bolt Circle
Dimensions In Inches

Figure 1. Split-Stirling linear-resonant cryocooler MX 7043

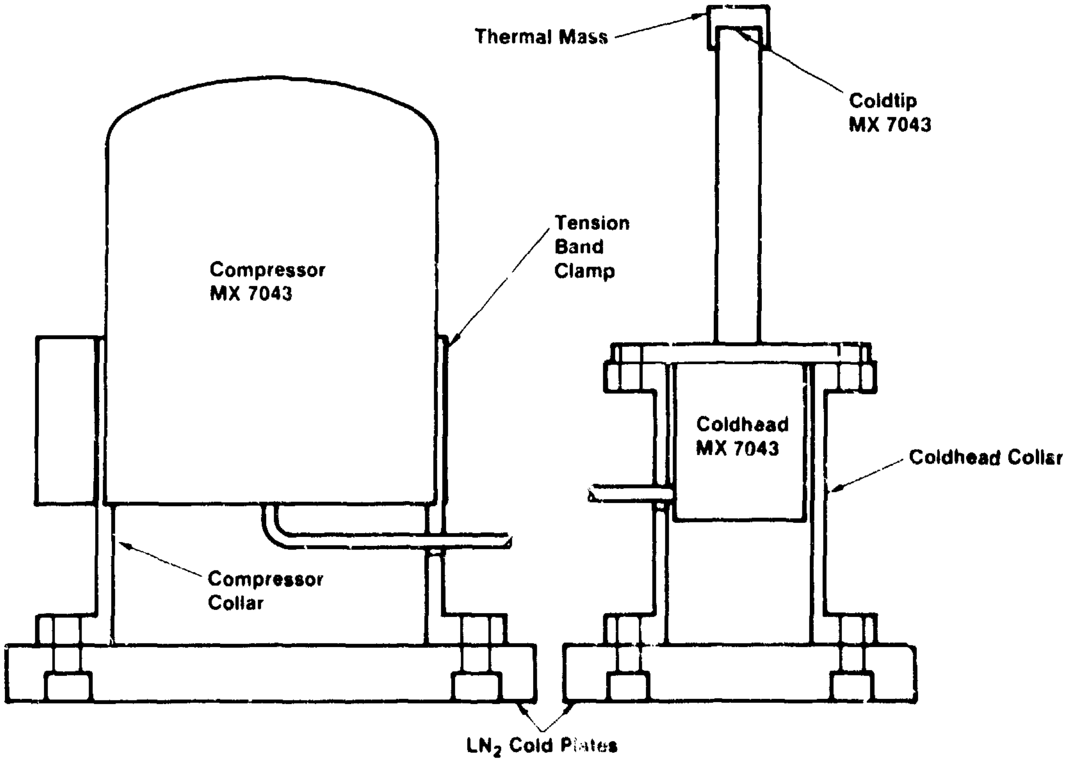
Thermal Mass
Coldtip
MX 7043
Compressor
MX 7043
Tension
Band
Clamp
Coldhead
MX 7043
Coldhead Collar
Compressor
Collar
LN$_2$ Cold Plates

Figure 2. Cooler performance test setup

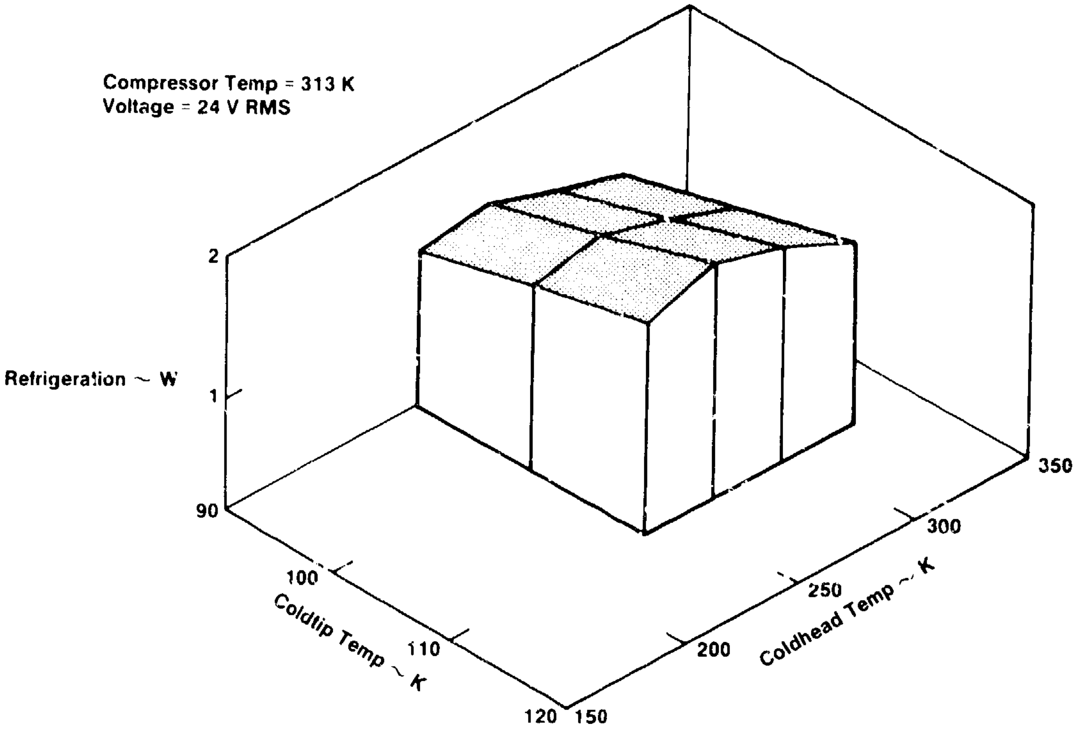

Figure 3. Cooler performance with 313 K compressor and 24 v rms

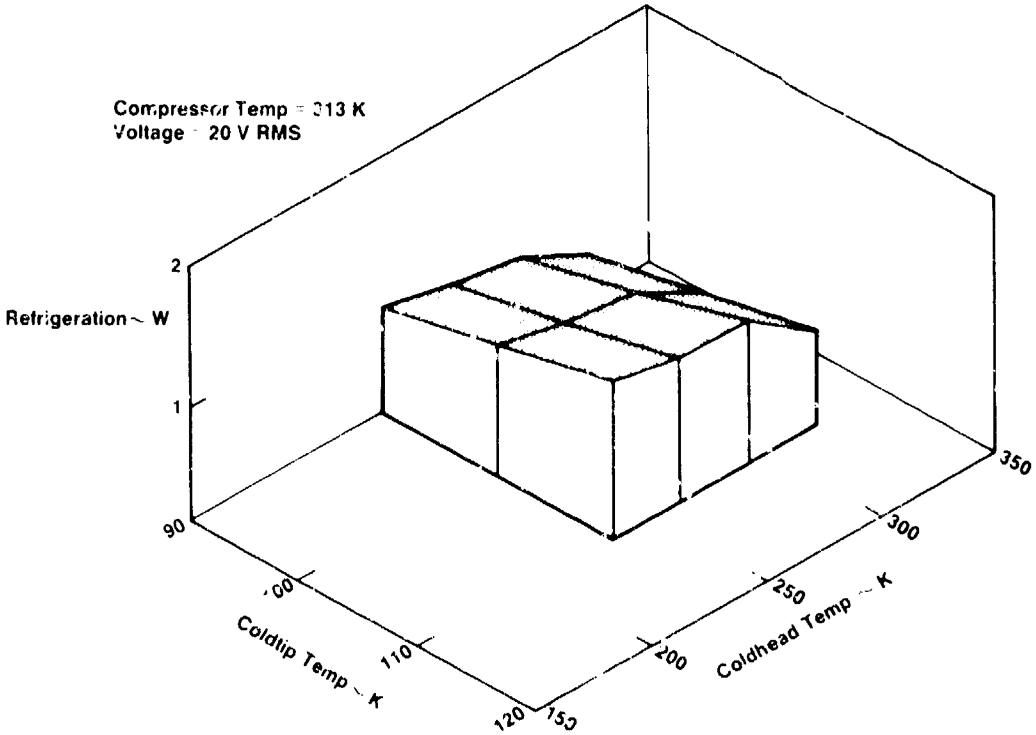

Figure 4. Cooler performance with 313 K compressor and 20 v rms

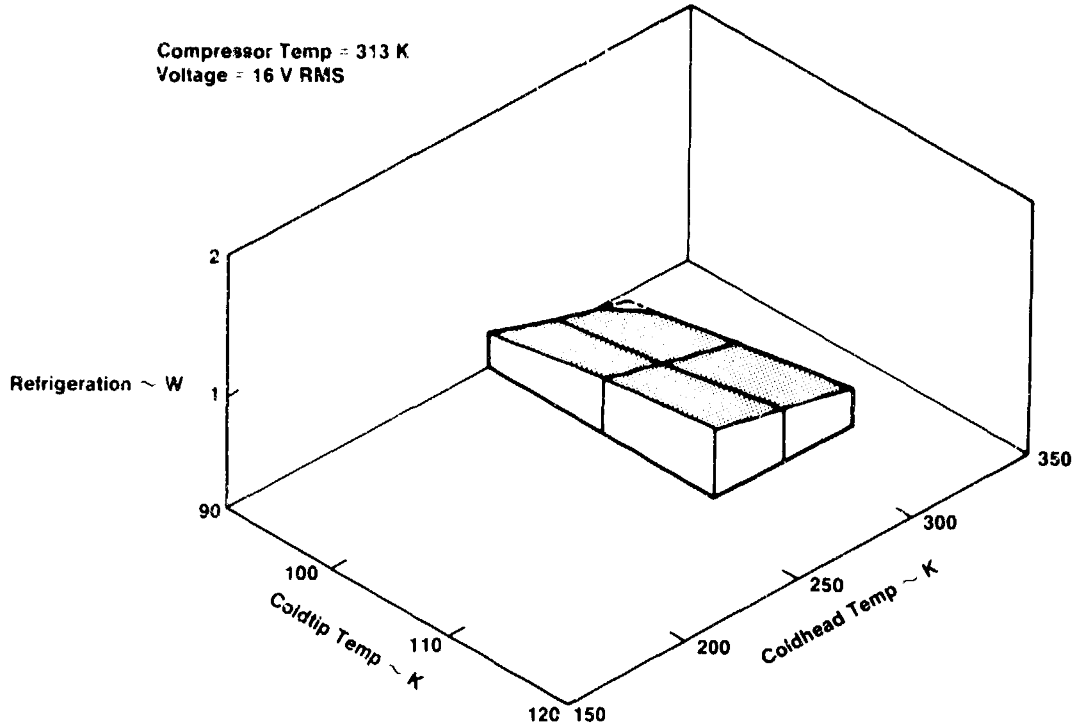

Figure 5. Cooler performance with 313 K compressor and 16 v rms

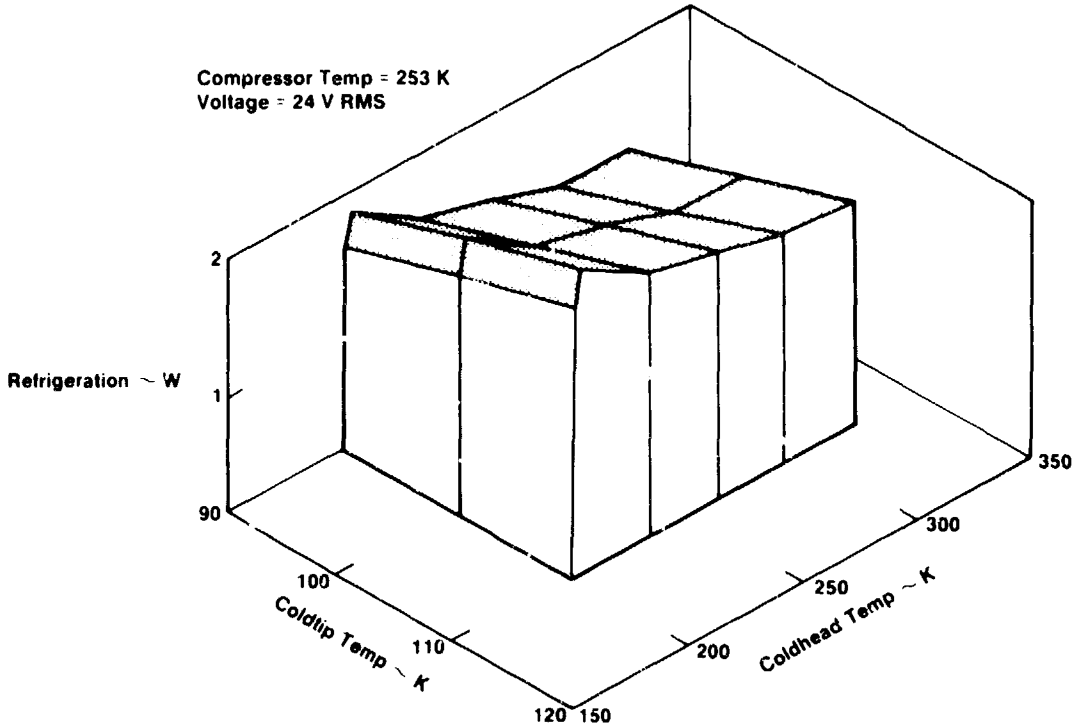

Figure 6. Cooler performance with 253 K compressor and 24 v rms

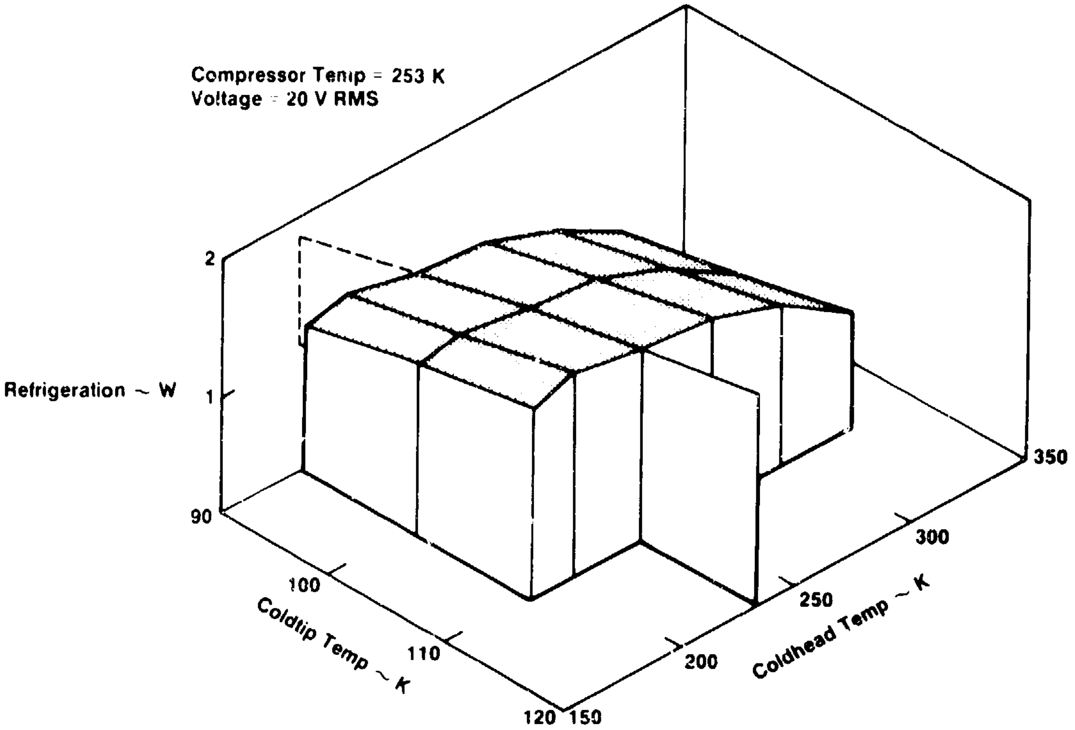

Figure 7. Cooler performance with 253 K compressor and 20 v rms

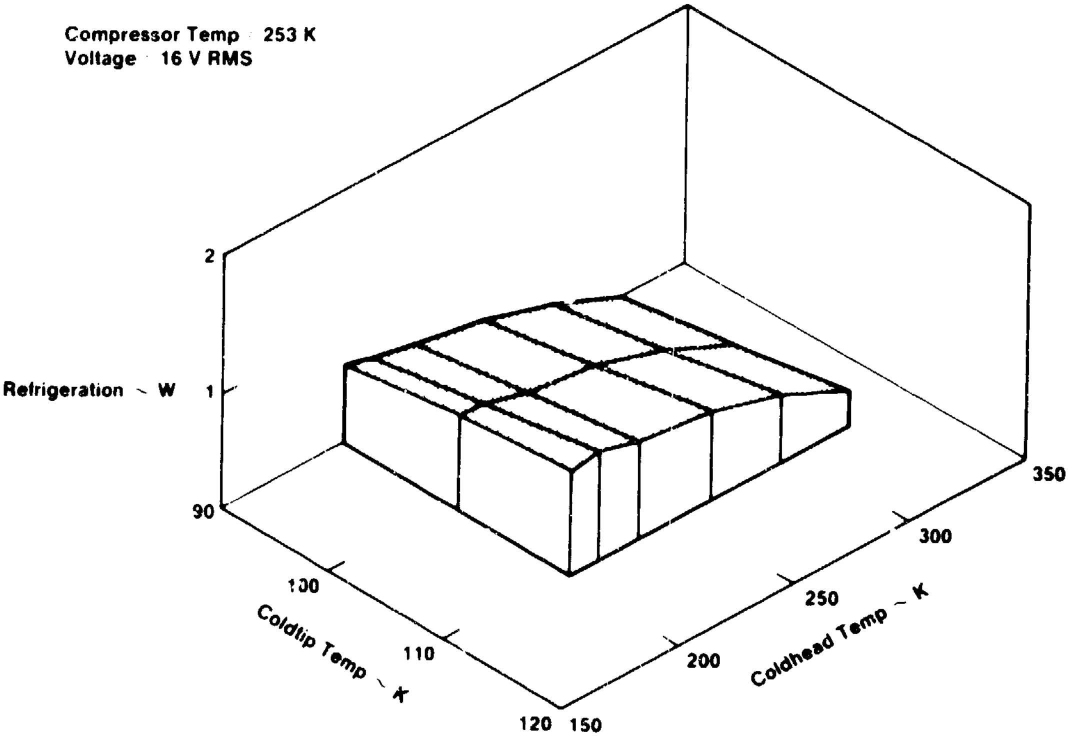

Figure 8. Cooler performance with 253 K compressor and 16 v rms

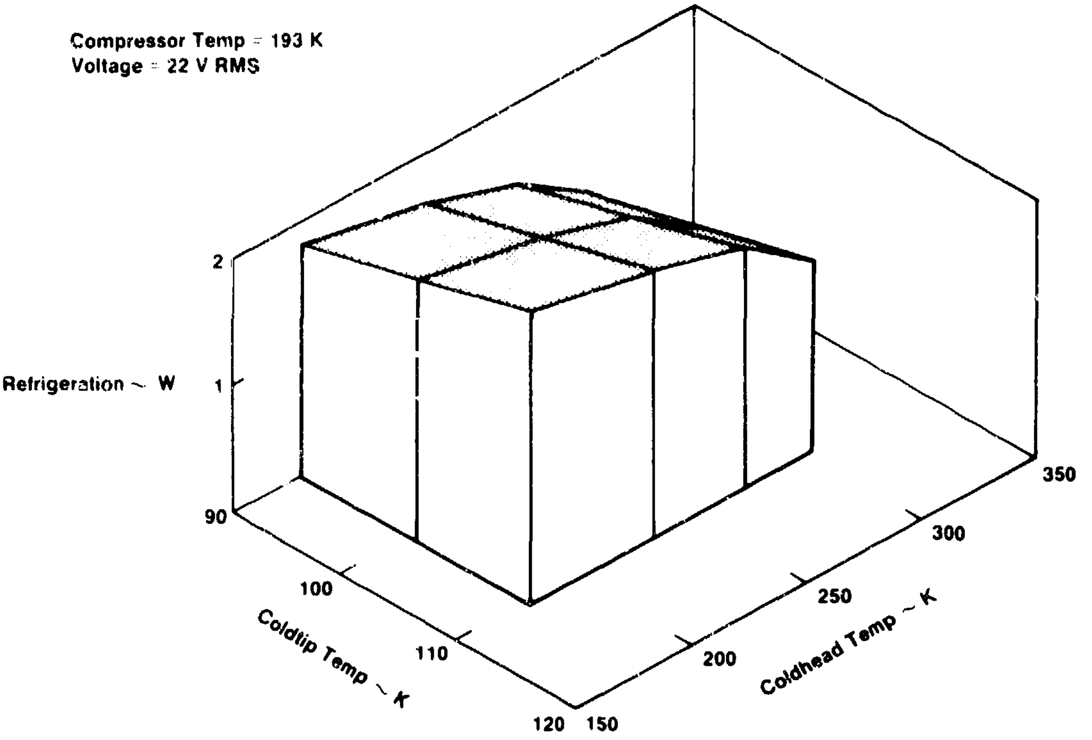

Figure 9. Cooler performance with 193 K compressor and 22 v rms

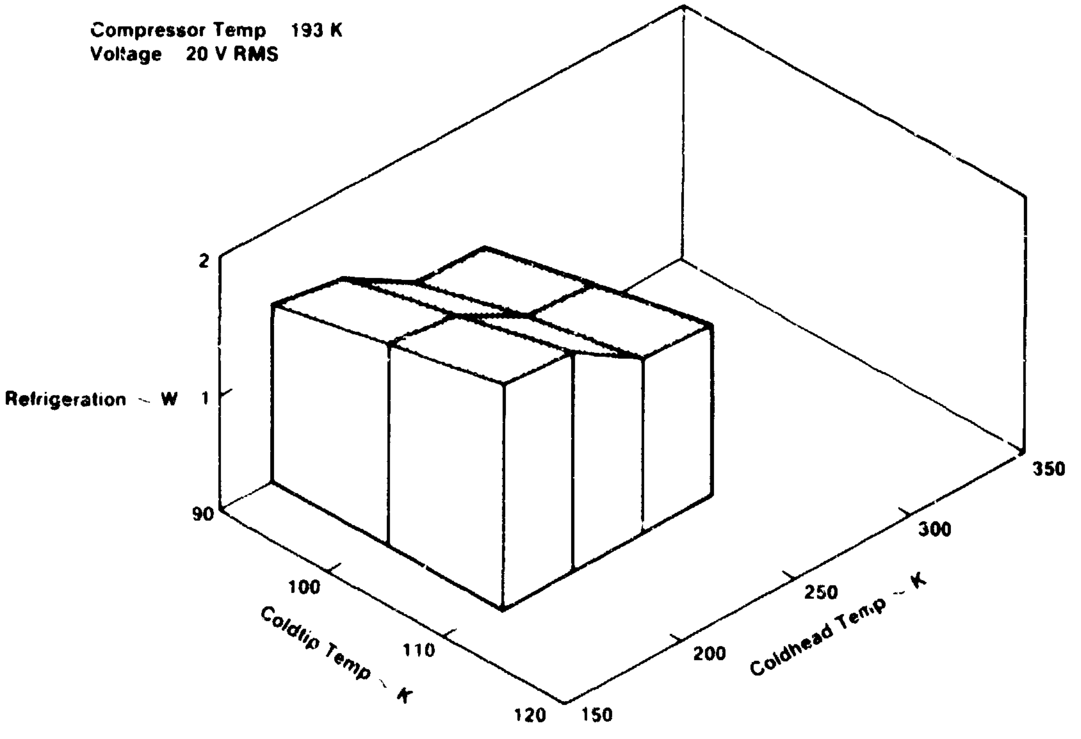

Figure 10. Cooler performance with 193 K compressor and 20 v rms

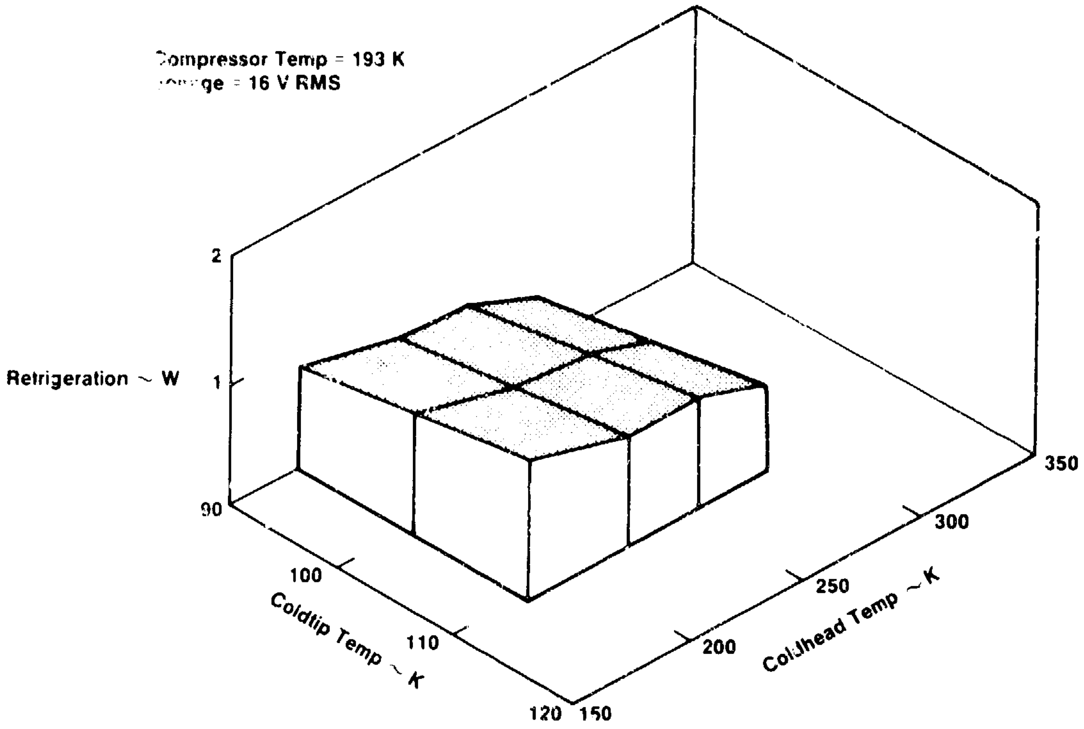

Figure 11. Cooler performance with 193 K compressor and 16 v rms

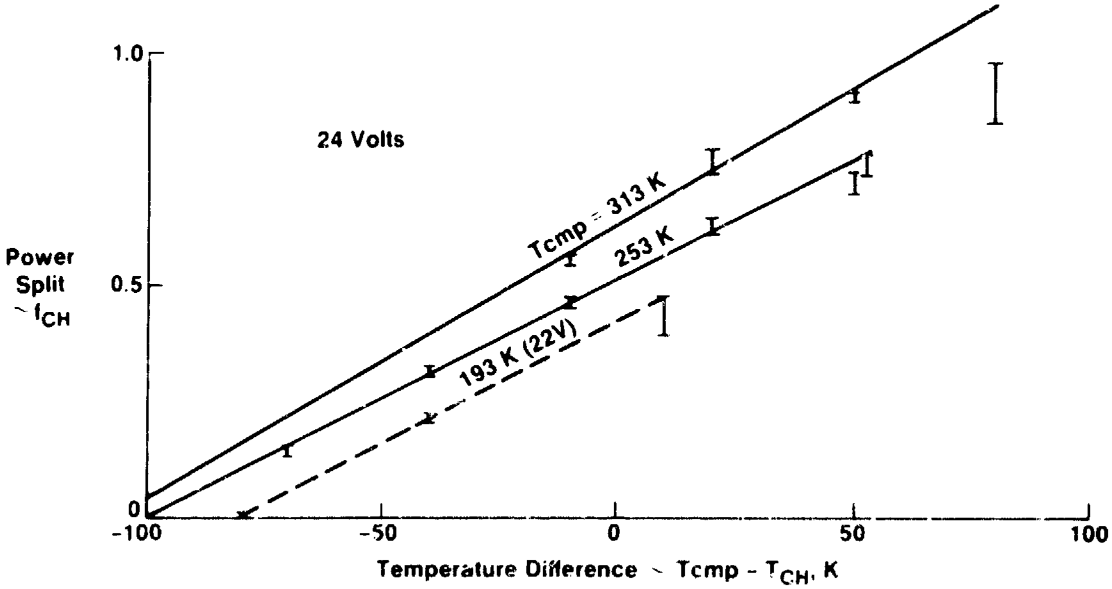

Figure 12a. Power split with 24 v rms

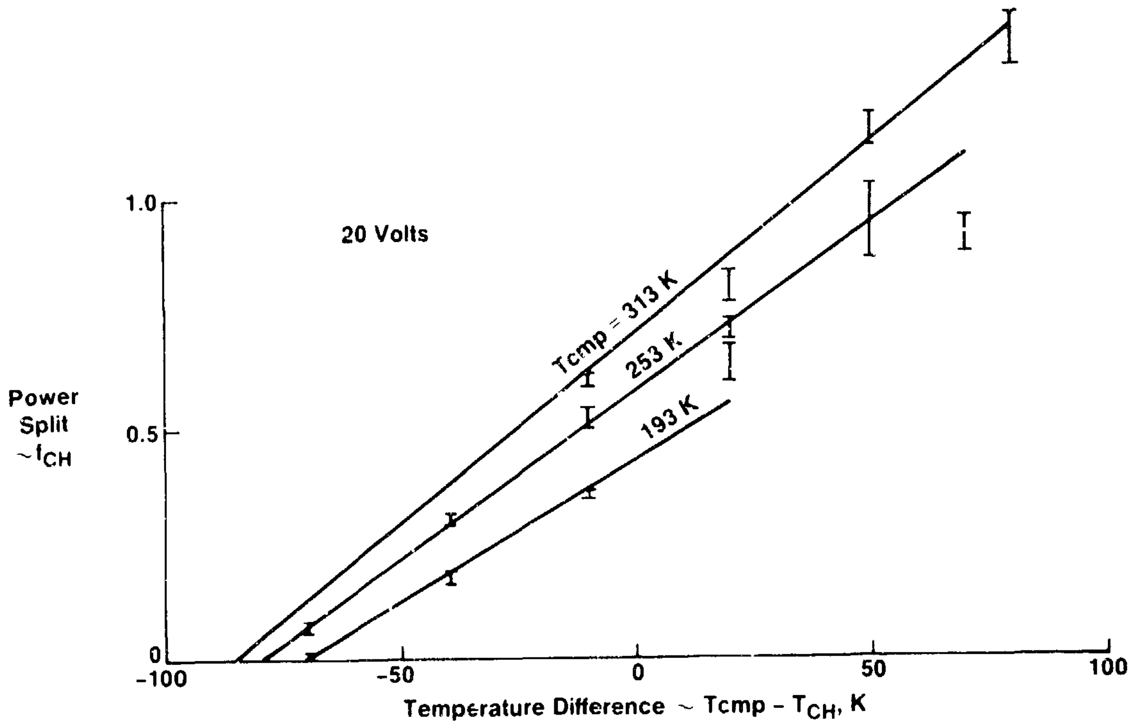

Figure 12b. Power split with 20 v rms

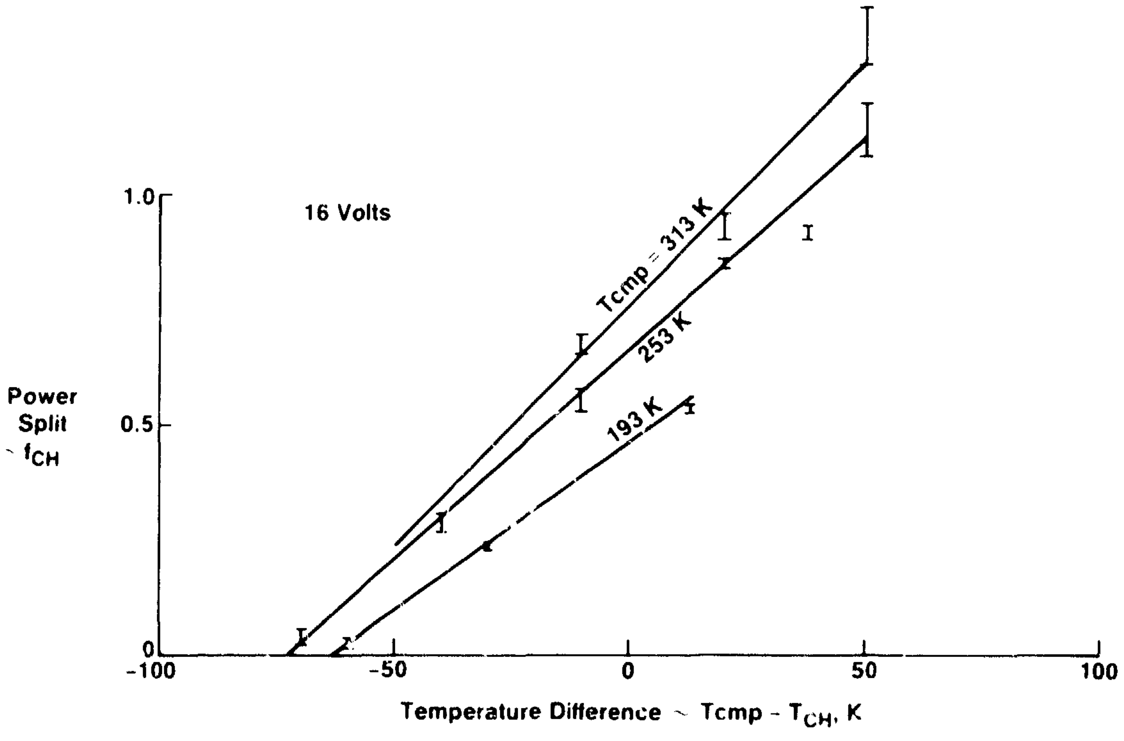

Figure 12c. Power split with 16 v rms

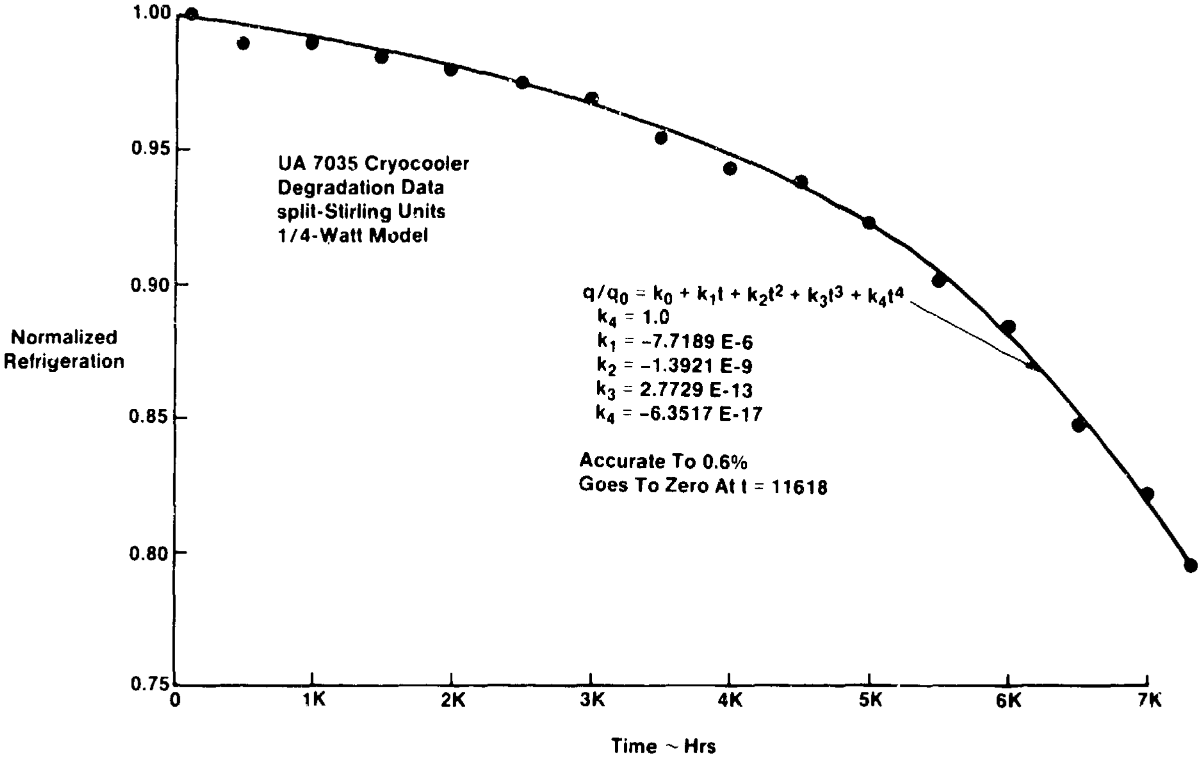

Figure 13. Cooler degradation, average of five units

Preceding Page Blank

DEVELOPMENT OF THE STIRLING CYCLE COOLERS FOR THE IMPROVED STRATOSPHERIC AND MESOSPHERIC SOUNDER

S.T.Werrett and G.D.Peskett

Oxford University
Department of Atmospheric Physics
Parks Road
Oxford OX1 3PU
United Kingdom

A long life miniature Stirling cycle cooler has been developed for the Improved Stratospheric And Mesospheric Sounder on the NASA Upper Atmosphere Research Satellite. The cooler, which was described at the Cryogenic Engineering Conference in 1985, uses a spring suspension and clearance seals. Testing of the prototypes carried out since then has included: qualification level vibration testing; thermal vacuum operation, including performance mapping; measurement of the effect on performance of increasing the connecting pipe length; optical measurement of the residual imbalance of a pair of electronically balanced compressors; continuation of the life test, with a compressor now having run for 11,500 hours. The flight model cooler design incorporates improvements in thermal interfacing and assembly methods, made as a result of the experience gained with the prototypes. The flight coolers are described and preliminary performance data for the first one presented. These data show that the cooler exceeds the ISAMS requirement.

Key words: Atmosphere; clearance seal; cooler; infra-red detectors; radiometer; spaceflight; spring suspension; Stirling cycle.

1. Introduction

The Improved Stratospheric And Mesospheric Sounder (ISAMS) is a limb sounding infra-red radiometer which will form part of the payload of the NASA Upper Atmosphere Research Satellite (UARS). Linear split Stirling cycle coolers capable of extracting 0.5 W at 80 K for the 30 months of the UARS mission have been developed to cool the infra-red detectors. The compressors and displacer-regenerators both employ clearance seals, spring suspension and linear motors. Both mechanisms are operated under servo control with LVDTs being used for shaft position measurement. In ISAMS two co-

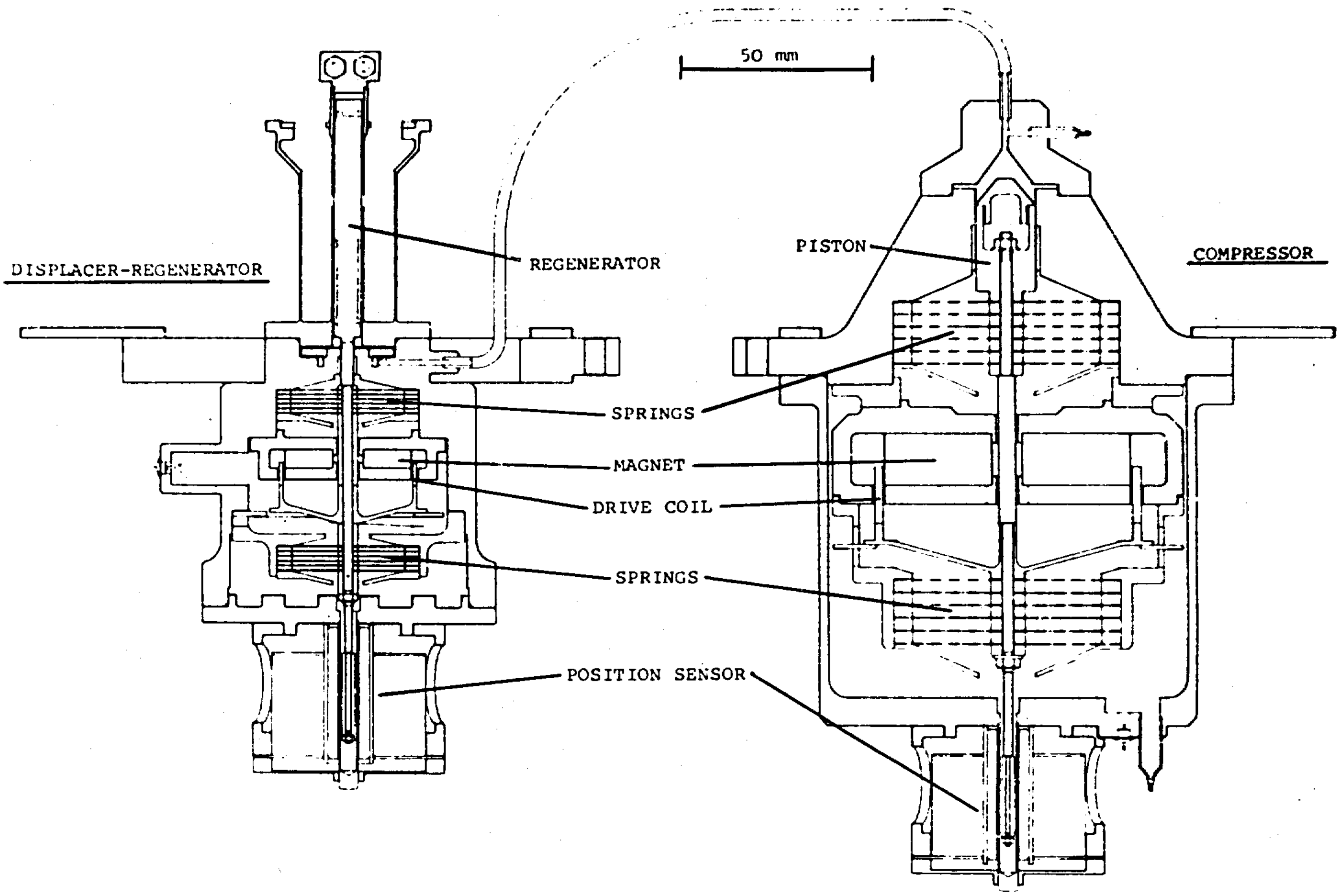
50 mm
DISPLACER-REGENERATOR
REGENERATOR
PISTON
COMPRESSOR
SPRINGS
MAGNET
DRIVE COIL
SPRINGS
POSITION SENSOR

Figure 1. Arrangement of the prototype cooler

olers are employed with the two compressors and two displacers linearly opposed so as to minimise unbalanced momentum.

The design, construction and performance of the prototype coolers have been previously described [1,2][1]. A diagram of their arrangement is reproduced in figure 1.

2. Testing of the prototypes

2.1. Approach

The development of a mechanism for use in space involves demostration of its ability to survive the environments encountered before reaching orbit as well as the adequacy of its performance for the duration of the mission. The test programme described here has been designed to satisfy the above requirement and to provide information on the performance of the coolers over a range of operating conditions. In parallel with this programme, British Aerospace (BAe) have performed an evaluation of the cooler on behalf of the European Space Agency (ESA) [3].

---

[1] Numbers in brackets refer to the literature references listed at the end of this report.

2.2. Vibration testing

After its performance had been characterised, one of the six prototype coolers was vibrated to the levels shown in table 1, the duration of the test being 1 minute in the axis parallel to the mechanism shafts and 90 seconds in a transverse direction. The intention was to run the device after vibration, to test for performance changes, and then to strip it down and examine the components. However, during the test it became clear that a failure had occurred in the compressor motor or suspension so that running the whole cooler again was not possible. The displacer-regenerator was then driven alone, no change in its characteristics was discernable.

Table 1. Qualification vibration levels

frequency / Hz	20 - 80	80 - 350	350 - 2000
power spectral density	+3 dB oct^{-1}	0.24 g^2Hz^{-1}	-3 dB oct^{-1}

The strip down of the cooler was attended by quality assurace personnel from BAe. The compressor failure was found to be due to separation of the motor coil from its support. The remainder of the compressor and displacer-regenerator showed no evidence of damage. A small amount of particulate debris was collected from the mechanisms.

Examination of the failed joint in the quality assurance laboratory at BAe revealed contamination of the joint epoxy with silicone rubber. The particulate contamination was found to be mostly chips of aluminium, titanium, copper and brass. The aluminium and titanium were thought to be machining debris from the cooler components and the brass, which is not used in the cooler, from the assembly jigs. The copper particles appeared to have come from the compressor drive coil which was free to move after the joint failure.

A drive coil of the same type as the one which failed had been successfully tested to higher levels previously, and we thus had no reason to doubt the suitability of a correctly made joint. It is almost certain that the failure was caused by the silicone rubber contamination (used in error to seal the encapsulation jig). However, since the strength of the original butt joint design could be increased easily by introducing an overlap between windings and support, this has been done in the flight models. Cleaning and inspection procedures have been tightened.

Table 2. Life test pre-conditioning vibration levels

frequency / Hz	20 - 120	120 - 600	600 - 2000
power spectral density	+9 dB oct^{-1}	0.08 g^2Hz^{-1}	-9 dB oct^{-1}

2.3. Life testing

At the time of writing the previous paper [1], one of the prototype coolers had been vibration tested, to the level shown in table 2, and subsequently run almost continuously for 6000 hours with no change in its performance. After a further 500 hours of unchanged operation, the displacer-regenerator mechanism failed. The failure was found to be due to a short circuit having developed between one of the static wires leading to the drive coil and the (grounded) body of the mechanism. The short circuit caused the control electronics to become unstable and overdrive the mechanism, eventually damaging it. The leadwire had been incorrectly positioned on assembly, its insulation being trapped and eventually cut through. (Due to shortage of assembly effort this mechanism had been assembled by a contractor).

On stripping down the failed mechanism no sign was seen of wear or fatigue, in particular the displacer appeared unmarked and no wear debris was found.

Another displacer-regenerator was connected to the life test compressor and the whole cooler was then vibrated to the level shown in table 2. Following this vibration, the life test was restarted and has since run for 5000 hours with no change in performance. The compressor has now accumulated 11,500 hours of operation.

2.4. Thermal performance measurement

2.4.1. Test set-up

Two of the prototype coolers were mounted as linearly opposed mechanism pairs in a vacuum chamber, as shown in figure 2. The temperatures of the compressor and displacer mounts could be independently varied, with the power input to the displacer mount monitored, permitting measurement of the power transfer from compressor to displacer. The two coolers were connected, through the vacuum chamber wall, to a pumping and filling rig. Instrumentation consisted of temperature sensors on the mechanisms and a multiplexed power and current measuring system on the drive motor inputs.

2.4.2. Test sequences

Most measurement sequences began with the setting of initial conditions of fill pressure, frequency of operation and heat sink temperatures. The coolers were then run and the load line (cold end temperature vs applied heat input) measured.

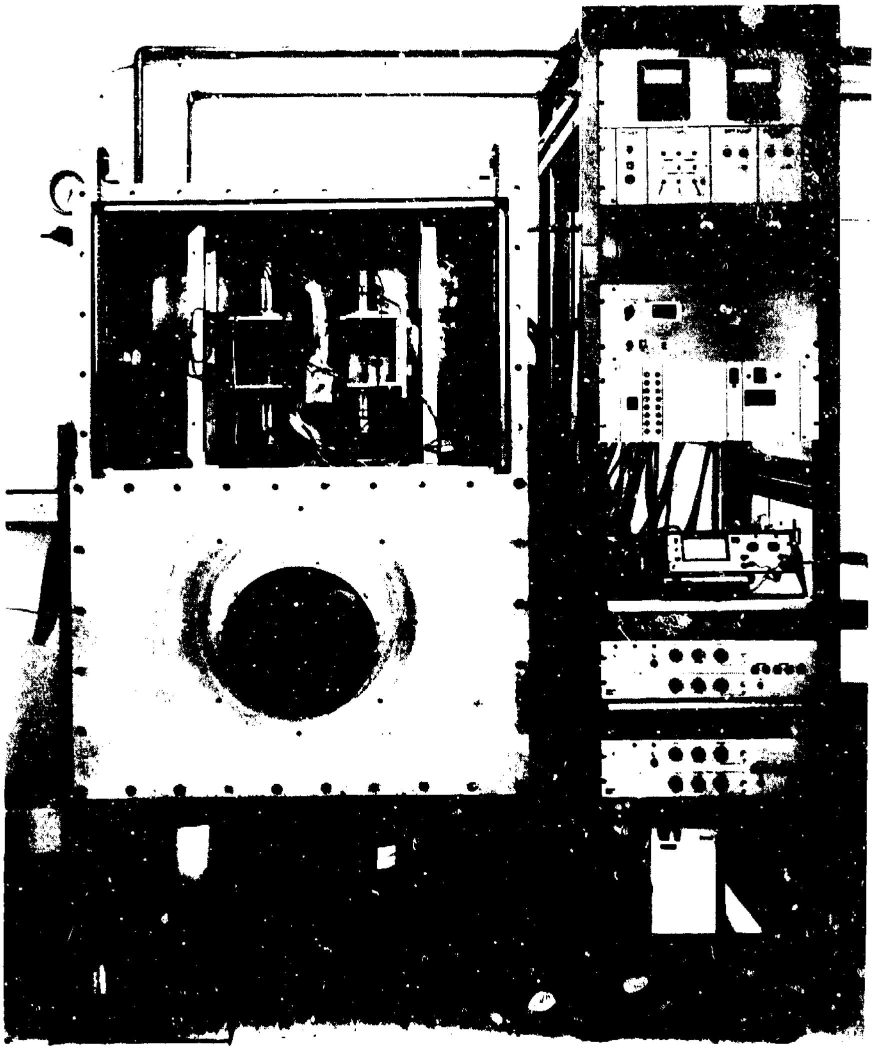

Figure 2. Thermal vacuum test set up

Measurements were made with a constant net power input of 20 W to the compressors, where net power is given by:

$$Wnet = Wgross - ((Irms)^2 * Rcoil)$$

Wgross is total input power measured with an electronic Watt meter; Irms is true rms input current measured with a purpose built meter; Rcoil is the resistance of the compressor drive coil. This measure of net power is used since it removes motor efficiency, which is device and frequency dependent, from the performance characteristics. Previous measurements [2] have shown that power deduced from the PV loop measured immediately above the compressor piston is equal to net motor power.

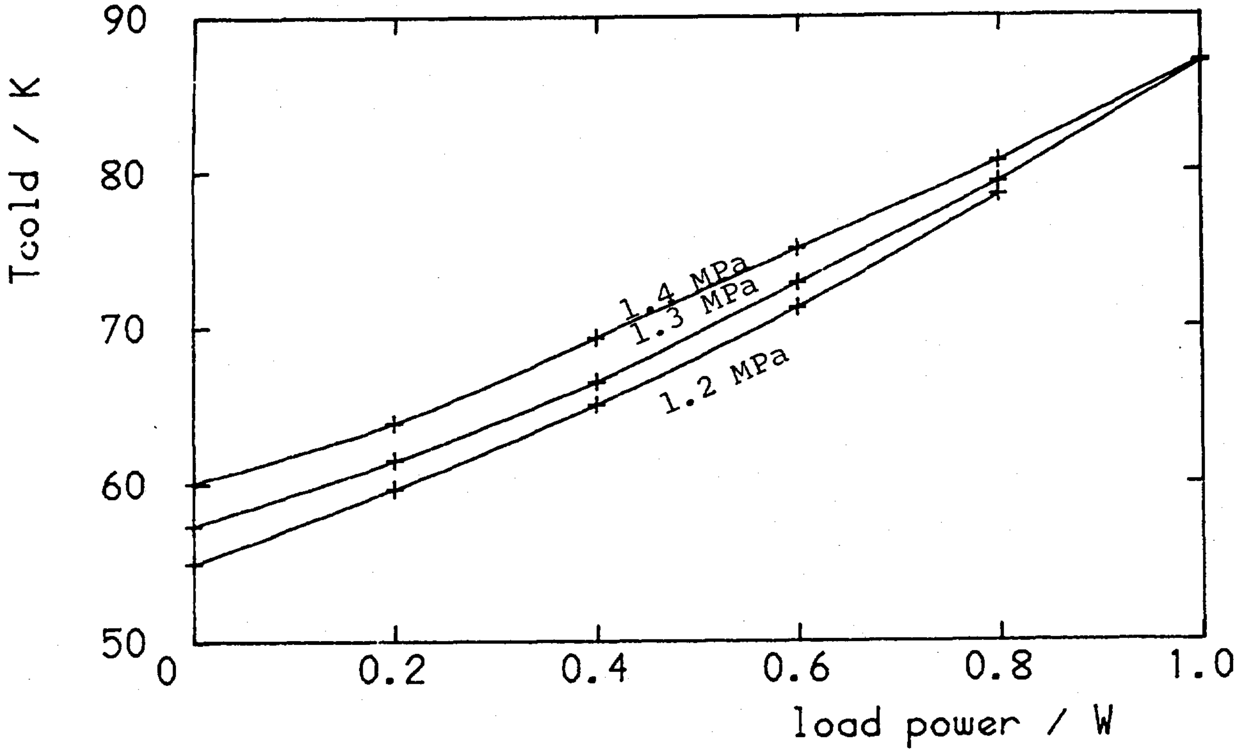

Figure 3. Performance vs fill pressure

2.4.3. Results

Figures 3 and 4 show a selection of the results from the measurements, made with the compressor and displacer heat sink temperatures equal. In figure 3, the effect of increasing the mounting face temperatures can be seen to increase the cold end temperature at all points on the load line. The effect of increasing fill pressure is shown in figure 4: performance is reduced at low load powers, but is less affected at higher ones. Monitoring of temperature distribution on the compressor showed that heat flow paths were such as to cause a temperature rise of up to 20 degrees at the cylinder head. Measurement of power input to the displacer-regenerator mount during several runs showed that approximately 9 W was transferred from the compressor to the displacer-regenerator. Figure 5 shows results obtained when one mechanism sink temperature was held constant and the other varied; compressor temperature can be seen to have the greater effect.

For the above measurements the length of the connecting pipe was approximately 250 mm, as it was for all of the prototypes. The connecting pipe length needed in the ISAMS installation was known to be greater (it is now fixed at 600 mm), so performance was measured with two longer pipes. The results are shown in figure 6.

2.4.4 Discussion of results

The reduction of efficiency as the fill pressure is increased is probably due to an increase in the heat input to the cold end at the low temperatures, possibly as a result of a reduction in regenerator efficiency. This effect restricts the choice of

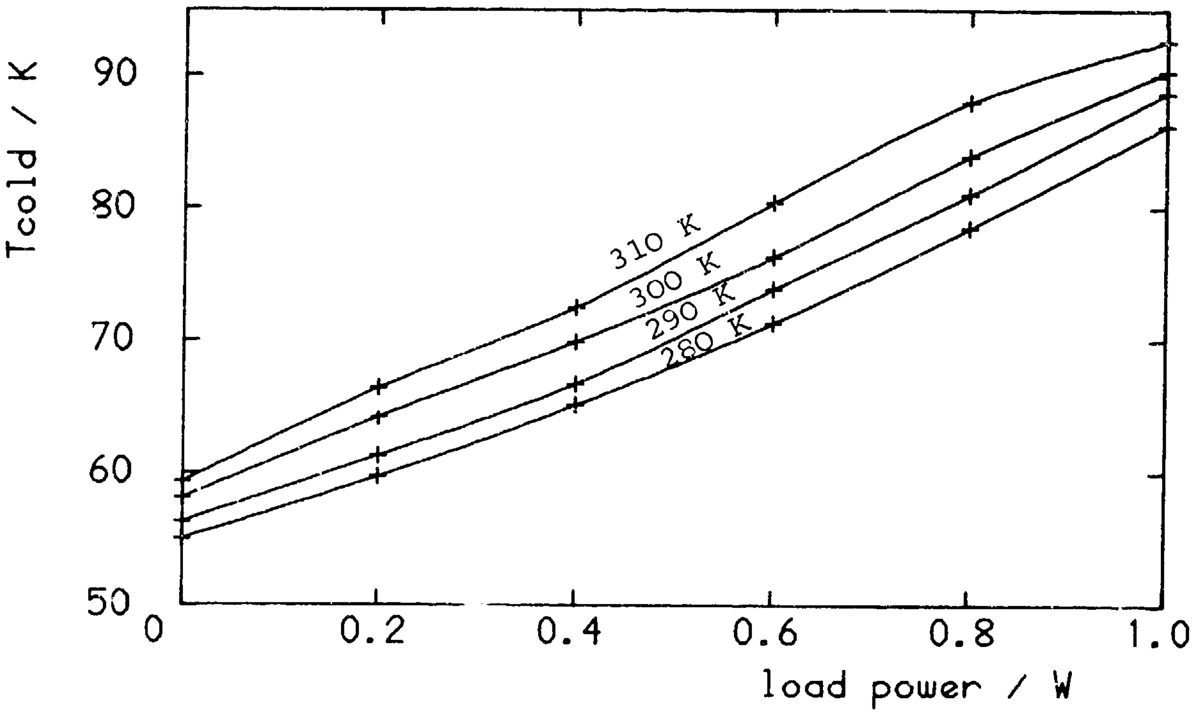

Figure 4. Performance vs mount temperature

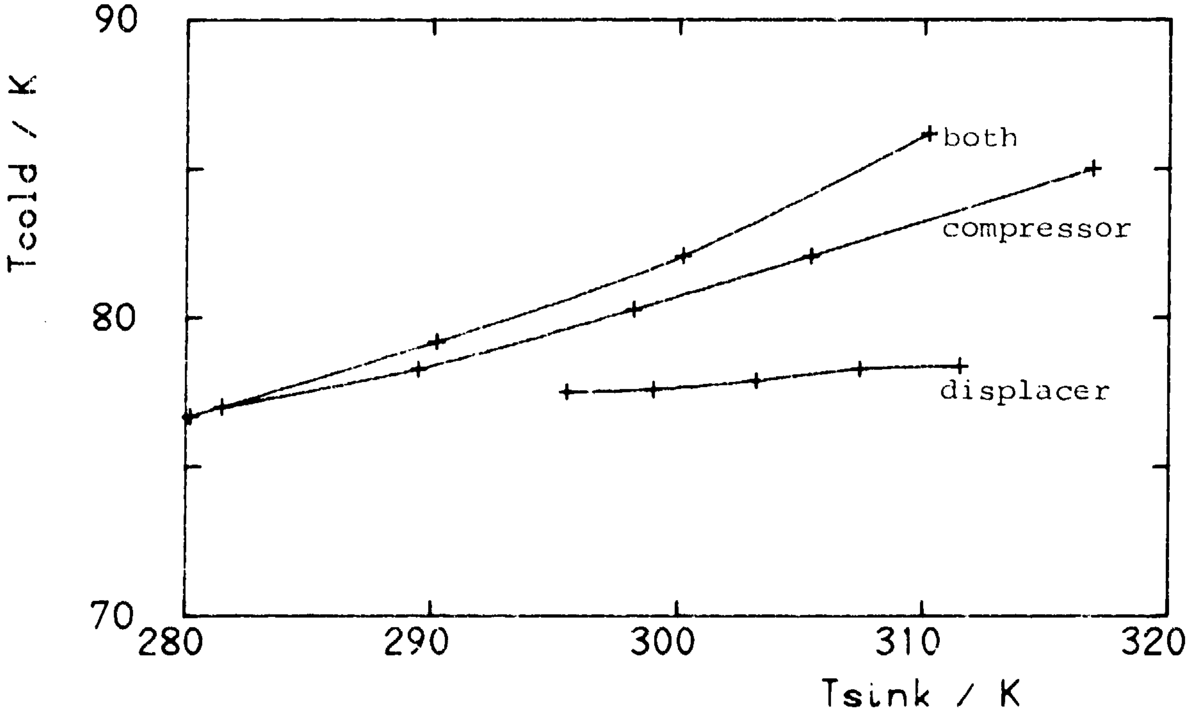

Figure 5. Separation of mount temperature effects

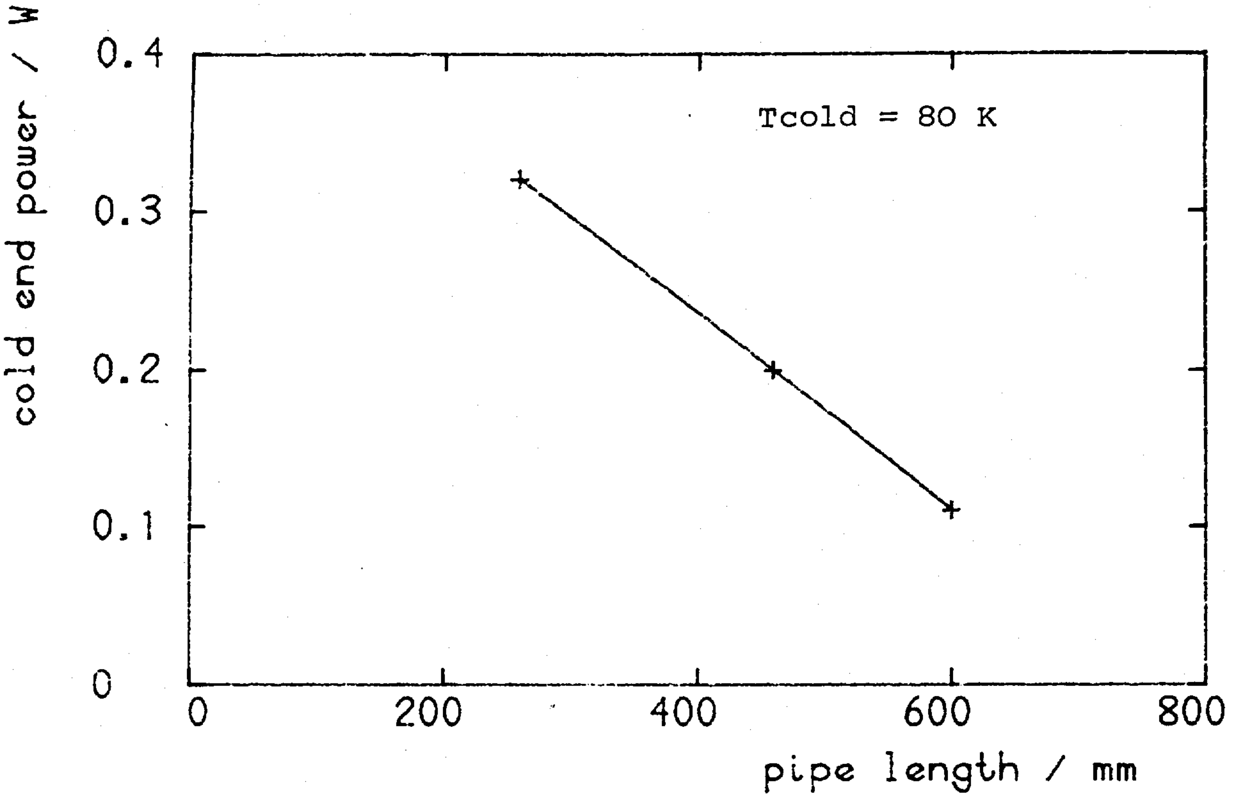

Figure 6. Effect of pipe length on performance

operating parameters for the flight coolers. It will generally be better to increase input power by increasing compressor amplitude rather than fill pressure.

The effect of mount temperature on performance was expected, but the much greater effect of the compressor mount temperature was not foreseen. The large amount of heat transferred to the displacer-regenerators is partly a consequence of the high compressor head temperature.

The falling off in performance as connecting pipe length is increased is presumed to be due to increased losses, although previous measurements and calculation have shown that the pressure drop losses in the pipe are small. The loss of cooling power should be considered as a proportion of the gross cold end load of approximately 1.2 W rather than the net figure shown in figure 6 (conductive and dynamic heat leaks accounting for the rest).

2.5. Residual vibration

For thermal reasons the mechanism mounts were not very stiff mechanically. Measurement of residual vibration of these mounts when the mechanisms were nominally balanced was used to provide a measure of the effectiveness of the servo controlled balance system. BAe were able to measure such vibrations by means of a speckle interferometric technique [4]. Since the moving mass and stroke are greater in the compressors than in the displacer-regenerators, and the control systems are the same, only the compressors were tested. Measurements were made with known imbalances in order to calibrate the results, at nominal balance with equal fill pressures and at nominal balance with a 10% pressure difference (to measure the effect of an otherwise tolerable leak).

Results of the measurements are given in table 3. The limit of resolution of the system was approximately one tenth of the movement seen in the 10% imbalance case. The null result in the balanced conditions thus implies a residual error of less than 1% in balancing the two compressors. Such an imbalance would result in peak residual momentum of 0.0013 Ns.

Table 3. Residual vibration measurements.

Conditions	Measured peak to peak movement
10% imbalance	25.3 micrometres
balanced, equal fill pressures	less than 2.5 micrometres
balanced, 10% pressure difference	less than 2.5 micrometres

3. Flight model coolers

3.1. Design

During the prototype phase of the cooler development it became clear that improvements in the heat sinking and ease of assembly of the mechanisms was desirable. Design changes which meet these objectives whilst having little impact on the proven mechanical arrangement were devised. We considered the implementation of these to be of sufficiently low risk to permit their incorporation into the ISAMS flight coolers.

In the flight design the thermal contact area at the mounting face of the compressor has been increased and the impedance of the path to the head greatly reduced. Similar changes have been made in the displacer-regenerator design. On the mechanical side, the stronger design of joint between the compressor drive coil and its support has been adopted, the displacer assembly has been made self aligning, with features which shrink out of contact on cool down, and adhesive locking of internal fasteners has been discontinued in favour of mechanical methods. The connecting pipe length has been increased to the 600 mm necessary for installation in ISAMS. The layout of the flight model mechanisms is shown in figure 7, with a photograph of the first one in figure 8. Five flight units are to be built.

3.2. Performance

The first flight cooler, fitted with a small vacuum jacket over the cold end, has been run on the bench to confirm satisfactory operation. Preliminary testing has been with no heat sinking of the mechanisms (other than free air convection). Figure 9 shows a load line for the flight unit and figure 10 the performance as a function of frequency of operation. (The running frequency in ISAMS will be programmable around 40 Hz.) The performance requirement for ISAMS, that each cooler produce 0.5 W of cooling at 80 K for less than 27 W of gross input power to the compressor, is exceed-

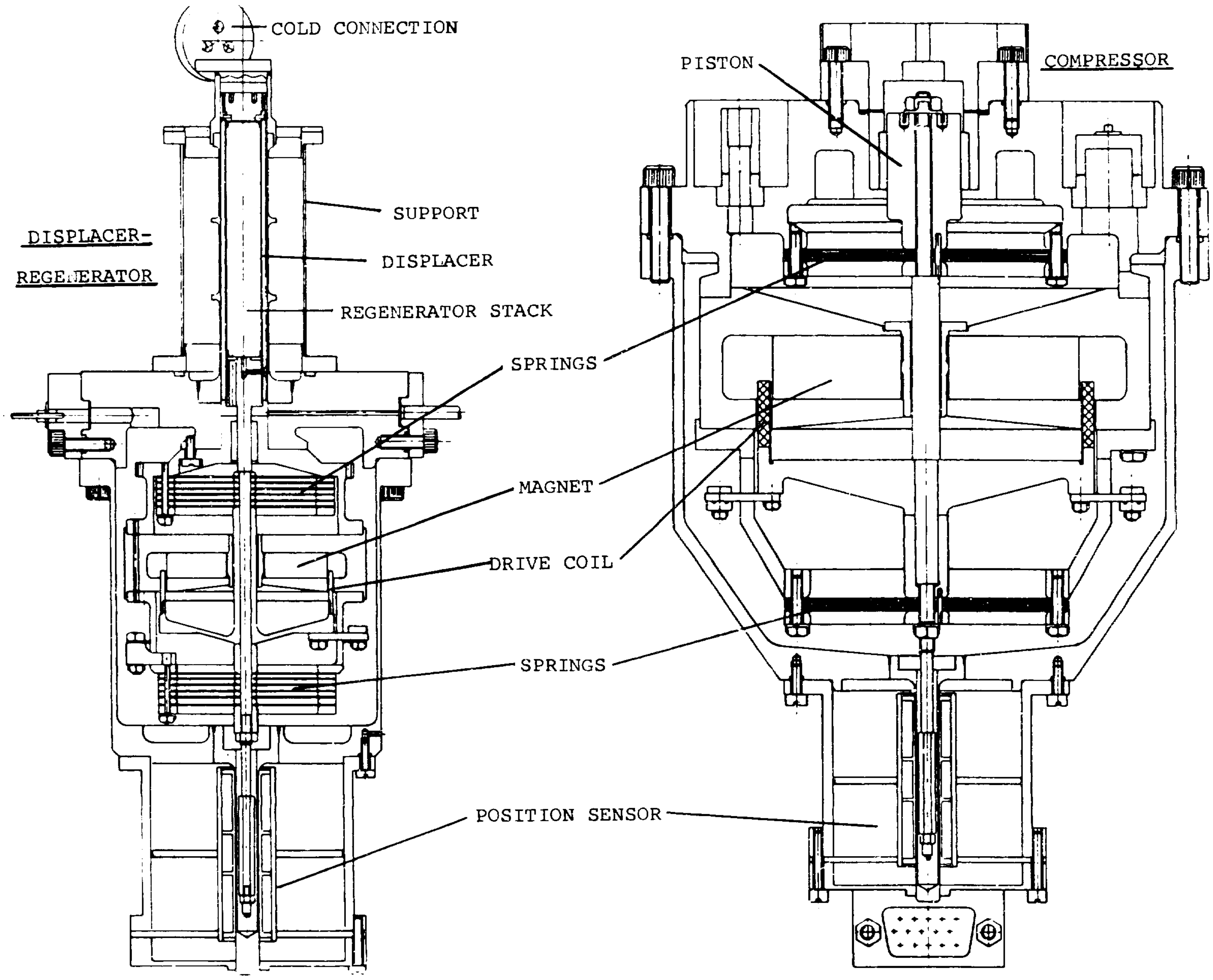
COLD CONNECTION
SUPPORT
DISPLACER-
REGENERATOR
DISPLACER
REGENERATOR STACK
PISTON
COMPRESSOR
SPRINGS
MAGNET
DRIVE COIL
SPRINGS
POSITION SENSOR

Figure 7. Arrangement of flight model cooler

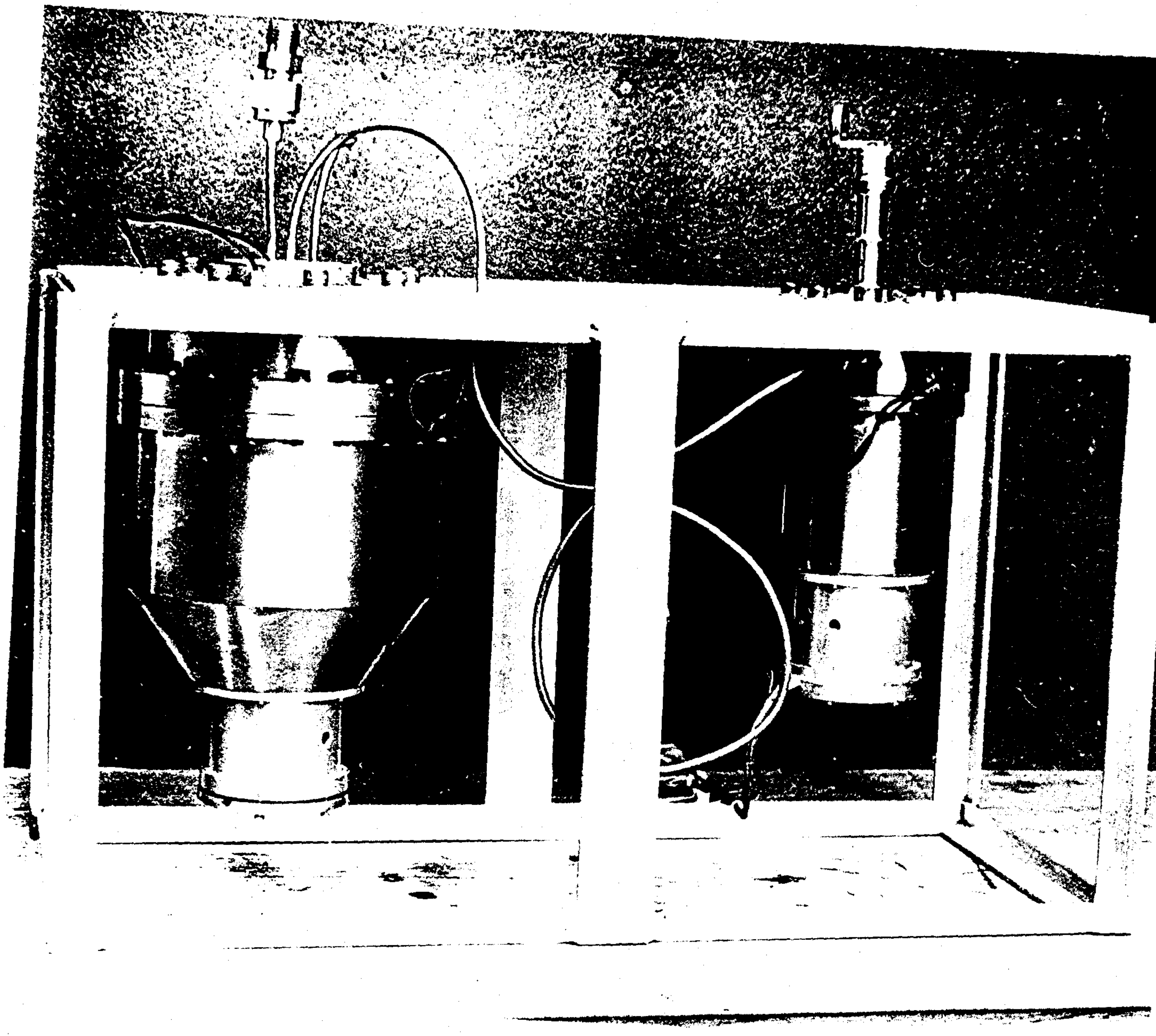

Figure 8. First flight model cooler

ed in these tests.

A pair of flight units is to be installed in the vacuum chamber for more complete performance assessment. The more representative thermal mounting of the cooler will reduce temperatures, particularly at the compressor head, and, based upon prototype results, the performance will further improve.

3.3. Safety tests

The coolers are classed as pressure vessels by the STS safety office and the ISAMS flight units must undergo additional screening for flaws in materials and faults in fabrication. The envelope components and welds have been subjected to dye

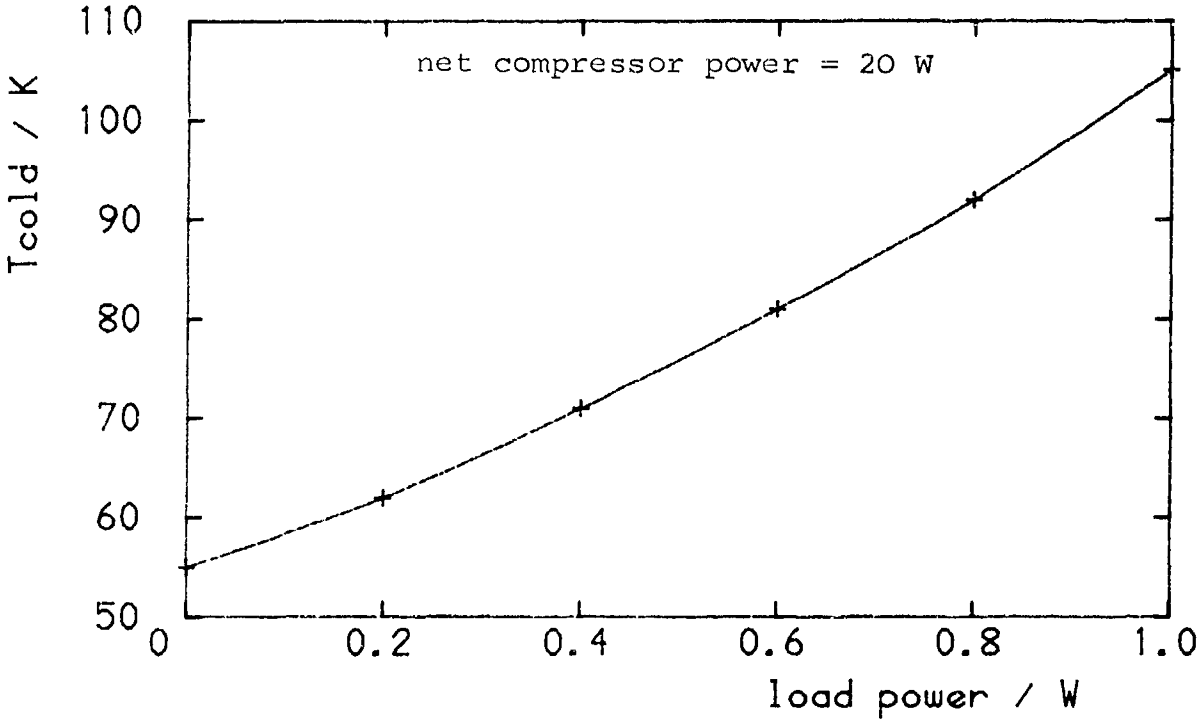

Figure 9. Preliminary performance measurement

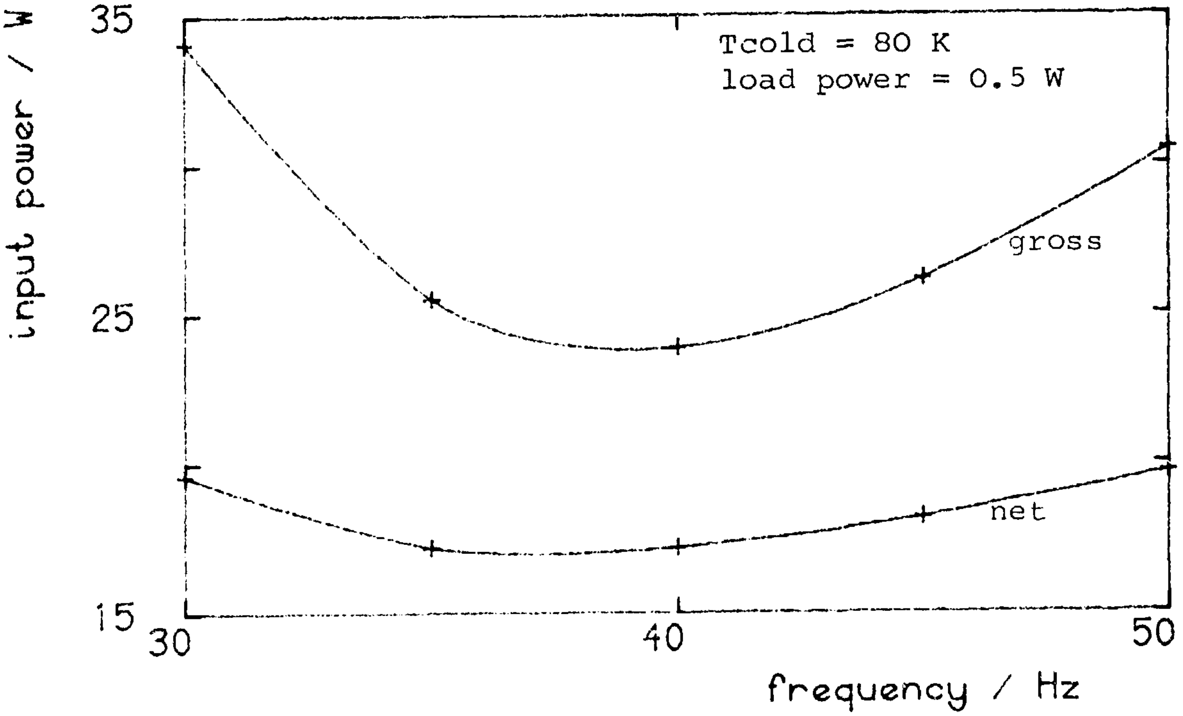

Figure 10. Performance vs frequency

penetrant and radiographic examination and the completed coolers will be proof pressure tested to 6 MPa.

4. Conclusions

The failures which have occurred in the life and vibration tests, whilst disappointing, have both been due to incorrect assembly rather than design weaknesses. A tightening up of assembly procedures is expected to reduce the risk of such problems in the future. In all other respects the tests have been successful and have given us confidence in the basic design of the cooler.

Operation of the coolers in the thermal-vacuum chamber has produced a map of performance against thermal and operational parameters. This map has been used to specify heat sinking requirements in ISAMS and to define what freedom we have in choosing running conditions. The performance achieved by the first flight unit is more than adequate to fulfill the ISAMS requirement.

Drawing office support in detailed design of the flight coolers has been supplied by R.Wolfenden, B.Smith and F.Row of the Rutherford Appleton Laboratory. Mechanism assembly has been carried out with care and patience by M.Clark and S.Delph at Oxford. T.Bradshaw provided valuable assistance in setting up the thermal vacuum tests. Many of the measurements presented here have been made by C.Adams and Zhang Zhimin.

This development programme has been funded by the United Kingdom Science and Engineering Research Council.

5. References

[1] Werrett et al., Development of a Stirling cycle cooler for spaceflight applications, in: "Advances in Cryogenic Engineering", vol 31, Plenum, New York (1986).

[2] Bradshaw et al., Performance of the Oxford miniature Stirling cycle refrigerator, in: "Advances in Cryogenic Engineering", vol 31, Plenum, New York (1986).

[3] "Evaluation of a cryogenic refrigerator for focal plane instrumentation", BAe document TP8095, ESA contract number 5089/82/NL/PB.

[4] Gregory D.A., Engineering applications of laser speckle photography for sub-micron measurement, in: "Proceedings of the Industrial and Engineering Survey Conference", London (1980), p.4.2/1-16

FIRST RESULTS ON A PROTOTYPE TWO STAGE MINIATURE STIRLING CYCLE COOLER FOR SPACEFLIGHT APPLICATIONS

T. W. Bradshaw

Rutherford Appleton Laboratory
Chilton, Didcot, Oxon, OX11 0QX, U.K.

Work is underway at the Rutherford Appleton Laboratory on a miniature Stirling cycle cooler for the temperature region below 40 K. The cooler has all the design features associated with the 80 K Oxford cooler which makes it suitable for long life spaceflight applications. The design and performance of the single stage Oxford cooler has been reported in two papers at the 1985 Cryogenic Engineering Conference. The mechanics of the prototype cooler presented here are similar, and in some cases identical, to the single stage cooler. The prototype cooler has a two stage displacer fed by two compressors working in opposition. The cooler has no rubbing parts, clearance seals are used throughout and are maintained by diaphragm springs. Each moving element has its own linear motor and position sensor, allowing for servo control. The cooling power as a function of cold end temperature is presented, the cooler giving approximately 100 mwatts at 37 K with a base temperature of around 30 K, the cooler has achieved a base temperature of 26 K. The optimum operating phase between the compressor and the displacer of 58° is somewhat lower than expected, this is discussed.

Key words: Cryocooler; cryogenic; low power refrigeration; multi stage; regenerative cooler; split Stirling; Stirling cycle.

1. Introduction

The Rutherford Appleton Laboratory (RAL) has been involved for several years in the development of single stage Stirling cycle coolers in support of two space projects, these are ISAMS (Improved Stratospheric and Mesospheric Sounder) to be flown on the Upper Atmosphere Research Satellite and ATSR (Along Track Scanning Radiometer) on the European Space Agency remote sensing satellite ERS-1. The need to cool the detectors for ISAMS to around 80 K led to the development, several years ago, of a small prototype single stage Stirling cycle cooler by the Department of Engineering Science at Oxford University using an idea for the linear drive and suspension system from an instrument developed by the Department of Atmospheric Physics. RAL later became involved with the department of Atmospheric Physics in the development of these coolers for space use. It was soon recognised that this cooler had wider applicability, and a decision was made to use it on ATSR. It has

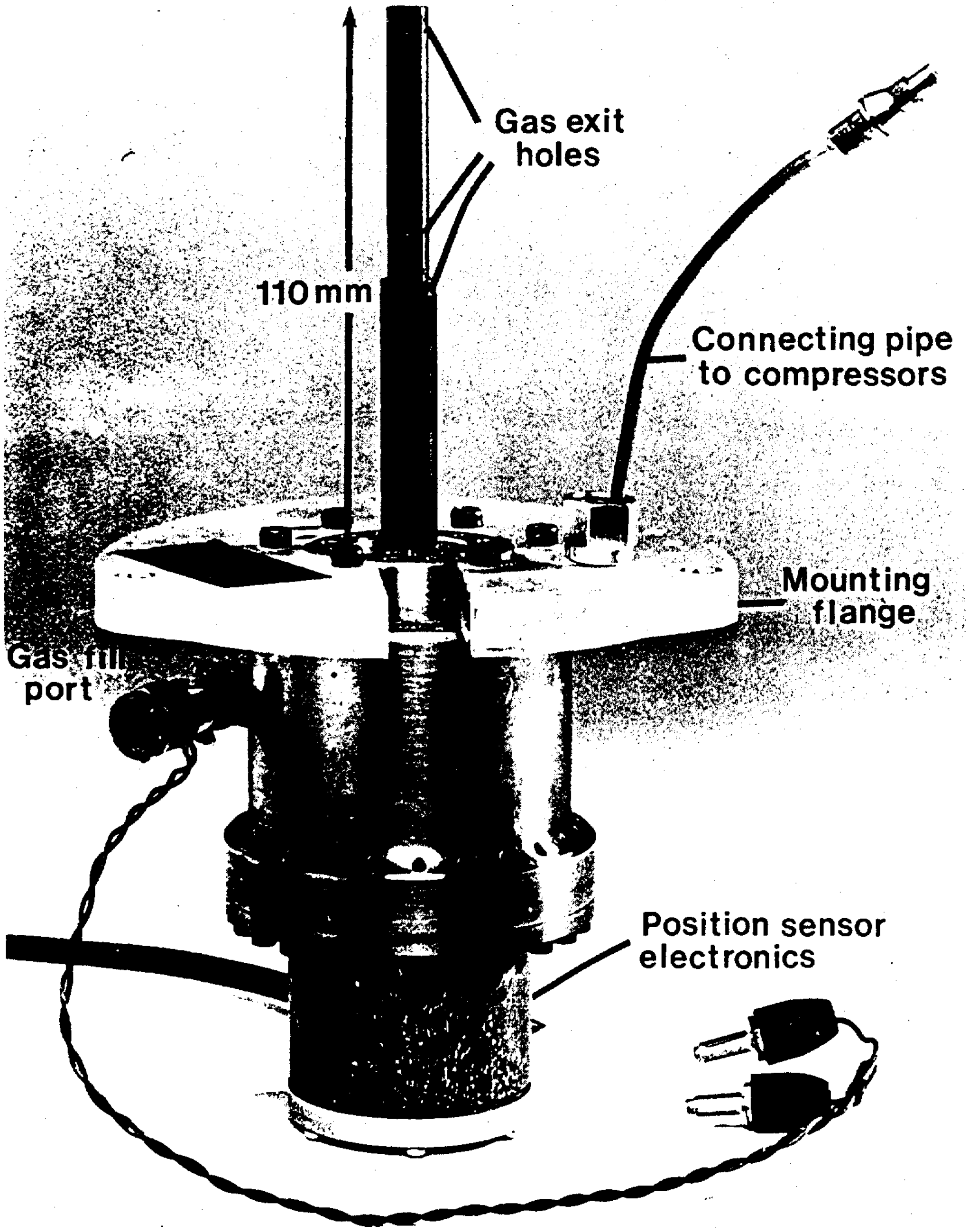
Gas exit holes
110mm
Connecting pipe to compressors
Mounting flange
Gas fill port
Position sensor electronics

Figure 1. The displacer unit of the two stage cooler

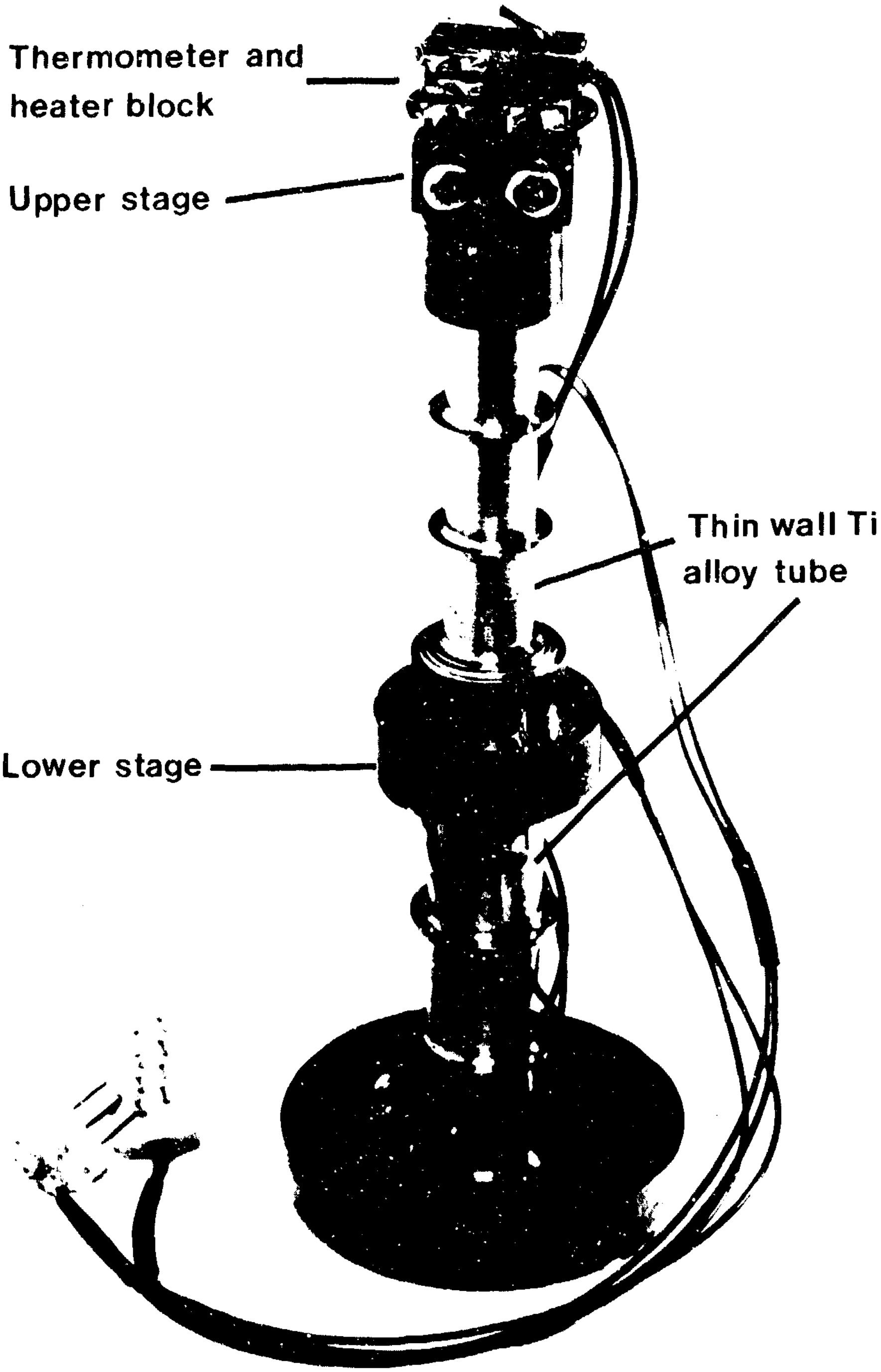
Thermometer and heater block
Upper stage
Thin wall Ti alloy tube
Lower stage

Figure 2. The outer sleeve of the displacer (the radiation shield is not shown).

been noted [1,2][1] that future space missions will require closed cycle coolers capable of achieving temperatures well below 80 K and which may be used as a pre-cooler for a further cooling stage. Experiments are being proposed that require low power focal plane cooling with lifetimes that rule out conventional cooling techniques involving solid or liquid cryogens. It was clear that in order to meet these requirements the work on the single stage cooler would have to be extended to cover lower temperatures. To this end, the prototype cooler described here was built to act as a test bed, and to give experience in the operation and performance of these devices.

2. Description of the cooler

The design of the cooler utilises all the long-life design features associated with the single stage Oxford miniature Stirling cycle cooler that has been developed for space use. The details of its design and performance have been described in detail elsewhere [3,4]. The cooler is of the split Stirling type with the displacer unit remote from the compressors, connected only by a gas feed pipe. There are no rubbing parts in the cooler, clearance seals are used throughout, maintained by beryllium-copper diaphragm springs operating well below their fatigue failure level. The moving parts are driven by loudspeaker - type linear drive motors. Two compressors are used, feeding one displacer unit, these are run on, or near, resonance at around 35 Hz and have a swept volume of approximately 2614 mm^3. A benefit of using two compressors is the ability to reduce the vibration levels from the cooler. The moving parts in the compressors are servo-controlled and a high degree of momentum compensation can be achieved by having the moving elements in the compressor running in opposition to each other.

The displacer unit has been modified from the single stage cooler, by having a stepped displacer as shown in figure 1. This introduces an expansion space intermediate in temperature between the cold stage and room temperature. The diameters of the upper and lower displacers are 9 and 12mm respectively. The lower regenerator is of 250 mesh phosphor bronze discs while the upper regenerator is composed of two different materials: the bottom two thirds are of 250 mesh phosphor bronze discs, and the remainder of 450 micron nominal diameter gold plated lead balls in single layers separated by gauze discs. This is a trial configuration, the performance of the cooler with different regenerator materials is undergoing assessment. The dimensions of both regenerators are the same: 7.2mm in diameter and 42 mm long. Having the regenerators the same diameter has greatly eased fabrication. The gauze discs were held within a thin wall titanium alloy (6% Al, 4% V) tube inside the plastic displacer (Vespel SP-3 [5]). The displacer has a nominal stroke of 3mm. The outer sleeve is shown in figure 2. This was constructed from copper and titanium alloy (with a wall thickness approximately 0.1 mm). The displacer was machined to have a radial clearance on this item of 35 microns. A thin wall copper radiation shield (not shown) fits on to the intermediate stage surrounding the cold end.

The regenerators are separated by a plastic interface piece containing a gas feed hole. The gas enters the upper expansion space via six gas exit holes and an

---

[1] Numbers in brackets refer to the literature references at the end of this report.

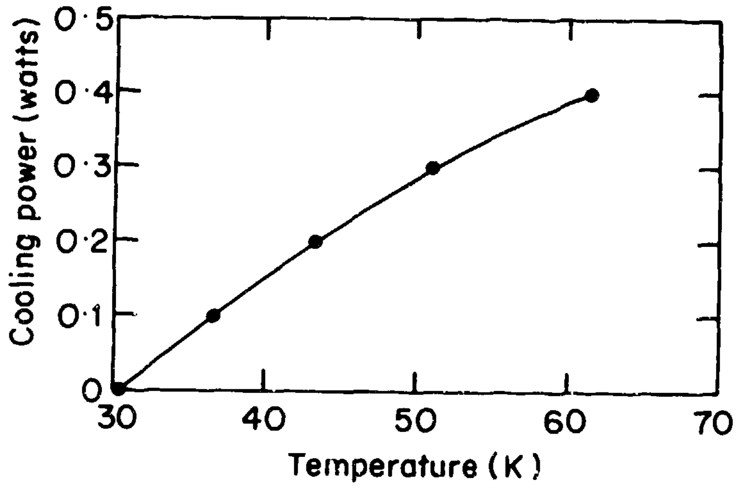

Figure 3. The cooling power vs. temperature (P=0.85 MPa, f=30 Hz, phase=58°).

annular heat exchanger. The intermediate expansion space has two such heat exchangers.

The temperature is measured using a platinum resistance thermometer on the cold end and a reverse-biased silicon diode on the intermediate stage, these measure to an accuracy of about 0.1 K and 1 K respectively.

3. Preliminary test results

3.1 Cooling power

The cold end is fitted with a heater to enable the temperature of the cold end vs. applied heat load to be measured, this is shown in figure 3. At temperatures below 50 K there is a marked reduction in cooling power which suggests a reduction in regenerator efficiency. The input power varied from 60 watts at 30 K to 57 watts at 62 K. The intermediate stage temperature varied between 142 and 166 K over this interval. A base temperature of 26 K was achieved with 380 mesh phosphor bronze discs in place of the lead regenerator material.

3.2 The optimum operating phase

An investigation is being made with the department of Atmospheric Physics at Oxford University regarding the phase relationship between the motion of the compressor, displacer and the pressure pulse for optimum performance. The optimum performance

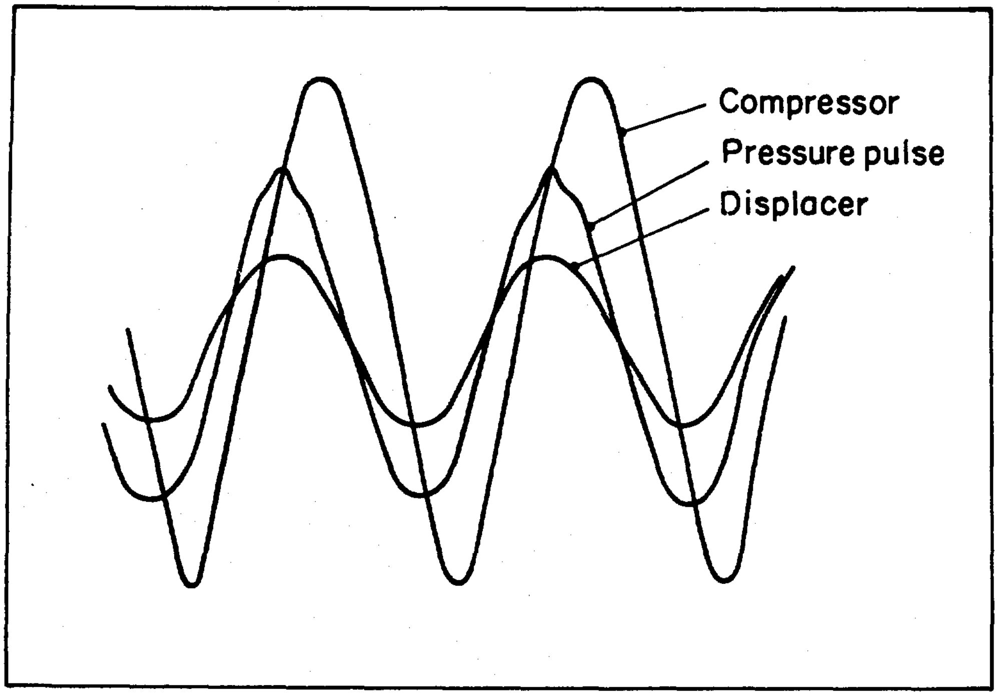

Figure 4. The phase between the compressor piston, displacer and the pressure as measured at the compressor (P=0.9 MPa, f=37 Hz, phase=50°).

in terms of cold end base temperature (no applied load) was with a phase (between the motion of the moving elements in the compressor and the displacer) of about 58° at a frequency of 30 Hz (this setting did not give the best intermediate stage temperature which was achieved with a phase angle of about 70°). The cold end base temperature is relatively insensitive to phase, around the optimum. For instance, a 5° deviation from the optimum at 30 Hz caused a 1 K increase in cold end temperature. This sensitivity rapidly increases outside these limits. The relative phase between the compressor piston motion, the pressure waveform and the displacer motion can be seen in figure 4. This is a tracing of an oscilloscope photograph showing the output from the position sensors on one of the compressors, the displacer and a pressure transducer located in the head of one of the compressors (the output from the position transducers indicate minimum volume in the compressor cylinder or expansion space for positive output). It can be seen that the pressure waveform leads the motion of the compressor piston by about 35° as previously reported for the single stage cooler [4]. The displacer/regenerator acts as a thermal compressor, producing a pressure pulse in phase with its motion. An additional component in this phase relationship is leakage past the piston of the compressor. These two effects combine to produce the phase lead in the pressure pulse with respect to the compressor piston motion. The optimum phase setting for this type of cooler is therefore quite different than expected from classical arguments. The phase lag between the pressure waveform in the compression and expansion spaces in a single stage cooler has been independently measured [6] but does not fully explain this behaviour.

4. Future work

The testing of the prototype is continuing, with measurements being made on the performance of the cooler with various types of regenerator material. The phase relationship between the pressure pulse and the motions of the compressor and the displacer is under investigation with the department of Atmospheric Physics at Oxford University. This effect greatly influences the performance of this type of cryocooler and a detailed explanation is required for design purposes. It is hoped to extend the work on two stage coolers to lower temperatures with the addition of a further cooling stage, either with the development of a three stage Stirling cycle cooler, or by using the cooler to pre-cool a Joule Thomson stage.

The development program is funded by the United Kingdom Science and Engineering Research Council. A design study on this cooler was funded by the European Space Agency under contract number 6342/85/nl/pb(sc). I would like to thank S.T. Werrett and J. Delderfield for useful discussions and J.M.D. Lister for his careful work in taking the measurements.

6. References

[1] Stultz, V.W., Spaceborne cooler technology for future JPL instruments, JPL White Paper, Jan 25 1985.

[2] Sherman, A., National Aeronautics and Space Administration needs and trends in Cryogenic Cooling, Cryogenics 23, (7), 348-352 (July 1983).

[3] Werrett, S.T., Peskett, G.D., Davey, G., Bradshaw, T.W., and Delderfield, J., Development of a small Stirling cycle cooler for spaceflight applications, Adv. Cryo. Eng. 31, 791-799 (Plenum, New York, 1986).

[4] Bradshaw, T.W., Delderfield, J., Werrett, S.T., and Davey, G., Performance of the Oxford Miniature Stirling cycle refrigerator, Adv. Cryo. Eng. 31,801-809 (Plenum, New York, 1986).

[5] Vespel is a trade mark of; DuPont de Nemours, p.o. box CH-1211, Geneva 24, Switzerland.

[6] Werrett, S.T., private communication

Preceding Page Blank

A DYNAMOMETER FOR TESTING LINEAR MOTORS FOR MINIATURE CRYOCOOLERS

Wilfred J. Gully and Robert L. Berry

Hughes Aircraft Company
Electron Dynamics Division
Torrance, CA 90509

The compressor design of small split-stirling cryocoolers may be simplified by the use of linear motors. In an effort to optimize the design of such motors, a special dynamometer system having several useful configurations was constructed. In one configuration, a motor could be driven as a generator and magnetic circuit information could be obtained. In another configuration, the efficiency of the motor for converting electical energy into work against an gas load could be studied. With this device motor versions were evaluated and the proper operating conditions determined. The details of this dynamometer will be described, and some general results illustrating its use will be presented.

Key Words: Cooler; cryogenic; dynamometer; generator; linear motor; resonance.

1. Introduction

In order to create reliable and efficient minature cryocoolers, we have been[1] developing compressors that employ linear motors operated at resonance. [1,2] To aid in compressor motor design, we have built a linear motor dynamometer to help us establish dynamic motor parameters. The obvious advantage was to separate the motor development from the cryogenic system and not rely solely on cryogenic performance as a measure of motor effectiveness. Our device can both extract power from a motor driven at resonance to determine its efficiency, and drive the motor in reverse as a generator for an evaluation of its electrical properties. We shall discuss its design and operation, and illustrate its use with some specific examples.

2. Motor Dynamometer Mode of Operation

This dynamometer differs substantially in detail, but not in principal from ordinary rotary motor dynamometers. The two new factors are the linear motion and the resonant operation. The linear motion is an important aspect because it

[1] Numbers in brackets refer to the literature references listed at the end of of the report.

reduces wear and simplifies the compressor design. With linear motion it is possible to align the force of the gas on the piston with the electrical force of the motor. In this way forces perpendicular to the moving surfaces are substantially reduced which enables us to replace rotary ball or needle bearings with simple unlubricated bearing surfaces. For the dynamometer, the linear motion complicates the way the load can be applied to the motor. We incorporated a piston assembly with a leak to apply this load force.

The second new factor is the resonant operation of the motor. This is important in order to attain high conversion efficiency of electrical to mechanical energy. The resonance frequency is given by:

$$w = \mathrm{sqrt}\ (k/m)$$

Where the spring constant k is given by a combination of the spring of the gas in the cylinder and of physical springs and m is the total moving mass of the armature and piston. At resonance, the phase angle between the force and velocity is zero so power is continuously transferred to the motor. In this way the work is done without an oscillatory excess flow of energy which minimizes the ohmic losses and leads to the high efficiency. The second new feature of this dynamometer therefore had to be the ability to adjust the spring constant to bring the unit into resonance at the desired frequency.

2.1. Hardware

A schematic of the apparatus is presented in Figure 1. The main body of the device provides support for the stator, the bearing surfaces for the armature, and the mounting surfaces for the auxiliary hardware. The unit has several provisions for adjusting the force on the motor. The force must have a magnitude and a phase relative to the motion of the armature. The magnitude is determined in large part by the pressure in the cylinder and the area of the piston. The piston area was made much larger than that of an actual cryoengine compressor so the device could work around ambient pressure and have the proper force. The dead volume in the cylinder could be adjusted with shims to change the compression ratio and consequently the spring constant of the gas for a given stroke. An adjustable leak from the cylinder to the atmosphere added a hysteretic component to the force of the gas by allowing the amount of gas in the cylinder to change during a cycle. This simulates the effects of gas flow and the refrigeration cycle on the operation of the compressor. Furthermore, various mechanical centering springs could be inserted between the housing and the armature. In this way, a specified in-phase and out-of-phase load could be applied to the motor while the resonance frequency could be independently determined.

2.2. Efficiency

The typical measure of efficiency of the motor is the motor constant K_m, which is the amount of power transfered to the armature relative to the ohmic losses sustained providing that power. In our dynamometer, we further subdivided the armature power into the amount transfered to the gas and the amount lost to the frictional drag on the armature. We employed the fraction of the input power dissipated in the gas as the figure of merit in our tests.

The total force on the armature is composed of that of the gas, the springs, and of friction in the bearing surfaces. Assuming that the springs are lossless, the average power delivered to the armature over a cycle only goes into PV work and to drag. The PV work was obtained by measuring the gauge pressure of the cylinder with a sensitive diaphragm pressure gauge, and monitoring the piston motion with a LVDT mutual inductance sensor. By plotting these on an oscilloscope, the PV diagram could be measured and the power delivered to the gas determined. The drag force was not routinely obtained, but its magnitude could be estimated by measuring the decay of the motion of the armature. It is a complex term that depends on the nature of the bearings, the weight of the moving assembly, magnetic sideforces, and the detailed alignment of the components. It was only approximately that found in a compressor, but since it remained reasonably constant from run to run the dynamometer was still useful in evaluating changes to the motor.

As discussed, power transferred to the armature divides between useful gas work and heat due to drag. Additional losses occur in the motor that can be characterized by electrical measurements on a motor where the armature is prevented from moving. In this fixed armature mode, the input power to the device can be measured as a function of frequency and current with a wattmeter. The effective resistance obtained by dividing the power by I^2 exceeds the simple dc resistance by the amount due to the hysteretic losses in the premeable material and to eddy currents. These can be separated by their frequency dependence, and by separate hysteresis measurements on the laminations. This total effective resistance at the operating frequency is used to estimate the electrical losses when the motor is operating. It errs by the small amount the moving armature affects the processes involved.

The distribution of power could now be determined. The current was measured with an ammeter and the input power was measured with a wattmeter. The power P(in) became:

$$P(in) = I*I*R + f* \S\ PdV + P(drag)$$

Where all but the drag could be determined reasonably well. The true efficiency of the motor was given by f* § PdV/P(in), and was generally the figure of merit. It was a function of the phase and magnitude of the load and the stroke, so these parameters were controlled while motor variations were being evaluated. Because of changes in drag, the dynamometer results after disassembly were reproducible to only ± 3%.

3. Generator Dynamometer Mode of Operation

The dynamometer could be reconfigured as in Figure 2, to enable us to measure the output voltage of the motor as it was driven by an auxilliary rotary motor. In this mode the springs, cylinder head, and pressure gauge are removed and the crank assembly added. The open circuit emf induced in the coil is a dynamic measure of the force/amp rating "g" of the motor since the armature power:

$$P(\text{armature})=F*\text{velocity}=(g*I)*\text{velocity}=I*(g*\text{velocity})=I*\text{emf}.$$

The generator is a sensitive way to monitor this coefficient as small changes are made to the motor because the output voltage is insensitive to the effects of the drag force on the armature. Variations in drag simply require variations in power delivered by the external motor to operate the armature at the desired frequency.

The output voltage is not necessarily sinusoidal, even though the armature is driven sinusoidally. Equivalently, the force/amp rating can depend upon the position of the armature which has significant design consequences. This can be measured by plotting the induced Emf versus a differentiated position waveform on the oscilloscope, as shown in Figure 3. Since the armature is driven harmonically, the velocity is a known function of position. In Figure 3a the motor constant is clearly independent of position because the voltage is proportional to velocity throughout the cycle. In Figure 3b, however, the voltage is depressed during the low velocity part of the cyle at the extremes of travel. This can be caused by saturation in a moving magnet motor, or by the coil leaving the magnet in a moving coil motor.

The generator can be run with various resistive loads across its output. This provides information on the change in motor performance when flux due to the flow of current is present. However, since the power is coming from the motor, the phase of the flux is evidently different from that occurring in motor operation and is of limited use. One finds primarily that the output power is maximized when the impedance is matched to the load. The maximum output power does depend on the effectiveness of the magnetic circuit, so it generally correllates with motor efficiency.

There was a useful operating mode we had neglected to include. The addition of a strain gauge on the shaft connecting the crank to the armature would allow during generator operation a measure of the drag friction due to the bearings and that due to any magnetic interaction between the stator and armature at the operating frequency. This would have allowed a more quantitive evaluation of these effects in our motor.

4. Applications

Many configurations of linear motors were evaluated with the dynamometer. Sizing and other details of the magnetic circuit were optimized empirically while the motor operated under realistic conditions. Modifications were crosschecked in the motor and generator modes to insure that the observed effects were consistent.

Two specific applications of the dynamometer will now be discussed. The first illustrates the importance of operating the motor at its resonance frequency. In Figure 4, we plot the power delivered to the gas and the power dissipated as ohmic loss in a motor, as the frequency of the drive oscillator was varied on both sides of the dynamometer resonance at 58 Hz. This was measured at constant stroke, so the fraction of power lost to drag can be expected to be the same throughout. Clearly, the maximum power transfer to the gas occurs at resonance where the power flows directly to the load. The impedance of the motor depends upon the phasing of the emf induced by the armature relative to the drive current. It is resistive at resonance which accounts for the efficient power transfer, but inductive below resonance and capacitive above.

The second application illustrates the usefulness of the dynamometer in evaluating the performance of a motor driver breadboard circuit. We have been developing electronic circuits to drive the coolers that, among other requirements, must operate from a DC voltage that ranges from 18 to 32 volts. The dynamometer in Figure 1 was excited at its resonance frequency by the drive waveform shown in Figure 5. We illustrate a square wave voltage pulse with approximately a 20% duty cycle that was applied across the terminals of the motor. The motor current responded with a modified inductive rise. The supply was then disconnected, and current decayed through a diode back across the switch which caused a momentary negative spike across the motor. This was followed by the open circuit voltage of the moving armature as it turned around, and then a voltage pulse in the opposite direction. The force applied to the armature is proportional to the current and is, therefore, roughly a triangular pulse with a width determined by the duty cycle.

The power delivered to the armature was proportional to the magnitude of the voltage and the duration of the pulse. In one series of tests, the dynamometer was operated at constant output power as a function of the input voltage. As the voltage was raised, the duty cycle was decreased until the PV work performed was at a specified value. The total input power was then recorded and the result is displayed in Figure 6. The power required to drive the unit increased by approximately 30%, indicating that the high voltage and short duty cycle pulse was much less efficient in driving the motor than was the low voltage long duty cycle pulse. The cause is apparently the harmonic content of the driving force waveform at short duty cycles, and its effectiveness in driving a resonant system. The average current flow during a short pulse had to be higher to deliver the same impulse and power to the armature. However, the ohmic losses increased substantually during a short pulse since they are proportional to the square of the current. The total input power, therefore, increases leading to the decrease in motor efficiency. Because of this shortcoming alternate methods of driving the motor were initiated.

5. Conclusions

A versatile device for evaluating the operation of resonant linear motors has been described. It provides for the adjustment and determination of primary load on the motor under reasonably well controlled conditions. Because of its flexibility various motor effects were successfully sorted and a detailed understanding of the motors obtained

We would like to express our appreciation to H. Kroebig for his splendid design and to A. Nickels for his fabrication support.

6. References

1. D. Lehrfeld, Split-Stirling, Linear Resonant, Cryogenic Refrigerators, Second biennial conference on Refrigeration for Cryogenic Sensors and Electronic Systems December7th and 8th, 1982, Goddard Space Flight Center, Greenbelt, Maryland (NASA Publication 2287).

2. A. K. Dejonge, A Small Free-Piston Stirling Refrigerator, Proceedings of the 14th IECEC, Boston, August 1979.

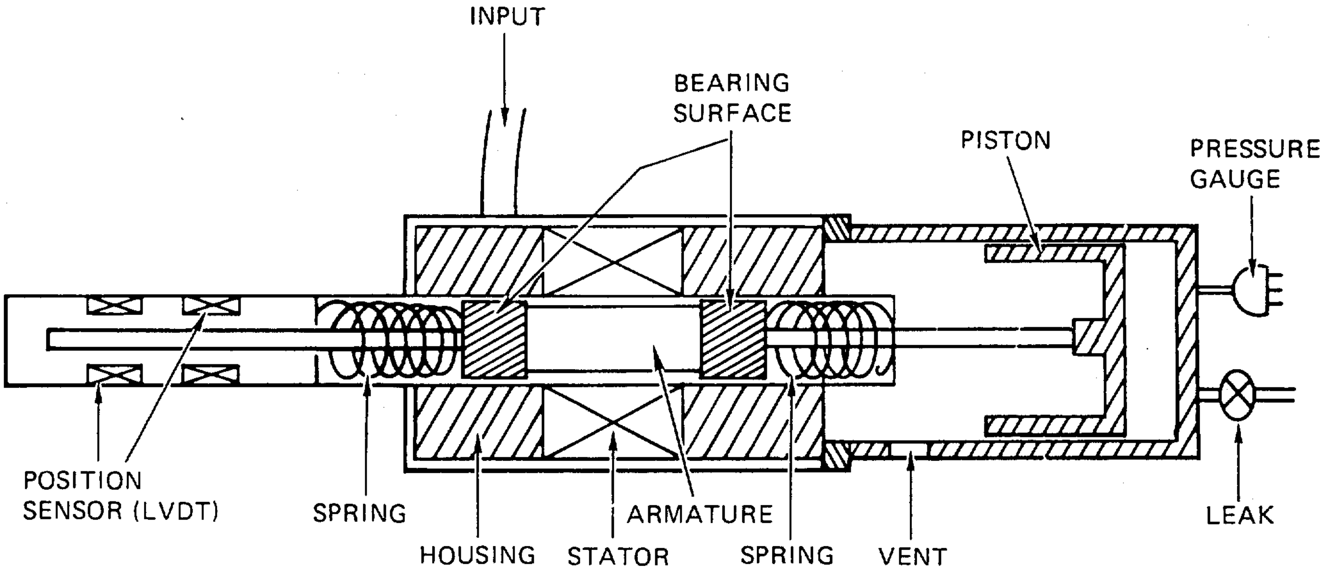
INPUT
BEARING SURFACE
PISTON
PRESSURE GAUGE
POSITION SENSOR (LVDT)
SPRING
HOUSING
STATOR
ARMATURE
SPRING
VENT
LEAK

Figure 1. A diagram of the motor dynamometer described in the text, illustrating its principal components.

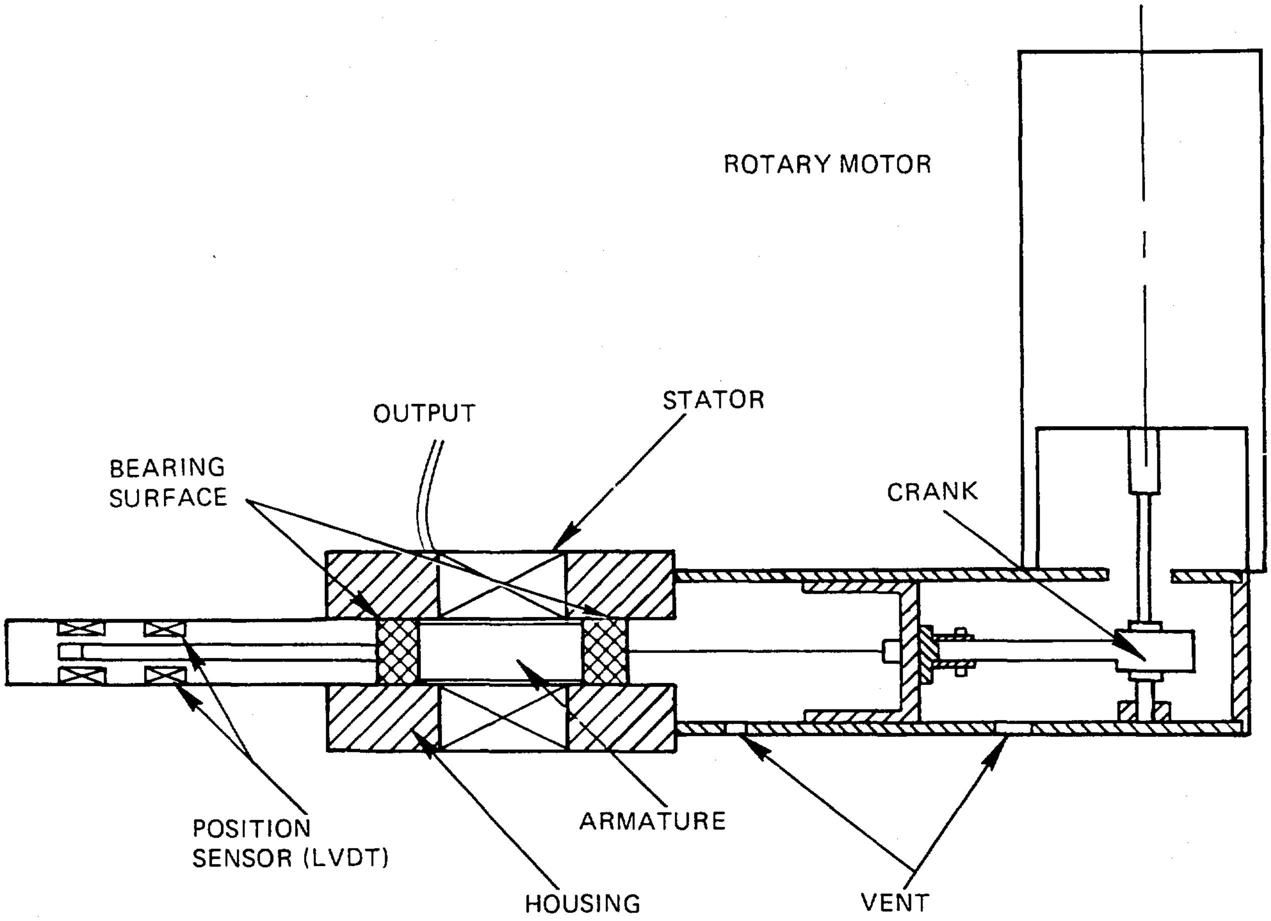

ROTARY MOTOR
OUTPUT
STATOR
BEARING SURFACE
CRANK
POSITION SENSOR (LVDT)
ARMATURE
HOUSING
VENT

Figure 2. A diagram of the generator version of the dynamometer, in which the rotary motor drives the armature to generate an output voltage.

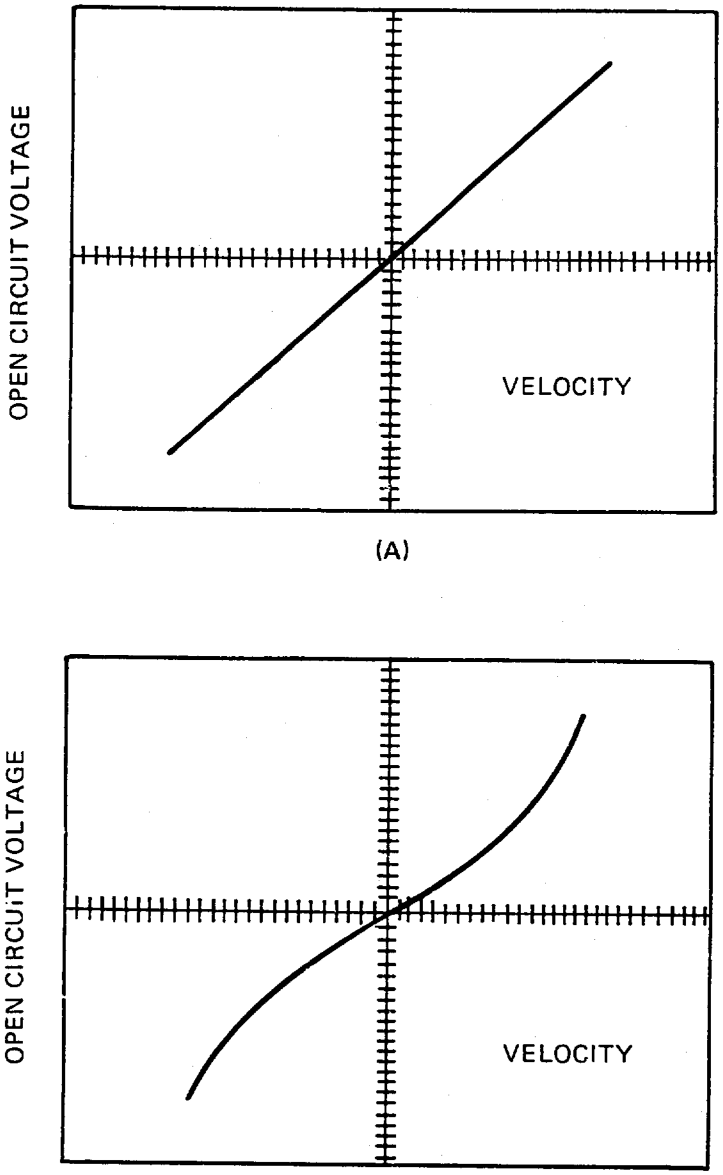

(A)

(B)

Figure 3. Open circuit generator voltage plotted against measured armature velocity illustrating position dependent non-linear behavior.

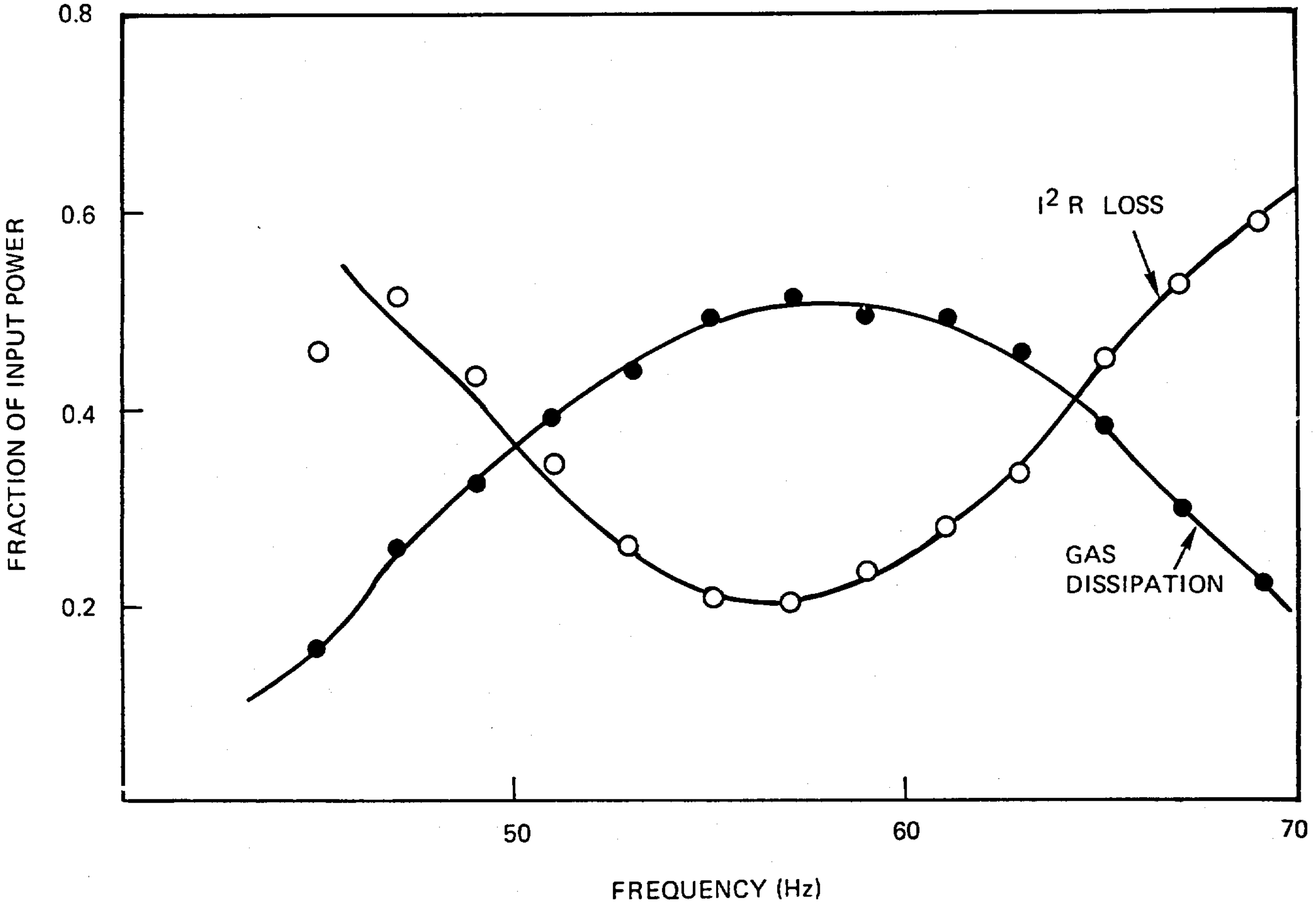

Figure 4. Demonstrating the dynamometer by showing the advantage of operating the motor at resonance.

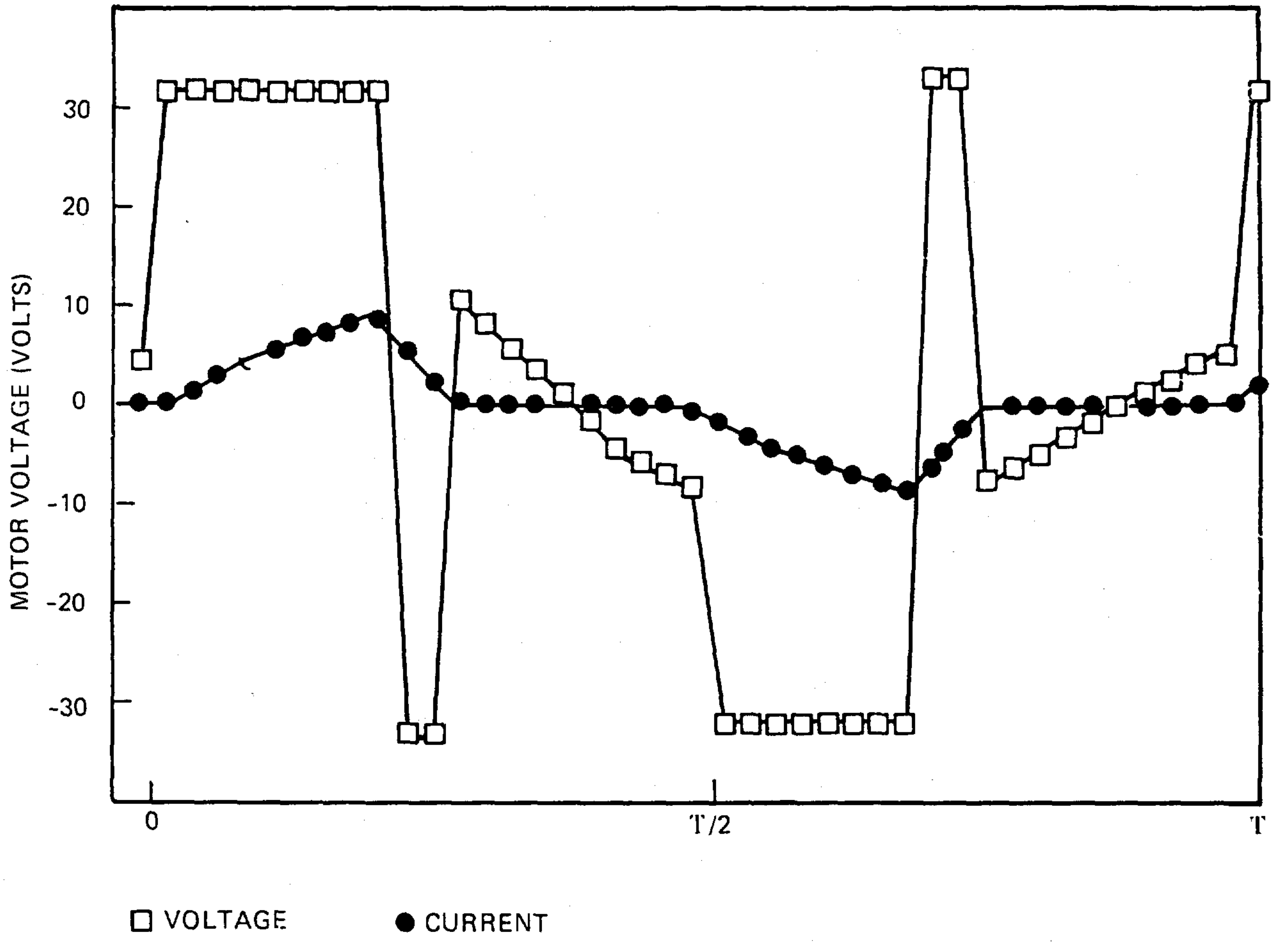

Figure 5. Drive waveform applied to the linear motor dynamometer during breadboard efficiency evaluation tests.

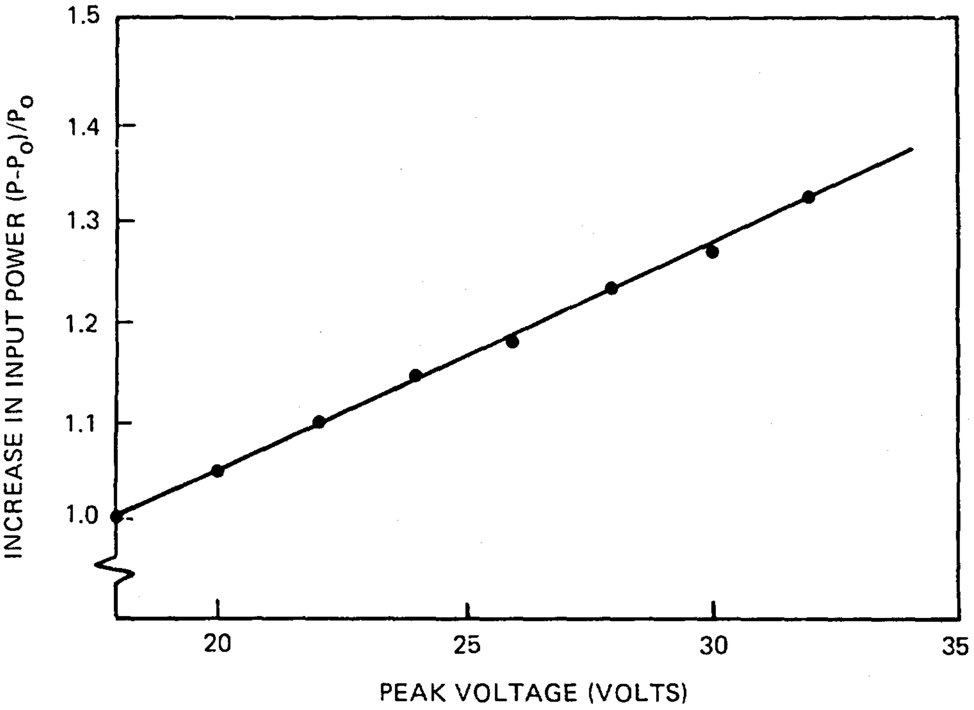

Figure 6. Fractional increase in input power due to increased I^2R losses during short high voltage drive pulses.

Preceding Page Blank

MINIATURE MULTISTAGE HIGH-PRESSURE GAS COMPRESSOR FOR LINDE-HAMPSON CRYOCOOLERS

E. Atkins, G. Walker, S. Zylstra
General Pneumatics Corporation
Western Research Center
Scottsdale, AZ 85260

A novel configuration for a compact multistage gas compressor was investigated. The compressor is intended for inclusion in small closed cycle Linde-Hamson cryocoolers with gas liquefaction by Joule-Thomson expansion.

The compressor arrangement may be described as a four or five stage pressure balanced opposed piston, twin-tandem compressor with a Scotch-yoke drive mechanism energized by an electric motor with electronic control. The new compressor is simple, very compact, easy to manufacture at relatively low cost and has the potential for long, maintenance free operating life.

A prototype compressor was fabricated in the course of the Phase I SBIR project entitled "Compact Reliable Low-Capacity Helium Liquefier"*. Test results and operating experience are reviewed.

Key Words: High pressure, multistage gas compressor, Linde-Hampson cryocooler, Joule-Thomson expansion

1. Introduction

Gas compressors are utilized in a large number of applications from miniature high pressure gas compressors for Linde-Hampson closed cycle cryocoolers and Joule-Thomson liquefiers to portable recharging units for self-contained underwater breathing apparatus (SCUBA). The applications cover a wide range of sizes, flow capacities and pressure ratings.

A new miniature multistage high pressure gas compressor concept was developed at the General Pneumatics Corporation's (GPC) Western Research Center for closed cycle Linde-Hampson cryocoolers, with Joule-Thomson expansion for gas liquefaction, intended for use in a "Compact Reliable Low-Capacity Helium

---

*Supported in part by the United States Department of Energy Contract No. DE-AC02-85ER80271.

Reliquefier". The technology of Linde-Hampson cryocoolers and Joule-Thomson liquefiers has been summarized by Walker (1983) [1].

2. Miniature Multistage High Pressure Gas Compressor

This new development in multistage high pressure gas compressors is less complicated, more compact, more reliable and easier to manufacture at less cost than some of the more conventional compressors. The device is a four stage reciprocating piston type compressor with a sliding Scotch-yoke drive mechanism. The compressor accomplishes the overall 100:1 compression ratio in four stages. As a consequence, the overall performance characteristics, in terms of input power vs. output flow and pressure, are drastically improved and since the duty of the valves is reduced, the rate of valve failure is significantly decreased (no valve failures were experienced throughout the performance and evaluation testing).

Compressors previously developed at GPC's Western Research Center, for Linde-Hampson cryocoolers, were primarily of the diaphragm type. The intent was to eliminate contaminants induced by rubbing and sliding seals which tends to cause cryostat blockage and flow restriction at the orifice (Joule-Thomson valve). A new breakthrough in cryostat design, specifically the Joule-Thomson expansion valve, by GPC's Western Research Center has virtually eliminated these problems. These new cryostats, which are not susceptible to contamination, have been summarized by Hedegard (1986) [2].

Diaphragm type compressors, comparable in size to piston type compressors, must run several times faster (usually 3 to 6) than piston type compressors to pump an equivalent amount of fluid. This is due to the smaller displacement volumes caused by the small stroke to diameter ratios required, usually about 1:100. Also, because of these much smaller displacement volumes the volumetric and valve efficiencies become much more critical.

The new compressor consists of four (4) pistons reciprocating in cylinders closed at the top and bottom ends. The pistons and cylinders are stepped so the ends are at different diameters. At the large diameter end the space between the end of the piston and the cylinder head is the first stage compression chamber. The small diameter end space between the piston and its cylinder head is the second stage compression chamber. The third and fourth stage compression chambers are inside the second and first stage chambers, respectively.

Each stage compression chamber is provided with a delivery and exhaust valve. The delivery valves for all four stages are hard conical poppet with soft conical seat type reverse check valves. The exhaust valves for all four stages are metal-to-metal ball and sharp edge seat type check valves. The valves are sized proportionally for each stage.

External plumbing connects the first stage exhaust valve with the second stage delivery valve and the second stage exhaust valve with the third stage delivery valve. Internal plumbing connects the third stage exhaust valve with the fourth stage delivery valve. High pressure compressed gas leaves the fourth stage through its exhaust valve and low pressure return gas enters the first stage through its delivery valve.

The piston was designed with piston rings and guide bushings of Rulon A, (a proprietary polytetrafluorothylene based glass filled composite material widely accepted for dry rubbing seals and bearings).

The piston rings and guide bushings ultimately would be replaced with close tolerance labyrinth seals, and gas bearings, respectively, to eliminate all the rubbing surfaces. Elimination of all these rubbing surfaces allows for very long, maintenance free, compressor operation. The compressor module can be equipped for water cooling with intercooling heat exchangers incorporated in the compressor module between compression stages and an aftercooler downstream of the high pressure stage.

The pistons oscillate with short strokes, in the cylinders, by means of a simple Scotch-yoke mechanism. With this configuration a single throw crankshaft passes along the transverse axis through the piston and is mounted on main bearings attached to the cylinder. The crankpin carries a slider block which is constrained to slide in a groove in the piston. Therefore, as the crankshaft is rotated by the electric motor, the crankpin rotates about, but offset from the axis of the crankshaft. The slider mounted on the crankpin slides in the piston groove and the piston reciprocates in the cylinder at the crankshaft speed and with a stroke equal to the diameter of rotation of the crankpin.

The stroke of the piston is small relative to the piston diameter to reduce the slider velocity (and so increase the compressor life), to reduce the inertia loads and to facilitate compact construction.

The ratio of the cylinder diameters may be selected so that the pressure ratios and work inputs to the four stages are approximately equal. In compressor design it is customary to equalize the work of compression for the various stages so as to maximize the savings in power input inherent in the process of intercooling the fluid between stages.

In the case of high pressure compressors used for Joule-Thomson gas liquefiers an overall compression ratio (P_{max}/P_{min}) of 100:1 or so is required. Two stages of compression would require compression ratios of 10:1 in each stage. Four stages of compression require compressor ratios of only 3.16:1 (i.e. 10) in each stage.

Consider a compressor to pressurize gas from 1 atm (14.7 psia) to 100 atm (1470 psia). As described above, the compression ratio is:

$$(P_{max}/P_{min}) = 100:1$$

Assume the compression is isothermal and, neglecting clearance effects, the compression process is as shown in figure 1.

Reproduced From
Best Available Copy

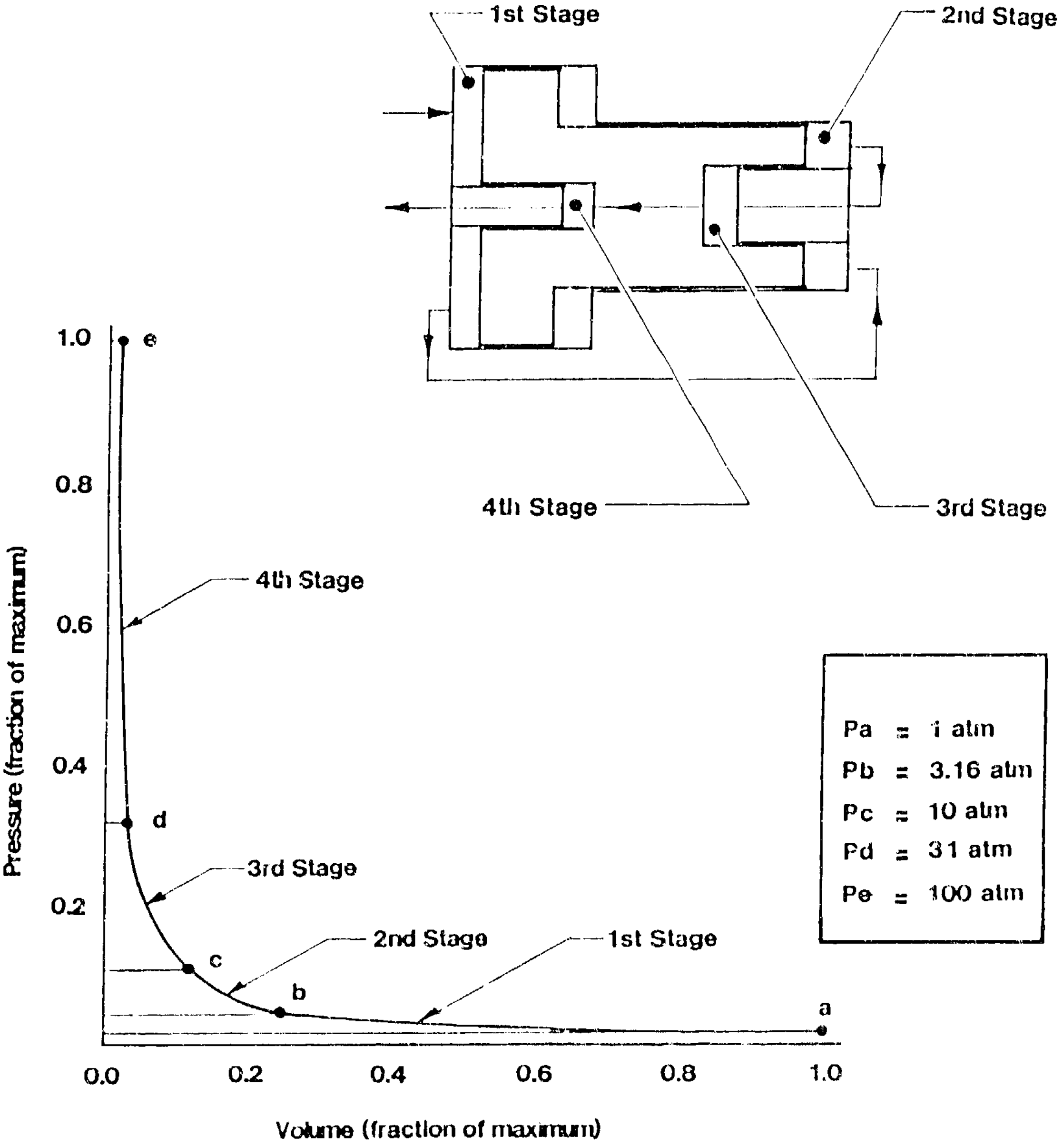
1st Stage
2nd Stage
4th Stage
3rd Stage
1.0
0.8
0.6
0.4
0.2
Pressure (fraction of maximum)
e
d
c
b
a
4th Stage
3rd Stage
2nd Stage
1st Stage
0.0
0.2
0.4
0.6
0.8
1.0
Volume (fraction of maximum)
Pa = 1 atm
Pb = 3.16 atm
Pc = 10 atm
Pd = 31 atm
Pe = 100 atm

FIGURE 1. COMPRESSION DIAGRAM FOR COMPACT FOUR STAGE GAS COMPRESSOR

The work of each stage is the same when the pressure ratio of each stage is the same:

$$\text{i.e. } \sqrt[4]{(P_{max}/P_{min})} = \sqrt[4]{100/1} = 3.16.$$

Now for each stage the mass of gas compressed is:

$$m_1 = \frac{\pi}{4} (D_1^2 - D_4^2) \frac{Pa}{T} \cdot \frac{S}{R}$$

$$m_2 = \frac{\pi}{4} (D_2^2 - D_3^2) \frac{Pb}{T} \cdot \frac{S}{R}$$

$$m_3 = \frac{\pi}{4} (D_3^2) \frac{Pc}{T} \cdot \frac{S}{R}$$

$$m_4 = \frac{\pi}{4} (D_4^2) \frac{Pd}{T} \cdot \frac{S}{R}$$

where the subscripts 1, 2, 3, 4 refer to compression stages 1, 2, 3, 4 and the subscripts a, b, c, d refer to respective pressures in the compression stages at the start of compression. D refers to piston diameter, S refers to piston stroke. T refers to absolute temperature and R refers to the characteristic gas constant of the fluid being compressed.

Neglecting fluid used to energize hydrostatic gas bearings the mass of fluid at the start of each compression stage is the same, i.e.

$$m_1 = m_2 = m_3 = m_4$$

Hence it can be shown by elementary algebraic manipulation that, for the above equality the following is obtained:

$$D_1 = 1.57\ D_2$$

$$D_2 = 2.03\ D_3$$

$$D_3 = 1.77\ D_4$$

Now consider a four stage compressor of the type discussed above with a first stage cylinder diameter of 10 cm (4 in approx), a fourth stage cylinder diameter of 1.5 cm (0.625 in approx) and a stroke of 1.5 cm. A large bore/short stroke arrangement is preferred so as to reduce the sliding velocity (and hence extend the life) of the Scotch-yoke mechanism.

Assume that at the start of compression the fluid in the first stage compression cylinder has a pressure and temperature of 1 atm and 15°C respectively (14.7 psia and 60°F). The mass of gas contained in the first stage at the start of compression is then:

$$m_1 = \frac{pV}{RT} = \frac{100 \times \frac{\pi}{4}(0.1^2 - 0.015^2)\, 0.015}{2.078 \times 288}$$

$$= 1.924 \times 10^{-5} \text{ kg}$$

and at a speed of 8 Hz (500 rev per min) the mass flow per sec is:

$$m_1 = 1.924 \times 10^{-5} \times 8 = 1.539 \times 10^{-4} \text{ kg/sec}$$

In accordance with our previous estimate of the ratio of cylinder diameters we can select the stage cylinder diameters and other principal parameters as follows:

1st stage - 10 cm (4 in approx)
2nd stage - 6 cm (2.5 in approx)
3rd stage - 3 cm (1.2 in approx)
4th stage - 1.5 cm (0.6 in approx)
Stroke - 1.5 cm (0.6 in approx)
Speed - 8 Hz (480 rev per min)

The compression power input for isothermal compression is

$$W = f\, p_1\, V_1\, \ln(r)$$

Where

W = work of compression
f = frequency (8 Hz)
p_1 = initial pressure (100 kPa)
V_1 = initial volume ($1.17 \times 10^{-4}\ \text{m}^3$)
r = pressure ratio (P_{max}/P_{min}) (3.16)

$$(V = \frac{\pi}{4} D_1^2 S = \frac{\pi}{4} \times 0.1^2 \times 0.015)$$

Therefore

$$W = 8 \times 100 \times 1.17 \times 10^{-4} \ln (3.16)$$
$$W = 0.108 \text{ kw}$$

and since there are four stages of approximately equal work input the total theoretical power input is 0.108 x 4 = 0.433 kw.

An isothermal efficiency of 60% and a mechanical efficiency of 70% may be realistic for the compressor so that the actual power input:

$$W = \frac{0.433}{0.6 \times 0.7} = 1.03 \text{ kw}$$

Diagrams of the input shaft torque as a function of crankangle are shown in figure 2. The zero datum crankangle occurs with the piston at the extreme right hand position with clockwise or anti-clockwise rotation. The torque/crankangle characteristics for all four stages are virtually identical with those for stages 2 and 3 out of phase by $\pi/2$ with those for stages 1 and 4. The four diagrams were summarized to find the net torque diagram shown at the bottom of figure 2. The net torque characteristic has two equal peaks, 180° apart with zero torque at the piston dead points. The peak torque to mean torque ratio was computed to be approximately 2:1. This indicates a moderate size flywheel will be sufficient to assure compressor operation at a steady speed of operation.

3. Four Stage Compressor Testing

The test set-up for the compact four stage compressor is shown diagrammatically in figure 3.

The compressor performance characteristics, using N_2 gas as the working fluid, were tested measuring the following parameters:

a) inlet pressure to the first stage
b) compressor speed
c) compressor housing temperature
d) ambient temperature
e) input power consumption
f) compressor output pressure and flow

The test procedure was as follows:

1) Start compressor with downstream needle valve wide open for maximum flow. Set inlet pressure and compressor speed at specified setting.
2) Measure the parameters a through f, listed above.

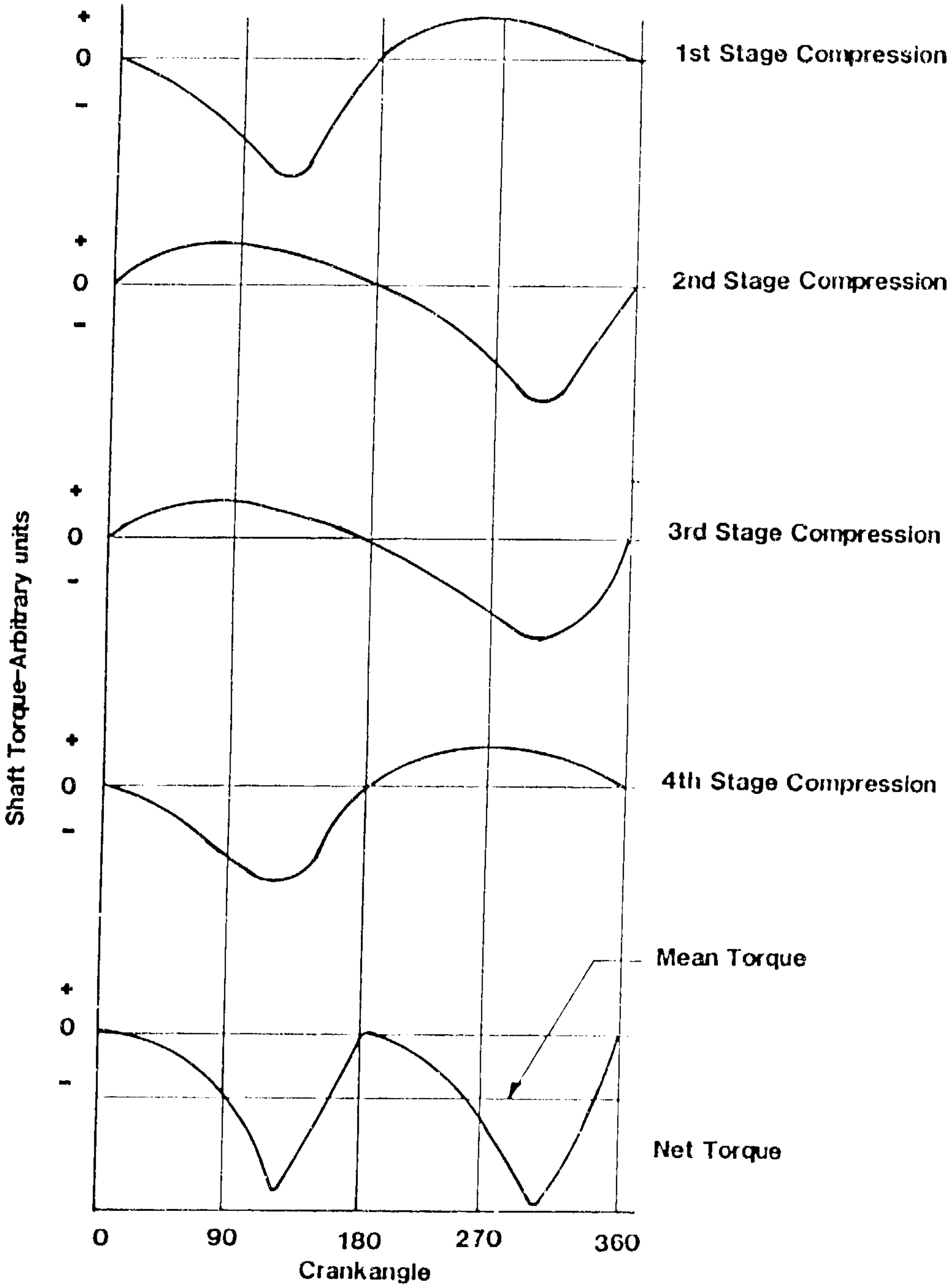

FIGURE 2. INPUT SHAFT TORQUE AS A FUNCTION OF CRANKANGLE

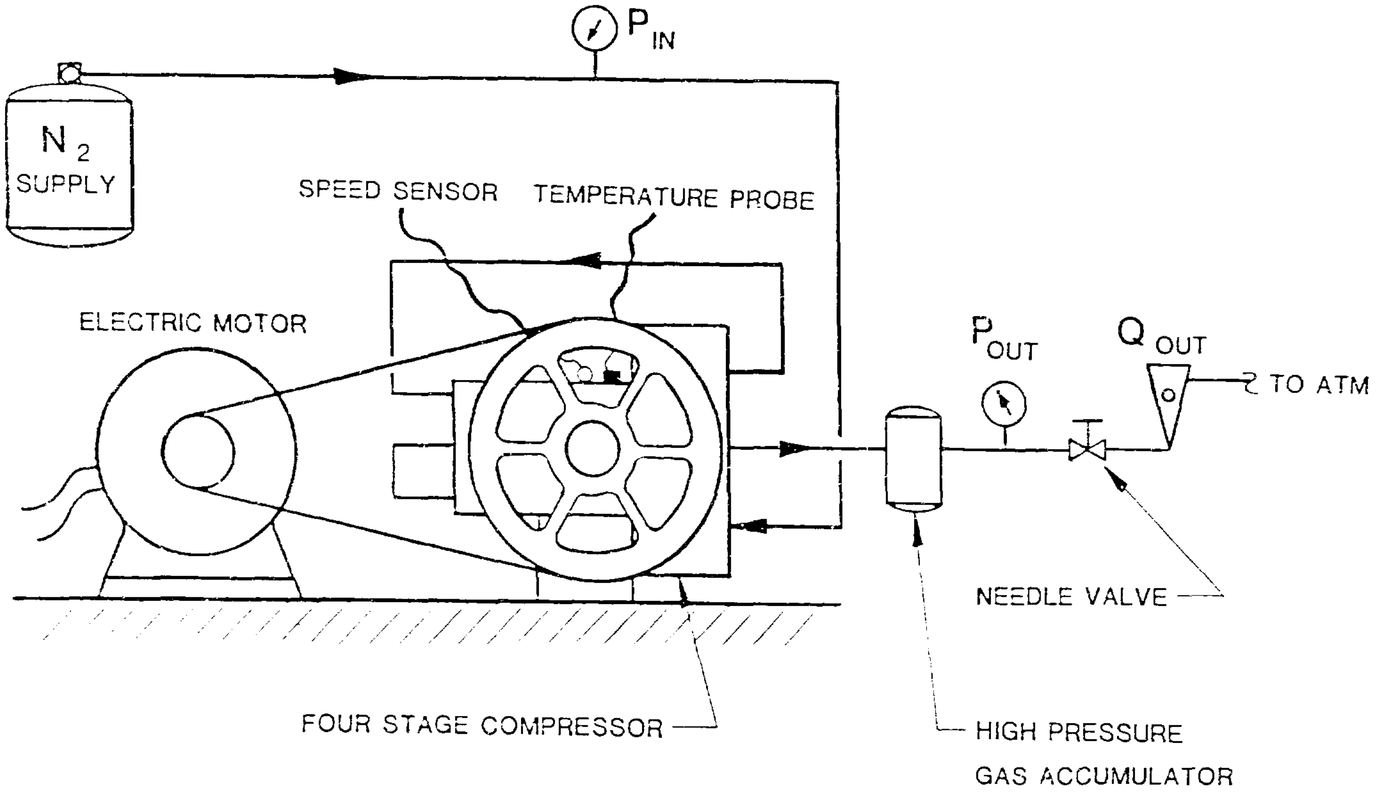
P_{IN}
N_2 SUPPLY
SPEED SENSOR
TEMPERATURE PROBE
ELECTRIC MOTOR
P_{OUT}
Q_{OUT}
TO ATM
NEEDLE VALVE
FOUR STAGE COMPRESSOR
HIGH PRESSURE GAS ACCUMULATOR

FIGURE 3. DIAGRAM OF THE COMPACT FOUR STAGE HIGH PRESSURE GAS COMPRESSOR TEST ARRANGEMENT

3) Close needle valve, to reduce outlet flow, and note the increase in outlet pressure
4) Repeat with decreasing outlet flow until needle valve is closed, (no flow). This gives maximum outlet pressure from the compressor.

The results of these tests showing the compressor outlet pressure as a function of outlet flow at constant compressor speed and inlet pressure are shown in figure 4.

As previously described high pressure compressors for Joule-Thomson gas liquefiers require an overall compression ratio (P_{max}/P_{min}) of 100:1. The compression ratio for each stage, of a four stage compressor is:

$$\sqrt[4]{P_{max}/P_{min}} = \sqrt[4]{100/1} = 3.16$$

The prototype compressor, built and tested here, easily met and exceeded these requirements reaching pressures in excess of 4000 psig, as shown in figure 4. The overall compression ratio (P_{max}/P_{min}) exceeded 200:1 giving an individual stage compression ratio is:

$$(\sqrt[4]{P_{max}/P_{min}}) \text{ of } 3.76:1.$$

4. Conclusion

The miniature multistage high pressure gas compressor developed for Linde-Hampson cryocoolers is presently continuing performance and life testing.

Primary concentration is being focused on the Scotch-yoke drive mechanism to increase the operating life by reducing the sliding friction and wear.

Alternative concepts for the delivery and exhaust valves, piston rings and guide bushings are also being investigated to improve reliability and overall system efficiency while at the same time further reducing the package size, weight and cost.

5. References

[1] Walker, G., (1983), Cryocooler, Vol. I & II, Plenum Publishing Company, New York.

[2] Hedegard, K., Temperature Sensitive Variable Area Flow Regulator for Joule-Thomson Nozzles, 4th International Cryocooler Conference, 1986.

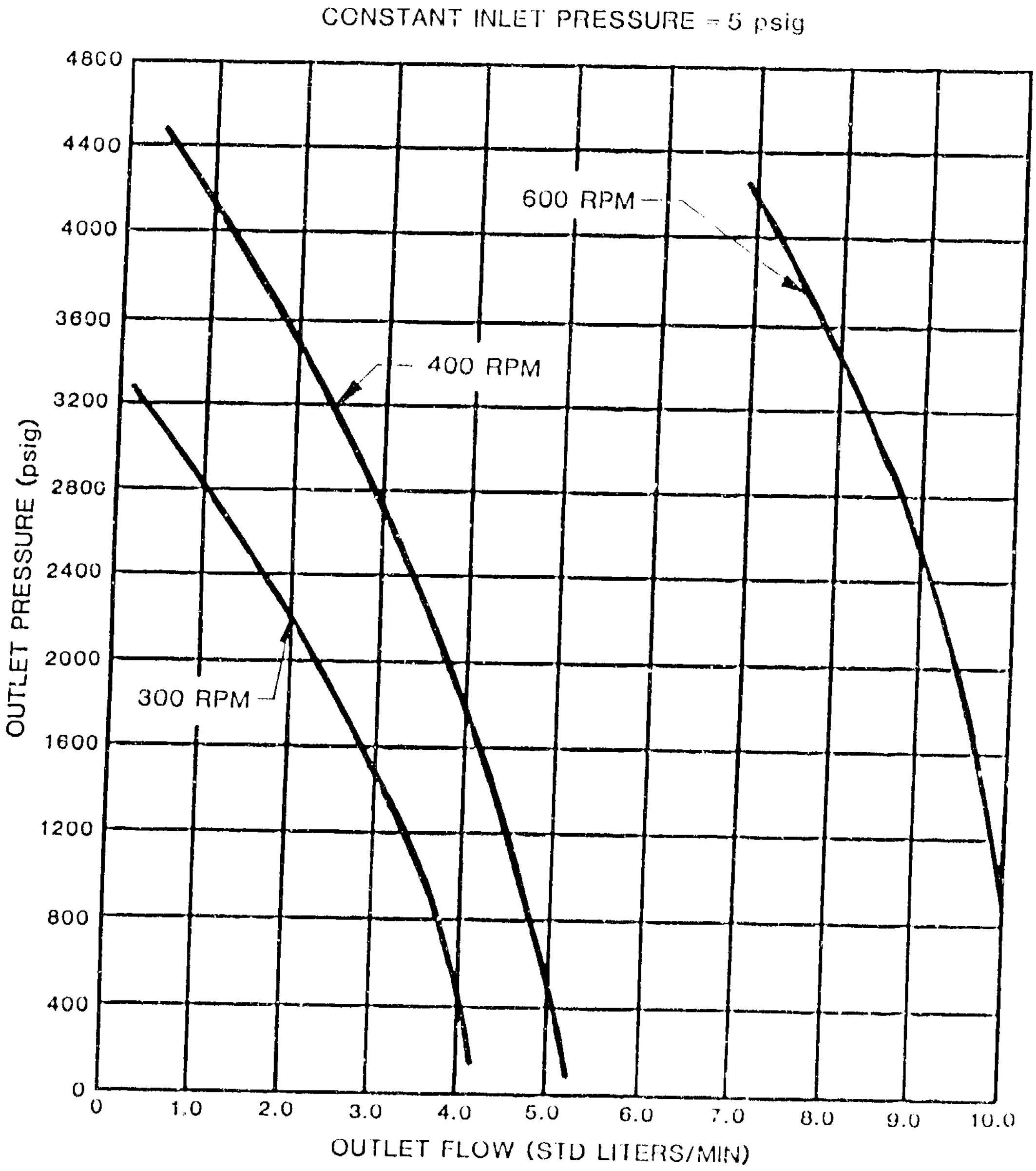

FIGURE 4. COMPRESSOR OUTLET FLOW AS A FUNCTION OF OUTLET PRESSURE WITH CONSTANT COMPRESSOR SPEED AND INLET PRESSURE

Preceding Page Blank

PROGRESS IN DEVELOPMENT OF OIL-FREE RESONANT-PISTON COMPRESSORS FOR CRYOGENIC APPLICATIONS

Peter W. Curwen

Mechanical Technology Incorporated
Latham, New York 12110

Oil-free helium compressors offer potential cost and reliability advantages for cryogenic systems. Recent progress has been made at Mechanical Technology Incorporated (MTI) in the development of linear-motor-driven, oil-free resonant-piston compressors (RPC). Particularly noteworthy is the development of a new type of linear motor having significantly reduced reciprocating mass. This motor has been incorporated into a single-stage, helium compressor with a 2.7:1 pressure ratio. The primary objectives of this compressor are low manufacturing cost and long operating life.

Key words: Linear motors; oil-free compressors; resonant-piston compressors

1. Introduction

At the 1981 Cryogenic Engineering Conference, MTI reported on a U.S. Navy-sponsored program to develop a linear-motor-driven, oil-free resonant-piston compressor (RPC) for helium liquefaction [1]*. This development was for a 54 lb/hr, 16:1 pressure ratio, two-stage compressor. The RPC was equipped with hydrostatic helium gas bearings to eliminate the need for oil lubrication and clearance seals to eliminate life-limiting, wear-couple seals.

Figure 1 shows the reciprocating assembly for the second-stage module of this two-stage compressor. Pistons for the two parallel-flow, second-stage cylinders are located at each end of the assembly. These pistons are dwarfed by two double-acting gas-spring pistons needed to resonate the 46-lb mass of the reciprocating assembly at 60 Hz. The 27-lb plunger of the reciprocating linear motor is located in the center of the assembly. Although the second-stage RPC successfully demonstrated the feasibility of oil-free, wear-free compressor operation, the demonstration had to be performed at reduced flow rates due to a shortfall of power from the linear motor. The complete two-stage compressor was not developed due to MTI's inability to develop a 17-hp linear motor having a plunger specific power of 0.63 hp/lb.

---

*Numbers in brackets refer to the literature references listed at the end of this report.

Plunger specific power is perhaps the most critical parameter for any free-piston compressor. This parameter is obtained by dividing the rated shaft power of the reciprocating linear motor by the weight of the motor's plunger. The highest possible value of this parameter is desired in order to minimize size and maximize efficiency of the RPC.

The plunger specific power that was actually achieved with the Navy motor was 0.31 hp/lb, which was typical of MTI motors developed during the 1970s. By the early 1980s, it was apparent that significant increases in plunger specific power were needed if the full potential of free-piston, resonant compressors was to be realized. This paper describes MTI's efforts to achieve such increases and the application of one such advanced motor to an oil-free, helium compressor.

2. Advances in linear motor design

Figure 2 shows a doubly excited (electrodynamic) linear motor of the type used in the Navy compressor. The plunger and stator are of round geometry. This particular motor produced 3.5 hp at 84% efficiency with a 16-lb plunger, resulting in a plunger specific power of 0.22 hp/lb. The path of the dc field flux through the motor is shown in Figure 3. As illustrated, the flux travels axially through the center of the plunger. Sufficient magnetic iron must be provided in the plunger centerbody to carry this flux without saturation. It is the weight of this magnetic centerbody that results in the low plunger specific power for this type of motor.

Figure 4 shows the plunger assembly for a recently developed 3.5-hp linear motor that has demonstrated a plunger specific power of 1.0 hp/lb (a factor of 4.5 increase over the motor shown in Figure 2). The plunger geometry in this case is flat rather than round. The path of the dc field flux through this motor is shown in Figure 5. As illustrated, the dc flux travels transversely (rather than axially) through the two-plunger pole packs, resulting in a substantial reduction in the weight of iron needed in the plunger.

Efficiency of the newly developed flat motor is currently about 73%. To bring this efficiency up to that of the motor shown in Figure 2, more iron and copper are needed. Our calculations indicate that the total weight of the flat motor must be increased to almost that of the round motor if the same levels of efficiency are to be achieved. However, most of this weight increase will occur in the stator. Plunger specific weight will decrease slightly but will still be three to four times greater than that of the round motor.

3. Oil-free helium compressor using new motor

For the past several years, MTI has conducted an internally funded program to demonstrate the feasibility of an oil-free helium compressor using the flat motor described above. Design-point ratings of the compressor are 15.6 lb/hr (1.96 g/sec) at 100 psig inlet and 300 psig discharge pressures. These conditions are typical of those used in commercial cryopump systems. A major objective of this development is to achieve a low-cost, hermetic compressor capable of 30,000 hours of maintenance-free life.

Figure 6 shows a cross section of this new oil-free helium RPC. The motor plunger assembly for this compressor is shown in Figure 4. In addition to using the flat motor, this design incorporates another innovation specifically directed at reducing the cost of the compressor; the RPC is equipped with just one cylinder and one piston (as shown in Figure 6). All previous RPCs developed by MTI have used opposed cylinders and pistons (i.e., a piston and cylinder located at each end of the reciprocating assembly). This was done to obtain a zero net average pressure force acting on the free-piston assembly. Pressure balancing is highly desirable since it greatly simplifies the problem of maintaining centered operation of the reciprocating assembly.

This single-cylinder RPC is also pressure balanced. Piston stroke is 0.8 in. at 3600 strokes/min. The piston is double acting. Helium compression is performed on one side of the piston using conventional, pressure-actuated reed valves to control inlet and discharge flow through the cylinder. The other side of the piston operates in a "balance" cylinder that pressure balances and stabilizes the reciprocating, free-piston assembly. The balance cylinder also provides about 50% of the "spring stiffness" needed to resonate the reciprocating assembly at 60 Hz. The remaining 50% of the resonance stiffness is obtained from the compression cylinder. Comparison of Figures 1 and 6 indicates the significant advantage of high plunger specific power. The size of auxiliary gas-spring cylinders needed to achieve resonant operation of the compressor is greatly reduced, as are also gas-spring losses.

Figure 7 shows a side view of the flat motor assembly for the helium RPC. Also shown is one of the hydrostatic helium gas bearing shafts used to support the motor plunger without sliding contact. Pressurized helium for these bearings is obtained from compressor discharge.

Figure 8 shows recently measured flow delivered by the compressor as a function of inlet pressure and motor current while maintaining a constant discharge pressure of 300 psig. This plot demonstrates how variable-capacity operation of a free-piston RPC can be easily obtained by simply changing the voltage (current) applied to the linear motor.

Testing of the present RPC configuration has been underway for only several weeks. Continuous steady-state operation has been demonstrated at motor currents of 22 and 25 A; steady-state operation at progressively higher currents is the objective of our continuing test program. Design-point operation has, in fact, been achieved in short-duration runs at 33 A. Operation of the helium hydrostatic bearings thus far has been trouble free.

4. Summary

Substantial progress has been made toward achievement of a low-cost, oil-free helium RPC as a result of a significant improvement in plunger specific power for the linear motor. Further development will concentrate on RPC performance improvement, endurance testing, and an assessment of whether current fabrication materials are acceptable from a contamination standpoint.

5. References

[1] Curwen, P. W., and Hurst, R., Development of an oil-free resonant piston compressor for helium liquefaction, Cryogenic Engineering Conference, San Diego, CA, August 1981.

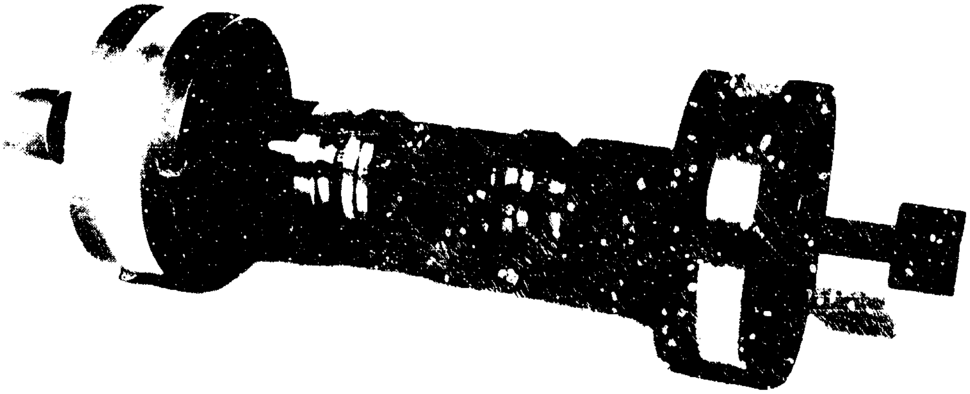

V6 187

Fig. 1 Second-Stage Reciprocating Assembly for Navy Helium RPC

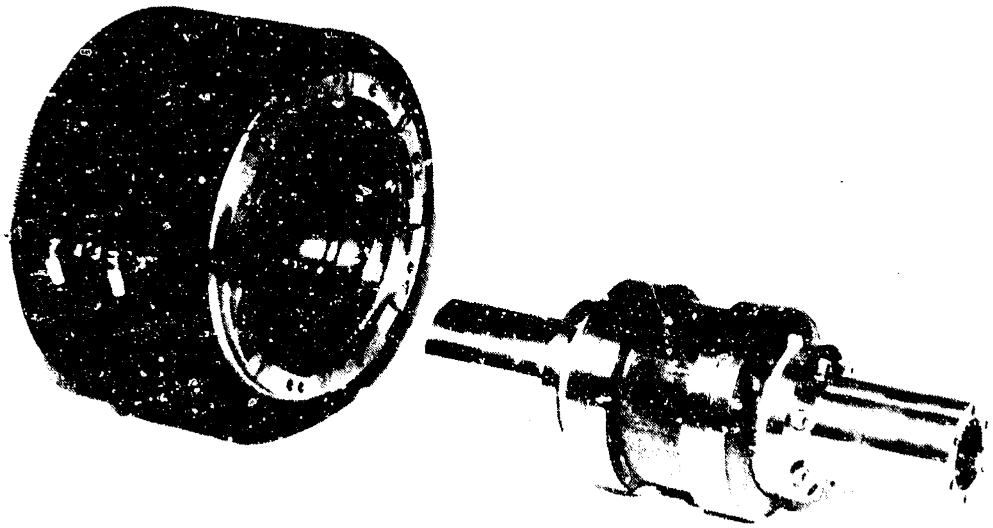

8617502 V6-63

Fig. 2 3.5-hp Electrodynamic, Round-Geometry Linear Motor

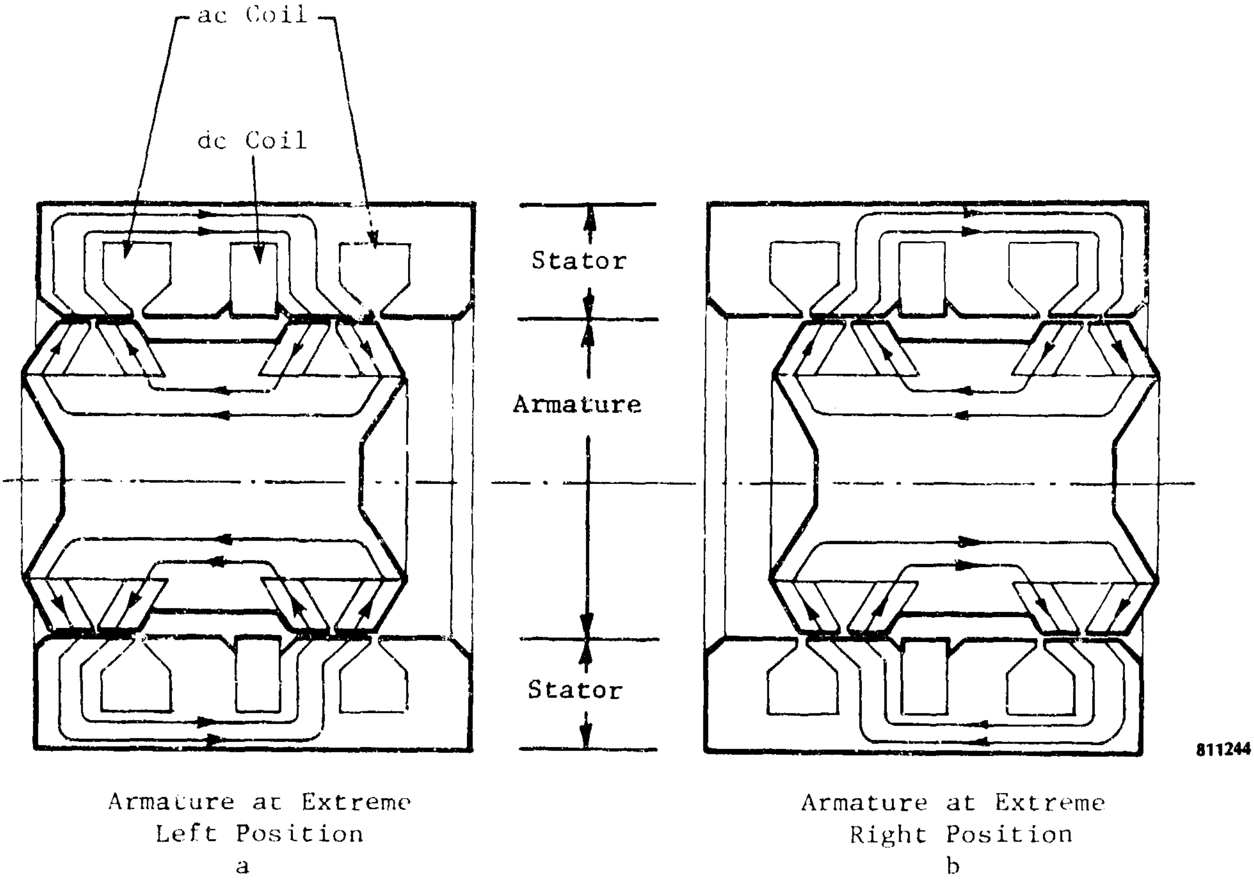
ac Coil
dc Coil
Stator
Armature
Stator
811244
Armature at Extreme
Left Position
a
Armature at Extreme
Right Position
b

Fig. 3 dc Flux Path in Round-Geometry Electrodynamic Linear Motor

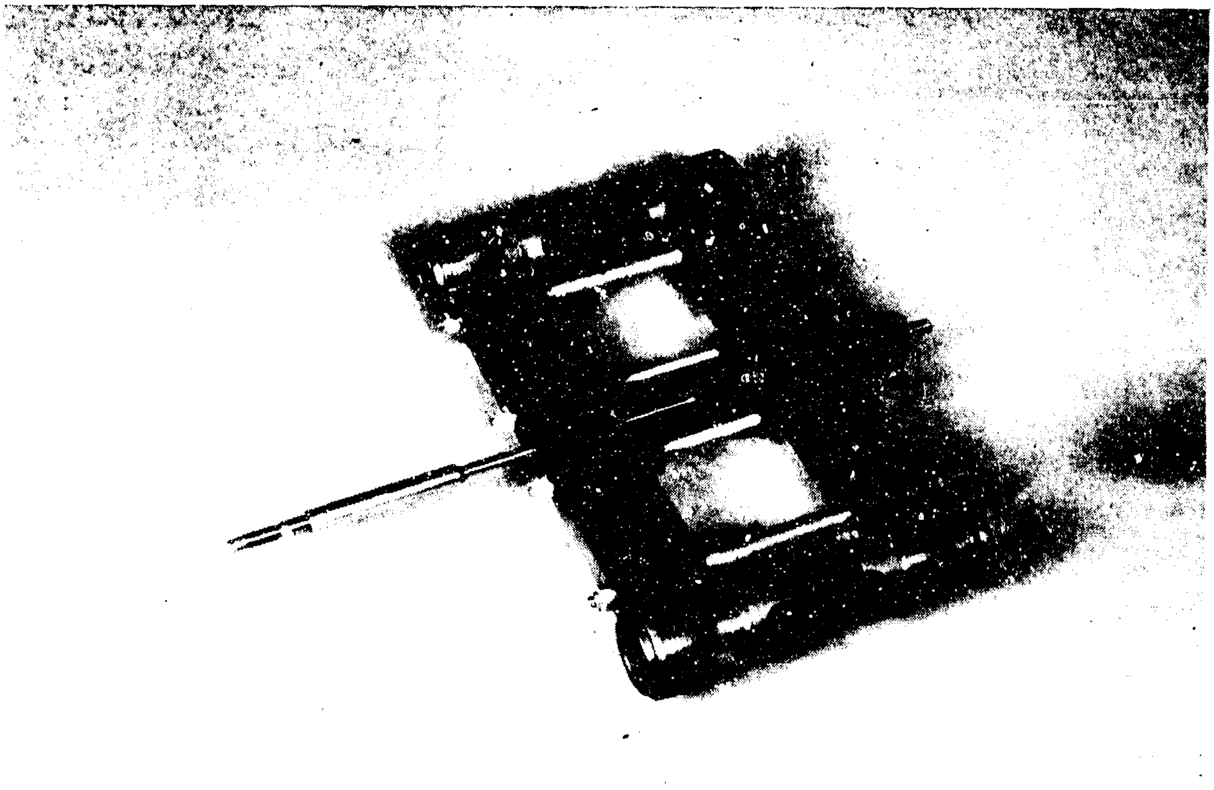

CT85468-15 V6-189

Fig. 4 Plunger Assembly for 3.5-hp Flat Geometry Linear Motor

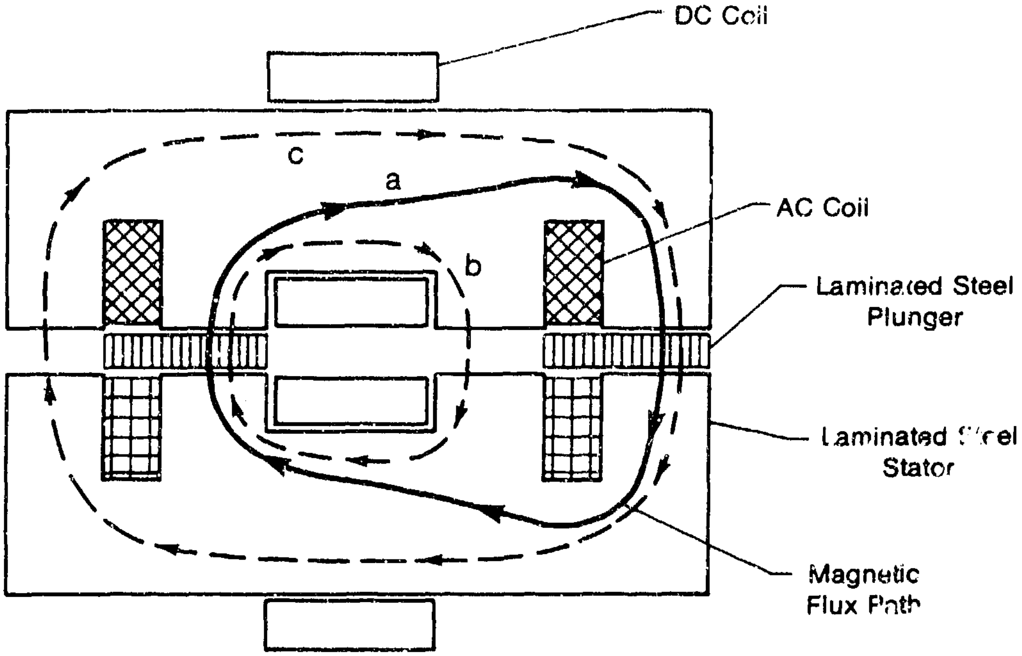
DC Coil
c
a
b
AC Coil
Laminated Steel Plunger
Laminated Steel Stator
Magnetic Flux Path

Extreme Right Position

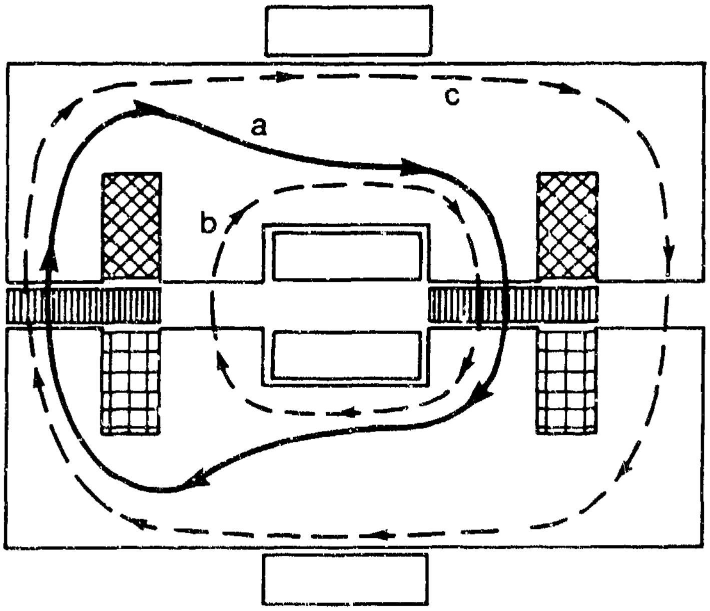

86678

Extreme Left Position

Fig. 5 dc Flux Path in Flat-Geometry Electrodynamic Linear Motor

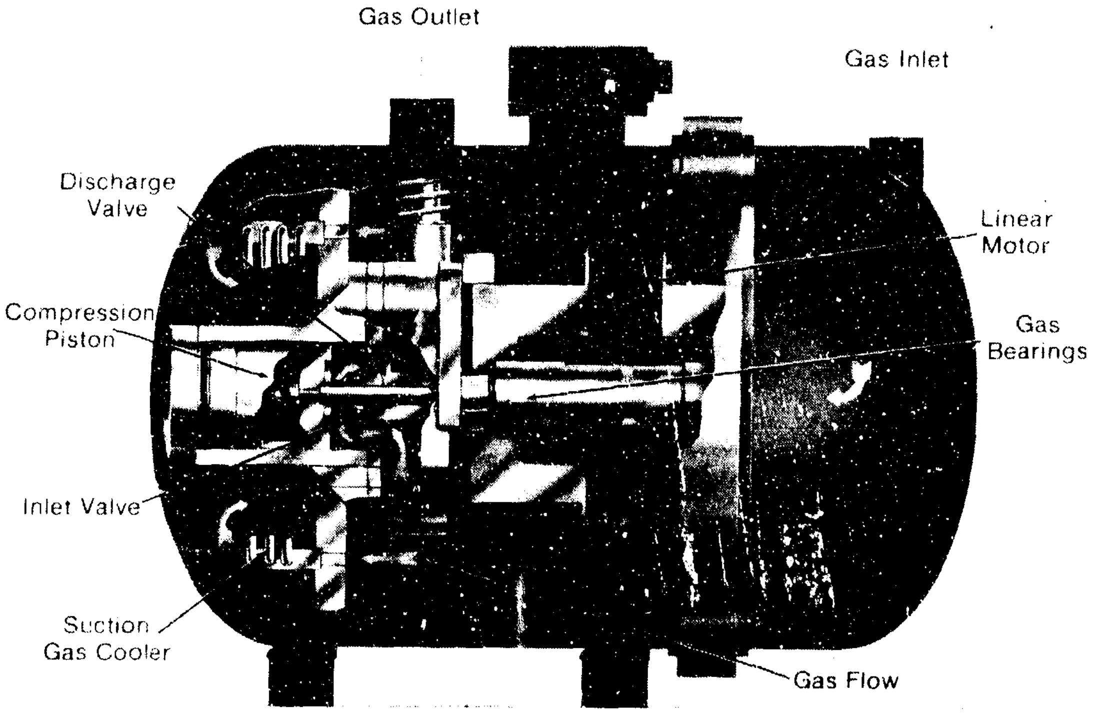
Gas Outlet
Gas Inlet
Discharge Valve
Linear Motor
Compression Piston
Gas Bearings
Inlet Valve
Suction Gas Cooler
Gas Flow

1469422 V6-168

Fig. 6 Cross Section of New Oil-Free Helium RPC

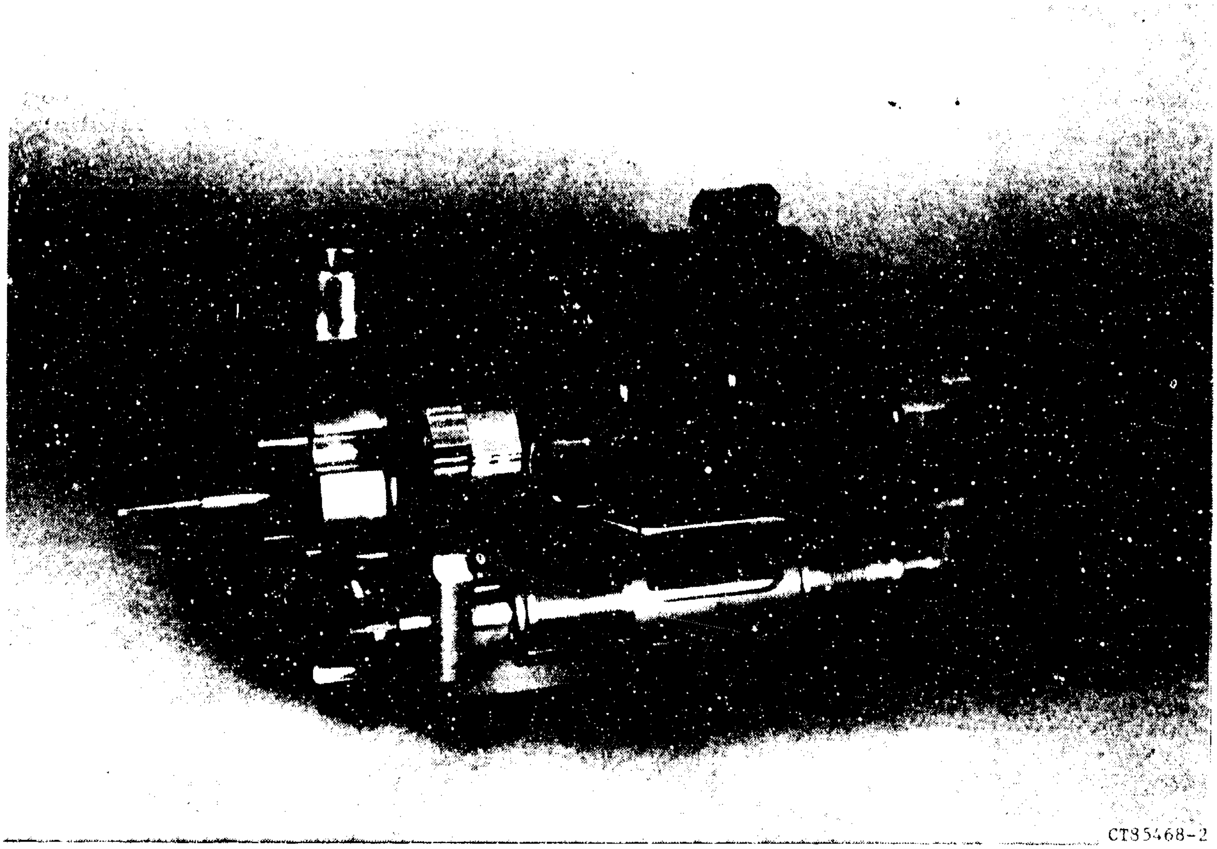

CT85468-2 V6-138

Fig. 7 Side View of Flat Motor Assembly for New Helium RPC

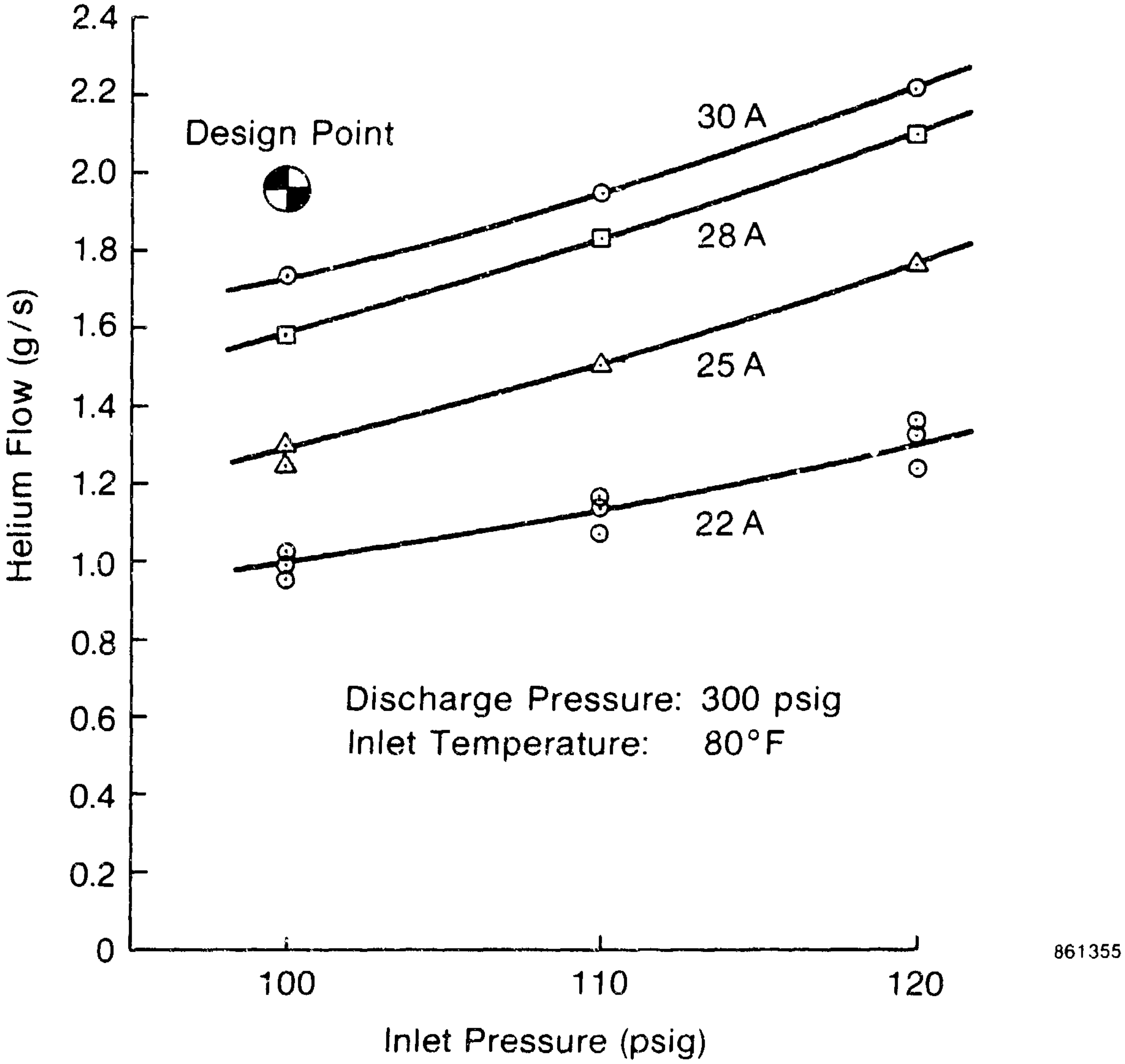

Fig. 8 Measured RPC Flow as a Function of Inlet Pressure and Current at Constant 300 psig Discharge Pressure

Final Attendance List
4th International Cryocooler Conference - September 24-26, 1986
Easton, MD

Argiro, Larry J.
DTNSRDC
Code 274
Annapolis, MD 21402
301-267-2649

Atkins, Ernest E.
General Pneumatics Corp.
7662 E. Gray Road Suite 107
Scottsdale, AZ 85260
602-998-1856

Augustynowicz, Stanislaw D.
Cryodynamics Inc.
191 Mill Lane
Mountainside, NJ 07092
201-654-7700

Averill, Robert D.
NASA Langley Research Center
M.A. 322
Hampton, VA 23665
804-865-4621

Backovsky, Zdenek
Rockwell International
2600 Westminster
Seal Beach, CA 90740

Baebler, Miha
Institut Zoran Rant
Kidriceva 66 (POB 88)
Skofjaloka, Yugoslavia 64220
064-62-675

Ballster, Michael
National Radio Astronomy OBS
2015 Ivy Road
Charlottesville, VA 22903
804-296-0365

Barbanera, Sandro
Istituto Elettronica Statosolido
Via Cineto Romano, 42
Rome, Italy 00156
39 6 4124851

Barclay, John A.
Astronautics Tech. Center
5800 Cottage Grove Road
Madison, Wisconsin 53716
608-221-9001

Barnard, Bryan
GEC Research Limited
East Lane, Wembley
London, England
OL 904 L262

Bello, Mel
Aerospace Corporation
P.O. Box 92947
Los Angeles, CA 90009
213-336-7277

Benedict, Becky A.
Ball Aerospace Systems Div.
P.O. Box 1062
Boulder, CO 80306
303-939-4794

Birmingham, Bascom W.
Birmingham Associates
5440 White Place
Boulder, CO 80202
303-442-1248

Blaugher, Richard D.
Westinghouse Electric Corp.
1310 Beulah Road
Pittsburgh, PA 15235
412-256-1352

Bogner, Dr. Guenther
Siemens AG, Corporate R&T
Paul-Gossen-Str. 100
8520 Ellangen, Germany
9131-731228

Bradshaw, Thomas W.
Rutherford Appleton Laboratory
Chilton Didcot Oxon OX11 0QX
UK
0235 21900

Brown, Michael T.
Hughes Aircraft Company
P.O. Box 902 E5S/G232
El Segundo, CA 90245
213-616-9702

Breckenridge, R. Warren
Arthur D. Little, Inc.
Acorn Park
Cambridge, MA 02140
617-684-5770

Buchanan, David S.
Biomagnetic Technologies Inc.
4174 Sorrento Valley Road
San Diego, CA 92121
619-453-6300

Buckley, Dan J.
Naval Weapons Center
Code 36213
China Lake, CA 93555
619-939-1686

Burt, William
TRW Inc.
One Space Park, MS 01-2044
Redondo Beach, CA 90278
213-535-2920

Busby, Michael S.
TRW
One Space Park R4-2066
Redondo Beach, CA 90278

Buzerak, Robert F.
Ford Aerospace & Communications Co.
Ford Road
Newport Beach, CA 92633

Carpetis, Constantin
DFVLR, German Aero Est.
Pfaffenwardring 38-40
7000 Stuttgart 80 West Germany

Castles, Stephen H.
NASA Goddard SFC
Greenbelt, MD 20771
301-286-8378

Chen, Guo-Bang
Zhejiang University
Hangzhou, China
21701 2427

Chen, Yen H.
TWR Space & Technology Group
One Space Park MS 154/2027
Redondo Beach, CA 90278

Christensen, Charles L.
Moog Inc.
Jamison Road
East Aurora, NY 14052
716-687-4610

Clark, Dr. Alan F.
National Bureau of Standards
325 S. Broadway MS 724.05
Boulder, CO 80303
303-497-3253

Cleveland, Forrest R.
Aerojet Electro Systems
1100 W. Hollyvale
Azusa, CA 91702
818-812-1764

Costello, Frederick
12864 Tewksbury Drive
Herndon, VA 22071
703-620-4942

Cranmer, David C.
The Aerospace Corporation
P.O. Bos 92957, MS M2/248
Los Angeles, CA 90009
213-648-5879

Curwen, Peter W.
Mechanical Technology Incorporated
968 Albany-Shaker Road
Latham, NY 12110
518-785-2285

Czipott, Peter V.
Physical Dynamics, Inc.
4350 Executive Drive, Suite [35]
San Diego, CA 92121
619-457-3201

Daunt, Prof. John G.
Queen's University
Kingston, Ontario Canada K7L 3N6

Davies, Kenneth
Rutherford Appleton Laboratory
Chilton NR Didcot Oxon 11 OQX
England

DeVilliers, Andre L.
Riverside Research Institute
1701 N. Fort Meyer Drive (700)
Arlington, VA 22209
703-522-2310

Deak, Michael
Oxford Superconducting Technology
600 Millk Street
Carteret, NJ 07008
201-541-1300

Dewanckel, Bernard
CEA/CEN-GRENOBLE
85X 38041 Grenoble, France

Edeskuty, Fred
Los Alamos National Laboratory
P.O. Box 1663 MS F611
Los Alamos, NM 87545
505-667-4240

Fagan, Thomas J., Jr.
Westinghouse Electric Corporation
1310 Beulah Road
Pittsburgh, PA 15235
412-256-1985

Fife, Allstair A.
CTF Systems Inc.
15-1750 McLean Avenue
Port Coquitiam, BC Canada V3C1M9
604-941-8651

Francis, Arthur W.
Union Carbide Corp. Linde Div.
Tarrytown Technical Center
Tarrytown, New York 10591
914-354-1908

Frederking, T.H.K.
University of California
Los Angeles, CA 90024
213-825-2491

Galassi, Anthony K.
DOD
7221 Calamo Street
Springfield, VA 22150
703-281-8064

Gasser, Max G.
NASA Goddard SFC
Greenbelt, MD 20771

Giellis, R.T.
Martin Marietta Corporation
Denver, Colorado 80201

Gifford, Peter E.
Cryomech Inc.
1630 Erie Blvd E.
Syracuse, NY 13210
315-475-9692

Glassford, Alexander P.
Lockheed Missiles & Space Co.
0/59-40, B589, 1111 Lockheed Way
Sunnyvale, CA 94089
408-743-0169

Green, Geoffrey
DTNSRDC
Annapolis Laboratory
Annapolis, MD 21402
301-267-3632

Gully, Wilfred J.
Hughes Aircraft Company
3100 W. Lomita Blvd.
Torrance, CA 90509-2999
213-517-5664

Gygax, Suso
Simon Fraser University
Burnaby, BV, V5A156, Canada
609-291-4845

Harada, Susumu
Hitachi, Ltd.
794 Higashitoyoi Kudamatsu Yamagucn

Hedegard, Kelly W.
General Pneumatics Corp.
7662 E. Gray Road, Suite 107
602-998-1856

Heiden, Christoph
University of Giessen
Heinrich-Buff-Ring 16
Giessen D6300 FRG

Hendricks, John B.
Alabama Cryogenic Engineering, Inc.
P.O. Box 2451
Huntsville, AL 35804
205-536-8629

Hickey, Thomas N.
Cryogeneral Corporation
506 11th St. North
Naples, FL 33940
813-263-2666

Hiroyasu, Makoto
Kaikin Industries, LTD
108 Decatur Street #5
Arlington, MA 02174
617-641-0692

Hocking, Barry N.
Lucas Aerospace-Engine Systems
The Radleys, Marston Green
Birmingham B33 OH2 England
021-779-6531

Hood, Charles B.
Cryogeneral Corporation
506 11th St North
Naples, FL 33940
813-263-2666

Horsley, William J.
Lockheed R&D, Dept 92/40
Bldg 205 3251 Hanover St
Palo Alto, CA 94304-1191
415-424-2409

Hunter, William H.
Space & Naval Warfare Sys Command
Surface EW PMW 171-4B
Washington, DC 20362-5100
703-920-6573

Hyman, Nelson L.
Naval Research Laboratory
4555 Overlook Ave., SW
Washington, DC 20375-5000
202-767-6997

Ishige, Takashi
HOXAN Corporation
16-2, Nonomlya 3-chome Yatebe-machl
Tsukuba-gum ibaraki 302 Japan

Iwasa, Yuki
MIT Room NW17-201
Cambridge, MA 02139
617-253-5548

Jensen, Jack E.
CVI Inc.
P.O. Box 2138
Columbus, Ohio 43216
614876-7381

Johnson, Al
Aerospace Corporation
P.O. Box 92957
El Segundo, CA 90009

Johnson, Dean L.
Jet Propulsion Laboratory
4800 Oak Grove Drive
Pasadena, CA 91109
818-354-4942

Kadi, Frank J., Dr.
Leybold-Heraeus/Vacuum Products, Inc.
5700 Mellon Road
Export, PA 15632

Kamioka, Yasuharu, Dr.
Toyo Oxygen Co., Ltd.
3-3 Mizuecho
Kawasaki, Kanagawa 210 Japan

Kanazawa, Yoshiaki
Sumitomo Heavy Industries, Ltd.
63-30 Yuhigaoka
Hiratsuka, Kanagawa 254 Japan
0463 23-1811

Kaneko, Mitsuhuro
Nihon University
7-24-1 Narashinoidal, Funabashi-SH
Chiba-Ken 274 Japan

Karperos, Kurt
Aerojet Electro Systems Co.
1100 W. Hollyvale P.O. Box 296
Azusa, CA 91702
818-812-1704

Kaufmann, Dr. Rainer
Dornler System Gmbh
P.O. Box 1360
7990 Friedrichshafen, FRG
7545 8-4024

Kerney, Peter J.
CTI-Cryogenics
266 Second Avenue
Waltham, MA 02254
617-890-9400

Kittel, Peter
NASA Ames Research Center
MS 244-10
Moffett Field, CA 94035
415-694-6525

Knowles, Tim
Energy Science Laboratories
11404 Sorrento Valley Road
San Diego, CA 92121

Koisumi, Tatsuo
Sumitomo Heavy Industries, Ltd.
Z-I-I Yato-Cho
Tanashi, Tokyo 188 Japan
0424 68-2263

Kuo, Daniel T.
Hughes Aircraft Company
3100 W. Lomita Blvd, Bldg 230
Torrance, CA 90509
213-517-6523

Kuroaka, Yasuo
Hoxan Corporation
Ninimlya 3-chome, Yatabe-machi
Ibaraki 305 Japan

Kushnir, Mark
ICE Cryogenic Engr. Ltd.
92 Remez Street
Rehovoth, Israel 76449
972-8-454108

Lam, Wim
Moog Inc., Carleton Group
Jamison Road
East Aurora, NY 14052
716-687-4549

Ledford, Otto C.
Advanced Technology
222 N. Sepulveda Blvd
Suite 130
El Segundo, CA 90245

Lehrfeld, Daniel
Magnovox EOS
46 Industrial Avenue
Mahwah, NJ 07430
201-529-1700

Lhota, James R.
The Aerospace Corporation
P.O. Box 92957 MS/250
Los Angeles, CA 90009
213-648-5298

Ligda, John R.
The Aerospace Corporation
P.O. Box 9113
Albuquerque, NM 87119
595-846-0231

Lightsey, E. Glenn
NASA Goddard SFC
Greenbelt, MD 20771
301-286-8378

Lindquist, Paul D.
AFWAL/FIEE
Wright Patterson AFB Ohio 45433
513-255-4853

Linenberger, Del D.
Ball Aerospace Systems Division
P.O. Box 1062
Boulder, CO 80306
303-939-4797

Lipp, Larry C.
Hughes Aircraft Company
M/S F150, P.O. Box 902
El Segundo, CA 90245
213-616-6162

Longsworth, Ralph C.
Air Products and Chemicals, Inc.
1833 Vultee Street,P.O. Box 2802
Allentown, PA 18105
215-481-3708

Ludwigsen, Jill
Nicholes Research Corporation
251 Edgewater Drive
Wakefield, MA 01880

Marsden, David
British Aerospace
Manor Road
Hatfield Hertfordshire, England
070 72-77403

Matsubara, Yoichi
Nihon University
7-24-1 Narashinosi
Funabashi-shi, Chiba-Ken Japan 274
0474-66-1111

McFarlane, Robert
Philips Laboratories
345 Scarborough Road
Briarcliff Manor, NY 10510
914-945-6329

Mayer, John
NIMBUS
2945 Kilgore
Rancho Cordova, CA 95670

Mitchell, Archer S.
Westinghouse Electric Company
P.O. Box 1521
Baltimore, MD 21203
301-765-7228

Moore, Raymond W.
Koch Process Systems
20 Walkup Drive
Westborough, MA 01581
617-366-9111

Moyer, Richard P.
Air Products & Chemicals, Inc.
P.O. Box 2802
Allentown, PA 18105
215-481-3800

Naiman, Charles S.
ICE Inc.
160 Lancaster Terrace
Brookline, MA 02146
617-277-4184

Nakashima, Hiroshi
Rwy Tech. Res. Instit. JNR
2-8-39 Hikari-cho
Kokuvunji-ahi, Tokyo, Japan 185
0425-72-2151

Nast, Ted
Lockheed Research Laboratory
3251 Hanover Street
Palo Alto, CA 94304

Ohtsuka, Taiichiro
Tohoku University
Aramaki AZA-AOBA
Sendai 980, Japan

Nesbitt, John R.
Aerojet Electrosystems
1100 W. Hollyvale
Azusa, CA 91702
818-812-2397

Neumueller, Heinz Werner
Siemens Research Laboratory
Dept ZFE TPHn,
8520 Erlangen, Germany (FRG)
09131 76928

Nisenoff, Martin
Naval Research Lab, Code 6854
4555 Overlook Road, SW
Washington, DC 20375-5000
202-767-3099

Noguchi, Takashi
Furukawa Oxford Tech. Ltd.
6, Yawata-kaigan-dori
Ichihaa, Chiba, 290, Japan
0436-43-2505

Novotny, Shlomo
Digital Equipment Corporation
100 Minuteman Road
Andover, MA 01810
617-689-126

Patton, George
DTNSRDC
Annapolis, MD 21402
301-267-3632

Paustian, D.A.
Clifton Precision
Instrument & Life Support Division
Davenport, IA 52808
800-553-1860

Penswick, Laurence Barry
Sunpower, Inc.
6 Byard Street
Athens, OH 45710
614-594-2222

Peschka, Walter
DFVLR-German Aerospace Est.
Pfaffenwaldring 38-40
7000 Stuttgart, West Germany 7000
711-6862-430

Peskett, Guy
Oxford Univ. Clarendon Lab
Oxford, England OX1 3PU
865 53344

Petrick, S. Walter
Jet Propulsion Laboratory
4800 Oak Grove Drive
Pasadena, CA 91109
818-354-2869

Pirtle, F. William
CTI Cryogenics
266 2nd Avenue
Waltham, MA 02254
617-890-9400

Powers, Gregory M.
AFSTC/USAF
Kirtland AFB, Albuquerque, NM 87117
505-846-4958

Radebaugh, Ray
National Bureau of Standards
325 Broadway, MS/773.30
Boulder, CO 80303
303-497-3710

Ravex, Alain Edouard
L'Air Liquide Enginieres
38360 Sassenage, France
76 43 60 30

Robinson, George Y. Jr.
MIT Cryogenic Engineering Lab
Bldg 41-203 MIT
Cambridge, MA 01239
617-253-5209

Rose, Daniel J.
Ball Aerospace Systems Div.
P.O. Box 1062
Boulder, CO 80306-1062
303-939-4509

Rosenbaum, Ralph Lewis
Tel-Aviv University
Ramat-Avis, Israel 69978

Rosser, Robin W.
Hughes Aircraft Company
P.O. Box 902-EO/E1-F187
El Segundo, CA 90245
213-616-5873

Russo, Samuel C.
Hughes Aircraft Co.
El Segundo, CA
213-616-9651

Ryschkewitsch, Michael G.
NASA/GSFC Cryogenics Tech Sect
Greenbelt, MD 20771
301-286-8568

Sarwinski, Raymond E.
Cryogenic Designs, Inc.
4275 Rodeo Drive
San Diego, CA 92124
619-455-0913

Savage, Christopher J.
ESA/ESTEC
Keplerlaan 1
The Netherlands 2201 AZ
31 1719 8401

Schepler, Bernard
Clifton Precision
Instrument & Life Support Div
Davenport, IA 52808
800-553-1860

Seyfert, Peter
CEA/CEN Grenoble
85X 38041 Grenoble, France

Sherman, Neil I.
Hughes Aircraft Company
P.O. Box 902 E55/G232
El Segundo, CA 90245
213-616-9653

Shields, William R.
Janis Research Co., Inc.
2 Jewel Drive
Wilmington, MA 01887
617-657-8750

Shigeru, Yoshida
Toyo Sanso Co. Ltd
3-3 Mizue-cho Kawasaki-60
Kawasaki Kanagawa 210 Japan

Silver, Arnold H.
TRW
One Space Park-Bldg R1-2170
Redondo Beach, CA 90278
213-535-2500

Sixsmith, Dr. Herbert
Creare, Inc.
P.O. Box 71
Hanover, NH 03755
603-643-3800

Smith, Glen A.
AFSTC USAF
Kirtland AFB, Albuquerque NM 87123
505-846-4958

Smith, Joseph L. Jr,
MIT
73 Vassar St
Cambridge, MA 02139
617-253-2296

Sobel, Lawrence D.
Ricor Ltd
En Harod Ihud, Israel
065-3170

Soldner, Leonhard
8520 Erlangen
Bayeon, West German
09131 731811

Stetson, Norman B.
Inframetrics, Inc
12 Oak Park Drive
Bedford, MA 01730
617-275-4510

Stevens, John
DTNSRDC
Annapolis, MD 21402
301-267-3632

Steyert, William A.
Air Products & Chemicals, Inc.
1833 Vultee St. P.O. Box 2802
Allentown, PA 18105
215-481-3700

Stockwell, Grant
Garrett Corporation
9851 Sepulveda Blvd
Los Angeles, CA 90009
213-417-6505

Stoddard, Mary
Sandia National Laboratory
P.O. Box 969, Div. 8434
Livermore, CA 94550
415-422-2056

Stolfi, Fred. R.
Philips Laboratories
345 Scarborough Road
Briarcliff Manor, NY 10510
914-945-6334

Strasser, Dipl.-Ing Wilhelm
Postfach 510760
5000 Koln 51, Germany
0221-3471203

Straubs, V. George
Dowty Aerospace Corp.
P.O. Box 5000, Sully Road
Sterling, VA 22170
703-450-5930

Superczynski, Michael
DTNSRDC
Annapolis, MD 21402
301-267-2149

Suter, Joseph
Applied Physics Laboratory
Johns Hopkins Road
Laurel, MD 20707
301-953-5000

Sweet, Richard C.
Philips Laboratories
345 Scarborough Road
Briarcliff Manor, NY 10510
914-945-6114

Swift, Walter L.
Creare, Inc.
P.O. Box 71
Hanover, NH 03755
603-643-3800

Thompson, William
Aerojet Electrosystems Co.
1100 W. Hollyvale St. P.O. Box 296
Azusa, CA 91702
818-812-2267

Timmerhaus, Klaus D.
University of Colorado
Eng. Center 424
Boulder, CO 80309
303-492-7680

Twigg, William Paul
Westinghouse AESD
P.O. Box 746
Baltimore, MD 21203
301-765-3606

Tzemos, Costas
CVI Inc.
P.O. Box 2138
Columbus, OH 42316
614-876-7381

Vourgourakis, Emmanuel J.
Hughes Aircraft Co.-EDSG
P.O. Box 902, E54 M/S F204
El Segundo, CA 90245-0902
213-616-9646

Vukovojac, Marija
Butterworth Scientific
P.O. Box 63, Bury Street
Guildford Surrey GU 2 SBH UK
0483 31261

Wade, Lawrence A.
Aerojet Electro Systems Co.
1100 W. Hollyvale St. P.O. Box 296
Azusa, CA 91702

Walker, Graham
General Pneumatics Corp.
7662 E. Gray Road, Suite 107
Scottsdale, AZ 85260
602-998-1856

Weinstock, Harold
AFOSR/NE
Bolling Air Force Base
Washington, DC 20332-6448
202-767-4933

Weiz, Albert W.
15 Acorn Park
Cambridge, MA 02140
617-864-5770

Werrett, Stephen
Oxford University
Parks Road
Oxford, UK OXI 3PU

White, Ronard
AFWAL/FIEE
Wright-Patterson AFB, Ohio 45433
513-255-4853

Wiemken, Albert J.
Sandia National Laboratories
P.O. Box 969
Livermore, CA 94550
415-422-2353

Yetman, Albert A.
NASA/GSCF, Code 713
Greenbelt, MD 20771
301-286-5405

York, Gary M.
Hughes Aircraft Company
P.O. Box 902 E55/G232
El Segundo, CA 90245-0902

Zimmerman, James E.
National Bureau of Standards
M.S. 724.03, 325 Broadwa
Boulder, CO 80303

Zyistra, Steven G.
7662 E. Gray Road
Suite 107
Scottsdale, AZ 85260
602-998-1856